Supplementary Material to accompany:

Highlighting the Origins and Consequences of Thermodynamic Non-Idealities in Mixture Separations using Zeolites and Metal-Organic Frameworks

Rajamani Krishna[a],[*] Jasper M. van Baten[b] and Richard Baur[a,c]

[a] Van 't Hoff Institute for Molecular Sciences, University of Amsterdam, Science Park 904, 1098 XH Amsterdam, The Netherlands

[b] AmsterCHEM, Almería, Spain; E-mail: jasper@amsterchem.com

[c] Current affiliation: Shell Global Solutions International BV, Amsterdam, The Netherlands; E-mail: richard.baur@shell.com

Table of Contents

1. Preamble

This Supplementary material accompanying our manuscript *Highlighting the Origins and Consequences of Thermodynamic Non-Idealities in Mixture Separations using Zeolites and Metal-Organic Frameworks* provides:

(a) Detailed structural information on all of the zeolites, and MOFs analyzed and discussed in the article

(b) Details of the IAST, and RAST methodologies and calculations for mixture adsorption equilibria,

(c) Input data on unary isotherm fits for the wide variety of guest/host combinations examined in this article,

(d) Detailed comparisons of CBMC simulations of mixture adsorption equilibrium, with IAST and RAST calculations,

(e) Summary of the Maxwel-Stefan formulation for mixture diffusion in zeolites and MOFs

(f) Maxwell-Stefan modeling of mixture permeation across microporous membranes

(g) Modeling of transient uptake of mixtures within spherical crystalline particle

(h) Modeling of transient breakthroughs in fixed bed adsorbers.

For ease of reading, this Supplementary Material is written as a stand-alone document. As a consequence, there is some overlap of material with the main manuscript. Researchers who are interested in specific sections can use the Table of Contents to skip to that specific section, without the need to browse through the entire material that is presented here.

Video animations

The following set of ten video animations have been uploaded as e-components; these are created from MD simulations of self-diffusion of unary and binary mixtures in different host materials.

1. Video 1: Water diffusion in DDR zeolite, demonstrating molecular clustering
2. Video 2: Methanol diffusion in DDR zeolite, demonstrating molecular clustering
3. Video 3: Ethanol diffusion in DDR zeolite, demonstrating molecular clustering
4. Video 4: methanol diffusion in all-silica FER zeolite, demonstrating molecular clustering
5. Video 5: methanol/ethanol mixture diffusion in all-silica FER zeolite, demonstrating molecular clustering
6. Video 6: Methanol/ethanol mixture diffusion in CHA zeolite, demonstrating molecular clustering
7. Video 7: CH_4 (=labelled C1)/CO_2 mixture diffusion in all-silica LTA zeolite, demonstrating perching of CO_2 at the window regions. CO_2 hinders inter-cage hopping of CH_4.
8. Video 8: CH_4 (=labelled C1)/CO_2 mixture diffusion in all-silica ERI zeolite, demonstrating perching of CO_2 at the window regions. CO_2 hinders inter-cage hopping of CH_4.
9. Video 9: CH_4/CO_2 mixture diffusion in AFX zeolite, demonstrating perching of CO_2 at the window regions. CO_2 is also located in pockets, and these molecules are stagnant.
10. Video 10: N_2/CO_2 mixture diffusion in AFX zeolite, demonstrating perching of CO_2 at the window regions. CO_2 is also located in pockets, and these molecules are stagnant.

2. Structural topology and connectivity of some common zeolites, MOFs, and ZIFs

The crystallographic data are available on the zeolite atlas website of the International Zeolite Association (IZA).[1, 2] Further details on the structure, landscape, pore dimensions of a very wide variety of micro-porous materials are available in the published literature.[3-10]

The pore topology and structural details of the crystalline structures that are discussed and analyzed in this article are provided in Figures 1- 32; further details are provided by Krishna and van Baten.[11-13]

One-dimensional channels

The pore landscape and structural details of all-silica AFI are provided in Figure 1.

Cages separated by narrow windows

AFX zeolite consists of cages of volume 490 $Å^3$, separated by 3.4 Å × 3.9 Å windows; the cages are also connected to pockets of 98$Å^3$ by 3.1 Å × 4.62 Å windows; see Figures 2, and 3.

CHA zeolite consists of cages of volume 316 $Å^3$, separated by 3.8 Å × 4.2 Å 8-ring windows as shown in Figures 4, and 5. SAPO-34 has the same structural topology of CHA zeolite.

DDR consists of cages of 277.8 $Å^3$ volume, separated by 3.65 Å × 4.37 Å 8-ring windows; the pore landscapes and structural details are provided in Figures 6, and 7.

ERI consists of cages of 408.7 $Å^3$ volume, separated by 3.8 Å × 4.9 Å 8-ring windows; the pore landscapes and structural details are provided in Figures 8, and 9.

LTA, LTA-5A, and LTA-4A consist of cages of 743 $Å^3$ volume, separated by 4.11 Å × 4.47 Å 8-ring windows; the pore landscapes and structural details are provided in Figures 10, 11, 12, and 13.

Per unit cell, LTA-5 has 96 Si, 96 Al, 32 Na^+, 32 Ca^{++} with Si/Al=1.

Per unit cell LTA-4A has 96 Si, 96 Al, 96 Na^+, Si/Al=1.

ZIF-8 consists of cages of 1168 $Å^3$ volume, separated by 3.3 Å windows; the pore landscapes and structural details are provided in Figures 14, 15.

Intersecting channels

MFI zeolite (also called silicalite-1) has a topology consisting of a set of intersecting straight channels, and zig-zag (or sinusoidal) channels of 5.4 Å × 5.5 Å and 5.4 Å × 5.6 Å size. The pore landscapes and structural details are provided in Figures 16, and 17. The crystal framework density $\rho = 1796$ kg m^{-3}. The pore volume $V_p = 0.165$ cm^3/g.

FER zeolite has two sets of intersecting channels; see Figures 18, 19, 20.

1D channels with side pockets

MOR zeolite (Mordenite) consists of 12-ring (7.0 Å × 6.5 Å) 1D channels, connected to 8-ring (5.7 Å × 2.6 Å) pockets; the pore landscapes and structural details are provided in Figures 21, and 22.

Cages separated by large windows

FAU-Si (= all-silica FAU) (cages of 408.7 $Å^3$ volume, separated by 3.8 Å × 4.9 Å 8-ring windows; see Figures 23, 24.

There are two variants of NaY zeolite.

Figure 25 provides structural details of NaY zeolite with 144 Si, 48 Al, 48 Na^+, Si/Al=3. Figure 26 provides structural details of NaY zeolite with 138 Si, 54 Al, 54 Na^+, Si/Al=2.55.

Figure 27 shows the structural details of NaX (= 86 Na^+/uc = 13X) zeolite. Per unit cell of NaX zeolite we have 106 Si, 86 Al, 86 Na^+ with Si/Al=1.23. This material is also commonly referred to by its trade name: 13X zeolite.

CuBTC (= $Cu_3(BTC)_2$ with BTC = 1,3,5-benzenetricarboxylate, also known as HKUST-1) framework is composed of copper atoms connected by benzene-1,3,5-tricarboxylate (BTC) linkers, which form a characteristic paddle-wheel structure: two copper atoms bonded to the oxygen atoms of four BTC linkers, generating four-connected square-planar vertexes; see Figures 28, and 29. The framework contains two types of large cavities (9 Å diameter) and small cavities (of 5 Å diameter). The larger cavities (L_2 and L_3) are similar in size and shape but as a result of the paddle-wheel, the copper atoms are only accessible from the L_3 cages. L_2 and L_3 cavities are connected through triangular-shaped windows. The small cavities (T_1) are tetrahedral pockets enclosed by the benzene rings; these are connected to L_3 cages by small triangular windows (3.5 Å in size), as shown in Figure 30.

For IRMOF-1 (= MOF 5 = $Zn_4O(BDC)_3$ with BDC^{2-} = 1-4 benzenedicarboxylate), the structural data, and pore landscapes are provided in Figures **31**, and 32.

3. Summary of IAST calculation methodology

Within microporous crystalline materials, the guest molecules exist in the adsorbed phase. The Gibbs adsorption equation[14] in differential form is

$$Ad\pi = \sum_{i=1}^{n} q_i d\mu_i \qquad (1)$$

The quantity A on the left side of Equation (1) is the surface area per kg of framework, with units of m^2 per kg of the framework of the crystalline material; q_i is the molar loading of component i in the adsorbed phase with units moles per kg of framework; μ_i is the molar

chemical potential of component *i*. The spreading pressure π has the same units as surface tension, i.e. N m^{-1}.

The chemical potential of any component in the adsorbed phase, μ_i, equals that in the bulk fluid phase. If the partial fugacities in the bulk fluid phase are f_i, we have

$$d\mu_i = RTd \ln f_i \tag{2}$$

where R is the gas constant (= 8.314 J mol^{-1} K^{-1}).

Briefly, the basic equation of Ideal Adsorbed Solution Theory (IAST) of Myers and Prausnitz[15] is the analogue of Raoult's law for vapor-liquid equilibrium, i.e.

$$f_i = P_i^0 x_i; \quad i = 1,2,...n \tag{3}$$

where x_i is the mole fraction in the adsorbed phase

$$x_i = \frac{q_i}{q_1 + q_2 + ...q_n} \tag{4}$$

and P_i^0 is the pressure for sorption of every component *i*, which yields the same spreading pressure, π for each of the pure components, as that for the mixture:

$$\frac{\pi A}{RT} = \int_0^{P_1^0} \frac{q_1^0(f)}{f} df = \int_0^{P_2^0} \frac{q_2^0(f)}{f} df = \int_0^{P_3^0} \frac{q_3^0(f)}{f} df = ... \tag{5}$$

where $q_i^0(f)$ is the *pure* component adsorption isotherm. The molar loadings $q_i^0(f)$ are expressed in the units of moles adsorbed per kg of framework, i.e. mol kg^{-1}. The units of $\frac{\pi A}{RT}$, also called the adsorption potential,[16] are mol kg^{-1}. If the isotherm fits are expressed in terms of molecules per unit cell, then the units of $\frac{\pi A}{RT}$ are also in molecules per unit cell.

The unary isotherm may be described by say the 1-site Langmuir isotherm

$$q^0(f) = q_{sat}\frac{bf}{1+bf}; \quad \theta = \frac{bf}{1+bf} \tag{6}$$

where we define the fractional *occupancy* of the adsorbate molecules, $\theta = q^0(f)/q_{sat}$. The superscript 0 is used to emphasize that $q^0(f)$ relates the *pure component* loading to the bulk fluid fugacity. More generally, the unary isotherms may need to be described by the dual-Langmuir-Freundlich model

$$q^0(f) = q_{A,sat}\frac{b_A f^{\nu A}}{1+b_A f^{\nu A}} + q_{B,sat}\frac{b_B f^{\nu B}}{1+b_B f^{\nu B}} \tag{7}$$

or the 3-site Langmuir-Freundlich model:

$$q^0 = q_{A,sat}\frac{b_A f^{\nu_A}}{1+b_A f^{\nu_A}} + q_{B,sat}\frac{b_B f^{\nu_B}}{1+b_B f^{\nu_B}} + q_{c,sat}\frac{b_C f^{\nu_C}}{1+b_C f^{\nu_C}} \tag{8}$$

Each of the integrals in Equation (5) can be evaluated analytically. For the 3-site Langmuir-Freundlich isotherm, the integration yields for component *i*,

$$\begin{aligned}
\int_{f=0}^{P_i^0}\frac{q^0(f)}{f}df &= \frac{q_{A,sat}}{\nu_A}\ln\left(1+b_A\left(P_i^0\right)^{\nu_A}\right)+\frac{q_{B,sat}}{\nu_B}\ln\left(1+b_B\left(P_i^0\right)^{\nu_B}\right)+\frac{q_{c,sat}}{\nu_C}\ln\left(1+b_C\left(P_i^0\right)^{\nu_C}\right)\\
\int_{f=0}^{P_i^0}\frac{q^0(f)}{f}df &= \frac{q_{A,sat}}{\nu_A}\ln\left(1+b_A\left(\frac{f_i}{x_i}\right)^{\nu_A}\right)+\frac{q_{B,sat}}{\nu_B}\ln\left(1+b_B\left(\frac{f_i}{x_i}\right)^{\nu_B}\right)+\frac{q_{c,sat}}{\nu_C}\ln\left(1+b_C\left(\frac{f_i}{x_i}\right)^{\nu_C}\right)
\end{aligned} \tag{9}$$

The right hand side of equation (9) is a function of P_i^0. For multicomponent mixture adsorption, each of the equalities on the right hand side of Equation (5) must satisfied. For specified partial fugacities in the bulk fluid phase, f_i, these constraints may be solved using a suitable root-finder, to yield the set of values of the adsorbed phase mole fractions, x_i, and P_i^0, all of which must satisfy Equation (5). The corresponding values of the integrals using these as

upper limits of integration must yield the same value of $\frac{\pi A}{RT}$ for each component; this ensures that the obtained solution is the correct one.

A key assumption of the IAST is that the enthalpies and surface areas of the adsorbed molecules do not change upon mixing. If the total mixture loading is q_t, the area covered by the adsorbed mixture is $\frac{A}{q_t}$ with units of m^2 (mol mixture)$^{-1}$. Therefore, the assumption of no surface area change due to mixture adsorption translates as $\frac{A}{q_t} = \frac{Ax_1}{q_1^0\left(P_1^0\right)} + \frac{Ax_2}{q_2^0\left(P_2^0\right)} + \cdots \frac{Ax_n}{q_n^0\left(P_n^0\right)}$; the total mixture loading is q_t is calculated from

$$q_t \equiv q_1 + q_2 \ldots + q_n = \frac{1}{\frac{x_1}{q_1^0(P_1^0)} + \frac{x_2}{q_2^0(P_2^0)} + \ldots + \frac{x_n}{q_n^0(P_n^0)}} \tag{10}$$

in which $q_1^0(P_1^0)$, $q_2^0(P_2^0), \ldots$ $q_n^0(P_n^0)$ are determined from the unary isotherm fits, using the sorption pressures for each component P_1^0, P_2^0, $P_3^0, .. P_n^0$ that are available from the solutions to equations (9), and (10).

The set of equations (3), (4), (5), (7), (8), (9), and (10) need to be solved numerically to obtain the loadings, q_i of the individual components in the mixture.

4. Activity coefficients and the Real Adsorbed Solution Theory (RAST)

To account for non-ideality effects in mixture adsorption, we introduce activity coefficients γ_i into Equation (3)[15]

$$f_i = P_i^0 x_i \gamma_i \tag{11}$$

Following the approaches of Myers, Talu, and Sieperstein[16-18] we model the excess Gibbs free energy for binary mixture adsorption as follows

$$\frac{G^{excess}}{RT} = x_1 \ln(\gamma_1) + x_2 \ln(\gamma_2) \tag{12}$$

The Wilson model for activity coefficients are given for binary mixtures by

$$\begin{aligned}
\ln(\gamma_1) &= \left(1 - \ln(x_1\Lambda_{11} + x_2\Lambda_{12}) - \frac{x_1\Lambda_{11}}{x_1\Lambda_{11} + x_2\Lambda_{12}} - \frac{x_2\Lambda_{21}}{x_2 + x_1\Lambda_{21}}\right)\left(1 - \exp\left(-C\frac{\pi A}{RT}\right)\right) \\
\ln(\gamma_2) &= \left(1 - \ln(x_1\Lambda_{21} + x_2\Lambda_{22}) - \frac{x_1\Lambda_{12}}{x_1\Lambda_{11} + x_2\Lambda_{12}} - \frac{x_2\Lambda_{22}}{x_1\Lambda_{21} + x_2\Lambda_{22}}\right)\left(1 - \exp\left(-C\frac{\pi A}{RT}\right)\right)
\end{aligned} \tag{13}$$

In equation (13), $\Lambda_{11} \equiv 1;\ \ \Lambda_{22} \equiv 1$, and C is a constant with the units kg mol^{-1}. The introduction of $\left(1 - \exp\left(-C\frac{\pi A}{RT}\right)\right)$ imparts the correct limiting behaviors $\gamma_i \to 1;\ \ \frac{\pi A}{RT} \to 0$ for the activity coefficients in the Henry regime, $f_t \to 0;\ \ \frac{\pi A}{RT} \to 0$. As pore saturation conditions are approached, this correction factor tends to unity $\left(1 - \exp\left(-C\frac{\pi A}{RT}\right)\right) \to 1$.

The choice of $\Lambda_{12} = \Lambda_{21} = 1$ in Equation (13) yields unity values for the activity coefficients.

The excess reciprocal loading for the mixture can be defined as

$$\left(\frac{1}{q_t}\right)^{excess} = \frac{1}{q_t} - \left(\frac{x_1}{q_1^0(P_1^0)} + \frac{x_2}{q_2^0(P_2^0)}\right) \tag{14}$$

The excess reciprocal loading for the mixture can be related to the partial derivative of the Gibbs free energy with respect to the adsorption potential at constant composition

$$\left(\frac{1}{q_t}\right)^{excess} = \left.\frac{\partial\left(\frac{G^{excess}}{RT}\right)}{\partial\left(\frac{\pi A}{RT}\right)}\right|_{T,x} = \left[-x_1\ln(x_1+x_2\Lambda_{12}) - x_2\ln\left(x_2+x_1\Lambda_{21}\right)\right]C\exp\left(-C\frac{\pi A}{RT}\right) \qquad (15)$$

For calculation of the total mixture loading we need to replace Equation (10) by

$$q_t \equiv q_1 + q_2 = \frac{1}{\frac{x_1}{q_1^0(P_1^0)} + \frac{x_2}{q_2^0(P_2^0)} + \left[-x_1\ln(x_1+x_2\Lambda_{12}) - x_2\ln\left(x_2+x_1\Lambda_{21}\right)\right]C\exp\left(-C\frac{\pi A}{RT}\right)} \qquad (16)$$

The parameters Λ_{12}, Λ_{21}, and C can be fitted to match the experimental data on mixture adsorption or CBMC mixture simulations. The implementation of the activity coefficients is termed as the Real Adsorbed Solution Theory (RAST). For all the mixtures investigated in this article, the reported parameters Λ_{12}, Λ_{21}, and C are obtained by using the Excel solver to minimize the sum of deviations of each of the component loadings predicted by the RAST and the CBMC (or experimental) data.

A different approach to introduce the correction factor $\left(1-\exp\left(-C\frac{\pi A}{RT}\right)\right)$ into the Wilson equations has been adopted by Hefti et al.[19] for developing a RAST description of adsorption equilibrium for CO_2/N_2 mixtures in ZSM-5 and 13X zeolites for a variety of pressures ranging to 1 MPa. In their approach the Wilson coefficients Λ_{12}, and Λ_{21} are each corrected as follows

$$\Lambda_{ij} = \left(\Lambda_{ij}^0 - 1\right)\left(1-\exp\left(-C\frac{\pi A}{RT}\right)\right) + 1 \qquad (17)$$

Use of the modified Wilson parameters as defined in equation (17) ensures the correct limiting behaviors $\gamma_i \to 1$; $\frac{\pi A}{RT} \to 0$ for the activity coefficients.

The above set of equations for binary mixture adsorption may be generalized for *n*-component mixtures in a straightforward manner as follows

$$\frac{G^{excess}}{RT} = \sum_{i=1}^{n} x_i \ln(\gamma_i) \tag{18}$$

$$\ln(\gamma_i) = \left[1 - \ln\left(\sum_{j=1}^{n} x_j \Lambda_{ij} \right) - \sum_{k=1}^{n} \frac{x_k \Lambda_{ki}}{\sum_{j=1}^{n} x_j \Lambda_{kj}} \right] \left(1 - \exp\left(-C \frac{\pi A}{RT} \right) \right); \quad i = 1,2,..n \tag{19}$$

$$q_t \equiv \sum_{i=1}^{n} q_i = \frac{1}{\sum_{i=1}^{n} \frac{x_i}{q_i^0(P_i^0)} + \left. \frac{\partial\left(\frac{G^{excess}}{RT} \right)}{\partial\left(\frac{\pi A}{RT} \right)} \right|_{T,x}} \tag{20}$$

Equations (18), (19), and (20) are applied in this article to model adsorption of ternary mixtures in NaX zeolite.

5. The Maxwell-Stefan description of *n*-component mixture permeation across microporous membranes

The need for invoking RAST model for modeling water/alcohol pervaporation processes across zeolite membrane will be demonstrated in this article. For this purpose, we need to use an appropriate model to describe intra-crystalline diffusion within the membranes. Below, we summarize the model equations as presented in the Supplementary material of our recent publication on the Maxwell-Stefan diffusion equations.[20]

The Maxwell-Stefan (M-S) equations represent a balance between the force exerted per mole of species *i* with the drag, or friction, experienced with each of the partner species in the mixture. We may expect that the frictional drag to be proportional to differences in the velocities of the

diffusing species $\left(u_i - u_j\right)$, where u_i is the velocity of motion of the adsorbate. For a mixture containing a total of *n* penetrants, 1, 2, 3,..*n* we write

$$
\begin{aligned}
-\frac{d\mu_1}{dz} &= \frac{RT}{Đ_{12}} x_2\left(u_1 - u_2\right) + \frac{RT}{Đ_{13}} x_3\left(u_1 - u_3\right) + ... + \frac{RT}{Đ_1}\left(u_1\right) \\
-\frac{d\mu_2}{dz} &= \frac{RT}{Đ_{21}} x_1\left(u_2 - u_1\right) + \frac{RT}{Đ_{23}} x_3\left(u_2 - u_3\right) + ... + \frac{RT}{Đ_2}\left(u_2\right) \\
&\cdots\cdots \\
-\frac{d\mu_n}{dz} &= \frac{RT}{Đ_{n1}} x_1\left(u_n - u_1\right) + \frac{RT}{Đ_{n2}} x_2\left(u_n - u_3\right) + ... + \frac{RT}{Đ_n}\left(u_n\right)
\end{aligned}
\tag{21}
$$

The left members of equation (21) are the negative of the gradients of the chemical potentials, with the units N mol^{-1}; it represents the driving force acting per mole of species 1, 2, 3,..*n*.

For zeolite, MOF and ZIF membranes, it is convenient to use as composition measures the mole fractions of the components in the adsorbed phase, x_i, $x_i = q_i / q_t$ where q_i is the molar loading of adsorbate, and q_t is the *total* mixture loading $q_t = \sum_{i=1}^{n} q_i$.

The term $RT/Đ_{ij}$ is interpreted as the friction coefficient for the *i-j* pair of penetrants. The term $RT/Đ_i$ is interpreted as the drag or friction coefficient between the penetrant *i* and the pore wall.

An important, persuasive, argument for the use of the M-S formulation for mixture diffusion is that the M-S diffusivity $Đ_i$ in mixtures can be estimated using information on the loading dependence of the corresponding unary diffusivity values. Molecular Dynamics (MD) simulation data for "small" guest molecules such as H_2 and Ne in FAU, LTA, and CHA indicate that the M-S diffusivities, $Đ_i$, are practically loading independent. This scenario has been termed the "weak confinement" scenario by Krishna and Baur:[21]

$$Đ_i = Đ_i(0) \tag{22}$$

where $Đ_i(0)$ is the M-S diffusivity at "zero-loading". It must be emphasized that the use of the weak confinement scenario is a simplified, idealized, picture of reality.

Generally speaking, unary M-S diffusivities $Đ_i$ show strong dependence on the molar loadings. See the publications of Krishna and van Baten[6, 8] for the theoretical background to the variety of loading dependencies that are encountered. For certain guest/host combinations, the M-S diffusivities $Đ_i$ decrease with loadings, approaching near-zero values at pore saturation; the simplest model to describe this loading dependence is

$$Đ_i = Đ_i(0)\left(1-\theta_t\right) = Đ_i(0)\theta_V \tag{23}$$

where $\theta_V = \left(1-\theta_t\right)$ is the fractional vacancy. Equation (23) is essentially based on a simple hopping model in which a molecule can jump from one adsorption site to an adjacent one, provided it is not already occupied. The loading dependence portrayed in equation (23) has been termed the "strong confinement" scenario by Krishna and Baur.[21]

The M-S diffusivity $Đ_{ij}$ has the units $m^2\ s^{-1}$ and the physical significance of an *inverse* drag coefficient. The magnitudes of the M-S diffusivities $Đ_{ij}$ do not depend on the choice of the mixture reference velocity because equation (21) is set up in terms of velocity differences. At the molecular level, the $Đ_{ij}$ reflect how the facility for transport of species *i correlates* with that of species *j*; they are also termed *exchange coefficients*. For mesoporous materials with pores in the 20 Å to 100 Å size range the values of the exchange coefficient $Đ_{12}$ are the nearly the same as the binary *fluid phase* M-S diffusivity, $Đ_{12,fl}$, over the entire range of pore concentrations.[3, 5, 22, 23] For micro-porous materials, the exchange coefficient $Đ_{12}$ cannot be directly identified with the

corresponding fluid phase diffusivity $Đ_{12,fl}$ because the molecule-molecule interactions are also significantly influenced by molecule-wall interactions.

The Maxwell-Stefan diffusion formulation (21) is consistent with the theory of irreversible thermodynamics. The Onsager Reciprocal Relations imply that the M-S pair diffusivities are symmetric $Đ_{ij} = Đ_{ji}$. We define N_i as the number of moles of species *i* transported per m^2 of crystalline material per second

$$N_i \equiv \rho q_i u_i \tag{24}$$

where ρ is the framework density with units of kg m^{-3}. Multiplying both sides of equation (21) by ρq_i, the M-S equations for *n*-component diffusion in zeolites, MOFs, and ZIFs take the form[4, 23, 24]

$$-\rho \frac{q_i}{RT}\frac{d\mu_i}{dz} = \sum_{\substack{j=1 \\ j\neq i}}^{n} \frac{x_j N_i - x_i N_j}{Đ_{ij}} + \frac{N_i}{Đ_i}; \quad i = 1,2,..n \tag{25}$$

At thermodynamic equilibrium, the chemical potential of component *i* in the bulk gas mixture equals the chemical potential of that component in the adsorbed phase within the membrane at both upstream and downstream faces. For the bulk gas phase mixture we have

$$\frac{1}{RT}\frac{d\mu_i}{dz} = \frac{d\ln f_i}{dz} = \frac{1}{p_i}\frac{df_i}{dz}; \quad i = 1,2 \tag{26}$$

The chemical potential gradients $d\mu_i/dz$ can be related to the gradients of the molar loadings, q_i, by defining thermodynamic correction factors Γ_{ij}

$$\frac{q_i}{RT}\frac{d\mu_i}{dz} = \sum_{j=1}^{n} \Gamma_{ij}\frac{dq_j}{dz}; \quad \Gamma_{ij} = \frac{q_i}{f_i}\frac{\partial f_i}{\partial q_j}; \quad i, j = 1,....n \tag{27}$$

The thermodynamic correction factors Γ_{ij} can be calculated by numerical differentiation of the RAST model describing mixture adsorption equilibrium. In some special cases, the mixed-gas Langmuir model

$$\frac{q_i}{q_{i,sat}} = \theta_i = \frac{b_i f_i}{1 + \sum_{i=1}^{n} b_i f_i}; \quad i = 1,2,...n \tag{28}$$

may be of adequate accuracy. Analytic differentiation of equation (28) yields

$$\Gamma_{ij} = \delta_{ij} + \left(\frac{q_{i,sat}}{q_{j,sat}}\right)\left(\frac{\theta_i}{\theta_V}\right); \quad i, j = 1,2\ldots n \tag{29}$$

where the fractional vacancy θ_V is defined as $\theta_V = 1 - \theta_t = 1 - \sum_{i=1}^{n} \theta_i$.

The elements of the matrix of thermodynamic factors Γ_{ij} can be calculated explicitly from information on the component loadings q_i in the adsorbed phase; this is the persuasive advantage of the use of the mixed-gas Langmuir model. By contrast, the IAST and RAST does not allow the calculation of Γ_{ij} explicitly from knowledge on the component loadings q_i in the adsorbed phase; an numerical procedure is required.

Specifically for binary mixtures, the mixed-gas Langmuir model is

$$\theta_i = \frac{q_i}{q_{i,sat}} = \frac{b_i f_i}{1 + b_1 f_1 + b_2 f_2}; \quad i = 1,2 \tag{30}$$

and the four elements of the matrix of thermodynamic factors $\begin{bmatrix} \Gamma_{11} & \Gamma_{12} \\ \Gamma_{21} & \Gamma_{22} \end{bmatrix}$ are:[21]

$$\begin{bmatrix} \Gamma_{11} & \Gamma_{12} \\ \Gamma_{21} & \Gamma_{22} \end{bmatrix} = \frac{1}{1-\theta_1-\theta_2} \begin{bmatrix} 1-\theta_2 & \frac{q_{1,sat}}{q_{2,sat}}\theta_1 \\ \frac{q_{2,sat}}{q_{1,sat}}\theta_2 & 1-\theta_1 \end{bmatrix} \tag{31}$$

The persuasive advantage of equation (31) is that the matrix of thermodynamic correction factors can be determined explicitly from the component loadings, and occupancies, without the need for numerical differentiation.

For steady-state membrane permeation calculations, presented hereunder, we use equation (31) for calculation of the thermodynamic correction factors, by taking the saturation capacities of each component as the sum of the saturation capacities of the different adsorption sites, A, B, C in Equation (8), i.e. $q_{sat} = q_{A,sat} + q_{B,sat} + q_{c,sat}$.

6. The Maxwell-Stefan description of binary mixture permeation across zeolite membranes

For binary mixture diffusion inside zeolites, MOFs, and ZIFs, the Maxwell-Stefan equations (25) are written as

$$\begin{aligned} -\rho\frac{q_1}{RT}\frac{d\mu_1}{dz} &= \frac{x_2N_1 - x_1N_2}{Đ_{12}} + \frac{N_1}{Đ_1} \\ -\rho\frac{q_2}{RT}\frac{d\mu_2}{\partial z} &= \frac{x_1N_2 - x_2N_1}{Đ_{12}} + \frac{N_2}{Đ_2} \end{aligned} \tag{32}$$

The first members on the right hand side of Equation (32) are required to quantify slowing-down effects that characterize binary mixture diffusion.[3, 5, 7] There is no experimental technique for direct determination of the exchange coefficients $Đ_{12}$, that quantify molecule-molecule interactions.

Let us define the square matrix [B]

$$[B]=\begin{bmatrix} \frac{1}{Đ_1}+\frac{x_2}{Đ_{12}} & -\frac{x_1}{Đ_{12}} \\ -\frac{x_2}{Đ_{12}} & \frac{1}{Đ_2}+\frac{x_1}{Đ_{12}} \end{bmatrix} \tag{33}$$

Equation (32) can be re-cast into 2-dimensional matrix notation

$$-\rho\begin{pmatrix} \frac{q_1}{RT}\frac{d\mu_1}{dz} \\ \frac{q_2}{RT}\frac{d\mu_2}{dz} \end{pmatrix}=[B]\begin{pmatrix} N_1 \\ N_2 \end{pmatrix};\quad \begin{pmatrix} N_1 \\ N_2 \end{pmatrix}=-\rho[B]^{-1}\begin{pmatrix} \frac{q_1}{RT}\frac{d\mu_1}{dz} \\ \frac{q_2}{RT}\frac{d\mu_2}{dz} \end{pmatrix} \tag{34}$$

We define the square matrix $[\Lambda]\equiv[B]^{-1}$; The inverse of the square matrix $[B]$ can be obtained explicitly

$$[\Lambda]\equiv[B]^{-1}=\frac{1}{1+\frac{x_1Đ_2}{Đ_{12}}+\frac{x_2Đ_1}{Đ_{12}}}\begin{bmatrix} Đ_1\left(1+\frac{x_1Đ_2}{Đ_{12}}\right) & \frac{x_1Đ_1Đ_2}{Đ_{12}} \\ \frac{x_2Đ_1Đ_2}{Đ_{12}} & Đ_2\left(1+\frac{x_2Đ_1}{Đ_{12}}\right) \end{bmatrix} \tag{35}$$

Combining equations (32), (34), and (35) we obtain

$$\begin{pmatrix} N_1 \\ N_2 \end{pmatrix}=-\rho[\Lambda][\Gamma]\begin{pmatrix} \frac{dq_1}{dz} \\ \frac{dq_2}{dz} \end{pmatrix};$$
$$\begin{pmatrix} N_1 \\ N_2 \end{pmatrix}=-\frac{\rho}{1+\frac{x_1Đ_2}{Đ_{12}}+\frac{x_2Đ_1}{Đ_{12}}}\begin{bmatrix} Đ_1\left(1+\frac{x_1Đ_2}{Đ_{12}}\right) & \frac{x_1Đ_1Đ_2}{Đ_{12}} \\ \frac{x_2Đ_1Đ_2}{Đ_{12}} & Đ_2\left(1+\frac{x_2Đ_1}{Đ_{12}}\right) \end{bmatrix}\begin{bmatrix} \Gamma_{11} & \Gamma_{12} \\ \Gamma_{21} & \Gamma_{22} \end{bmatrix}\begin{pmatrix} \frac{dq_1}{dz} \\ \frac{dq_2}{dz} \end{pmatrix} \tag{36}$$

Extensive Molecular Dynamics (MD) simulations have shown that correlation effects are of negligible importance for mixture diffusion across materials such as LTA, ZIF-8, CHA, DDR, ERI that consist of cages separated by windows in the 3.4 Å – 4.2 Å size range.[3, 5, 7, 25] Molecules

jump one-at-a-time across the narrow windows, and the assumption of negligible correlations is justified.

In the limiting scenario in which correlations effects are of negligible importance:

$$\frac{Đ_i}{Đ_{ij}} \to 0; \quad \text{correlations negligible}$$

In cases in which correlations are negligible, Equation (36) simplifies to yield

$$N_i = -\rho\, Đ_i \frac{q_i}{RT}\frac{d\mu_i}{dz}; \quad i = 1,2$$

$$[\Lambda] \to \begin{bmatrix} Đ_1 & 0 \\ 0 & Đ_2 \end{bmatrix}; \quad \begin{pmatrix} N_1 \\ N_2 \end{pmatrix} = -\rho \begin{bmatrix} Đ_1 & 0 \\ 0 & Đ_2 \end{bmatrix} \begin{bmatrix} \Gamma_{11} & \Gamma_{12} \\ \Gamma_{21} & \Gamma_{22} \end{bmatrix} \begin{pmatrix} \frac{dq_1}{dz} \\ \frac{dq_2}{dz} \end{pmatrix} \tag{37}$$

7. Linearized solution for steady-state permeation across zeolite membranes

Figure 33 provides a schematic of binary mixture permeation of components 1, and 2 across a zeolite membrane of thickness, δ. We define a dimensionless distance coordinate along the membrane $\eta = \frac{z}{\delta}$. The first objective is to develop appropriate models to determine the steady-state permeation fluxes for the following set of boundary conditions

$$\text{upstream face}: \; z = 0; \quad f_i = f_{i0}; \quad q_i = q_{i0}; \quad \theta_i = \theta_{i0}; \quad \pi_i = \pi_{i0}; \quad \theta_V = \theta_{V0} \tag{38}$$

$$\text{downstream face}: \; z = \delta; \quad f_i = f_{i\delta}; \quad q_i = q_{i\delta}; \quad \theta_i = \theta_{i\delta}; \quad \pi_i = \pi_{i\delta}; \quad \theta_V = \theta_{V\delta} \tag{39}$$

Numerical solutions of the set of coupled ordinary differential equations (36) (ODEs) is required; shooting methods are required for the determination of the steady-state fluxes. An

alternative, practical, approach is to determine the two matrices $[\Lambda]$, and $[\Gamma]$ at the adsorbed phase loadings, mole fractions, and occupancies at the upstream face of the membrane.

In the linearized model, the fluxes are given by

$$\begin{pmatrix} N_1 \\ N_2 \end{pmatrix} = \frac{\rho}{\delta}[\Lambda][\Gamma]\begin{pmatrix} q_{10} - q_{1\delta} \\ q_{20} - q_{2\delta} \end{pmatrix} \tag{40}$$

The linearized model essentially assumes that the component loading profiles within the membrane layer are linear. The accuracy of the linearized model for calculation of the steady-state membrane permeation fluxes has been established in our earlier work.[20]

8. Simulation methodology for transient uptake inside microporous crystalline particles

The radial distribution of molar loadings, q_i, within a spherical crystallite, of radius r_c, is obtained from a solution of a set of differential equations describing the uptake

$$\rho\frac{\partial q_i(r,t)}{\partial t} = -\frac{1}{r^2}\frac{\partial}{\partial r}\left(r^2 N_i\right) \tag{41}$$

The fluxes N_i, in turn, are related to the radial gradients in the molar loadings by Equation (36), or the simplified equation (37), as appropriate for the material. At time t = 0, i.e. the initial conditions, the molar loadings $q_i(r,0)$ at all locations r within the crystal are uniform (zero loadings). For all times $t \geq$ 0, the exterior of the crystal is brought into contact with a bulk gas mixture at partial pressures $p_i(r_c,t)$ that is maintained constant till the crystal reaches thermodynamic equilibrium with the surrounding gas mixture.

$$t \geq 0; \quad q_i(r_c,t) \text{ in equilibrium with the initial values } p_i(r_c,t) \tag{42}$$

At any time t, during the transient approach to thermodynamic equilibrium, the spatial-averaged component loading within the crystallites of radius r_c is calculated using

$$\bar{q}_i(t) = \frac{3}{r_c^3}\int_0^{r_c} q_i(r,t) r^2 dr \qquad (43)$$

The spatial-averaged $\bar{q}_i(t)$ can be compared directly with experimental transient uptake data.

There is no generally applicable analytical solution to describe transient diffusion of binary mixtures and the set of Equations (36), (41), (42), and (43) need to be solved numerically using robust computational techniques. Equations (41) are first subjected to finite volume discretization. One of two strategies can be adopted: (a) equi-volume discretization, or (b) equi-distant discretization; see Figure 34. The choice of the discretization scheme used is crucially important in obtaining accurate, converged results. The choice of equi-volume slices is needed when the gradients of the loadings are particularly steep nearer to $r = r_c$. For either strategy, about 100 – 400 slices are required, depending on the guest/host combination. Combination of the discretized partial differential equations (41) along with algebraic equations describing mixture adsorption equilibrium, results in a set of differential-algebraic equations (DAEs), which are solved using BESIRK.[26] BESIRK is a sparse matrix solver, based on the semi-implicit Runge-Kutta method originally developed by Michelsen,[27] and extended with the Bulirsch-Stoer extrapolation method.[28] Use of BESIRK improves the numerical solution efficiency in solving the set of DAEs. The evaluation of the sparse Jacobian required in the numerical algorithm is largely based on analytic expressions.[21] Further details of the numerical procedures used in this work, are provided by Krishna and co-workers;[21, 29-31] interested readers are referred to our website that contains the numerical details.[29]

9. Simulation methodology for transient breakthrough in fixed bed adsorbers

Fixed beds, packed with crystals of microporous materials, are commonly used for separation of mixtures (see schematic in Figure 34); such adsorbers are commonly operated in a transient mode, and the compositions of the gas phase, and component loadings within the crystals, vary with position and time. During the initial stages of the transience, the pores are loaded up gradually, and only towards the end of the adsorption cycle are conditions corresponding to pore saturation attained. Put another way, separations in fixed bed adsorbers are influenced by both the Henry regime of adsorption as well as the conditions corresponding to pore saturation. For a given separation task, transient breakthroughs provide more a realistic evaluation of the efficacy of a material, as they reflect the combined influence of adsorption selectivity, and adsorption capacity.[4, 32]

We describe below the simulation methodology used to perform transient breakthrough calculations that are presented in this work. This simulation methodology is the same as that used in our previous published works.[4, 32-34]

Assuming plug flow of an *n*-component gas mixture through a fixed bed maintained under isothermal, isobaric, conditions, the molar concentrations in the gas phase at any position and instant of time are obtained by solving the following set of partial differential equations for each of the species *i* in the gas mixture.[21]

$$\frac{\partial c_i(t,z)}{\partial t}+\frac{\partial\left(v(t,z)c_i(t,z)\right)}{\partial z}+\frac{\left(1-\varepsilon\right)}{\varepsilon}\rho\frac{\partial \bar{q}_i(t,z)}{\partial t}=0;\quad i=1,2,...n \tag{44}$$

In equation (44), t is the time, z is the distance along the adsorber, ρ is the framework density, ε is the bed voidage, v is the interstitial gas velocity, and $\bar{q}_i(t,z)$ is the *spatially averaged* molar

loading within the crystallites of radius r_c, monitored at position z, and at time t. The time $t = 0$, corresponds to the time at which the feed mixture is injected at the inlet to the fixed bed. Prior to injection of the feed, it is assumed that an inert, non-adsorbing, gas flows through the fixed bed.

At any time t, during the transient approach to thermodynamic equilibrium, the spatially averaged molar loading within the crystallite r_c is obtained by integration of the radial loading profile

$$\bar{q}_i(t) = \frac{3}{r_c^3}\int_0^{r_c} q_i(r,t) r^2 dr \tag{45}$$

For transient unary uptake within a crystal at any position and time with the fixed bed, the radial distribution of molar loadings, q_i, within a spherical crystallite, of radius r_c, is obtained from a solution of a set of differential equations describing the uptake

$$\frac{\partial q_i(r,t)}{\partial t} = -\frac{1}{\rho}\frac{1}{r^2}\frac{\partial}{\partial r}\left(r^2 N_i\right) \tag{46}$$

The molar flux N_i of component i may be described by the appropriate formulations of Maxwell-Stefan equations, discussed in the foregoing sections.

Summing equation (**45**) over all n species in the mixture allows calculation of the *total average* molar loading of the mixture within the crystallite

$$\bar{q}_t(t,z) = \sum_{i=1}^{n} \bar{q}_i(t,z) \tag{47}$$

The *interstitial* gas velocity is related to the *superficial* gas velocity by

$$v = \frac{u}{\varepsilon} \tag{48}$$

The adsorber bed is assumed to be initially free of adsorbates, i.e. we have the initial condition

$$t = 0; \quad q_i(0,z) = 0 \tag{49}$$

Equation (49) is relevant to the operation of the transient breakthrough experiments on a laboratory scale, but are not truly reflective of industrial operations.

At time, $t = 0$, the inlet to the adsorber, $z = 0$, is subjected to a step input of the n-component gas mixture and this step input is maintained till the end of the adsorption cycle when steady-state conditions are reached.

$$t \geq 0; \quad p_i(0,t) = p_{i0}; \quad u(0,t) = u_0 \tag{50}$$

where $u_0 = v_0\varepsilon$ is the superficial gas velocity at the inlet to the adsorber.

If the value of $\frac{Đ_i}{r_c^2}$ is large enough to ensure that intra-crystalline gradients are absent and the entire crystallite particle can be considered to be in thermodynamic equilibrium with the surrounding bulk gas phase at that time t, and position z of the adsorber

$$\bar{q}_i(t,z) = q_i(t,z) \tag{51}$$

The molar loadings at the *outer surface* of the crystallites, i.e. at $r = r_c$, are calculated on the basis of adsorption equilibrium with the bulk gas phase partial pressures p_i at that position z and time t. The adsorption equilibrium can be calculated on the basis of the IAST or RAST descriptions of mixture adsorption equilibrium, as appropriate.

For convenience, the set of equations describing the fixed bed adsorber are summarized in Figure 35. Typically, the adsorber length is divided into 100 – 200 slices. Combination of the discretized partial differential equations (PDEs) along with the algebraic IAST or RAST equilibrium model, results in a set of differential-algebraic equations (DAEs), which are solved using BESIRK.[26] BESIRK is a sparse matrix solver, based on the semi-implicit Runge-Kutta

method originally developed by Michelsen,[27] and extended with the Bulirsch-Stoer extrapolation method.[28] Use of BESIRK improves the numerical solution efficiency in solving the set of DAEs. The evaluation of the sparse Jacobian required in the numerical algorithm is largely based on analytic expressions.[21] Further details of the numerical procedures used in this work, are provided by Krishna and co-workers;[21, 29-31] interested readers are referred to our website that contains the numerical details.[29]

For presenting the breakthrough simulation results, we use the dimensionless time, $\tau = \frac{tu}{L\varepsilon}$, obtained by dividing the actual time, t, by the characteristic time, $\frac{L\varepsilon}{u}$, where L is the length of adsorber, u is the superficial fluid velocity, ε is the bed voidage.[35]

For all the simulations reported in this article we choose the following: adsorber length, L = 0.3 m; cross-sectional area, A = 1 m^2; superficial gas velocity entering the bed, u_0 = 0.04 m s^{-1}; voidage of the packed bed, ε = 0.4. Also, the total pressures is assumed to be constant along the length of the fixed bed. Please note that since the superficial gas velocity is specified, the specification of the cross-sectional area of the tube, A, is not relevant in the simulation results presented. The total volume of the bed is $V_{bed} = LA$. The volume of MOF used in the simulations is $V_{ads} = LA(1-\varepsilon)$ = 0.18 m^3. If ρ is the framework density, the mass of the adsorbent in the bed is $m_{ads} = \rho LA(1-\varepsilon)$ kg. It is important to note that the volume of adsorbent, V_{ads}, includes the pore volume of the adsorbent material. In these breakthrough simulations we use the same volume of adsorbent in the breakthrough apparatus, i.e. (1 - ε) A L = 0.18 m^3 = 180 L.

In all of the transient breakthrough simulations in fixed bed adsorbers reported in this work, the value of $\frac{Đ_i}{r_c^2}$ is chosen to be large enough to ensure that intra-crystalline gradients are absent and the entire crystallite particle can be considered to be in thermodynamic equilibrium.

10. Hydrogen bonding and molecular clustering

In recent years there have been several molecular simulation and experimental studies on unary and mixture adsorption characteristics of polar compounds such as water, methanol, and ethanol in a variety of microporous materials; on the basis of these studies there is clear evidence of clustering of the polar guest molecules caused due to hydrogen bonding.[8, 36-43] To demonstrate that the cause of molecular clustering is the hydrogen bonding between molecular pairs, we examine the radial distribution functions (RDFs) for distances between all combinations of O and H atoms of molecule pairs. Figure 36 presents the data of Krishna and van Baten[36] for RDF of O···H ("hydrogen bonds") bond distances of water-water, methanol-methanol, and ethanol-ethanol pairs during for unary adsorption of (a) water, (b) methanol, and (c) ethanol at 300 K in ZIF-8, LTA, FAU, DDR, and MFI. In all cases we note the first peaks in the RDFs occur at a distance less than 2 Å, that is characteristic of hydrogen bonding.[44]

For adsorption of water/methanol mixtures, Figure 37 presents the RDFs for O···H ("hydrogen bonds") of water-water, methanol-methanol, and water-methanol pairs for (a) DDR, (b) LTA (all-silica), (c) FAU (all-silica), and (d) MFI zeolites. The first peak of the RDF manifests at distances smaller than 2 Å for all three molecular pairs in the four zeolites. Furthermore, we note that the first peak value is significantly higher for the water-methanol pair, indicating that clustering between water-methanol pairs is the strongest.

For adsorption of water/ethanol mixtures, Figure 38 presents the RDFs for O···H bonding of water-water, ethanol-ethanol, and water-ethanol pairs for (a) DDR, and (b) FAU (all-silica) zeolites. The first peak of the RDF manifests at distances smaller than 2 Å for all three molecular pairs in the two zeolites. Furthermore, we note that the first peak value is significantly higher for the water-ethanol pair, indicating that clustering between water-ethanol pairs is the strongest.

For adsorption of methanol/ethanol mixtures in FER zeolite, Figure 39 presents data on RDFs for three different component loadings (a) Θ_1= 0.5/uc, Θ_2= 4/uc, (b) Θ_1= 1/uc, Θ_2= 4/uc, (c) Θ_1= 2/uc, Θ_2= 2/uc. The O···H distances for methanol-methanol, ethanol-ethanol, and methanol-ethanol are compared. For all three molecular pairs, the first peaks manifest at distances smaller than 2 Å indicating H-bonding for all three pairs. The H-bonding of the methanol-methanol pair is strongest as the peak height is the highest. Figure 39d presents a comparison of the O-H distances for methanol-ethanol pairs for FER (Θ_1= 2/uc, Θ_2= 2/uc) with the corresponding binary liquid phase mixture, i.e. without restraining walls. The data show that the H-bonding for the methanol-ethanol pairs occurs both in liquid mixtures and within the adsorbed phase.

For adsorption of mixtures of polar molecules in CuBTC, Gutierrez-Sevillano et al;[41, 42] determined the radial distribution functions (RDFs) for distances between all combinations of O and H atoms of molecule pairs. Figure 40, panels a, b, c, and d, presents a comparison of the RDFs for $H_{benzene}$-$O_{molecule}$ and $H_{molecule}$-$O_{molecule}$ distances for water/benzene, methanol/benzene, ethanol/benzene, and water/methanol/ethanol/benzene mixtures in CuBTC at 298 K and total fluid fugacity of 1000 Pa. We note that the RDFs for H_{water}-O_{water}, $H_{methanol}$-$O_{methanol}$, and $H_{ethanol}$-$O_{ethanol}$ pairs each exhibit a first peak at an intermolecular distance of 2 Å, that is characteristic of

hydrogen bonding.[36, 44] The results presented in Figure 40d show that H-bonding between alcohol/alcohol pairs are stronger than the bonding between water/water pairs.

Remarkably, the corresponding values for $H_{benzene}$-O_{water}, $H_{benzene}$-$O_{methanol}$, and $H_{benzene}$-$O_{ethanol}$ do not display any peaks in the RDFs. This would indicate that guest molecules do not form clusters with benzene molecules, and clustering effects are restricted to water/water, methanol/methanol, and ethanol/ethanol pairs.

11. Influence of hydrogen bonding and molecular clustering on unary isotherms

Due to cluster formation, the unary isotherms of water, alcohols, acetone, benzene displays step-like characteristics.[45-51] As illustration, Figures 41a,b,c,d present data obtained from CBMC simulations[12, 36] for unary isotherms of water, methanol, and ethanol in (a) FAU, (b) MFI, (c) DDR, (d) CHA, and (e) ZIF-8. Figure 41f presents CBMC simulated isotherms[46, 47] for water, methanol, ethanol, acetone, and benzene in CuBTC at 298 K. These isotherms are not amenable to fitting by the simple Langmuir model; the continuous solid lines are the dual-site or 3-site Langmuir-Freundlich model fits, using equation (7), or (8); these fits are shown by the continuous solid lines. Particularly noteworthy are the differences in the saturation capacities, $q_{sat} = q_{A,sat} + q_{B,sat} + q_{C,sat}$, of the various guest molecules. For CuBTC, for example, water = 54 mol kg^{-1}; methanol = 19.9 mol kg^{-1}; ethanol = 13 mol kg^{-1}; acetone = 9.9 mol kg^{-1}; benzene = 6.7 mol kg^{-1}.

Besides the RDF data on O-H distances, another way of underscoring the manifestation of molecular clustering is by examining the unary isotherms and calculating the inverse thermodynamic factor, $1/\Gamma_i$, defined by

$$\frac{1}{\Gamma_i} \equiv \frac{\partial \ln q_i}{\partial \ln f_i} = \frac{f_i}{q_i}\frac{\partial q_i}{\partial f_i} \tag{52}$$

that can determined by analytic differentiation of equation (7), or (8).

Figures 42, and 43 present the calculations of $1/\Gamma_i$ for adsorption of water, and alcohols in FAU, MFI, DDR, ZIF-8 and CuBTC. The values of $1/\Gamma_i$ exceeds unity for a range of molar loadings, q_i; this is indicated by the shaded regions.

In order to fully appreciate the import of $1/\Gamma_i > 1$, it is best to first discuss the simple case for which the adsorbed phase loading follows a single-site Langmuir isotherm $q_i = q_{i,sat}\frac{b_i f_i}{1+b_i f_i}$, whose differentiation yields

$$\frac{1}{\Gamma_i} = 1 - \theta_i \tag{53}$$

where we define the fractional *occupancies* $\theta_i \equiv q_i / q_{i,sat}$. Equation (53) shows that inverse thermodynamic factor, $1/\Gamma_i$, equals the fractional *vacancy* $\theta_V = (1-\theta_i)$ for a Langmuirian adsorbed phase, and in this case we must have $1/\Gamma_i \le 1$. When there is no molecular clustering, increasing the loading, q_i, by increasing the bulk fluid phase fugacity, leads to *linear decrease* in the number of vacant sites. For the data presented in Figures 42, and 43 there is an *increase* in the number of vacant sites with for a range of loadings, q_i; this deserves further explanation. We present below the arguments as put forward by Krishna and van Baten;[40] the explanation is based on a simple lattice model for unary adsorption. Consider a square lattice containing 64 adsorption sites; see Figure 44a. If the molecular species, 10 in total, are all unclustered the fractional occupancy is $\theta_i = 10/64$, and the fractional vacancy $\theta_V = 1-\theta_i = 54/64$. A molecular cluster can be regarded as a *k*-mer. A *k*-mer occupies the same vacant adsorbed site as a normal,

unclustered, molecule. As a consequence, it is feasible to have the fractional vacancy exceed unity, i.e. $1/\Gamma_i > 1$. If clustering occurs and dimers are formed, the same number of molecules will occupy only 5 sites; see Figure 44b. The remaining number of vacant locations, 59, are still available for occupation. Even if no more clusters are formed, this would imply that a total of 10 + 59 = 69 molecules could be accommodated on the square lattice. Cluster formation has the effect of increasing the fractional vacancy θ_V to the value of 69/64. Therefore, it is possible to have $1/\Gamma_i > 1$ when clustering occurs. Equivalently, the occurrence of $1/\Gamma_i > 1$ can be taken to imply the existence of molecular clusters.

Experimental confirmation of clustering effects is provided by the experimental data of Tsotsalas et al.[52] for adsorption of methanol in CuBTC.

12. Non-ideality effects for mixture adsorption in CuBTC

The CBMC simulations for adsorption of various mixtures in CuBTC are published by Gutierrez-Sevillano et al;[41, 42] their data are re-analyzed to quantify non-ideality effects in mixture adsorption.

Figure 45 presents the results for CBMC simulations of the component loadings for adsorption of equimolar (a) water/methanol, (b) water/ethanol, (c) water/1-propanol, (d) water/methanol/ethanol/1-propanol, and (e) methanol/ethanol mixtures in CuBTC at 298 K. In all cases, we note a reversal in the hierarchy of component loadings as conditions approach pore saturation. In all five cases, we note that at conditions close to pore saturation, the adsorption is in favor of the component with the higher saturation capacity. For aqueous mixtures, the selectivity is in favor of water at conditions close to 100 kPa. For methanol/ethanol mixtures, the adsorption is in favor of the shorter alcohol, i.e. methanol, as pore saturation is approached.

Figure 46, panels a, b, c, d, and e, present the results for CBMC simulations of the component loadings for adsorption of equimolar water/benzene, methanol/benzene, ethanol/benzene, methanol/ethanol, and acetone/benzene mixtures in CuBTC at 298 K. In all cases, we note a reversal in the hierarchy of component loadings as conditions approach pore saturation. In all cases, we note that at conditions close to pore saturation, the adsorption is in favor of the component with the higher saturation capacity. For water/benzene mixtures, the selectivity is in favor of water at fugacities $f_t > 10$ kPa. For methanol/benzene and ethanol/benzene mixtures, the selectivity is in favor of the alcohol as pore saturation conditions are approached. For methanol/ethanol mixtures, the adsorption is in favor of the shorter alcohol as pore saturation is approached. For acetone/benzene mixtures, the selectivity is in favor of acetone as pore saturation conditions are approached. From the data in Figure 46 we conclude that CuBTC has the potential of separation of separating binary mixtures of benzene with water, methanol, ethanol, and acetone. For operation at pore saturation the selectivity is in favor of the smaller partner molecule in the mixture.

Figure 47 compares the IAST calculations with CBMC simulations of component loadings of equimolar (a) water/methanol, (b) water/ethanol, (c) water/1-propanol, (d) water/methanol/ethanol/1-propanol, and (e) methanol/ethanol mixtures. Though entropy effects are qualitatively captured by the IAST calculations, the quantitative agreement between the CBMC mixtures simulations and IAST is rather poor in all cases.

Figure 48 compare the IAST calculations with CBMC simulations of component loadings of equimolar (a) water/benzene, (b) methanol/benzene, (c) ethanol/benzene, (d) methanol/ethanol, (e) acetone/benzene, and (f) water/methanol/ethanol/benzene mixtures in CuBTC at 298 K. In all cases, the IAST correctly anticipates that the adsorption is favorable to the component with the

higher saturation capacity as saturation conditions are approached. However, the quantitative agreement between the CBMC mixtures simulations and IAST is generally poor. The reasons for the deviations are most likely attributed to the influence of molecular clustering engendered by hydrogen bonding effects, as explained in detail in our earlier work.[36]

It is clear from the results presented in Figure 47, and Figure 48 that the assumption of an *ideal* adsorbed phase is not of adequate accuracy.

The departures of IAST estimates from CBMC mixtures simulations depend both on the composition of the adsorbed phase and the adsorption potential, $\frac{\pi A}{RT}$. This is verified for the six mixtures: methanol/ethanol, methanol/benzene, ethanol/benzene, acetone/benzene, water/methanol, and water/ethanol mixtures in CuBTC at 298 K by the plots in Figures 49a,b. In all cases, the departures of IAST from CBMC simulations tend to vanish as $\frac{\pi A}{RT} \to 0$; this stresses the importance of introducing the $\left(1-\exp\left(-C\frac{\pi A}{RT}\right)\right)$ into the Wilson equations for activity coefficients.

Figures 50a,b,c,d compare the IAST and RAST calculations with CBMC simulations of component loadings of (a) methanol/ethanol, (b) methanol/benzene, (c) ethanol/benzene, and (d) acetone/benzene mixtures. In the RAST calculations, the Wilson parameters, along with the parameter *C* were fitted to match the CBMC simulation data; the values of the fitted parameters are provided in Table 3. We see that the RAST calculations offer significant improvement over the corresponding IAST calculations. The corresponding RAST calculations of the activity coefficients are shown in Figures 51a,b,c,d.

The influence of thermodynamic non-idealities on mixture separations can be quantified by comparing the IAST and RAST calculations of the adsorption selectivities. For separation of a binary mixture of A (more strongly adsorbed) and B (more poorly adsorbed), the adsorption selectivity is defined by

$$S_{ads} = \frac{q_A / q_B}{y_A / y_B} \tag{54}$$

where the q_A, and q_B represent the molar loadings within the zeolite or MOF that is in equilibrium with a bulk fluid mixture with mole fractions y_A, and $y_B = 1 - y_A$. The molar loadings, also called *gravimetric uptake capacities*, are usually expressed with the units mol kg^{-1}. The *volumetric uptake capacities* are

$$Q_A = \rho q_A; \quad Q_B = \rho q_B \tag{55}$$

where ρ is the crystal framework density of the zeolite or MOF, expressed say in units of kg m^{-3}, or kg L^{-1}. For CuBTC, the crystal framework density $\rho = 879$ kg m^{-3}.

Figures 52a,b,c,d present comparisons of CBMC simulations with IAST and RAST calculations of the adsorption selectivities for methanol/ethanol, methanol/benzene, ethanol/benzene, and acetone/benzene mixtures in CuBTC. In all four cases, the IAST predictions become increasing poorer as the bulk fluid phase fugacity, $f_t = f_1 + f_2$, increases.

13. Separation of binary mixtures in fixed bed adsorber packed with CuBTC adsorbent

We now investigate the influences of thermodynamic non-idealities on the separation of methanol/ethanol, methanol/benzene, ethanol/benzene, and acetone/benzene mixtures in fixed bed adsorbers packed with CuBTC crystals. For a binary mixture of A (more strongly adsorbed) and B (more poorly adsorbed), the more poorly adsorbed component B can be recovered in

nearly pure state during a finite interval during the transient breakthrough of the mixtures exiting the bed. The maximum productivity of pure B is realized if the following set of conditions are satisfied: (a) plug flow of the fluid mixture, i.e. negligible axial dispersion, (b) negligible intra-crystalline diffusion resistance, (c) negligible resistance to mass transfer from bulk fluid mixture to the surface of the crystals, and the concentrations "fronts" of the fluid mixture traverse the fixed bed in the form of shock waves.[33, 53] The maximum achievable productivity, ΔQ, can be calculated using the shock-wave model; the result is

$$\Delta Q = \left(Q_A \frac{y_B}{1 - y_B} - Q_B \right) \tag{56}$$

The physical significance of ΔQ, conveniently expressed in the units of mol per L of adsorbent, is that it represents the *maximum* amount of pure component B (= the more poorly adsorbed component) that can be recovered during the *adsorption* phase of fixed bed separations. The quantity ΔQ is an appropriate combination of selectivity and uptake capacity that is reflective of the *separation potential* of separations in fixed beds packed with a specific adsorbent.[33]

Figures 53a,b,c,d presents calculations of the separation potential, ΔQ, for methanol(A)/ethanol(B), methanol(A)/benzene(B), ethanol(A)/benzene(B), and acetone(A)/benzene(B) mixtures in fixed beds packed with CuBTC crystals and operating at 298 K, for varying total fluid phase fugacities, $f_t = f_1 + f_2$, Due to entropy effects, for operations at high values of the bulk fluid fugacities, the component that is produced in pure form is the component with the lower saturation capacity: (a) ethanol, (b) benzene, (c) benzene, and (d) benzene. The corresponding productivities are significantly lowered due to thermodynamic non-idealities. For example, the separations of ethanol/benzene mixtures at 100 kPa, the productivity

of pure benzene that is “rejected” due to entropy effects is reduced by about 100% due to thermodynamic non-idealities. Put another way, neglect of thermodynamic non-idealities tend to over-estimate the consequence of entropy effects that favor the component with the higher saturation capacities. Another important point to note is that for all four mixtures, the bulk fluid fugacity, $f_t = f_1 + f_2$, at which selectivity reversal occurs is also influenced by thermodynamic non-idealities.

In order to underscore the conclusions drawn on the basis of the shock wave model , Figure 54 presents transient breakthrough simulations of 50/50 methanol/ethanol feed mixtures in fixed bed adsorbed packed with CuBTC at 298 K, operating at total fluid mixture fugacities: (a) $f_t = 2$ kPa, (b) $f_t = 4$ kPa, (c) $f_t = 8$ kPa, and (d) $f_t = 30$ kPa.

For operation at $f_t = 2$ kPa, both IAST and RAST anticipate that the more strongly adsorbed component is the longer chain alcohol, and the shorter chain alcohol is rejected. This separation is “normal”, and dictated by the stronger binding of the longer chain alcohol.

For operations at $f_t = 8$ kPa, and $f_t = 30$ kPa, entropy effects cause the shorter chain alcohol to be preferentially adsorbed and the longer chain ethanol is “rejected”. In view of the larger differences in the breakthrough times of ethanol and methanol, the IAST predicts that the production of pure ethanol is larger, in agreement with the shock wave model calculations shown in Figure 53a.

For operations at $f_t = 4$ kPa, the differences in the breakthroughs with IAST and RAST are particularly striking. The IAST anticipates that methanol is the component that is preferentially adsorbed, but the RAST predicts the selective adsorption of ethanol.

14. Non-ideality effects for adsorption of methanol/n-hexane mixtures in CuBTC

Figure 55a presents the unary isotherm data of van Assche et al.[54] for adsorption of methanol, and n-hexane at 313 K in CuBTC, along with the dual-site Langmuir-Freundlich fits. The experimental data of van Assche et al.[54] for component loadings for methanol/n-hexane mixture adsorption in CuBTC as a function of the total pressure, p_t are compared in Figure 55b with IAST estimates of component loadings. Figure 55c compares the experimental data on the methanol/n-hexane adsorption selectivity, as a function of the total pressure, p_t, with IAST and RAST calculations. It is interesting to note that the IAST calculations anticipate a selectivity reversal at p_t = 200 Pa; the selectivity is in favor of n-hexane for p_t < 100 Pa. However, the IAST estimates of the methanol/n-hexane adsorption selectivities are about about an order of magnitude higher than the values determined experimentally. The strong deviations of the IAST estimates from the experimental data are most likely due to hydrogen bonding between the adsorbed methanol molecules. Use of the RAST and introduction of activity coefficients (cf. Figure 55d) are necessary to obtain good description of mixture adsorption.

15. Non-ideality effects for adsorption of methanol/n-hexane mixtures in MSC-5A (Takeda)

One of the early experimental investigations demonstrating inadequacies of the IAST for description of mixture adsorption equilibria is by Konno et al.[55] who investigated adsorption of mixtures containing one or more polar compounds: methanol, acetone, benzene, and n-hexane (nC6) in three different adsorbents: 13 X zeolite, Takeda Molecular Sieve Carbon MSC-5A, and activated carbon G-2X. As illustration, Figure 56a presents data on the component loadings of methanol and nC6 in MSC-5A at a total pressure of 4 kPa and 303.15 K, as a function of the mole fraction of methanol in the bulk vapor phase. In Figure 56b, the data on the adsorbed phase

mole fraction of methanol is plotted as a function the mole fraction of methanol in the bulk vapor phase. It is interesting to note that mixture adsorption exhibits azeotropic behavior. The phenomenon of azeotropic mixture adsorption is characterized by the equality of mole fractions in the bulk vapor phase and in the adsorbed phase, $y_1 = x_1$. For bulk vapor phase methanol fractions lower than 0.5, the adsorbed phase is richer in methanol, the adsorbate of the smaller molecular size. However, for bulk vapor phase richer in methanol, the adsorbed phase is richer in n-hexane, the adsorbate with the larger molecular size.

For the IAST calculations, the pure component Langmuir isotherm fits used are taken from Table S1 of Bartholdy et al.[56] The IAST estimations of the adsorbate composition, shown by the dashed line, does not anticipate such selectivity reversals. Use of the RAST, shown by the continuous solid line, with fitted Wilson parameters are $\Lambda_{12} = 1.2$; $\Lambda_{21} = 68$; $C = 0.15$ kg mol^{-1} is able to capture the selectivity reversal phenomena reasonably accurately. Figure 56c presents the RAST calculations of the activity coefficients in the adsorbed phase. It is interesting to note that the activity coefficients are below unity, whereas the corresponding activity coefficients for bulk liquid phase mixtures, both exceed unity; see Figure 56d.

16. Non-ideality effects for adsorption of toluene/1-propanol mixtures in DAY-13 at 298.15 K

In Figures 57a,b the experimental data of Sakuth et al.[57, 58] of toluene/1-propanol mixture adsorption in DAY-13 (dealuminated Y zeolite, with FAU topology) at $T = 298.15$ K and two different total pressures $p_t = 0.36$ kPa, and $p_t = 1.06$ kPa. In these plots, the adsorbed phase mole fraction of toluene is plotted as a function of the mole fraction of toluene in the bulk vapor phase. It is interesting to note that mixture adsorption exhibits azeotropic behavior. The phenomenon of azeotropic mixture adsorption is characterized by the equality of mole fractions in the bulk vapor

phase and in the adsorbed phase, $y_1 = x_1$. For bulk vapor phase toluene fractions lower than 0.5, the adsorbed phase is richer in toluene, the component with the lower saturation capacity. However, for bulk vapor phase richer in toluene, the adsorbed phase is richer in 1-propanol, the adsorbate with the highest saturation capacity. The IAST estimations of the adsorbate composition, shown by the dashed line, does not anticipate such selectivity reversals; for the IAST calculations, the pure component data are provided in Table 1 of Sakuth et al.[57] In Figure 57c the differences in the estimation of the total mixture loading, $q_{t,IAST}$ from the experimental data, $q_{t,exp}$ is plotted as function of the adsorbed phase mole fraction of toluene. It is noteworthy that the deviations of the IAST estimates from experimental data is not just a function of the adsorbed phase mole fraction, but are also dependent on the total pressure in the bulk vapor phase.

Use of the RAST, shown by the continuous solid lines in Figures 57a,b, with fitted Wilson parameters are $\Lambda_{12} = 0.52$; $\Lambda_{21}= 12.2$; $C = 1.1$ kg mol^{-1}, is able to capture the selectivity reversal reasonably accurately; the Wilson parameters were obtained by fitting the experimental data at both pressures. Figures 57d,e present the RAST Wilson calculations of the activity coefficients in the adsorbed phase. It is interesting to note that the activity coefficients for both toluene and 1-propanol are below unity.

We now investigate the influence of thermodynamic non-idealities for separation of separation of toluene(1)/1-propanol(2) mixtures in DAY-13 at a total pressure $p_t = 1.06$ kPa, and with varying mole fractions of toluene in the bulk vapor phase. Figure 58a presents a comparison of IAST and RAST calculations for toluene(1)/1-propanol(2) adsorption selectivity, $S_{ads} = \frac{q_1/q_2}{y_1/y_2}$, plotted as function of mole fractions of toluene in the bulk vapor phase, y_1. The IAST predicts that the selectivity is practically independent of composition, and in favor of toluene that has the

stronger binding constant for adsorption. The predictions of the RAST are remarkably different. For bulk vapor phase toluene fractions lower than 0.2, the RAST selectivity is in favor of toluene. However, for $y_1 > 0.2$, the RAST selectivity is in favor of the 1-propanol.

Figure 58b,c compare the IAST and RAST calculations of the toluene, and 1-propanol uptake capacities.

Let us say that the toluene/1-propanol separations are conducted in fixed bed adsorbers with varying compositions of inlet feed mixtures, with the objective of selective adsorption of toluene. Using the theory of shock waves in fixed bed adsorbers,[33] the maximum amount of pure 1-propanol that can be recovered during the adsorption cycle is given by the separation potential, $\Delta Q_{1-propanol/toluene} = Q_{toluene} \frac{y_{1-propanol}}{1-y_{1-propanol}} - Q_{1-propanol}$, expressed in the units mol L^{-1}; for these calculations the crystal framework density of DAY-13 is taken as ρ = 1421 kg m^{-3}. Figure 58d presents a comparison of the IAST and RAST calculations of $\Delta Q_{1-propanol/toluene}$. The RAST anticipates shows that for a range of feed mixture compositions, $y_1 > 0.4$, the separation potential is negative. This implies that toluene will be rejected in the adsorption cycle and 1-propanol will be selectively adsorbed. In order to demonstrate these strong influences of termodynamic non-idealities, we undertook transient breakthrough simulations.

Figures 59a,b present transient breakthrough simulations of toluene(1)/1-propanol(2) feed mixtures in fixed bed adsorbed packed with DAY-13, operating at 298 K and p_t = 1.06 kPa with two different feed mixture compositions: (a) $y_1 = 0.1$, and (b) $y_1 = 0.5$.

For operation with feed mixture composition $y_1 = 0.1$, both IAST and RAST anticipate that the more strongly adsorbed component is toluene that has the stronger binding with the framework. We also note that the IAST implementation produces distended breakthroughs, and lower

productivity of pure 1-propanol. Purified 1-propanol can be recovered during the time interval $\Delta\tau$ as indicated in Figure 59a. Due to higher adsorption selectivity anticipated by RAST (cf. Figure 58a), the transient breakthroughs are sharper using the RAST and the productivity of 1-propanol is significantly higher because of the larger value of $\Delta\tau$.

The situation is completely different for transient breakthroughs with an equimolar feed mixture, $y_1 = 0.5$. In this case, the RAST anticipates that 1-propanol is selectively adsorbed and toluene is rejected. The IAST, on the other hand, anticipates that toluene is selectively adsorbed and pure 1-propanol can be produced in the adsorption cycle. Inclusion of thermodynamic non-idealities reverses the separation capability in this case.

The differences between IAST and RAST estimates of separation performance are also significant for operations at a lower total pressure of 0.36 kPa. For separation of toluene(1)/1-propanol(2) mixtures in DAY-13 at a total pressure $p_t = 0.36$ kPa, Figure 60a presents a comparison of IAST and RAST calculations for separation potential, $\Delta Q_{1-propanol/toluene} = Q_{toluene}\dfrac{y_{1-propanol}}{1-y_{1-propanol}} - Q_{1-propanol}$ and with varying mole fractions of toluene in the bulk vapor phase. For a feed mixture containing 0.6 mole fraction toluene, the RAST anticipates a negative separation potential, i.e. that 1-propanol is preferentially adsorbed. On the other hand, the IAST anticipates a positive separation potential, i.e. toluene is preferentially adsorbed. In order to confirm these contradictory behaviors, Figure 60b presents the corresponding transient breakthrough simulations for 60/40 toluene(1)/1-propanol(2) feed mixtures in fixed bed adsorbed packed with DAY-13, operating at 298 K and $p_t = 0.36$ kPa. The IAST shows that 1-propanol is rejected, and toluene is preferentially adsorbed. The RAST anticipates that pure toluene can be recovered during the adsorption cycle, and 1-propanol is preferentially adsorbed.

17. Non-ideality effects for adsorption of toluene/1-propanol mixtures in DAY-55 at 298.15 K

Sakuth et al.[57] also present data on adsorption of toluene/1-propanol mixtures in DAY-55 (dealuminated Y zeolite) at T = 298.15 K. The re-analysis of the experimental data proceeds along precisely the same lines as for DAY-13; the results are presented in Figure 61. As was the case for DAY-13, DAY-55 exhibits the phenomenon of azeotropic mixture adsorption, characterized by the equality of mole fractions in the bulk vapor phase and in the adsorbed phase, $y_1 = x_1$. The IAST does not anticipate the phenomenon of selectivity reversal. The proper accounting of non-ideality effects in mixture adsorption is required to properly capture selectivity reversal phenomenon.

18. Water/alcohols mixture adsorption in FAU zeolite

Using published data on CBMC mixture simulations, we shall examine the non-ideality effects for mixture adsorption in four different zeolites, FAU, DDR, MFI, and CHA.

Let us consider the adsorption of water/methanol, and water/ethanol mixtures in all-silica FAU zeolite that consists of 786 $Å^3$ cages, that are separated by 7.3 Å size windows. Figure 62 shows CBMC simulations of Krishna and van Baten[36] for pure component adsorption isotherms for water, methanol, and ethanol in all-silica FAU zeolite at 300 K. Above fluid phase fugacities of 10^4 Pa, pore saturation is reached and the hierarchy of saturation capacities water >> methanol > ethanol is a reflection of the size of the molecules.

Figure 63a presents CBMC simulations for adsorption of equimolar (partial fugacities f_1=f_2) water/methanol mixtures in FAU zeolite at 300 K. In the Henry regime of adsorption, the water loading is significantly below that of the alcohol. However, we note that at partial fluid phase fugacities, $f_i > 5\times10^3$ Pa, the adsorption is in favor of water, a consequence of entropy effects.

The continuous solid lines are the IAST calculations using the pure component isotherm fits. IAST calculations are able to provide a reasonably good description of mixture adsorption equilibrium for partial fugacities $f_i < 1\times10^3$ Pa. For $f_i > 2\times10^3$ Pa, there are significant quantitative deviations between IAST calculations and CBMC simulations of water loadings.

The departures of IAST estimates from CBMC mixtures simulations depend both on the composition of the adsorbed phase and the adsorption potential, $\frac{\pi A}{RT}$. This is verified by the plots in Figure 63b, showing the dependence of $q_{t,IAST} - q_{t,CBMC}$ on adsorbed phase mole function of water determined from CBMC (bottom axis), and the adsorption potential, $\frac{\pi A}{RT}$ (top axes). The departures of IAST from CBMC simulations tend to vanish as $\frac{\pi A}{RT} \to 0$; this stresses the importance of introducing the $\left(1-\exp\left(-C\frac{\pi A}{RT}\right)\right)$ into the Wilson equations for activity coefficients.

A good match of the CBMC simulations is obtained by accounting for thermodynamic non-idealities using Wilson parameters. The comparison of the Real Adsorbed Solution Theory (RAST) with CBMC simulations is shown in Figure 63c; the corresponding calculations of the activity coefficients are shown in Figure 63d. The departures of CBMC simulations from IAST get reflected in the values of activity coefficients. In particular, the activity coefficient of methanol falls significantly below unit with increasing bulk fluid phase fugacities, f_t.

Figure 64a presents CBMC simulation[36] data for adsorption of water/methanol mixture in FAU zeolite at 300 K at 1 kPa total pressure, and varying composition in the bulk fluid phase. The continuous and dashed lines are the RAST and IAST estimates of component loadings. Figure

64b presents the corresponding RAST calculations of the activity coefficients γ_i, for water and methanol.

Figure 65a presents CBMC simulations for adsorption of equimolar (partial fugacities $f_1=f_2$) water/ethanol mixture in FAU zeolite at 300 K. In the Henry regime of adsorption, the water loading is significantly below that of the alcohol. However, we note that at partial phase fugacities, $f_i > 8\times10^3$ Pa, the adsorption is in favor of water, a consequence of entropy effects. The continuous solid lines are the IAST calculations using the pure component isotherm fits. IAST calculations are able to provide a reasonably good description of mixture adsorption equilibrium for $f_i < 3\times10^2$ Pa. For $f_i > 3\times10^2$ Pa, there are significant quantitative deviations between IAST calculations and CBMC simulations of water loadings.

The departures of IAST estimates from CBMC mixtures simulations depend both on the composition of the adsorbed phase and the adsorption potential, $\frac{\pi A}{RT}$. This is verified by the plots in Figure 65b, showing the dependence of $q_{t,IAST} - q_{t,CBMC}$ on adsorbed phase mole function of water determined from CBMC (bottom axis), and the adsorption potential, $\frac{\pi A}{RT}$ (top axes).

A good match of the CBMC simulations is obtained by accounting for thermodynamic non-idealities using Wilson parameters. The comparison of the Real Adsorbed Solution Theory (RAST) with CBMC simulations is shown in Figure 65c; the corresponding calculations of the activity coefficients are shown in Figure 65d. The departures of CBMC simulations from IAST get reflected in the values of activity coefficients that depart from unity.

19. Steady-state water/ethanol mixture permeation across all-silica FAU zeolite membrane

Faujasite (FAU) zeolite is most commonly used for separations in two different structural forms, with varying Si/Al ratios; Zeolite X has 1 < Si/Al < 1.5, whereas the Zeolite Y has 1.5 < Si/Al < 3. For example, the use of ultrathin zeolite X membrane for pervaporation dehydration of ethanol is described by Zhou et al.[59]

For illustrating the influence of thermodynamic non-idealities, we analyze water(1)/ethanol(2) mixture permeation across all-silica FAU zeolite membrane at 300 K. The upstream composition is 5/95, i.e. f_{10}/f_{20}=5/95. The total mixture fugacity in the upstream compartment, $f_{t0}= f_{10}+ f_{20,}$ is varied from 2 Pa to 100 kPa. The partial fugacities of the two components in the downstream compartment are taken to be $f_{1\delta}= f_{2\delta}= 1$ Pa. Figure 66a compares the water/ethanol adsorption selectivity calculations for the IAST and RAST models. The IAST severely underestimates the values of S_{ads}. To rationalize this observation, Figures 66b,c present calculations of the mole fractions of water in the adsorbed phase, x_{10} at the upstream face, and the activity coefficients of water, γ_1, and ethanol, γ_2. For water/ethanol/FAU, the activity coefficient of water, γ_1 is significantly lower than unity. Consequently, the corresponding mole fractions of water in the adsorbed phase, x_1, calculated by the RAST are significantly higher than that estimated by the IAST. The higher loadings of water, as estimated by the RAST, results in estimates of S_{ads} that are higher than those calculated using the IAST.

For calculation of the water/ethanol permeation selectivities we assume that the Maxwell-Stefan diffusivities to be loading-independent, with the ratio $\frac{Đ_1}{Đ_2}=\frac{Đ_1(0)}{Đ_2(0)}=10$. Within the large open cages of FAU zeolite, correlation effects are of significant importance. Based on the MD

simulation data in previous works,[20] we take $\frac{Đ_1}{Đ_{12}} = 10$; $\frac{Đ_2}{Đ_{12}} = 1$. Figures 66d compares the water/ethanol permeation selectivities estimated using the IAST and RAST; as expected, the RAST estimates are significantly higher than those based on the IAST.

20. Water/alcohols mixture adsorption in DDR zeolite

Consider the adsorption of water/methanol, and water/ethanol mixtures in all-silica DDR zeolite that consists of 278 Å^3 cages, that are separated by 3.65 Å × 4.37 Å size windows. Figure 67 shows CBMC simulations of Krishna and van Baten[36] for pure component adsorption isotherms for water, methanol, and ethanol in DDR at 300 K. Above fluid phase fugacities of 10^5 Pa, pore saturation is reached and the hierarchy of saturation capacities water >> methanol > ethanol is a reflection of the size of the molecules.

Figure 68a presents CBMC simulations for adsorption of equimolar (partial fugacities f_1=f_2) water/methanol mixture in DDR zeolite at 300 K. In the Henry regime of adsorption, the water loading is significantly below that of methanol. However, we note that at partial fugacities, f_i > 8×10^3 Pa, the adsorption is in favor of water, a consequence of entropy effects. The continuous solid lines are the IAST calculations using pure component isotherm fits. IAST calculations are able to provide a reasonably good description of mixture adsorption equilibrium for f_i < 20 Pa. For f_i > 20 Pa, there are significant quantitative deviations between IAST calculations and CBMC simulations of water loadings in the mixture.

The departures of IAST estimates from CBMC mixtures simulations depend both on the composition of the adsorbed phase and the adsorption potential, $\frac{\pi A}{RT}$. This is verified by the

plots in Figure 68b, showing the dependence of $q_{t,IAST} - q_{t,CBMC}$ on adsorbed phase mole function of water determined from CBMC (bottom axis), and the adsorption potential, $\frac{\pi A}{RT}$ (top axes).

A good match of the CBMC simulations is obtained by accounting for thermodynamic non-idealities using Wilson parameters. The comparison of the Real Adsorbed Solution Theory (RAST) with CBMC simulations is shown in Figure 68c; the corresponding calculations of the activity coefficients are shown in Figure 68d. The departures of CBMC simulations from IAST get reflected in the values of activity coefficients that depart from unity.

Figure 69a presents CBMC simulations for adsorption of equimolar (partial fugacities f_1=f_2) water/ethanol mixture in DDR zeolite at 300 K. In the Henry regime of adsorption, the water loading is significantly below that of ethanol. However, we note that at partial fugacities, f_i = 8×10^3 Pa, the loading of water equals that of ethanol. The continuous solid lines are the IAST calculations using pure component isotherm fits. IAST calculations are able to provide a reasonably good description of mixture adsorption equilibrium for f_i < 10 Pa. For f_i > 10 Pa, there are significant quantitative deviations between IAST calculations and CBMC simulations of water loadings in the mixture.

The departures of IAST estimates from CBMC mixtures simulations depend both on the composition of the adsorbed phase and the adsorption potential, $\frac{\pi A}{RT}$. This is verified by the plots in Figure 69b, showing the dependence of $q_{t,IAST} - q_{t,CBMC}$ on adsorbed phase mole function of water determined from CBMC (bottom axis), and the adsorption potential, $\frac{\pi A}{RT}$ (top axes).

A good match of the CBMC simulations is obtained by accounting for thermodynamic non-idealities using Wilson parameters. The comparison of the Real Adsorbed Solution Theory

(RAST) with CBMC simulations is shown in Figure 69c; the corresponding calculations of the activity coefficients are shown in Figure 69d. The departures of CBMC simulations from IAST get reflected in the values of activity coefficients that depart from unity.

21. Water/alcohol mixture permeation across DDR zeolite membrane

The potential of DDR membranes for water/alcohol separations is demonstrated by Kuhn et al.[60] Our objective here is to demonstrate the strong influence of thermodynamic non-idealities on the water/alcohol pervaporation characteristics of DDR membranes. Toward this end, we consider permeation of water(1)/methanol(2), and water(1)/ethanol(2) feed mixtures, containing 5 mole % water across DDR zeolite membrane at 300 K.

The inter-cage hopping of water and alcohol molecules across the 3.65 Å × 4.37 Å size windows of DDR membrane may be taken to be uncorrelated, and the appropriate expression for the permeation fluxes is given by equation (37). Invoking the linearized solution for steady-state permeation, and using equation (40), we can calculate the permeation fluxes for water and alcohol. We compare the adsorption and permeation selectivity calculations using both the IAST and RAST models:

$$S_{ads} = \frac{q_{10}/q_{20}}{f_{10}/f_{20}}; \quad S_{perm} = \frac{N_1/N_2}{f_{10}/f_{20}} \tag{57}$$

where f_{10}/f_{20} is taken to be 5/95.

We take the Maxwell-Stefan diffusivities to be loading-independent, with the ratio $\frac{Đ_1}{Đ_2} = \frac{Đ_1(0)}{Đ_2(0)} = 10$. The matrix of thermodynamic correction factors is calculated using the simplified equation (31), in which the component loadings, and occupancies are calculated using

the IAST or RAST models. The results for water/methanol adsorption and permeation selectivtities are summarized in Figures 70a,b as a function of the total mixture fugacity in the upstream compartment, $f_{t0}= f_{10}+ f_{20}$. The IAST severely underestimates both S_{ads} and S_{perm}. For rationalization of these observations, Figures 70c,d present calculations of the mole fractions of water in the adsorbed phase, x_{10} at the upstream face, and the activity coefficients of water, γ_1, and alcohol, γ_2. The activity coefficients of water, γ_1 are significantly lower than unity. Consequently, the corresponding mole fractions of water in the adsorbed phase, x_1, calculated by the RAST are significantly higher than that estimated by the IAST. The higher loadings of water, as estimated by the RAST, results in estimates of both S_{ads} and S_{perm} that are higher than those calculated using the IAST.

Precisely analogous results are obtained for 5/95 water(1)/ethanol(2) mixture permeation across DDR membrane; the results are presented in Figure 71.

During transient approach to steady-state, the water flux displays overshoots for both water/methanol, and water/ethanol mixtures; see Figures 72a,b. The origin of the flux overshoots can be traced to thermodynamic coupling in the permeation fluxes, induced the matrix of thermodynamic correction factors $\begin{bmatrix} \Gamma_{11} & \Gamma_{12} \\ \Gamma_{21} & \Gamma_{22} \end{bmatrix}$; this has been explained in detail in our earlier work.[24] The corresponding permeation selectivities are plotted in Figures 72c,d. During a brief period of initial transient, water/ethanol permeation selectivities reach values about 10-100 times higher than the selectivities at steady-state. The precise method to be adopted to benefit from such transient operation techniques needs further detailed investigation.

22. Water/alcohols mixture adsorption in MFI zeolite

Consider the adsorption of water/methanol, and water/ethanol mixtures in all-silica MFI zeolite that consists of intersecting channels of 5.5 Å. Figure 73 shows CBMC simulations of Krishna and van Baten[36] for pure component adsorption isotherms for water, methanol, and ethanol in MFI at 300 K. Above fluid phase fugacities of 10^5 Pa, pore saturation is reached and the hierarchy of saturation capacities water >> methanol > ethanol is a reflection of the size of the molecules.

Figure 74a presents CBMC simulations for adsorption of equimolar (partial fugacities f_1=f_2) water/methanol mixture in MFI zeolite at 300 K. In the Henry regime of adsorption, the water loading is significantly below that of methanol. However, we note that at partial fugacities, f_i > 2×10^4 Pa, the adsorption is in favor of water, a consequence of entropy effects. The continuous solid lines are the IAST calculations using pure component isotherm fits. IAST calculations are able to provide a good description of mixture adsorption equilibrium for the entire range of fluid phase fugacities. Very slight improvements are realized by introduction of activity coefficients, and the use of the RAST; see Figure 74b and Figure 74c.

Figure 75a presents CBMC simulations for adsorption of equimolar (partial fugacities f_1=f_2) water/ethanol mixture in MFI zeolite at 300 K. In the Henry regime of adsorption, the water loading is significantly below that of ethanol. The estimations of the IAST are particularly unsatisfactory for water at fugacities in excess of 100 Pa. The departures of IAST estimates from CBMC mixtures simulations depend both on the composition of the adsorbed phase and the adsorption potential, $\frac{\pi A}{RT}$. This is verified by the plots in Figure 75b, showing the dependence of $q_{t,IAST} - q_{t,CBMC}$ on adsorbed phase mole function of water determined from CBMC (bottom axis),

and the adsorption potential, $\frac{\pi A}{RT}$ (top axes). Introduction of activity coefficients, and use of the RAST provides a good match with the CBMC simulated loadings; see Figures 75c and 75d. It is noteworthy that the activity coefficient of water is significantly higher than unity for a range of bulk fluid phase fugacities.

23. Steady-state water/ethanol mixture permeation across all-silica MFI zeolite membrane

Hydrophobic MFI membranes have potential use in the recovery of ethanol from dilute aqueous solutions.[61, 62] In order to demonstrate the significance of thermodynamic non-idealities on the MFI pervaporation characteristics, we analyze water(1)/ethanol(2) mixture permeation across all-silica MFI zeolite membrane at 300 K. The upstream feed mixture composition is 95 mole% water, 5 mole% ethanol, i.e. f_{10}/f_{20} = 95/5. The total mixture fugacity in the upstream compartment, $f_{t0}= f_{10}+ f_{20,}$ is varied from 2 Pa to 100 kPa. The partial fugacities of the two components in the downstream compartment are taken to be $f_{1\delta}= f_{2\delta}$= 1 Pa. Figure 76a compares the ethanol/water adsorption selectivity calculations for the IAST and RAST models. The IAST severely underestimates the values of S_{ads}. To rationalize this observation, Figures 76b,c present calculations of the mole fractions of water in the adsorbed phase, x_{10} at the upstream face, and the activity coefficients of water, γ_1, and ethanol, γ_2. For water/ethanol/MFI, the activity coefficient of water, γ_1 is significantly higher than unity. Consequently, the corresponding mole fractions of water in the adsorbed phase, x_1, calculated by the RAST are significantly lower than that estimated by the IAST. The lower loadings of water, as estimated by the RAST, results in estimates of S_{ads} that are significantly higher than those calculated using the IAST.

For calculation of the permeation selectivities we assume that the Maxwell-Stefan diffusivities to be loading-independent, with the ratio $\frac{Đ_1}{Đ_2}=\frac{Đ_1(0)}{Đ_2(0)}=10$. Within the intersecting 5.5 Å channels of MFI zeolite, correlation effects are not negligible. Based on the MD simulation data in previous works,[20] we take $\frac{Đ_1}{Đ_{12}}=10$; $\frac{Đ_2}{Đ_{12}}=1$. Figure 76d compares the ethanol/water permeation selectivities estimated using the IAST and RAST; as expected, the RAST estimates are significantly higher than those based on the IAST.

24. Non-idealities in adsorption of mixtures of 1-alcohols in CHA zeolite

Let us examine the data on the pure component isotherms for a series of 1-alcohols in CHA, which is a cage type zeolite that consists of 316 Å^3 sized cages separated by 3.8 Å × 4.2 Å sized windows. CBMC simulations of pure component 1-alcohols with C atoms in the 1 – 6 range in CHA at 300 K, as reported in the work of Krishna and van Baten,[12] are shown in Figure **77**a. The continuous solid lines in Figure **77**a are fits using the dual-site Langmuir-Freundlich model with parameters as specified in Table 10. The saturation capacities, $\Theta_{i,sat}$, decreases from 5.4 molecules per cage for methanol to 1 molecule per cage for 1-hexanol; see data in Figure **77**b. Figure **77** also presents snapshots of the location, and conformations, of the 1-alcohols within the cages of CHA at saturation conditions. Except for methanol, the saturation cage capacity has an integer value because 1-alcohol molecules cannot locate at the window regions.

The CBMC simulations for six different binary mixtures: (a) methanol/ethanol, (b) ethanol/1-propanol, (c) ethanol/1-hexanol, (d) 1-butanol/1-pentanol, (e) 1-butanol/1-hexanol, and (f) 1-pentanol/1-hexanol mixtures in CHA at 300 K are shown in Figure 78. The partial fugacities in the bulk fluid phase are taken to be equal, i.e. f_1=f_2. In all six cases, we note a tendency for

selectivity to reverse in favor of the component with the higher saturation capacity. The shaded regions in Figure 78 indicate that the bulk fluid phase is in the liquid phase for the range of fugacities, f_t. Operations with bulk liquid phase mixtures ensures that the shorter 1-alcohol will be preferentially adsorbed. The dashed lines represent calculations of the IAST using dual-Langmuir-Freundlich fits of pure component isotherms. The IAST correctly anticipates selectivity reversals for all six mixtures.

Experimental confirmation of the selectivity reversal phenomena observed in Figure 78 are provided by Remy et al.[63] who report data transient breakthroughs of ethanol/1-propanol and ethanol/1-hexanol mixtures in a fixed bed adsorber packed with SAPO-34, that has the same structural topology as CHA zeolite; see Figure 79a,b. The experiments show that the component that is eluted first from the adsorber is the alcohol with the longer chain length. In other words, the separations are not dictated by the binding strengths in the Henry regime. Rather, the breakthroughs confirm the selectivity reversal phenomena and preferential adsorption of the shorter 1-alcohol.

From Figure 78, we note that the quantitative agreement of the IAST with CBMC simulations are especially poor for ethanol/1-hexanol, 1-butanol/1-pentanol, and 1-pentanol/1-hexanol mixtures. The departures from IAST do not accrue solely from hydrogen bonding effects. A significant part of the deviations from IAST arises from the fact, that the cage capacity of 1-pentanol and 1-hexanol are both 1 molecule per cage. For mixtures containing one or more of these molecules, there is only room for one of these molecules. Consequently, the competition between 1-pentanol and 1-hexanol and partner species is not uniform over the entire pore space. Since the competition is less severe than anticipated by IAST, entropy effects favoring the shorter 1-alcohols are less strong than anticipated by the IAST.

We now apply the RAST for describing the adsorption of methanol/ethanol mixtures. Consider adsorption of binary equimolar fluid mixtures of methanol and ethanol in CHA. The saturation capacities are 5.5 and 4 molecules per cage, respectively. CBMC simulations on the component loadings in equilibrium with an equimolar methanol-ethanol mixture is shown in Figure 80a for varying partial fluid phase fugacities, f_i.

At $f_i < 5$ kPa, the selectivity is in favor of the component with the longer chain length, ethanol; this is "normal" behavior for mixture adsorption. However, for $f_i > 10$ kPa selectivity reversal occurs and methanol is preferentially adsorbed due to its higher packing efficiency. The IAST calculations are shown by the dashed lines. For total fugacities, $f_t < 10$ kPa, the IAST calculations are in good agreement with CBMC mixture simulations. IAST calculations are not in good quantitative agreement with CBMC simulations for $f_t < 10$ kPa.

The departures of IAST estimates from CBMC mixtures simulations depend both on the composition of the adsorbed phase and the adsorption potential, $\frac{\pi A}{RT}$. This is verified by the plots in Figure 80b, showing the dependence of $q_{t,IAST} - q_{t,CBMC}$ on adsorbed phase mole function of methanol determined from CBMC (bottom axis), and the adsorption potential, $\frac{\pi A}{RT}$ (top axes).

Introduction of activity coefficients and use of the RAST results in good match with CBMC simulated values of the component loadings; see Figures 80b,c.

Thermodynamic non-idealities have a strong effect on the permeation fluxes across CHA membrane. To demonstrate this we consider permeation of methanol(1)/ethanol(2) mixtures, containing 50 mole % methanol across CHA zeolite membrane at 300 K.

The inter-cage hopping of methanol and ethanol molecules across the 3.8 Å × 4.2 Å size windows of CHA membrane may be taken to be uncorrelated, and the appropriate expression for

the permeation fluxes is given by equation (37). Invoking the linearized solution for steady-state permeation, and using equation (40), we can calculate the permeation fluxes for methanol and ethanol. We compare the adsorption and permeation selectivity calculations using both the IAST and RAST models: $S_{ads} = \frac{q_{10}/q_{20}}{f_{10}/f_{20}}$; $S_{perm} = \frac{N_1/N_2}{f_{10}/f_{20}}$ where f_{10}/f_{20} =50/50.

We take the Maxwell-Stefan diffusivities to be loading-independent, with the ratio $\frac{Đ_1}{Đ_2} = \frac{Đ_1(0)}{Đ_2(0)} = 20$. The matrix of thermodynamic correction factors is calculated using the simplified equation (31), in which the component loadings, and occupancies are calculated using the IAST or RAST models. The results for methanol/ethanol adsorption and permeation selectivities are summarized in Figures 81a,b as a function of the total mixture fugacity in the upstream compartment, f_{t0}= f_{10}+ f_{20}. The IAST overestimates both S_{ads} and S_{perm}. For rationalization of these observations, Figures 81c,d present calculations of the mole fractions of ethanol in the adsorbed phase, x_{20} at the upstream face, and the activity coefficients of methanol, γ_1, and ethanol, γ_2. The activity coefficient of ethanol, γ_2 is significantly lower than unity. Consequently, the corresponding mole fractions of ethanol in the adsorbed phase, x_2, calculated by the RAST are significantly higher than that estimated by the IAST. The higher loadings of ethanol, as estimated by the RAST, results in estimates of both S_{ads} and S_{perm} that are lower than those calculated using the IAST.

25. Adsorption of water/ethanol mixtures in LTA-4A zeolite

The use of LTA-4A zeolite in a hybrid distillation-membrane separation scheme is illustrated in Figure 82. Distillation can produce ethanol with a purity close to 95 wt% owing to azeotrope formation. For obtaining say 99.5% pure ethanol, we need to feed the obtained 95 wt% ethanol

product to an azeotropic distillation column with an entrainer such as benzene, or cyclohexane. A better alternative, avoiding the use of entrainers, is to adopt a hybrid scheme (see Figure 82) in which the 95 wt% ethanol top product is fed to a hydrophilic LTA-4A zeolite membrane pervaporation unit. LTA-4A zeolite has 11 Å sized cages separated by windows with an aperture of 4 Å. Water has a significantly higher diffusivity than ethanol due to the narrow window aperture; diffusion selectivity strongly favors water. The desired 99.5% pure ethanol product is recovered as retentate. The water-rich permeate is returned to the distillation column.

We now analyze water/ethanol separations with LTA-4A membranes.

Figures 83a,b shows the experimental data of Pera-Titus et al.[64] for pure component isotherms for water and ethanol in LTA-4A zeolite at a variety of temperatures. Their data on unary isotherms are used to determine the Langmuir-Freundlich fit parameters at 333 K, as reported in Table 11.

Pera-Titus et al.[64] also published experimental data of the component loadings for water/ethanol mixtures at 2.1 kPa and 333 K as a function of mole fraction of water in the bulk vapor phase; see Figure 84. The experimental data on component loadings in the mixture were used to determine the Wilson parameters, as reported in Table 11. The continuous solid lines in Figure 84 are RAST estimations, that offer improvement over the corresponding IAST estimations (shown by the dashed lines).

26. Transient water/ethanol mixture permeation across LTA-4A zeolite membrane

Water/ethanol separations are effectively carried out with LTA-4A zeolite because the adsorption selectivity is significantly higher than in DDR zeolite; see calculations in Figure 85a of water/ethanol adsorption selectivity, S_{ads}, for water(1)/ethanol(2) mixtures in LTA-4A at 333

K p_t = 2.1 kPa, and varying bulk vapor phase compositions. There are some quantitative differences in the IAST and RAST estimations of S_{ads}, that can be rationalized on the basis of the deparatures of the activity coefficients of both water and ethanol from unity; both values are lowered below unity; see Figure 85b.

For permeation of 5/95 water(1)/ethanol(2) mixtures across LTA-4A membrane, the permeation fluxes, calculated using the RAST (indicated by the continuous solid lines), and the IAST (dashed lines), for transient approach to state-state are plotted in Figure 86a. Both the IAST and RAST anticipate overshoots in the water permeation fluxes. The origin of these overshoots are traceable to thermodynamic coupling in the permeation fluxes, induced the matrix of thermodynamic correction factors $\begin{bmatrix} \Gamma_{11} & \Gamma_{12} \\ \Gamma_{21} & \Gamma_{22} \end{bmatrix}$. In order to prove this, Figure 86b compares the permeation fluxes including thermodynamic coupling (solid lines) with those calculated assuming $\begin{bmatrix} \Gamma_{11} & \Gamma_{12} \\ \Gamma_{21} & \Gamma_{22} \end{bmatrix}$ equals the identity matrix $[I] = \begin{bmatrix} 1 & 0 \\ 0 & 1 \end{bmatrix}$, indicated by the dotted lines. Ignoring thermodynamic coupling, does not result in any water flux overshoots.

The permeation selectivities during the early transience are about three orders of magnitude higher than those obtained at steady-state; see Figure 86c. The deliberate exploitation of high water/ethanol permeation selectivities during the initial stages of transience remains a practical challenge.

The use of LTA-4A membrane for water/ethanol pervaporation is discussed in more detail by Pera-Titus et al.[64]

27. Adsorption of water/alcohol mixtures in ZIF-71

ZIF-71 possess a three-dimensional pore network formed by large cages interconnected via small windows;[65] see pore landscapes in Figure 87. CBMC simulations[65] of the pure component isotherms of water, methanol and ethanol in ZIF-71 at 298 K are shown in Figure 87a. The significantly higher saturation capacity of water compared to that of methanol and ethanol is evident. The CBMC simulations of Nalaparaju et al.[65] for water/methanol and water/ethanol mixtures in ZIF-71 provide convincing evidence of the entropy effects that manifest at pore saturation conditions. Figures 87b, and 87c shows CBMC simulations of the component loadings for equimolar (b) water/methanol, (c) water/ethanol mixtures in ZIF-71. For total pressures below 20 kPa, the adsorption is in favor of the alcohol. However, as the total pressure increase above 20 kPa, entropy effects cause the water loadings to exceed that the partner alcohol molecules. These results imply that for adsorption from *liquid phase* mixtures, water can be selectively adsorbed from water/alcohol mixtures. The IAST calculations afford only a qualitative prediction of mixture adsorption. Thermodynamic non-ideality effects need to be accounted for in process design calculations of separation equipment.

28. Segregation effects for CO_2/CH_4 mixture adsorption in cage-type zeolites

In the modeling of mixture separations in fixed bed adsorbers and membrane devices, a common practice is to use the IAST for estimating the component loadings in the microporous crystalline materials from information of unary isotherm fits.[66-68] A key assumption of the IAST is that the composition of the adsorbed phase is homogeneously and uniformly distributed within zeolite or metal-organic frameworks. Preferential location of molecules at certain locations

within the crystalline, causes segregated adsorption and deviations from the assumption of homogeneous distribution.

For separation of CO_2 from gaseous mixtures with CH_4, cage-type zeolites such as DDR, CHA, LTA, ERI, and ZIF-8 are of practical interest; these materials consist of cages separated by narrow windows, in the 3.3 – 4.5 Å range. The selectivity of separation of CO_2 is dictated by both adsorption and diffusion characteristics. For adsorption of CO_2/CH_4 mixtures, CBMC simulations[69] show that the window regions of cage-type zeolites has a significantly higher proportion of CO_2 than within the cages. Due to the segregated nature of mixture adsorption, the IAST is unable to predict the mixture loadings accurately.

Consider adsorption of pure CH_4, Ar, N_2, CO_2, Ne, and Kr in CHA, DDR, ERI, and LTA zeolites. CBMC simulations were run by Krishna and van Baten[69] to determine the adsorption equilibrium at 300 K and 1 MPa. Each GCMC simulation was run for 10^7 cycles. The centers of the molecules were captured every 1000 cycles, starting at cycle 1000. Statistics of 10^4 samples of the equilibrium positions within the CHA, ERI, LTA, and DDR, frameworks were collected for each molecule. From the collected statistics the % probability of locating a molecule within the window region can be determined; the data are summarized in Figures 88a, 90a, 89a, and 91a for, respectively, CHA, LTA, ERI, and DDR zeolites. For all four zeolites, CO_2 has the highest probability, about 30%-40%, of locating at the window regions. With increasing molecular diameter (Ar, N_2, Kr, CH_4), probability of locating at the window region decreases.

CBMC simulations for the component loadings in equilibrium with equimolar CO_2/CH_4 gas mixtures for a range of partial fugacities f_i are shown in Figures 88b, 90b, 89b, and 91b for CHA, LTA, ERI, and DDR zeolites, respectively. We note that for all four zeolites, the IAST under-predicts the loading of the more weakly adsorbed CH_4 in the CO_2/CH_4 mixture. The

conventional IAST calculation assumes that CH_4 molecules compete with *all* of the CO_2, making no allowance for segregation. Due to segregation effects the competition faced by CH_4 molecules within the cages, where they almost exclusively reside, is *smaller* than that in the entire pore space. The IAST anticipates a stiffer competition between CO_2 and CH_4 as it assumes a uniform distribution of composition; consequently, the separation selectivity is *over*estimated.

Introduction of activity coefficients, and use of the RAST is necessary to properly match CBMC simulations of mixture adsorption equilibrium, and model segregated mixture adsorption. The RAST calculations for CO_2/CH_4/ERI are summarized in Figure 92. For this purpose the RAST model was implemented as an Excel macro, and the Excel solver was used to determine the set of three parameters Λ_{12}, Λ_{21}, and C. The continuous solid lines in Figure 92a are RAST calculations that match the CBMC data on component loadings. Figure 92b shows the corresponding RAST calculations of the activity coefficients γ_i, for CO_2 and CH_4. The activity coefficient of CH_4 decreases to values significantly below unity with increasing bulk fugacities. For total bulk fluid phase fugacities exceeding 1 MPa, the adsorption selectivity predicted by the IAST is significantly higher than those determined from using the RAST.

The RAST calculations for CO_2/CH_4/DDR are summarized in Figure 93. Figure 93a compares the CBMC simulations for adsorption of equimolar (partial fugacities $f_1=f_2$) CO_2/CH_4 in DDR zeolite at 300 K with the RAST model with Wilson parameters. Segregation effects are properly captured using the RAST. Figure 93b shows the corresponding RAST calculations of the activity coefficients γ_i, for CO_2 and CH_4. Segregation effects have the effect of reducing the CO_2/CH_4 selectivity below the values calculated with IAST; see Figure 93c.

29. Segregation effects for CO_2/CH_4 mixture adsorption in AFX zeolite

The adsorbent with the highest selectivity for a given CO_2 separation duty can selected on the basis of screening of available zeolites and MOFs.[70-72] The screening can be done on the basis of experiments,[73-77] or molecular simulations.[5, 70, 72, 78] As illustration, Figure 94 presents data obtained from Configurational-Bias Monte Carlo (CBMC) simulations[70, 71] on the selectivity for CO_2/CH_4 mixtures as a function of the fluid fugacity, f_t, for a selection of all-silica zeolites: AFX, JBW, BIK, SIV, LOV, LEV, EPI, CHA, MFI, and FAU-Si. The simulations were carried out up to a total pressure of 10 MPa in order to be of relevance to natural gas and H_2 purification technologies for which pressures as high as 5 MPa are used. For any mixture, the values of S_{ads} are seen to vary by 2-3 orders of magnitude. It is noteworthy that for JBW, BIK, and AFX, selectivities in the range 100-1000 are obtained.

In order to understand the reasons for the high selectivities exhibited by AFX, we need to examine the pore landscapes as shown in Figures 2, and 3. In one unit cell of AFX there are 4 cages, and 4 small pockets. The 8-ring windows separating two cages are 3.44 Å × 3.88 Å in size. The window regions and the small pockets are preferred locations for CO_2;[69-71, 79] the pockets can be viewed as providing an "egg-carton" structure. CH_4, N_2, or H_2 do not prefer to locate at the window regions, and are preferentially located within the cages. Since there are 12 windows per unit cell of AFX, the adsorption selectivity for CO_2 is exceptionally high. Due to the slow diffusion of CO_2 it is likely that that the CO_2 ensconced in the pockets are practically stagnant, and the high selectivities predicted by CBMC simulations may not be realizable in practice.

JBW and BIK are both one-dimensional 8-ring channel structures of about 3.7 Å size. The channel topologies are such that CO_2 can nestle nicely in each channel segment (cf. Figure 94);

these are like "egg-cartons" for CO_2. Interestingly, JBW and BIK have the lowest values of pore volumes and surface areas.

Figure 95a presents a comparison of the estimations using the IAST with CBMC simulations of component loadings of equimolar (partial fugacities f_1=f_2) CO_2/CH_4 mixtures in AFX zeolite at 300 K. We note that the IAST under-predicts the loading of the more weakly adsorbed CH_4 in the CO_2/CH_4 mixture; these results are entirely analogous to those obtained for CHA, ERI, LTA, and DDR, shown in Figures 88b, 90b, 89b, and 91b. The conventional IAST calculation assumes that CH_4 molecules compete with *all* of the CO_2, making no allowance for segregation. Due to segregation effects the competition faced by CH_4 molecules within the cages, where they almost exclusively reside, is *smaller* than that in the entire pore space. The IAST anticipates a stiffer competition between CO_2 and CH_4 as it assumes a uniform distribution of composition; consequently the separation selectivity is *over*estimated. The estimations of the RAST with fitted Wilson parameters, are shown by the continuous solid lines in Figure 95b. The corresponding RAST calculations for the component activity coefficients γ_i, for CO_2 and CH_4 are shown in Figure 95c. Segregation effects have the effect of reducing the CO_2/CH_4 adsorption selectivity; see comparison of RAST and IAST estimates in Figure 95d.

30. Segregation effects for CO_2/N_2 mixture adsorption in AFX zeolite

The comparisons of IAST and RAST estimations with CBMC simulations for adsorption of 15/85 CO_2/N_2 mixtures in AFX zeolite at 300 K are shown in Figures 96a,b. In this case the failure of the IAST is only marginal. This is because the N_2 molecule can also locate at the window regions; see snapshots in Figure 96. However, the pockets of AFX zeolite seem to be the exclusive province of the CO_2 molecules; so segregation effects are not entirely negligible.

Figure 96c presents the RAST calculations of the component activity coefficients γ_i, for CO_2 and N_2. The activity coefficient of N_2 falls below unity at high bulk fluid phase fugacities. The IAST estimations of the CO_2/N_2 adsorption selectivities are slightly optimistic because the IAST assumes a uniform distribution of adsorbates in the pore space; see Figure 96d.

31. Segregation effects for CO_2/CH_4 mixture adsorption in MOR zeolite

MOR zeolite (Mordenite) consists of 12-ring (7.0 Å × 6.5 Å) 1D channels, connected to 8-ring (5.7 Å × 2.6 Å) pockets; the pore landscapes and structural details are provided in Figures 21, and 22. Computational snapshots (cf. Figure 97) of the location of molecules for CO_2/CH_4 mixture adsorption show that CO_2 get preferentially ensconced in the side-pockets. Figure 97a presents a comparison of the estimations using the IAST and RAST with CBMC simulations of component loadings of equimolar (partial fugacities $f_1=f_2$) CO_2/CH_4 mixtures in MOR zeolite at 300 K. We note that the IAST under-predicts the loading of the more weakly adsorbed CH_4 in the CO_2/CH_4 mixture. The conventional IAST calculation assumes that CH_4 molecules compete with *all* of the CO_2, making no allowance for segregation. Due to segregation effects the competition faced by CH_4 molecules within the 12-ring channels, where they almost exclusively reside, is *smaller* than that in the entire pore space. The IAST anticipates a stiffer competition between CO_2 and CH_4 as it assumes a uniform distribution of composition; consequently the separation selectivity is *over*estimated.

Figure 97b shows RAST calculations of the component activity coefficients γ_i, for CO_2 and CH_4. Figure 97c compares CO_2/CH_4 adsorption selectivities obtained from CBMC with IAST and RAST estimations. As for AFX zeolite, the influence of segregation is to reduce the CO_2/CH_4 adsorption selectivity, as compared with IAST estimates.

32. Congregation effects for CO_2/CH_4, CO_2/N_2, and CO_2/H_2 mixture adsorption in NaX, and NaY zeolites

For CO_2 capture from natural gas, predominantly containing CH_4, at high pressures, NaX zeolite is a potential adsorbent. This zeolite, commonly called 13X zeolite, has 106 Si, 86 Al, and 86 Na^+ per unit cell Si/Al=1.23; see Figure 27 for the structural details of NaX. Due to strong coulombic interactions of CO_2 with the extra-framework Na^+ ions, the selectivity is strongly in favor of CO_2. There is a tendency of CO_2 molecules to congregate around the cations; as evidenced by the snapshot in Figure 98; this results in an inhomogeneous distribution of adsorbates CO_2 and CH_4. The IAST calculation assumes that CH_4 molecules compete with *all* of the CO_2, making no allowance for congregation. Due to congregation effects, the competition faced by CH_4 molecules within the cages is *smaller* than that in the entire pore space. The IAST anticipates a stiffer competition between CO_2 and CH_4 as it assumes a uniform distribution of composition; consequently the separation selectivity is *over*estimated. This is confirmed by comparisons of the IAST estimations of CO_2/CH_4 adsorption selectivities with CBMC simulation data; see Figure 98b.

The RAST model, with activity coefficients described by the Wilson model, can be used to model congregation effects in mixture adsorption. Figure 98a compares the CBMC simulations[74, 76] for adsorption of equimolar (partial fugacities $f_1=f_2$) CO_2/CH_4 in NaX zeolite at 300 K with the RAST model. Congregation effects are properly modelled using the RAST. Figure 98c shows the corresponding RAST calculations of the activity coefficients γ_i, for CO_2 and CH_4. Congregation effects cause the activity coefficient of CH_4 to fall significantly below unity with increase fluid phase fugacity, f_i.

Congregation effects also manifest for adsorption of CO_2/N_2 mixtures in NaX zeolite. Figure 99a presents a comparison of CBMC simulated component loadings for 15/85 CO_2/N_2 mixture

adsorption in NaX zeolite at 313 K with estimations using the IAST, and RAST. The IAST tends to overestimate the adsorption selectivities are high bulk fluid fugacities; see Figure 99b. Figure 99c presents RAST calculations of the component activity coefficients γ_i, for CO_2 and N_2; it is noteworthy that the activity coefficient of N_2 falls significantly below unity.

Figure 100 presents an analysis of 15/85 CO_2/H_2 mixture adsorption in NaX zeolite at 313 K. The deviations from IAST are also ascribable to congregation effects.

Congregation effects may be expected to become decreasingly significant as the number of extra-framework cations is reduced. To demonstrate this, Figure 101 presents a comparison CBMC CO_2/CH_4 adsorption selectivities determined from CBMC simulations at 300 K for all-silica FAU (192 Si, 0 Al, 0 Na^+, Si/Al=∞), NaY (138 Si, 54 Al, 54 Na^+, Si/Al=2.56), and NaX (106 Si, 86 Al, 86 Na^+, Si/Al=1.23) zeolites with IAST estimations. For all-silica FAU, the IAST estimates are in perfect agreement with CBMC simulations. The agreement of IAST estimates with CBMC simulated data becomes progressively worse with decreasing Si/Al ratios.

33. Congregation effects for CO_2/CH_4 mixture adsorption in LTA-4A zeolite

Congregation effects also manifest for CO_2/CH_4 mixture adsorption in LTA-4A (per unit cell, LTA-4A has 96 Si, 96 Al, 96 Na^+, with Si/Al=1). Figure 102a shows the comparison of the CBMC simulated component loadings for adsorption of equimolar (partial fugacities $f_1=f_2$) CO_2/CH_4 mixtures in LTA-4A zeolite at 300 K with the estimations using the IAST, and RAST. There is a tendency of CO_2 molecules to congregate around the Na+ cations; this results in an inhomogeneous distribution of adsorbates CO_2 and CH_4. The IAST calculation assumes that CH_4 molecules compete with *all* of the CO_2, making no allowance for segregation. Due to segregation effects, the competition faced by CH_4 molecules within the cages is *smaller* than that in the

entire pore space. The IAST anticipates a stiffer competition between CO_2 and CH_4 as it assumes a uniform distribution of composition; consequently the separation selectivity is *over*estimated by the IAST. This is confirmed by comparisons of the IAST estimations of CO_2/CH_4 adsorption selectivities with CBMC simulation data; see Figure 102b.

The RAST model, with activity coefficients described by the Wilson model, can be used to model segregated mixture adsorption. Figure 102a compares the CBMC simulations[70, 72] for adsorption of equimolar (partial fugacities $f_1=f_2$) CO_2/CH_4 in LTA-4A zeolite at 300 K with the RAST model. Segregation effects are properly modelled using the RAST. Figure 102c shows the corresponding RAST calculations of the activity coefficients γ_i, for CO_2 and CH_4. Segregation effects cause the activity coefficient of CH_4 to fall significantly below unity with increase fluid phase fugacity, f_t.

34. CO_2/CH_4 mixture adsorption in 13X zeolite; Re-analysis of Gholipour-Mofarahi experimental data

Gholipour and Mofarahi[80] report the results of a comprehensive experimental investigation of adsorption equilibrium of describe CO_2/CH_4 mixture adsorption in 13X zeolite at pressures of 0.4 MPa and 0.6 MPa, and varying compositions of the bulk gas mixture. We present a re-analysis of their binary experimental data at 303 K as presented in their Table 4. Figure 103 presents a plot of the adsorbed phase mole fraction of CO_2 as a function of the mole fraction of CO_2 in the bulk gas mixture; the plotted data is for 0.6 MPa total pressure. As compared to the experimental data, the IAST severely overpredicts the mole fraction of the adsorbed phase mole fraction of CO_2. The overprediction is most likely caused by congregation of CO_2 around the cations.

It is noteworthy that Gholipour and Mofarahi[80] model non-ideality effects for CO_2/CH_4 mixture adsorption in 13X zeolite , without invoking the correction factor $\left(1-\exp\left(-C\frac{\pi A}{RT}\right)\right)$.

35. CO_2/N_2 mixture adsorption in 13X zeolite; Re-analysis of Hefti experimental data

Hefti et al.[19] report the results of a comprehensive experimental investigation of adsorption equilibrium for CO_2/N_2 mixtures in ZSM-5 and 13X zeolites for pressures ranging to 1 MPa. As illustration, Figures 104a,b present experimental data (indicated by symbols) of Hefti et al.[19] for (a) component loadings, q_i, and (b) adsorbed phase mole fractions, x_i, of CO_2, and N_2 for adsorption of CO_2/N_2 mixtures in 13X zeolite at 298 K and total pressure p_t = 1 MPa, as function of the mole fraction of CO_2 in the bulk gas phase. The IAST (shown by the dashed lines) overestimates the CO_2 loading, and underestimates the N_2 loading; consequently the adsorption selectivities are overly optimistic.

The overestimation of selectivities by IAST can be rationalized on the same basis as for CO_2/CH_4 separations with NaX zeolite, as discussed in the foregoing section. Due to strong coulombic interactions of CO_2 with the extra-framework Na^+ ions, the selectivity is strongly in favor of CO_2 There is a tendency of CO_2 molecules to congregate around the cations; as evidenced by the snapshot in Figure 99; this results in an inhomogeneous distribution of adsorbates CO_2 and N_2. The IAST calculation assumes that N_2 molecules compete with *all* of the CO_2, making no allowance for congregation of CO_2 around the cations. Due to congregation effects, the competition faced by N_2 molecules within the cages is *smaller* than that in the entire pore space. The IAST anticipates a stiffer competition between CO_2 and N_2 as it assumes a uniform distribution of composition; consequently, the separation selectivity is *over*estimated.

Use of the RAST model, shown by the continuous solid line, with fitted Wilson parameters Λ_{12} = 1.95; Λ_{21} = 64; C = 0.044 kg mol^{-1} in Equation (13), is able to model the congregation/segregation effects in mixture adsorption. The fitted Wilson parameters are based on the entire data set at 298 K, as reported in Section 2.2 of the Supplementary Material of Hefti et al.[19] It is worthy of note here, that the RAST model calculations as presented by Hefti et al.[19] use modified Wilson parameters, described by equation (17).

The experimental data of Hefti et al.[19] for CO_2/N_2 mixture adsorption in 13X zeolite also demonstrates that the IAST overestimates the adsorption selectivity for the same reasons as outlined above for CO_2/CH_4 and CO_2/N_2 mixture separations, as discussed in foregoing sections.

36. CO_2/C_3H_8 and C_2H_4/C_2H_6 mixture adsorption in NaX zeolite; re-analysis of Siperstein data

Siperstein and Myers[16] report experimental data for adsorption of $CO_2(1)/C_3H_8(2)$ mixtures in NaX zeolite at 293 K. A re-analysis of the data, as reported in Table C1 of their paper, is presented in Figure 105. The difference in the total mixture loading, $q_t = q_1 + q_t$, estimated from the IAST and experimental data is plotted in Figure 105a, as function of the adsorbed phase mole fraction of CO_2, x_1. The deviation of IAST from experimental data is not uniquely determined by x_1. Figure 105b plots $q_{tIAST} - q_{t,\exp}$, as a function of the adsorption potential, $\frac{\pi A}{RT}$; the deviations of the IAST from experiments is also dependent on the adsorption potential. It is noteworthy that the deviations tend to zero as $\frac{\pi A}{RT} \to 0$.

The deviations from ideality are adequately described with the Wilson parameters listed in Table 24. Figure 105c presents the RAST calculations of the activity coefficients of CO_2, and C_3H_8 plotted as a function of the adsorbed phase mole fraction of CO_2, determined

experimentally. It is particularly noteworthy, that the activity coefficient of propane falls significantly below unity for mole fractions of CO_2 larger than about 0.9. Figures 105d,e are parity plots, comparing the IAST and RAST estimates of the component loadings of (d) CO_2, and (e) C_3H_8 with the values determined experimentally. The IAST estimates of propane loadings are seen to be in poorer agreement with experimental data as compared to RAST estimates.

Thermodynamic non-ideality effects are considerably less significant for adsorption of C_2H_4/C_2H_6 mixtures in NaX zeolite at 293 K, as reported in Table C4 of Siperstein and Myers.[16] their paper. Figure 106a presents RAST calculations of the activity coefficients of C_2H_4, and C_2H_6 plotted as a function of the adsorbed phase mole fraction of C_2H_4, determined experimentally. The activity coefficients deviate from unity by about 20%. Consequently, the difference between the RAST and IASt estimates of the component loadings are significantly lower than that for CO_2/C_3H_8 mixtures.

We now investigate the influence of thermodynamic non-idealities for separation of 50/50 $CO_2(1)/C_3H_8(2)$ with NaX zeolite at 293 K, using the unary isotherm fits and Wilson parameters. Figure 107a presents a comparison of IAST and RAST calculations for adsorption selectivity, $S_{ads} = \frac{q_1/q_2}{y_1/y_2}$, plotted as function of the total pressure, p_t. Due to Coulombic interactions with the Na^+ cations, carbon-dioxide is more strongly adsorbed, and the selectivities are in favor of CO_2. Due to congregation of CO_2 around the cations, there is segregated adsorption. The IAST assumes a uniform distribution of adsorbates in the pore space of NaX zeolite, and overestimates the degree of competition between CO_2, and C_3H_8. Consequently, the CO_2/C_3H_8 selectivity predicted by the IAST is significantly higher than those predicted by the RAST. Figures 107b,c compare the IAST and RAST calculations of the CO_2, and C_3H_8 uptake capacities.

The main influence of thermodynamic non-idealities is to reduce the extent to which C_3H_8 is "rejected" due to mixture adsorption. If the CO_2/C_3H_8 separations are conducted in fixed bed adsorbers, the important influence of thermodynamic non-idealities to reduce the amount of pure C_3H_8 that can be recovered in the adsorption cycle. Using the theory of shock waves in fixed bed adsorbers,[33] the maximum amount of pure C_3H_8 that can be recovered during the adsorption cycle is given by the separation potential, $\Delta Q = Q_{CO2}\frac{y_{C3H8}}{1-y_{C3H8}} - Q_{C3H8}$, expressed in the units mol L^{-1}; for these calculations the crystal framework density of NaX zeolite is taken as ρ = 1421 kg m^{-3}. Figure 107d presents a comparison of the IAST and RAST calculations of ΔQ. For a total mixture fugacity, f_t = 40 kPa, the values of ΔQ, are respectively 4, and 2.8 mol L^{-1}, respectively. Thermodynamic non-idealities reduce the productivity of pure C_3H_8 in a fixed bed adsorber by about 40%.

In order to confirm this anticipated result, Figure 108 presents transient breakthrough simulations of 50/50 CO_2/C_3H_8 feed mixtures in fixed bed adsorber packed with NaX zeolite, operating at total pressure, p_t = 40 kPa and 293 K. Arbitrarily setting the purity requirement of C_3H_8 as containing 0.1% CO_2 as impurity, we can determine the productivity of 99.9% pure C_3H_8. Expressing the productivity in terms of mole of 99.9% pure C_3H_8 produced per kg of NaX packed in the bed, the productivity values are determined to be 2.96 and 2.04 mol L^{-1}, respectively for the IAST and RAST model implementations. These values are somewhat lower than those estimated from the shock wave model because of the small degree of distention in the transient breakthroughs in the fixed bed adsorber.

37. CO_2/C_3H_8 mixture adsorption in NaX zeolite; re-analysis of Costa data

Costa et al.[81] report experimental data for adsorption of $CO_2(1)/C_3H_8(2)$ mixtures in NaX zeolite at 293 K, that are analogous to those analyzed in the foregoing section for the experimental data of Siperstein and Myers[16]. The re-analysis of the data of Costa et al.[81] is presented below.

Figure 109a presents a plot of the mole fraction of CO_2 in the bulk gas phase, y_1, versus the mole fraction of CO_2 in the adsorbed phase, x_1. The experimental data clearly demonstrates the occurrence of the phenomenon of azeotropic adsorption, i.e. $y_1 = x_1$. The phenomenon of azeotropy is not anticipated by the IAST; as demonstrated the IAST calculations of x_1 versus y_1 for a total pressure of 50 kPa; see Figure 109b. Introduction of the activity coefficients in the adsorbed phase is required for quantitative modeling of mixture adsorption. The deviations from ideality are adequately described with the Wilson parameters listed in Table 25. The RAST model, with Wilson parameters fitted to match the experimental data, anticipates the phenomenon of azeotropy for bulk vapor phase mole fraction $y_1 \approx 0.8$, at a total pressure of 50 kPa; see Figure 109b.

Figure 109c presents the RAST calculations of the activity coefficients of CO_2, and C_3H_8 plotted as a function of the adsorbed phase mole fraction of CO_2, determined experimentally. It is particularly noteworthy, that the activity coefficient of propane falls significantly below unity for mole fractions of CO_2 larger than about 0.8. Figures 109d,e are parity plots, comparing the IAST and RAST estimates of the component loadings of CO_2, and C_3H_8 with the values determined experimentally. The IAST estimates of propane loadings are seen to be in poorer agreement with experimental data.

We now investigate the influence of thermodynamic non-idealities for separation of 80/20 CO_2(1)/C_3H_8(2) with NaX zeolite at 293 K, using the unary isotherm fits and Wilson parameters listed in Table 25. Figure 110a presents a comparison of IAST and RAST calculations for adsorption selectivity, $S_{ads} = \frac{q_1/q_2}{y_1/y_2}$, plotted as function of the total pressure, p_t. Due to Coulombic interactions with the Na^+ cations, carbon-dioxide is more strongly adsorbed, and the selectivities are in favor of CO_2. Due to congregation of CO_2 around the cations, there are significant deparatures from IAST estimates of selectivity. The IAST assumes a uniform distribution of adsorbates in the pore space of NaX zeolite, and overestimates the degree of competition between CO_2, and C_3H_8. Consequently, the CO_2/C_3H_8 selectivity predicted by the IAST is significantly higher than those predicted by the RAST. Figures 110b,c compare the IAST and RAST calculations of the CO_2, and C_3H_8 uptake capacities.

The main influence of thermodynamic non-idealities is to reduce the extent to which C_3H_8 is "rejected" due to mixture adsorption. If the 80/20 CO_2/C_3H_8 separations are conducted in fixed bed adsorbers, the important influence of thermodynamic non-idealities to reduce the amount of pure C_3H_8 that can be recovered in the adsorption cycle. Using the theory of shock waves in fixed bed adsorbers,[33] the maximum amount of pure C_3H_8 that can be recovered during the adsorption cycle is given by the separation potential, $\Delta Q = Q_{CO2}\frac{y_{C3H8}}{1-y_{C3H8}} - Q_{C3H8}$, expressed in the units mol L^{-1}; for these calculations the crystal framework density of NaX zeolite is taken as ρ = 1421 kg m^{-3}.

Figure 110d presents a comparison of the IAST and RAST calculations of ΔQ. At p_t = 50 kPa, the values of ΔQ, are respectively 0.67, and ≈ 0 mol L^{-1}, respectively. For a total pressure, p_t = 50 kPa, introduction of thermodynamic non-idealities anticipates the phenomenon of

azeotropic adsorption (see Figure 109b); consequently no separation is possible, i.e. $\Delta Q \approx 0$. In order to further investigate the phenomenon of azeotropic adsorption, Figure 111a presents transient breakthrough simulations of 80/20 CO_2/C_3H_8 feed mixtures in fixed bed packed with NaX zeolite, operating at total pressure, p_t = 50 kPa and 293 K. The IAST predicts that CO_2 is preferentially adsorbed, and that pure C_3H_8 can be recovered during a finite time interval. The RAST predicts that the component breakthroughs occur concomitantly and that no separation is achievable; pure C_3H_8 cannot be recovered in the adsorption cycle.

The corresponding simulations for 85/15 CO_2/C_3H_8 feed mixtures in fixed bed packed with NaX zeolite, operating at total pressure, p_t = 50 kPa and 293 K are presented in Figure 111b. In this case, the RAST anticipates that C_3H_8 is preferentially adsorbed, and purified CO_2 can be recovered during the early transience. Using the IAST estimates of mixture adsorption equilibrium, we note that CO_2 is preferentially adsorbed, and purified C_3H_8 can be recovered during the early transience.

The corresponding re-analysis of the experimental data of Costa et al.[81] for adsorption of four other binary mixtures is presented in Figure 112 (C_3H_6/C_3H_8), Figure 113 (CO_2/C_3H_6), Figure 114 (CO_2/C_2H_4), and Figure 115 (C_2H_4/C_3H_8). Of these four mixtures, the non-ideality effects are particularly strong for C_3H_6/C_3H_8 mixture adsorption. For CO_2/C_2H_4, and C_2H_4/C_3H_8 mixture adsorption, non-ideality effects are relatively minor.

38. $CO_2/C_2H_4/C_3H_8$ and $CO_2/C_3H_6/C_3H_8$ mixture adsorption in NaX zeolite; re-analysis of Calleja data

Calleja et al.[82] also report experimental data for adsorption of ternary $CO_2/C_2H_4/C_3H_8$ and $CO_2/C_3H_6/C_3H_8$ mixtures at 293 K in NaX (=13 X) zeolite, with varying compositions of the bulk gas phase. Using the unary isotherm fit parameters, along with the Wilson parameters, fitted

for the constituent *binary* pairs (as specified in Table 25), we apply equations (18), (19), and (20) to determine the component loadings in the ternary adsorbed phase.

Figures 116a,b,c present parity plots, comparing the IAST and RAST estimates of the component loadings of (a) CO_2, (b) C_2H_4, and (c) C_3H_8 with the values determined experimentally for $CO_2/C_2H_4/C_3H_8$ mixture adsorption. Use of the IAST, and neglect of non-ideality effects in the adsorbed phase leads to poorer agreement with the experimental data.

Figures 117a,bc present parity plots, comparing the IAST and RAST estimates of the component loadings of (a) CO_2, (b) C_3H_6, and (c) C_3H_8 with the values determined experimentally for $CO_2/C_3H_6/C_3H_8$ mixture adsorption. Use of the IAST, and neglect of non-ideality effects in the adsorbed phase tend to underestimate the loadings of CO_2, and C_3H_8; concomitantly, the C_3H_6 loading is somewhat overestimated. It is also noteworthy, that the RAST estimates of C_3H_8 loadings are also not perfect. This points to the limitations of predicting ternary mixture adsorption using Wilson fits of the corresponding binary pairs; this aspect needs further detailed investigation.

39. C_2H_4/iso-C_4H_{10} mixture adsorption in NaX zeolite; re-analysis of Hyun-Danner data

Congregation effects may also be expect to manifest for adsorption of unsaturated alkenes in zeolites containing extra-framework cations. Hyun and Danner[83] report experimental data for adsorption of C_2H_4/iso-C_4H_{10} mixtures in 13X zeolite. For adsorption at 298 K and 137.8 kPa, their experimental data clearly demonstrates the occurrence of the phenomenon of azeotropic adsorption, i.e. $y_1 = x_1$; see Figure 118a. The phenomenon of azeotropy is not anticipated by the IAST; see Figure 118b. To account for azeotropic adsorption, activity coefficients need to be introduced; see RAST calculations in Figures 118b,c. Figure 118d,e are parity plots, comparing

the IAST and RAST estimates of the component loadings of C_2H_4, and iso-C_4H_{10} with the values determined experimentally. The IAST estimates of both component loadings are seen to be in poorer agreement with experiment.

40. CO_2/C_2H_4, CO_2/C_3H_8, and C_2H_4/C_3H_8 mixture adsorption in ZSM-5 zeolite; re-analysis of Calleja data

Congregation effects may also be expect to manifest for adsorption of CO_2 in other zeolites containing extra-framework cations. To demonstrate this, we present a re-analysis of the experimental data of Calleja et al.[84] for adsorption of the binary mixtures of CO_2/C_2H_4, CO_2/C_3H_8 and C_2H_4/C_3H_8 at 293 K in ZSM-5 (with MFI topology) zeolite with Si/Al ratio = 15, as reported in Table 5 of their paper; see Figure 119. Figure 120, and Figure 121.

Figure 119 presents the analysis of the experimental data of Calleja et al.[84] for adsorption of CO_2/C_2H_4 mixtures at 293 K in ZSM-5 (with MFI topology) zeolite with Si/Al ratio = 15. The mixture adsorption is nearly ideal, and the activity coefficients of both components are close to unity.

For adsorption of CO_2/C_3H_8 and C_2H_4/C_3H_8 mixtures, on the other hand, non-ideality effects are significant.

Figure 120a presents a plot of the mole fraction of CO_2 in the bulk gas phase, y_1, versus the mole fraction of CO_2 in the adsorbed phase, x_1 for CO_2/C_3H_8 mixture The experimental data clearly demonstrates the occurrence of the phenomenon of azeotropic adsorption, i.e. $y_1 = x_1$. The phenomenon of azeotropy is not anticipated by the IAST; as demonstrated the IAST calculations of x_1 versus y_1 for a total pressure of 40 kPa; see Figure 120b. Introduction of the activity coefficients in the adsorbed phase is required for quantitative modeling of mixture adsorption. Figure 120c presents RAST calculations of the activity coefficients of CO_2, and C_3H_8 plotted as a

function of the adsorbed phase mole fraction of C_2H_4, determined experimentally. Figure 120d,e are parity plots, comparing the IAST and RAST estimates of the component loadings of CO_2, and C_3H_8 with the values determined experimentally. The IAST estimates are in poorer agreement with experimental data.

Congregation effects may also be expect to manifest for adsorption of unsaturated alkenes in zeolites containing extra-framework cations. To demonstrate this, we present a re-analysis of the experimental data of Calleja et al.[84] for adsorption of C_2H_4/C_3H_8 mixtures at 293 K in ZSM-5 (with MFI topology) zeolite with Si/Al ratio = 15, as reported in Table 5 of their paper; see Figure 121. Figure 121a presents a plot of the mole fraction of C_2H_4 in the bulk gas phase, y_1, versus the mole fraction of C_2H_4 in the adsorbed phase, x_1. The experimental data clearly demonstrates the occurrence of the phenomenon of azeotropic adsorption, i.e. $y_1 = x_1$. The phenomenon of azeotropy is not anticipated by the IAST; as demonstrated in the IAST calculations of x_1 versus y_1 for a total pressure of 40 kPa; see Figure 121a,b. Introduction of the activity coefficients in the adsorbed phase is required for quantitative modeling of mixture adsorption. Figure 121c presents RAST calculations of the activity coefficients of C_2H_4, and C_3H_8 plotted as a function of the adsorbed phase mole fraction of C_2H_4, determined experimentally. Figure 121d,e are parity plots, comparing the IAST and RAST estimates of the component loadings of C_2H_4, and C_3H_8 with the values determined experimentally. The IAST estimates of both component loadings are seen to be in poorer agreement with experiment.

In order to demonstrate the consequence of non-idealities in mixture adsorption, Figure 122 presents transient breakthrough simulations of 10/20 C_2H_4/C_3H_8 feed mixtures in fixed bed packed adsorber ZSM-5 (Si/Al ratio = 15) zeolite, operating at total pressure, p_t = 30 kPa and 293 K. The transient breakthroughs using the RAST estimation of mixture adsorption

equilibrium shows a clear separation, with preferential adsorption of C_3H_8. In sharp contrast, use of the IAST model shows that both guest molecules breakthrough at the same time, and no separation is achievable.

41. CO_2/C_3H_8, CO_2/H_2S, C_3H_8/H_2S, and $CO_2/C_3H_8/H_2S$ mixture adsorption in H-MOR; re-analysis of Talu-Zwiebel data

Talu and Zwiebel[18] report experimental data of adsorption of CO_2/C_3H_8 mixtures at 303 K in H-MOR (= H-Mordenite) that provides convincing evidence of non-idealities engendered by both segregation/congregation effects; see Figures 123a,b,d,e. Two sets of experimental data are reported: (a, b) 17/83 $CO_2(1)/C_3H_8(2)$ mixtures and varying total gas phase pressures, p_t, and (d, e) $CO_2(1)/C_3H_8(2)$ mixtures at a total gas phase pressure p_t = 41 kPa, and varying CO_2 mole fractions in the bulk gas phase, y_1. The combined data set on mixture adsorption were used to determine the Wilson parameters of the RAST model; these are reported in Table 28. The corresponding RAST calculations of the activity coefficients of CO_2, and C_3H_8 for $CO_2(1)/C_3H_8(2)$ mixtures for the two data sets are shown in Figures 123c,f.

Due to congregation/segregation effects, the adsorption selectivities determined experimentally for 17/83 $CO_2(1)/C_3H_8(2)$ mixtures are significantly higher than those predicted by the IAST that assumes a uniform distribution of adsorbates within the pore topology of H-MOR; see Figures 123a,b.

The experimental data for adsorption of $CO_2(1)/C_3H_8(2)$ mixtures at a total gas phase pressure p_t = 41 kPa, and varying CO_2 mole fractions in the bulk gas phase, y_1, clearly show the phenomenon of azeotropy, at $y_1 = x_1 \approx 0.6$; the IAST does not anticipate azeotropy. Use of the RAST model, with fitted Wilson parameters captures the azeotropic effects with good accuracy.

If 17/83 CO_2/C_3H_8 mixture separations are conducted in fixed bed adsorbers, the important influence of thermodynamic non-idealities to influence the amount of pure C_3H_8 that can be recovered in the adsorption cycle. Using the theory of shock waves in fixed bed adsorbers,[33] the maximum amount of pure C_3H_8 that can be recovered during the adsorption cycle is given by the separation potential, $\Delta Q = Q_{CO2}\frac{y_{C3H8}}{1-y_{C3H8}} - Q_{C3H8}$, expressed in the units mol L^{-1}; for these calculations the crystal framework density of H-MOR zeolite is taken as ρ = 1715 kg m^{-3}.

Figure 124a presents a comparison of the IAST and RAST calculations of ΔQ for 17/83 CO_2/C_3H_8 mixture separations. For a total pressure p_t = 41 kPa the values of ΔQ, are respectively 0.54, and 3.5 mol L^{-1}, respectively. Figure 124b presents transient breakthrough simulations of 17/83 CO_2/C_3H_8 feed mixtures in fixed bed packed with H-MOR, operating at total pressure, p_t = 41 kPa and 303 K. The RAST predicts that CO_2 is preferentially adsorbed, and that pure C_3H_8 can be recovered during a finite time interval $\Delta\tau$, as indicated. For transient breakthrough simulations using the IAST, the time interval $\Delta\tau$ between the two breakthroughs is considerably shorter. From a material balance on the adsorber, we can determine the amount of purified C_3H_8 that can be recovered. Setting the purity requirement arbitrarily at 90%, the productivities of 90%+pure C_3H_8 are determined to be 0.44, and 3.16 mol L^{-1}; these values are somewhat lower than those calculated using the "shock wave" formula because of the distended nature of breakthroughs in Figure 124b. Neglect of thermodynamic non-idealities severely underestimates the productivity of 90%+ pure C_3H_8.

Figures 125a,b present a re-analysis of the experimental data of Talu and Zwiebel[18] for adsorption of (a) CO_2/H_2S, and (b) C_3H_8/H_2S mixtures at 303 K in H-MOR, as reported in Table

5 of their paper. Particularly noteworthy is the strong azeotropy for C_3H_8/H_2S mixture adsorption, for which the IAST predictions are exceedingly poor.

Talu and Zwiebel[18] also report experimental data for adsorption of ternary $CO_2/C_3H_8/H_2S$ mixtures at 303 K in H-MOR, as reported in Table 7 of their paper; the experimental data consist of four different campaigns. Using the unary isotherm fit parameters, along with the Wilson parameters, fitted for the constituent *binary* pairs (as specified in Table 28), we apply equations (18), (19), and (20) to determine the component loadings in the adsorbed phase. Figures 126a,b,c present parity plots, comparing the IAST and RAST estimates of the component loadings of (a) CO_2, (b) C_3H_8, and (c) H_2S with the values determined experimentally for ternary $CO_2/C_3H_8/H_2S$ mixture adsorption. The unary isotherm fit parameters, along with the Wilson parameters, determined from fitting the non-idealities in the constituene binary pairs, are specified in Table 28.

Use of the IAST, and neglect of non-ideality effects in the adsorbed phase tend to severely underestimate the loadings of C_3H_8. It is also noteworthy, that the RAST estimates of component loadings are also not perfect.

For one of the four campaigns of Talu and Zwiebel:[18] $y_2/y1=0.96$; $p_t=13.4$ kPa, the adsorbed phase compositions are plotted in ternary composition space; the RAST and IAST estimates follow different trajectories in composition space. This points to the limitations of predicting ternary mixture adsorption using Wilson fits of the corresponding binary pairs; this aspect needs further detailed investigation.

42. CO_2/CH_4 mixture adsorption in LTA-5A zeolite; Re-analysis of Mofarahi-Gholipour experimental data

Mofarahi and Gholipour[85] report the results of a comprehensive experimental investigation of adsorption equilibrium of describe CO_2/CH_4 mixture adsorption in LTA-5A zeolite at 303 K, 0.4 MPa, and varying compositions of the bulk gas mixture. We present a re-analysis of their binary experimental data as presented in their Table 4, Table 9, and Table 11. Figure 127 presents a plot of the adsorbed phase mole fraction of CO_2 as a function of the mole fraction of CO_2 in the bulk gas mixture; the plotted data is for 0.4 MPa total pressure. As compared to the experimental data, the IAST severely overpredicts the mole fraction of the adsorbed phase mole fraction of CO_2. The overprediction is most likely caused by congregation of CO_2 around the cations.

It is noteworthy that Mofarahi and Gholipour[85] model non-ideality effects for CO_2/CH_4 mixture adsorption in LTA-5A , without invoking the correction factor $\left(1-\exp\left(-C\frac{\pi A}{RT}\right)\right)$.

43. C_2H_4/C_2H_6 mixture adsorption in LTA-5A zeolite; Re-analysis of Mofarahi-Salehi experimental data

Mofarahi and Salehi[86] present a comprehensive set of experimental data for $C_2H_4(1)/C_2H_6(2)$ mixture adsorption in LTA-5A zeolite. Figure 128 presents ar re-analysis of the experimental data of Mofarahi and Salehi[86] at 283 K, for three different bulk gas phase mole fractions, y_1 of $C_2H_4(1)$. The IAST overpredicts the total mixture loading. The overprediction by IAST is significantly lower than witnessed above for CO_2/CH_4 mixture adsorption in 13X and LTA-5A zeolites.

The consequences of non-ideality effects on transient mixture breakthroughs are nicely underscored in the transient breakthrough experiments reported by van Zandvoort et al.[87] for $H_2/N_2/Ar/CH_4/C_2H_6/C_2H_4/CO_2$ mixtures in tubes packed with LTA-5A zeolite, operating at 313

K, and 0.5 MPa; see Figure 129a. In this mixture CO_2 is most strongly adsorbed; the sequence of experimental breakthroughs is H_2, N_2, Ar, CH_4, C_2H_6, C_2H_4, and CO_2. The breakthrough of CO_2 occurs less than 1 minute after the breakthrough of C_2H_4.

Figure 129b presents the results of transient breakthrough simulations, determined using the IAST for gas-zeolite mixture adsorption equilibrium. In the simulations, the breakthrough of CO_2 occurs about 7 minutes after the breakthrough of C_2H_4. This indicates that the adsorption strength of CO_2 is vastly overestimated by the IAST; this conclusion is congruent with the earlier observations in Figure 127 and Figure 128; apparently congregation effects have a much stronger influence of CO_2 adsorption than on C_2H_4 adsorption.

44. Segregation effects for adsorption of CH_4/N_2 mixtures in Ba-ETS-4

By tuning the size of the microporous channels and using ETS-4 as adsorbent, both adsorption and diffusion characteristics favor the selective uptake of N_2 from $CH_4(1)/N_2(2)$ mixtures.[88-90] Nitrogen is a "pencil-like" molecule, of 4.4 Å × 3.3 Å size; CH_4 is a spherical molecule of 3.7 Å size. The pores of Ba-ETS-4 virtually exclude methane molecules. Figures 130a, and 130b compare the experimental data (represented by symbols) of Bhadra[91] for binary mixture adsorption equilibrium of (a) 50/50, and (b) 90/10 $CH_4(1)/N_2(2)$ mixtures in Ba-ETS-4 with IAST calculations. Due to the segregated nature of mixture adsorption, the IAST calculations of adsorption equilibrium are in extremely poor agreement with the experimental data.

45. Preferential location of branched alkanes and cyclic hydrocarbons at the intersections of MFI zeolite

CBMC simulations of the unary adsorption isotherms for linear alkanes, with carbon numbers ranging from 1 to 6 in MFI zeolite at 300 K are shown in Figure 131a. The linear alkanes can

locate anywhere along the straight channels and zig-zag channels, and there are no perceptible isotherm inflections. Due to configurational considerations, branched alkanes prefer to locate at the channel intersections because of the extra "leg room" that is available here. An extra "push" is required to locate these molecules within the channel interiors. This extra push results in an inflection in the pure component isotherms at a loading of 4 molecules per unit cell.[92-95] See CBMC simulation data for iso-butane (iC4), 2-methylpentane (2MP), and 2,2dimethylbutane (22DMB) in Figure 131b. Cyclic hydrocarbons, such as cyclohexane, Benzene (Bz), and ethylbenzene (EthBz) also prefer to locate at the intersections; the unary isotherm for benzene also exhibits a strong inflection at a loading, $\Theta = 4$ molecules per unit cell.

Due to the preferential location of branched and cyclic hydrocarbons at the channel intersections, the adsorption of mixtures containing these types of hydrocarbons along with linear alkanes and alkenes, exhibit non-ideality effects.

Using published data on CBMC simulations,[4, 93, 96-99] we examine the extent of departures of the IAST from CBMC simulations of a wide variety of mixtures in MFI zeolite.

46. Alkane/benzene, and alkene/benzene mixture adsorption in MFI zeolite

CH_4/benzene mixture adsorption in MFI zeolite at 300 K

Figure 132a shows the unary isotherms of CH_4 and Benzene in MFI zeolite at 300 K. Benzene is more strongly adsorbed than methane for total fluid phase fugacities $f_t < 10^6$ Pa. However, for $f_t > 10^6$ Pa, the loadings of CH_4 exceed that of benzene because the alkane can locate anywhere within the channels, whilst the adsorption of benzene is restricted to the intersection sites. Figure 132b provides a comparison of the estimations using the IAST and RAST with CBMC simulations of component loadings of binary 50/50 CH_4/Benzene mixtures in MFI zeolite at 300

K. It is noteworthy that methane loading nearly coincides with that of benzene at $f_t \approx 10^9$ Pa. The IAST calculations overestimate the benzene/methane adsorption selectivity because it assumes a homogeneous distribution of adsorbates; see Figure 132c. The IAST calculation assumes that CH_4 molecules compete with *all* of the benzene molecules, making no allowance for segregation and preferential adsorption of benzene at the intersections. Due to segregation effects the competition faced by CH_4 molecules within the channels is *smaller* than that in the entire pore space. The IAST anticipates a stiffer competition between benzene and CH_4 as it assumes a uniform distribution of composition; consequently, the separation selectivity is *over*estimated. Use of the RAST, with fitted Wilson parameters, results in improved match with the CBMC simulated component loadings in the mixture. It is noteworthy that the activity coefficient of methane falls significantly below unity with increasing bulk fluid phase fugacities; see Figure 132d.

C_2H_4/benzene mixture adsorption in MFI zeolite at 300 K

Figure 133 presents the analysis of C_2H_4/Benzene mixture adsorption in MFI at 300 K. Figure 133a shows the unary isotherms of C_2H_4 and Benzene in MFI zeolite at 300 K. Benzene is more strongly adsorbed than ethene at total fluid phase fugacities $f_t < 10^4$ Pa. However, for $f_t > 10^4$ Pa, the loadings of C_2H_4 exceed that of benzene because the alkene can locate anywhere within the channels, whilst the adsorption of benzene is restricted to the intersection sites. Figure 133b provides a comparison of the estimations using the IAST and RAST with CBMC simulations of component loadings of binary 50/50 C_2H_4/Benzene mixtures in MFI zeolite at 300 K. It is noteworthy that ethene loading coincides with that of benzene at the $f_t \approx 10^6$ Pa. The IAST calculation assumes that C_2H_4 molecules compete with *all* of the benzene molecules, making no allowance for segregation and preferential adsorption of benzene at the intersections. Due to

segregation effects the competition faced by C_2H_4 molecules within the channels is *smaller* than that in the entire pore space. The IAST anticipates a stiffer competition between benzene and C_2H_4 as it assumes a uniform distribution of composition; consequently, the separation selectivity is *over*estimated; see Figure 133c. Use of the RAST, with fitted Wilson parameters, results in improved match with the CBMC simulated component loadings in the mixture. It is noteworthy that the activity coefficient of ethene falls significantly below unity with increasing bulk fluid phase fugacities; see Figure 133d.

C_2H_4/benzene mixture adsorption in MFI zeolite at 653 K

The analysis of C_2H_4/Benzene mixture adsorption in MFI at a higher temperature of 653 K are presented in Figure 134. In this case, the differences in the IAST and RAST calculations are considerably smaller, as compared to data for 300 K. Both IAST and RAST models predict the selectivity reversal phenomenon at $f_t \approx 5\times10^7$ Pa, observed in the CBMC mixture simulation data.

C_3H_6/benzene mixture adsorption in MFI zeolite at 300 K

Figure 135 presents the corresponding analysis for adsorption of C_3H_6/Benzene mixtures in MFI zeolite at 300 K. Figure 135a shows the unary isotherms of C_3H_6 and Benzene in MFI zeolite at 300 K. Benzene molecule is much more strongly adsorbed than propene at total fluid phase fugacities $f_t < 10^3$ Pa. However, for $f_t > 10^3$ Pa, the loadings of C_3H_6 exceed that of benzene because the alkene can locate anywhere within the channels, whilst the adsorption of benzene is restricted to the intersection sites. Figure 135b provides a comparison of the estimations using the IAST and RAST with CBMC simulations of component loadings of binary 50/50 C_3H_6/Benzene mixtures in MFI zeolite at 300 K. It is noteworthy that propene loading coincides with that of benzene at the $f_t \approx 5\times10^3$ Pa. For total mixture fugacities $f_t > 5\times10^3$ Pa,

propene is preferentially adsorbed due to entropy effects that favor the alkene that has the higher saturation capacity. The IAST calculation assumes that C_3H_6 molecules compete with *all* of the benzene molecules, making no allowance for segregation and preferential adsorption of benzene at the intersections. Due to segregation effects the competition faced by C_3H_6 molecules within the channels is *smaller* than that in the entire pore space. The IAST anticipates a stiffer competition between benzene and C_3H_6 as it assumes a uniform distribution of composition; consequently, the separation selectivity is *over*estimated; see Figure 135c. Use of the RAST, with fitted Wilson parameters, results in improved match with the CBMC simulated component loadings in the mixture. It is noteworthy that the activity coefficient of both benzene and propene fall significantly below unity with increasing bulk fluid phase fugacities; see Figure 135d.

47. Adsorption of linear and branched alkanes in MFI zeolite

Segregated adsorption manifests for mixtures of linear alkanes and branched alkanes in MFI zeolite, as highlighted by a number of examples below.

CH_4/iso-butane(iC4) mixture adsorption in MFI zeolite at 300 K

Figure 136a shows the unary isotherms of CH_4 and iso-butane (iC4) in MFI zeolite at 300 K. Iso-butane is more strongly adsorbed than methane for fluid phase fugacities $f_t < 10^6$ Pa. Due to configurational considerations, iC4 molecules prefer to locate at the channel intersections because of the extra "leg room" that is available here. An extra "push" is required to locate iC4 within the channel interiors. This extra push results in an inflection in the iC4 at a loading of 4 molecules per unit cell.[92-95] For $f_t > 10^6$ Pa, the loadings of CH_4 exceed that of iC4 because the alkane can locate anywhere within the channels, whilst the adsorption of iC4 is restricted to the intersection sites. Figure 136b provides a comparison of the estimations using the IAST and RAST with CBMC simulations of component loadings of binary 50/50 CH_4/iC4 mixtures in MFI

zeolite at 300 K. It is noteworthy that methane loading nearly coincides with that of iC4 at $f_t \approx 10^8$ Pa. The IAST calculations overestimate the iC4/methane adsorption selectivity because it assumes a homogeneous distribution of adsorbates; see Figure 136c. The IAST calculation assumes that CH_4 molecules compete with *all* of the iC4 molecules, making no allowance for segregation and preferential adsorption of iC4 at the intersections. Due to segregation effects the competition faced by CH_4 molecules within the channels is *smaller* than that in the entire pore space. The IAST anticipates a stiffer competition between iC4 and CH_4 as it assumes a uniform distribution of adsorbates; consequently, the separation selectivity is *over*estimated. Use of the RAST, with fitted Wilson parameters, results in improved match with the CBMC simulated component loadings in the mixture. It is noteworthy that the activity coefficients of both methane and iC4 fall significantly below unity with increasing bulk fluid phase fugacities; see Figure 136d.

C_2H_6/iso-butane(iC4) mixture adsorption in MFI zeolite at 300 K

Figure 137a shows the unary isotherms of C_2H_6 and iso-butane (iC4) in MFI zeolite at 300 K. Iso-butane is more strongly adsorbed than ethane for total fluid phase fugacities $f_t < 10^4$ Pa. Due to configurational considerations, iC4 molecules prefer to locate at the channel intersections because of the extra "leg room" that is available here. An extra "push" is required to locate iC4 within the channel interiors. This extra push results in an inflection in the iC4 at a loading of 4 molecules per unit cell.[92-95] For $f_t > 10^4$ Pa, the loadings of C_2H_6 exceed that of iC4 because the alkane can locate anywhere within the channels, whilst the adsorption of iC4 is restricted to the intersection sites. Figure 137b provides a comparison of the estimations using the IAST and RAST with CBMC simulations of component loadings of binary 50/50 C_2H_6/iC4 mixtures in MFI zeolite at 300 K. It is noteworthy that ethane loading nearly coincides with that of iC4 at $f_t \approx$

5×10^4 Pa. Entropy effects cause the loadings of ethane to exceed that of iso-butane for $f_t > 5\times10^4$ Pa. The IAST calculations overestimate the iC4/C_2H_6 adsorption selectivity because it assumes a homogeneous distribution of adsorbates; see Figure 137c. The IAST calculation assumes that C_2H_6 molecules compete with *all* of the iC4 molecules, making no allowance for segregation and preferential adsorption of iC4 at the intersections. Due to segregation effects the competition faced by C_2H_6 molecules within the channels is *smaller* than that in the entire pore space. The IAST anticipates a stiffer competition between iC4 and C_2H_6 as it assumes a uniform distribution of adsorbates; consequently, the separation selectivity is *over*estimated. Use of the RAST, with fitted Wilson parameters, results in improved match with the CBMC simulated component loadings in the mixture. It is noteworthy that the activity coefficients of both ethane and iC4 fall significantly below unity with increasing bulk fluid phase fugacities; see Figure 137d.

C_3H_8/iso-butane(iC4) mixture adsorption in MFI zeolite at 300 K

Figure 138a shows the unary isotherms of C_3H_8 and iso-butane (iC4) in MFI zeolite at 300 K. Iso-butane is more strongly adsorbed than propane for fluid phase fugacities $f_t < 10^3$ Pa. Due to configurational considerations, iC4 molecules prefer to locate at the channel intersections because of the extra "leg room" that is available here. An extra "push" is required to locate iC4 within the channel interiors. This extra push results in an inflection in the iC4 at a loading of 4 molecules per unit cell.[92-95] However, for $f_t > 10^3$ Pa, the loadings of C_3H_8 exceed that of iC4 because the alkane can locate anywhere within the channels, whilst the adsorption of iC4 is restricted to the intersection sites. Figure 138b provides a comparison of the estimations using the IAST and RAST with CBMC simulations of component loadings of binary 50/50 C_3H_8/iC4 mixtures in MFI zeolite at 300 K. It is noteworthy that propane loading nearly coincides with that of iC4 at $f_t \approx 5\times10^3$ Pa. Entropy effects cause the loadings of propane to exceed that of iso-

butane for $f_t > 5\times10^3$ Pa. The IAST calculations overestimate the iC4/C_3H_8 adsorption selectivity because it assumes a homogeneous distribution of adsorbates; see Figure 138c. The IAST calculation assumes that C_3H_8 molecules compete with *all* of the iC4 molecules, making no allowance for segregation and preferential adsorption of iC4 at the intersections. Due to segregation effects the competition faced by C_3H_8 molecules within the channels is *smaller* than that in the entire pore space. The IAST anticipates a stiffer competition between iC4 and C_3H_8 as it assumes a uniform distribution of adsorbates; consequently, the iC4/C_3H_8 separation selectivity is *over*estimated for $f_t < 5\times10^3$ Pa. Selectivity reversal manifests for $f_t > 5\times10^3$ Pa, and entropy effects favor the adsorption of propane; consequently, the iC4/C_3H_8 separation selectivity falls below unity. Use of the RAST, with fitted Wilson parameters, results in improved match with the CBMC simulated component loadings in the mixture. It is noteworthy that the activity coefficients of both propane and iC4 fall significantly below unity with increasing bulk fluid phase fugacities; see Figure 138d.

n-butane(nC4)/iso-butane(iC4) mixture adsorption in MFI zeolite at 300 K

Figure 139a shows the unary isotherms of nC4 and iC4 in MFI zeolite at 300 K. Due to configurational considerations, iC4 molecules prefer to locate at the channel intersections because of the extra "leg room" that is available here. An extra "push" is required to locate iC4 within the channel interiors. This extra push results in an inflection in the iC4 at a loading of 4 molecules per unit cell.[92-95] Normal-butane is more strongly adsorbed than iso-butane for the entire range of fluid phase fugacities f_t. Figure 139b provides a comparison of the estimations using the IAST and RAST with CBMC simulations of component loadings of binary 50/50 nC4/iC4 mixtures in MFI zeolite at 300 K. The experimental data of Titze et al. [99] using Infra-Red Microscopy (IRM) are in good agreement with CBMC simulations; these provide

experimental verification of the entropy effects that favor nC4. The IAST correctly predicts the entropy effects that favor the linear nC4, but the quantitative agreement is not good because of the inhomogeneous distribution of adsorbates within the pore network; a detailed analysis, and quantification, of segregation effects for nC4/iC4 mixtures has been provided by Krishna and Paschek.[100] The IAST anticipates a stiffer competition between nC4 and iC4 as it assumes a uniform distribution of adsorbates; consequently, the nC4/iC4 separation selectivity is *over*estimated; see Figure 139c. The RAST model is able to quantitatively describe the mixture adsorption equilibrium. It is noteworthy that the activity coefficient of iC4 falls significantly below unity with increasing bulk fluid phase fugacities; see Figure 139d.

n-hexane(nC6)/2-methylpentane(2MP) mixture adsorption in MFI zeolite at 300 K

Figure 140a shows the unary isotherms of nC6 and 2MP in MFI zeolite at 300 K. Due to configurational considerations, 2MP molecules prefer to locate at the channel intersections because of the extra "leg room" that is available here. An extra "push" is required to locate 2MP within the channel interiors. This extra push results in an inflection in the 2MP at a loading of 4 molecules per unit cell.[92-95] Normal-hexane more strongly adsorbed than 2MP for the entire range of fluid phase fugacities f_t. Figure 140b provides a comparison of the estimations using the IAST and RAST with CBMC simulations of component loadings of binary 50/50 nC6/2MP mixtures in MFI zeolite at 300 K. The experimental data of Titze et al. [99] using Infra-Red Microscopy (IRM) are in good agreement with CBMC simulations; these provide experimental verification of the entropy effects that favor nC6. The IAST correctly predicts the entropy effects that favor the linear nC6, but the quantitative agreement is not perfect because of the inhomogeneous distribution of adsorbates within the pore network.

48. Transient uptake of nC4/iC4, and nC6/2MP mixtures in MFI zeolite

Figure 141 presents simulations of the transient uptake of n-butane(nC4)/iso-butane(iC4) mixtures in MFI. The linear *n*-butane has a mobility that is about 1-2 orders of magnitude higher than that of the branched isomer because of subtle configurational differences; this has been established PFG NMR experiments of Fernandez et al.[101] Configurational-entropy effects also cause the preferential adsorption of the linear isomer.[99] The continuous solid lines in Figure 141a are simulation results using the RAST, that include the influence of thermodynamic coupling. In these simulations, we use equation (37) for the transfer fluxes. The corresponding calculations using the IAST are shown with the dashed lines in Figure 141a. The RAST predicts a larger overshoot in the component loading of nC4 during transient uptake as compared to the IAST. In order to demonstrate that the nC4 overshoots are due to thermodynamic coupling effects, the dotted lines in Figure 141b are simulations in which the matrix of thermodynamic correction factors is taken to be the identity matrix $\begin{bmatrix}\Gamma_{11} & \Gamma_{12}\\ \Gamma_{21} & \Gamma_{22}\end{bmatrix}\rightarrow\begin{bmatrix}1 & 0\\ 0 & 1\end{bmatrix}$; no nC4 overshoots are detected in this scenario, as explained in earlier work.[24]

The transient uptake of *n*-hexane(nC6)/2-methylpentane(2MP) mixtures in microporous crystals of MFI zeolite, exposed to an equimolar gas phase mixture at constant total pressure (= 2.6 Pa) have been reported by Titze et al.[99] The transient equilibration of nC6 displays a pronounced overshoot, achieving supra-equilibrium loadings during transient equilibration. Titze et al.[99] have established the validity of the M-S equation (37) to model intra-crystalline fluxes by detailed consideration of correlation effects. The mixture adsorption equilibrium is determined using the RAST. The input data on diffusivities are: $Đ_1/r_c^2 = 0.016$ s^{-1}; $Đ_2/r_c^2 = 1.6\times10^{-4}$ s^{-1}.

Figure 142 shows the simulations for transient uptake of nC6/2MP mixture in MFI at 300 K. The initial partial pressures $p_1 = p_2 = 0$ Pa; final partial pressures $p_1 = p_2 = 1.3$ Pa. The continuous solid lines are RAST calculations using equation (37) that include thermodynamic coupling effects. The dotted lines are simulations in which the matrix of thermodynamic correction factors is taken to be the identity matrix $\begin{bmatrix}\Gamma_{11} & \Gamma_{12}\\ \Gamma_{21} & \Gamma_{22}\end{bmatrix}\rightarrow\begin{bmatrix}1 & 0\\ 0 & 1\end{bmatrix}$. The overshoot in the nC6 uptake is validated by the experimental data of Titze et al.[99]

49. Separation of nC4/iC4 mixtures in fixed bed adsorber packed with MFI zeolite adsorbent

We now investigate the influence of thermodynamic non-idealities for separation of 50/50 nC4(1)/iC4(2) mixtures in MFI at 300 K. Figure 143a presents a comparison of IAST and RAST calculations for adsorption selectivity, $S_{ads} = \frac{q_1/q_2}{y_1/y_2}$, plotted as function of the total fluid mixture fugacity, f_t. Due to configurational entropy effects, the adsorption selectivity becomes increasingly in favor of the linear isomer nC4. The IAST anticipates a much stronger increase in selectivity than the corresponding calculations using the RAST, taking due account of the thermodynamic non-idealities accruing from the segregated nature of mixture adsorption. Figure 143b compares the IAST and RAST calculations of the iC4 uptake capacities. The main influence of thermodynamic non-idealities is to reduce the extent to which the branched isomer is "rejected" due to mixture adsorption; see Figure 143b.

If the nC4/iC4 separations are conducted in fixed bed adsorbers, the important influence of thermodynamic non-idealities to reduce the amount of pure iC4 that can be recovered in the adsorption cycle. Using the theory of shock waves in fixed bed adsorbers,[33] the maximum amount of pure iC4 that can be recovered during the adsorption cycle is given by the separation

potential, $\Delta Q_{iC4/nC4} = Q_1 \frac{y_2}{y_1} - Q_2 = Q_1 - Q_2$, calculated as the difference in the uptake capacities of nC4 and iC4. Figure 143c presents a comparison of the IAST and RAST calculations of $\Delta Q_{iC4/nC4}$. For a total mixture fugacity, f_t = 10 kPa, the values of $\Delta Q_{iC4/nC4}$, are respectively 2.5, and 1.98 mol L^{-1}, respectively. Thermodynamic non-idealities reduce the productivity of pure iC4 in a fixed bed adsorber by about 40%.

In order to confirm this anticipated result, Figure 144 presents transient breakthrough simulations of 50/50 nC4/iC4 feed mixtures in fixed bed packed adsorber with MFI at 300 K, operating at total fluid mixture fugacity, f_t = 10 kPa. Arbitrarily setting the purity requirement of iC4 as containing 0.05% nC4 as impurity, we can determine the productivity of 99.95% pure iC4. Expressing the productivity in terms of mole of 99.95% pure iC4 produced per kg of MFI zeolite packed in the bed, the productivity values are determined to be 2.2 and 1.77 mol L^{-1}, respectively for the IAST and RAST model implementations. These values are slightly lower than those estimated from the shock wave model because of the small degree of distention in the breakthroughs in the fixed bed adsorber.

50. Molecular clustering at sub-critical temperatures

From an energy-saving perspective, there is incentive to separate CO_2 from natural gas, predominantly consisting of CH_4, by adsorption separations in fixed beds that operate at cryogenic temperatures.[102] The critical temperature of CO_2 is 301 K, and there is a significant amount of cluster formation for adsorption at temperatures lower than 300 K.[70, 79, 103] Due to cluster formation the isotherms become increasingly steeper as the temperature is lowered; this is witnessed in CBMC simulations[70, 79, 103] for CO_2 isotherms in in (a) IRMOF-1, (b) all-silica FAU, and (c) all-silica AFI at 200 K, and 300 K.; see Figures 145a,b,c. The manifestation of

formation of CO_2 clusters can be verified by calculating the inverse thermodynamic factor, $\frac{1}{\Gamma_i} \equiv \frac{\partial \ln q_i}{\partial \ln f_i} = \frac{f_i}{q_i}\frac{\partial q_i}{\partial f_i}$; see Figures 145d,e,f. For CO_2 adsorption in IRMOF-1, FAU, and AFI at 200 K, there is a range of loading for which $1/\Gamma_i$, exceeds unity to a significant extent, signaling cluster formation. In sharp contrast, for CO_2 adsorption in IRMOF-1, FAU, and AFI at 300 K, the value of $1/\Gamma_i$ remains essentially below unity for the entire range of loadings in all three materials. It is also noteworthy, that molecular clustering effects appear to be stronger in IRMOF-1 at 200 K.

The critical temperature of CH_4 is 191 K, and for adsorption at temperatures below 194 K, there is CBMC simulation and experimental data to confirm cluster formation.[8, 79, 104]

At 300 K, with practically no cluster formation of either guest molecules CO_2 and CH_4, the IAST estimates are in excellent agreement with CBMC simulated data for 50/50 CO_2/CH_4 mixture adsorption in IRMOF-1, FAU, and AFI; see Figures 146a,b,c.

At 200 K, CO_2 forms clusters but CH_4 does not. Figure 147a presents a comparison of CBMC simulated loadings for 50/50 CO_2/CH_4 mixture adsorption in IRMOF-1 at 200K with IAST, and RAST estimates. Due to CO_2 cluster formation, the competition faced by individual CH_4 molecules is effectively strengthened, resulting in an enhanced selectivity in favor of CO_2. The use of the IAST underestimates the adsorption selectivity; see Figure 147b. The RAST calculations of the activity coefficients γ_i, for CO_2 and CH_4 are shown in Figure 147c.

51. Notation

A	surface area per kg of framework, $m^2\ kg^{-1}$
b_i	Langmuir-Freundlich parameter, $Pa^{-\nu}$
$[B]$	M-S matrix, $m^{-2}\ s$
c_i	molar concentration of species i, $mol\ m^{-3}$
c_t	total molar concentration in mixture, $mol\ m^{-3}$
c_{i0}	molar concentration of species i in fluid mixture at inlet to adsorber, $mol\ m^{-3}$
C	constant used in equation (13), $kg\ mol^{-1}$ or $uc\ molecule^{-1}$
$Đ_i$	M-S diffusivity of component i for molecule-pore interactions, $m^2\ s^{-1}$
$Đ_i(0)$	M-S diffusivity at zero-loading, $m^2\ s^{-1}$
$Đ_{ij}$	M-S exchange coefficient, $m^2\ s^{-1}$
$Đ_{12}$	M-S exchange coefficient for binary mixture, $m^2\ s^{-1}$
E	energy parameter, $J\ mol^{-1}$
f_i	partial fugacity of species i, Pa
f_t	total fugacity of bulk fluid mixture, Pa
$[I]$	Identity matrix with elements δ_{ij}, dimensionless
L	length of packed bed adsorber, m
n	number of species in the mixture, dimensionless
N_i	molar flux of species i defined in terms of the membrane area, $mol\ m^{-2}\ s^{-1}$
p_i	partial pressure of species i, Pa
p_t	total system pressure, Pa
P_i^0	sorption pressure, Pa
q_A	molar loading species A, $mol\ kg^{-1}$
$q_{i,sat}$	molar loading of species i at saturation, $mol\ kg^{-1}$
q_t	total molar loading of mixture, $mol\ kg^{-1}$

Q_A	volumetric uptake of species A, mol m^{-3}
ΔQ	separation potential, mol m^{-3}
r	radial coordinate, m
r_c	radius of crystallite, m
R	gas constant, 8.314 J mol^{-1} K^{-1}
S_{ads}	adsorption selectivity, dimensionless
S_{perm}	permeation selectivity, dimensionless
t	time, s
T	absolute temperature, K
u_i	velocity of motion of i, m s^{-1}
u	superficial gas velocity in packed bed, m s^{-1}
v	interstitial gas velocity in packed bed, m s^{-1}
V_p	pore volume, m^3 kg^{-1}
x_i	mole fraction of species i in adsorbed phase, dimensionless
y_i	mole fraction of species i in bulk fluid mixture, dimensionless
z	distance along the adsorber, and along membrane layer, m

Greek letters

γ_i	activity coefficient of component i in adsorbed phase, dimensionless
Γ_{ij}	thermodynamic factors, dimensionless
$[\Gamma]$	matrix of thermodynamic factors, dimensionless
δ	thickness of membrane, m
δ_{ij}	Kronecker delta, dimensionless
ε	voidage of packed bed, dimensionless
η	dimensionless distance, dimensionless
θ_i	fractional occupancy of component i, dimensionless
θ_t	fractional occupancy of adsorbed mixture, dimensionless

θ_V	fractional vacancy, dimensionless
Θ_i	loading of species *i*, molecules per unit cage, or per unit cell
$\Theta_{i,sat}$	saturation loading of species *i*, molecules per unit cage, or per unit cell
Θ_t	total mixture loading, molecules per unit cage, or per unit cell
$[\Lambda]$	matrix of Maxwell-Stefan diffusivities, $m^2\ s^{-1}$
Λ_{ij}	Wilson parameters, dimensionless
μ_i	molar chemical potential, J mol^{-1}
ν	Freundlich exponent in unary isotherm, dimensionless
π	spreading pressure, N m^{-1}
ρ	framework density, kg m^{-3}
τ	time, dimensionless

Subscripts

0	upstream face of membrane
1	referring to species 1
2	referring to species 2
i,j	components in mixture
η	position along membrane
δ	downstream face of membrane
i	referring to component *i*
t	referring to total mixture
s	referring to surface at position $\xi = 1$.
sat	referring to saturation conditions
V	vacancy

Superscripts

0	referring to pure component loading
excess	referring to excess parameter

Vector and Matrix Notation

( )	component vector
[ ]	square matrix

Table 1. 3-site Langmuir-Freundlich isotherm fits for adsorption of water in CuBTC at 298 K.

	Site A			Site B			Site C		
	$q_{A,sat}$ / mol kg^{-1}	b_A / Pa$^{-\nu_{iA}}$	ν_A	$q_{B,sat}$ / mol kg^{-1}	b_B / Pa$^{-\nu_{iB}}$	ν_B	$q_{C,sat}$ / mol kg^{-1}	b_C / Pa$^{-\nu_C}$	ν_C
water	22	5.48 $\times 10^{-4}$	1	22	6.24 $\times 10^{-32}$	10	10	2.51 $\times 10^{-4}$	0.6

Table 2. Dual-site Langmuir-Freundlich parameters for adsorption of methanol, ethanol, acetone, and benzene at 298 K in CuBTC.

Adsorbate	Site A			Site B		
	$q_{A,sat}$ mol kg^{-1}	b_A Pa$^{-\nu_A}$	ν_A dimensionless	$q_{B,sat}$ mol kg^{-1}	b_B Pa$^{-\nu_B}$	ν_B dimensionless
methanol	8.4	3.82×10^{-4}	1.03	11.5	9.3×10^{-16}	6.5
ethanol	5	2.29×10^{-3}	0.97	8	6.41×10^{-7}	3.2
acetone	5	4.83×10^{-17}	7.5	4.9	1.39×10^{-2}	0.7
1-propanol	8	4.83×10^{-4}	2.7	2	2.07×10^{-2}	0.5
benzene	4.6	2.76×10^{-6}	3.1	2.1	3.96×10^{-3}	1

Table 3. Wilson non-ideality parameters for binary mixtures in CuBTC at 298 K. The units of C are kg mol^{-1}, the reciprocal of the units of the loadings.

	Λ_{12}	Λ_{21}	C / kg mol^{-1}
methanol/ethanol	0.5	5	0.05
methanol/benzene	12	12	0.05
ethanol/benzene	6.6	22.4	0.031
acetone/benzene	10	10	0.05

Table 4. Dual-site Langmuir-Freundlich parameters for adsorption of methanol, and n-hexane at 313 K in CuBTC. The unary isotherm fits are based on the data scanned from Figure 2 of van Assche et al.[54]

Adsorbate	Site A			Site B		
	$q_{A,sat}$ mol kg^{-1}	b_A Pa$^{-\nu_A}$	ν_A dimensionless	$q_{B,sat}$ mol kg^{-1}	b_B Pa$^{-\nu_B}$	ν_B dimensionless
methanol	13.5	8.57×10^{-3}	0.62	6.5	2.5×10^{-3}	1.56
n-hexane	2.3	1.06×10^{-1}	0.6	2.8	4.81×10^{-8}	6.85

The fitted Wilson parameters using the data scanned from Figure 4 of van Assche et al.[54] The units of C are kg mol^{-1}.

	Λ_{12}	Λ_{21}	C / kg mol^{-1}
methanol/n-hexane/CuBTC	13	72	0.07

Table 5. Langmuir-Freundlich fits of the unary isotherms of toluene, and 1-propanol in DAY-13 zeolite at 298 K. The parameters were obtained by fitting the unary isotherm data in Table 1 of Sakuth et al.[57]

	q_{sat} mol kg^{-1}	b Pa$^{-\nu}$	ν dimensionless
toluene	2.26	0.2585	0.74
1-propanol	3.26	0.09743	0.56

The fitted Wilson parameters using the data from Table 3 Sakuth et al.[57] for toluene/1-propanol mixture adsorption in DAY-13. The units of C are kg mol^{-1}.

	Λ_{12}	Λ_{21}	C / kg mol^{-1}
Toluene/1-propanol/DAY-13	0.52	12.2	1.1

Table 6. Langmuir-Freundlich fits of the unary isotherms of toluene, and 1-propanol in DAY-55 zeolite at 298 K. The parameters were obtained by fitting the unary isotherm data in Table 1 of Sakuth et al.[57]

	q_{sat} mol kg^{-1}	b Pa$^{-\nu}$	ν dimensionless
toluene	2	0.01292	1.4
1-propanol	3.2	0.005524	1.06

The fitted Wilson parameters using the data from Table 3 Sakuth et al.[57] for toluene/1-propanol mixture adsorption in DAY-55. The units of C are kg mol^{-1}.

	Λ_{12}	Λ_{21}	C / kg mol^{-1}
Toluene/1-propanol/DAY-55	3.95	0.25	1

Table 7. Dual-site Langmuir-Freundlich parameters for adsorption of water, methanol, and ethanol at 300 K in all-silica FAU zeolite. The fit parameters are based on the CBMC simulations of pure component isotherms presented in earlier work.[36]

Adsorbate	Site A			Site B		
	$q_{A,sat}$ mol kg^{-1}	b_A $Pa^{-\nu_A}$	ν_A dimensionless	$q_{B,sat}$ mol kg^{-1}	b_B $Pa^{-\nu_B}$	ν_B dimensionless
water	16	1.54×10^{-121}	33	4.6	624×10^{-5}	1
methanol	3.4	6.36×10^{-16}	4.6	5.8	1.68×10^{-4}	1
ethanol	2.5	3.19×10^{-13}	4.9	2.9	1×10^{-3}	1.05

Wilson non-ideality parameters for binary water/methanol and water/ethanol mixtures in FAU at 300 K. The units of C are kg mol^{-1}.

	Λ_{12}	Λ_{21}	C / kg mol^{-1}
water/methanol in FAU	3.1	2.1	0.515
water/ethanol in FAU	1.88	1.25	0.24

Table 8. Dual-site Langmuir-Freundlich parameters for pure component water, methanol, and ethanol at 300 K in all-silica DDR zeolite. The fit parameters are based on the CBMC simulations of pure component isotherms presented in earlier work.[36]

	Site A			Site B		
	$q_{A,sat}$ mol kg^{-1}	b_A Pa$^{-\nu_i}$	ν_A dimensionless	$q_{B,sat}$ mol kg^{-1}	b_B Pa$^{-\nu_i}$	ν_B dimensionless
water	6.727	3.85×10^{-16}	4	2.219	1.73×10^{-5}	1
methanol	1.803	1.49×10^{-4}	1.25	1.595	6×10^{-4}	0.77
ethanol	1.512	7.66×10^{-3}	1	0.645	8.59×10^{-6}	1

Wilson non-ideality parameters for binary water/methanol and water/ethanol mixtures in DDR at 300 K. The units of C are kg mol^{-1}.

	Λ_{12}	Λ_{21}	C / kg mol^{-1}
water/methanol in DDR	2.1	3.3	9.1
water/ethanol in DDR	2.7	7.1	0.4

Table 9. Dual-site Langmuir-Freundlich parameters for adsorption of water, methanol, and ethanol at 300 K in all-silica MFI zeolite. The fit parameters are based on CBMC simulations of Krishna and van Baten.[36]

Adsorbate	Site A			Site B		
	$q_{A,sat}$ mol kg^{-1}	b_A Pa$^{-\nu_A}$	ν_A dimensionless	$q_{B,sat}$ mol kg^{-1}	b_B Pa$^{-\nu_B}$	ν_B dimensionless
water	6.7	6.37×10^{-24}	6.2	3.6	1.09×10^{-5}	1.04
methanol	2.4	1×10^{-4}	1.64	1.4	1.92×10^{-3}	0.7
ethanol	1.1	2.82×10^{-4}	2.7	1.7	1.91×10^{-2}	0.9

Wilson non-ideality parameters for binary water/methanol and water/ethanol mixtures in MFI at 300 K. The units of C are kg mol^{-1}.

	Λ_{12}	Λ_{21}	C / kg mol^{-1}
water/methanol in MFI	0.52	1.2	0.7
water/ethanol in MFI	0.23	0.62	0.6

Table 10. Dual-site Langmuir-Freundlich parameters for pure component water, and 1-alcohols in CHA at 300 K. The fit parameters are based on the CBMC simulations of pure component isotherms presented in earlier work.[12] Note that the saturation capacities are specified in molecules per cage; multiply these by 1.387 to obtain the values in mol per kg framework.

	Site A			Site B		
	$\Theta_{A,sat}$ Molecules cage^{-1}	b_A Pa$^{-\nu_A}$	ν_A dimensionless	$\Theta_{B,sat}$ molecules cage^{-1}	b_B Pa$^{-\nu_B}$	$\nu_{i,B}$ dimensionless
water	12	7.86×10^{-59}	17	9	8.32×10^{-6}	1
methanol	2.7	6.77×10^{-11}	3.3	2.7	4.45×10^{-4}	1
ethanol	2	7.93×10^{-5}	0.87	2	3.6×10^{-3}	1.14
1-propanol	1	1.28×10^{-2}	1.8	1	9.11×10^{-2}	1
1-butanol	1	0.231	1.46	1	0.5066	1
1-pentanol	0.5	19.26	1.72	0.5	6.91	1
1-hexanol	0.5	2561	2.4	0.5	24.8	1

Wilson non-ideality parameters for binary methanol/ethanol mixture adsorption

	Λ_{12}	Λ_{21}	C / cage molecule^{-1}
methanol/ethanol in CHA	3.3	2.4	0.04

Table 11. Langmuir-Freundlich fits of the unary isotherms of water, and ethanol in LTA-4A zeolite at 333 K. The isotherm fits are based on the experimental data of Pera-Titus et al.[64]

	q_{sat} mol kg^{-1}	b Pa$^{-\nu}$	ν dimensionless
water	11.3	8.63×10^{-3}	0.9
ethanol	3.8	4.46×10^{-3}	0.89

The fitted Wilson parameters for water/ethanol/LTA-4A using the experimental data of Pera-Titus et al.[64] The units of C are kg mol^{-1}.

	Λ_{12}	Λ_{21}	C / kg mol^{-1}
water/ethanol/LTA-4A	10.3	3.2×10^{-6}	0.036

Table 12. Dual-site Langmuir-Freundlich parameters for pure component CO_2, and CH_4 at 300 K in all-silica ERI zeolite. The fit parameters are based on the CBMC simulations of pure component isotherms presented in earlier work.[69]

	Site A			Site B		
	$q_{A,sat}$ mol kg^{-1}	b_A Pa$^{-\nu_A}$	ν_A dimensionless	$q_{B,sat}$ mol kg^{-1}	b_B Pa$^{-\nu_B}$	ν_B dimensionless
CO_2	5	3.77×10^{-6}	1	1.45	7.56×10^{-8}	1
CH_4	2	3.43×10^{-8}	1	2.45	2.39×10^{-6}	1

Fitted Wilson non-ideality parameters for binary CO_2/CH_4 mixture adsorption in ERI at 300 K.

	Λ_{12}	Λ_{21}	C / kg mol^{-1}
CO_2/CH_4 in ERI	2.5	1.05	0.1

Table 13. Dual-site Langmuir-Freundlich parameters for pure component CO_2, and CH_4 at 300 K in all-silica DDR zeolite. The fit parameters are based on the CBMC simulations of pure component isotherms presented in earlier work.[69]

	Site A			Site B		
	$q_{A,sat}$ mol kg^{-1}	b_A Pa$^{-\nu_A}$	ν_A dimensionless	$q_{B,sat}$ mol kg^{-1}	b_B Pa$^{-\nu_B}$	ν_B dimensionless
CO_2	1.5	2.32×10^{-6}	0.74	3	5.89×10^{-6}	1
CH_4	1.4	4.04×10^{-6}	1	1.95	2.11×10^{-6}	0.74

Fitted Wilson non-ideality parameters for binary CO_2/CH_4 mixture adsorption in DDR at 300 K.

	Λ_{12}	Λ_{21}	C / kg mol^{-1}
CO_2/CH_4 in DDR	0.81	3	0.34

Table 14. Dual-site Langmuir-Freundlich parameters for pure components CO_2, and CH_4 at 300 K in all-silica AFX zeolite. The fit parameters are based on the CBMC simulations of pure component isotherms presented in earlier works.[70, 71]

	Site A			Site B		
	$q_{A,sat}$ mol kg^{-1}	b_A Pa$^{-\nu_A}$	ν_A dimensionless	$q_{B,sat}$ mol kg^{-1}	b_B Pa$^{-\nu_B}$	ν_B dimensionless
CO_2	3.0	1.07×10^{-5}	0.78	6.4	7.95×10^{-5}	0.92
CH_4	2.9	1.76×10^{-8}	1	3.1	1.24×10^{-6}	1
N_2	3.2	4.73×10^{-7}	1	3.3	1.74×10^{-8}	1

Fitted Wilson non-ideality parameters for binary CO_2/CH_4, and CO_2/N_2 mixture adsorption in AFX at 300 K.

	Λ_{12}	Λ_{21}	C / kg mol^{-1}
CO_2/CH_4 in AFX	3.1	0.32	0.16
CO_2/N_2 in AFX	0.45	2.2	0.84

Table 15. Dual-site Langmuir parameters for pure components CO_2, and CH_4 at 300 K in all-silica MOR zeolite. The fit parameters are based on the CBMC simulations of pure component isotherms presented in earlier works.[70, 71]

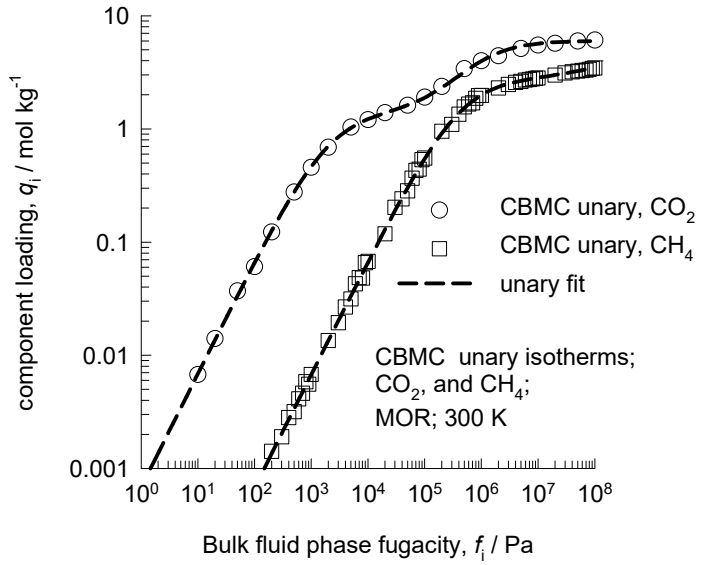

	Site A			Site B		
	$q_{A,sat}$ mol kg^{-1}	b_A Pa$^{-\nu_A}$	ν_A dimensionless	$q_{B,sat}$ mol kg^{-1}	b_B Pa$^{-\nu_B}$	ν_B dimensionless
CO_2	1.4	4.84×10^{-4}	1	4.6	1.27×10^{-6}	1
CH_4	1.05	1.59×10^{-8}	1	2.8	2.39×10^{-6}	1

Fitted Wilson non-ideality parameters for binary CO_2/CH_4 mixture adsorption in MOR at 300 K.

	Λ_{12}	Λ_{21}	C / kg mol^{-1}
CO_2/CH_4 in MOR	0.16	6.2	0.46

Table 16. Dual-site Langmuir-Freundlich parameters for pure components CO_2, and CH_4 at 300 K in NaX zeolite containing 86 Na^+/uc with Si/Al=1.23. The fit parameters are based on the CBMC simulations of pure component isotherms.

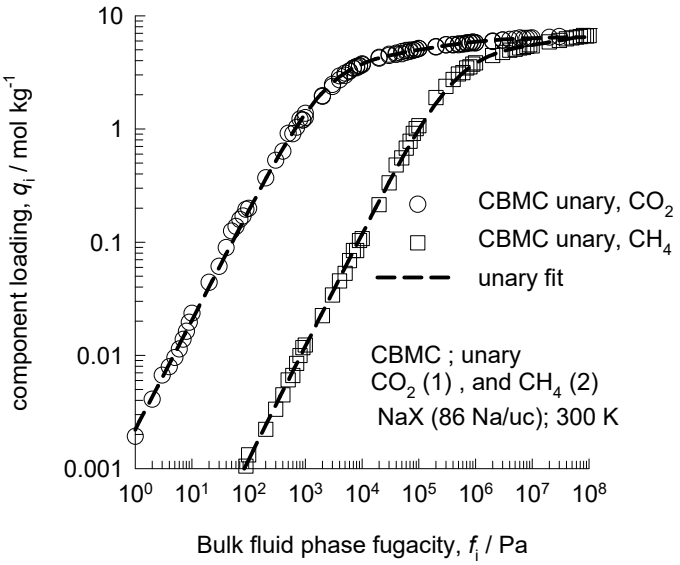

	Site A			Site B		
	$q_{A,sat}$ mol kg^{-1}	b_A Pa$^{-\nu_A}$	ν_A dimensionless	$q_{B,sat}$ mol kg^{-1}	b_B Pa$^{-\nu_B}$	ν_B dimensionless
CO_2	2.1	1.57×10^{-4}	0.7	4.4	4.26×10^{-4}	1
CH_4	2.3	1.24×10^{-8}	1	5.5	2.17×10^{-6}	1

Fitted Wilson non-ideality parameters for binary CO_2/CH_4 mixture adsorption in NaX at 300 K.

	Λ_{12}	Λ_{21}	C / kg mol^{-1}
CO_2/CH_4 in NaX (86 Na/uc) at 300 K	0.18	4.5	0.33

Table 17. Dual-site Langmuir-Freundlich parameters for pure components CO_2, N_2 and H_2 at 313 K in NaX zeolite containing 86 Na^+/uc with Si/Al=1.23. The fit parameters are based on the CBMC simulations of pure component isotherms.

	Site A			Site B		
	$q_{A,sat}$ mol kg^{-1}	b_A Pa$^{-\nu_A}$	ν_A dimensionless	$q_{B,sat}$ mol kg^{-1}	b_B Pa$^{-\nu_B}$	ν_B dimensionless
CO_2	2.25	6.64×10^{-5}	0.7	4.5	1.86×10^{-4}	1
N_2	5.6	2.85×10^{-9}	1	3.7	1.2×10^{-7}	1
H_2	9.8	4.33×10^{-10}	1	11	1.29×10^{-8}	1

Fitted Wilson non-ideality parameters for binary CO_2/N_2, and CO_2/H_2 mixture adsorption in NaX at 313 K.

	Λ_{12}	Λ_{21}	C / kg mol^{-1}
CO_2/N_2 in NaX (86 Na/uc) at 313 K	1.76	0.6	0.2
CO_2/H_2 in NaX (86 Na/uc) at 313 K	1	10^3	0.001

Table 18. Dual-site Langmuir-Freundlich parameters for pure components CO_2, and CH_4 at 300 K in NaY zeolite containing 54 Na^+/uc with Si/Al=2.56. The fit parameters are based on the CBMC simulations of pure component isotherms.

	Site A			Site B		
	$q_{A,sat}$ mol kg^{-1}	b_A Pa$^{-\nu_A}$	ν_A dimensionless	$q_{B,sat}$ mol kg^{-1}	b_B Pa$^{-\nu_B}$	ν_B dimensionless
CO_2	1.8	2×10^{-5}	0.7	5.9	4.16×10^{-5}	1
CH_4	3.4	6.53×10^{-9}	1	5.9	1.13×10^{-6}	1

Table 19. Dual-site Langmuir-Freundlich parameters for pure components CO_2, and CH_4 at 200 K, and 300K in all-silica FAU. The fit parameters are based on the CBMC simulations of pure component isotherms presented in earlier works.[70, 79, 103]

	Site A			Site B		
	$q_{A,sat}$ mol kg^{-1}	b_A Pa$^{-\nu_A}$	ν_A dimensionless	$q_{B,sat}$ mol kg^{-1}	b_B Pa$^{-\nu_B}$	ν_B dimensionless
CO_2 at 200 K	4.2	4.71×10^{-5}	1	5.9	5.14×10^{-17}	4.3
CH_4 at 200 K	2.3	2.04×10^{-12}	2.3	4.4	3.71×10^{-6}	1
CO_2 at 300 K	2.4	2.52×10^{-14}	2.4	6.7	6.74×10^{-7}	1
CH_4 at 300 K	4	7×10^{-9}	0.86	6.5	2.75×10^{-7}	1

Table 20. Dual-site Langmuir-Freundlich parameters for pure components CO_2, and CH_4 at 300 K in LTA-4A zeolite. The fit parameters are based on the CBMC simulations of pure component isotherms.

	Site A			Site B		
	$q_{A,sat}$ mol kg^{-1}	b_A Pa$^{-\nu_A}$	ν_A dimensionless	$q_{B,sat}$ mol kg^{-1}	b_B Pa$^{-\nu_B}$	ν_B dimensionless
CO_2	1.8	2.19×10^{-4}	0.5	2.9	4.19×10^{-4}	1
CH_4	1.6	1.72×10^{-7}	1	4	1.18×10^{-5}	1

Fitted Wilson non-ideality parameters for binary CO_2/CH_4 mixture adsorption in LTA-4A at 300 K.

	Λ_{12}	Λ_{21}	C / kg mol^{-1}
CO_2/CH_4 in LTA-4A at 300 K	49	0.12	0.012

Table 21. Dual-site Langmuir parameters for pure components CO_2, and CH_4 at 303 K in 13X zeolite. These parameters are based on the unary isotherm data reported in Figure 2 and Figure 3 of Gholipour and Mofarahi.[80]

	Site A		Site B	
	$q_{A,sat}$ mol kg^{-1}	b_A Pa^{-1}	$q_{B,sat}$ mol kg^{-1}	b_B Pa^{-1}
CO_2	3.1	9.38×10^{-6}	2.5	4.4×10^{-4}
CH_4	6.7	7.64×10^{-7}		

Table 22. Dual-site Langmuir parameters for pure components CO_2, and CH_4 at 303 K in LTA-5A zeolite. These parameters are based on the unary isotherm data reported in Figure 2 and Figure 3 of Mofarahi and Gholipour.[85]

	Site A		Site B	
	$q_{A,sat}$ mol kg^{-1}	b_A Pa^{-1}	$q_{B,sat}$ mol kg^{-1}	b_B Pa^{-1}
CO_2	1.4	7.33×10^{-6}	2.5	7.32×10^{-4}
CH_4	3.2	1.74×10^{-6}		

Table 23. Dual-site Langmuir parameters for pure components C_2H_4, and C_2H_6 at 283 K in LTA-5A zeolite. These parameters are based on the unary isotherm data reported in Table 2 and Table 3 of Mofarahi and Salehi.[86]

	Site A		Site B	
	$q_{A,sat}$ mol kg^{-1}	b_A Pa^{-1}	$q_{B,sat}$ mol kg^{-1}	b_B Pa^{-1}
C_2H_4	2.05	4.12×10^{-4}	1.15	2.05×10^{-5}
C_2H_6	2.44	5.56×10^{-5}		

Table 24. Dual-site Langmuir-Freundlich parameters for pure components CO_2, C_3H_8, C_2H_4,and C_2H_6 at 293 K in NaX zeolite.[16] The fit parameters were determined by fitting the unary isotherm data presented in Figure 1 of Siperstein and Myers.[16]

	Site A			Site B		
	$q_{A,sat}$ mol kg^{-1}	b_A Pa$^{-\nu_A}$	ν_A dimensionless	$q_{B,sat}$ mol kg^{-1}	b_B Pa$^{-\nu_B}$	ν_B dimensionless
CO_2	5.7	2.94×10^{-3}	0.64	1.1	1.63×10^{-2}	0.92
C_3H_8	1.8	1.47×10^{-5}	1.75	1.5	3.56×10^{-3}	0.75
C_2H_4	1.8	2.1×10^{-3}	1	2.6	1.19×10^{-3}	0.76
C_2H_6	3.4	7.27×10^{-7}	1.48	0.2	8.12×10^{-4}	1

Wilson non-ideality parameters for binary mixtures at 293 K in NaX zeolite. These are determined by fitting to the experimental data of Siperstein and Myers,[16] as reported in Table C1 of their publication.

	Λ_{12}	Λ_{21}	C / kg mol^{-1}
CO_2/C_3H_8 in NaX	1.85	5.1	0.08
C_2H_4/C_2H_6 in NaX	2.06	1	0.083

Table 25. Dual-site Langmuir parameters for pure components CO_2, C_2H_4, C_3H_6, and C_3H_8 at 293 K in 13X (= NaX) zeolite. The fit parameters were determined by fitting the unary isotherm data presented in Table I of Costa et al.[81]

	Site A		Site B	
	$q_{A,sat}$ mol kg^{-1}	b_A Pa^{-1}	$q_{B,sat}$ mol kg^{-1}	b_B Pa^{-1}
CO_2	2.2	6.7×10^{-4}	2.5	3.47×10^{-5}
C_2H_4	1.35	2.25×10^{-4}	1.4	2.57×10^{-4}
C_3H_6	0.95	5.72×10^{-4}	1.5	5.98×10^{-2}
C_3H_8	2.2	7.04×10^{-4}		

Wilson non-ideality parameters for binary mixtures at 293 K in NaX zeolite. These are determined by fitting to the experimental data of Costa et al.[81] as reported in their paper.

	Λ_{12}	Λ_{21}	C / kg mol^{-1}
CO_2/C_3H_8 in NaX	2	1.8	0.2
CO_2/C_2H_4 in NaX	3.35	0.07	0.2
CO_2/C_3H_6 in NaX	7.8	0.13	0.2
C_3H_6/C_3H_8 in NaX	0.15	6.7	0.2
C_2H_4/C_3H_8 in NaX	1.2	1.4	0.2

Table 26. Dual-site Langmuir-Freundlich parameters for pure components C_2H_4,and iso-C_4H_{10} at 298 K in NaX zeolite. The fit parameters were determined by fitting the unary isotherm data presented in Table I of Hyun and Danner.[83]

	Site A		Site B	
	$q_{A,sat}$ mol kg^{-1}	b_A Pa^{-1}	$q_{B,sat}$ mol kg^{-1}	b_B Pa^{-1}
C_2H_4	0.75	2.14×10^{-3}	2.15	1.27×10^{-4}
iso-C_4H_{10}	1.4	7.49×10^{-3}	0.5	6.44×10^{-5}

Wilson non-ideality parameters for binary mixture in NaX zeolite. These are determined by fitting to the experimental data in Table III of Hyun and Danner.[83]

	Λ_{12}	Λ_{21}	C / kg mol^{-1}
C_2H_4/ iso-C_4H_{10} in NaX	0.018	56	0.033

Table 27. Dual-site Langmuir parameters for pure components CO_2, C_2H_4, and C_3H_8 at 293 K in ZSM-5 (with MFI topology) zeolite with Si/Al ratio = 15. The fit parameters were determined by fitting the unary isotherm data presented in Table 2 of Calleja et al.[84]

	Site A		Site B	
	$q_{A,sat}$ mol kg^{-1}	b_A Pa^{-1}	$q_{B,sat}$ mol kg^{-1}	b_B Pa^{-1}
CO_2	1.35	3.32×10^{-5}	1.1	4.5×10^{-3}
C_2H_4	1.25	2.51×10^{-5}	1.1	1×10^{-2}
C_3H_8	0.76	3.62×10^{-4}	0.9	1×10^{-2}

Wilson non-ideality parameters for binary mixtures at 293 K in ZSM-5 (with MFI topology) zeolite with Si/Al ratio = 15. These are determined by fitting to the experimental data of Calleja et al.[84] as reported in Table 5 of their paper.

	Λ_{12}	Λ_{21}	C / kg mol^{-1}
CO_2/C_3H_8 in ZSM-5 (Si/Al=15)	0.2	5.1	0.9
CO_2/C_2H_4 in ZSM-5 (Si/Al=15)	2.8	10^{-6}	0.9
C_2H_4/C_3H_8 in ZSM-5 (Si/Al=15)	1.8	2	0.9

Table 28. Dual-site Langmuir parameters for pure components CO_2, C_3H_8, and H_2S at 303 K in H-MOR. The fit parameters were determined by fitting the unary isotherm data presented in Table 4 of Talu and Zwiebel.[18]

	Site A		Site B	
	$q_{A,sat}$ mol kg^{-1}	b_A Pa^{-1}	$q_{B,sat}$ mol kg^{-1}	b_B Pa^{-1}
CO_2	2.4	2.02×10^{-5}	0.6	1.37×10^{-3}
C_3H_8	0.65	1.63×10^{-5}	0.72	1.7×10^{-3}
H_2S	1.5	9.79×10^{-5}	1.2	4.99×10^{-3}

Wilson non-ideality parameters for binary mixtures at 303 K in H-MOR. These are determined by fitting to the experimental data of Talu and Zwiebel[18] as reported in Table 5 of their paper.

	Λ_{12}	Λ_{21}	C / kg mol^{-1}
CO_2/C_3H_8 in H-MOR	4.15	7.25	0.7
CO_2/H_2S in H-MOR	0.48	2.1	0.7
C_3H_8/H_2S in H-MOR	4.4	11.4	0.7

Table 29. Langmuir parameters for adsorption of CH_4, and N_2 in Ba-ETS-4 at 283.15 K. The isotherm parameters are taken from Table 3 of Majumdar et al.[89], and Table 3.2 of the Ph.D. dissertation of Bhadra.[91] The cited parameters are converted to the units that are consistent with the other data presented in our article. For conversion purposes, we use the framework density for BaETS-4 of 1720 kg m^{-3}.

	q_{sat} mol kg^{-1}	b Pa^{-1}
CH_4	0.5	9.3×10^{-6}
N_2	1.4	9.02×10^{-6}

Table 30. Dual-site Langmuir-Freundlich parameters for hydrocarbons in MFI at 300 K.

	Site A			Site B		
	$\Theta_{A,sat}$ molecules uc^{-1}	b_A Pa$^{-\nu}$	ν_A dimensionless	$\Theta_{B,sat}$ molecules uc^{-1}	b_B Pa$^{-\nu}$	ν_B dimensionless
CH_4	4.2	1.28×10^{-6}	0.77	16	3.23×10^{-6}	1
C_2H_6	3.3	4.08×10^{-7}	1	13	7.74×10^{-5}	1
C_2H_4	6.9	2×10^{-4}	0.65	10.1	6.96×10^{-6}	1.2
C_3H_8	1.4	3.35×10^{-4}	0.67	10.7	6.34×10^{-4}	1.06
C_3H_6	0.6	2.91×10^{-6}	1	11.4	6.53×10^{-4}	1
nC_4H_{10}	1.5	2.24×10^{-3}	0.57	8.7	9.75×10^{-3}	1.12
iC_4H_{10}	4	2.29×10^{-2}	1	6	2.87×10^{-5}	1
nC6	6.6	0.708	0.83	1.4	16.6	1.5
2MP	4	4.51	1.05	4	7.92×10^{-6}	1.13
Benzene	4	1.36×10^{-1}	1.06	8	2.34×10^{-3}	0.52

Table 31. Wilson non-ideality parameters for binary mixtures in all-silica MFI zeolite at 300 K. The units of C are uc molecule^{-1}.

	Λ_{12}	Λ_{21}	C / uc molecule^{-1}
CH_4/iC4 in MFI	3.3	2.3	0.083
C_2H_6/iC4 in MFI	14.3	0.76	0.09
C_3H_8/iC4 in MFI	4.1	2.9	0.048
nC4/iC4 in MFI	5.6	0.28	0.17
nC6/2MP in MFI	0.6	0.34	0.106
CH_4/Benzene in MFI	4.1	4.3	0.042
C_2H_4/Benzene in MFI	19.3	1.38	0.08
C_3H_6/Benzene in MFI	20.9	2.5	0.05

Note: The RAST model implementation of Titze et al. [99] for nC4/iC4 and nC6/2MP mixture adsorption does not include the correction factor $\left(1-\exp\left(-C\frac{\pi A}{RT}\right)\right)$. Consequently, the Wilson parameters reported in their work are different from those listed above.

Table 32. Dual-site Langmuir-Freundlich parameters for hydrocarbons in MFI at 653 K; the data are fitted to CBMC simulation data from earlier publications.[105-107]

	Site A			Site B		
	$\Theta_{A,sat}$ molecules uc^{-1}	b_A Pa$^{-\nu}$	ν_A dimensionless	$\Theta_{B,sat}$ molecules uc^{-1}	b_B Pa$^{-\nu}$	ν_B dimensionless
C_2H_4	5	4.03×10^{-9}	1	11	9.36×10^{-8}	1
Benzene	6.8	1.36×10^{-7}	0.77	4	1.82×10^{-6}	1

Wilson non-ideality parameters for binary mixtures in all-silica MFI zeolite at 653 K. The units of C are uc molecule^{-1}.

	Λ_{12}	Λ_{21}	C / uc molecule^{-1}
C_2H_4/Benzene in MFI	2.7	4.5	0.05

Table 33. Dual-site Langmuir-Freundlich parameters for pure components CO_2, and CH_4 at 200 K, and 300K in IRMOF-1. The fit parameters are based on the CBMC simulations of pure component isotherms presented in earlier works.[70, 79, 103]

	Site A			Site B		
	$q_{A,sat}$ mol kg^{-1}	b_A $Pa^{-\nu_A}$	ν_A dimensionless	$q_{B,sat}$ mol kg^{-1}	b_B $Pa^{-\nu_B}$	ν_B dimensionless
CO_2 at 200 K	26	5.31×10^{-58}	13	11	1.61×10^{-5}	1
CH_4 at 200 K	27	1.66×10^{-7}	1.2	12	6.62×10^{-6}	0.67
CO_2 at 300 K	12	6.93×10^{-19}	3	21	3.85×10^{-7}	1
CH_4 at 300 K	30	1.29×10^{-7}	1	11	2.21×10^{-7}	0.67

The fitted Wilson parameters for CO_2/CH_4 mixture adsorption in IRMOF-1 at 200 K are

	Λ_{12}	Λ_{21}	C / kg mol^{-1}
CO_2/CH_4/IRMOF-1/200K	0.001	1.15	0.35

Table 34. Dual-site Langmuir-Freundlich parameters for pure components CO_2, and CH_4 at 200 K, and 300 K in all-silica AFI. The fit parameters are based on the CBMC simulations of pure component isotherms presented in earlier works.[70, 79, 103]

	Site A			Site B		
	$q_{A,sat}$ mol kg^{-1}	b_A $Pa^{-\nu_A}$	ν_A dimensionless	$q_{B,sat}$ mol kg^{-1}	b_B $Pa^{-\nu_B}$	ν_B dimensionless
CO_2 at 200 K	2.25	3.8×10^{-13}	3.3	1.9	7.5×10^{-5}	1
CH_4 at 200 K	2.7	1.71×10^{-5}	1	1.5	4.03×10^{-8}	1
CO_2 at 300 K	3.6	3.39×10^{-7}	1.1	1.65	6.6×10^{-6}	0.6
CH_4 at 300 K	1.5	1.58×10^{-6}	1	1.5	1.18×10^{-7}	1

52. References

(1) Baerlocher, C.; Meier, W. M.; Olson, D. H. *Atlas of Zeolite Framework Types*; 5th Edition, Elsevier: Amsterdam, 2002.

(2) Baerlocher, C.; McCusker, L. B. Database of Zeolite Structures. http://www.iza-structure.org/databases/, International Zeolite Association, 10 January 2002.

(3) Krishna, R. Diffusion in Porous Crystalline Materials. *Chem. Soc. Rev.* **2012**, *41*, 3099-3118.

(4) Krishna, R. The Maxwell-Stefan Description of Mixture Diffusion in Nanoporous Crystalline Materials. *Microporous Mesoporous Mater.* **2014**, *185*, 30-50.

(5) Krishna, R. Describing the Diffusion of Guest Molecules inside Porous Structures. *J. Phys. Chem. C* **2009**, *113*, 19756-19781.

(6) Krishna, R.; van Baten, J. M. Investigating the Relative Influences of Molecular Dimensions and Binding Energies on Diffusivities of Guest Species Inside Nanoporous Crystalline Materials *J. Phys. Chem. C* **2012**, *116*, 23556-23568.

(7) Krishna, R.; van Baten, J. M. Investigating the Influence of Diffusional Coupling on Mixture Permeation across Porous Membranes *J. Membr. Sci.* **2013**, *430*, 113-128.

(8) Krishna, R.; van Baten, J. M. Influence of Adsorption Thermodynamics on Guest Diffusivities in Nanoporous Crystalline Materials. *Phys. Chem. Chem. Phys.* **2013**, *15*, 7994-8016.

(9) Krishna, R.; van Baten, J. M. Insights into diffusion of gases in zeolites gained from molecular dynamics simulations. *Microporous Mesoporous Mater.* **2008**, *109*, 91-108.

(10) Krishna, R.; van Baten, J. M. Diffusion of alkane mixtures in MFI zeolite. *Microporous Mesoporous Mater.* **2008**, *107*, 296-298.

(11) Krishna, R.; van Baten, J. M. Separating n-alkane mixtures by exploiting differences in the adsorption capacity within cages of CHA, AFX and ERI zeolites. *Sep. Purif. Technol.* **2008**, *60*, 315-320.

(12) Krishna, R.; van Baten, J. M. Entropy-based Separation of Linear Chain Molecules by Exploiting Differences in the Saturation Capacities in Cage-type Zeolites. *Sep. Purif. Technol.* **2011**, *76*, 325-330.

(13) Krishna, R. Separating Mixtures by Exploiting Molecular Packing Effects in Microporous Materials. *Phys. Chem. Chem. Phys.* **2015**, *17*, 39-59.

(14) Ruthven, D. M. *Principles of Adsorption and Adsorption Processes*; John Wiley: New York, 1984.

(15) Myers, A. L.; Prausnitz, J. M. Thermodynamics of Mixed Gas Adsorption. *A.I.Ch.E.J.* **1965**, *11*, 121-130.

(16) Siperstein, F. R.; Myers, A. L. Mixed-Gas Adsorption. *A.I.Ch.E.J.* **2001**, *47*, 1141-1159.

(17) Talu, O.; Myers, A. L. Rigorous Thermodynamic Treatment of Gas-Adsorption. *A.I.Ch.E.J.* **1988**, *34*, 1887-1893.

(18) Talu, O.; Zwiebel, I. Multicomponent Adsorption Equilibria of Nonideal Mixtures. *A.I.Ch.E.J.* **1986**, *32*, 1263-1276.

(19) Hefti, M.; Marx, D.; Joss, L.; Mazzotti, M. Adsorption Equilibrium of Binary Mixtures of Carbon Dioxide and Nitrogen on Zeolites ZSM-5 and 13X. *Microporous Mesoporous Mater.* **2015**, *215*, 215-228.

(20) Krishna, R. Using the Maxwell-Stefan formulation for Highlighting the Influence of Interspecies (1-2) Friction on Binary Mixture Permeation across Microporous and Polymeric Membranes. *J. Membr. Sci.* **2017**, *540*, 261-276.

(21) Krishna, R.; Baur, R. Modelling Issues in Zeolite Based Separation Processes. *Sep. Purif. Technol.* **2003**, *33*, 213-254.

(22) Krishna, R.; van Baten, J. M. Unified Maxwell-Stefan Description of Binary Mixture Diffusion in Micro- and Meso- Porous Materials. *Chem. Eng. Sci.* **2009**, *64*, 3159-3178.

(23) Krishna, R.; van Baten, J. M. Maxwell-Stefan modeling of slowing-down effects in mixed gas permeation across porous membranes. *J. Membr. Sci.* **2011**, *383*, 289-300.

(24) Krishna, R. Tracing the Origins of Transient Overshoots for Binary Mixture Diffusion in Microporous Crystalline Materials. *Phys. Chem. Chem. Phys.* **2016**, *18*, 15482-15495.

(25) Krishna, R.; van Baten, J. M. A molecular dynamics investigation of the diffusion characteristics of cavity-type zeolites with 8-ring windows. *Microporous Mesoporous Mater.* **2011**, *137*, 83-91.

(26) Kooijman, H. A.; Taylor, R. A dynamic nonequilibrium model of tray distillation columns. *A.I.Ch.E.J.* **1995**, *41*, 1852-1863.

(27) Michelsen, M. An efficient general purpose method of integration of stiff ordinary differential equations. *A.I.Ch.E.J.* **1976**, *22*, 594-597.

(28) Bulirsch, R.; Stoer, J. Numerical treatment of ordinary differential equations by extrapolation methods. *Numer. Math.* **1966**, *8*, 1-14.

(29) Krishna, R.; Baur, R. Diffusion, Adsorption and Reaction in Zeolites: Modelling and Numerical Issues. http://krishna.amsterchem.com/zeolite/, University of Amsterdam, Amsterdam, 1 January 2015.

(30) Krishna, R.; van Baten, J. M. Investigating the potential of MgMOF-74 membranes for CO_2 capture. *J. Membr. Sci.* **2011**, *377*, 249-260.

(31) He, Y.; Krishna, R.; Chen, B. Metal-Organic Frameworks with Potential for Energy-Efficient Adsorptive Separation of Light Hydrocarbons. *Energy Environ. Sci.* **2012**, *5*, 9107-9120.

(32) Krishna, R. Methodologies for Evaluation of Metal-Organic Frameworks in Separation Applications. *RSC Adv.* **2015**, *5*, 52269-52295.

(33) Krishna, R. Screening Metal-Organic Frameworks for Mixture Separations in Fixed-Bed Adsorbers using a Combined Selectivity/Capacity Metric. *RSC Adv.* **2017**, *7*, 35724-35737.

(34) Krishna, R. Methodologies for Screening and Selection of Crystalline Microporous Materials in Mixture Separations. *Sep. Purif. Technol.* **2018**, *194*, 281-300. https://doi.org/10.1016/j.seppur.2017.11.056.

(35) Krishna, R.; Long, J. R. Screening metal-organic frameworks by analysis of transient breakthrough of gas mixtures in a fixed bed adsorber. *J. Phys. Chem. C* **2011**, *115*, 12941-12950.

(36) Krishna, R.; van Baten, J. M. Hydrogen Bonding Effects in Adsorption of Water-alcohol Mixtures in Zeolites and the Consequences for the Characteristics of the Maxwell-Stefan Diffusivities. *Langmuir* **2010**, *26*, 10854-10867.

(37) Krishna, R.; van Baten, J. M. Highlighting Pitfalls in the Maxwell-Stefan Modeling of Water-Alcohol Mixture Permeation across Pervaporation Membranes. *J. Membr. Sci.* **2010**, *360*, 476-482.

(38) Krishna, R.; van Baten, J. M. Mutual slowing-down effects in mixture diffusion in zeolites. *J. Phys. Chem. C* **2010**, *114*, 13154-13156.

(39) Krishna, R.; van Baten, J. M. A Molecular Dynamics Investigation of the Unusual Concentration Dependencies of Fick Diffusivities in Silica Mesopores. *Microporous Mesoporous Mater.* **2011**, *138*, 228-234.

(40) Krishna, R.; van Baten, J. M. A rationalization of the Type IV loading dependence in the Kärger-Pfeifer classification of self-diffusivities. *Microporous Mesoporous Mater.* **2011**, *142*, 745-748.

(41) Gutierrez-Sevillano, J. J.; Calero, S.; Krishna, R. Selective Adsorption of Water from Mixtures with 1-Alcohols by Exploitation of Molecular Packing Effects in CuBTC. *J. Phys. Chem. C* **2015**, *119*, 3658-3666.

(42) Gutierrez-Sevillano, J. J.; Calero, S.; Krishna, R. Separation of Benzene from Mixtures with Water, Methanol, Ethanol, and Acetone: Highlighting Hydrogen Bonding and Molecular Clustering Influences in CuBTC. *Phys. Chem. Chem. Phys.* **2015**, *17*, 20114-20124.

(43) Kärger, J.; Binder, T.; Chmelik, C.; Hibbe, F.; Krautscheid, H.; Krishna, R.; Weitkamp, J. Microimaging of transient guest profiles to monitor mass transfer in nanoporous materials. *Nature Materials* **2014**, *13*, 333-343.

(44) Zhang, C.; Yang, X. Molecular dynamics simulation of ethanol/water mixtures for structure and diffusion properties. *Fluid Phase Equilib.* **2005**, *231*, 1-10.

(45) Fleys, M.; Thompson, R. W. Monte Carlo Simulations of Water Adsorption Isotherms in Silicalite and Dealuminated Zeolite Y. *J. Chem. Theory Comput.* **2005**, *1*, 453-458.

(46) Newalkar, B. L.; Jasra, R. V.; Kamath, V.; Bhat, S. G. T. Sorption of water in aluminophosphate molecular sieve $AlPO_4$-5. *Microporous Mesoporous Mater.* **1998**, *20*, 129-137.

(47) Pillai, R. S.; Jasra, R. V. Computational Study for Water Sorption in AlPO4-5 and AlPO4-11Molecular Sieves. *Langmuir* **2010**, *26*, 1755-1764.

(48) Halasz, I.; Kim, S.; Marcus, B. Uncommon Adsorption Isotherm of Methanol on a Hydrophobic Y-zeolite. *J. Phys. Chem. B* **2001**, *105*, 10788-10796.

(49) Di Lella, A.; Desbiens, N.; Boutin, A.; Demachy, I.; P., U.; Bellat, J. P.; Fuchs, A. H. Molecular simulation studies of water physisorption in zeolites. *Phys. Chem. Chem. Phys.* **2006**, *8*, 5396-5406.

(50) Narasimhan, L.; Boulet, P.; Kuchta, B.; Schaef, O.; Denoyel, R.; Brunet, P. Molecular Simulations of Water and Paracresol in MFI Zeolite - A Monte Carlo Study. *Langmuir* **2009**, *25*, 11598-11607.

(51) Chmelik, C.; Bux, H.; Caro, J.; Heinke, L.; Hibbe, F.; Titze, T.; Kärger, J. Mass transfer in a Nanoscale Material Enhanced by an Opposing Flux. *Phys. Rev. Lett.* **2010**, *104*, 085902.

(52) Tsotsalas, M.; Hejcik, P.; Sumida, K.; Kalay, Z.; Furukawa, S.; Kitagawa, S. Impact of Molecular Clustering inside Nanopores on Desorption Processes. *J. Am. Chem. Soc.* **2013**, *135*, 4608-4611.

(53) Kluge, G.; Franke, T.; Schöllner, R.; Nagel, G. Estimation of Component Loadings in Fixed-Bed Adsorption from Breakthrough Curves of Binary Gas Mixtures in Nontrace Systems. *Chem. Eng. Sci.* **1991**, *46*, 368-371.

(54) Van Assche, T. R. C.; Duerinck, T.; Van der Perre, S.; Baron, G. V.; Denayer, J. F. M. Prediction of Molecular Separation of Polar−Apolar Mixtures on Heterogeneous Metal−Organic Frameworks: HKUST-1. *Langmuir* **2014**, *30*, 7878−7883.

(55) Konno, M.; Teranayabashi, M.; Takako, Y.; Saato, S. Adsorption Equilibria of Hydrocarbon Gaseous Mixtures Containing Polar Components. *J. Chem. Eng. Japan.* **1985**, *18*, 398-408.

(56) Bartholdy, S.; Bjørner, M. G.; Solbraa, E.; Shapiro, A.; Kontogeorgis, G. M. Capabilities and Limitations of Predictive Engineering Theories for Multicomponent Adsorption. *Ind. Eng. Chem. Res.* **2013**, *52*, 11552-11563.

(57) Sakuth, M.; Meyer, J.; Gmehling, J. Vapor Phase Adsorption Equilibria of Toluene + 1-Propanol Mixtures on Y-Zeolites with Different Silicon to Aluminum Ratios. *J. Chem. Eng. Data* **1995**, *40*, 895-899.

(58) Sakuth, M.; Meyer, J.; Gmehling, J. Measurement and Prediction of Binary Adsorption Equilibria of Vapors on Dealuminated Y-zeolites (DAY). *Chem. Eng. Process.* **1998**, *37*, 267-277.

(59) Zhou, H.; Korelskiy, D.; Leppäjärvi, T.; Grahn, M.; Tanskanen, J.; Hedlund, J. Ultrathin Zeolite X Membranes for Pervaporation Dehydration of Ethanol. *J. Membr. Sci.* **2012**, *399-400*, 106-111.

(60) Kuhn, J.; Castillo-Sanchez, J. M.; Gascon, J.; Calero, S.; Dubbeldam, D.; Vlugt, T. J. H.; Kapteijn, F.; Gross, J. Adsorption and Diffusion of Water, Methanol, and Ethanol in All-Silica DD3R: Experiments and Simulation. *J. Phys. Chem. C* **2009**, *113*, 14290-14301.

(61) Shu, X.; Wang, X.; Kong, Q.; Gu, X.; Xu, N. High-Flux MFI Zeolite Membrane Supported on YSZ Hollow Fiber for Separation of Ethanol/Water. *Ind. Eng. Chem. Res.* **2012**, *51*, 12073-12080.

(62) Mittal, N.; Bai, P.; Siepmann, I.; Daoutidis, P.; Tsapatsis, M. Bioethanol Enrichment using Zeolite Membranes: Molecular Modeling, Conceptual Process Design and Techno-Economic Analysis. *J. Membr. Sci.* **2017**, *540*, 464-476.

(63) Remy, T.; Saint-Remi, J. C.; Singh, R.; Webley, P. A.; Baron, G. V.; Denayer, J. F. M. Adsorption and Separation of C1-C8 Alcohols on SAPO-34. *J. Phys. Chem. C* **2011**, *115*, 8117-8125.

(64) Pera-Titus, M.; Fité, C.; Sebastián, V.; Lorente, E.; Llorens, J.; Cunill, F. Modeling Pervaporation of Ethanol/Water Mixtures within 'Real' Zeolite NaA Membranes. *Ind. Eng. Chem. Res.* **2008**, *47*, 3213-3224.

(65) Nalaparaju, A.; Zhao, X. S.; Jiang, J. W. Molecular Understanding for the Adsorption of Water and Alcohols in Hydrophilic and Hydrophobic Zeolitic Metal-Organic Frameworks. *J. Phys. Chem. C* **2010**, *114*, 11542-11550.

(66) Li, S.; Falconer, J. L.; Noble, R. D.; Krishna, R. Interpreting unary, binary and ternary mixture permeation across a SAPO-34 membrane with loading-dependent Maxwell-Stefan diffusivities. *J. Phys. Chem. C* **2007**, *111*, 5075-5082.

(67) Krishna, R.; van Baten, J. M.; García-Pérez, E.; Calero, S. Incorporating the loading dependence of the Maxwell-Stefan diffusivity in the modeling of CH_4 and CO_2 permeation across zeolite membranes. *Ind. Eng. Chem. Res.* **2007**, *46*, 2974-2986.

(68) van den Bergh, J.; Zhu, W.; Groen, J. C.; Kapteijn, F.; Moulijn, J. A.; Yajima, K.; Nakayama, K.; Tomita, T.; Yoshida, S. Natural Gas Purification with a DDR Zeolite Membrane; Permeation Modelling with Maxwell-Stefan Equations. *Stud. Surf. Sci. Catal.* **2007**, *170*, 1021-1027.

(69) Krishna, R.; van Baten, J. M. Segregation effects in adsorption of CO_2 containing mixtures and their consequences for separation selectivities in cage-type zeolites. *Sep. Purif. Technol.* **2008**, *61*, 414-423.

(70) Krishna, R.; van Baten, J. M. In silico screening of metal-organic frameworks in separation applications. *Phys. Chem. Chem. Phys.* **2011**, *13*, 10593-10616.

(71) Krishna, R.; van Baten, J. M. A comparison of the CO_2 capture characteristics of zeolites and metal-organic frameworks. *Sep. Purif. Technol.* **2012**, *87*, 120-126.

(72) Krishna, R.; van Baten, J. M. In Silico Screening of Zeolite Membranes for CO_2 Capture. *J. Membr. Sci.* **2010**, *360*, 323-333.

(73) Herm, Z. R.; Swisher, J. A.; Smit, B.; Krishna, R.; Long, J. R. Metal-Organic Frameworks as Adsorbents for Hydrogen Purification and Pre-Combustion Carbon Dioxide Capture *J. Am. Chem. Soc.* **2011**, *133*, 5664-5667.

(74) Mason, J. A.; Sumida, K.; Herm, Z. R.; Krishna, R.; Long, J. R. Evaluating Metal-Organic Frameworks for Post-Combustion Carbon Dioxide Capture via Temperature Swing Adsorption. *Energy Environ. Sci.* **2011**, *4*, 3030-3040.

(75) Palomino, M.; Corma, A.; Rey, F.; Valencia, S. New Insights on CO_2−Methane Separation Using LTA Zeolites with Different Si/Al Ratios and a First Comparison with MOFs. *Langmuir* **2010**, *26*, 1910-1917.

(76) Simmons, J. M.; Wu, H.; Zhou, W.; Yildirim, T. Carbon capture in metal–organic frameworks—a comparative study. *Energy & Environ. Sci.* **2011**, *4*, 2177-2185.

(77) Bao, Z.; Yu, L.; Ren, Q.; Lu, X.; Deng, S. Adsorption of CO_2 and CH_4 on a magnesium-based metal organic framework. *J. Colloid Interface Sci.* **2011**, *353*, 549-556.

(78) Krishna, R.; van Baten, J. M. Using molecular simulations for screening of zeolites for separation of CO_2/CH_4 mixtures. *Chem. Eng. J.* **2007**, *133*, 121-131.

(79) Krishna, R.; van Baten, J. M. Investigating cluster formation in adsorption of CO_2, CH_4, and Ar in zeolites and metal organic frameworks at sub-critical temperatures. *Langmuir* **2010**, *26*, 3981-3992.

(80) Gholipour, F.; Mofarahi, M. Adsorption Equilibrium of Methane and Carbon Dioxide on Zeolite13X: Experimental and Thermodynamic Modeling. *J. of Supercritical Fluids* **2016**, *111*, 47-54.

(81) Costa, E.; Calleja, G.; Jimenez, A.; Pau, J. Adsorption Equilibrium of Ethylene, Propane, Propylene, Carbon Dioxide, and Their Mixtures in 13X Zeolite. *J. Chem. Eng. Data* **1991**, *36*, 218-224.

(82) Calleja, G.; Jimenez, A.; Pau, J.; Domínguez, L.; Pérez, P. Multicomponent Adsorption Equilibrium of Ethylene, Propane, Propylene and CO_2 on 13X Zeolite. *Gas Sep. Purif.* **1994**, *8*, 247-256.

(83) Hyun, S. H.; Danner, R. P. Equiilbrium Adsorption of Ethane, Ethylene, Isobutane, Carbon Dioxide, and Their Binary Mixtures on 13X Molecular Sieves. *J. Chem. Eng. Data* **1982**, *27*, 196-200.

(84) Calleja, G.; Pau, J.; Calles, J. A. Pure and Multicomponent Adsorption Equilibrium of Carbon Dioxide, Ethylene, and Propane on ZSM-5 Zeolites with Different Si/Al Ratios. *J. Chem. Eng. Data* **1998**, *43*, 994-1003.

(85) Mofarahi, M.; Gholipour, F. Gas Adsorption Separation of CO_2/CH_4 System using Zeolite 5A. *Microporous Mesoporous Mater.* **2014**, *200*, 47-54.

(86) Mofarahi, M.; Salehi, S. M. Pure and Binary Adsorption Isotherms of Ethylene and Ethane on Zeolite 5A. *Adsorption* **2013**, *19*, 101-110.

(87) van Zandvoort, I.; van Klink, G. P. M.; de Jong, E.; van der Waal, J. C. Selectivity and Stability of Zeolites [Ca]A and [Ag]A towards Ethylene Adsorption and Desorption from Complex Gas Mixtures. *Microporous Mesoporous Mat.* **2018**, *263*, 142-149.

(88) Kuznicki, S. M.; Bell, V. A.; Nair, S.; Hillhouse, H. W.; Jacubinas, R. M.; Braunbarth, C. M.; Toby, B. H.; Tsapatsis, M. A titanosilicate molecular sieve with adjustable pores for size-selective adsorption of molecules. *Nature* **2001**, *412*, 720-724.

(89) Majumdar, B.; Bhadra, S. J.; Marathe, R. P.; Farooq, S. Adsorption and Diffusion of Methane and Nitrogen in Barium Exchanged ETS-4. *Ind. Eng. Chem. Res.* **2011**, *50*, 3021-3034.

(90) Bhadra, S. J.; Farooq, S. Separation of Methane Nitrogen Mixture by Pressure Swing Adsorption for Natural Gas Upgrading. *Ind. Eng. Chem. Res.* **2011**, *50*, 14030-14045.

(91) Bhadra, S. J. *Methane-Nitrogen Separation by Pressure Swing Adsorption*. Ph.D. Dissertation, National University of Singapore, Singapore, 2007.

(92) Vlugt, T. J. H.; Zhu, W.; Kapteijn, F.; Moulijn, J. A.; Smit, B.; Krishna, R. Adsorption of linear and branched alkanes in the silicalite-1. *J. Am. Chem. Soc.* **1998**, *120*, 5599-5600.

(93) Vlugt, T. J. H.; Krishna, R.; Smit, B. Molecular Simulations of Adsorption Isotherms for Linear and Branched Alkanes and Their Mixtures in Silicalite. *J. Phys. Chem. B* **1999**, *103*, 1102-1118.

(94) Krishna, R.; Smit, B.; Calero, S. Entropy effects during sorption of alkanes in zeolites. *Chem. Soc. Rev.* **2002**, *31*, 185-194.

(95) Schenk, M.; Vidal, S. L.; Vlugt, T. J. H.; Smit, B.; Krishna, R. Separation of alkane isomers by exploiting entropy effects during adsorption on silicalite-1: A configurational-bias Monte Carlo simulation study. *Langmuir* **2001**, *17*, 1558-1570.

(96) Dubbeldam, D.; Calero, S.; Vlugt, T. J. H.; Krishna, R.; Maesen, T. L. M.; Smit, B. United Atom Forcefield for Alkanes in Nanoporous Materials. *J. Phys. Chem. B* **2004**, *108*, 12301-12313.

(97) Dubbeldam, D.; Krishna, R.; Calero, S.; Yazaydın, A. Ö. Computer-Assisted Screening of Ordered Crystalline Nanoporous Adsorbents for Separation of Alkane Isomers. *Angew. Chem. Int. Ed.* **2012**, *51*, 11867-11871.

(98) Frenkel, D.; Smit, B. *Understanding Molecular Simulations: From Algorithms to Applications*; 2nd Edition, Academic Press: San Diego, 2002.

(99) Titze, T.; Chmelik, C.; Kärger, J.; van Baten, J. M.; Krishna, R. Uncommon Synergy Between Adsorption and Diffusion of Hexane Isomer Mixtures in MFI Zeolite Induced by Configurational Entropy Effects *J. Phys. Chem. C* **2014**, *118*, 2660-2665.

(100) Krishna, R.; Paschek, D. Molecular simulations of adsorption and siting of light alkanes in silicalite-1. *Phys. Chem. Chem. Phys.* **2001**, *3*, 453-462.

(101) Fernandez, M.; Kärger, J.; Freude, D.; Pampel, A.; van Baten, J. M.; Krishna, R. Mixture Diffusion in Zeolites Studied by MAS PFG NMR and Molecular Simulation. *Microporous Mesoporous Mater.* **2007**, *105*, 124-131.

(102) Grande, C. A.; Blom, R. Cryogenic Adsorption of Methane and Carbon Dioxide on Zeolites 4A and 13X. *Energy Fuels* **2014**, *28*, 6688-6693.

(103) Krishna, R.; van Baten, J. M. Highlighting a variety of unusual characteristics of adsorption and diffusion in microporous materials induced by clustering of guest molecules. *Langmuir* **2010**, *26*, 8450-8463.

(104) Getzschmann, J.; Senkovska, I.; Wallacher, D.; Tovar, M.; Fairen-Jimenez, D.; Düren, T.; van Baten, J. M.; Krishna, R.; Kaskel, S. Methane storage mechanism in the Metal-Organic Framework $Cu_3(btc)_2$: An *in situ* neutron diffraction study. *Microporous Mesoporous Mater.* **2010**, *136*, 50-58.

(105) Hansen, N.; Krishna, R.; van Baten, J. M.; Bell, A. T.; Keil, F. J. Analysis of Diffusion Limitation in the Alkylation of Benzene over H-ZSM-5 by Combining Quantum Chemical Calculations, Molecular Simulations, and a Continuum Approach. *J. Phys. Chem. C* **2009**, *113*, 235-246.

(106) Hansen, N.; Krishna, R.; van Baten, J. M.; Bell, A. T.; Keil, F. J. Reactor simulation of benzene ethylation and ethane dehydrogenation catalyzed by ZSM-5: A multiscale approach. *Chem. Eng. Sci.* **2010**, *65*, 2472-2480.

(107) Krishna, R.; Baur, R.; Van Baten, J. M. Highlighting Diffusional Coupling Effects in Zeolite Catalyzed Reactions by Combining the Maxwell-Stefan and Langmuir-Hinshelwood Formulations. *React. Chem. Eng.* **2017**, *2*, 324-336.

(108) Clark, W. M.; Rowley, R. L. The mutual diffusion coefficient of methanol - n-hexane near the consolute point. *A.I.Ch.E.J.* **1986**, *32*, 1125-1131.

(109) Krishna, R.; van Baten, J. M. Onsager coefficients for binary mixture diffusion in nanopores. *Chem. Eng. Sci.* **2008**, *63*, 3120-3140.

(110) Bakhtyari, A.; Mofarahi, M. Pure and Binary Adsorption Equilibria of Methane and Nitrogen on Zeolite 5A. *J. Chem. Eng. Data* **2014**, *59*, 626-639.

(111) Pakseresht, S.; Kazemeini, M.; Akbarnejad, M. M. Equilibrium isotherms for CO, CO_2, CH_4 and C_2H_4 on the 5A molecular sieve by a simple volumetric apparatus. *Sep. Purif. Technol.* **2002**, *28*, 53-60.

(112) Krishna, R.; van Baten, J. M. Diffusion of Hydrocarbon Mixtures in MFI Zeolite: Influence of Intersection Blocking. *Chem. Eng. J.* **2008**, *140*, 614-620.

53. Captions for Figures

Figure 1. Pore landscape and structural details of all-silica AFI zeolite.

Figure 2. Pore landscape of all-silica AFX zeolite.

Figure 3. Structural details for AFX zeolite.

Figure 4. Pore landscape of all-silica CHA zeolite.

Figure 5. Structural details for CHA zeolite.

Figure 6. Pore landscape of all-silica DDR zeolite.

Figure 7. Structural details for DDR zeolite.

Figure 8. Pore landscape of all-silica ERI zeolite.

Figure 9. Structural details for ERI zeolite.

Figure 10. Pore landscape of all-silica LTA zeolite.

Figure 11. Structural details for all-silica LTA zeolite.

Figure 12. Structural details for LTA-5A zeolite.

Figure 13. Structural details for LTA-4A zeolite.

Figure 14. Pore landscape and structural data for ZIF-8.

Figure 15. Pore landscape and structural data for ZIF-8.

Figure 16. Pore landscape and structural data for MFI zeolite.

Figure 17. Pore landscape and structural data for MFI zeolite.

Figure 18, Figure 19, Pore landscape of all-silica FER zeolite.

Figure 20. Structural details for FER zeolite.

Figure 21. Pore landscape of all-silica MOR zeolite.

Figure 22. Structural details for MOR zeolite.

Figure 23. Pore landscape of all-silica FAU zeolite.

Figure 24. Structural details for FAU zeolite.

Figure 25. Structural details of NaY zeolite with 144 Si, 48 Al, 48 Na^{+}, Si/Al=3.

Figure 26. Structural details of NaY zeolite with 138 Si, 54 Al, 54 Na^{+}, Si/Al=2.55.

Figure 27. Structural details of NaX (= 86 Na^+/uc = 13X) zeolite. Snapshots of $CO_{2\ 4}$ in the cages.

Figure 28. Pore landscape of all-silica CuBTC.

Figure 29. Structural details for CuBTC.

Figure 30. Cage connectivity of CuBTC framework.

Figure 31. Pore landscape and structural data for IRMOF-1.

Figure 32. Pore landscape and structural data for IRMOF-1.

Figure 33. Schematic of zeolite membrane permeation device.

Figure 34. Schematic of a packed bed adsorber, showing two different discretization schemes for a single spherical crystallite.

Figure 35. Summary of model equations describing packed bed adsorber, along with discretization scheme.

Figure 36. Comparison of RDF of $H_{molecule}$-$O_{molecule}$ distances for (a) water, (b) methanol, and (c) ethanol at 300 K in ZIF-8, LTA, FAU, DDR, and MFI. These data are from Krishna and van Baten.[36]

Figure 37. RDFs for equimolar binary water/methanol mixtures at 300 K in (a) DDR (total loading = 36 molecules per unit cell, i.e. 3/cage), (b) all-silica LTA (total loading = 72 molecules per unit cell), (c) all-silica FAU (total loading = 72 molecules per unit cell), and (d) MFI (total loading = 10 molecules per unit cell). The O-H distances of water-water, methanol-methanol, and water-methanol pairs are shown. These data are from Krishna and van Baten.[36]

Figure 38. RDFs for binary water/ethanol mixtures at 300 K in (a) DDR (total loading = 24 molecules per unit cell), and (v) all-silica FAU (total loading = 56 molecules per unit cell). The O-H distances of water-water, ethanol-ethanol, and water-ethanol pairs are shown. These data are from Krishna and van Baten.[36]

Figure 39. (a, b, c) RDFs for binary methanol(1)/ethanol(2) mixtures at 323 K in FER with component loadings (a) Θ_1= 0.5/uc, Θ_2= 4/uc, (b) Θ_1= 1/uc, Θ_2= 4/uc, (c) Θ_1= 2/uc, Θ_2= 2/uc. The O-H distances for methanol-methanol, ethanol-ethanol, and methanol-ethanol are compared.

(d) Comparison of the O-H distances for methanol-ethanol pairs for FER (Θ_1= 2/uc, Θ_2= 2/uc) with binary liquid mixture, i.e. without restraining walls.

Figure 40. (a, b, c) Comparing the RDFs for $H_{benzene}$-$O_{molecule}$ and $H_{molecule}$-$O_{molecule}$ distances for (a) water/benzene, (b) methanol/benzene, and (c) ethanol/benzene mixtures in CuBTC at 298 K and total fluid fugacity of 1000 Pa. (d) Comparing the RDFs for $H_{molecule}$-$O_{molecule}$ distances for quaternary water/methanol/ethanol/benzene mixtures in CuBTC at 298 K and total fluid fugacity of 1000 Pa.

Figure 41. (a, b, c, d) Comparison of the CBMC simulations[12, 36] for unary isotherms of water, methanol, and ethanol in (a) FAU, (b) MFI, (c) DDR, (d) CHA, and (e) ZIF-8 at 300 K. The continuous solid lines are dual-site Langmuir-Freundlich isotherm fits. (f) Comparison of the CBMC simulations[41, 42] for unary isotherms of water, methanol, ethanol, acetone, and benzene in CuBTC at 298 K with 3-site (for water) or 2-site Langmuir-Freundlich isotherm fits. For CuBTC, the unary isotherm fit parameters are specified in Table 1, and Table 2.

Figure 42. The inverse thermodynamic factor, $1/\Gamma_i$, plotted as a function of the molar loading$_i$, for unary adsorption of water, methanol, and ethanol in FAU, MFI, DDR, and ZIF-8. The $1/\Gamma_i$ are calculated by differentiation of dual-site Langmuir-Freundlich fits of the isotherms.

Figure 43. The inverse thermodynamic factor, $1/\Gamma_i$, plotted as a function of the molar loadings of water, methanol, ethanol, acetone, and benzene in CuBTC at 298 K. The $1/\Gamma_i$ are calculated by differentiation of multi-site Langmuir-Freundlich fits of the isotherms. The unary isotherm fit parameters are specified in Table 1, and Table 2.

Figure 44. (a) Adsorption of 10 unclustered molecular species on a square lattice containing 64 adsorption sites. (b) Adsorption of dimers.

Figure 45. CBMC simulations[41, 42] for (a) water/methanol, (b) water/ethanol, (c) water/1-propanol, (d) water/methanol/ethanol/1-propanol, and (e) methanol/ethanol mixtures in CuBTC at 298 K. The partial fugacities in the bulk fluid phase are taken to be equal, i.e. $f_1=f_2$.

Figure 46. CBMC simulations[41, 42] for (a) water/benzene, (b) methanol/benzene, (c) ethanol/benzene, (d) methanol/ethanol, and (e) acetone/benzene mixtures in CuBTC at 298 K. The partial fugacities in the bulk fluid phase are taken to be equal, i.e. $f_1=f_2$.

Figure 47. Comparison of CBMC simulations[41, 42] for (a) water/methanol, (b) water/ethanol, (c) water/1-propanol, (d) water/methanol/ethanol/1-propanol, and (e) methanol/ethanol mixtures in

CuBTC at 298 K with IAST calculations. The partial fugacities in the bulk fluid phase are taken to be equal, i.e. $f_1=f_2=f_3=f_4$. The unary isotherm fit parameters are specified in Table 1, and Table 2.

Figure 48. Comparison of CBMC simulations[41, 42] for (a) water/benzene, (b) methanol/benzene, (c) ethanol/benzene, (d) methanol/ethanol, (e) acetone/benzene, and (f) water/methanol/ethanol/benzene mixtures in CuBTC at 298 K with IAST calculations. The partial fugacities in the bulk fluid phase are taken to be equal, i.e. $f_1=f_2=f_3=f_4$. The unary isotherm fit parameters are specified in Table 1, and Table 2.

Figure 49. (a, b) Dependence of $q_{t,IAST}-q_{t,CBMC}$ on (a) adsorption potential, $\frac{\pi A}{RT}$, and (b) adsorbed phase mole function of component 1 determined from CBMC simulation, for methanol/ethanol, methanol/benzene, ethanol/benzene, acetone/benzene, water/methanol, and water/ethanol mixtures in CuBTC at 298 K. The unary isotherm fit parameters are specified in Table 2.

Figure 50. (a, b, c, d) Comparison of CBMC simulations with IAST and RAST calculations of the component loadings for (a) methanol/ethanol, (b) methanol/benzene, (c) ethanol/benzene, and (d) acetone/benzene mixtures in CuBTC at 298 K. The partial fugacities in the bulk fluid

phase are taken to be equal, i.e. $f_1=f_2$. The unary isotherm fit parameters are specified in Table 2. The Wilson parameters as reported in Table 3.

Figure 51. (a, b, c, d) RAST calculations of the activity coefficients for equimolar (a) methanol/ethanol, (b) methanol/benzene, (c) ethanol/benzene, and (d) acetone/benzene mixtures in CuBTC at 298 K. The unary isotherm fit parameters are specified in Table 2. The partial fugacities in the bulk fluid phase are taken to be equal, i.e. $f_1=f_2$. The Wilson parameters as reported in Table 3.

Figure 52. (a, b, c, d) Comparison of CBMC simulations with IAST and RAST calculations of the adsorption selectivities for (a) methanol/ethanol, (b) methanol/benzene, (c) ethanol/benzene, and (d) acetone/benzene mixtures in CuBTC at 298 K. The partial fugacities in the bulk fluid phase are taken to be equal, i.e. $f_1=f_2$. The unary isotherm fit parameters are specified in Table 2. The Wilson parameters as reported in Table 3.

Figure 53. (a, b, c, d) Comparison of CBMC simulations with IAST and RAST calculations of the separation potential, ΔQ, for (a) methanol/ethanol, (b) methanol/benzene, (c) ethanol/benzene, and (d) acetone/benzene mixtures in CuBTC at 298 K. The partial fugacities in the bulk fluid phase are taken to be equal, i.e. $f_1=f_2$. The unary isotherm fit parameters are specified in Table 2. The Wilson parameters as reported in Table 3.

Figure 54. Transient breakthrough simulations of 50/50 methanol/ethanol feed mixtures in fixed bed adsorbed packed with CuBTC at 298 K, operating at total fluid mixture fugacities: (a) $f_t = 2$ kPa, (b) $f_t = 4$ kPa, (c) $f_t = 8$ kPa, and (d) $f_t = 30$ kPa. The unary isotherm fit parameters are specified in Table 2.The Wilson parameters as reported in Table 3.

Figure 55. (a) Unary isotherm data of van Assche et al.[54] for adsorption of methanol, and n-hexane at 313 K in CuBTC; the dual-site Langmuir-Freundlich parameters are provided in Table 4. (b) Experimental data of van Assche et al.[54] for component loadings for methanol/n-hexane mixture adsorption in CuBTC as a function of the total pressure, p_t; the partial fugacities in the bulk phase are equal, i.e. $p_1=p_2$. The dashed lines are IAST estimates of component loadings; the continuous solid lines are RAST calculations using the Wilson parameters specified in Table 4. (c) Comparison of the experimental data on the methanol/n-hexane adsorption selectivity, as a function of the total pressure, p_t, with IAST and RAST calculations. (d) RAST calculations of the activity coefficients in the adsorbed phase as function of the adsorption potential, $\frac{\pi A}{RT}$.

Figure 56. (a) Experimental data of Konno et al.[55] for component loadings for methanol and n-hexane (nC6) in MSC-5A (Takeda) at 4 kPa and 303.15 K as a function of the mole fraction of methanol in the bulk vapor phase. (b) Plot of the adsorbed phase mole fraction of methanol vs

the mole fraction of methanol in the bulk vapor phase. The dashed line represent IAST estimations; the continuous solid line are the RAST calculations. (c) RAST Wilson calculations of the activity coefficients in the adsorbed phase. The unary Langmuir isotherm fits are provided in Table S1 of Bartholdy et al.[56] The "fitted" Wilson parameters are Λ_{12} = 1.2; Λ_{21}= 68; C = 0.15 kg mol^{-1}. (d) Activity coefficient in bulk liquid mixtures, calculated using the NRTL parameters of Clark and Rowley.[108]

Figure 57. (a, b) Experimental data of Sakuth et al.[57] of toluene/1-propanol mixtures in DAY-13 (dealuminated Y zeolite) at T = 298.15 K and total pressure (a) p_t = 0.36 kPa, and (b) p_t = 1.06 kPa. (c) The differences in the estimation of the total mixture loading, $q_{t,IAST}$ from the experimental data, $q_{t,exp}$ is plotted as function of the adsorbed phase mole fraction of toluene., (d, e) RAST Wilson calculations of the activity coefficients in the adsorbed phase at T = 298.15 K and total pressure (d) p_t = 0.36 kPa, and (e) p_t = 1.06 kPa. The unary isotherms were fitted with the Langmuir-Freundlich model; the fit parameters are provided in Table 5. The "fitted" Wilson parameters are provided in Table 5.

Figure 58. Comparison of IAST and RAST calculations for (a) adsorption selectivity, (b, c) uptake capacities, and (c) separation potential, $\Delta Q_{1-propanol/toluene} = Q_{toluene}\frac{y_{1-propanol}}{1-y_{1-propanol}} - Q_{1-propanol}$ for separation of toluene(1)/1-propanol(2) mixtures in DAY-13 at a total pressure p_t = 1.06 kPa,

and with varying mole fractions of toluene in the bulk vapor phase. The unary isotherm fit parameters, along with Wilson parameters are provided in Table 5.

Figure 59. Transient breakthrough simulations of toluene(1)/1-propanol(2) feed mixtures in fixed bed packed with DAY-13, operating at 298 K and p_t = 1.06 kPa. The feed mixture compositions are: (a) y_1 = 0.1, and (b) y_1 = 0.5. The unary isotherm fit parameters, along with Wilson parameters are provided in Table 5.

Figure 60. (a) Comparison of IAST and RAST calculations for separation potential, $\Delta Q_{1-propanol/toluene} = Q_{toluene} \frac{y_{1-propanol}}{1-y_{1-propanol}} - Q_{1-propanol}$ for separation of toluene(1)/1-propanol(2) mixtures in DAY-13 at a total pressure p_t = 0.36 kPa, and with varying mole fractions of toluene in the bulk vapor phase. (b) Transient breakthrough simulations of toluene(1)/1-propanol(2) feed mixtures in fixed bed packed with DAY-13, operating at 298 K and p_t = 0.36 kPa. The feed mixture composition is y_1 = 0.6. The unary isotherm fit parameters, along with Wilson parameters are provided in Table 5.

Figure 61. (a, b) Experimental data of Sakuth et al.[57] of toluene/1-propanol mixtures in DAY-55 (dealuminated Y zeolite) at T = 298.15 K and total pressure (a) p_t = 0.36 kPa, and (b) p_t = 1.04 kPa. (c, d) RAST Wilson calculations of the activity coefficients in the adsorbed phase at T =

298.15 K and total pressure (c) p_t = 0.36 kPa, and (d) p_t = 1.04 kPa. The unary isotherm fit parameters, along with Wilson parameters are provided in Table 6.

Figure 62. CBMC simulations[36] of pure component adsorption isotherms for water, methanol, and ethanol in all-silica FAU zeolite at 300 K. The continuous solid lines are the Dual-Langmuir-Freundlich fits using the parameters specified in Table **7**.

Figure 63. (a) CBMC simulations[36] for adsorption of equimolar (f_1=f_2) water/methanol mixture in FAU zeolite at 300 K compared with IAST estimates of component loadings. (b) Dependence of $q_{t,IAST} - q_{t,CBMC}$ on adsorbed phase mole function of water determined from CBMC (in the bottom axis), and the adsorption potential, $\frac{\pi A}{RT}$ (top axes). (c) CBMC simulation data vs RAST estimates. (d) RAST calculations of the activity coefficients γ_i, for water and methanol. The unary isotherm fit parameters, along with the Wilson parameters, are provided in Table **7**.

Figure 64. (a) CBMC simulations[36] for adsorption of water/methanol mixture in FAU zeolite at 300 K at 1 kPa total pressure, and varying composition in the bulk fluid phase. The continuous and dashed lines are the RAST and IAST estimates of component loadings. (b) RAST

calculations of the activity coefficients γ_i, for water and methanol. The unary isotherm fit parameters, along with the Wilson parameters, are provided in Table **7**.

Figure 65. (a) CBMC simulations[36] for adsorption of equimolar (f_1=f_2) water/ethanol mixture in FAU zeolite at 300 K compared with IAST estimates of component loadings. (b) Dependence of $q_{t,IAST} - q_{t,CBMC}$ on adsorbed phase mole function of water determined from CBMC (in the bottom axis), and the adsorption potential, $\frac{\pi A}{RT}$ (top axes). (c) CBMC simulation data vs RAST estimates. (d) RAST calculations of the activity coefficients γ_i, for water and ethanol. The unary isotherm fit parameters, along with the Wilson parameters, are provided in Table **7**.

Figure 66. (a) IAST and RAST calculations of water/ethanol adsorption selectivities, S_{ads}, for 5/95 water(1)/ethanol(2) mixtures across all-silica FAU zeolite membrane at 300 K, plotted as a function of the total upstream fugacities in the upstream compartment, f_{t0}= f_{10}+ f_{20}. The partial fugacities of the two components in the downstream compartment are taken to be $f_{1\delta}$= $f_{2\delta}$= 1 Pa. The Maxwell-Stefan diffusivities are $Đ_1 = 10^{-9}$; $Đ_2 = 10^{-10}$ m^2 s^{-1}; the membrane thickness, δ = 50 μm. (b) Mole fractions of water in the adsorbed phase, x_1 at the upstream face. (c) Activity coefficients of water, γ_1, and ethanol, γ_2 in the adsorbed phase. (d) IAST and RAST calculations of water/ethanol permeation selectivities, S_{perm}.

Figure 67. CBMC simulations of pure component adsorption isotherms for water, methanol, and ethanol in all-silica DDR zeolite at 300 K. The continuous solid lines are the Dual-Langmuir-Freundlich fits using the parameters specified in Table **8**.

Figure 68. (a) CBMC simulations[36] for adsorption of equimolar (f_1=f_2) water/methanol mixture in DDR zeolite at 300 K compared with IAST estimates of component loadings. (b) Dependence of $q_{t,IAST} - q_{t,CBMC}$ on adsorbed phase mole function of water determined from CBMC (in the bottom axis), and the adsorption potential, $\frac{\pi A}{RT}$ (top axes). (c) CBMC simulation data vs RAST estimates. (d) RAST calculations of the activity coefficients γ_i, for water and methanol. The unary isotherm fit parameters, along with the Wilson parameters, are provided in Table 8.

Figure 69. (a) CBMC simulations[36] for adsorption of equimolar (f_1=f_2) water/ethanol mixture in DDR zeolite at 300 K compared with IAST estimates of component loadings. (b) Dependence of $q_{t,IAST} - q_{t,CBMC}$ on adsorbed phase mole function of water determined from CBMC (in the bottom axis), and the adsorption potential, $\frac{\pi A}{RT}$ (top axes). (c) CBMC simulation data vs RAST estimates. (d) RAST calculations of the activity coefficients γ_i, for water and methanol. The unary isotherm fit parameters, along with the Wilson parameters, are providedin Table 8.

Figure 70. (a) Water/methanol adsorption selectivity, S_{ads}, and (b) water/methanol permeation selectivities, S_{perm} for steady-state permeation of 5/95 water(1)/methanol(2) mixtures across all-silica DDR zeolite membrane at 300 K, calculated as a function of the total upstream fugacities in the upstream compartment, $f_{t0}= f_{10}+ f_{20}$. The partial fugacities of the two components in the downstream compartment are taken to be $f_{1\delta}= f_{2\delta}= 1$ Pa. The Maxwell-Stefan diffusivities are $Đ_1 = 10^{-10}$; $Đ_2 = 10^{-11}$ m^2 s^{-1}; the membrane thickness, $\delta = 50$ μm. (c) Mole fractions of water in the adsorbed phase, x_1, and (d) activity coefficients of water, γ_1, and methanol, γ_2 in the adsorbed phase The pure component fits are provided in Table 8. The dashed lines represent calculations based on IAST estimations of phase equilibrium at the upstream and downstream faces; the continuous solid lines are the corresponding estimations using RAST with Wilson parameters specified in Table 8.

Figure 71. (a) Water/alcohol adsorption selectivity, S_{ads}, and (b) water/alcohol permeation selectivities, S_{perm} for steady-state permeation of 5/95 water(1)/ethanol(2) mixtures across all-silica DDR zeolite membrane at 300 K, calculated as a function of the total upstream fugacities in the upstream compartment, $f_{t0}= f_{10}+ f_{20}$. The partial fugacities of the two components in the downstream compartment are taken to be $f_{1\delta}= f_{2\delta}= 1$ Pa. The Maxwell-Stefan diffusivities are $Đ_1 = 10^{-10}$; $Đ_2 = 10^{-11}$ m^2 s^{-1}; the membrane thickness, $\delta = 50$ μm. (c) Mole fractions of water

in the adsorbed phase, x_1, and (d) activity coefficients of water, γ_1, and ethanol, γ_2 in the adsorbed phase. The pure component fits are provided in Table 8. The dashed lines represent calculations based on IAST estimations of phase equilibrium at the upstream and downstream faces; the continuous solid lines are the corresponding estimations using RAST with Wilson parameters specified in Table 8.

Figure 72. (a, b) Permeation fluxes of water and alcohol, and (c, d) water/alcohol permeation selectivities for transient permeation of (a, c) 5/95 water(1)/methanol(2), and (b, d) 5/95 water(1)/ethanol(2) mixtures across DDR membrane at 300 K. The dashed lines represent calculations based on IAST estimations of phase equilibrium at the upstream and downstream faces; the continuous solid lines are the corresponding estimations using RAST with Wilson parameters, specified in Table 8.

Figure 73. CBMC simulations[36] of pure component adsorption isotherms for water, methanol, and ethanol in all-silica MFI zeolite at 300 K. The continuous solid lines are the Dual-Langmuir-Freundlich fits using the parameters specified in Table **9**.

Figure 74. (a, b) CBMC simulations[36] for adsorption of equimolar (partial fugacities f_1=f_2) water/methanol mixture in MFI zeolite at 300 K. The continuous solid lines are the (a) IAST,

and (b) RAST calculations using the pure component fits in Table **9**. (c) RAST calculations of the activity coefficients γ_i, for water and methanol. The unary isotherm fit parameters, along with the Wilson parameters, are specified in Table **9**.

Figure 75. (a) CBMC simulations[36] for adsorption of equimolar (f_1=f_2) water/ethanol mixture in MFI zeolite at 300 K compared with IAST estimates of component loadings. (b) Dependence of $q_{t,IAST} - q_{t,CBMC}$ on adsorbed phase mole function of water determined from CBMC (in the bottom axis), and the adsorption potential, $\frac{\pi A}{RT}$ (top axes). (c) CBMC simulation data vs RAST estimates. (d) RAST calculations of the activity coefficients γ_i, for water and ethanol. The unary isotherm fit parameters, along with the Wilson parameters, are specified in Table **9**.

Figure 76. (a) IAST and RAST calculations of ethanol/water adsorption selectivities, S_{ads}, for 95/5 water(1)/ethanol(2) mixtures across all-silica MFI zeolite membrane at 300 K, plotted as a function of the total upstream fugacities in the upstream compartment, f_{t0}= f_{10}+ f_{20}. The partial fugacities of the two components in the downstream compartment are taken to be $f_{1\delta}$= $f_{2\delta}$= 1 Pa. The Maxwell-Stefan diffusivities are $Đ_1 = 10^{-9}$; $Đ_2 = 10^{-10}$ m^2 s^{-1}; the membrane thickness, δ = 50 μm. (b) Mole fractions of water in the adsorbed phase, x_1 at the upstream face. (c) Activity

coefficients of water, γ_1, and ethanol, γ_2 in the adsorbed phase. (d) IAST and RAST calculations of ethanol/water permeation selectivities, S_{perm}.

Figure 77. (a) CBMC simulations[12] of pure component adsorption isotherms for 1-alcohols in CHA at 300 K. Table **10** provides the pure component isotherm fit parameters. (b) Saturation capacities for adsorption of 1-alcohols in CHA at 300 K. (c) Snapshots showing the conformations of 1-alcohols in CHA at saturation conditions.

Figure 78. CBMC mixture simulations for (a) methanol/ethanol, (b) ethanol/1-propanol, (c) ethanol/1-hexanol, (d) 1-butanol/1-pentanol, (e) 1-butanol/1-hexanol, and (f) 1-pentanol/1-hexanol mixtures in CHA at 300 K. The partial fugacities in the bulk fluid phase are taken to be equal, i.e. $f_1=f_2$. The dashed lines represent IAST calculations using dual-site Langmuir-Freundlich fits of pure component isotherms. Table 10 provides the pure component isotherm fit parameters. The range of liquid phase operation is indicated by the shaded region; the transition between vapor and liquid bulk phase is determined using the Peng-Robinson equation of state.

Figure 79. (a, b) Transient breakthrough experimental data of Remy et al.[63] for separation of (a) ethanol/1-propanol, and (b) ethanol/1-hexanol mixtures in a fixed bed adsorber packed with SAPO-34.

Figure 80. (a) CBMC simulations[12] for adsorption of equimolar (f_1=f_2) methanol/ethanol mixture in CHA zeolite at 300 K compared with IAST estimates of component loadings. (b) Dependence of $q_{t,IAST} - q_{t,CBMC}$ on adsorbed phase mole function of water determined from CBMC (in the bottom axis), and the adsorption potential, $\frac{\pi A}{RT}$ (top axes). (c) CBMC simulation data vs RAST estimates. (d) RAST calculations of the activity coefficients γ_i, for water and methanol. The pure component fit parameters, along with the Wilson parameters, are provided in Table **10**.

Figure 81. (a) Methanol/ethanol adsorption selectivity, S_{ads}, and (b) methanol/ethanol permeation selectivities, S_{perm} for steady-state permeation of 50/50 methanol(1)/ethanol(2) mixtures across all-silica CHA zeolite membrane at 300 K, calculated as a function of the total upstream fugacities in the upstream compartment, f_{t0}= f_{10}+ f_{20}. The partial fugacities of the two components in the downstream compartment are taken to be $f_{1\delta}$= $f_{2\delta}$= 1 Pa. The Maxwell-Stefan diffusivities are $Đ_1 = 6\times10^{-14}$; $Đ_2 = 3\times10^{-15}$ m^2 s^{-1}; the membrane thickness, δ = 50 μm. (c) Mole fractions of ethanol in the adsorbed phase, x_2, and (d) activity coefficients of methanol, γ_1, and ethanol, γ_2 in the adsorbed phase. The pure component fit parameters, along with the Wilson parameters, are provided in Table **10**. The dashed lines represent calculations based on IAST estimations of phase equilibrium at the upstream and downstream faces; the continuous solid lines are the corresponding estimations using RAST.

Figure 82. Water permeates preferentially across LTA-4A zeolite membrane used in hybrid scheme for production of 99.5% pure ethanol.

Figure 83. (a, b) Pure component isotherms for (a) water, and (b) ethanol in LTA-4A zeolite. Experimental data of Pera-Titus.[64] The unary isotherm fit parameters are specified in Table 11.

Figure 84. Experimental data of Pera-Titus[64] for component loadings for water and ethanol in LTA-4A zeolite at 2.1 kPa and 333 K as a function of the mole fraction of water in the bulk vapor phase. The dashed lines are IAST estimations. The continuous solid lines are RAST estimations. The unary isotherm fit parameters are specified in Table 11, along with the Wilson parameters.

Figure 85. (a) Water/ethanol adsorption selectivity, S_{ads}, for water(1)/ethanol(2) mixtures in LTA-4A at 333 K and total pressure 2.1 kPa; the bulk vapor phase composition is varied in the range 0 – 0.1. (b) Activity coefficients of water, γ_1, and ethanol, γ_2 in the adsorbed phase. The unary isotherm fit parameters are specified in Table 11, along with the Wilson parameters.

Figure 86. (a, b) Permeation fluxes of water and ethanol, and (c) water/ethanol permeation selectivities for transient permeation of 5/95 water(1)/ethanol(2) mixtures across LTA-4A membrane at 333 K. The partial pressures of the two components in the downstream compartment are taken to be $f_{1\delta}$ = $f_{2\delta}$= 0.001 Pa. The Maxwell-Stefan diffusivities are $Đ_1 = 10^{-10}$; $Đ_2 = 10^{-11}$ m^2 s^{-1}; the membrane thickness, δ = 50 μm. The dashed lines represent calculations based on IAST estimations of phase equilibrium at the upstream and downstream faces; the continuous solid lines are the corresponding estimations using RAST. The dotted lines represent simulations, using the RAST, but ignoring thermodynamic coupling effects. The unary isotherm fit parameters are specified in Table 11, along with the Wilson parameters.

Figure 87. (a) CBMC simulation data of Nalaparaju et al.[65] for pure component adsorption isotherms of water (only the "adsorption" branch of the isotherms are shown here), methanol and ethanol in ZIF-71 at 298 K. (b, c) CBMC simulations of the component loadings for equimolar (b) water/methanol, (c) water/ethanol mixtures in ZIF-71. The continuous solid lines are the IAST calculations of the component loadings.

Figure 88. Snapshots showing the location of CO_2 and CH_4 within the cage/window structure of CHA zeolite. (a) % probability for adsorption of component in the window region of CHA. (b)

CBMC simulations for the component loadings in equilibrium with equimolar CO_2/CH_4 mixtures in CHA; the continuous solid lines are the IAST calculations.

Figure 89. Snapshots showing the location of CO_2 and CH_4 within the cage/window structure of LTA zeolite. (a) % probability for adsorption of component in the window region of LTA. (b) CBMC simulations for the component loadings in equilibrium with equimolar CO_2/CH_4 mixtures in LTA; the continuous solid lines are the IAST calculations.

Figure 90. Snapshots showing the location of CO_2 and CH_4 within the cage/window structure of ERI zeolite. (a) % probability for adsorption of component in the window region of ERI. (b) CBMC simulations for the component loadings in equilibrium with equimolar CO_2/CH_4 mixtures in ERI; the continuous solid lines are the IAST calculations.

Figure 91. Snapshots showing the location of CO_2 and CH_4 within the cage/window structure of DDR zeolite. (a) % probability for adsorption of component in the window region of DDR. (b) CBMC simulations for the component loadings in equilibrium with equimolar CO_2/CH_4 mixtures in DDR; the continuous solid lines are the IAST calculations.

Figure 92. (a) CBMC simulations for adsorption of equimolar (partial fugacities f_1=f_2) CO_2/CH_4 mixtures in ERI zeolite at 300 K. The continuous solid lines are the RAST calculations using the pure component fits and Wilson parameters in Table 12. (b) RAST calculations of the activity coefficients γ_i, for CO_2 and CH_4. (c) Comparison of IAST and RAST calculations of the CO_2/CH_4 adsorption selectivity with those determined from CBMC simulations.

Figure 93. (a) CBMC simulations for adsorption of equimolar (partial fugacities f_1=f_2) CO_2/CH_4 mixtures in DDR zeolite at 300 K. The continuous solid lines are the RAST calculations using the pure component fits and Wilson parameters in Table 13. (b) RAST calculations of the activity coefficients γ_i, for CO_2 and CH_4. (c) Comparison of IAST and RAST calculations of the CO_2/CH_4 adsorption selectivity with those determined from CBMC simulations.

Figure 94. Adsorption selectivities for CO_2/CH_4 mixtures at 300 K in a variety of all-silica zeolite structures, obtained from Configurational-Bias Monte Carlo (CBMC) simulations; the partial fugacities in the gas phase are equal, i.e. f_1= f_2. The data plotted here are obtained from the Supplementary Material accompanying the article of Krishna and van Baten.[70, 71] Also shown are the pore landscapes of AFX, JBW, and BIK zeolites.

Figure 95. (a, b) Comparison of the estimations using the (a) IAST and (b) RAST with CBMC simulations of component loadings of equimolar (partial fugacities f_1=f_2) CO_2/CH_4 mixtures in AFX zeolite at 300 K. (c) RAST calculations of the component activity coefficients γ_i, for CO_2 and CH_4. (d) Comparison CO_2/CH_4 adsorption selectivities obtained from CBMC with IAST and RAST estimations. The unary isotherm fit parameters, along with the Wilson parameters, are provided in Table 14.

Figure 96. (a, b) Comparison of the estimations using the (a) IAST and (b) RAST with CBMC simulations of component loadings of 15/85 (partial fugacities f_1/f_2=15/85) CO_2/N_2 mixtures in AFX zeolite at 300 K. (c) RAST calculations of the component activity coefficients γ_i, for CO_2 and N_2. (d) Comparison CO_2/N_2 adsorption selectivities obtained from CBMC with IAST and RAST estimations. The unary isotherm fit parameters, and Wilson parameters, are provided in Table 14.

Figure 97. (a) Comparison of the estimations using the IAST and RAST with CBMC simulations[79, 109] of component loadings of equimolar (partial fugacities f_1=f_2) CO_2/CH_4 mixtures in MOR zeolite at 300 K. (b) RAST calculations of the component activity coefficients γ_i, for CO_2 and CH_4. (e) Comparison CO_2/CH_4 adsorption selectivities obtained from CBMC with IAST and RAST estimations. The unary isotherm fit parameters and Wilson parameters are provided in Table 15.

Figure 98. (a) Comparison of the estimations using the IAST, and RAST with CBMC simulations[70] of component loadings of equimolar (partial fugacities f_1=f_2) CO_2/CH_4 mixtures in NaX zeolite at 300 K. (b) Comparison CO_2/CH_4 adsorption selectivities obtained from CBMC with IAST and RAST estimations. (c) RAST calculations of the component activity coefficients γ_i, for CO_2 and CH_4. The unary isotherm fit parameters and Wilson parameters are provided in Table 16.

Figure 99. (a) Comparison of the estimations using the IAST, and RAST with CBMC simulations[70] of component loadings of 15/85 CO_2/N_2 mixtures in NaX zeolite at 313 K. (b) Comparison CO_2/N_2 adsorption selectivities obtained from CBMC with IAST and RAST estimations. (c) RAST calculations of the component activity coefficients γ_i, for CO_2 and N_2. The unary isotherm fit parameters and Wilson parameters are provided in Table 17.

Figure 100. (a) Comparison of the estimations using the IAST, and RAST with CBMC simulations[70] of component loadings of 15/85 CO_2/H_2 mixtures in NaX zeolite at 313 K. (b) Comparison CO_2/H_2 adsorption selectivities obtained from CBMC with IAST and RAST estimations. (c) RAST calculations of the component activity coefficients γ_i, for CO_2 and H_2. The unary isotherm fit parameters and Wilson parameters are provided in Table 17.

Figure 101. Comparison CBMC CO_2/CH_4 adsorption selectivities determined from CBMC simulations 300 K for all-silica FAU (192 Si, 0 Al, 0 Na^+, Si/Al=∞), NaY (138 Si, 54 Al, 54 Na^+, Si/Al=2.56), and NaX (106 Si, 86 Al, 86 Na^+, Si/Al=1.23) zeolites with IAST estimations. The unary isotherm parameters are provided in Table 19 (all-silica FAU), Table 18 (NaY), and Table 16 (NaX).

Figure 102. (a) Comparison of the estimations using the IAST, and RAST with CBMC simulations[70] of component loadings of equimolar (partial fugacities f_1=f_2) CO_2/CH_4 mixtures in LTA-4A zeolite at 300 K. (b) Comparison CO_2/CH_4 adsorption selectivities obtained from CBMC with IAST and RAST estimations. (c) RAST calculations of the component activity coefficients γ_i, for CO_2 and CH_4. The unary isotherm fit parameters and Wilson parameters are provided in Table 20.

Figure 103. Re-analysis of the experimental data of Gholipour and Mofarahi[80] for CO_2(1)/CH_4(2) mixture adsorption at 303 K in 13X zeolite. The unary isotherm fit parameters are specified in Table 21.

Figure 104. (a, b) Experimental data (indicated by symbols) of Hefti et al.[19] for (a) component loadings, q_i, and (b) adsorbed phase mole fractions, x_i, of CO_2, and N_2 for adsorption of CO_2/N_2 mixtures in 13X zeolite at 298 K and total pressure p_t = 1 MPa, as function of the mole fraction

of CO_2 in the bulk gas phase. The dashed lines are the IAST estimations, using the unary isotherm fits provided in Table 2 of Hefti et al.[19] The continuous solid lines are the estimations using RAST using Wilson parameters: $\Lambda_{12} = 1.95$; $\Lambda_{21} = 64$; $C = 0.044$ kg mol^{-1}

Figure 105. Re-analysis of the experimental data of Siperstein and Myers[16] for adsorption of CO_2/C_3H_8 mixtures in NaX zeolite at 293 K, as reported in Table C1 of their paper. (a, b) The differences in the estimation of the total mixture loading, $q_{t,IAST}$ from the experimental data, $q_{t,exp}$ is plotted as function of the (a) adsorbed phase mole fraction of CO_2, determined experimentally, and (b) the adsorption potential, $\frac{\pi A}{RT}$. (c) RAST calculations of the activity coefficients of CO_2, and C_3H_8 plotted as a function of the adsorbed phase mole fraction of CO_2, determined experimentally. (d, e) Parity plots, comparing the IAST and RAST estimates of the component loadings of (d) CO_2, and (e) C_3H_8 with the values determined experimentally. The unary isotherm fit parameters, along with the Wilson parameters, are specified in Table 24.

Figure 106. Re-analysis of the experimental data of Siperstein and Myers[16] for adsorption of C_2H_4/C_2H_6 mixtures in NaX zeolite at 293 K, as reported in Table C4 of their paper. (a) RAST calculations of the activity coefficients of C_2H_4, and C_2H_6 plotted as a function of the adsorbed phase mole fraction of C_2H_4, determined experimentally. (b, c) Parity plots, comparing the IAST and RAST estimates of the component loadings of (b) C_2H_4, and (c) C_2H_6 with the values determined experimentally. The unary isotherm fit parameters, along with the Wilson parameters, are specified in Table 24.

Figure 107. Comparison of IAST and RAST calculations for (a) adsorption selectivity, (b) CO_2 uptake capacities, (c) C_3H_8 uptake capacities, and (d) separation potential, $\Delta Q = Q_1 \frac{y_2}{y_1} - Q_2$ for separation of 50/50 $CO_2(1)/C_3H_8(2)$ feed mixtures in NaX zeolite at 293 K. The unary isotherm fit parameters, along with the Wilson parameters, are specified in Table 24.

Figure 108. Transient breakthrough simulations of 50/50 CO_2/C_3H_8 feed mixtures in fixed bed packed with NaX zeolite, operating at total pressure, p_t = 40 kPa and 293 K. The unary isotherm fit parameters, along with the Wilson parameters, are specified in Table 24.

Figure 109. Re-analysis of the experimental data of Costa et al.[81] for adsorption of CO_2/C_3H_8 mixtures at 293 K in NaX (=13 X) zeolite. (a) Plot of the experimental data on mole fraction of CO_2 in the bulk gas phase, y_1, versus the mole fraction of CO_2 in the adsorbed phase, x_1. (b) Comparison of IAST and RAST calculations of mole fraction of CO_2 in the adsorbed phase, x_1, as a function of the mole fraction of CO_2 in the bulk gas phase, y_1; the total pressure = 50 kPa. (c) RAST calculations of the activity coefficients of CO_2, and C_3H_8 plotted as a function of the adsorbed phase mole fraction of CO_2, determined experimentally. (d, e) Parity plots, comparing the IAST and RAST estimates of the component loadings of (d) CO_2, and (e) C_3H_8 with the

values determined experimentally. The unary isotherm fit parameters, along with the Wilson parameters, are specified in Table 25.

Figure 110. Comparison of IAST and RAST calculations for (a) adsorption selectivity, (b) CO_2 uptake capacities, (c) C_3H_8 uptake capacities, and (d) separation potential, $\Delta Q = Q_1 \frac{y_2}{y_1} - Q_2$ for separation of 80/20 $CO_2(1)/C_3H_8(2)$ feed mixtures in NaX zeolite at 293 K. The unary isotherm fit parameters, along with the Wilson parameters, are specified in Table 25.

Figure 111. Transient breakthrough simulations for (a) 80/20 CO_2/C_3H_8, and (b) 85/15 feed mixtures in fixed bed packed with NaX zeolite, operating at total pressure, p_t = 50 kPa and 293 K. The unary isotherm fit parameters, along with the Wilson parameters, are specified in Table 25.

Figure 112. Re-analysis of the experimental data of Costa et al.[81] for adsorption of C_3H_6/C_3H_8 mixtures at 293 K in NaX (=13 X) zeolite. (a) Plot of the experimental data on mole fraction of C_3H_6 in the bulk gas phase, y_1, versus the mole fraction of C_3H_6 in the adsorbed phase, x_1. (b) Comparison of IAST and RAST calculations of mole fraction of C_3H_6 in the adsorbed phase, x_1, as a function of the mole fraction of C_3H_6 in the bulk gas phase, y_1; the total pressure = 100 kPa. (c) RAST calculations of the activity coefficients of C_3H_6, and C_3H_8 plotted as a function of the

adsorbed phase mole fraction of C_3H_6, determined experimentally. (d, e) Parity plots, comparing the IAST and RAST estimates of the component loadings of (d) C_3H_6, and (e) C_3H_8 with the values determined experimentally. The unary isotherm fit parameters, along with the Wilson parameters, are specified in Table 25.

Figure 113. Re-analysis of the experimental data of Costa et al.[81] for adsorption of CO_2/C_3H_6 mixtures at 293 K in NaX (=13 X) zeolite. (a) Plot of the experimental data on mole fraction of CO_2 in the bulk gas phase, y_1, versus the mole fraction of CO_2 in the adsorbed phase, x_1. (b) Comparison of IAST and RAST calculations of mole fraction of CO_2 in the adsorbed phase, x_1, as a function of the mole fraction of CO_2 in the bulk gas phase, y_1; the total pressure = 50 kPa. (c) RAST calculations of the activity coefficients of CO_2, and C_3H_6 plotted as a function of the adsorbed phase mole fraction of CO_2, determined experimentally. (d, e) Parity plots, comparing the IAST and RAST estimates of the component loadings of (d) CO_2, and (e) C_3H_6 with the values determined experimentally. The unary isotherm fit parameters, along with the Wilson parameters, are specified in Table 25.

Figure 114. Re-analysis of the experimental data of Costa et al.[81] for adsorption of CO_2/C_2H_4 mixtures at 293 K in NaX (=13 X) zeolite. (a) Plot of the experimental data on mole fraction of CO_2 in the bulk gas phase, y_1, versus the mole fraction of CO_2 in the adsorbed phase, x_1. (b) Comparison of IAST and RAST calculations of mole fraction of CO_2 in the adsorbed phase, x_1, as a function of the mole fraction of CO_2 in the bulk gas phase, y_1; the total pressure = 100 kPa. (c) RAST calculations of the activity coefficients of CO_2, and C_2H_4 plotted as a function of the

adsorbed phase mole fraction of CO_2, determined experimentally. (d, e) Parity plots, comparing the IAST and RAST estimates of the component loadings of (d) CO_2, and (e) C_2H_4 with the values determined experimentally. The unary isotherm fit parameters, along with the Wilson parameters, are specified in Table 25.

Figure 115. Re-analysis of the experimental data of Costa et al.[81] for adsorption of C_2H_4/C_3H_8 mixtures at 293 K in NaX (=13 X) zeolite. (a) Plot of the experimental data on mole fraction of C_3H_6 in the bulk gas phase, y_1, versus the mole fraction of C_2H_4 in the adsorbed phase, x_1. (b) Comparison of IAST and RAST calculations of mole fraction of C_2H_4 in the adsorbed phase, x_1, as a function of the mole fraction of C_2H_4 in the bulk gas phase, y_1; the total pressure = 100 kPa. (c) RAST calculations of the activity coefficients of C_2H_4, and C_3H_8 plotted as a function of the adsorbed phase mole fraction of C_2H_4, determined experimentally. (d, e) Parity plots, comparing the IAST and RAST estimates of the component loadings of (d) C_2H_4, and (e) C_3H_8 with the values determined experimentally. The unary isotherm fit parameters, along with the Wilson parameters, are specified in Table 25.

Figure 116. Re-analysis of the experimental data of Calleja et al.[82] for adsorption of $CO_2/C_2H_4/C_3H_8$ mixtures at 293 K in NaX (=13 X) zeolite. Parity plots, comparing the IAST and RAST estimates of the component loadings of (a) CO_2, (b) C_2H_4, and (c) C_3H_8 with the values determined experimentally. The unary isotherm fit parameters, along with the Wilson parameters, are specified in Table 25.

Figure 117. Re-analysis of the experimental data of Calleja et al.[82] for adsorption of $CO_2/C_3H_6/C_3H_8$ mixtures at 293 K in NaX (=13 X) zeolite. Parity plots, comparing the IAST and RAST estimates of the component loadings of (a) CO_2, (b) C_3H_6, and (c) C_3H_8 with the values determined experimentally. The unary isotherm fit parameters, along with the Wilson parameters, are specified in Table 25.

Figure 118. Re-analysis of the experimental data of Hyun and Danner[83] for adsorption of C_2H_4/iso-C_4H_{10} mixtures at 298 K and 137.8 kPa in 13X zeolite, as reported in Table III of their paper. (a) Plot of the experimental data on mole fraction of C_2H_4 in the bulk gas phase, y_1, versus the mole fraction of C_2H_4 in the adsorbed phase, x_1; the total pressure = 137.8 kPa. (b) Comparison of IAST and RAST calculations of mole fraction of C_2H_4 in the adsorbed phase, x_1, as a function of the mole fraction of C_2H_4 in the bulk gas phase, y_1. (c) RAST calculations of the activity coefficients of C_2H_4, and iso-C_4H_{10} plotted as a function of the adsorbed phase mole fraction of C_2H_4, determined experimentally. (d, e) Parity plots, comparing the IAST and RAST estimates of the component loadings of (d) C_2H_4, and (e) iso-C_4H_{10} with the values determined experimentally. The unary isotherm fit parameters, along with the Wilson parameters, are specified in Table 26.

Figure 119. Re-analysis of the experimental data of Calleja et al.[84] for adsorption of CO_2/C_2H_4 mixtures at 293 K in ZSM-5 (with MFI topology) zeolite with Si/Al ratio = 15, as reported in

Table 5 of their paper. (a) Plot of the experimental data on mole fraction of CO_2 in the bulk gas phase, y_1, versus the mole fraction of CO_2 in the adsorbed phase, x_1. (b) Comparison of IAST and RAST calculations of mole fraction of CO_2 in the adsorbed phase, x_1, as a function of the mole fraction of CO_2 in the bulk gas phase, y_1; the total pressure = 34 kPa. (c) RAST calculations of the activity coefficients of CO_2, and C_2H_4 plotted as a function of the adsorbed phase mole fraction of CO_2, determined experimentally. (d, e) Parity plots, comparing the IAST and RAST estimates of the component loadings of (d) CO_2, and (e) C_2H_4 with the values determined experimentally. The unary isotherm fit parameters, along with the Wilson parameters, are specified in Table 27.

Figure 120. Re-analysis of the experimental data of Calleja et al.[84] for adsorption of CO_2/C_3H_8 mixtures at 293 K in ZSM-5 (with MFI topology) zeolite with Si/Al ratio = 15, as reported in Table 5 of their paper. (a) Plot of the experimental data on mole fraction of CO_2 in the bulk gas phase, y_1, versus the mole fraction of CO_2 in the adsorbed phase, x_1. (b) Comparison of IAST and RAST calculations of mole fraction of CO_2 in the adsorbed phase, x_1, as a function of the mole fraction of CO_2 in the bulk gas phase, y_1; the total pressure = 40 kPa. (c) RAST calculations of the activity coefficients of CO_2, and C_3H_8 plotted as a function of the adsorbed phase mole fraction of CO_2, determined experimentally. (d, e) Parity plots, comparing the IAST and RAST estimates of the component loadings of (d) CO_2, and (e) C_3H_8 with the values determined experimentally. The unary isotherm fit parameters, along with the Wilson parameters, are specified in Table 27.

Figure 121. Re-analysis of the experimental data of Calleja et al.[84] for adsorption of C_2H_4/C_3H_8 mixtures at 293 K in ZSM-5 (with MFI topology) zeolite with Si/Al ratio = 15, as reported in Table 5 of their paper. (a) Plot of the experimental data on mole fraction of C_2H_4 in the bulk gas phase, y_1, versus the mole fraction of C_2H_4 in the adsorbed phase, x_1; the total pressure = 40 kPa. (b) Comparison of IAST and RAST calculations of mole fraction of C_2H_4 in the adsorbed phase, x_1, as a function of the mole fraction of C_2H_4 in the bulk gas phase, y_1. (c) RAST calculations of the activity coefficients of C_2H_4, and C_3H_8 plotted as a function of the adsorbed phase mole fraction of C_2H_4, determined experimentally. (d, e) Parity plots, comparing the IAST and RAST estimates of the component loadings of (d) C_2H_4, and (e) C_3H_8 with the values determined experimentally. The unary isotherm fit parameters, along with the Wilson parameters, are specified in Table 27.

Figure 122. Transient breakthrough simulations of 10/20 C_2H_4/C_3H_8 feed mixtures in fixed bed packed with ZSM-5 (with MFI topology) zeolite with Si/Al ratio = 15, operating at total pressure, p_t = 30 kPa and 293 K. The unary isotherm fit parameters, along with the Wilson parameters, are specified in Table 27.

Figure 123. Re-analysis of the experimental data of Talu and Zwiebel[18] for adsorption of CO_2/C_3H_8 mixtures at 303 K in H-MOR, as reported in Table 5 of their paper. (a, b) Comparison

of experimental data with IAST and RAST calculations for the (a) adsorption selectivity, and (b) CO_2 uptake for 17/83 CO_2(1)/C_3H_8(2) mixtures and varying total gas phase pressures, p_t. (c) RAST calculations of the activity coefficients of CO_2, and C_3H_8 for 17/83 CO_2(1)/C_3H_8(2) mixtures, plotted as a function total gas phase pressures, p_t. (d, e) Comparison of experimental data for the (a) adsorption selectivity, and (b) adsorbed phase mole fraction of CO_2, x_1, for CO_2(1)/C_3H_8(2) mixtures at a total gas phase pressure p_t = 41 kPa, and varying CO_2 mole fractions in the bulk gas phase, y_1. (f) RAST calculations of the activity coefficients of CO_2, and C_3H_8 for CO_2(1)/C_3H_8(2) mixtures at a total gas phase pressure p_t = 41 kPa, and varying CO_2 mole fractions in the bulk gas phase, y_1. The unary isotherm fit parameters, along with the Wilson parameters, are specified in Table 28.

Figure 124. (a) Comparison of IAST and RAST calculations for the separation potential, $\Delta Q = Q_1 \frac{y_2}{y_1} - Q_2$ for separation of 17/83 CO_2(1)/C_3H_8(2) feed mixtures in H-MOR at 303 K, plotted as a function of the total gas pressure, p_t. (b) Transient breakthrough simulations of 17/83 C_2H_4/C_3H_8 feed mixtures in fixed bed packed with H-MOR, operating at total pressure, p_t = 41 kPa and 303 K.

Figure 125. Re-analysis of the experimental data of Talu and Zwiebel[18] for adsorption of (a) CO_2/H_2S, and (b) C_3H_8/H_2S mixtures at 303 K in H-MOR, as reported in Table 5 of their paper.

(a) Comparison of experimental data for adsorbed phase mole fraction of CO_2, x_1, for $CO_2(1)/H_2S(2)$ mixtures at a total gas phase pressure p_t = 15.6 kPa, and varying CO_2 mole fractions in the bulk gas phase, y_1. (b) Comparison of experimental data for adsorbed phase mole fraction of C_3H_8, x_1, for C_3H_8 (1)/H_2S(2) mixtures at a total gas phase pressure p_t = 8.1 kPa, and varying C_3H_8 mole fractions in the bulk gas phase, y_1. The unary isotherm fit parameters, along with the Wilson parameters, are specified in Table 28.

Figure 126. Re-analysis of the experimental data of Talu and Zwiebel[18] for adsorption of ternary $CO_2/C_3H_8/H_2S$ mixtures at 303 K in H-MOR, as reported in Table 7 of their paper. Parity plots, comparing the IAST and RAST estimates of the component loadings of (a) CO_2, (b) C_3H_8, and (c) H_2S with the values determined experimentally. The unary isotherm fit parameters, along with the Wilson parameters, are specified in Table 28.

Figure 127. Re-analysis of the experimental data of Mofarahi and Gholipour[85] for $CO_2(1)/CH_4(2)$ mixture adsorption at 303 K in LTA-5A zeolite. The unary isotherm fit parameters are specified in Table 22.

Figure 128. Re-analysis of the experimental data of Mofarahi and Salehi[86] for $C_2H_4(1)/ C_2H_6(2)$ mixture adsorption at 283 K in LTA-5A zeolite. The unary isotherm fit parameters are specified in Table 23.

Figure 129. (a) Experimental breakthrough determined by van Zandvoort et al.[87] for transient breakthrough of $H_2/N_2/Ar/CH_4/C_2H_6/C_2H_4/CO_2$ mixtures in tube packed with LTA-5A zeolite, operating at 313 K, and 0.5 MPa. The gas mixture composition at the inlet is determined using the information provided in the legend to Figure 4 of their paper. (b) Transient breakthrough simulations determined using the IAST for gas-zeolite mixture adsorption equilibrium. The unary isotherm fits used in the IAST calculations are culled from the publications of Mofarahi [85, 86, 110] and Pakseresht et al.[111]

Figure 130. (a, b) Experimental data (represented by symbols) of Bhadra[91] for binary mixture adsorption equilibrium of (a) 50/50, and (b) 90/10 $CH_4(1)/N_2(2)$ mixtures in Ba-ETS-4 at 283 K. The experimental data are scanned from Figure 3.7 of the PhD dissertation of Bhadra. The dashed lines are the IAST calculations of mixture adsorption equilibrium using the Langmuir parameters specified in Table 29.

Figure 131. (a) CBMC simulations for linear alkanes, with carbon numbers ranging from 1 to 6 in MFI zeolite at 300 K. (b) CBMC simulations for branched alkanes and benzene in MFI zeolite at 300 K.

Figure 132. (a) CBMC simulations[112] of unary isotherms of CH_4 and Benzene in MFI zeolite at 300 K. The continuous solid lines are dual-site Langmuir-Freundlich fits; the unary isotherm fit

parameters are provided in Table 30. (b) Comparison of the estimations using the IAST and RAST with CBMC simulations[112] of component loadings of binary 50/50 CH_4/Benzene mixtures in MFI zeolite at 300 K. (c) Plot of the Benzene/CH_4 adsorption selectivity as a function of the total fluid mixture fugacity, f_t. (d) RAST calculations of the component activity coefficients, γ_i. The Wilson parameters are specified in Table 31.

Figure 133. (a) CBMC simulations[112] of unary isotherms of C_2H_4 and Benzene in MFI zeolite at 300 K. The continuous solid lines are dual-site Langmuir-Freundlich fits; the unary isotherm fit parameters are provided in Table 30. (b) Comparison of the estimations using the IAST and RAST with CBMC simulations[112] of component loadings of binary 50/50 C_2H_4/Benzene mixtures in MFI zeolite at 300 K. (c) Plot of the Benzene/C_2H_4 adsorption selectivity as a function of the total fluid mixture fugacity, f_t. (d) RAST calculations of the component activity coefficients, γ_i. The Wilson parameters are specified in Table 31.

Figure 134. (a) CBMC simulations[105-107] of unary isotherms of C_2H_4 and Benzene in MFI zeolite at 653 K. The continuous solid lines are dual-site Langmuir-Freundlich fits; the unary isotherm fit parameters are provided in Table 32. (b) Comparison of the estimations using the IAST and RAST with CBMC simulations[105-107] of component loadings of binary 50/50 C_2H_4/Benzene mixtures in MFI zeolite at 653 K. (c) Plot of the Benzene/C_2H_4 adsorption selectivity as a function of the total fluid mixture fugacity, f_t. (d) RAST calculations of the component activity coefficients, γ_i. The Wilson parameters are specified in Table 32.

Figure 135. (a) CBMC simulations[112] of unary isotherms of C_3H_6 and Benzene in MFI zeolite at 300 K. The continuous solid lines are dual-site Langmuir-Freundlich fits; the unary isotherm fit parameters are provided in Table 30. (b) Comparison of the estimations using the IAST and RAST with CBMC simulations[112] of component loadings of binary 50/50 C_3H_6/Benzene mixtures in MFI zeolite at 300 K. (c) Plot of the Benzene/C_3H_6 adsorption selectivity as a function of the total fluid mixture fugacity, f_t. (d) RAST calculations of the component activity coefficients, γ_i. The Wilson parameters are specified in Table 31.

Figure 136. (a) CBMC simulations[112] of unary isotherms of CH_4 and iC4 in MFI zeolite at 300 K. The continuous solid lines are dual-site Langmuir-Freundlich fits; the unary isotherm fit parameters are provided in Table 30. (b) Comparison of the estimations using the IAST and RAST with CBMC simulations[112] of component loadings of binary 50/50 CH_4/iC4 mixtures in MFI zeolite at 300 K. (c) Plot of the iC4/CH_4 adsorption selectivity as a function of the total fluid mixture fugacity, f_t. (d) RAST calculations of the component activity coefficients, γ_i. The Wilson parameters are specified in Table 31.

Figure 137. (a) CBMC simulations[112] of unary isotherms of C_2H_6 and iC4 in MFI zeolite at 300 K. The continuous solid lines are dual-site Langmuir-Freundlich fits; the unary isotherm fit parameters are provided in Table 30. (b) Comparison of the estimations using the IAST and

RAST with CBMC simulations[112] of component loadings of binary 50/50 C_2H_6/iC4 mixtures in MFI zeolite at 300 K. (c) Plot of the iC4/C_2H_6 adsorption selectivity as a function of the total fluid mixture fugacity, f_t. (d) RAST calculations of the component activity coefficients, γ_i. The Wilson parameters are specified in Table 31.

Figure 138. (a) CBMC simulations[112] of unary isotherms of C_3H_8 and iC4 in MFI zeolite at 300 K. The continuous solid lines are dual-site Langmuir-Freundlich fits; the unary isotherm fit parameters are provided in Table 30. (b) Comparison of the estimations using the IAST and RAST with CBMC simulations[112] of component loadings of binary 50/50 C_3H_8/iC4 mixtures in MFI zeolite at 300 K. (c) Plot of the iC4/C_3H_8 adsorption selectivity as a function of the total fluid mixture fugacity, f_t. (d) RAST calculations of the component activity coefficients, γ_i. The Wilson parameters are specified in Table 31.

Figure 139. (a) CBMC simulations[99] of unary isotherms of nC4 and iC4 in MFI zeolite at 300 K. The continuous solid lines are dual-site Langmuir-Freundlich fits; the unary isotherm fit parameters are provided in Table 30. (b) Comparison of the estimations using the IAST and RAST with CBMC simulations[99] of component loadings of binary 50/50 nC4/iC4 mixtures in MFI zeolite at 300 K. (c) Plot of the nC4/iC4 adsorption selectivity as a function of the total fluid mixture fugacity, f_t. (d) RAST calculations of the component activity coefficients, γ_i. The Wilson parameters are specified in Table 31.

Figure 140. (a) CBMC simulations[99] of unary isotherms of nC6 and 2MP in MFI zeolite at 300 K. The continuous solid lines are dual-site Langmuir-Freundlich fits; the unary isotherm fit parameters are provided in Table 30. (b) Comparison of the estimations using the IAST and RAST with CBMC simulations[99] of component loadings of binary 50/50 nC6/2MP mixtures in MFI zeolite at 300 K. The Wilson parameters are specified in Table 31.

Figure 141. (a, b) Transient uptake of nC4/iC4 mixture in MFI at 298 K. The initial partial pressures $p_1 = p_2 = 0$ Pa; final partial pressures $p_1 = p_2 = 100$ Pa. Input data: $Đ_1/r_c^2 = 0.08$ s^{-1}; $Đ_2/r_c^2 = 4\times10^{-3}$ s^{-1}. The continuous solid lines are RAST calculations using equation (37) that include thermodynamic coupling effects. The dashed lines are simulations using the IAST. The dotted lines are simulations in which the matrix of thermodynamic correction factors is taken to be the identity matrix $\begin{bmatrix}\Gamma_{11} & \Gamma_{12}\\ \Gamma_{21} & \Gamma_{22}\end{bmatrix}\rightarrow\begin{bmatrix}1 & 0\\ 0 & 1\end{bmatrix}$. The unary isotherm fit parameters are provided in Table 30. The Wilson parameters are specified in Table 31.

Figure 142. Transient uptake of nC6/2MP mixture in MFI at 300 K. The initial partial pressures $p_1 = p_2 = 0$ Pa; final partial pressures $p_1 = p_2 = 1.3$ Pa. Input data: $Đ_1/r_c^2 = 0.016$ s^{-1}; $Đ_2/r_c^2 =$

1.6×10^{-4} s^{-1}. The continuous solid lines are RAST calculations using equation (37) that include thermodynamic coupling effects. The dotted lines are simulations in which the matrix of thermodynamic correction factors is taken to be the identity matrix $\begin{bmatrix}\Gamma_{11} & \Gamma_{12}\\ \Gamma_{21} & \Gamma_{22}\end{bmatrix}\rightarrow\begin{bmatrix}1 & 0\\ 0 & 1\end{bmatrix}$. The unary isotherm fit parameters are provided in Table 30. The Wilson parameters are specified in Table 31.

Figure 143. Comparison of IAST and RAST calculations for (a) adsorption selectivity, (b) iC4 uptake capacities, and (c) volumetric separation potential, $\Delta Q_{iC4/nC4} = Q_1\frac{y_2}{y_1} - Q_2 = Q_1 - Q_2$ for separation of 50/50 nC4(1)/iC4(2) mixtures in MFI zeolite at 300 K. The unary isotherm fit parameters are provided in Table 30. The Wilson parameters are specified in Table 31.

Figure 144. Transient breakthrough simulations of 50/50 nC4/iC4 feed mixtures in fixed bed packed adsorber with MFI, operating at total fluid mixture fugacity, f_t = 10 kPa and 300 K. The mixture adsorption equilibrium is determined using IAST and RAST. The unary isotherm fit parameters are provided in Table 30. The Wilson parameters are specified in Table 31.

Figure 145. (a, b, c) CBMC simulations of pure component isotherms for CO_2 adsorption in (a) IRMOF-1, (b) all-silica FAU, and (c) all-silica AFI at 200 K, and 300 K. (d, e, f) The inverse thermodynamic factor, $1/\Gamma_i$, plotted as a function of the molar loadings of CO_2 in (d) IRMOF-1, (e) all-silica FAU, and (f) all-silica AFI at 200 K, and 300 K. The $1/\Gamma_i$ are calculated by analytic differentiation of dual-site Langmuir-Freundlich fits of the isotherms. The unary isotherm fit parameters are specified in Table 33 (IRMOF-1), Table 19 (FAU), Table 34 (AFI).

Figure 146. (a) Comparison of CBMC simulated loadings for 50/50 CO_2/CH_4 mixture adsorption in (a) IRMOF-1, (b) all-silica FAU, and (c) all-silica AFI at 300 K with IAST estimates. The unary isotherm fit parameters are specified in Table 33 (IRMOF-1), Table 19 (FAU), Table 34 (AFI).

Figure 147. (a) Comparison of CBMC simulated loadings for 50/50 CO_2/CH_4 mixture adsorption in IRMOF-1 at 200K with IAST, and RAST estimates. (b) Comparison of IAST and RAST calculations of the CO_2/CH_4 adsorption selectivity for IRMOF-1 at 200 K with those determined from CBMC simulations. (c) RAST calculations of the activity coefficients γ_i, for CO_2 and CH_4. The unary isotherm fit parameters are specified in Table 33, along with the Wilson parameters.

AFI

Figure S1

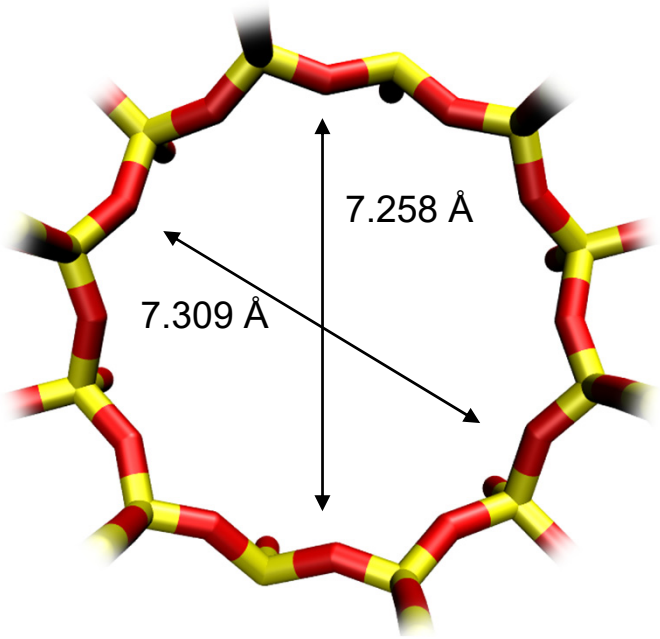

	AFI
a /Å	23.774
b /Å	13.726
c /Å	8.484
Cell volume / Å^3	2768.515
conversion factor for [molec/uc] to [mol per kg Framework]	0.3467
conversion factor for [molec/uc] to [kmol/m^3]	2.1866
ρ [kg/m3]	1729.876
MW unit cell [g/mol(framework)]	2884.07
ϕ, fractional pore volume	0.274
open space / Å^3/uc	759.4
Pore volume / cm^3/g	0.159
Surface area /m^2/g	466.0
DeLaunay diameter /Å	7.26

Snapshots of CH_4 and CO_2

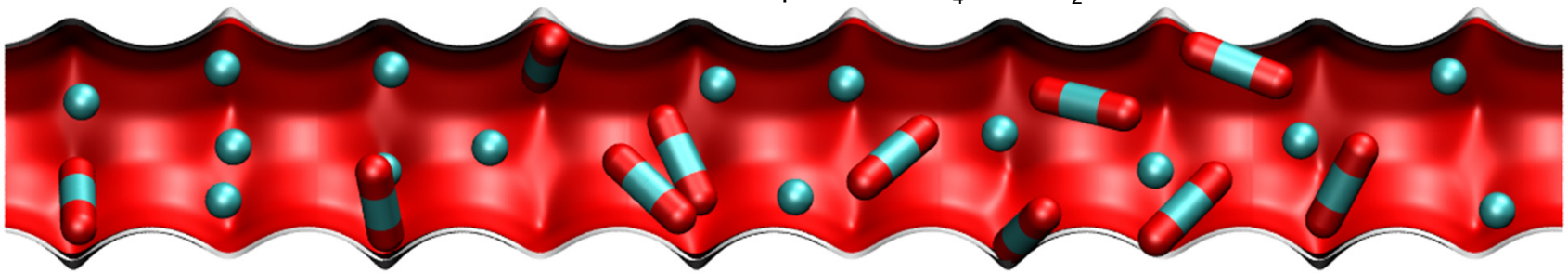

Structural information from: C. Baerlocher, L.B. McCusker, Database of Zeolite Structures, International Zeolite Association, http://www.iza-structure.org/databases/

Figure S2

AFX pore landscape

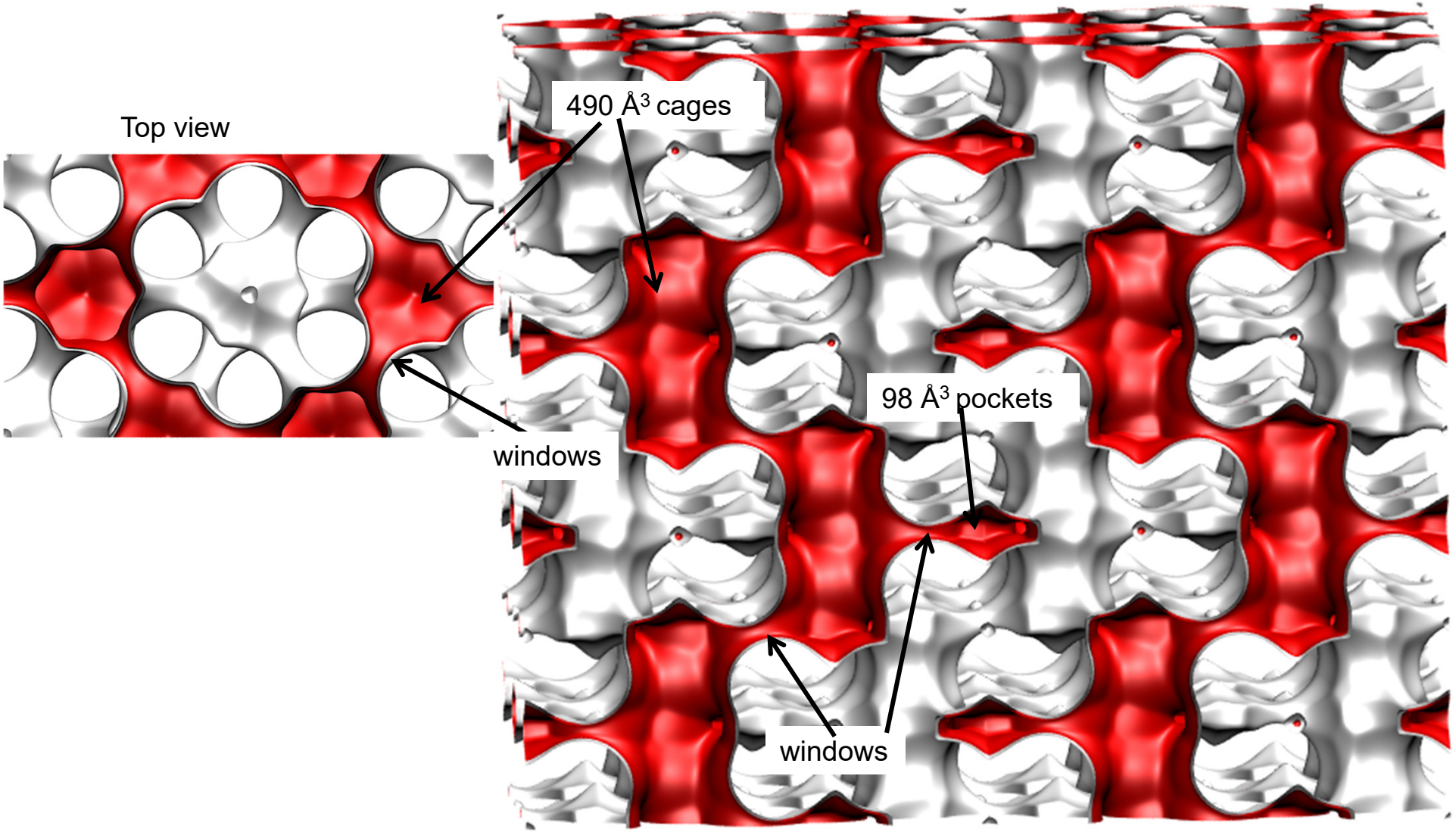

Structural information from: C. Baerlocher, L.B. McCusker, Database of Zeolite Structures, International Zeolite Association, http://www.iza-structure.org/databases/

Figure S3

AFX window sizes and pore dimensions

	AFX
a /Å	23.836
b /Å	13.762
c /Å	19.949
Cell volume / Å^3	6543.891
conversion factor for [molec/uc] to [mol per kg Framework]	0.1734
conversion factor for [molec/uc] to [kmol/m^3]	0.7059
ρ [kg/m3]	1463.713
MW unit cell [g/mol(framework)]	5768.141
ϕ, fractional pore volume	0.359
open space / Å^3/uc	2352.5
Pore volume / cm^3/g	0.246
Surface area /m^2/g	674.0
DeLaunay diameter /Å	3.44

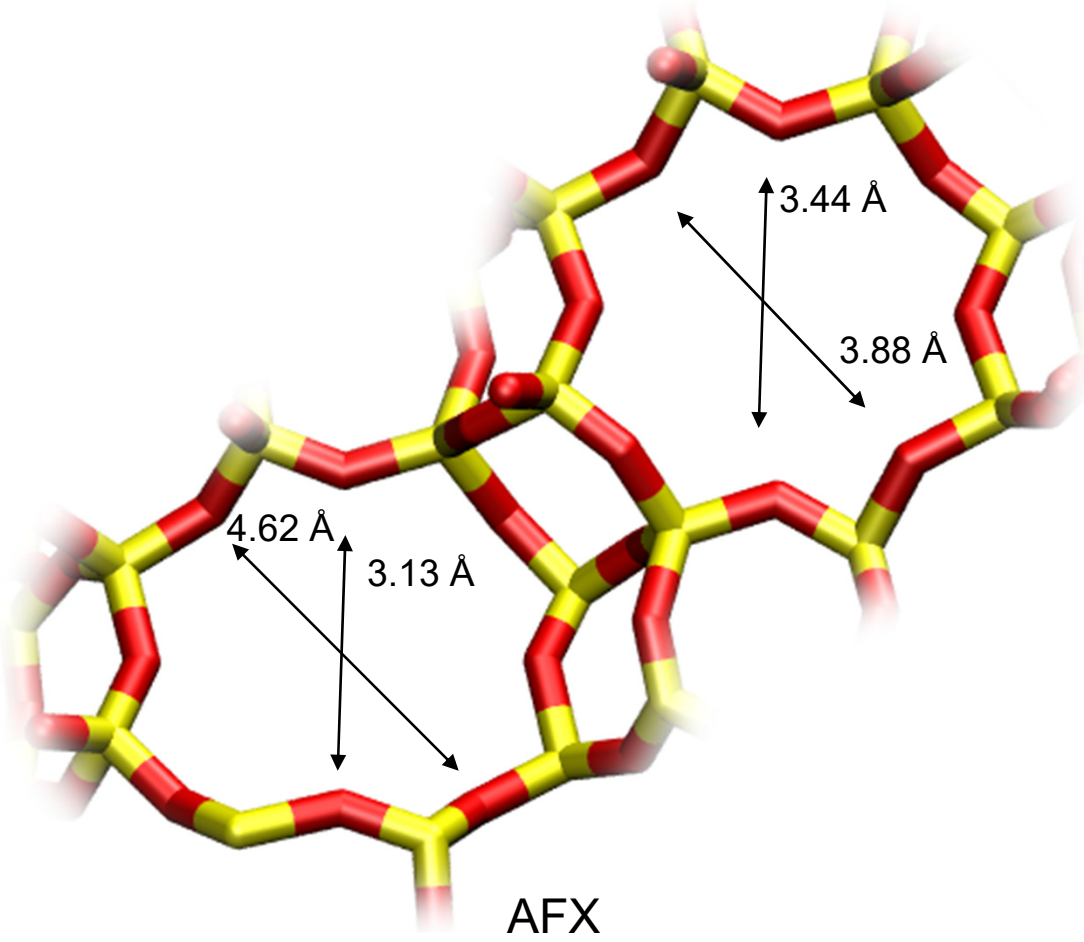

The window dimension calculated using the van der Waals diameter of framework atoms = 2.7 Å are indicated above by the arrows.

Figure S4

CHA landscape

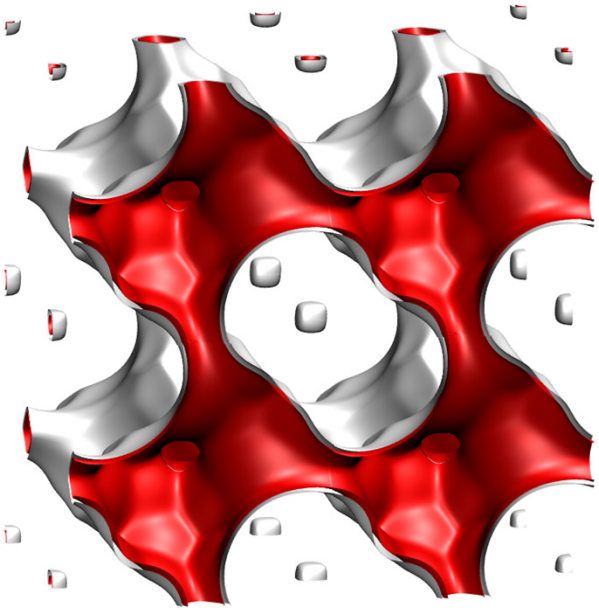

There are 6 cages per unit cell. The volume of one CHA cage is 316.4 Å^3, slightly larger than that of a single cage of DDR (278 Å^3), but significantly lower than FAU (786 Å^3).

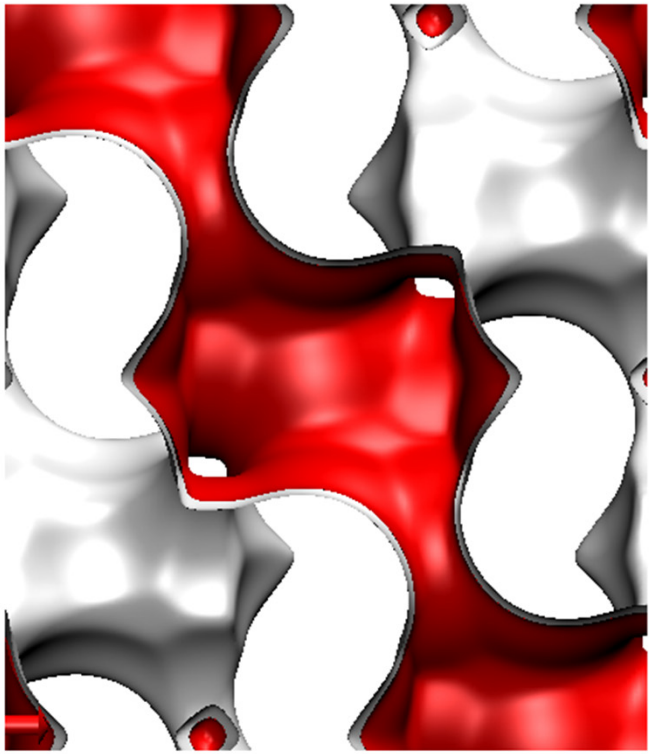

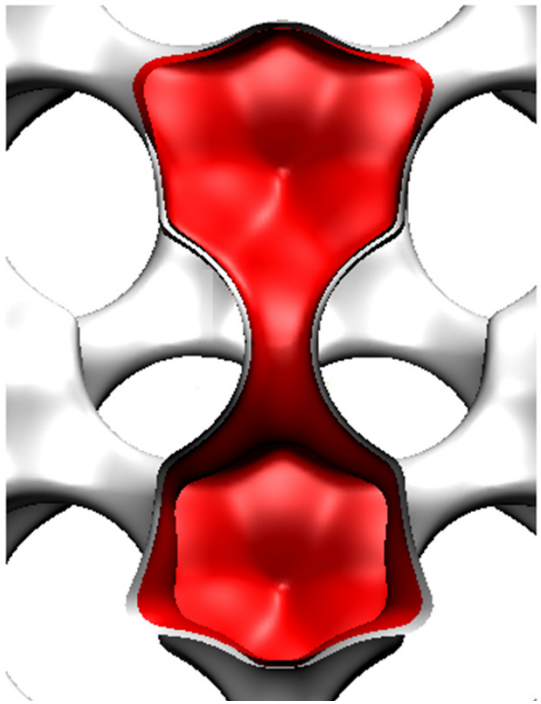

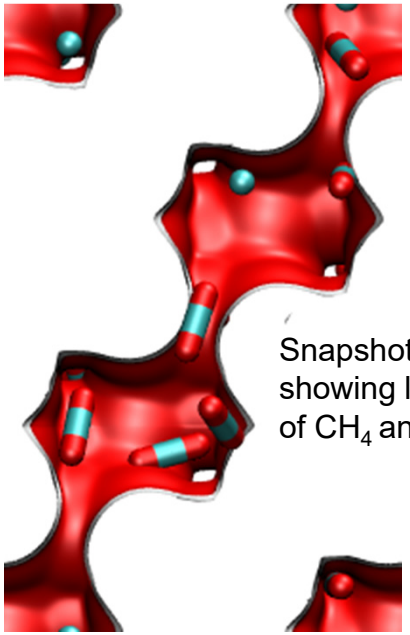

Snapshots showing location of CH_4 and CO_2

Snapshots showing location of CH_4

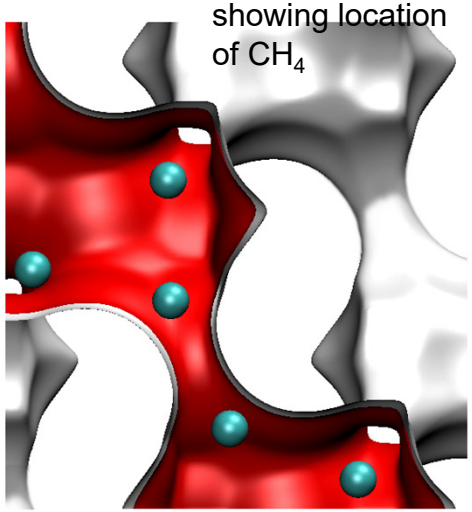

Structural information from: C. Baerlocher, L.B. McCusker, Database of Zeolite Structures, International Zeolite Association, http://www.iza-structure.org/databases/

Figure S5

CHA window and pore dimensions

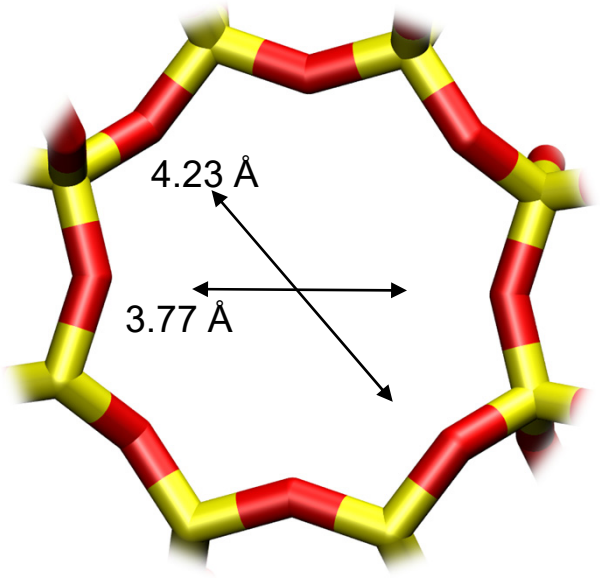

CHA

The window dimensions calculated using the van der Waals diameter of framework atoms = 2.7 Å are indicated above by the arrows.

	CHA
a /Å	15.075
b /Å	23.907
c /Å	13.803
Cell volume / Å^3	4974.574
conversion factor for [molec/uc] to [mol per kg Framework]	0.2312
conversion factor for [molec/uc] to [kmol/m^3]	0.8747
ρ [kg/m3]	1444.1
MW unit cell [g/mol(framework)]	4326.106
ϕ, fractional pore volume	0.382
open space / Å^3/uc	1898.4
Pore volume / cm^3/g	0.264
Surface area /m^2/g	758.0
DeLaunay diameter /Å	3.77

Figure S6

DDR landscape

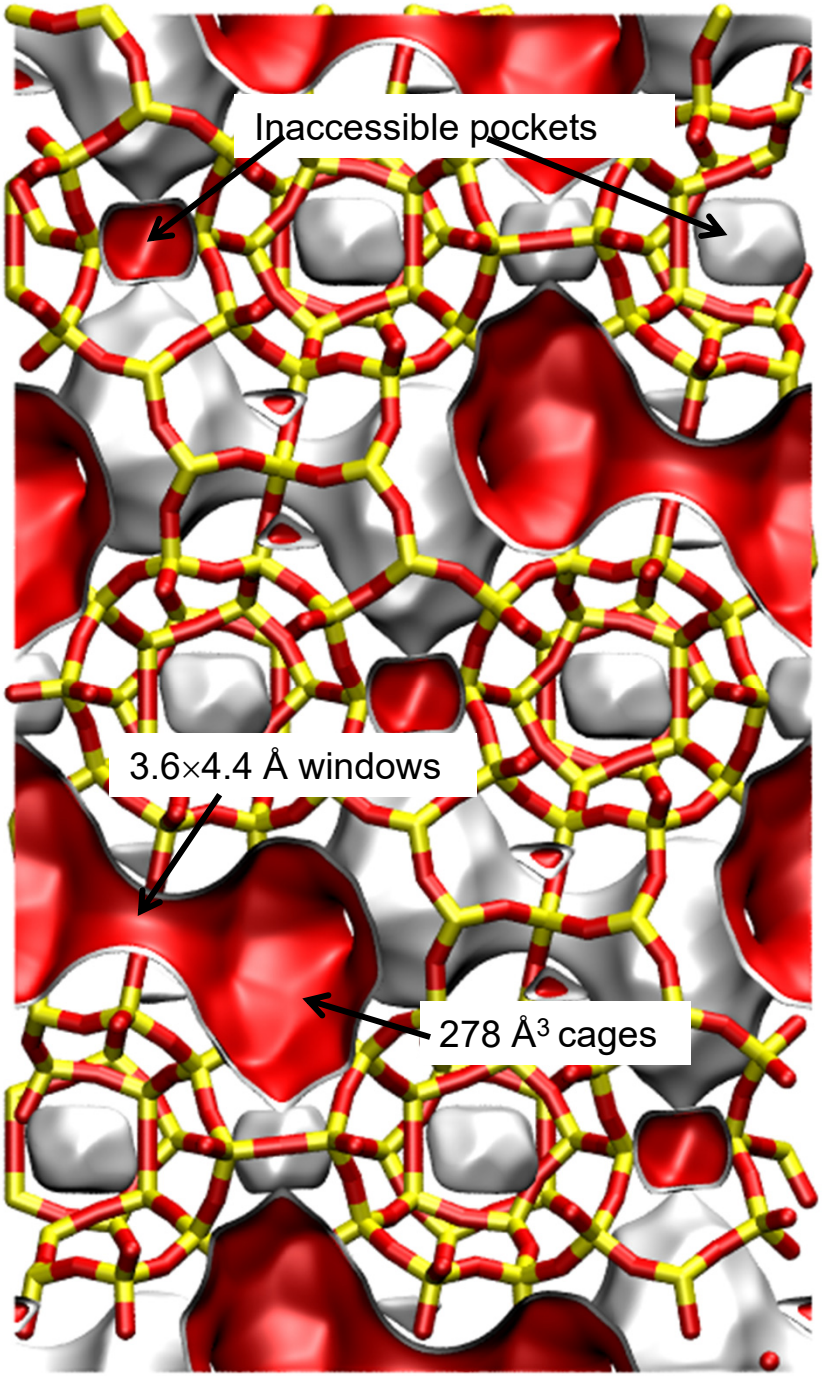

To convert from molecules per unit cell to mol kg^{-1}, multiply by 0.06936.
The pore volume is 0.182 cm^3/g.

There are 12 cages per unit cell. The volume of one DDR cage is 278 Å^3, significantly smaller than that of a single cage of FAU (786 Å^3), or ZIF-8 (1168 Å^3).

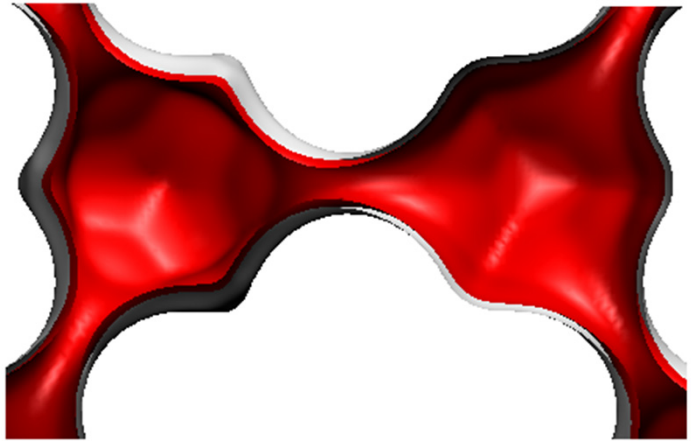

Structural information from: C. Baerlocher, L.B. McCusker, Database of Zeolite Structures, International Zeolite Association, http://www.iza-structure.org/databases/

Figure S7

DDR window and pore dimensions

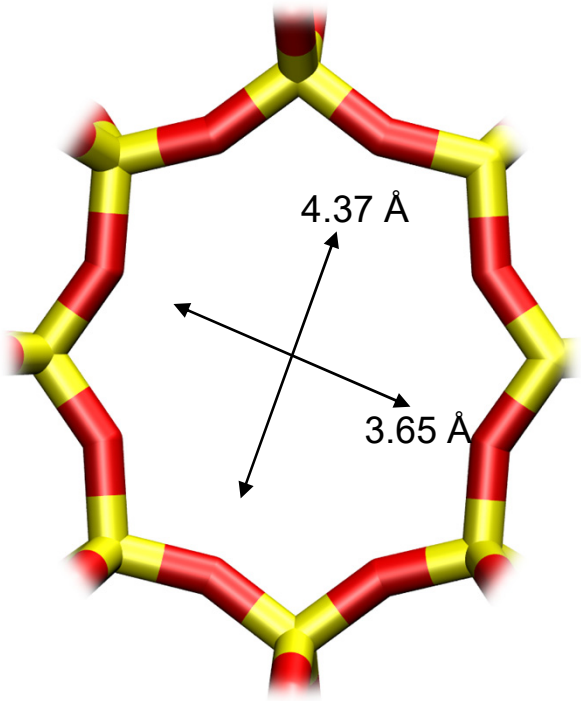

DDR

The window dimensions calculated using the van der Waals diameter of framework atoms = 2.7 Å are indicated above by the arrows.

	DDR
a /Å	24.006
b /Å	13.86
c /Å	40.892
Cell volume / Å^3	13605.72
conversion factor for [molec/uc] to [mol per kg Framework]	0.0693
conversion factor for [molec/uc] to [kmol/m^3]	0.4981
ρ [kg/m3]	1759.991
MW unit cell [g/mol(framework)]	14420.35
ϕ, fractional pore volume	0.245
open space / Å^3/uc	3333.5
Pore volume / cm^3/g	0.139
Surface area /m^2/g	350.0
DeLaunay diameter /Å	3.65

Figure S8

ERI pore landscape

There are 4 cages per unit cell.
The volume of one ERI cage is 408.7 Å^3, significantly smaller than that of a single cage of FAU-Si (786 Å^3), or ZIF-8 (1168 Å^3).

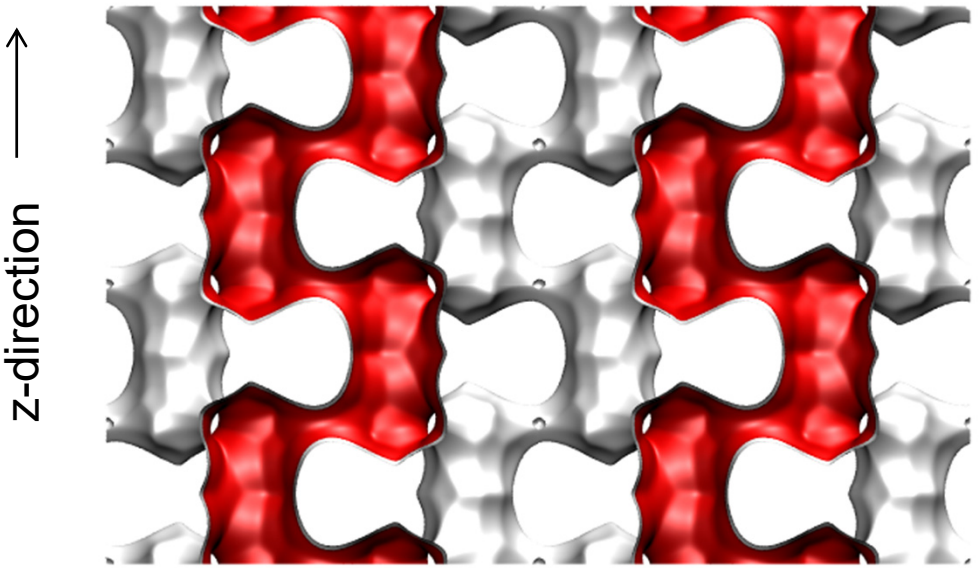

x-y projection

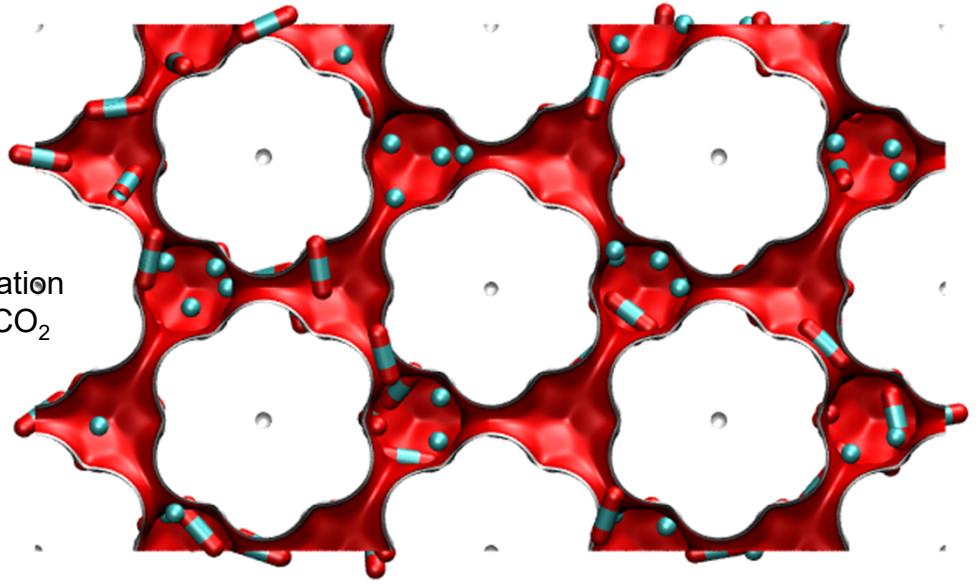

Snapshots showing location of CH_4 and CO_2

Structural information from: C. Baerlocher, L.B. McCusker, Database of Zeolite Structures, International Zeolite Association, http://www.iza-structure.org/databases/

Figure S9

ERI window and pore dimensions

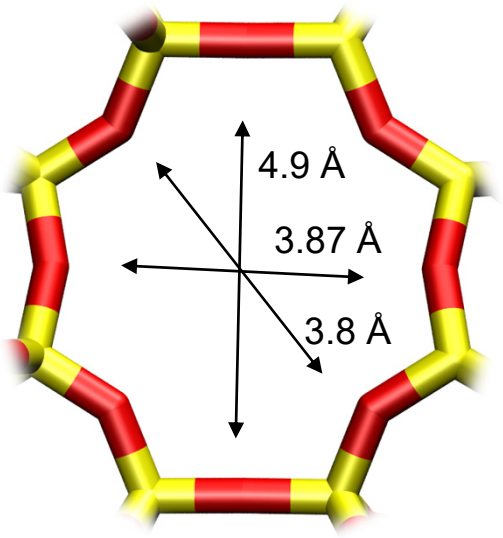

ERI

The window dimensions calculated using the van der Waals diameter of framework atoms = 2.7 Å are indicated above by the arrows.

	ERI
a /Å	22.953
b /Å	13.252
c /Å	14.81
Cell volume / Å^3	4504.804
conversion factor for [molec/uc] to [mol per kg Framework]	0.2312
conversion factor for [molec/uc] to [kmol/m^3]	1.0156
ρ [kg/m3]	1594.693
MW unit cell [g/mol(framework)]	4326.106
ϕ, fractional pore volume	0.363
open space / Å^3/uc	1635.0
Pore volume / cm^3/g	0.228
Surface area /m^2/g	635.0
DeLaunay diameter /Å	3.81

Figure S10

LTA-Si landscapes

This is a *hypothetical* structure

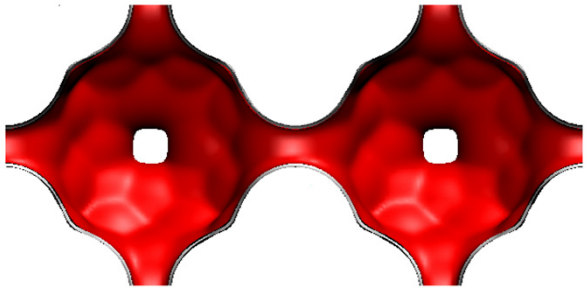

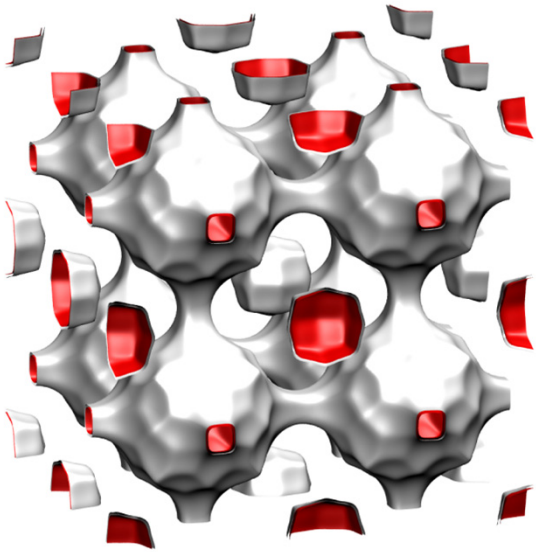

There are 8 cages per unit cell.
The volume of one LTA cage is 743 Å^3, intermediate in size between a single cage of ZIF-8 (1168 Å^3) and of DDR (278 Å^3).

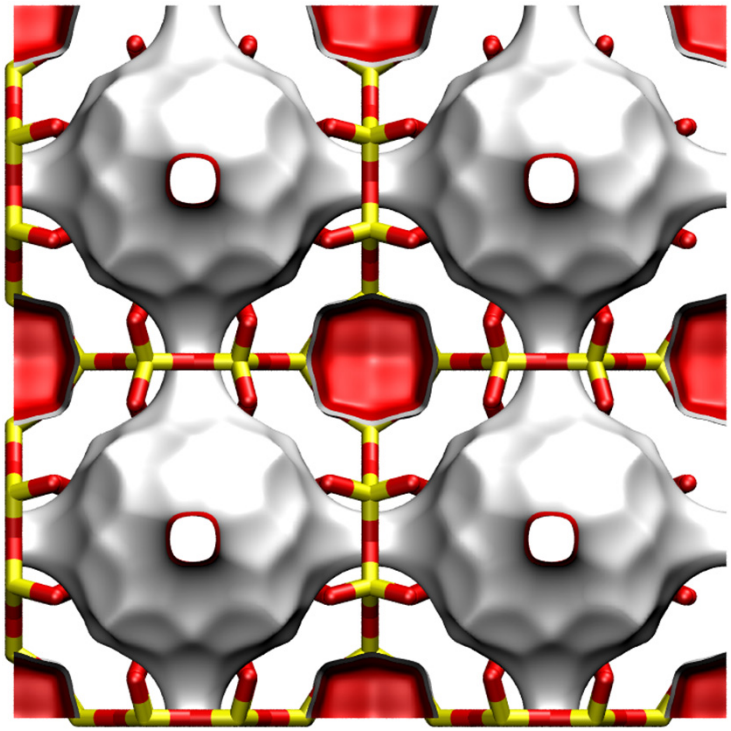

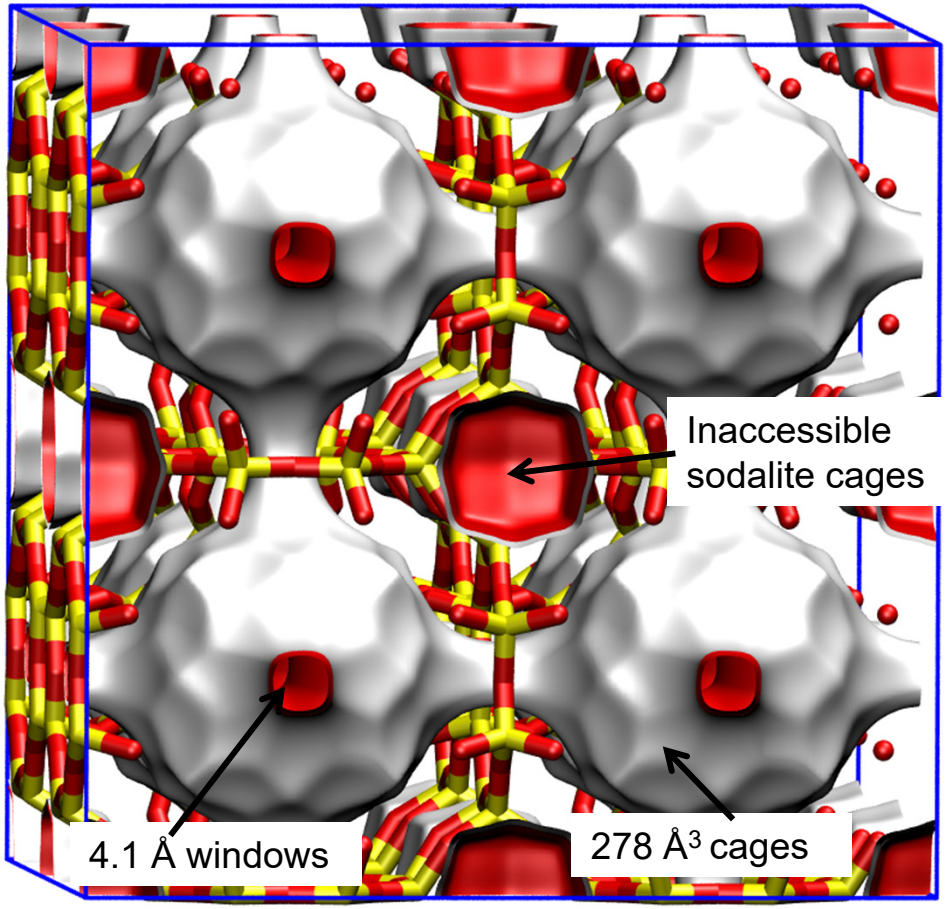

Figure S11

LTA-Si window and pore dimensions

8-ring window of LTA

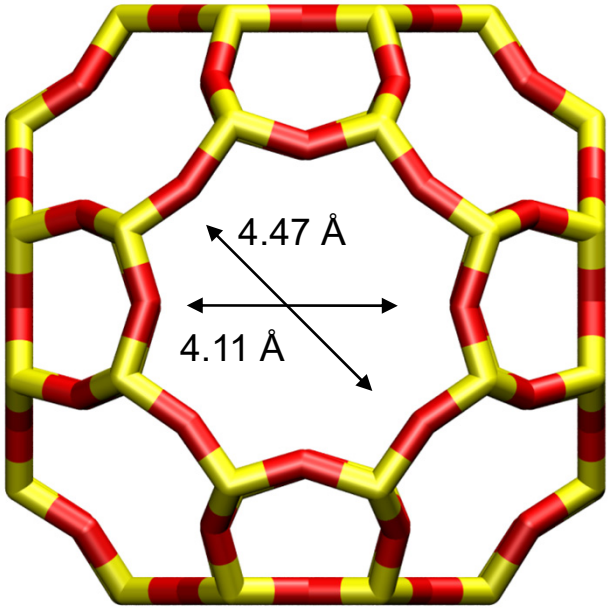

The window dimension calculated using the van der Waals diameter of framework atoms = 2.7 Å is indicated above by the arrows.

	LTA-Si
a /Å	24.61
b /Å	24.61
c /Å	24.61
Cell volume / Å^3	14905.1
conversion factor for [molec/uc] to [mol per kg Framework]	0.0867
conversion factor for [molec/uc] to [kmol/m^3]	0.2794
ρ [kg/m3]	1285.248
MW unit cell [g/mol(framework)]	11536.28
ϕ, fractional pore volume	0.399
open space / Å^3/uc	5944.4
Pore volume / cm^3/g	0.310
Surface area /m^2/g	896.0
DeLaunay diameter /Å	4.10

LTA-5A

Figure S12

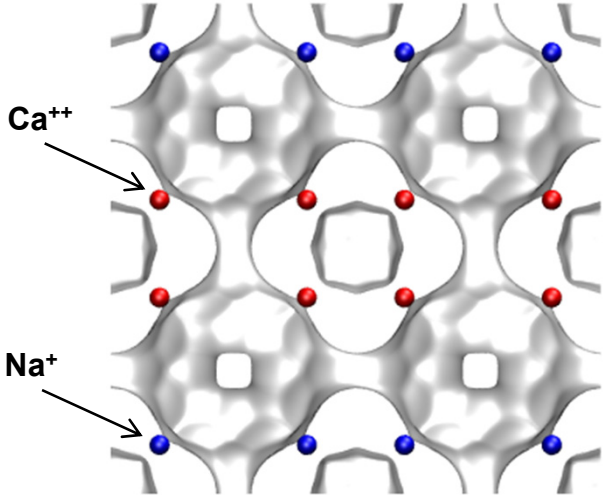

LTA-5A (32 Na+, 32 Ca++)

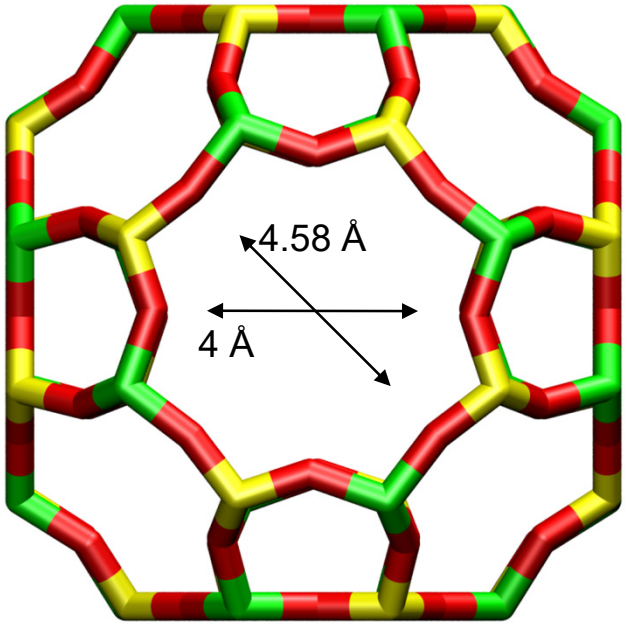

LTA-5A

The window dimension calculated using the van der Waals diameter of framework atoms = 2.7 Å is indicated above by the arrow.

	LTA-5A
a /Å	24.555
b /Å	24.555
c /Å	24.555
Cell volume / Å^3	14805.39
conversion factor for [molec/uc] to [mol per kg Framework]	0.0744
conversion factor for [molec/uc] to [kmol/m^3]	0.2955
ρ [kg/m3] (with cations)	1508.376
MW unit cell [g/mol(framework+cations)]	13448.48
ϕ, fractional pore volume	0.380
open space / Å^3/uc	5620.4
Pore volume / cm^3/g	0.252
Surface area /m^2/g	
DeLaunay diameter /Å	4.00

LTA-4A

Figure S13

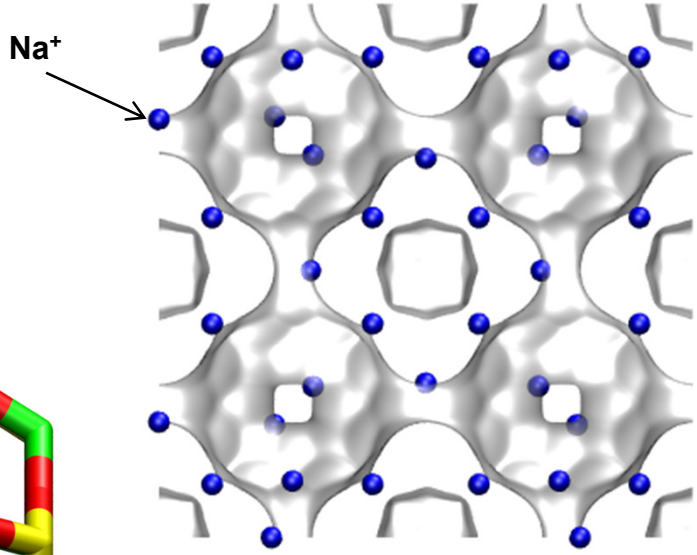

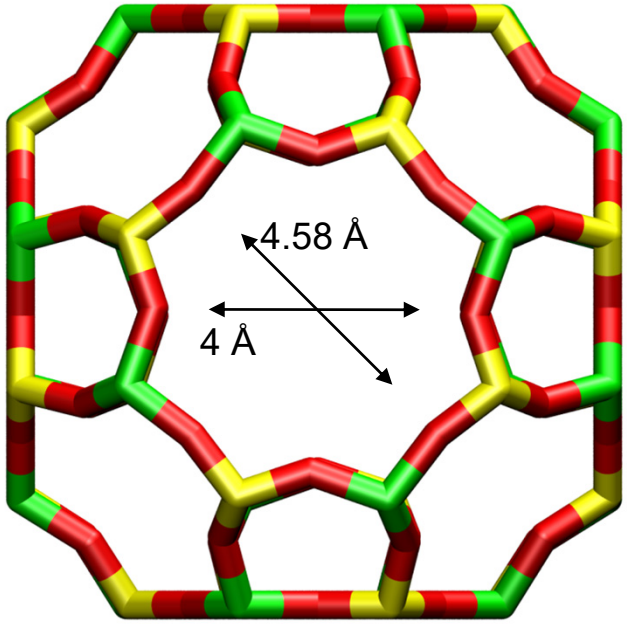

LTA-4A

The window dimension calculated using the van der Waals diameter of framework atoms = 2.7 Å is indicated above by the arrow.

Note that the Na^+ ions partially block the windows and therefore the diffusivities in LTA-4A are significantly lower than that for LTA Si. These cannot be determined from MD.

LTA-4A (96 Na+)

	LTA-4A
a /Å	24.555
b /Å	24.555
c /Å	24.555
Cell volume / $Å^3$	14805.39
conversion factor for [molec/uc] to [mol per kg Framework]	0.0733
conversion factor for [molec/uc] to [kmol/m^3]	0.2991
ρ [kg/m3] (with cations)	1529.55
MW unit cell [g/mol(framework+cations)]	13637.27
ϕ, fractional pore volume	0.375
open space / $Å^3$/uc	5552.0
Pore volume / cm^3/g	0.245
Surface area /m^2/g	
DeLaunay diameter /Å	4.00

ZIF-8 pore landscapes

Figure S14

There are 2 cages per unit cell. To convert from molecules per cage to mol kg^{-1}, multiply by 0.7325.

There are 2 cages per unit cell. The volume of one ZIF-8 cage is 1168 $Å^3$, significantly larger than that of a single cage of DDR (278 $Å^3$), or FAU (786 $Å^3$).

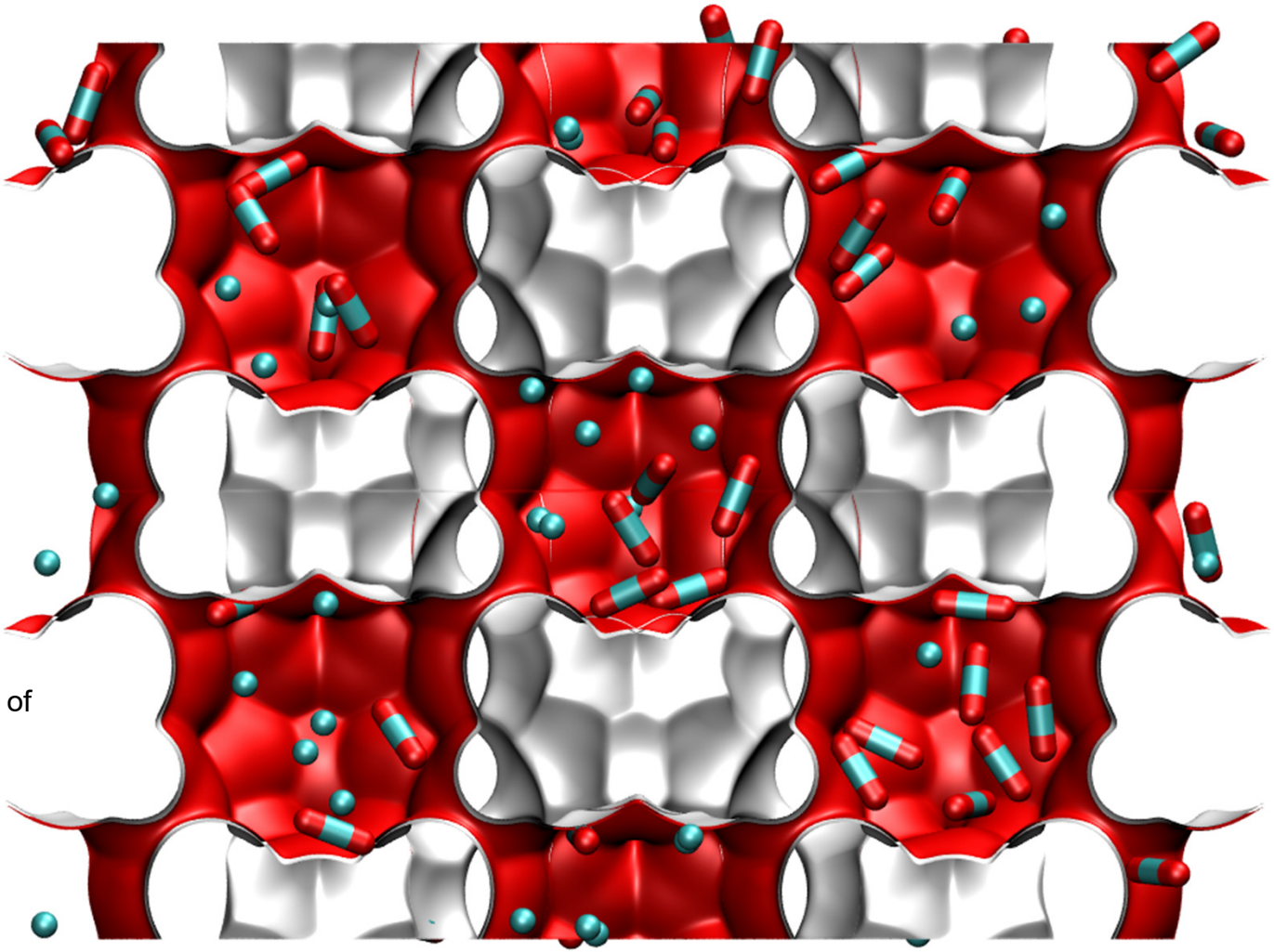

Snapshots showing the locations of CO_2 and CH_4 in ZIF-8

ZIF-8 dimensions

Figure S15

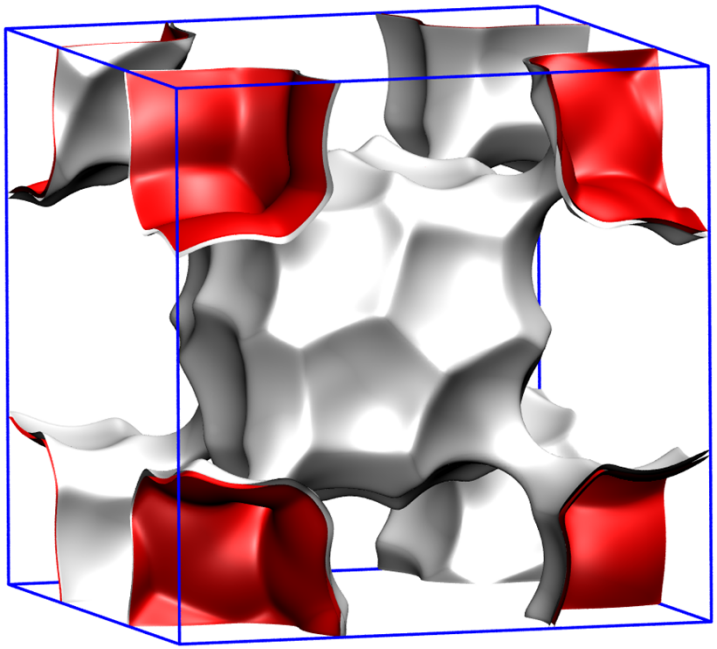

Unit cell of ZIF-8

	ZIF-8
a /Å	16.991
b /Å	16.991
c /Å	16.991
Cell volume / Å^3	4905.201
conversion factor for [molec/uc] to [mol per kg Framework]	0.3663
conversion factor for [molec/uc] to [kmol/m^3]	0.7106
ρ [kg/m3]	924.253
MW unit cell [g/mol(framework)]	2730.182
ϕ, fractional pore volume	0.476
open space / Å^3/uc	2337.0
Pore volume / cm^3/g	0.515
Surface area /m^2/g	1164.7
DeLaunay diameter /Å	3.26

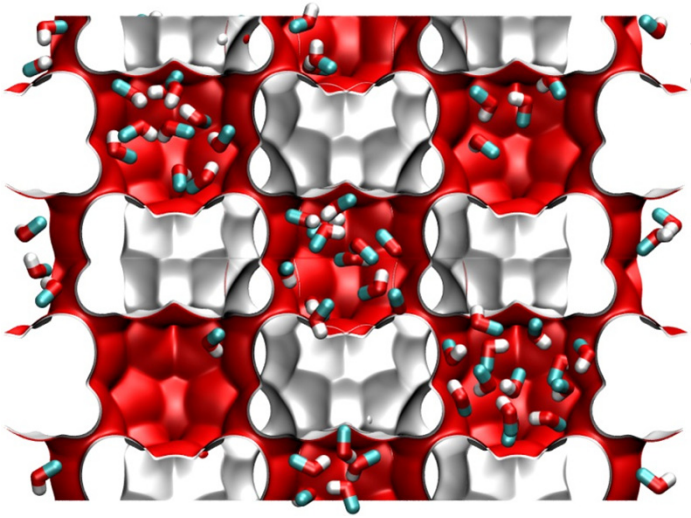

Snapshot showing clustering of methanol molecules in ZIF-8

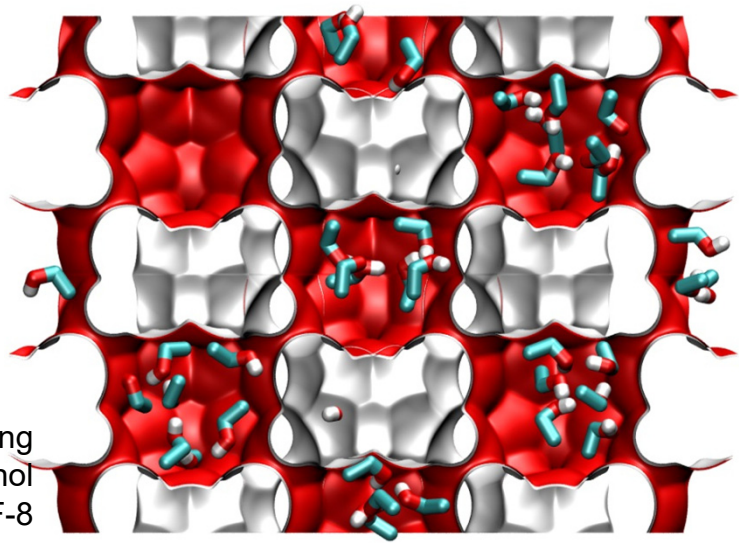

Snapshot showing clustering of ethanol molecules in ZIF-8

MFI pore landscape

Figure S16

	MFI
a /Å	20.022
b /Å	19.899
c /Å	13.383
Cell volume / Å^3	5332.025
conversion factor for [molec/uc] to [mol per kg Framework]	0.1734
conversion factor for [molec/uc] to [kmol/m^3]	1.0477
ρ [kg/m3]	1796.386
MW unit cell [g/mol(framework)]	5768.141
ϕ, fractional pore volume	0.297
open space / Å^3/uc	1584.9
Pore volume / cm^3/g	0.165
Surface area /m^2/g	487.0
DeLaunay diameter /Å	5.16

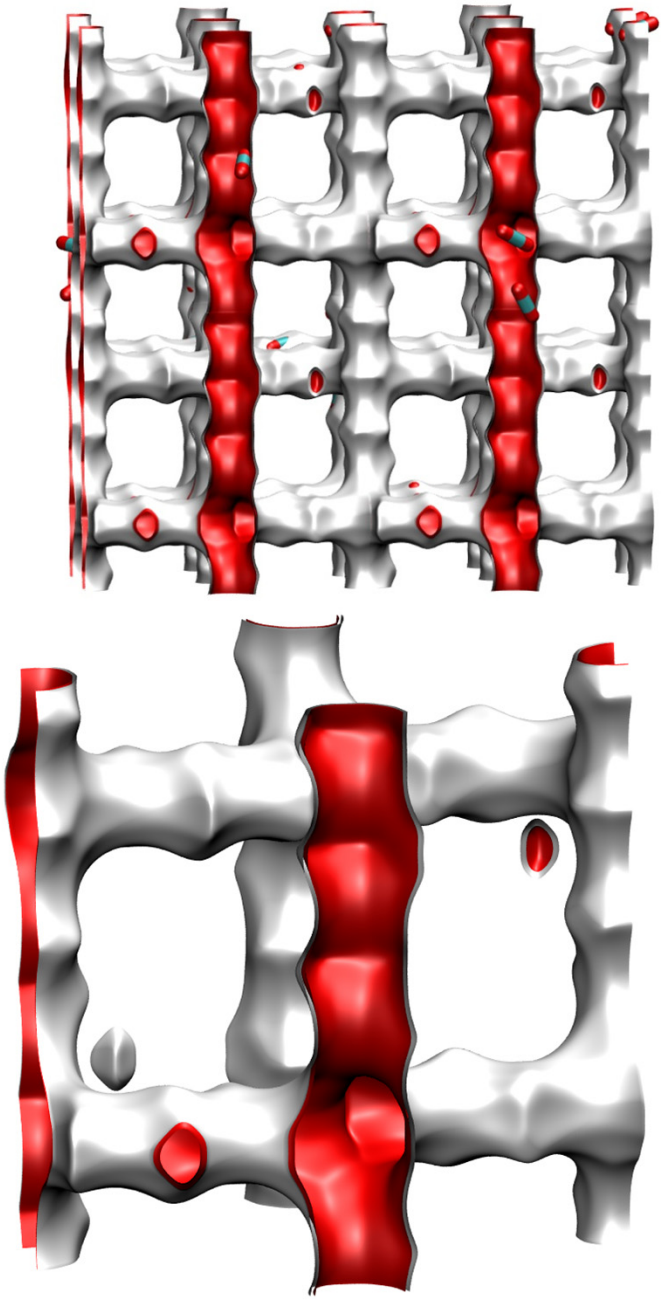

Figure S17

MFI pore dimensions

10 ring channel of MFI viewed along [100]

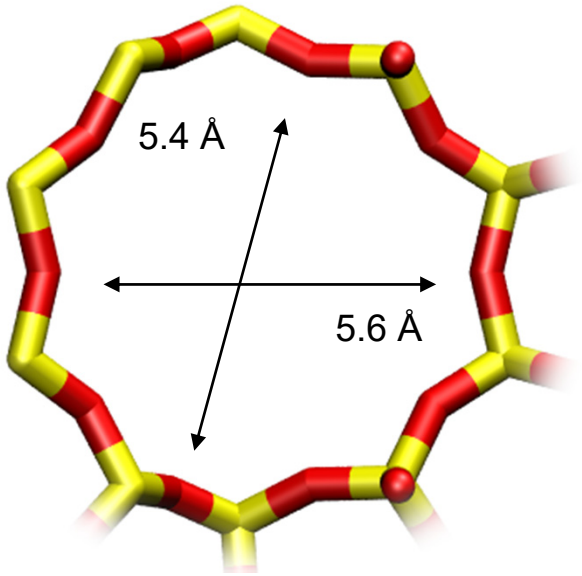

10 ring channel of MFI viewed along [010]

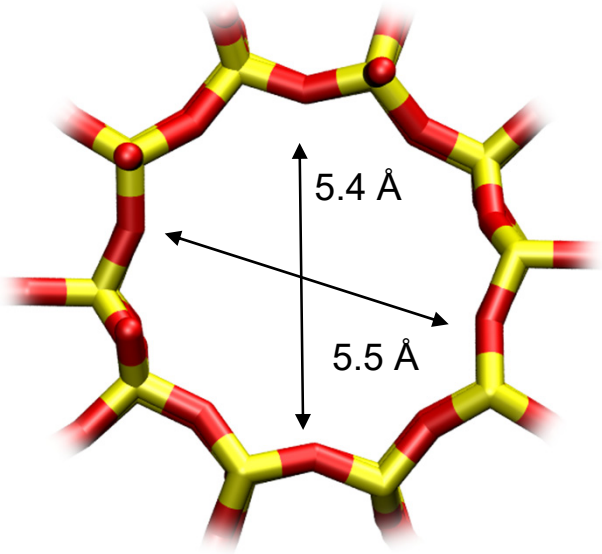

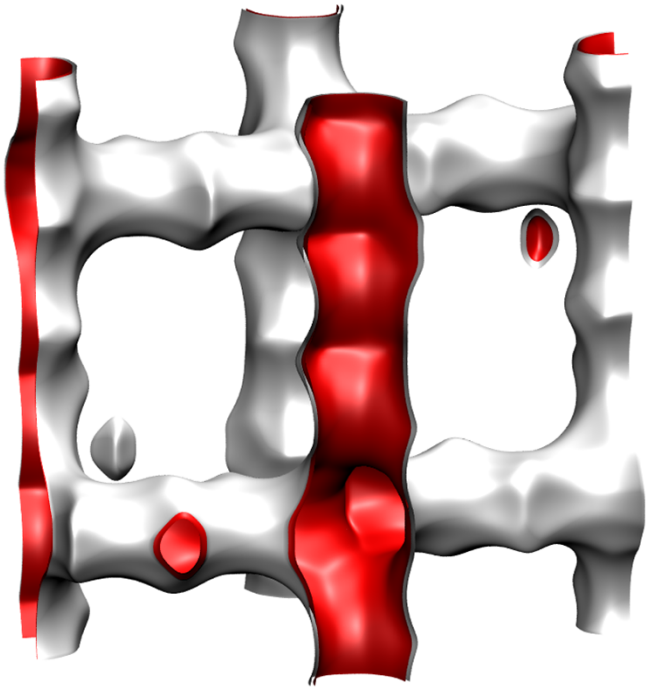

Figure S18

FER pore landscape

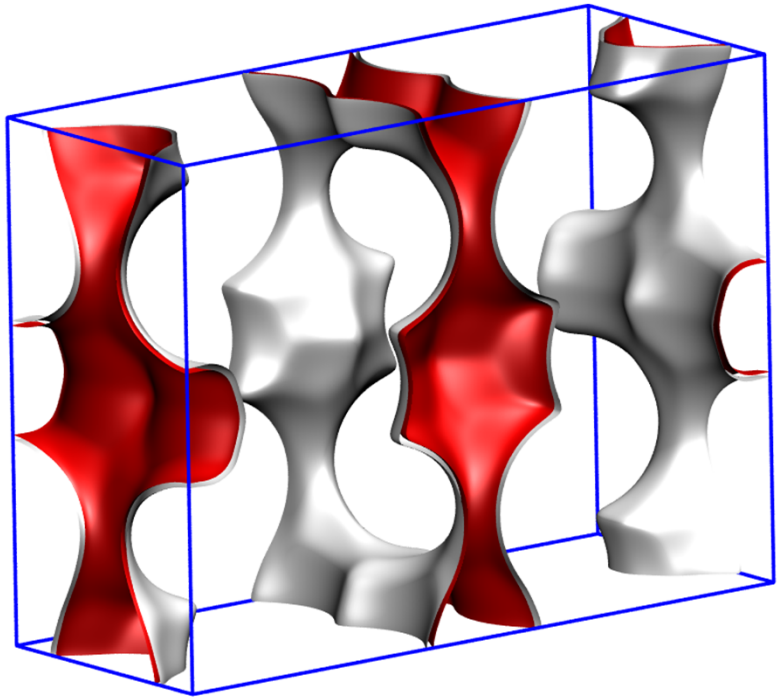

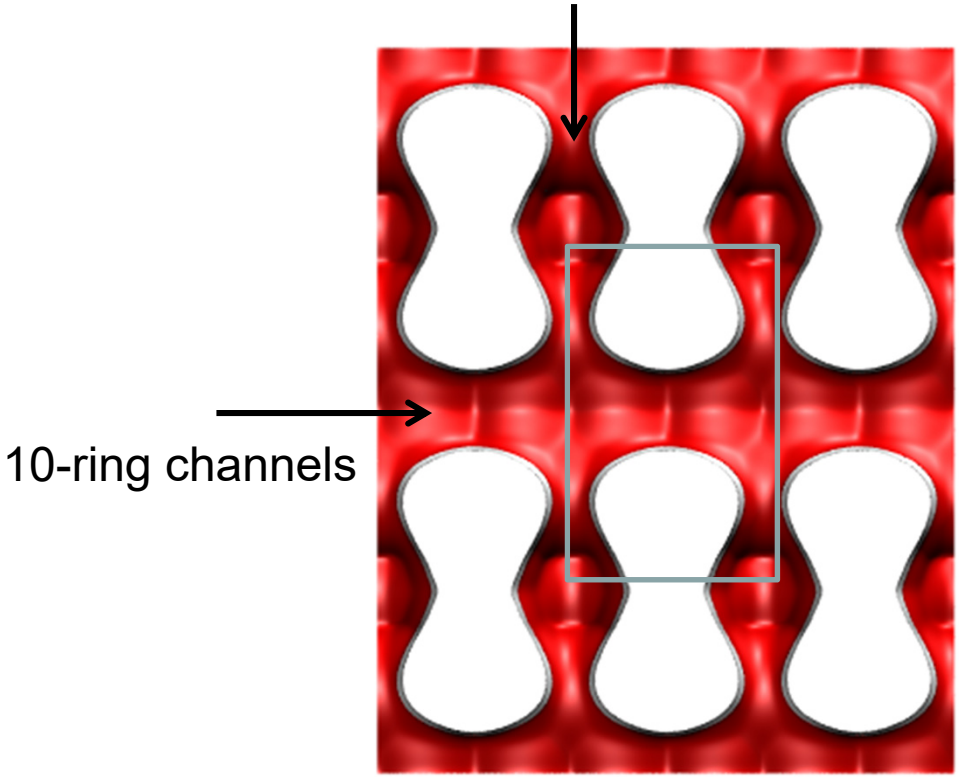

This is one unit cell

There are two 10-ring channels
There are two 8-ring channels

Structural information from: C. Baerlocher, L.B. McCusker, Database of Zeolite Structures, International Zeolite Association, http://www.iza-structure.org/databases/

FER pore dimensions

Figure S19

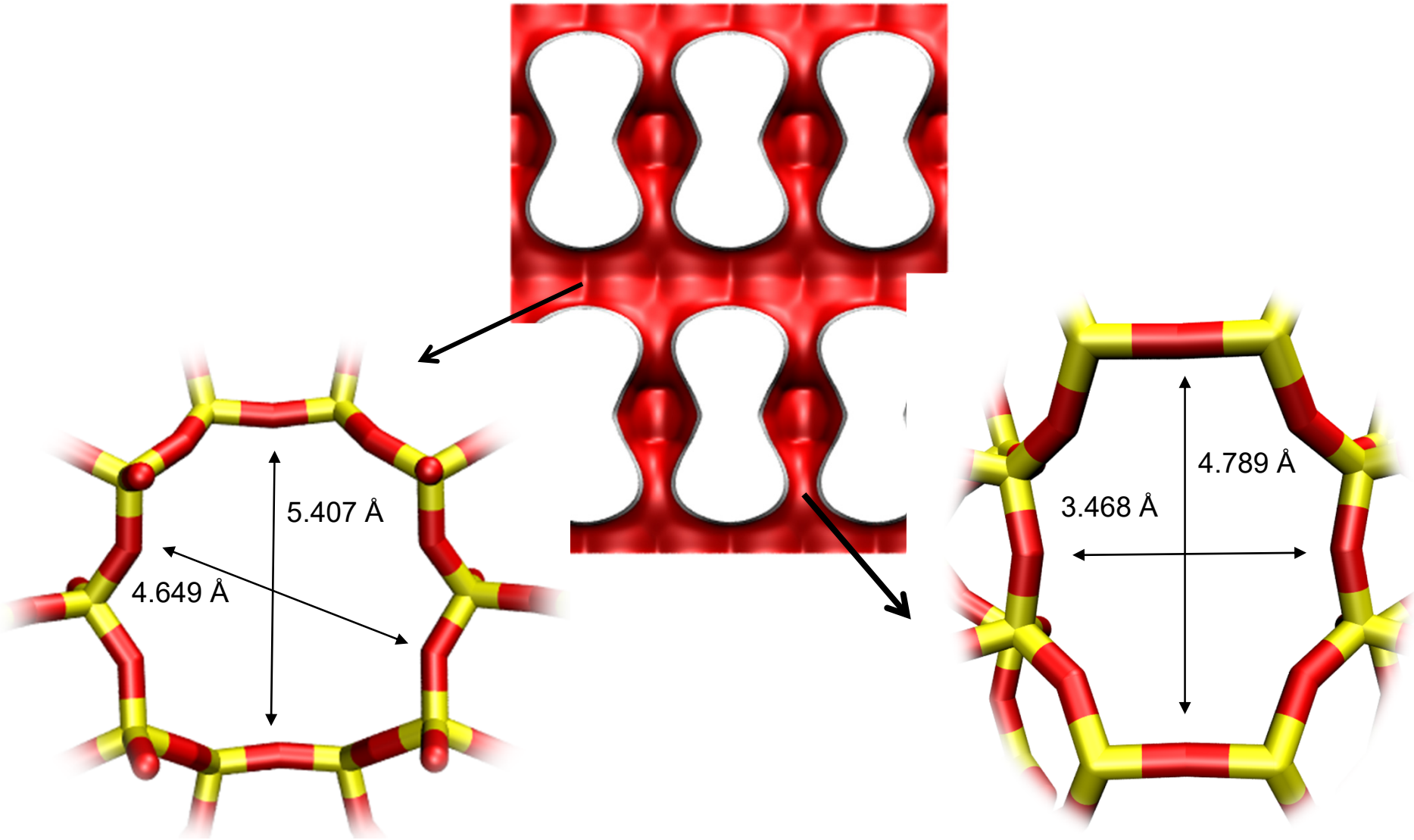

FER channel [0 0 1]

FER [0 1 0]

Figure S20

FER pore landscape

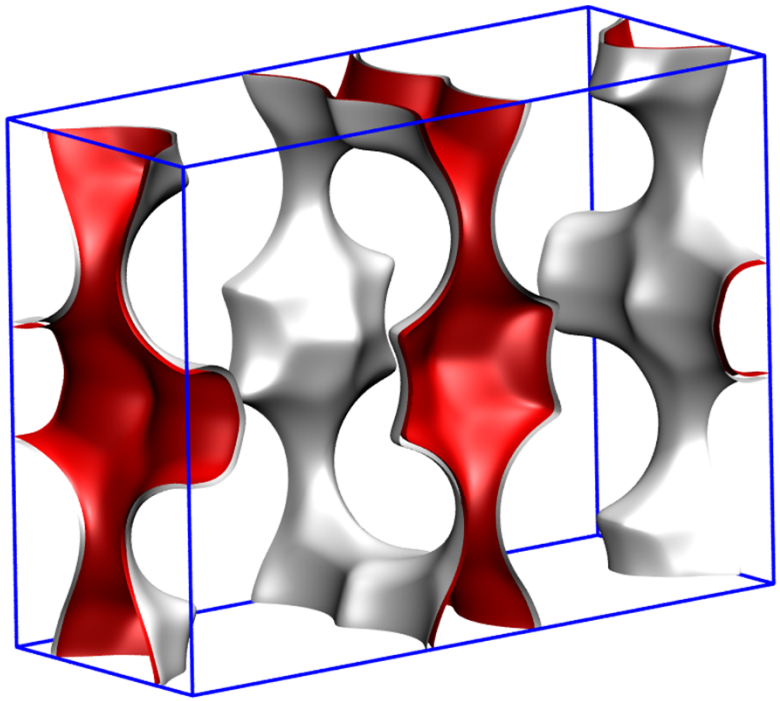

	FER
a /Å	19.156
b /Å	14.127
c /Å	7.489
Cell volume / Å^3	2026.649
conversion factor for [molec/uc] to [mol per kg Framework]	0.4623
conversion factor for [molec/uc] to [kmol/m^3]	2.8968
ρ [kg/m3]	1772.33
MW unit cell [g/mol (framework)]	2163.053
ϕ, fractional pore volume	0.283
open space / Å^3/uc	573.2
Pore volume / cm^3/g	0.160
Surface area /m^2/g	403.0
DeLaunay diameter /Å	4.65

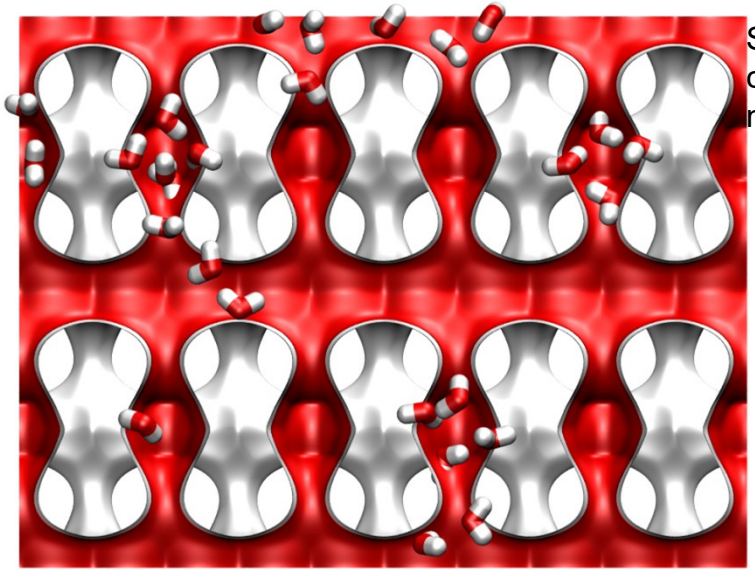

Snapshot showing clustering of water molecules in FER

Snapshot showing clustering of methanol molecules in FER

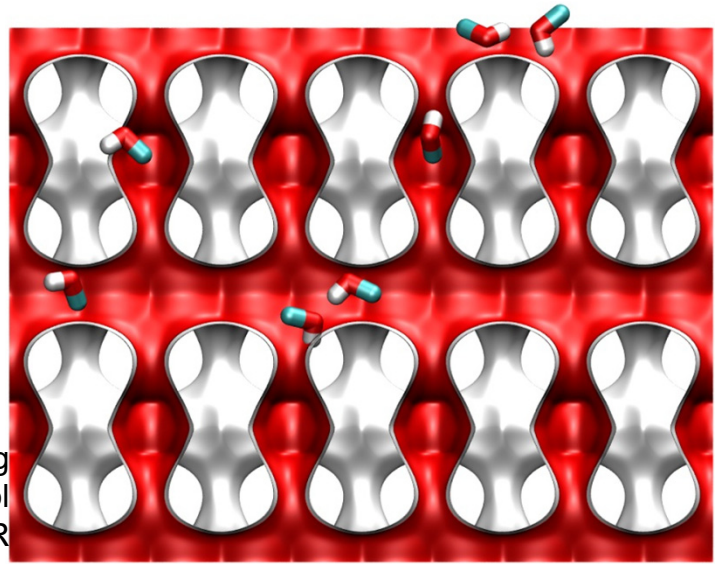

Figure S21

MOR pore landscape

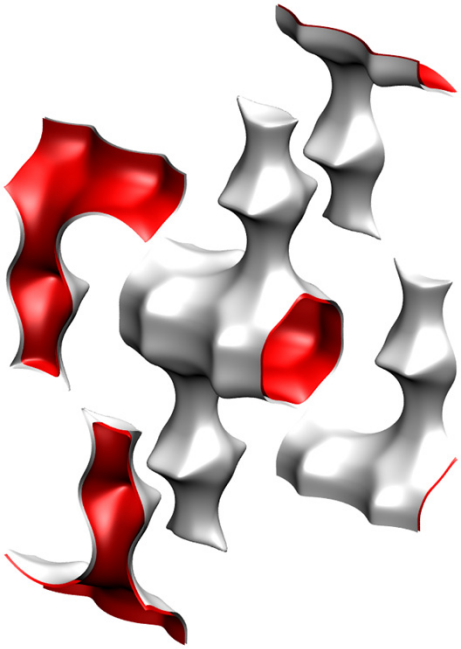

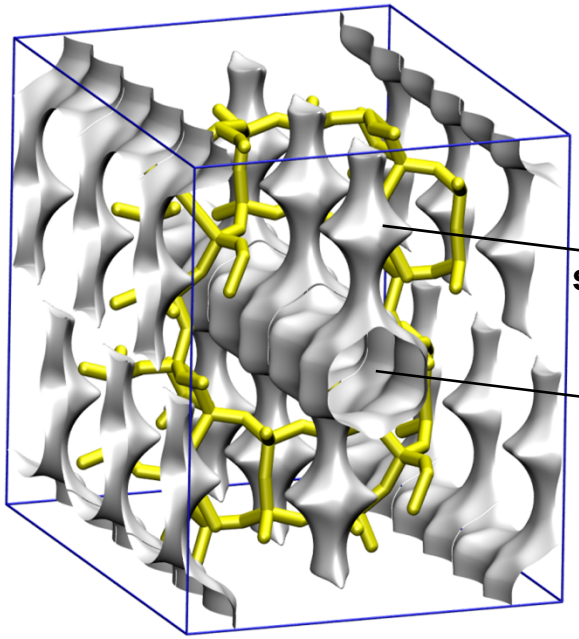

	MOR
a /Å	18.094
b /Å	20.516
c /Å	7.524
Cell volume / Å^3	2793.033
conversion factor for [molec/uc] to [mol per kg Framework]	0.3467
conversion factor for [molec/uc] to [kmol/m^3]	2.0877
ρ [kg/m3]	1714.691
MW unit cell [g/mol(framework)]	2884.07
ϕ, fractional pore volume	0.285
open space / Å^3/uc	795.4
Pore volume / cm^3/g	0.166
Surface area /m^2/g	417.0
DeLaunay diameter /Å	6.44

Figure S22

MOR pore dimensions

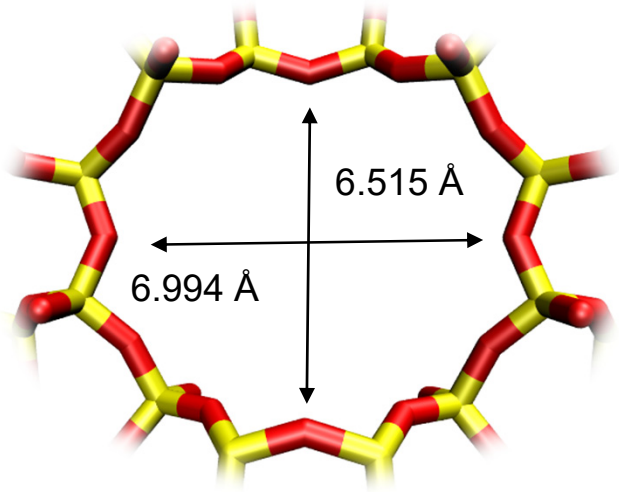

MOR Channel [1 0 0]

12-ring
main channels

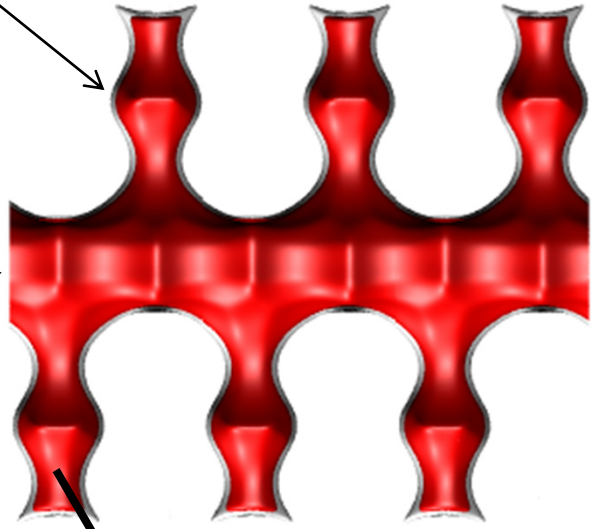

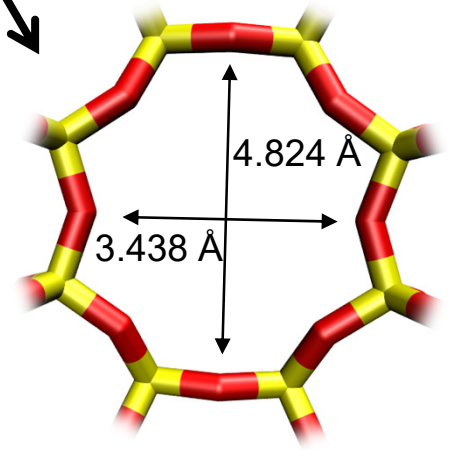

MOR [0 1 0]

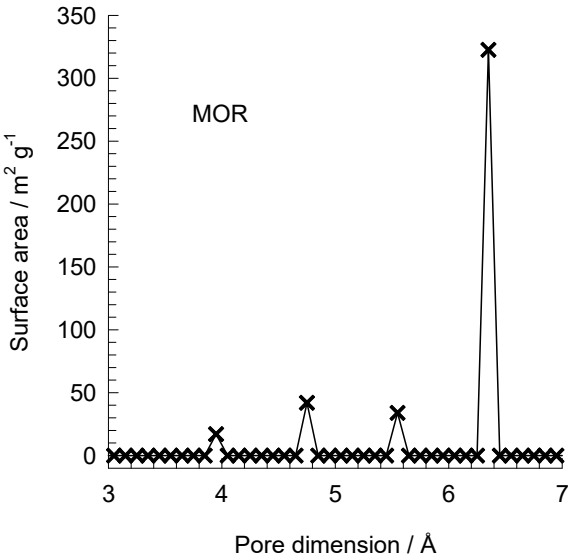

This plot of surface area versus pore dimension is determined using a combination of the DeLaunay triangulation method for pore dimension determination, and the procedure of Düren for determination of the surface area.

FAU-Si pore landscape

Figure S23

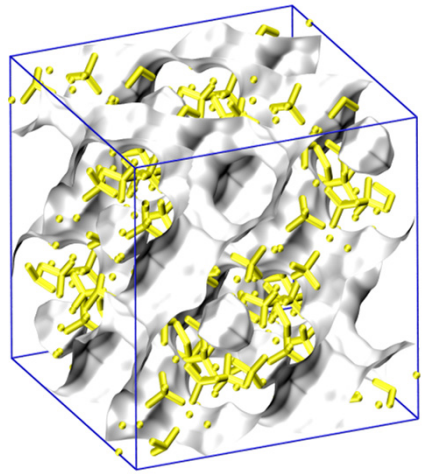

The sodalite cages are blocked in simulations and are not accessible to guest molecules; these are excluded for pore volume determination.

12-ring window of FAU

There are 8 cages per unit cell. The volume of one FAU cage is 786 Å^3, larger in size than that of LTA (743 Å^3) and DDR (278 Å^3).

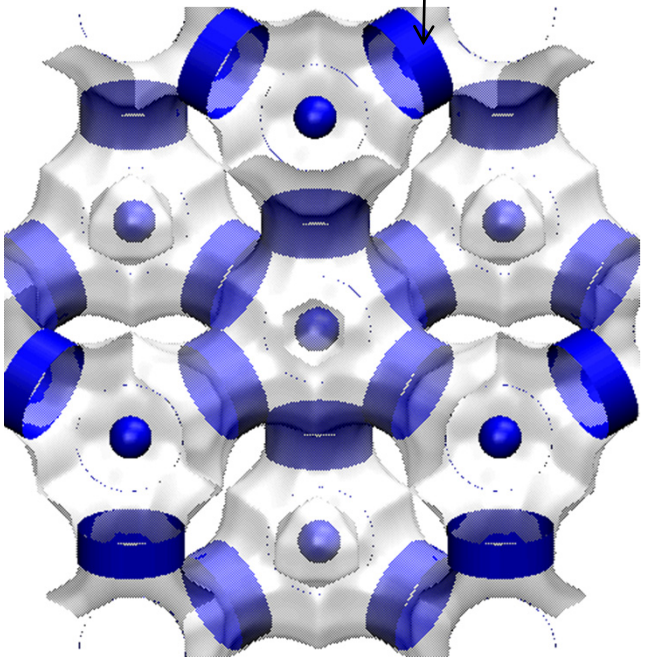

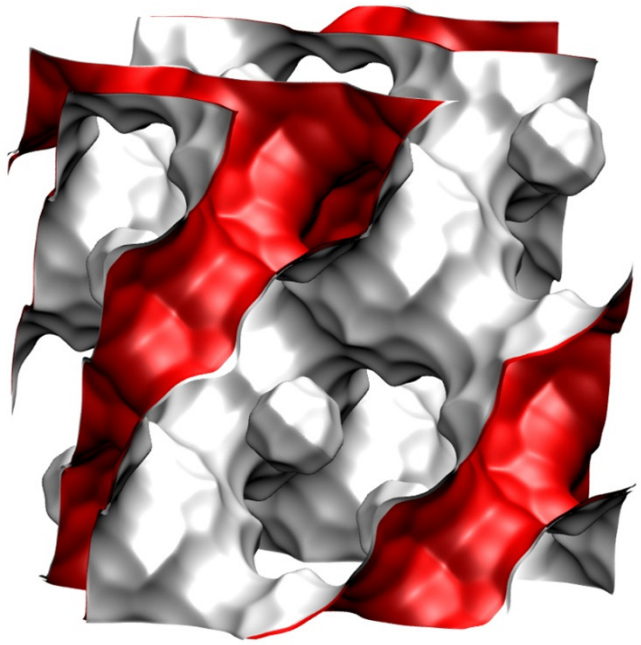

Structural information from: C. Baerlocher, L.B. McCusker, Database of Zeolite Structures, International Zeolite Association, http://www.iza-structure.org/databases/

Figure S24

FAU-Si window and pore dimensions

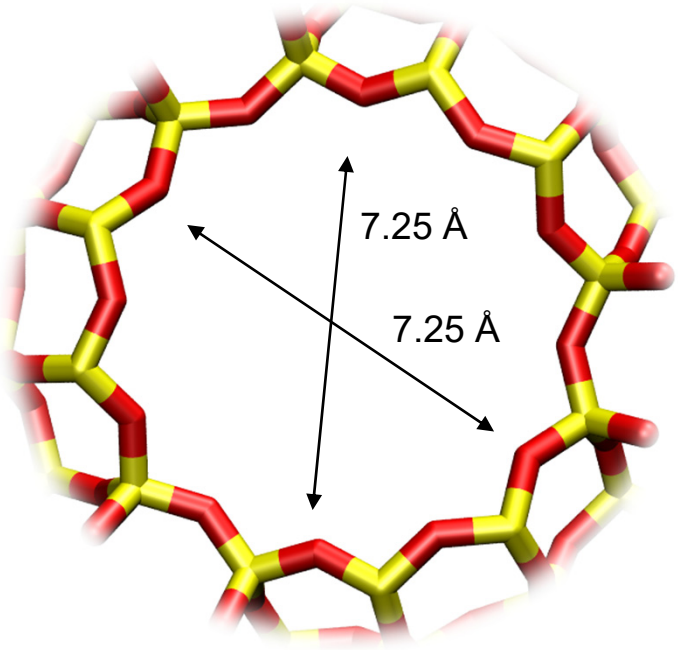

	FAU-Si
a /Å	24.28
b /Å	24.28
c /Å	24.28
Cell volume / Å^3	14313.51
conversion factor for [molec/uc] to [mol per kg Framework]	0.0867
conversion factor for [molec/uc] to [kmol/m^3]	0.2642
ρ [kg/m3]	1338.369
MW unit cell [g/mol (framework)]	11536.28
ϕ, fractional pore volume	0.439
open space / Å^3/uc	6285.6
Pore volume / cm^3/g	0.328
Surface area /m^2/g	1086.0
DeLaunay diameter /Å	7.37

NaY (144 Si, 48 Al, 48 Na+, Si/Al=3)

Figure S25

Blue spheres are cations

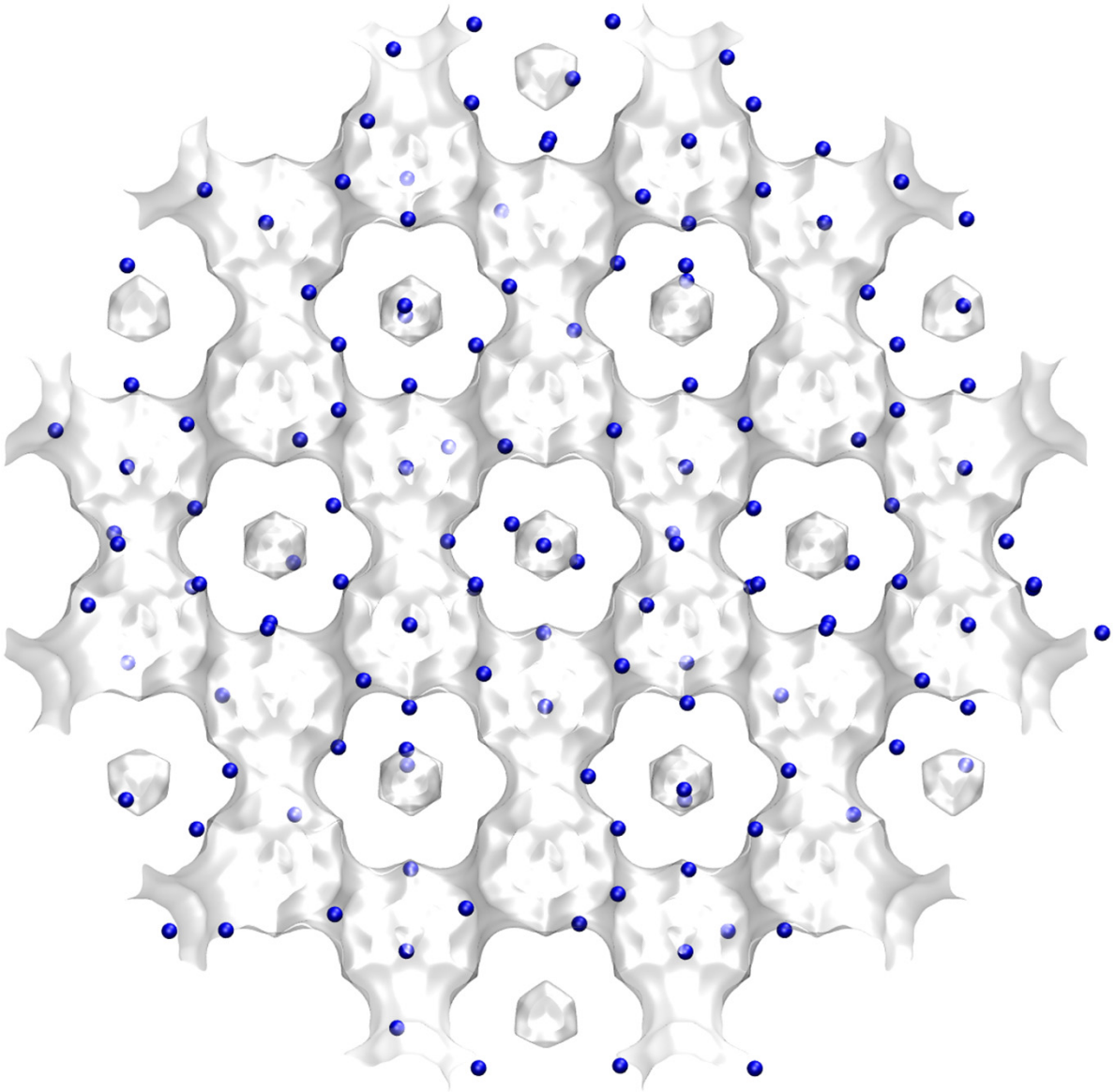

	FAU-48Al
a /Å	25.028
b /Å	25.028
c /Å	25.028
Cell volume / Å^3	15677.56
conversion factor for [molec/uc] to [mol per kg Framework]	0.0794
conversion factor for [molec/uc] to [kmol/m^3]	0.2596
ρ [kg/m3] (with cations)	1333.19
MW unit cell [g/mol(framework+cations)]	12586.78
ϕ, fractional pore volume	0.408
open space / Å^3/uc	6396.6
Pore volume / cm^3/g	0.306
Surface area /m^2/g	
DeLaunay diameter /Å	7.37

NaY (138 Si, 54 Al, 54 Na+, Si/Al=2.55)

Figure S26

Blue spheres are cations

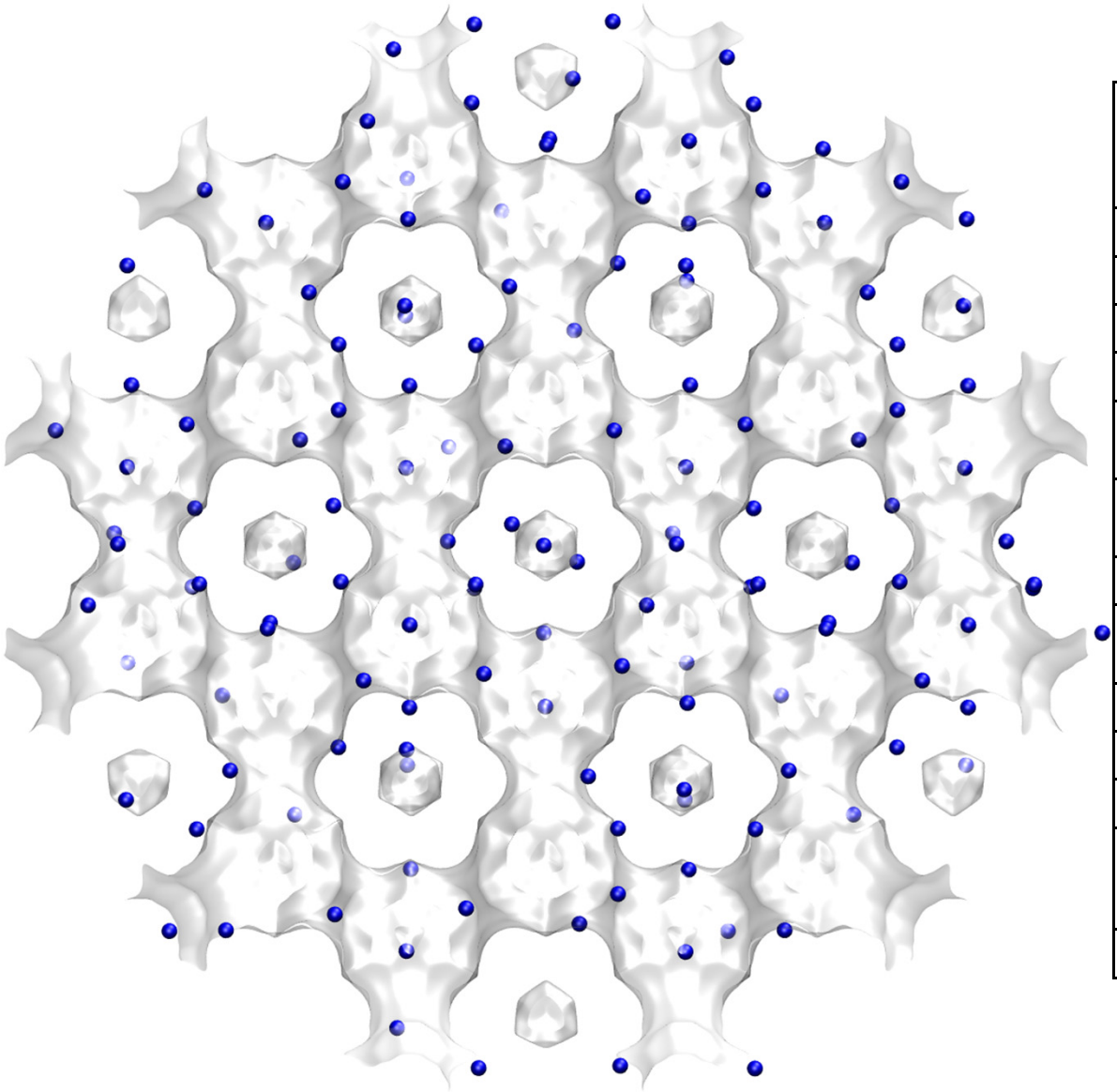

	FAU-54Al
a /Å	25.028
b /Å	25.028
c /Å	25.028
Cell volume / Å^3	15677.56
conversion factor for [molec/uc] to [mol per kg Framework]	0.0786
conversion factor for [molec/uc] to [kmol/m^3]	0.2596
ρ [kg/m3] (with cations)	1347.1
MW unit cell [g/mol(framework+cations)]	12718.08
ϕ, fractional pore volume	0.408
open space / Å^3/uc	6396.6
Pore volume / cm^3/g	0.303
Surface area /m^2/g	
DeLaunay diameter /Å	7.37

NaX (106 Si, 86 Al, 86 Na+, Si/Al=1.23)

Figure S27

This material is commonly referred to by its trade name 13X zeolite

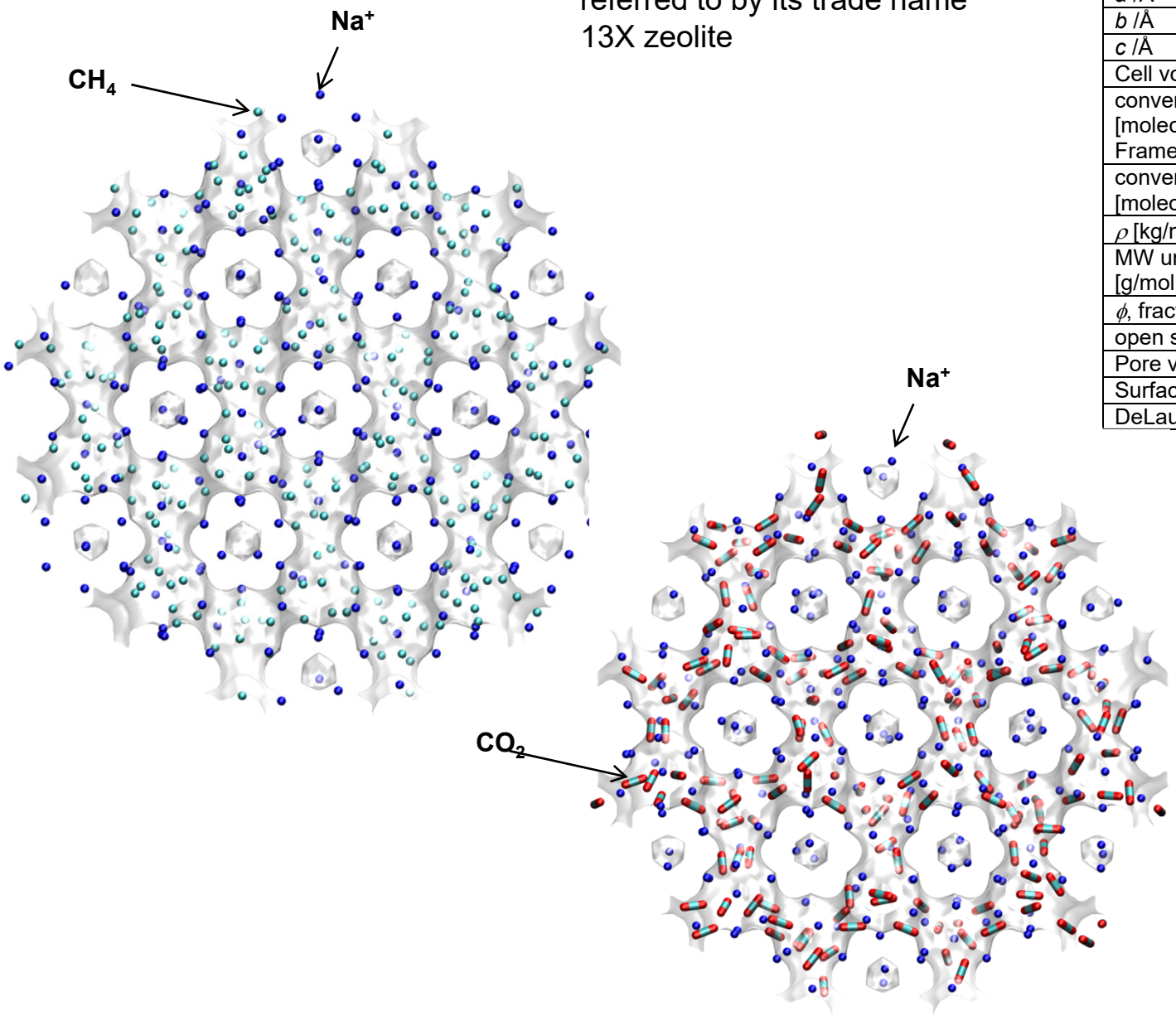

	NaX 86 Na/uc
a /Å	25.028
b /Å	25.028
c /Å	25.028
Cell volume / Å^3	15677.56
conversion factor for [molec/uc] to [mol per kg Framework]	0.0745
conversion factor for [molec/uc] to [kmol/m^3]	0.2658
ρ [kg/m3] (with cations)	1421.277
MW unit cell [g/mol(framework+cations)]	13418.42
ϕ, fractional pore volume	0.399
open space / Å^3/uc	6248.0
Pore volume / cm^3/g	0.280
Surface area /m^2/g	
DeLaunay diameter /Å	7.37

Figure S28

CuBTC pore landscapes

The structural information for CuBTC (= $Cu_3(BTC)_2$ with BTC = 1,3,5-benzenetricarboxylate) have been taken from

S.S.Y. Chui, S.M.F. Lo, J.P.H. Charmant, A.G. Orpen, I.D. Williams, A chemically functionalizable nanoporous material $[Cu_3(TMA)_2(H2O)_3]_n$, Science 283 (1999) 1148-1150.
The crystal structure of Chui et al. includes axial oxygen atoms weakly bonded to the Cu atoms, which correspond to water ligands. Our simulations have been performed on the dry CuBTC with these oxygen atoms removed.

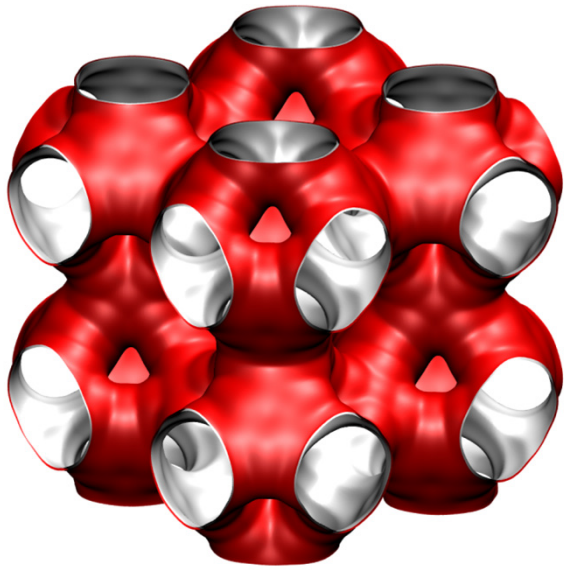

Q. Yang, C. Zhong, Electrostatic-Field-Induced Enhancement of Gas Mixture Separation in Metal-Organic Frameworks: A Computational Study, ChemPhysChem 7 (2006) 1417-1421.

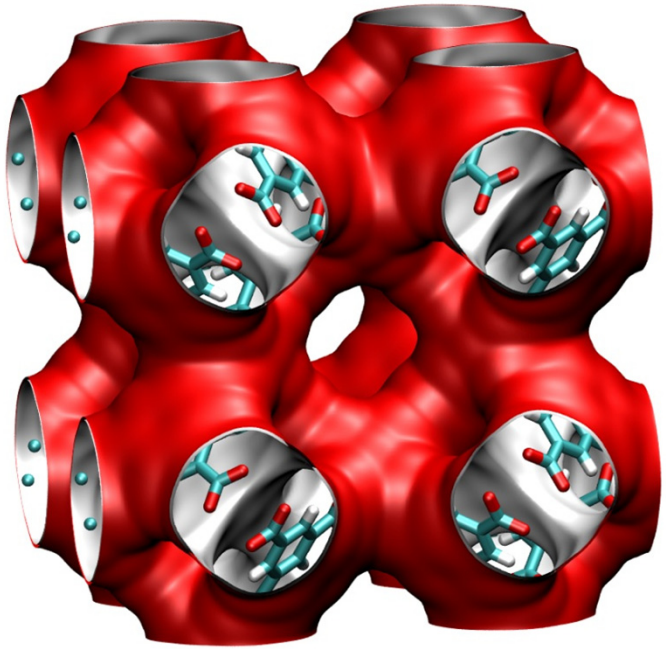

Snapshot of CO_2/CH_4 mixture

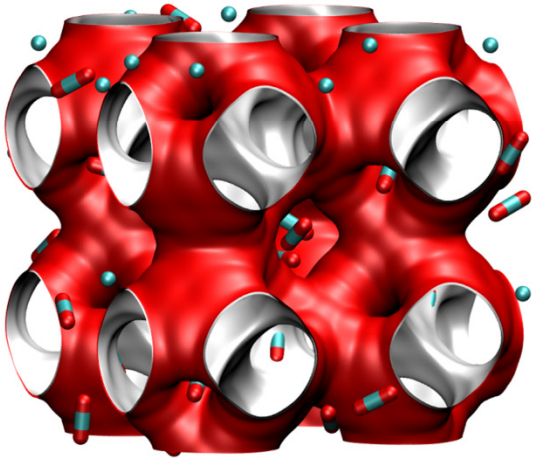

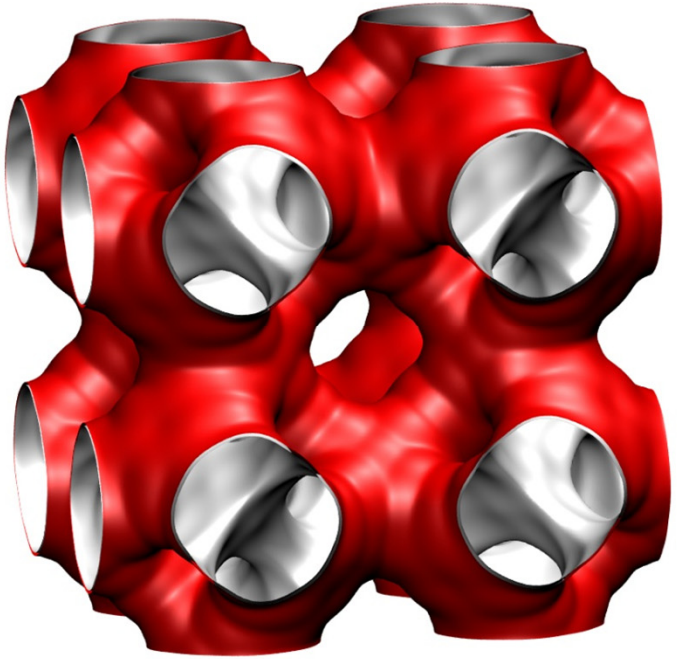

CuBTC pore dimensions

Figure S29

	CuBTC
a /Å	26.343
b /Å	26.343
c /Å	26.343
Cell volume / Å^3	18280.82
conversion factor for [molec/uc] to [mol per kg Framework]	0.1034
conversion factor for [molec/uc] to [kmol/m^3]	0.1218
ρ [kg/m3]	878.8298
MW unit cell [g/mol(framework)]	9674.855
ϕ, fractional pore volume	0.746
open space / Å^3/uc	13628.4
Pore volume / cm^3/g	0.848
Surface area /m^2/g	2097.0
DeLaunay diameter /Å	6.23

The CuBTC structure consists of two types of “cages” and two types of “windows” separating these cages. Large cages are inter-connected by 9 Å windows of square cross-section. The large cages are also connected to tetrahedral-shaped pockets of ca. 6 Å size through triangular-shaped windows of ca. 4.6 Å size

Figure S30

CuBTC framework

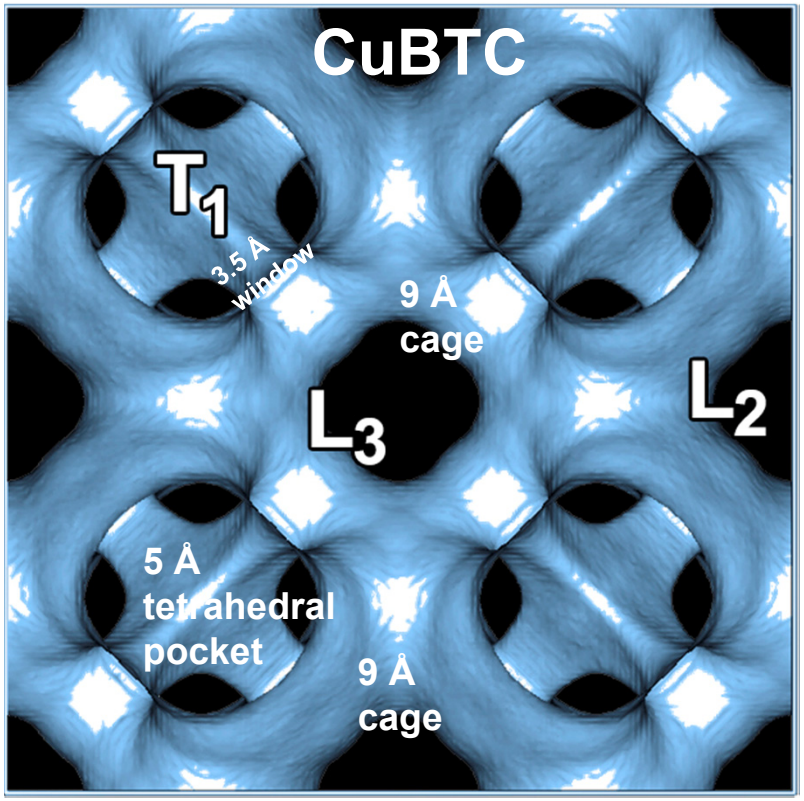

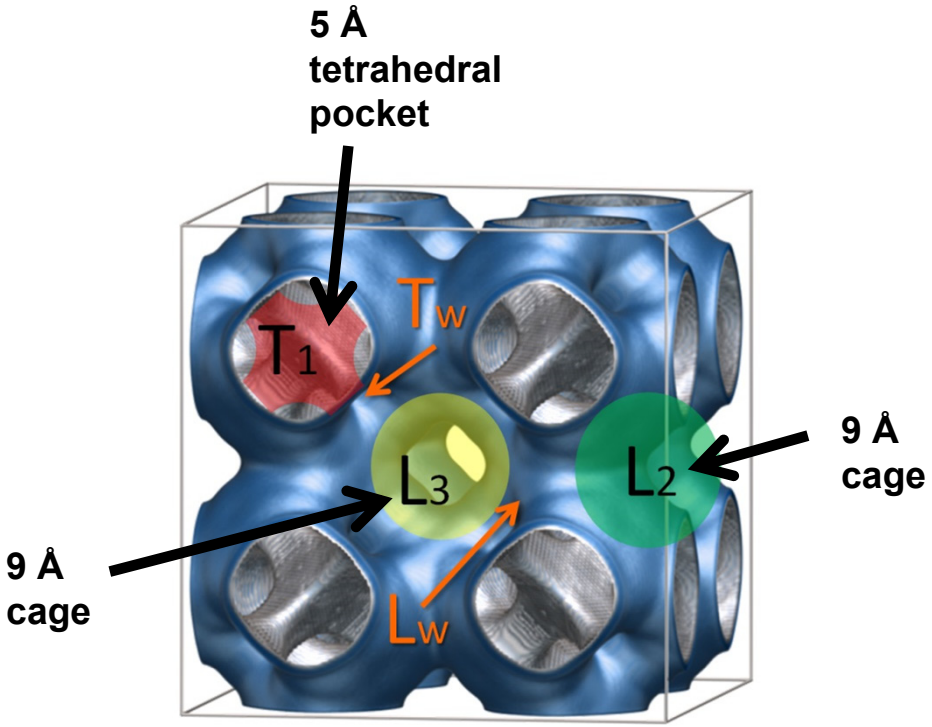

Figure S31

IRMOF-1 pore landscape

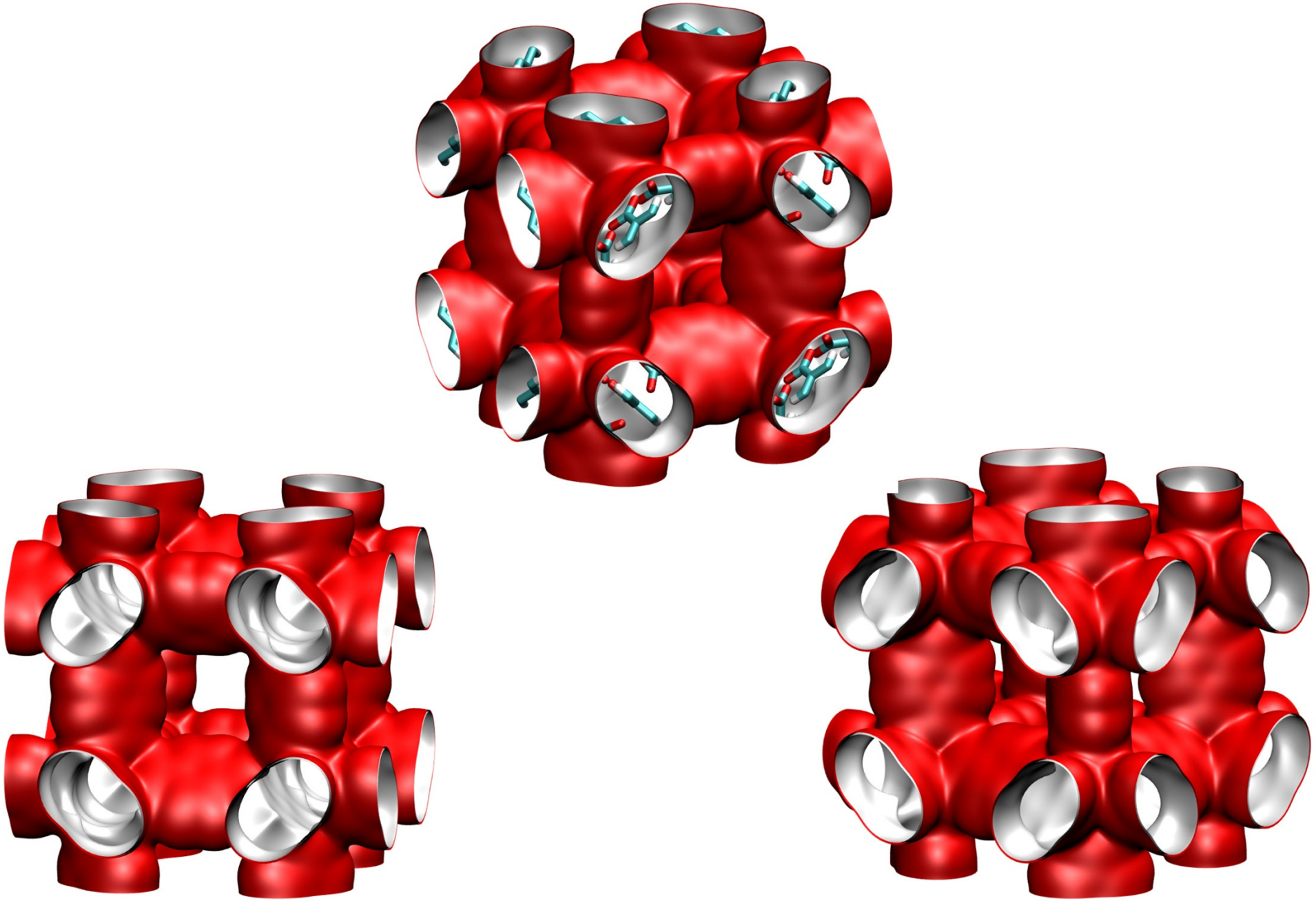

Figure S32

IRMOF-1 pore dimensions

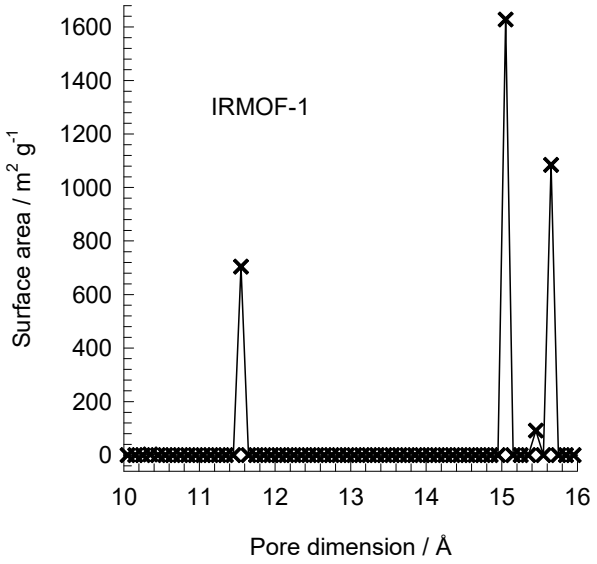

This plot of surface area versus pore dimension is determined using a combination of the DeLaunay triangulation method for pore dimension determination, and the procedure of Düren for determination of the surface area.

	IRMOF-1
a /Å	25.832
b /Å	25.832
c /Å	25.832
Cell volume / Å^3	17237.49
conversion factor for [molec/uc] to [mol per kg Framework]	0.1624
conversion factor for [molec/uc] to [kmol/m^3]	0.1186
ρ [kg/m3]	593.2075
MW unit cell [g/mol(framework)]	6157.788
ϕ, fractional pore volume	0.812
open space / Å^3/uc	13996.3
Pore volume / cm^3/g	1.369
Surface area /m^2/g	3522.2
DeLaunay diameter /Å	7.38

Figure S33

Schematic for zeolite membrane permeation

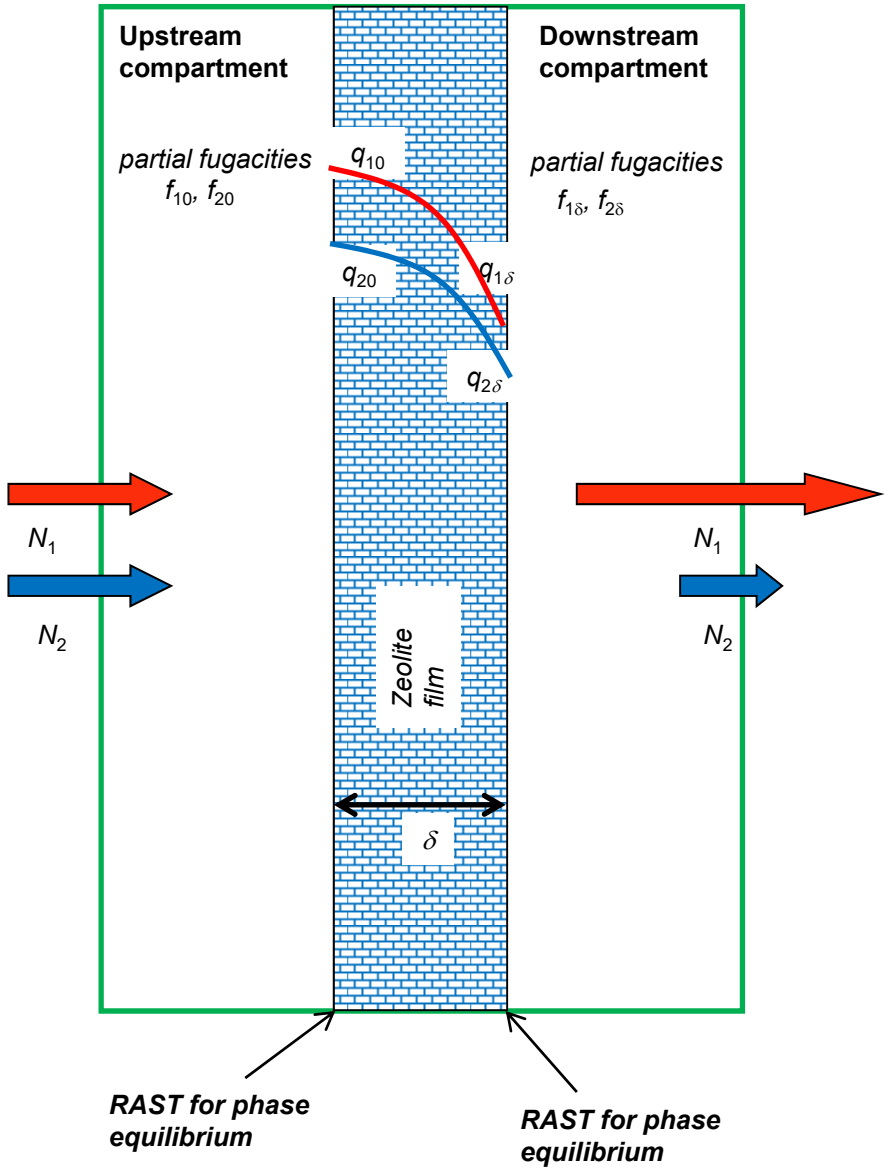

Figure S34

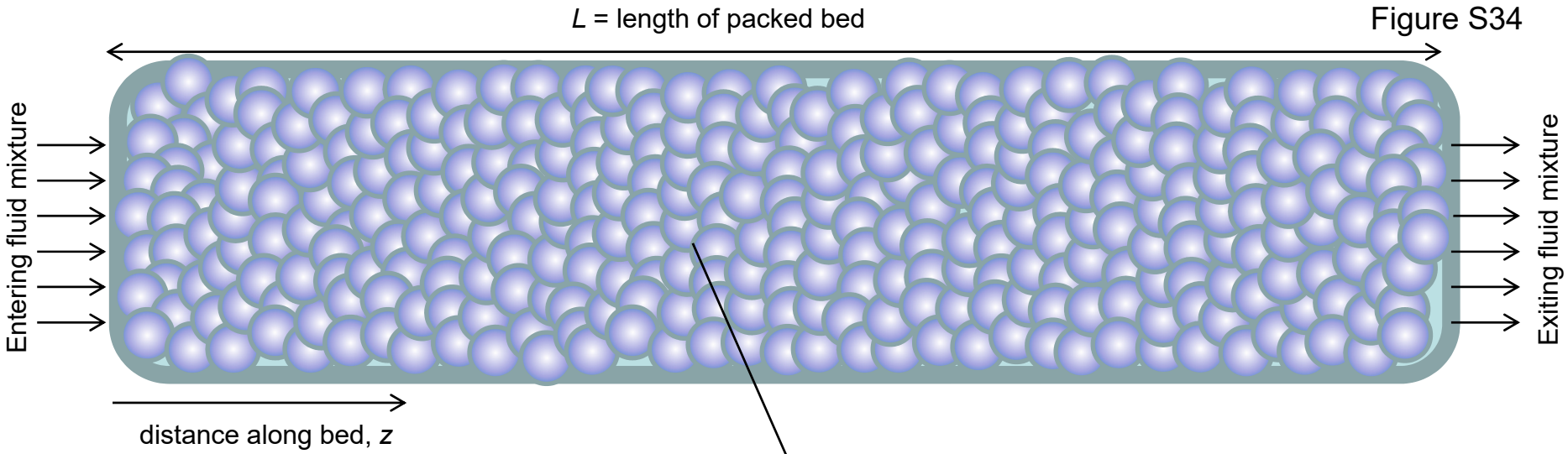

Two different discretization strategies for adsorbent particle

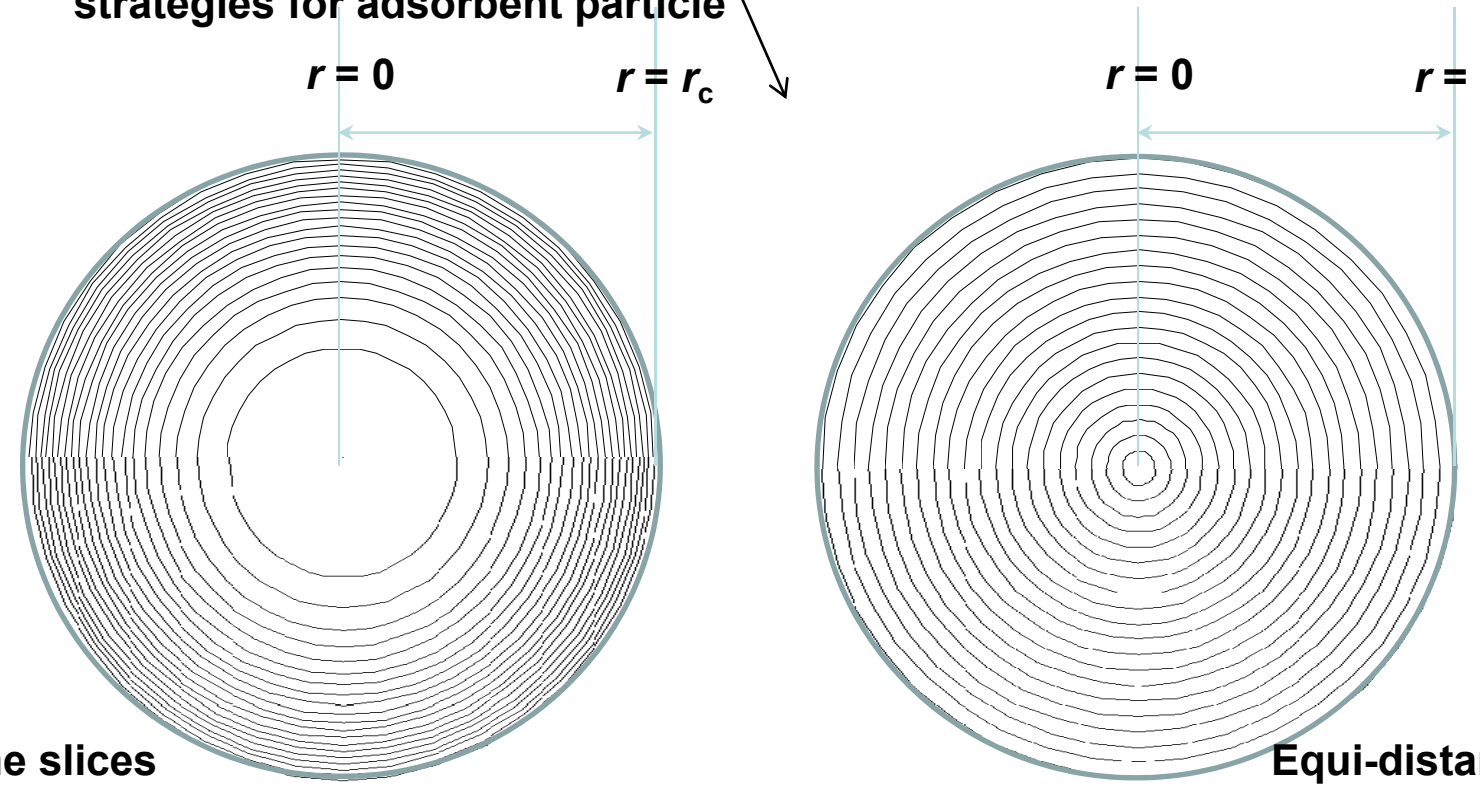

Equi-volume slices

Equi-distant slices

Fixed bed breakthrough model

Figure S35

Component balance

$$\frac{1}{RT}\frac{\partial p_i}{\partial t} = -\frac{1}{RT}\frac{\partial (v p_i)}{\partial z} - \frac{(1-\varepsilon)}{\varepsilon}\rho\frac{\partial \bar{q}_i}{\partial t}; \quad i = 1,2,...n$$

Balance for mixture

$$\frac{1}{RT}p_t\frac{\partial (v(t,z))}{\partial z} = -\frac{(1-\varepsilon)}{\varepsilon}\rho\frac{\partial \bar{q}_t(t,z)}{\partial t}$$

Average loading within crystal

$$\bar{q}_i = \frac{3}{r_c^3}\int_0^{r_c} q_i r^2 dr$$

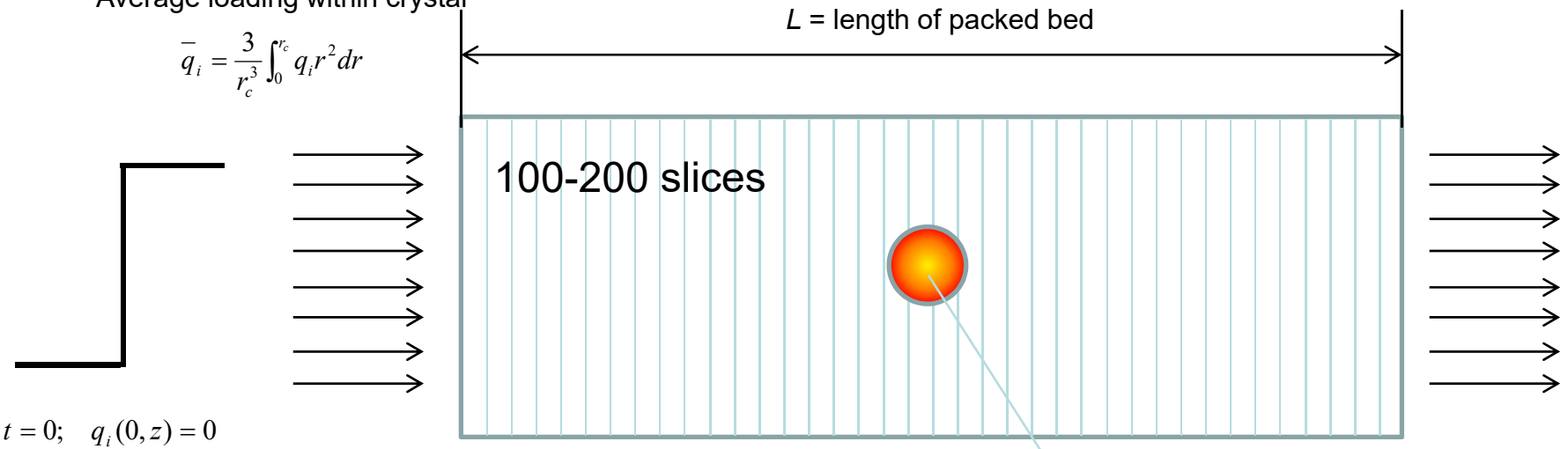

$t = 0; \quad q_i(0,z) = 0$

$t \geq 0; \quad p_i(0,t) = p_{i0}; \quad u(0,t) = u_0$

Uptake within crystal

$$\frac{\partial q_i}{\partial t} = -\frac{1}{\rho}\frac{1}{r^2}\frac{\partial}{\partial r}\left(r^2 N_i\right)$$

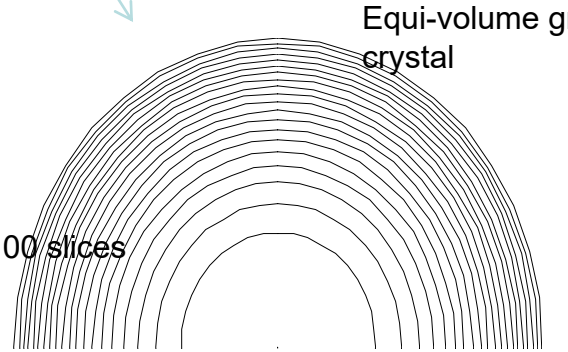

Maxwell-Stefan equations

$$-\rho\frac{q_i}{RT}\nabla\mu_i = \sum_{\substack{j=1 \\ j\neq i}}^{n}\frac{x_j N_i - x_i N_j}{Đ_{ij}} + \frac{N_i}{Đ_i}; \quad i = 1,2,..n$$

RDF

Figure S36

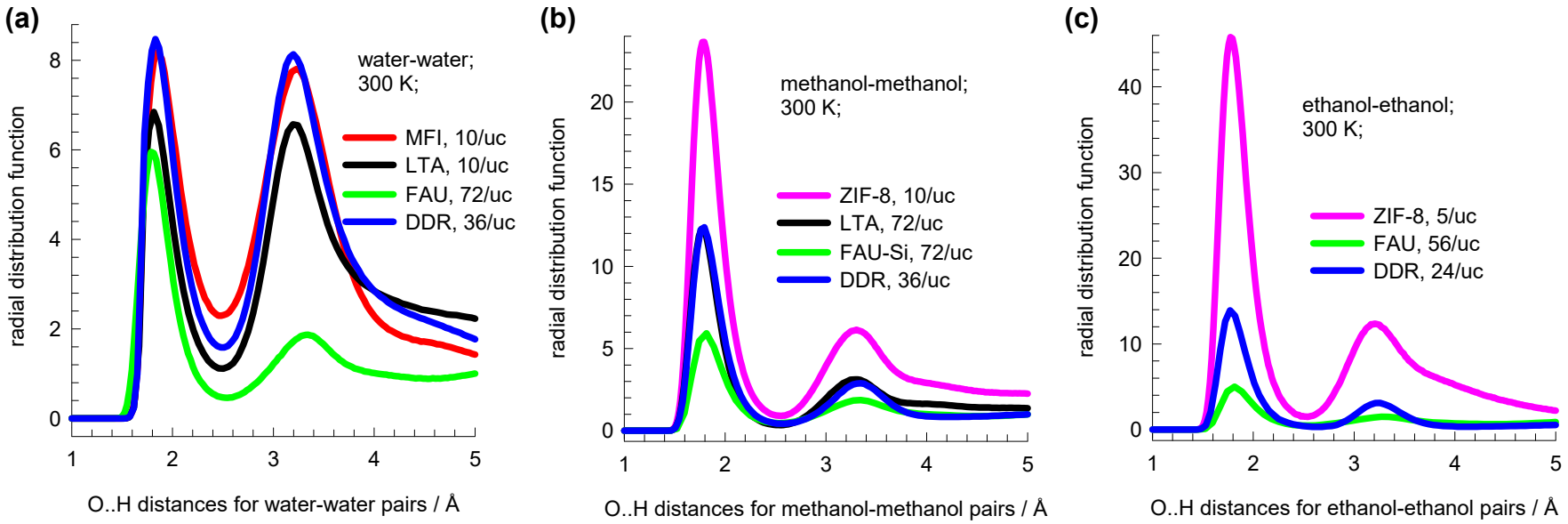

Figure S37

RDF

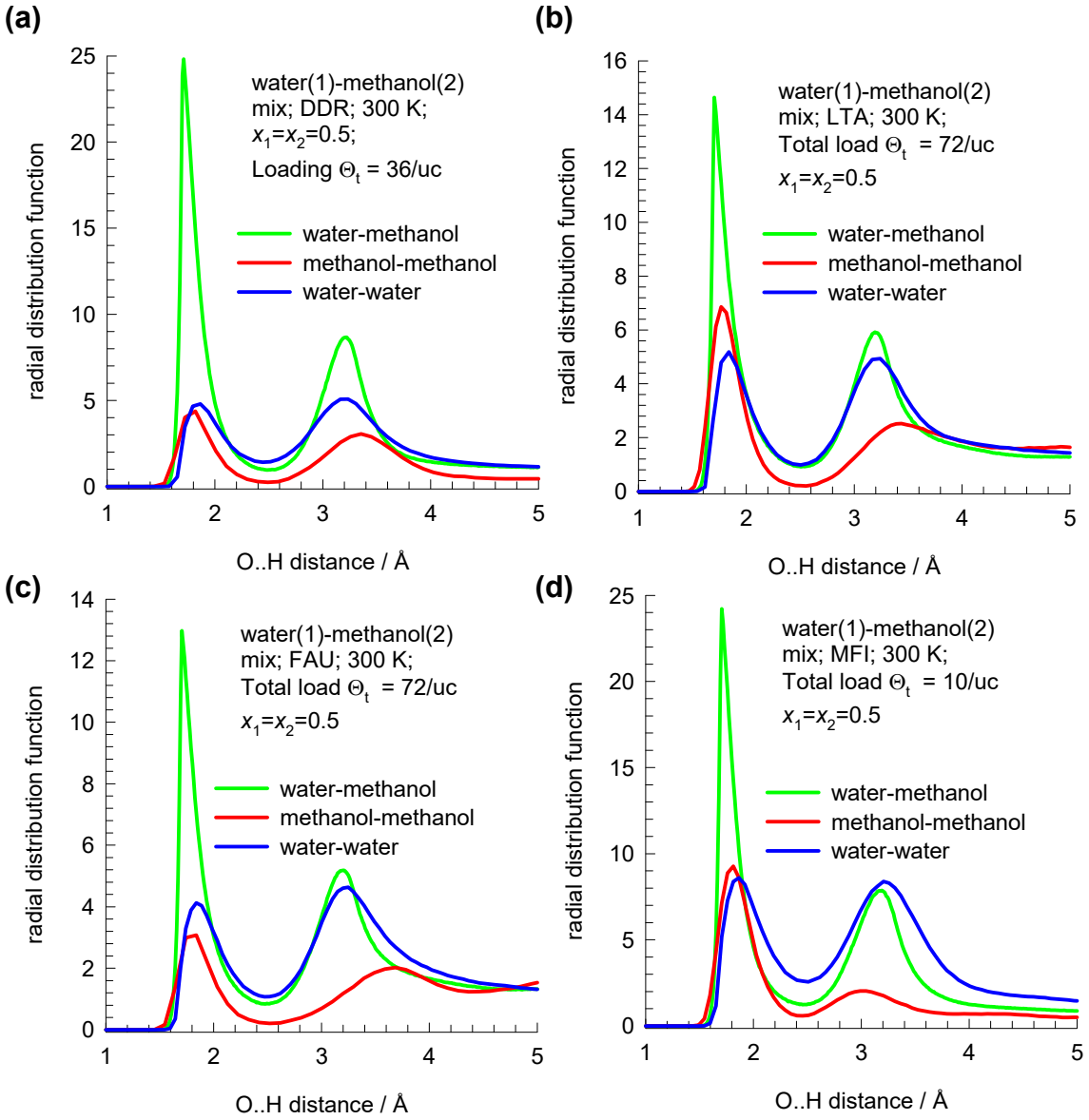

RDF

Figure S38

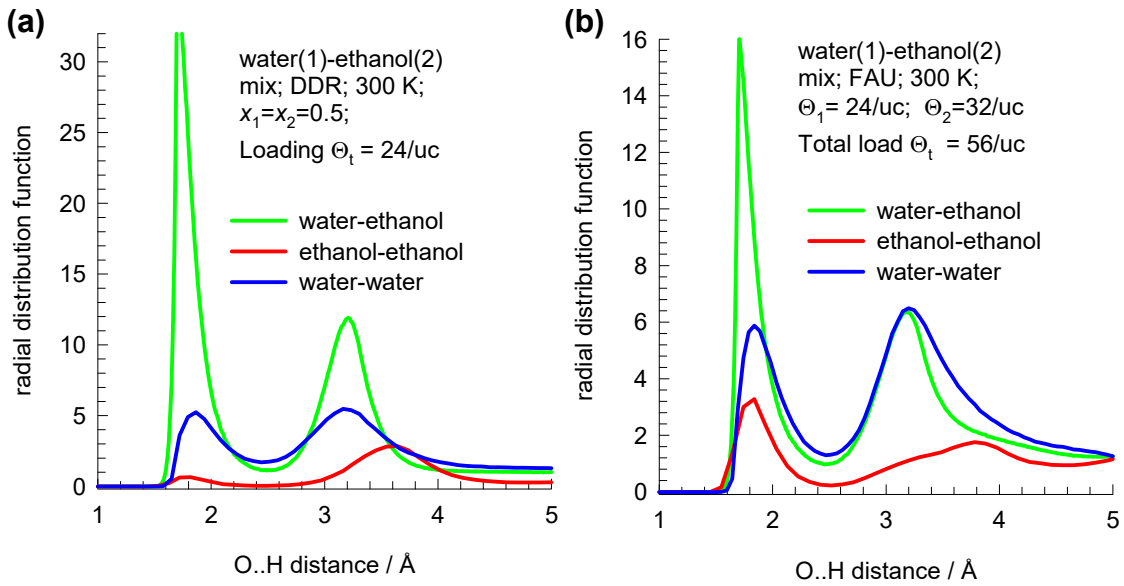

RDF

Figure S39

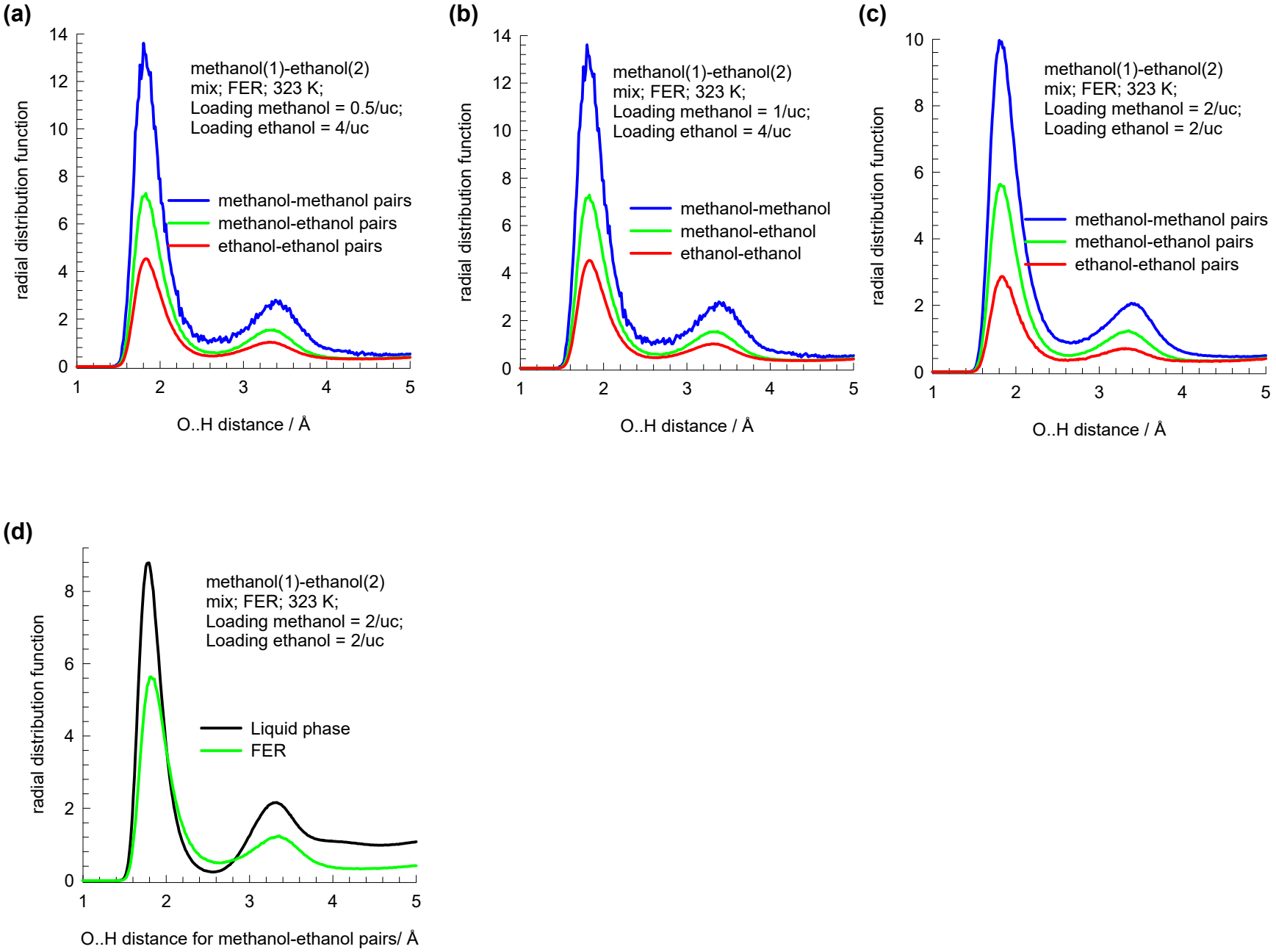

Figure S40

RDF

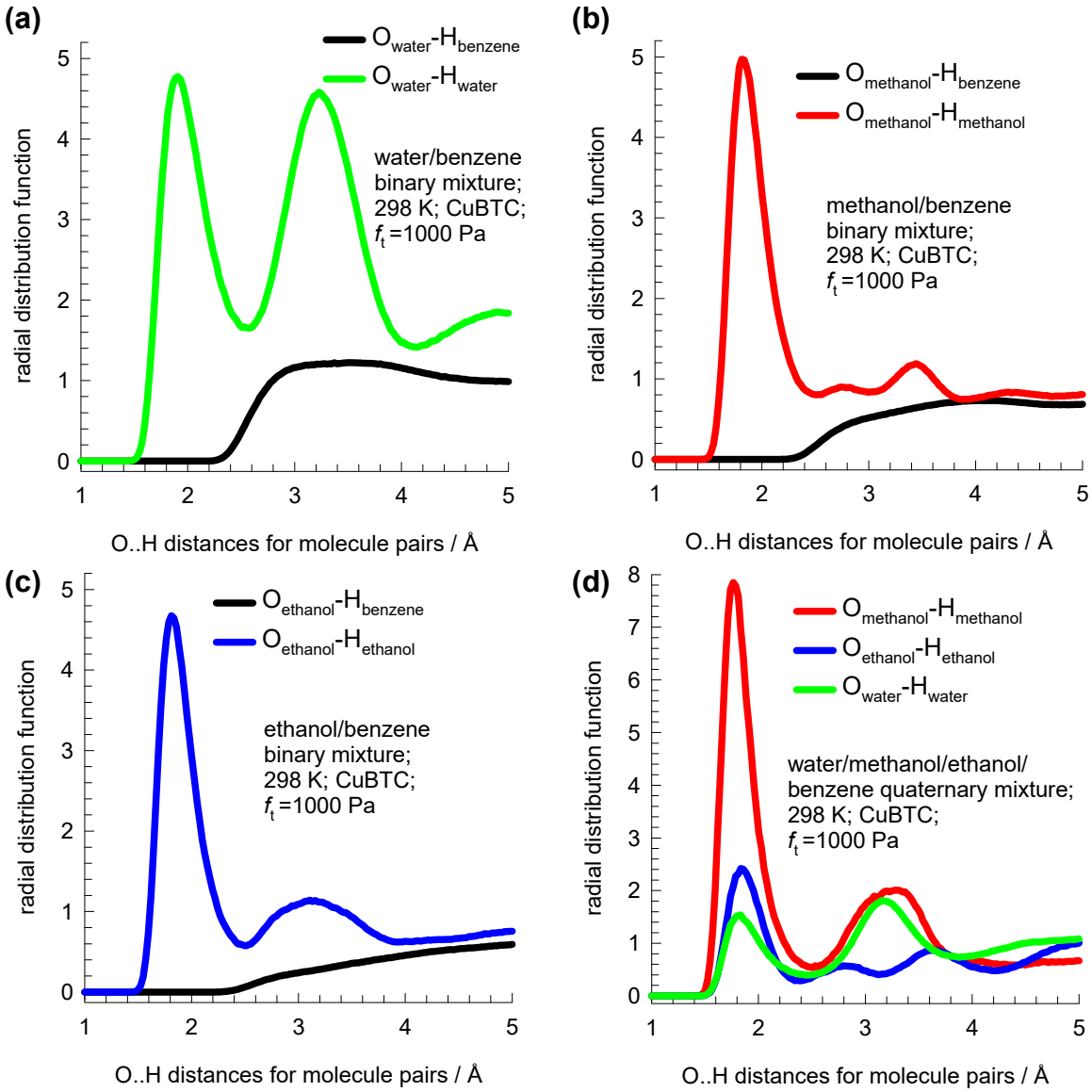

Figure S41

Unary isotherms

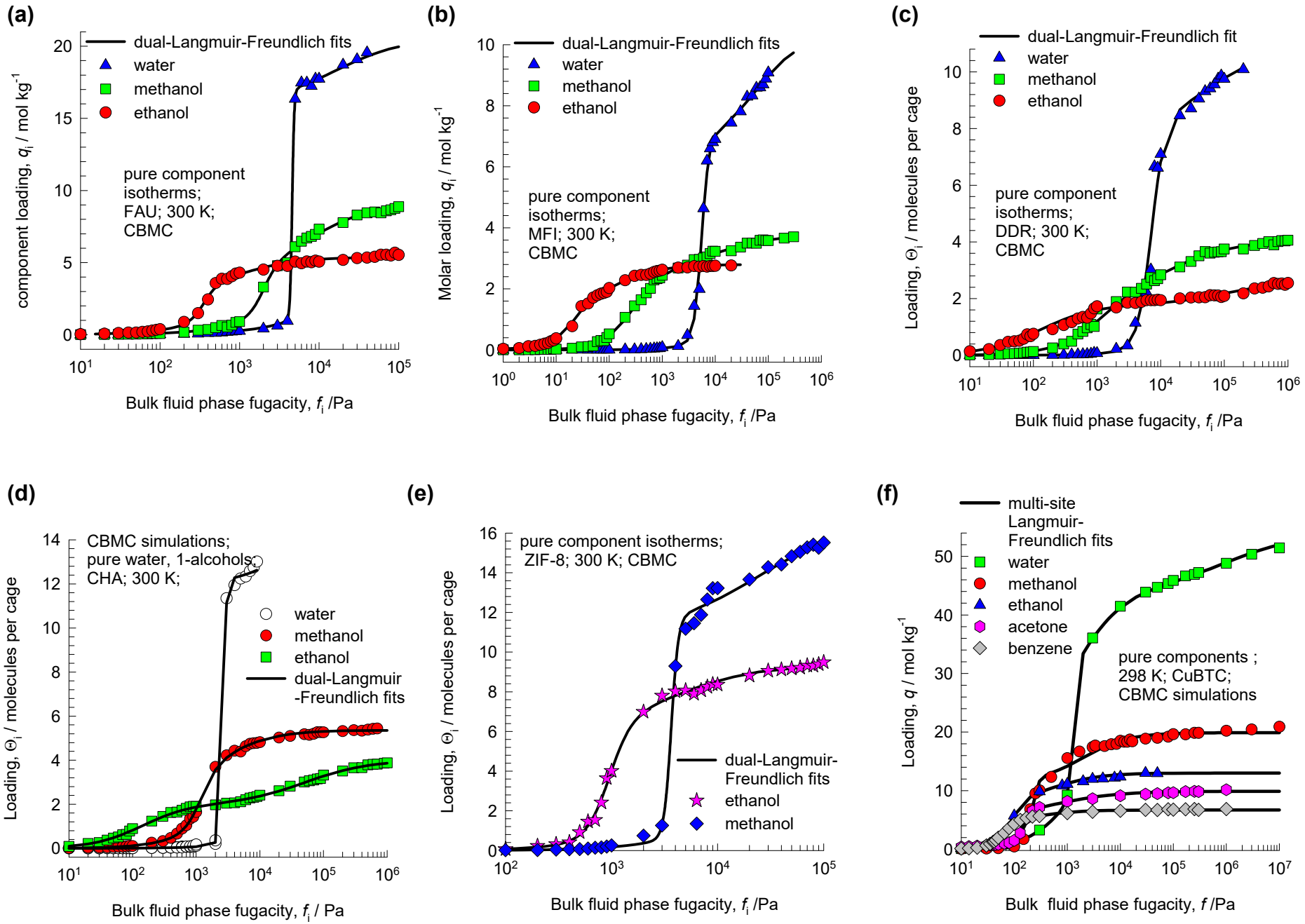

Inverse Thermodynamic Factor

Figure S42

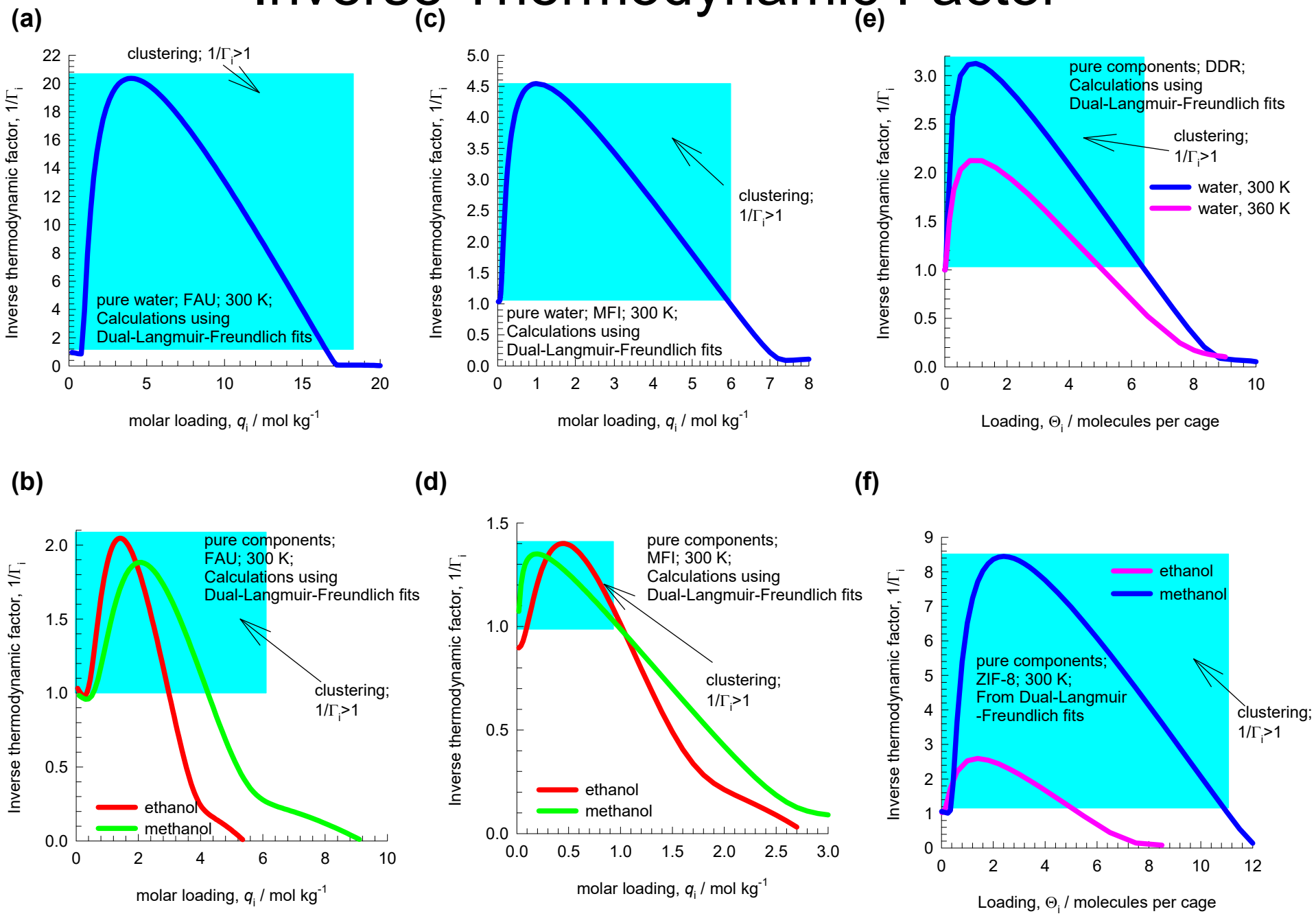

Inverse Thermodynamic Factor

Figure S43

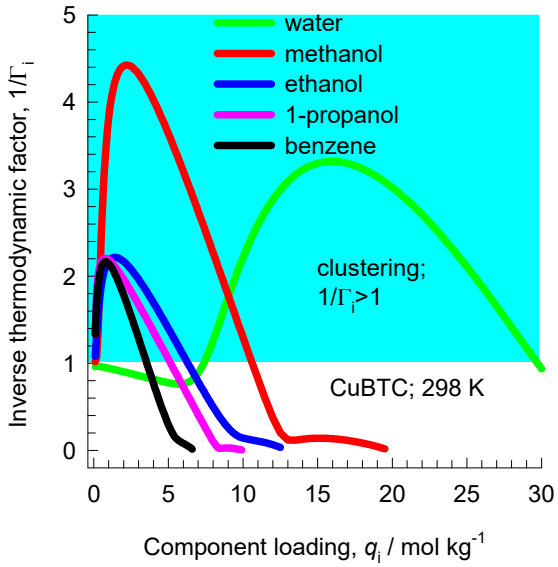

Figure S44

(a) Unclustered molecules

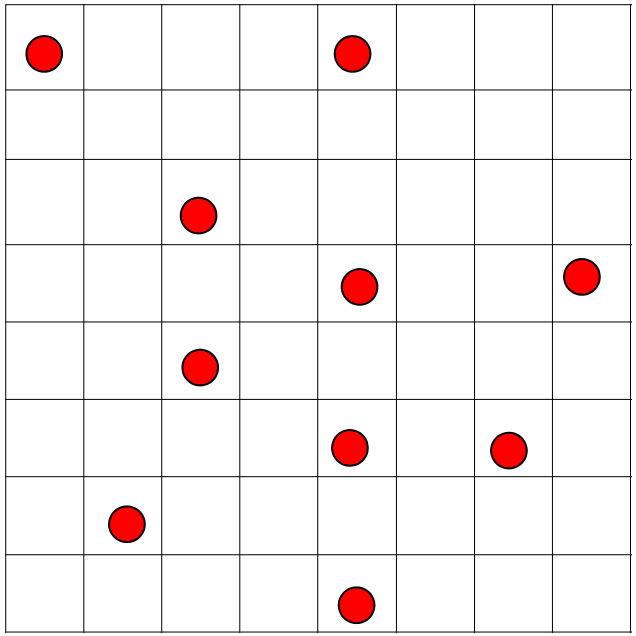

(b) Dimers

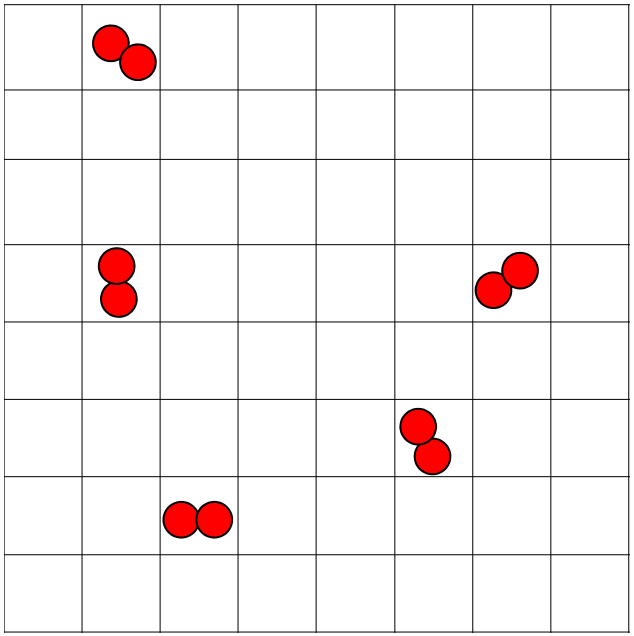

Figure S45

CBMC mixture simulations

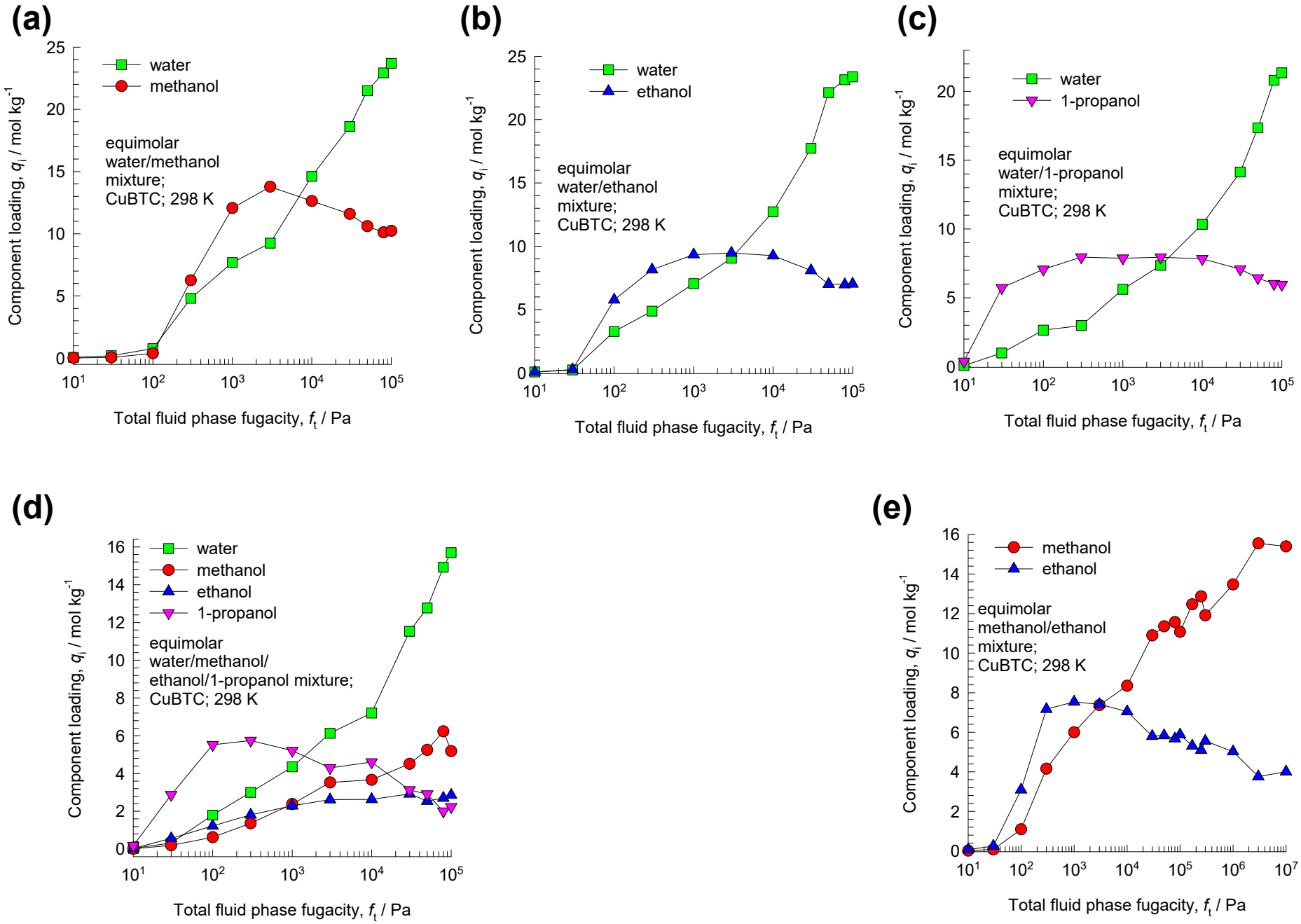

CBMC binary mixture simulations

Figure S46

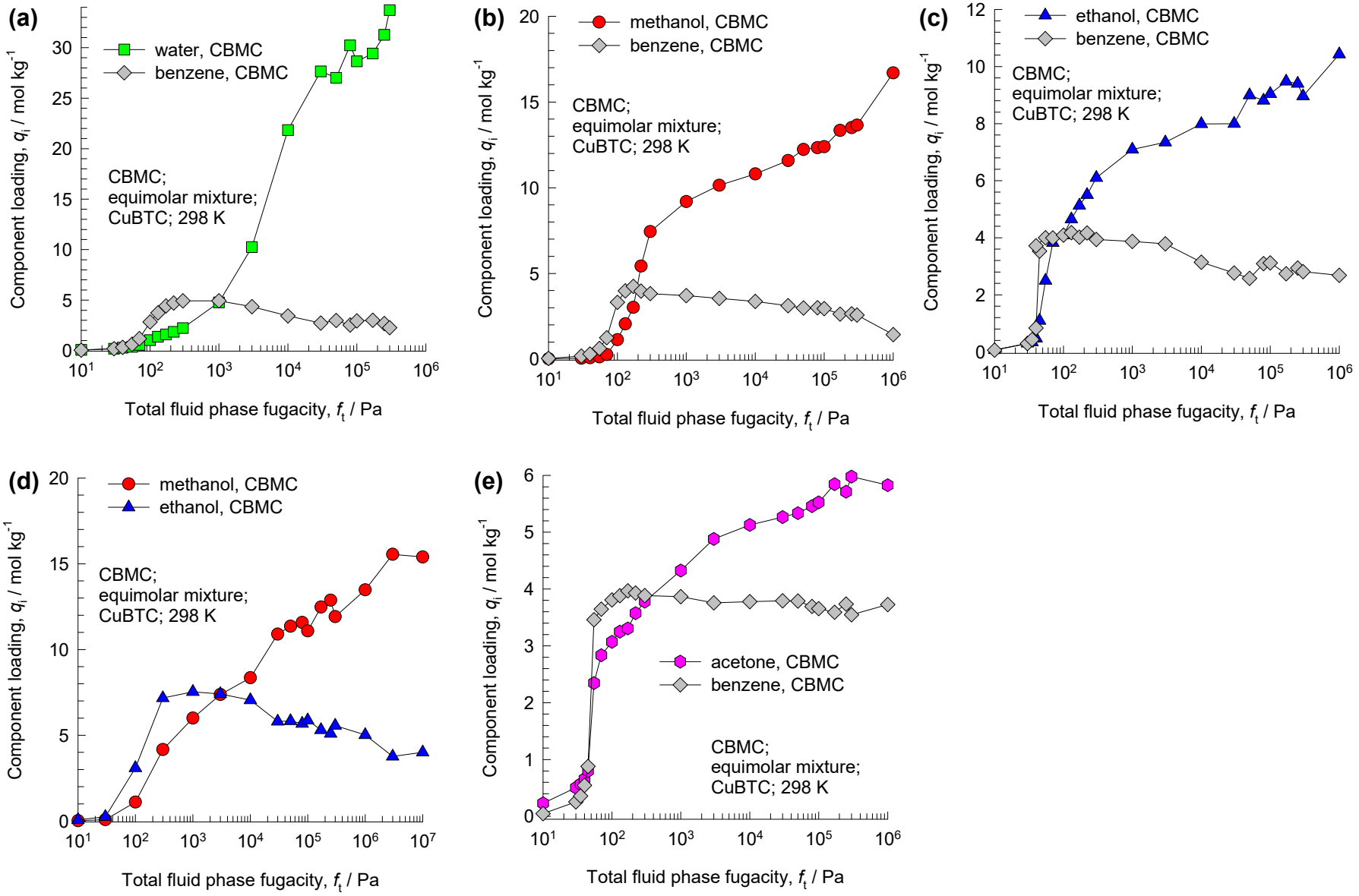

Figure S47

IAST vs CBMC mixture

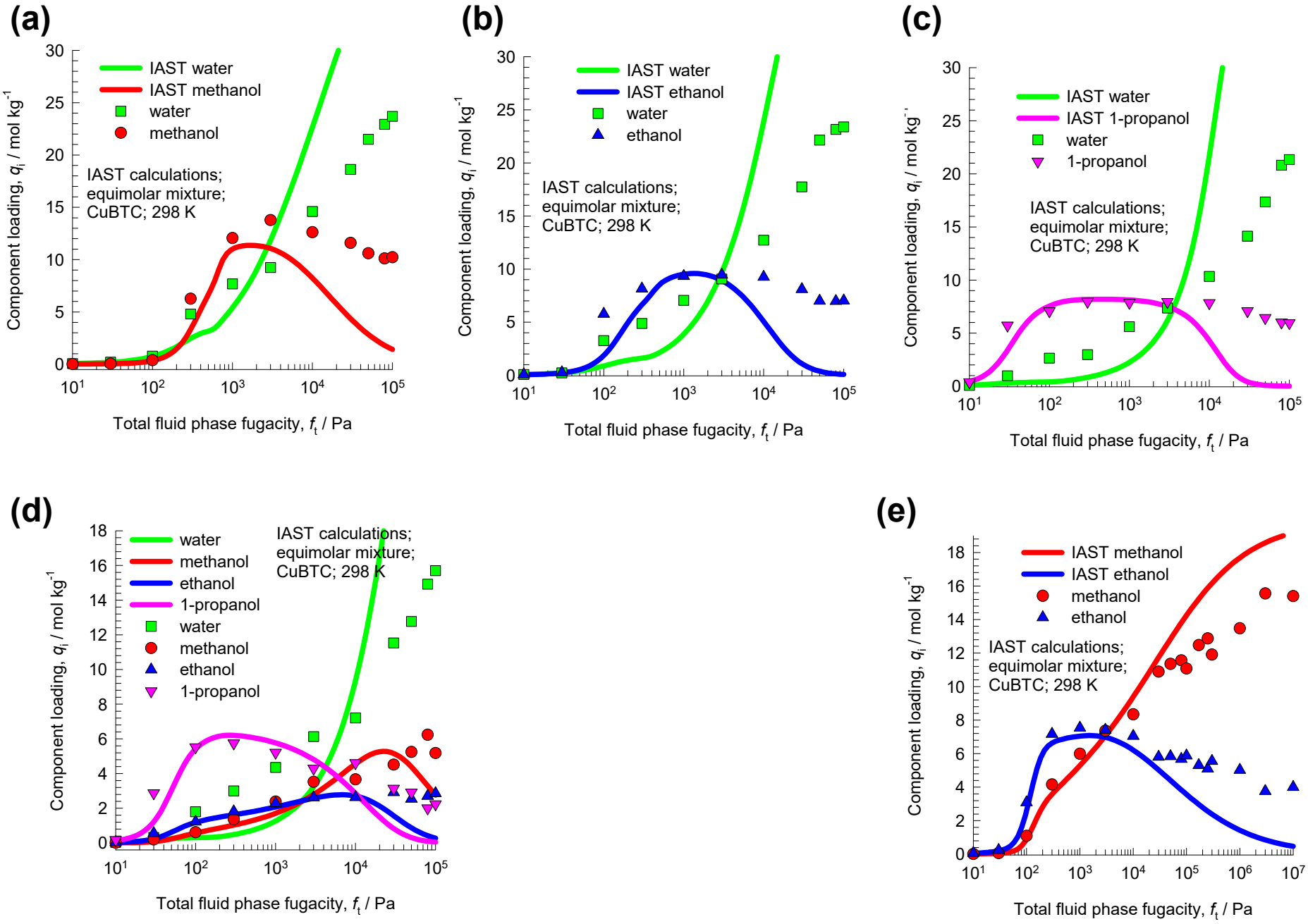

IAST vs CBMC mixture

Figure S48

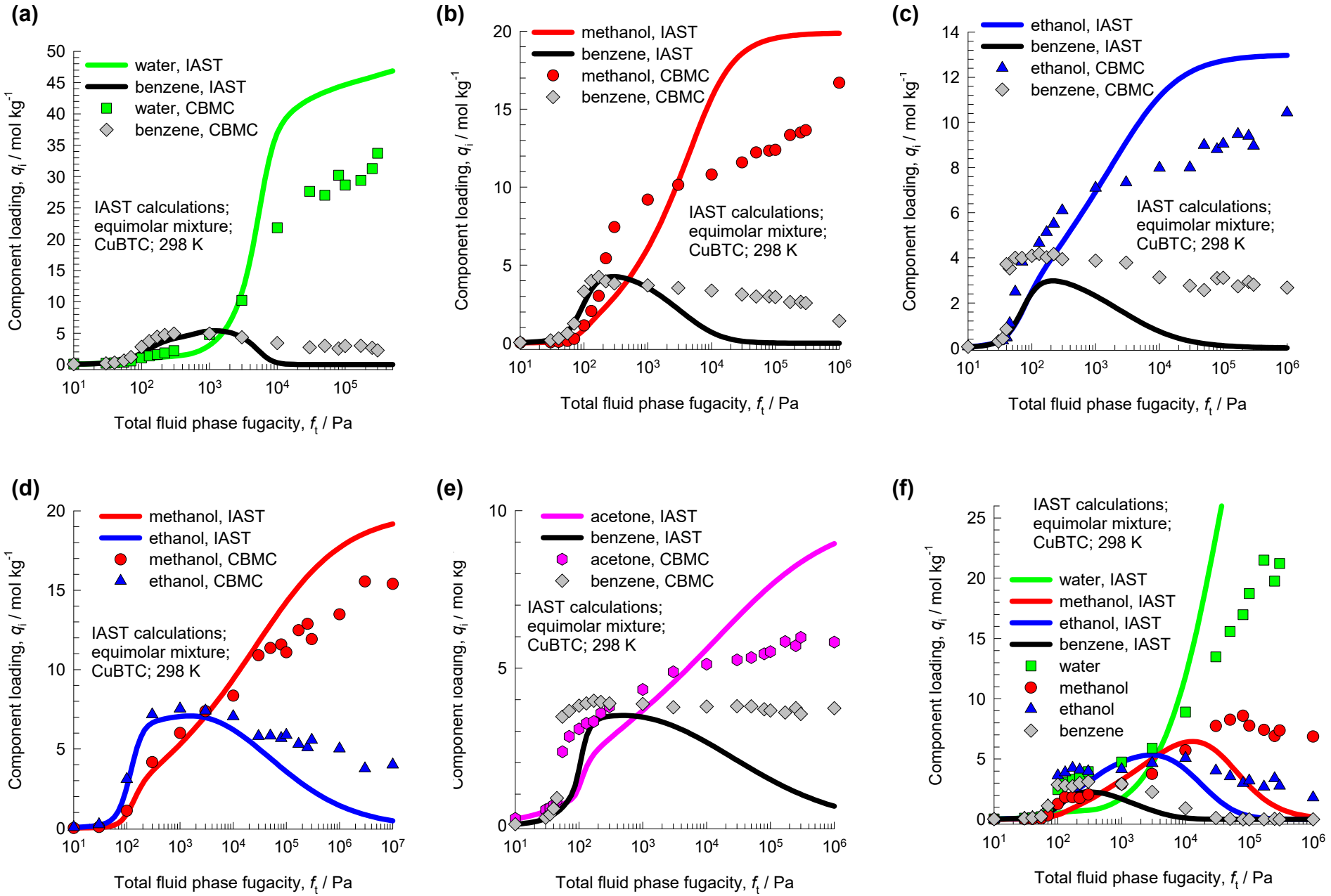

Figure S49

$q_{t,IAST}$ - $q_{t,CBMC}$

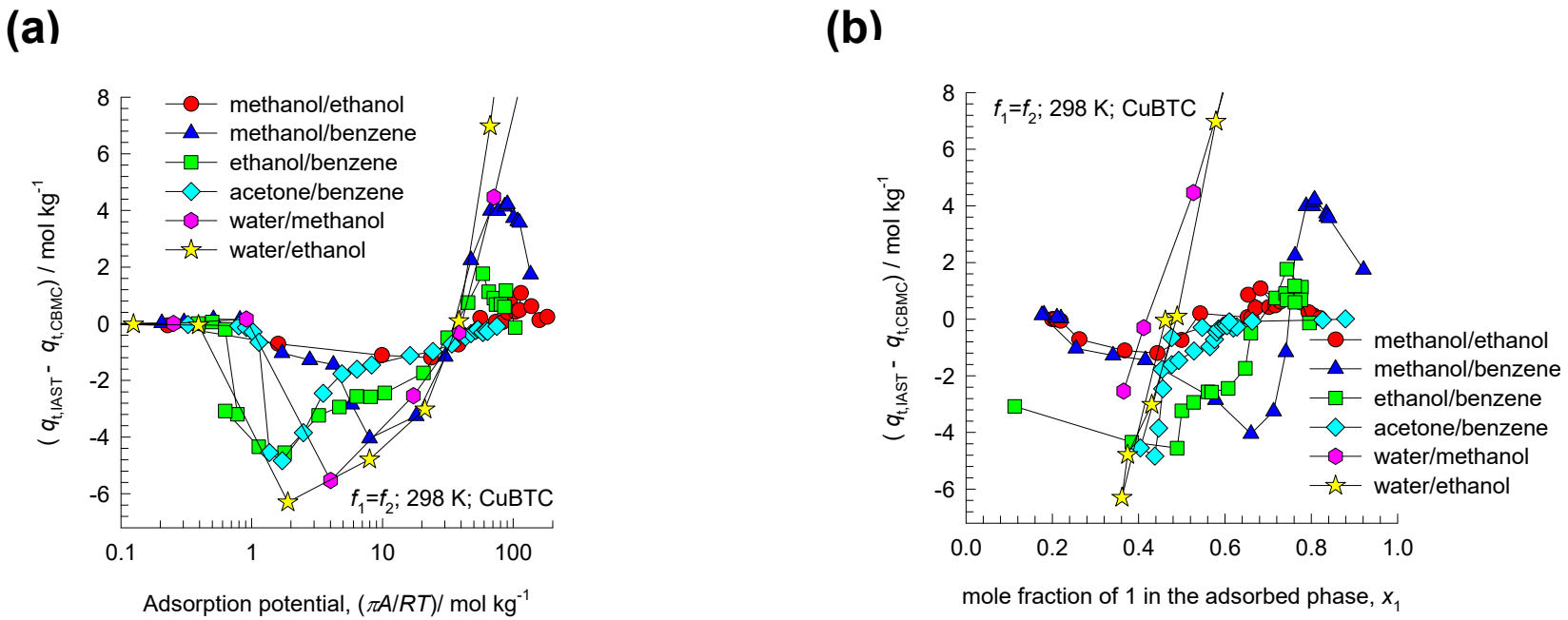

Figure S50

CBMC vs IAST/RAST calculations

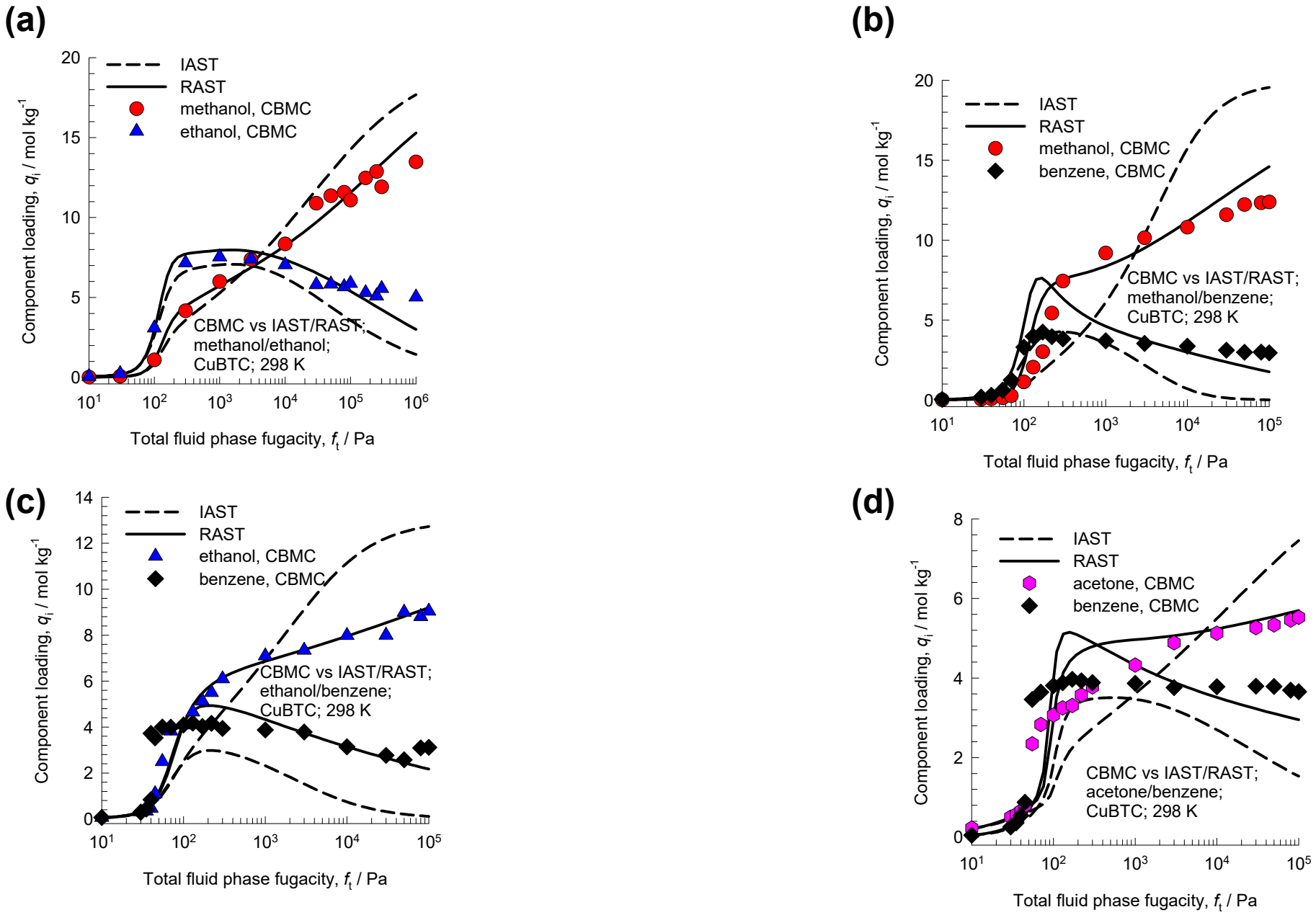

Figure S51

RAST activity coefficients

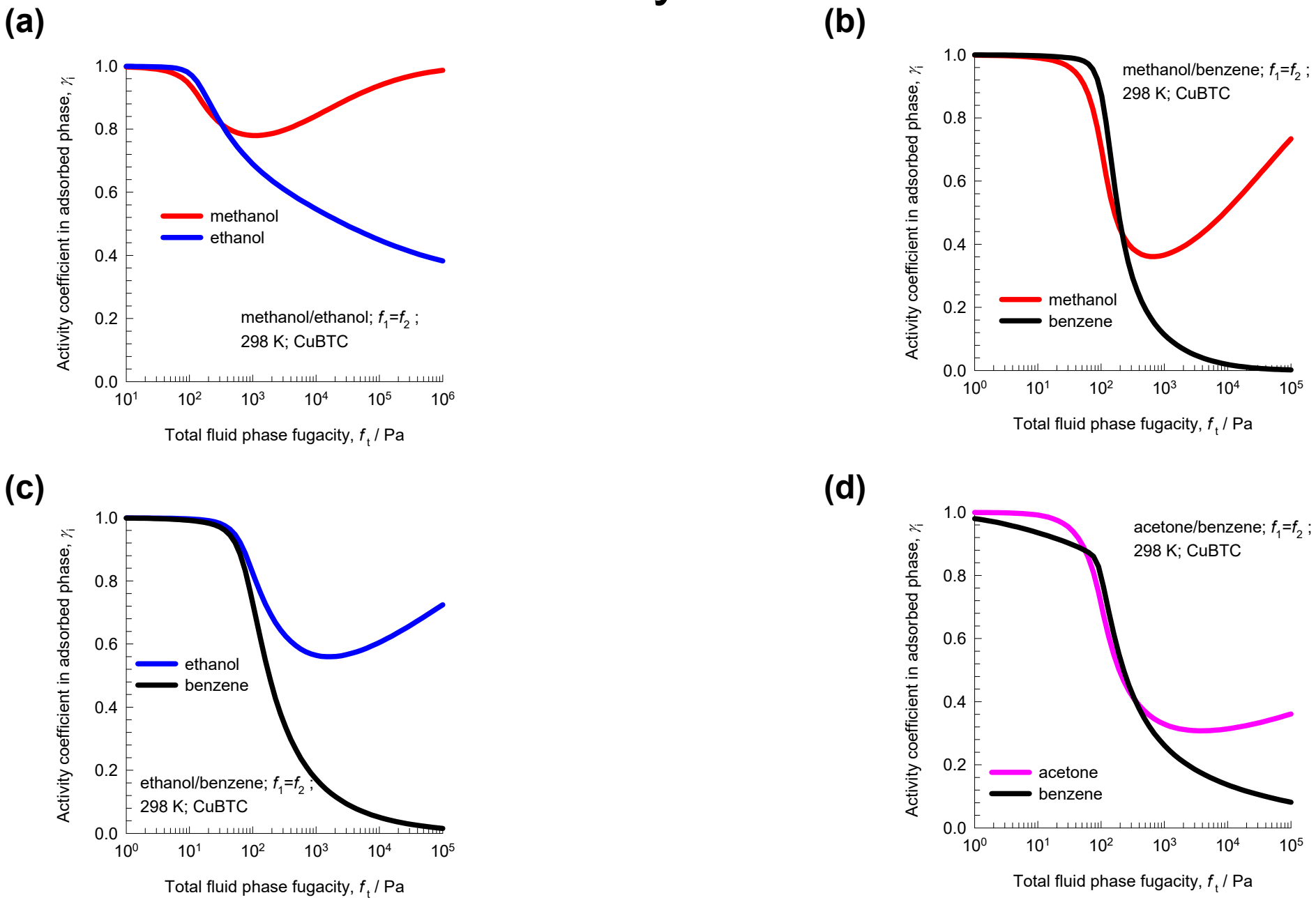

Figure S52

S_{ads}: IAST/RAST vs CBMC

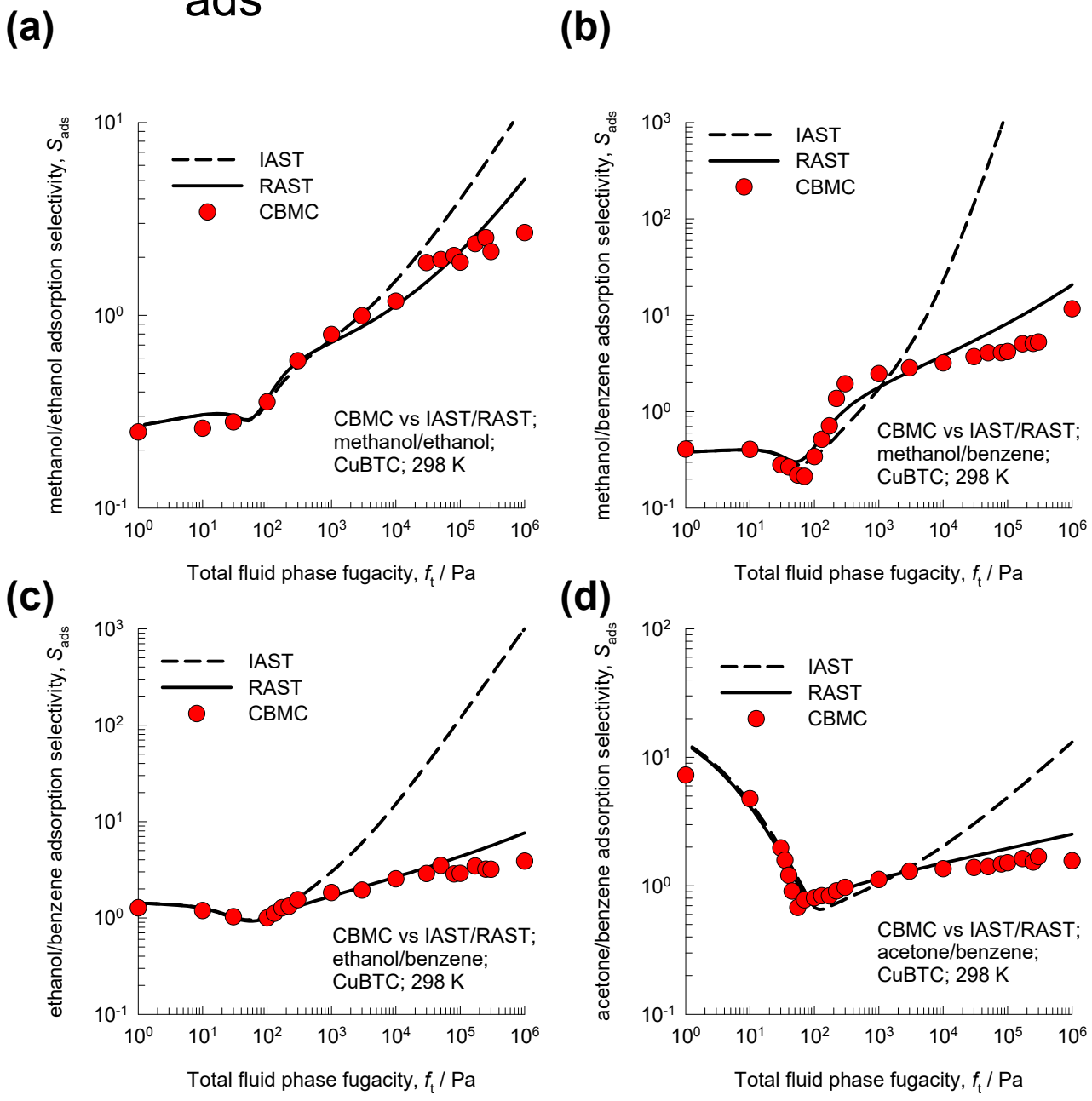

Figure S53

ΔQ: IAST/RAST vs CBMC

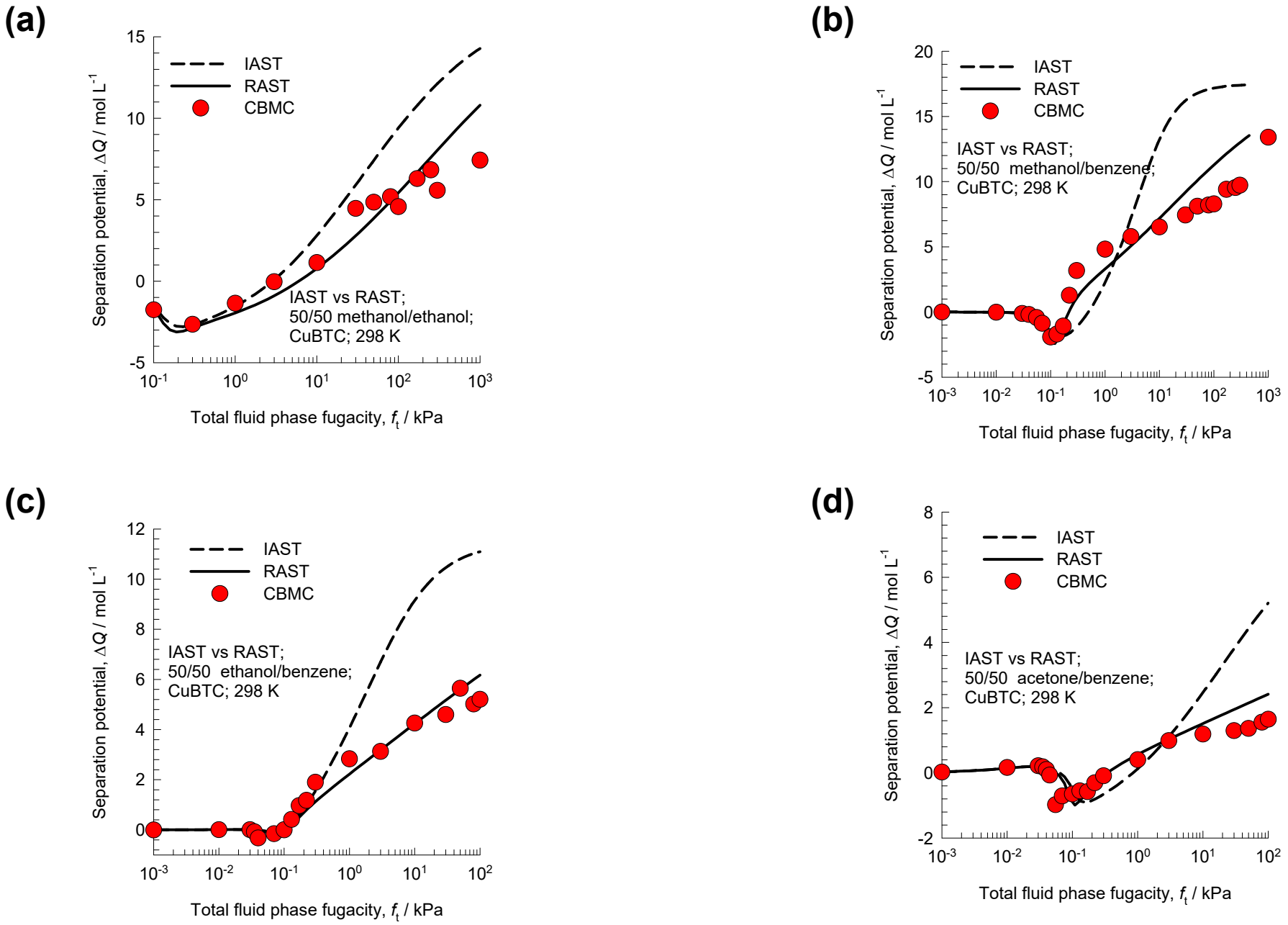

Figure S54

Selectivity reversal methanol/ethanol/CuBTC

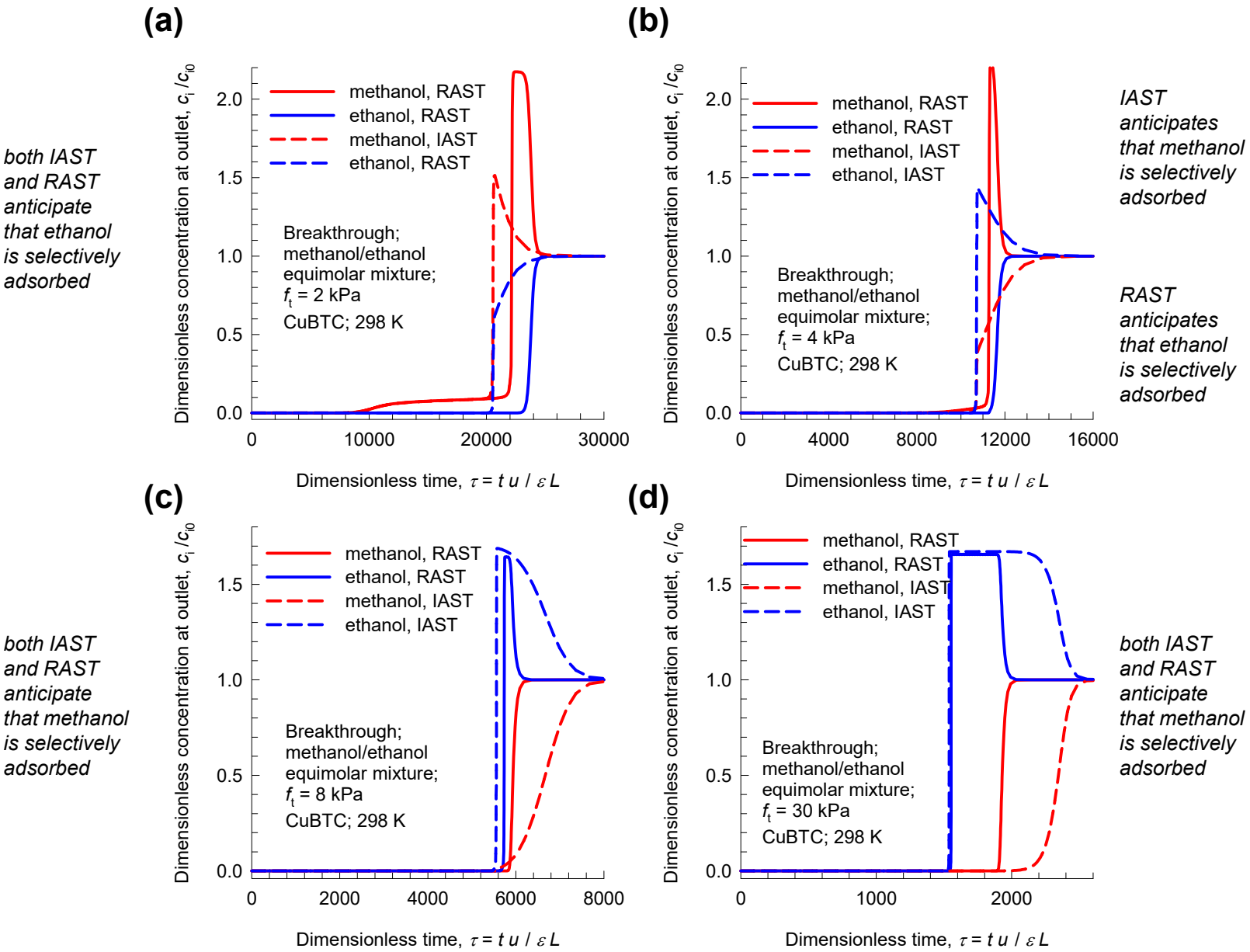

Figure S55

Methanol/n-hexane adsorption in CuBTC

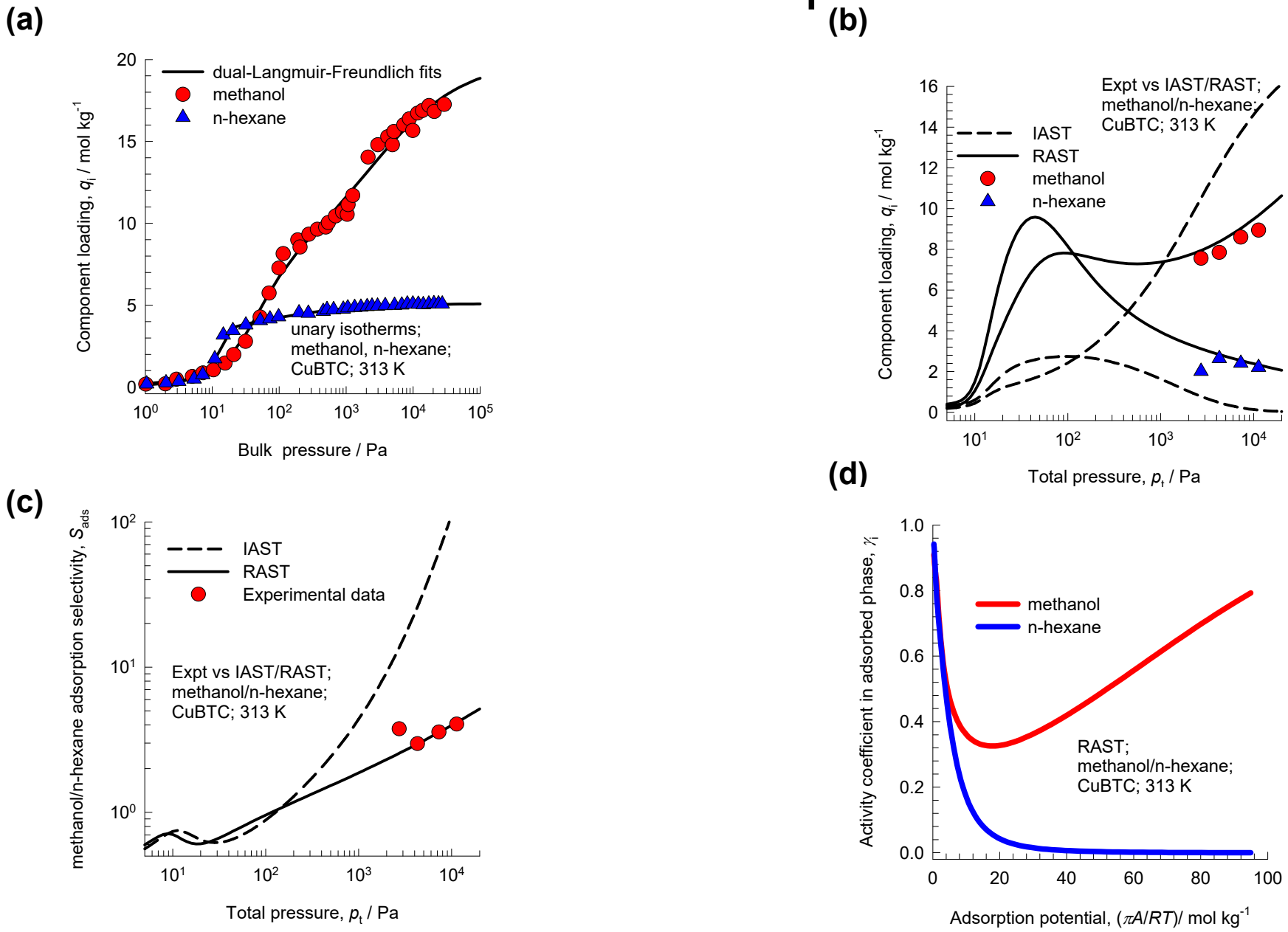

Figure S56

Methanol/nC6 adsorption in MSC-5A (Takeda)

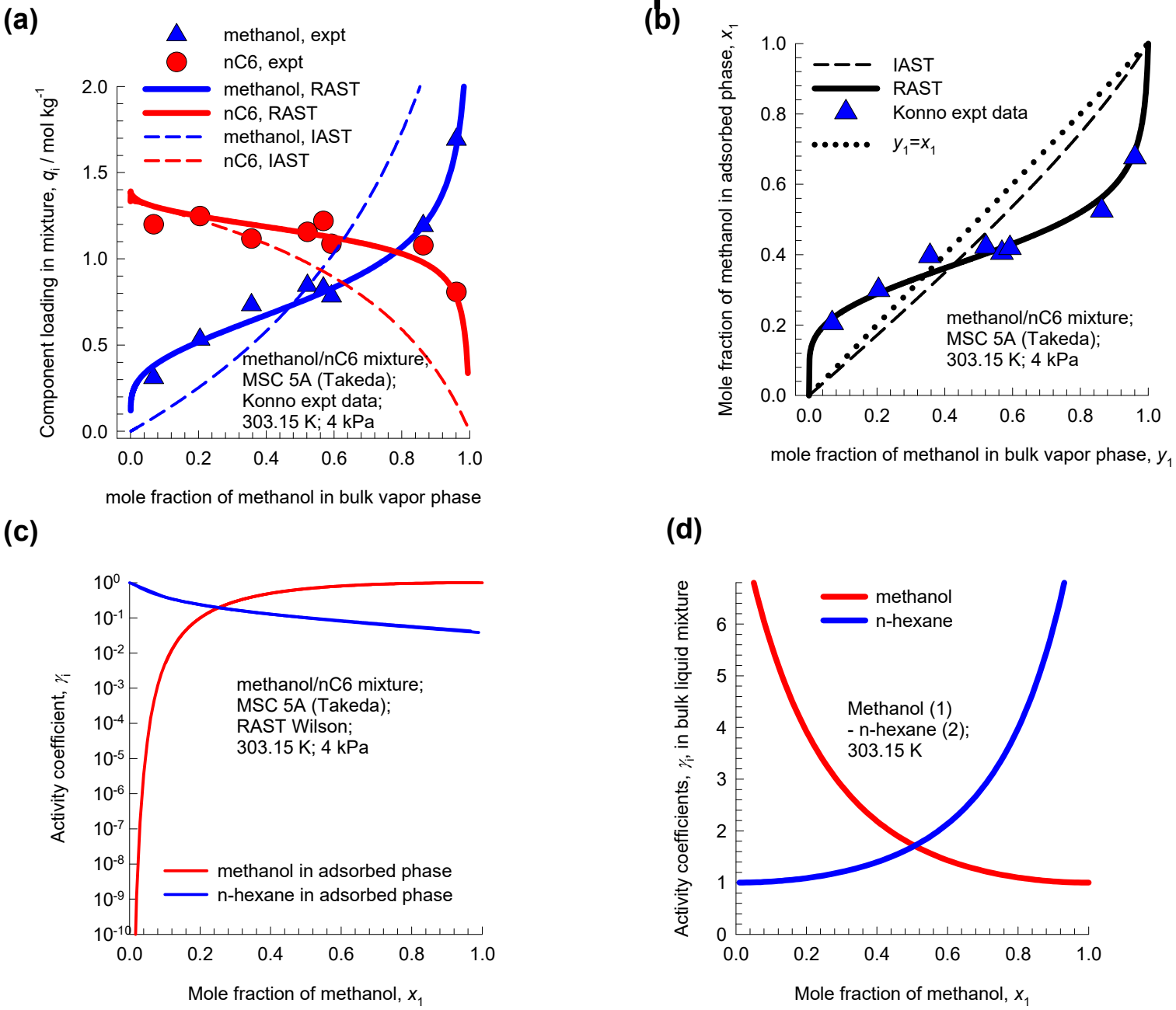

Figure S57

Toluene/1-propanol adsorption in DAY-13

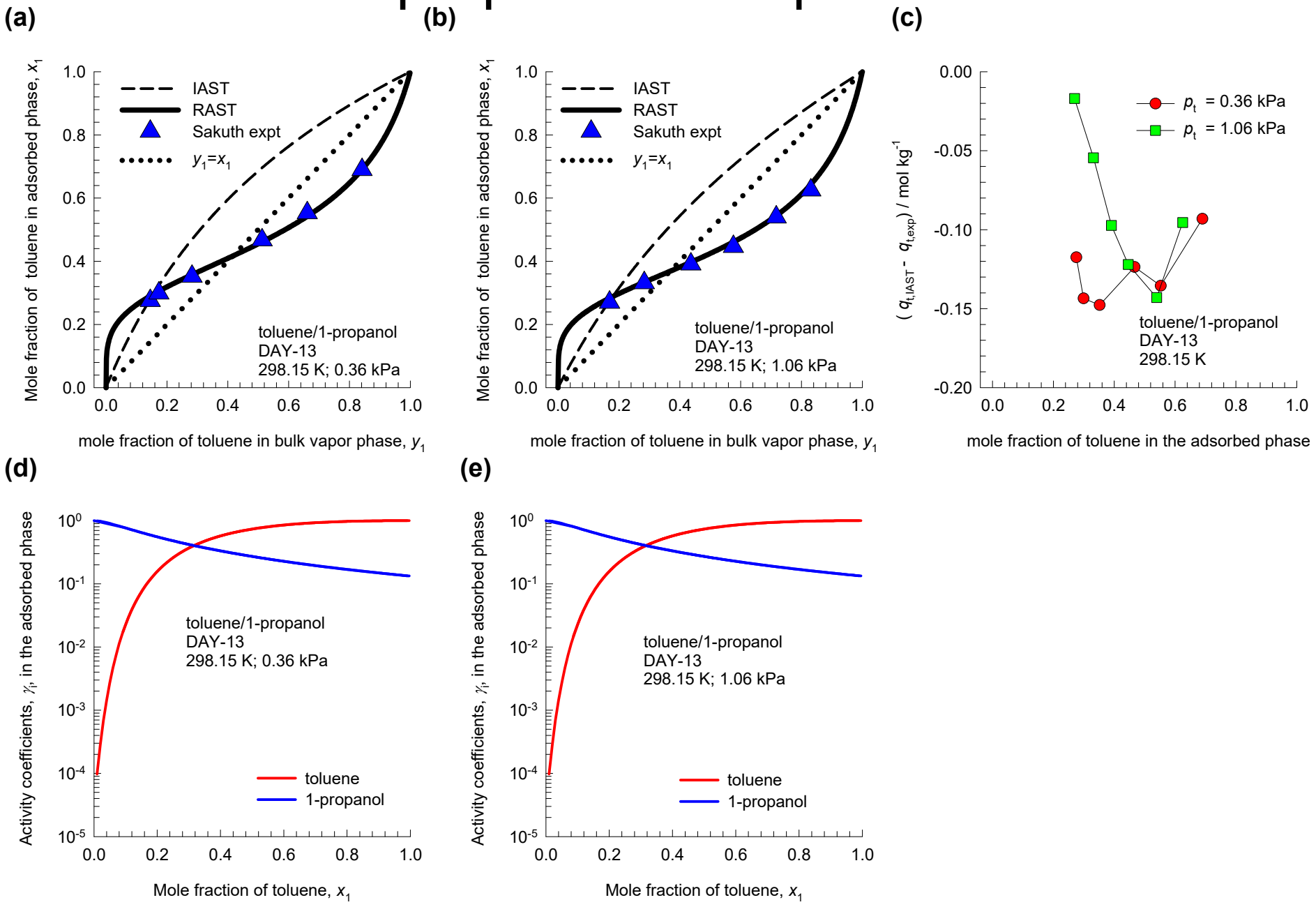

toluene/1-propanol/DAY-13; p_t = 1.06 kPa

Figure S58

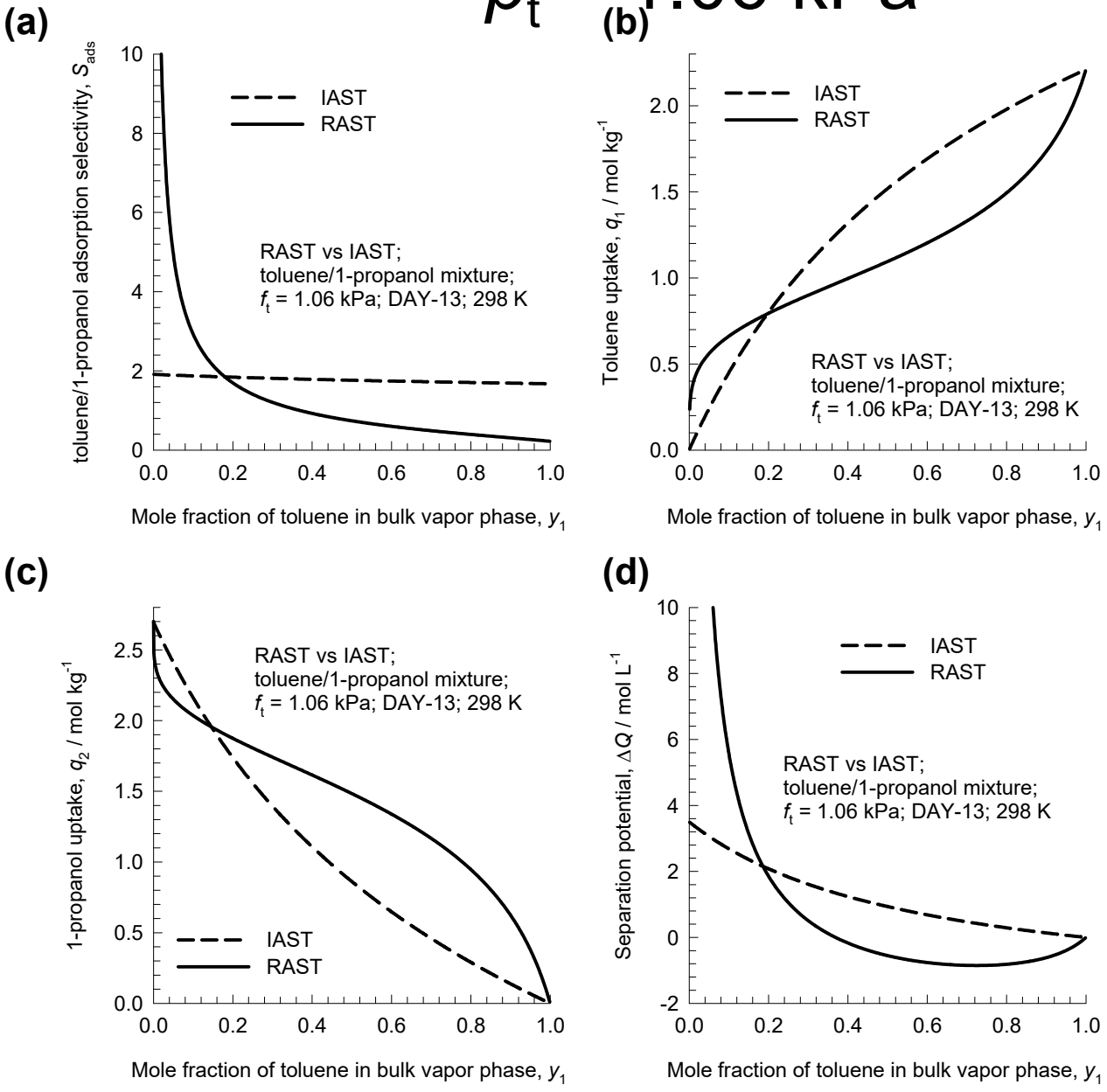

Figure S59

Transient breakthrough toluene/1-propanol/DAY-13: RAST vs IAST Total pressure = 1.06 kPa

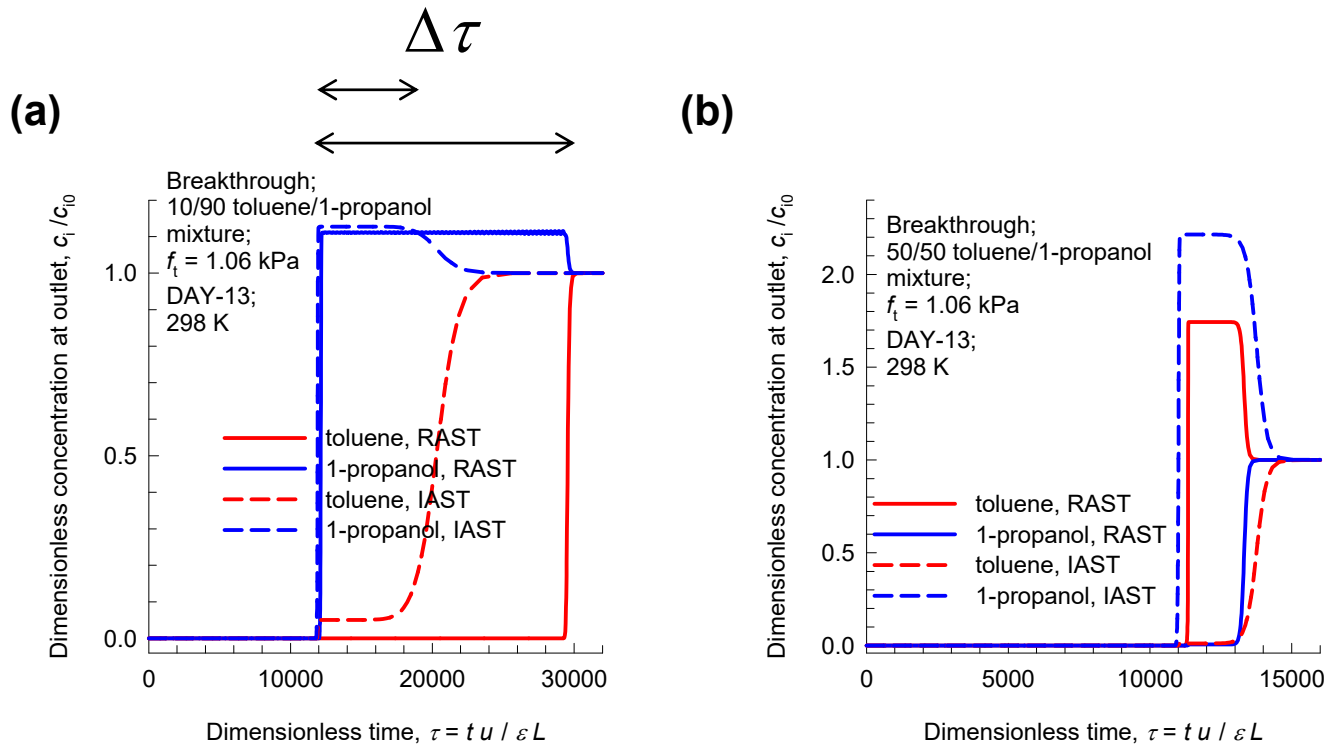

toluene/1-propanol/DAY-13
Total pressure = 0.36 kPa

Figure S60

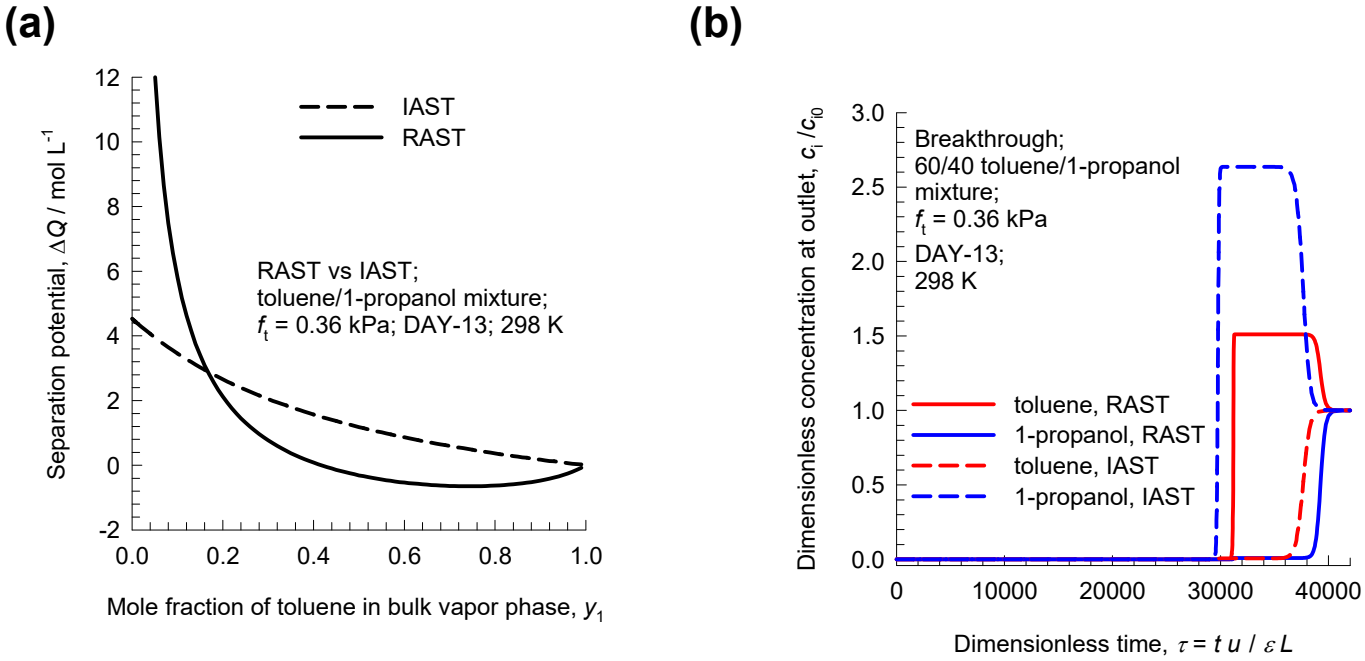

Figure S61

Toluene/1-propanol adsorption in DAY-55

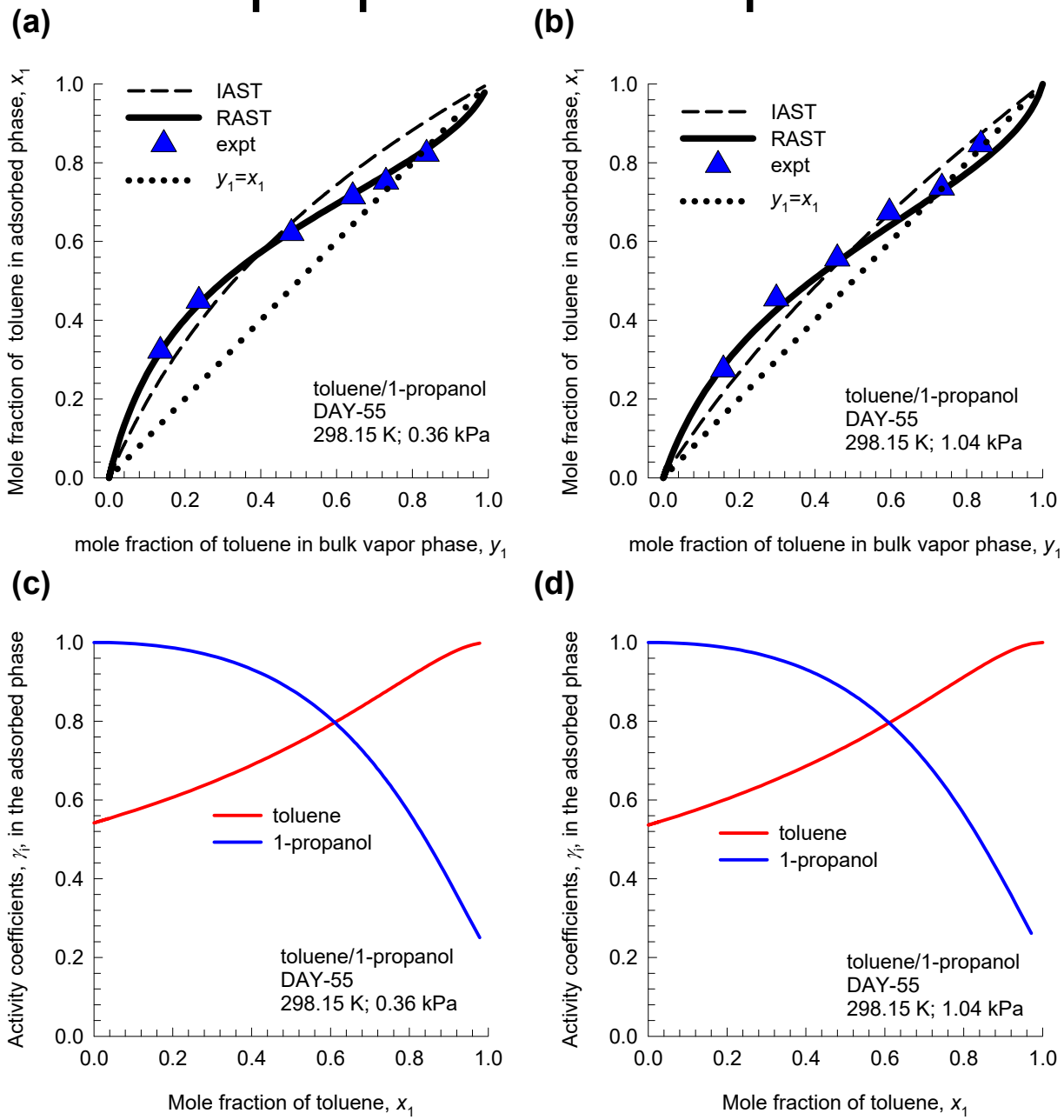

Water, methanol, ethanol unary isotherms in FAU

Figure S62

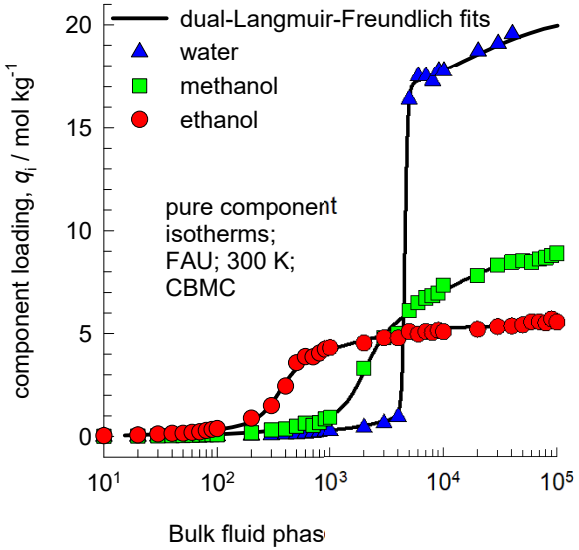

snapshot showing ethanol adsorption in FAU

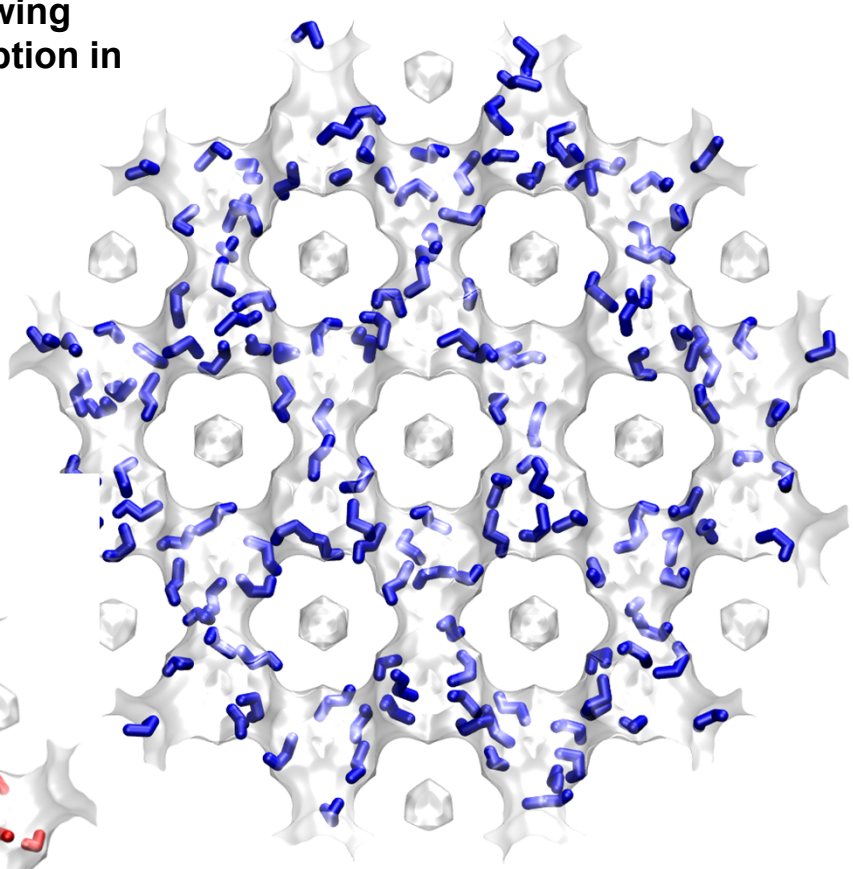

snapshot showing methanol adsorption in FAU

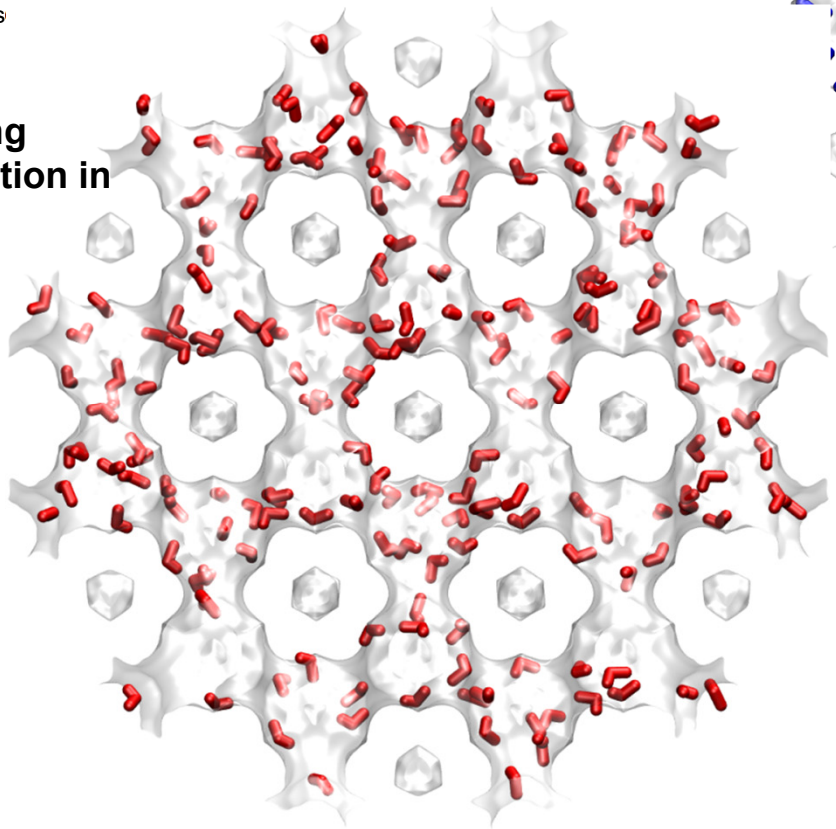

Water/methanol mixture adsorption in FAU

Figure S63

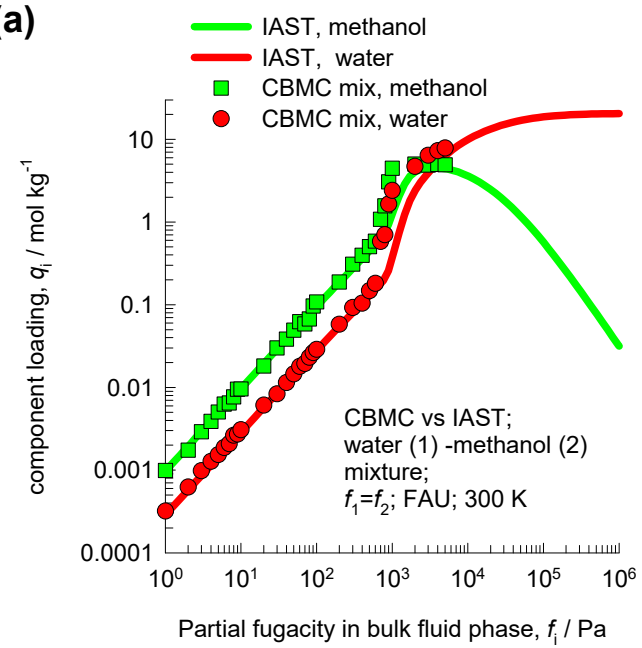

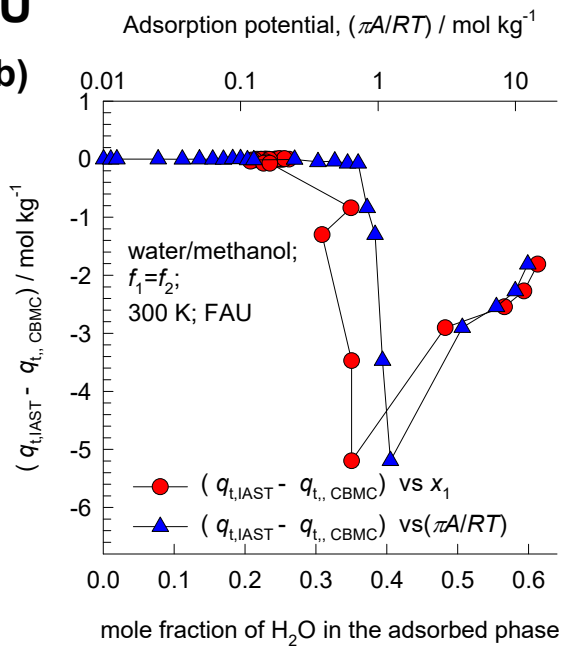

snapshot showing water/methanol mixture adsorption in FAU

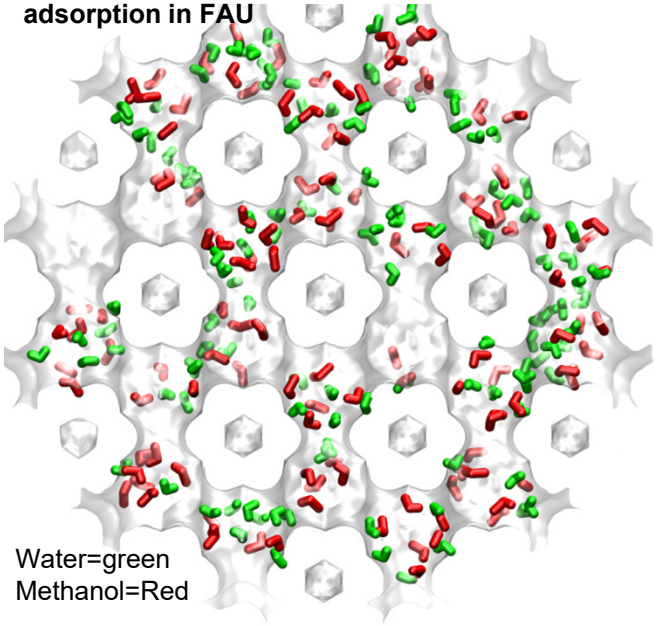

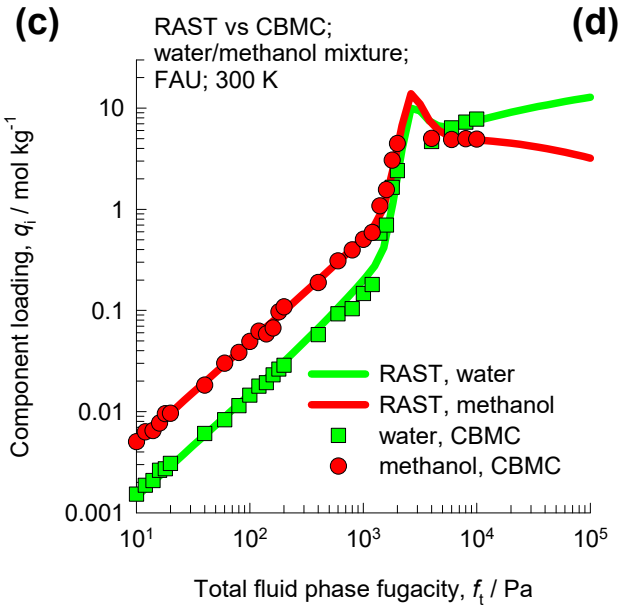

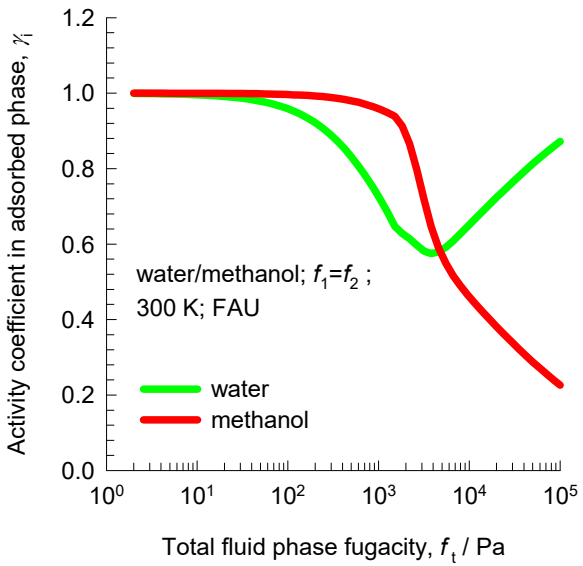

Water/methanol mixture adsorption in FAU

Figure S64

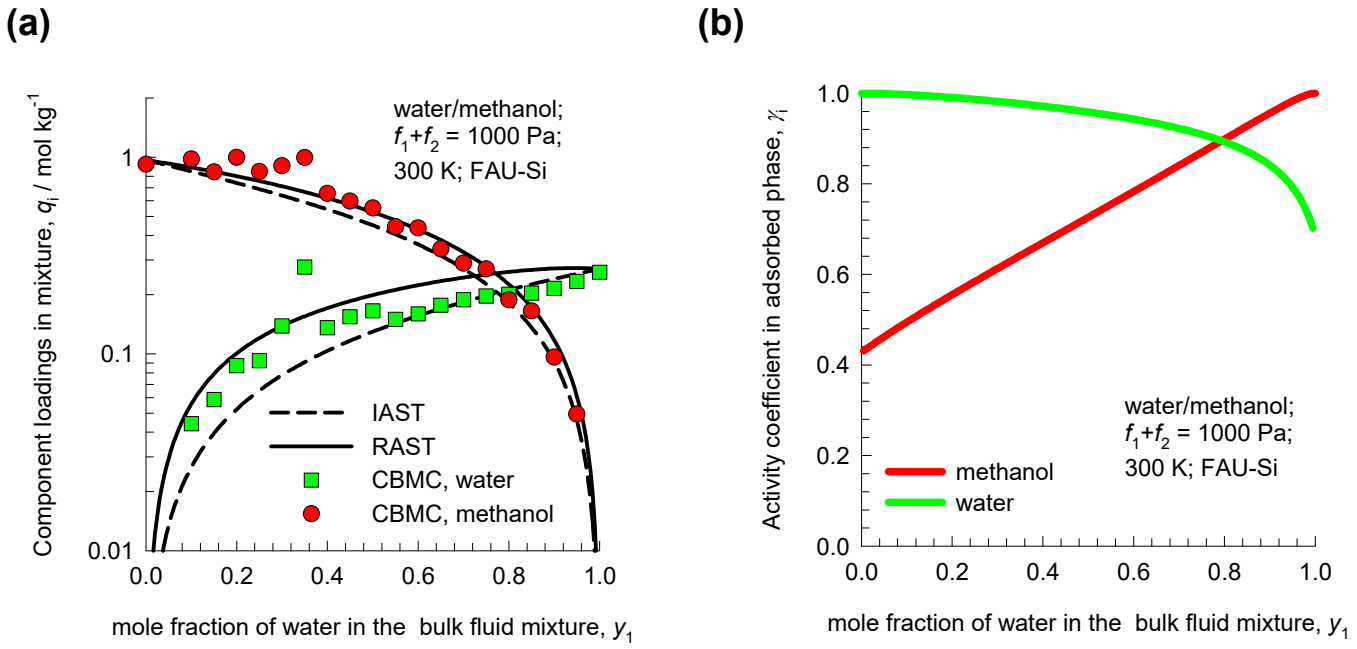

Water/ethanol mixture adsorption in FAU

Figure S65

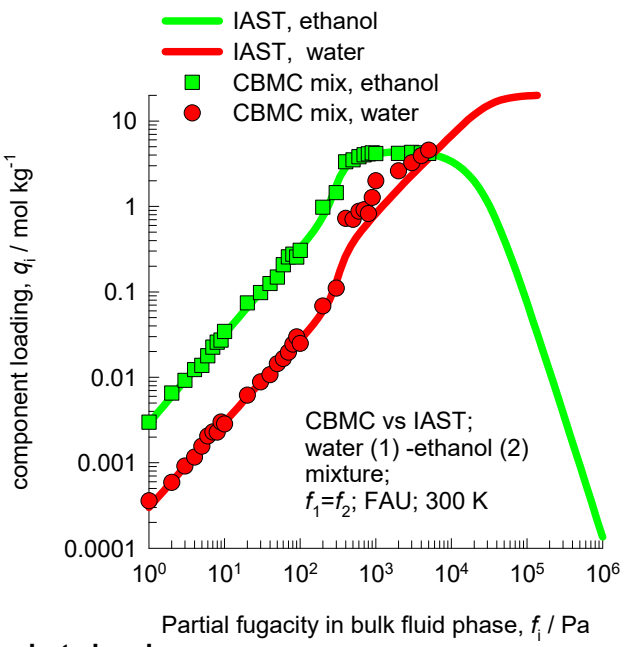

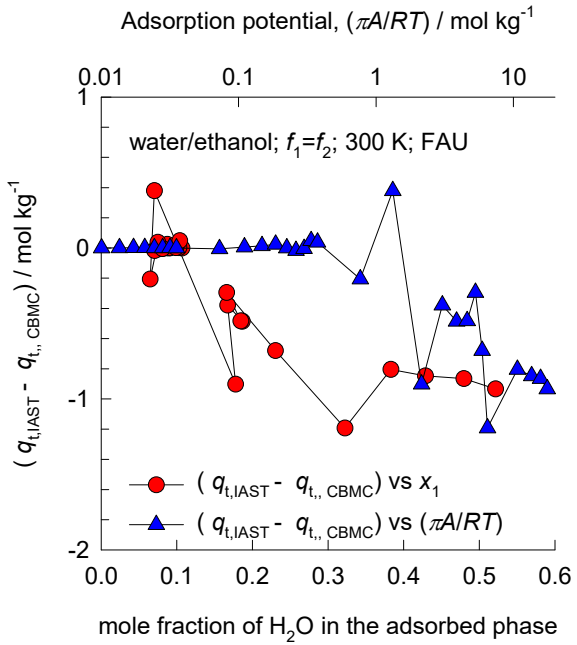

snapshot showing water/ethanol mixture adsorption in FAU

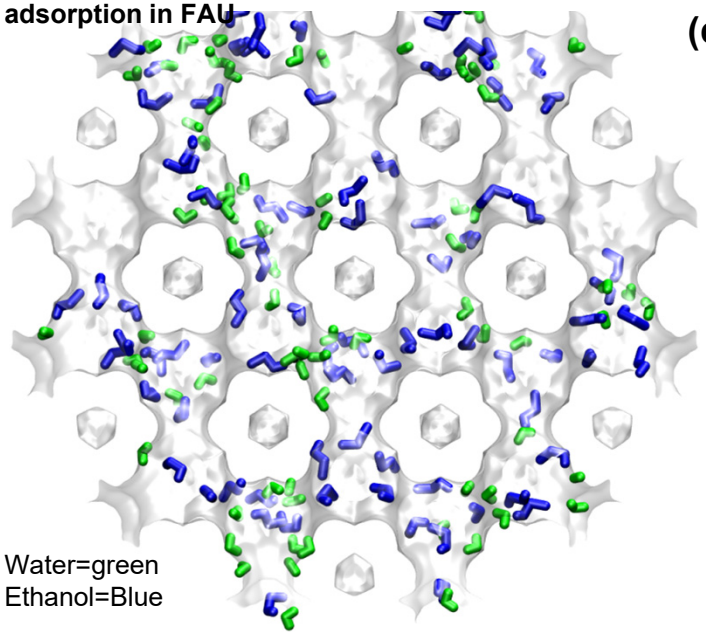

Water=green
Ethanol=Blue

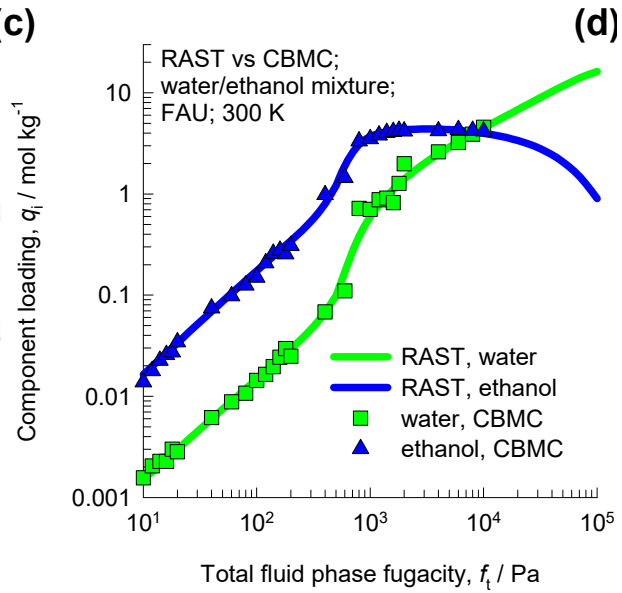

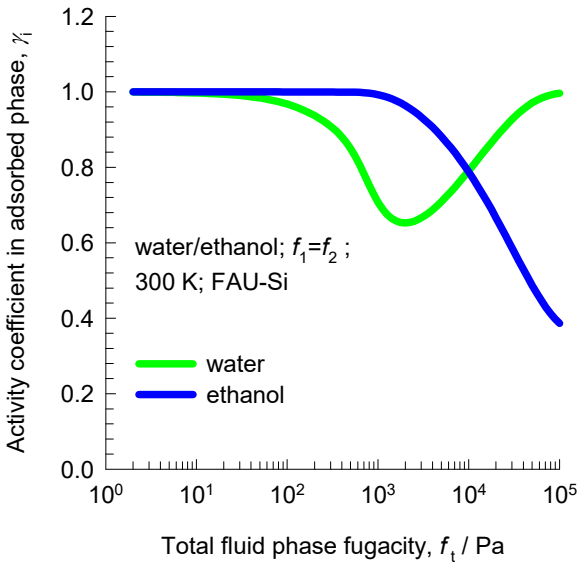

Figure S66

Water/ethanol permeation across FAU membrane

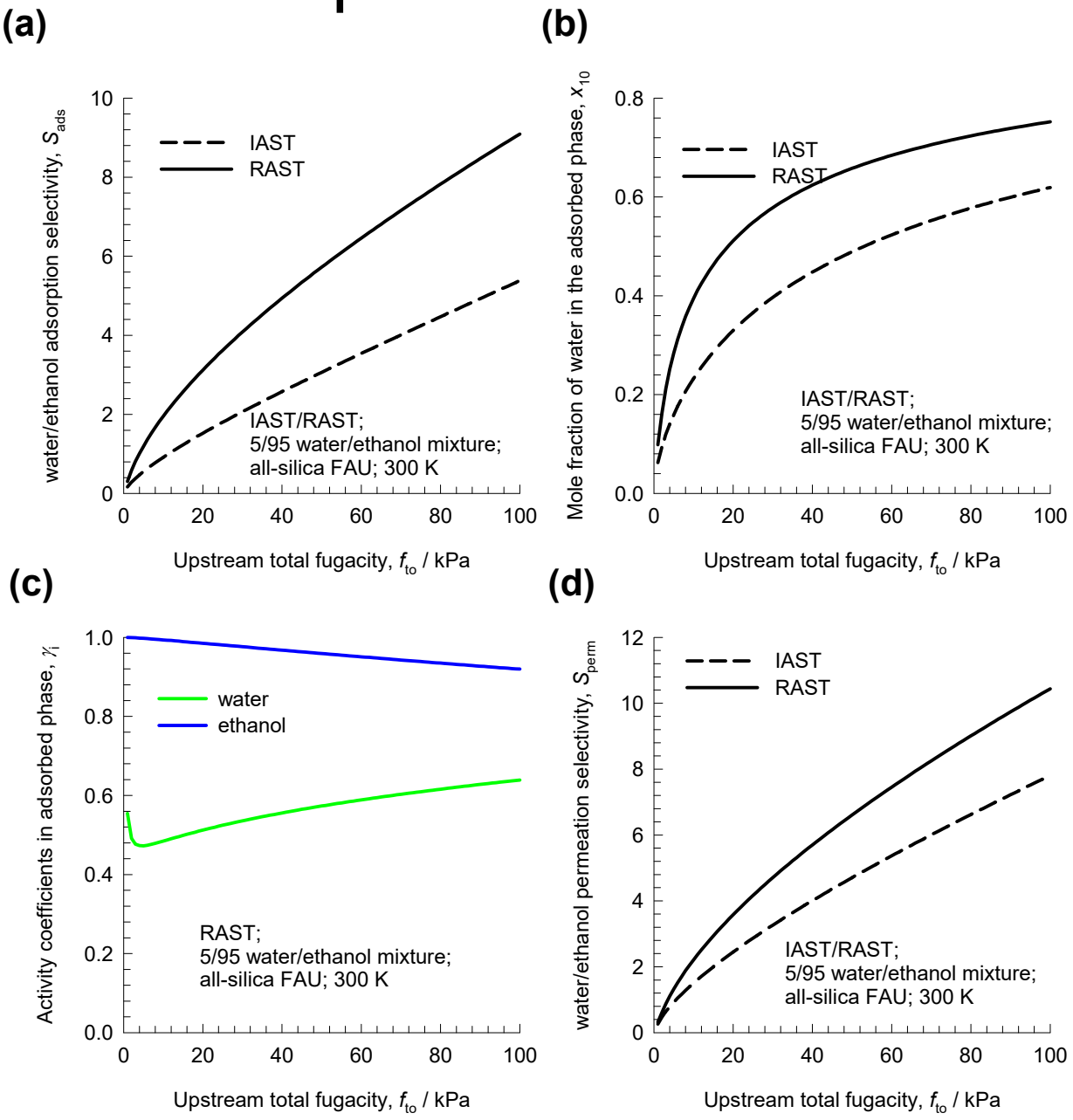

Water, methanol, ethanol unary isotherms in DDR

Figure S67

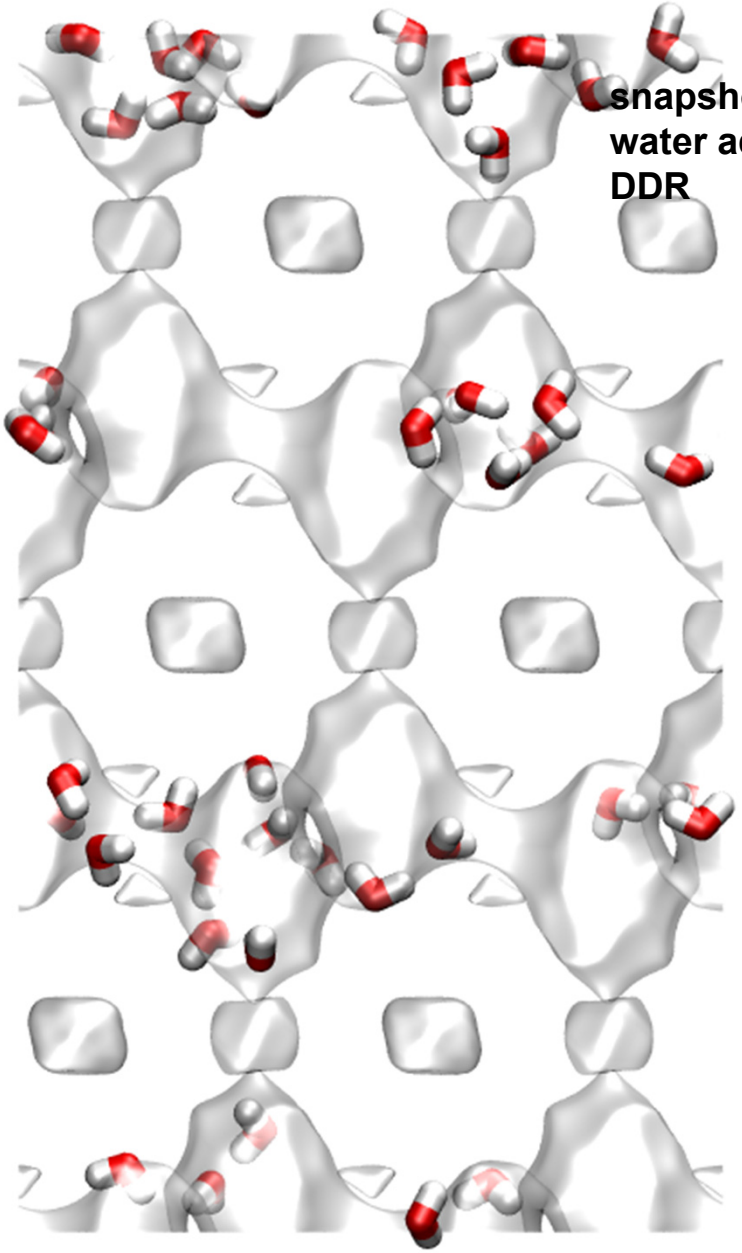

snapshot showing water adsorption in DDR

There are 12 cages per unit cell. The volume of one DDR cage is 278 Å^3, significantly smaller than that of a single cage of FAU (786 Å^3), or ZIF-8 (1168 Å^3).

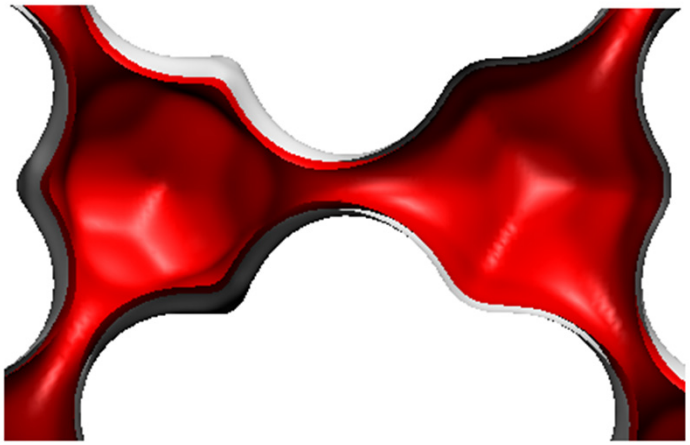

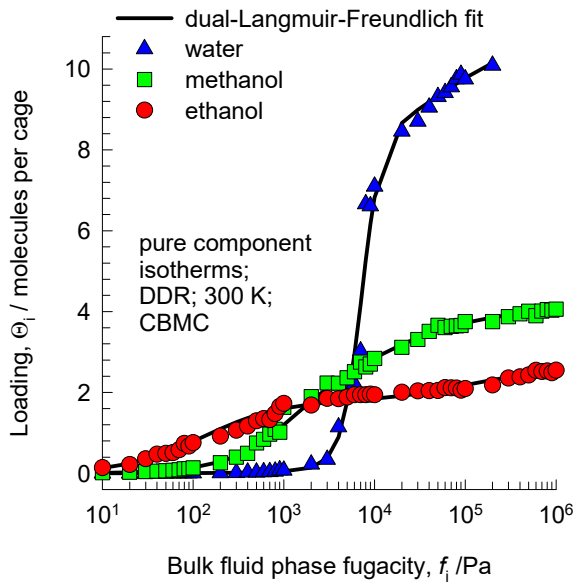

Water/methanol mixture adsorption in DDR

Figure S68

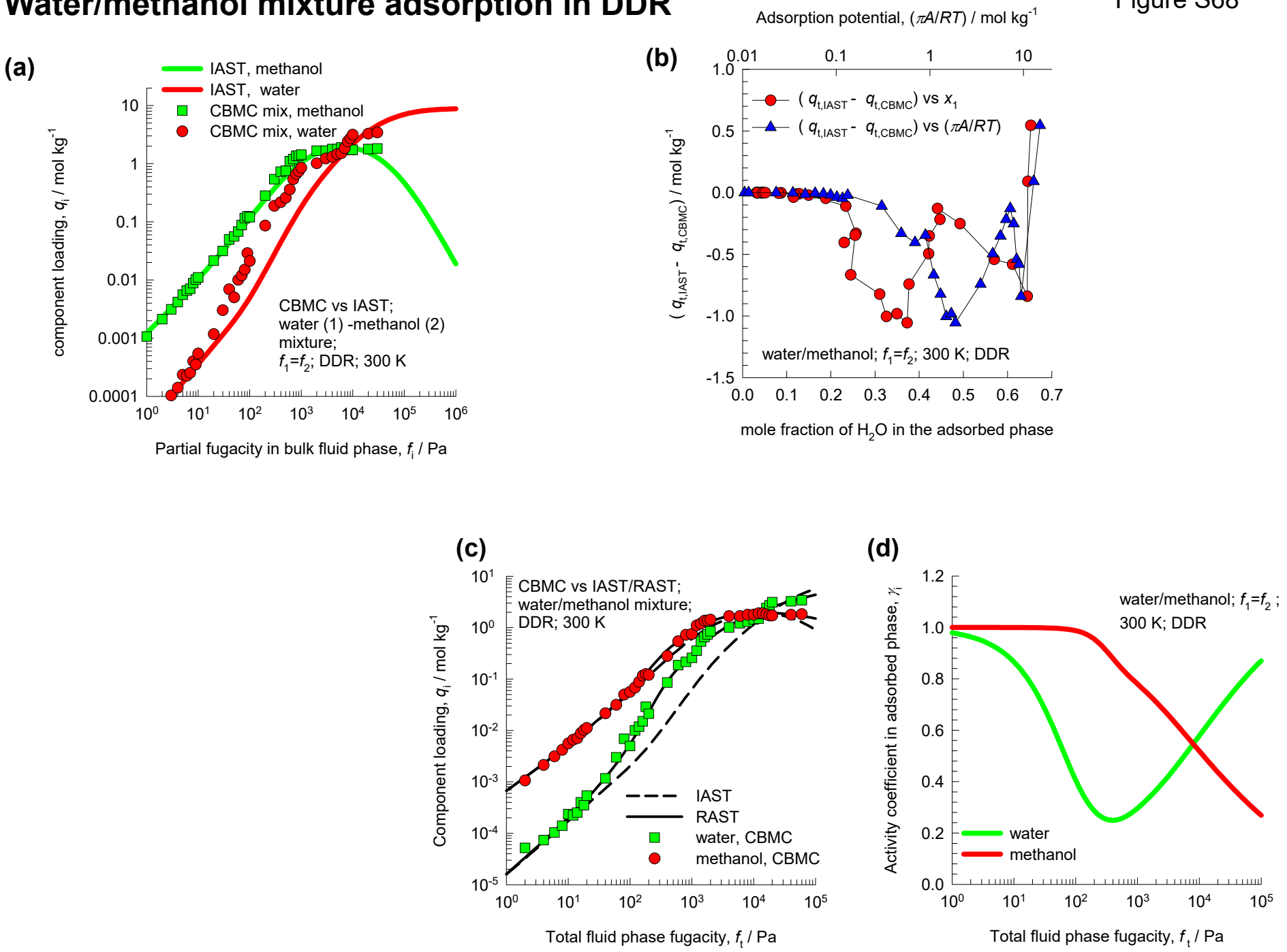

Water/ethanol mixture adsorption in DDR

Figure S69

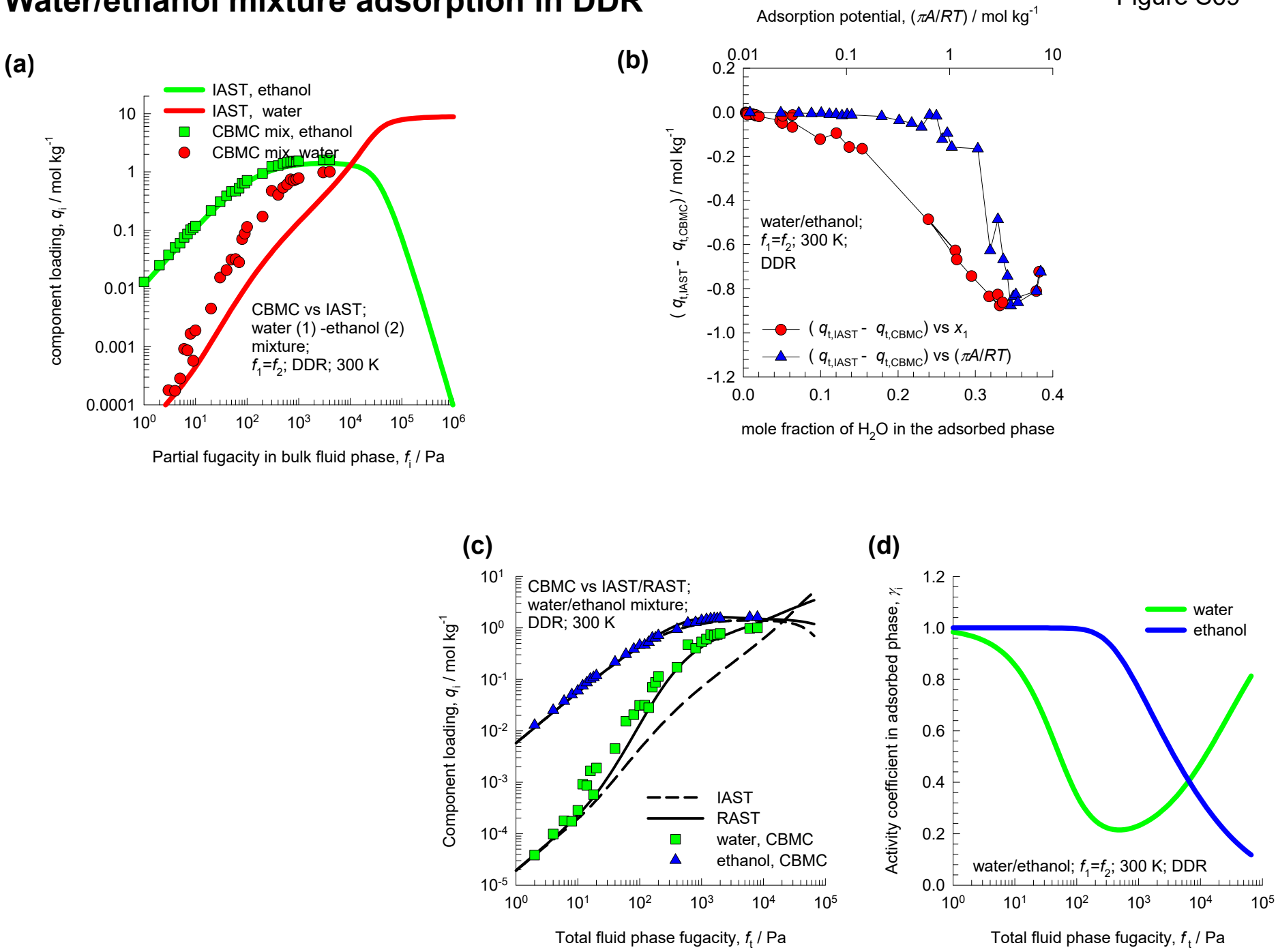

Figure S70

Water/methanol permeation across DDR membrane

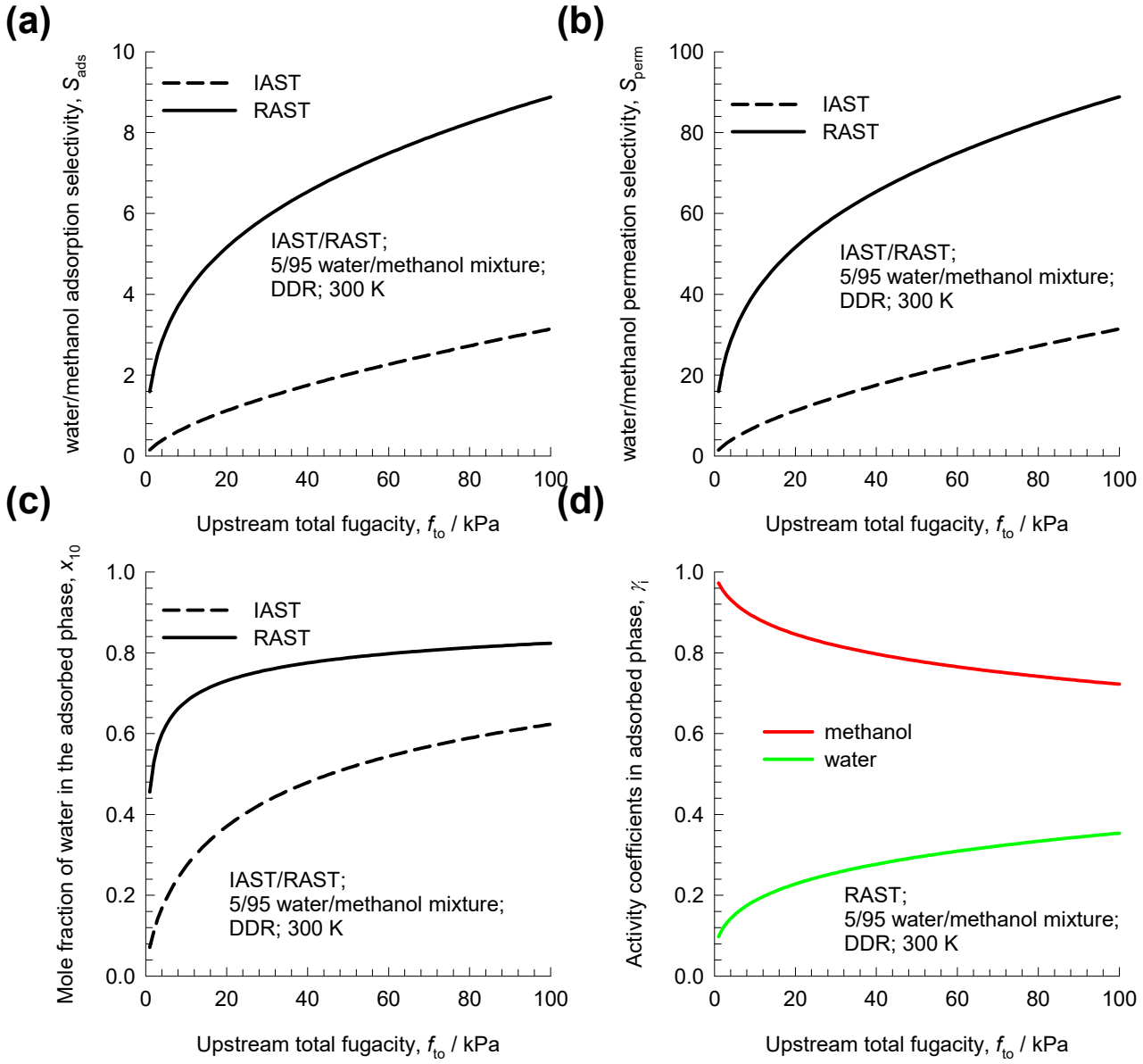

Water/ethanol permeation across DDR membrane

Figure S71

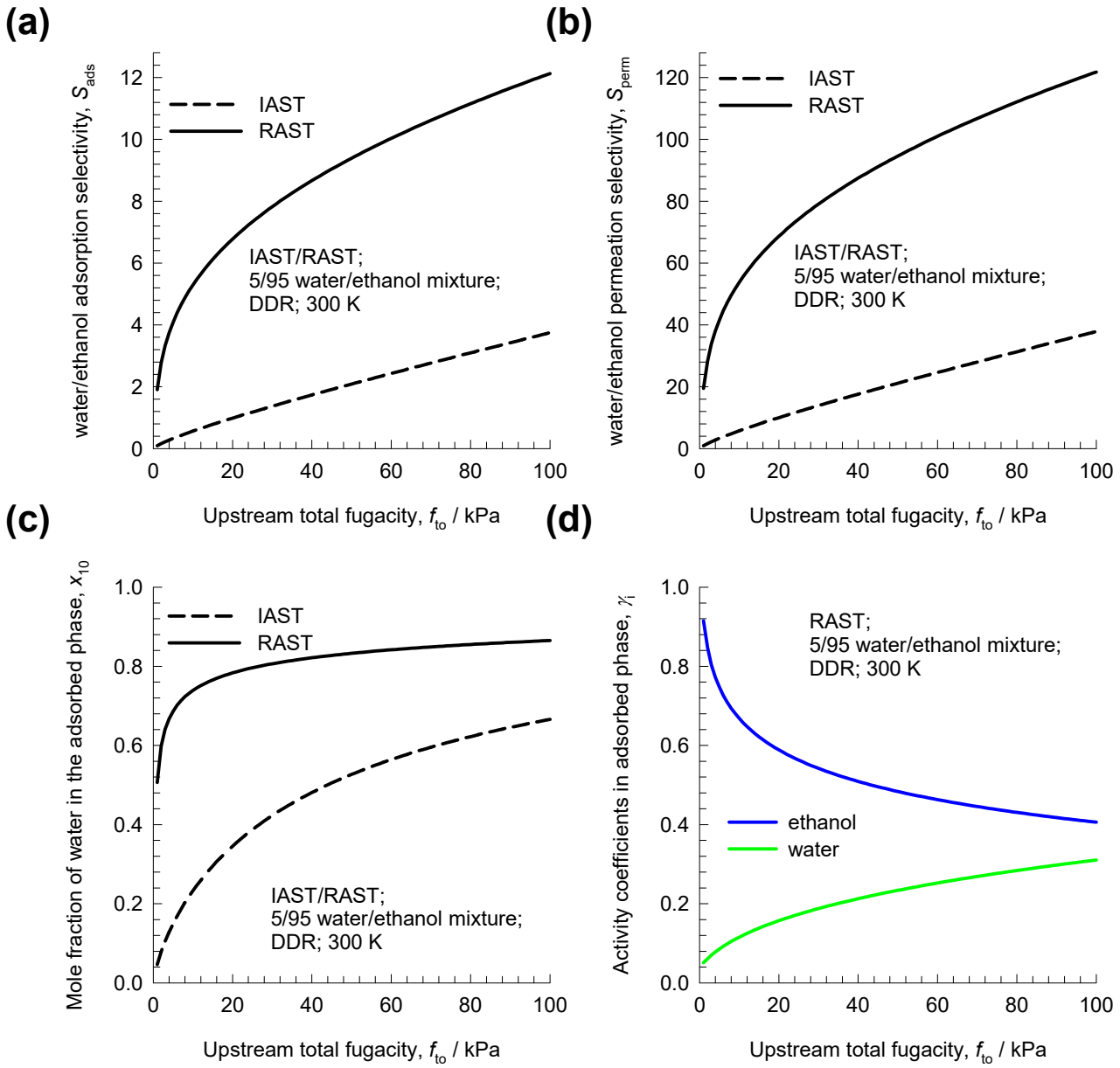

Transient water/alcohol permeation across DDR membrane

Figure S72

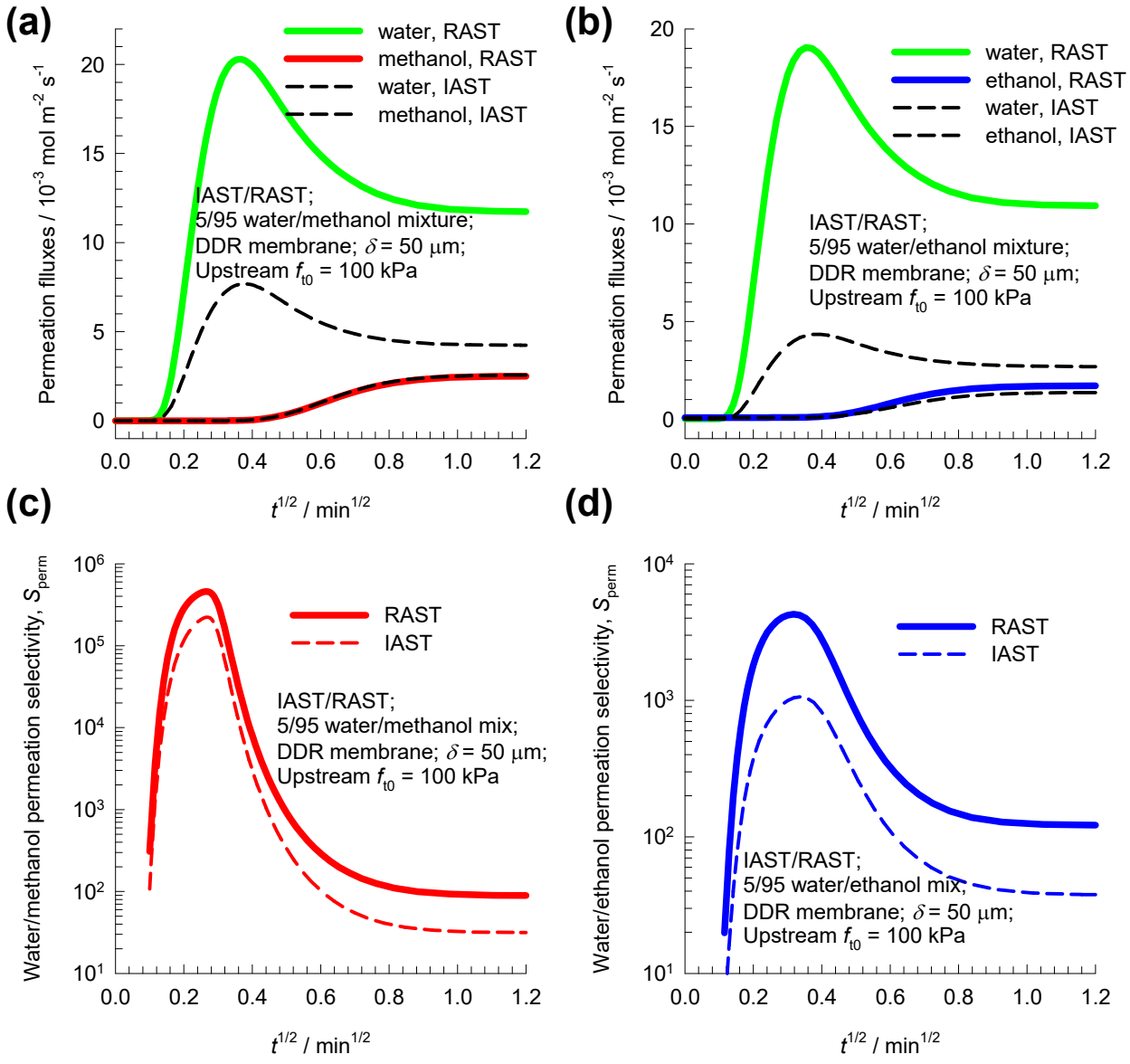

Water, methanol, ethanol isotherms in MFI

Figure S73

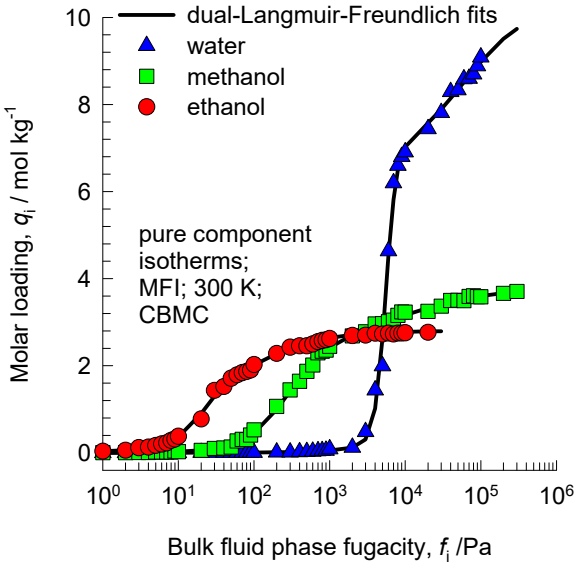

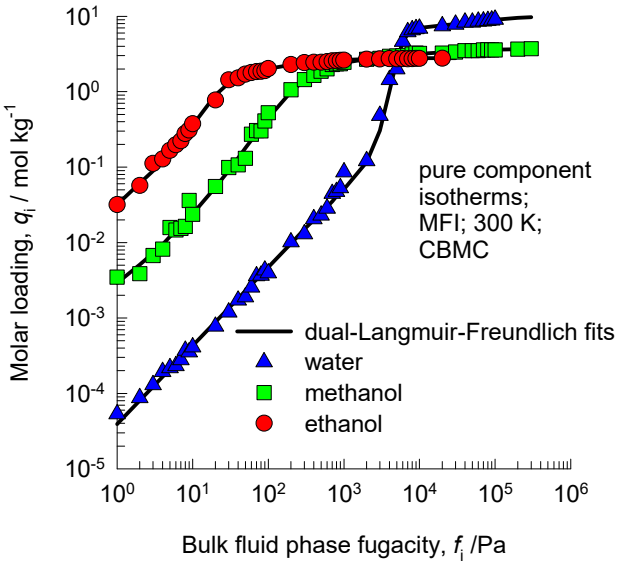

water

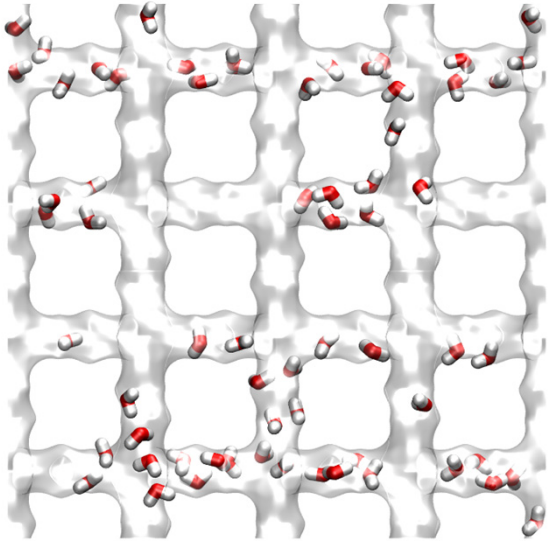

methanol

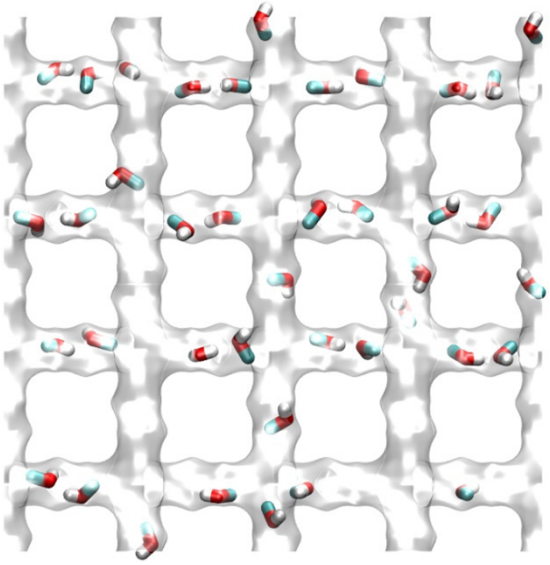

ethanol

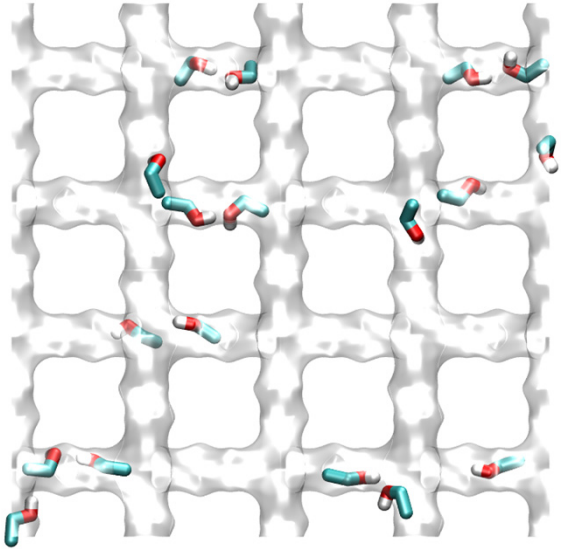

Water/methanol mixture adsorption in MFI

Figure S74

(a)

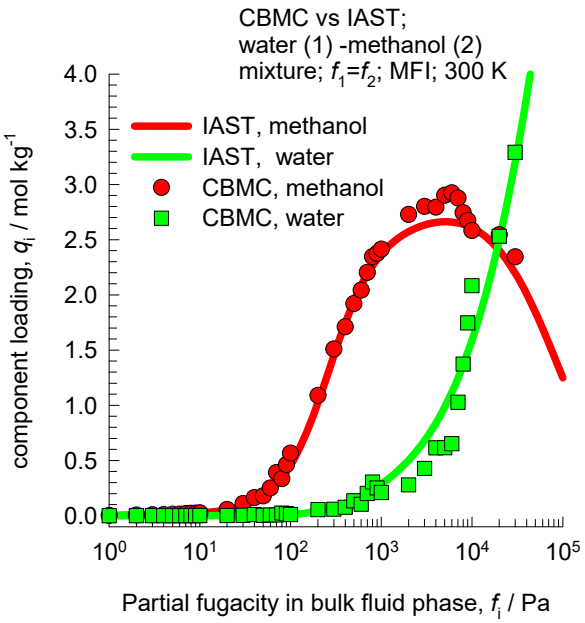

snapshot showing water/methanol mixture adsorption in MFI

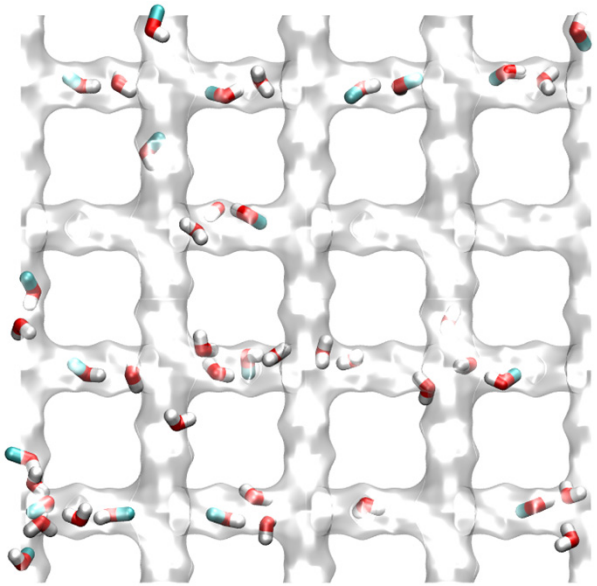

(b)

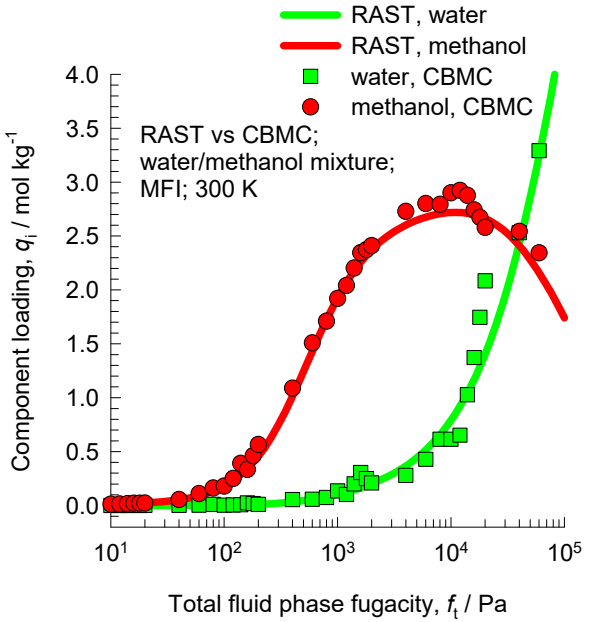

(c)

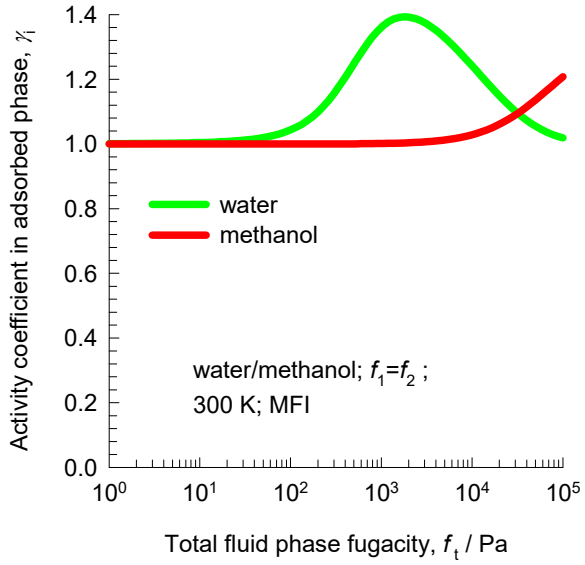

Water/ethanol mixture adsorption in MFI

Figure S75

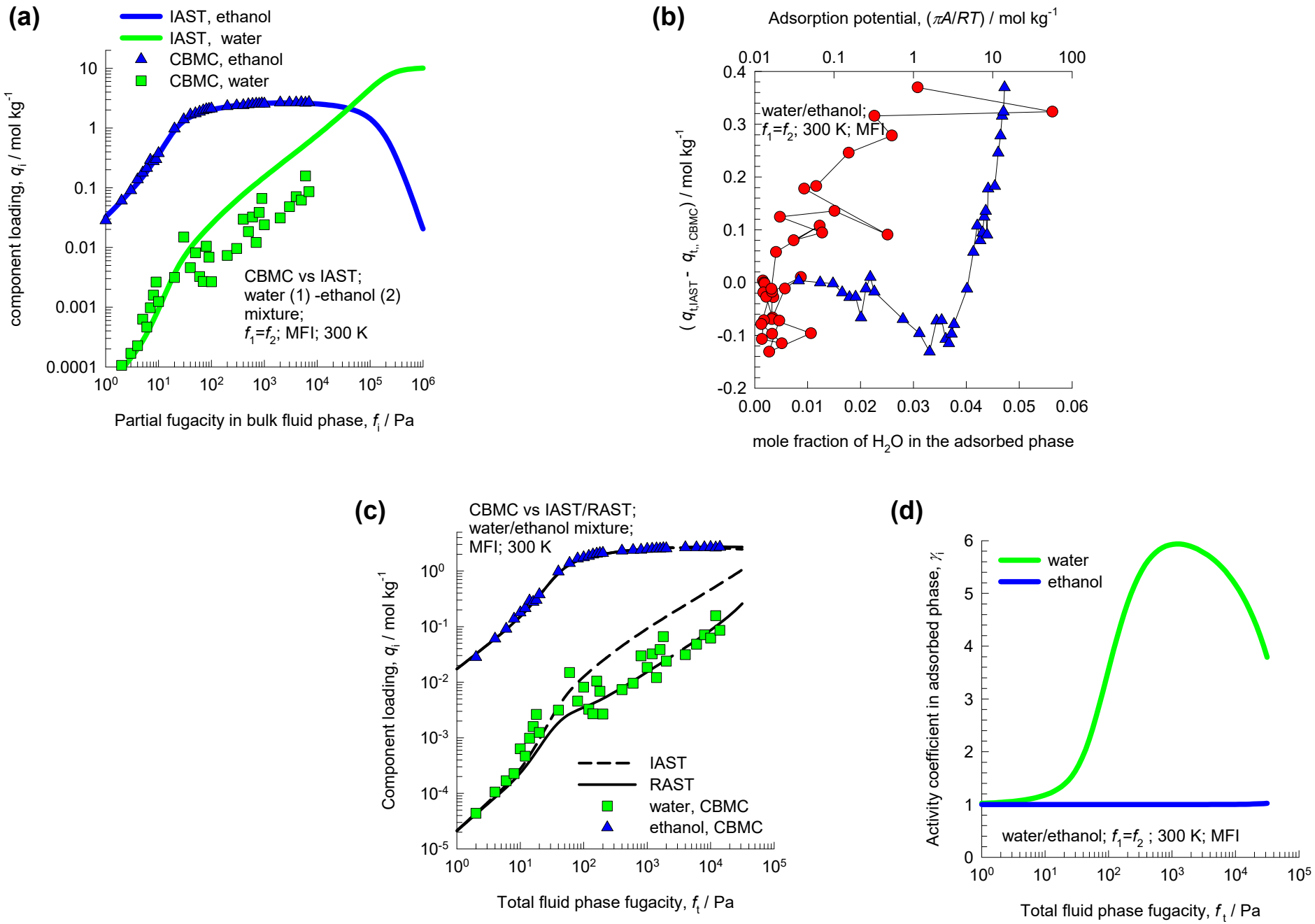

Figure S76

Water/ethanol permeation across MFI membrane

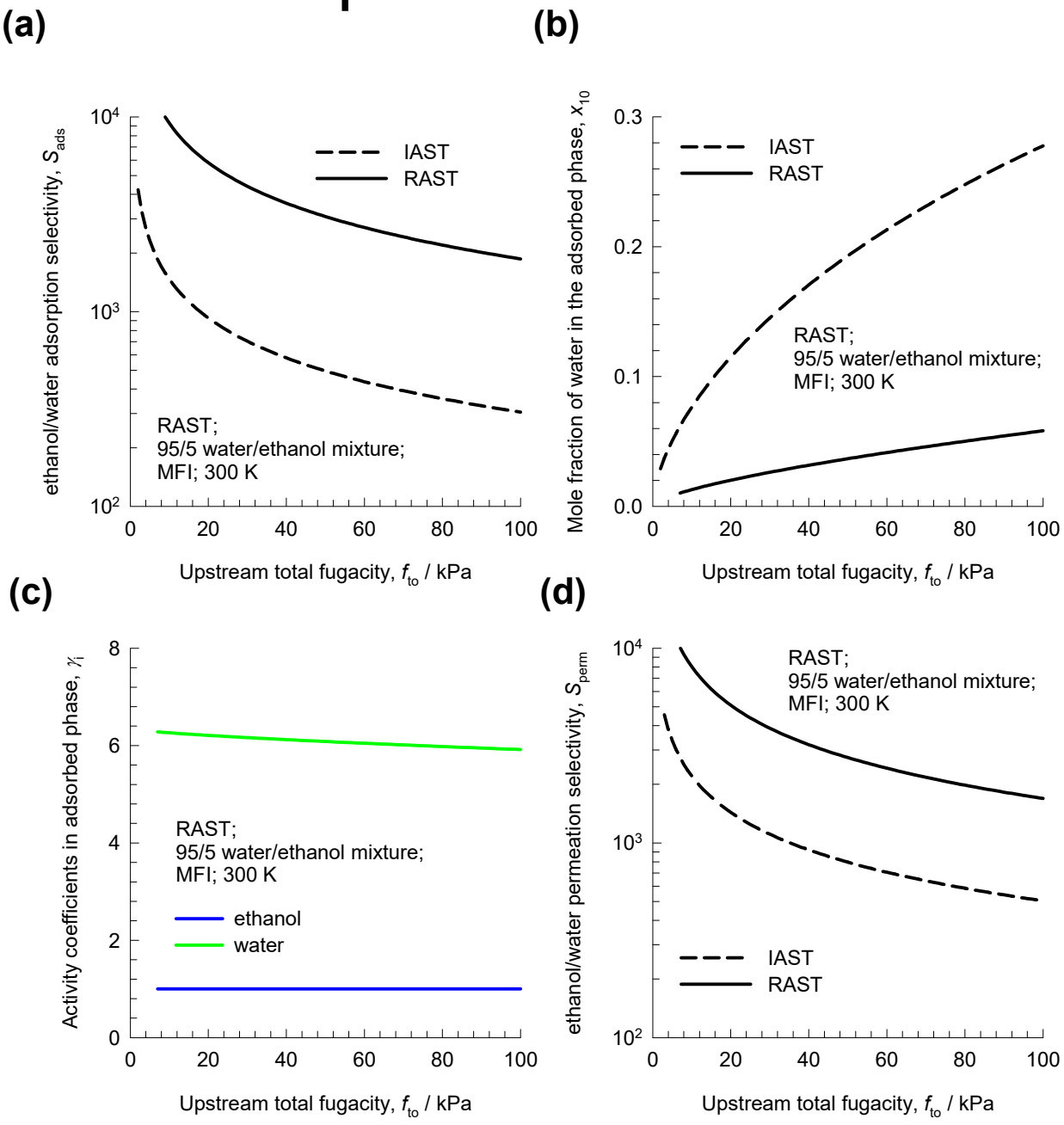

1-alcohols unary isotherms in CHA zeolite

Figure S77

(a)

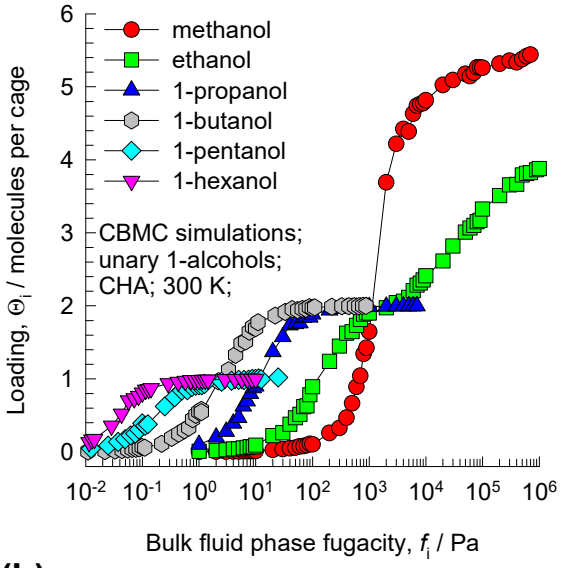

(b)

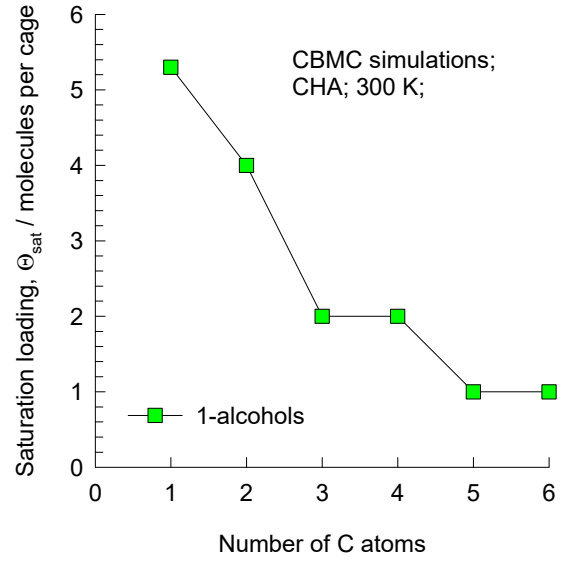

There are 6 cages per unit cell.
The volume of one CHA cage is 316.4 Å^3, slightly larger than that of a single cage of DDR (278 Å^3), but significantly lower than FAU (786 Å^3).

(c)

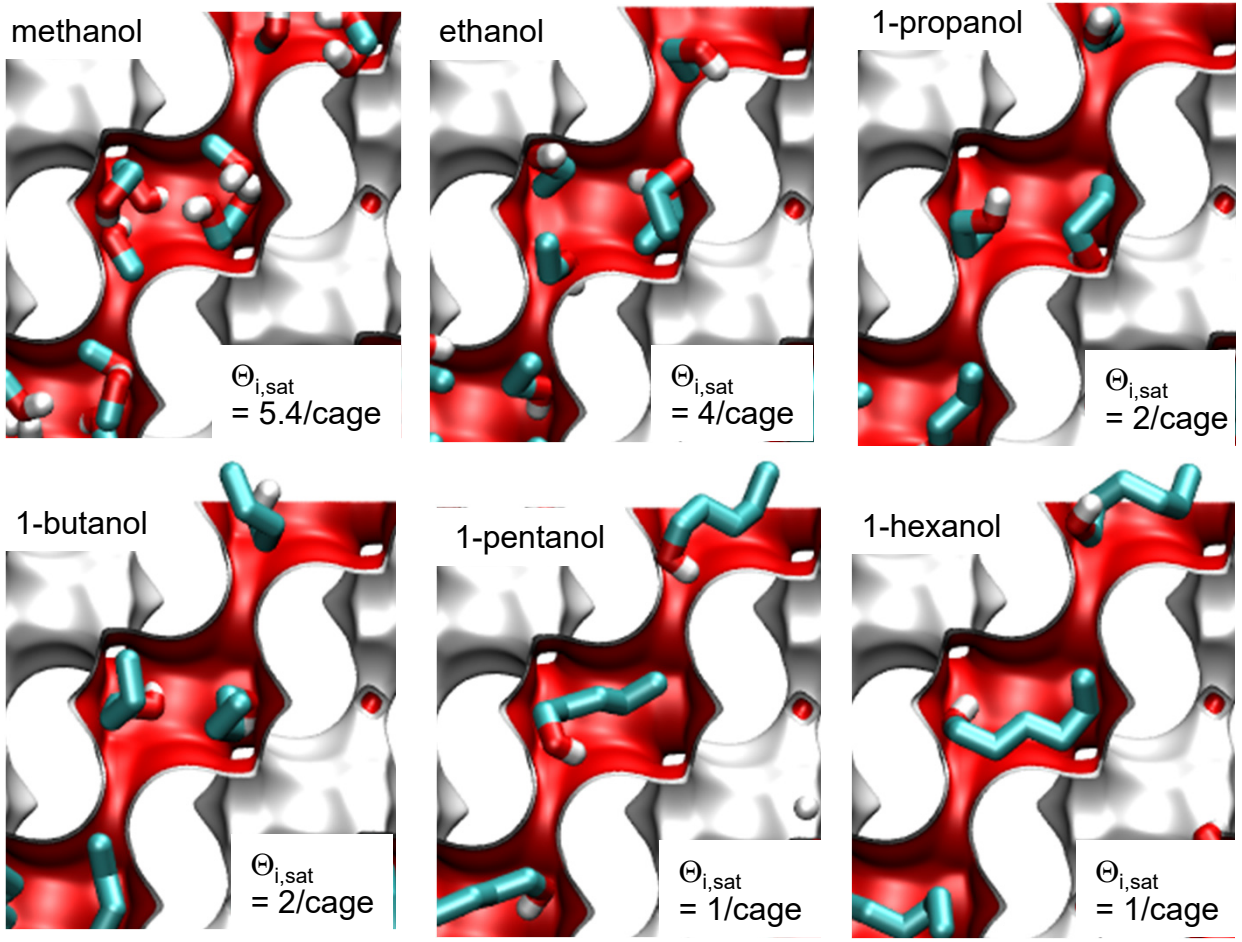

1-alcohols mixture adsorption in CHA zeolite

Figure S78

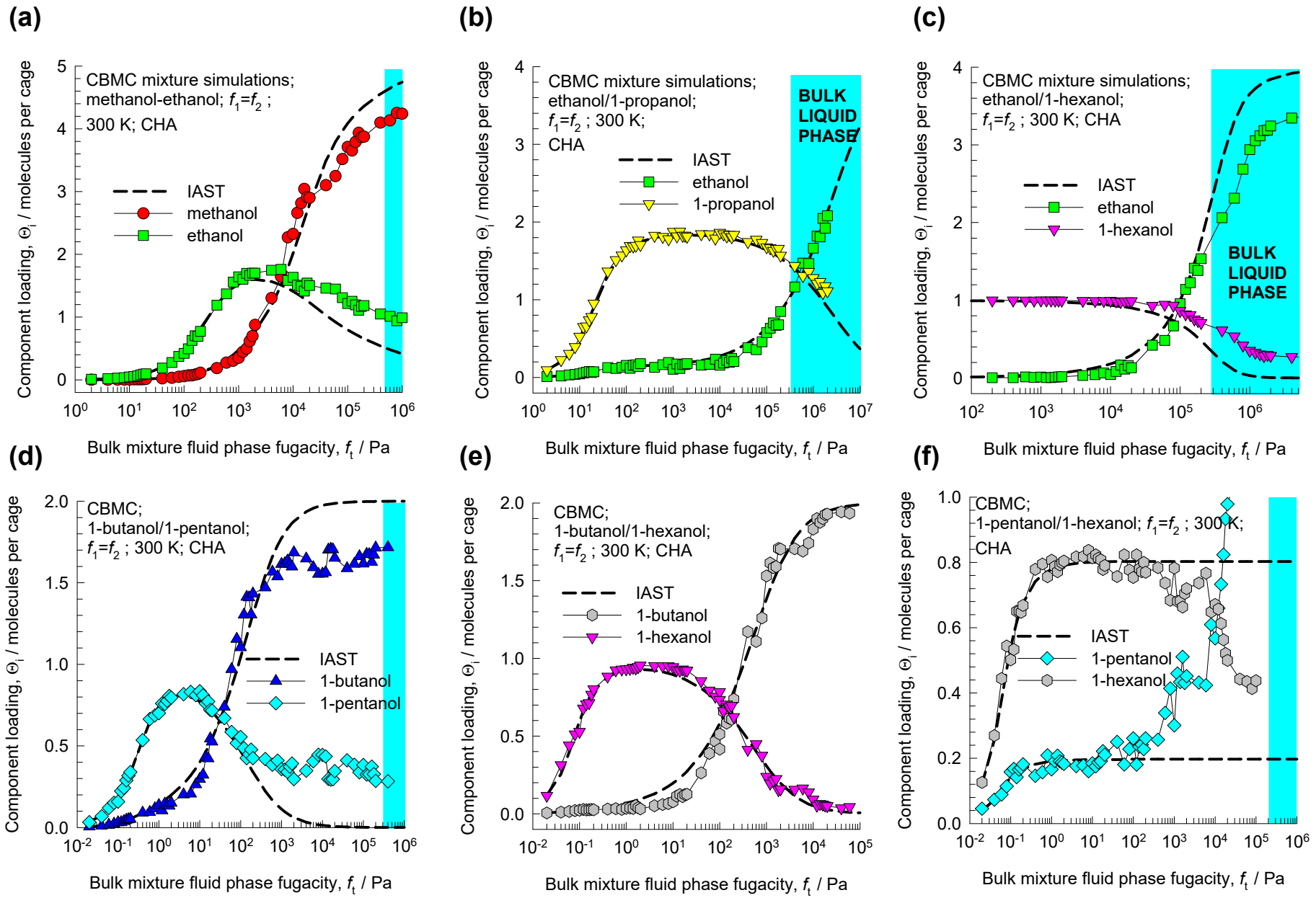

Experimental confirmation of selectivity reversals

Figure S79

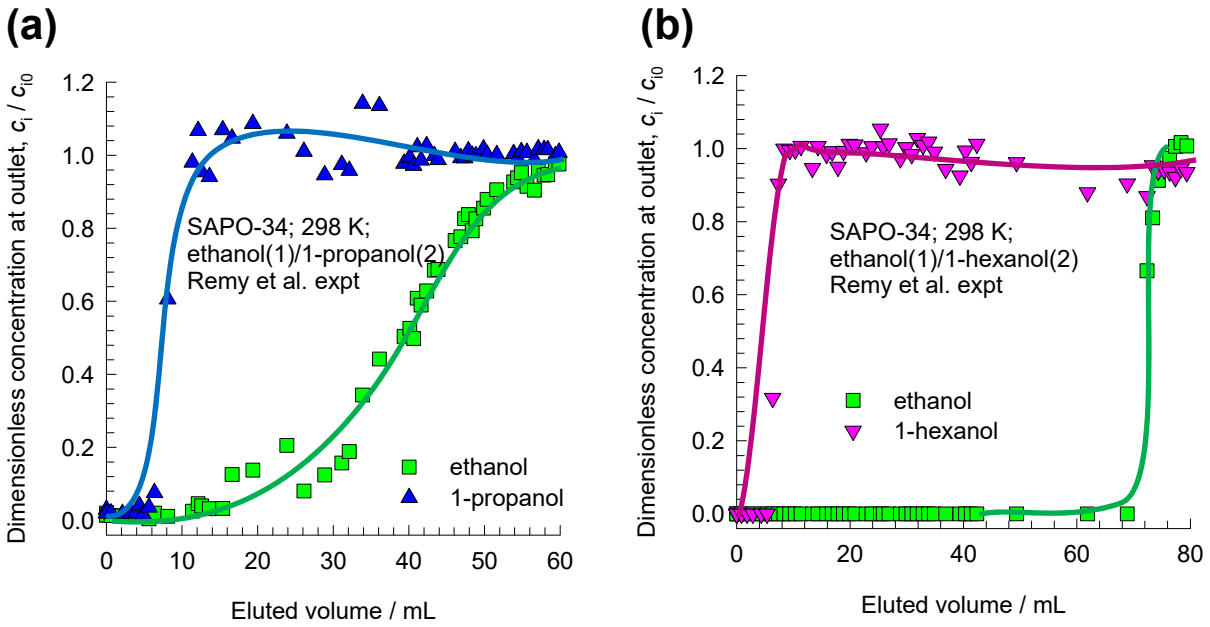

Methanol/ethanol mixture adsorption in CHA zeolite

Figure S80

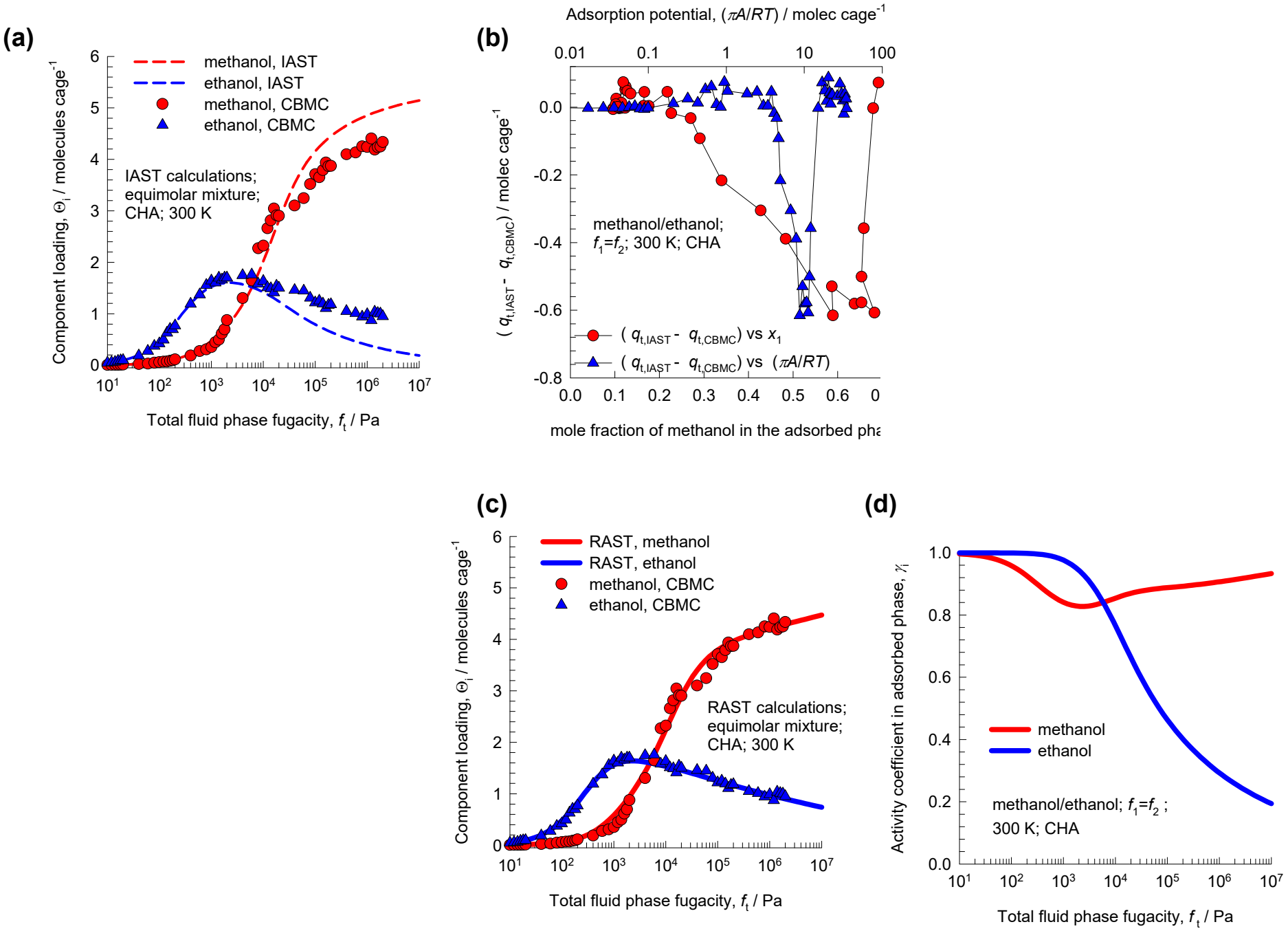

Methanol/ethanol permeation across CHA membrane

Figure S81

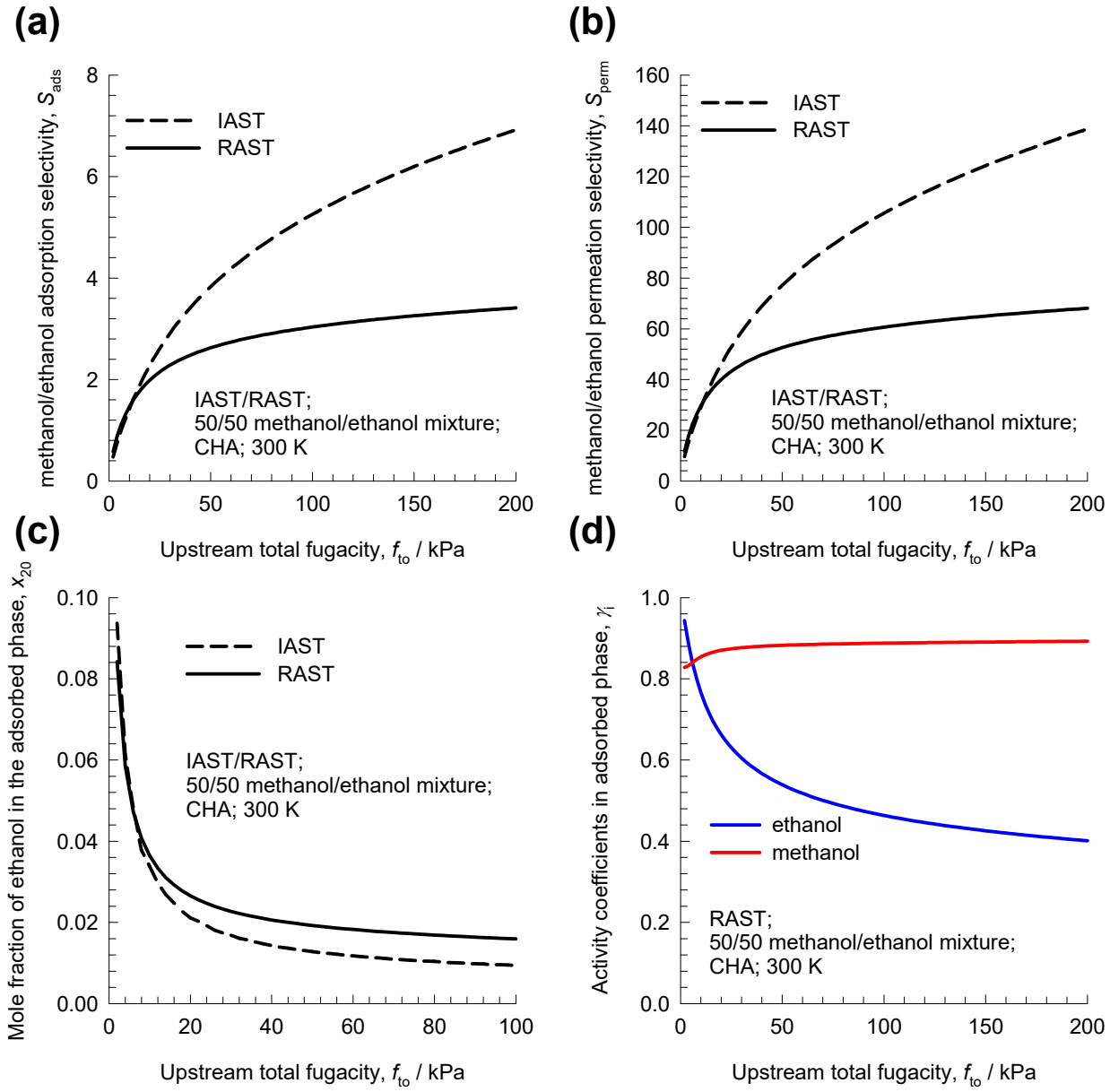

Figure S82

Breaking the azeotrope with LTA-4A

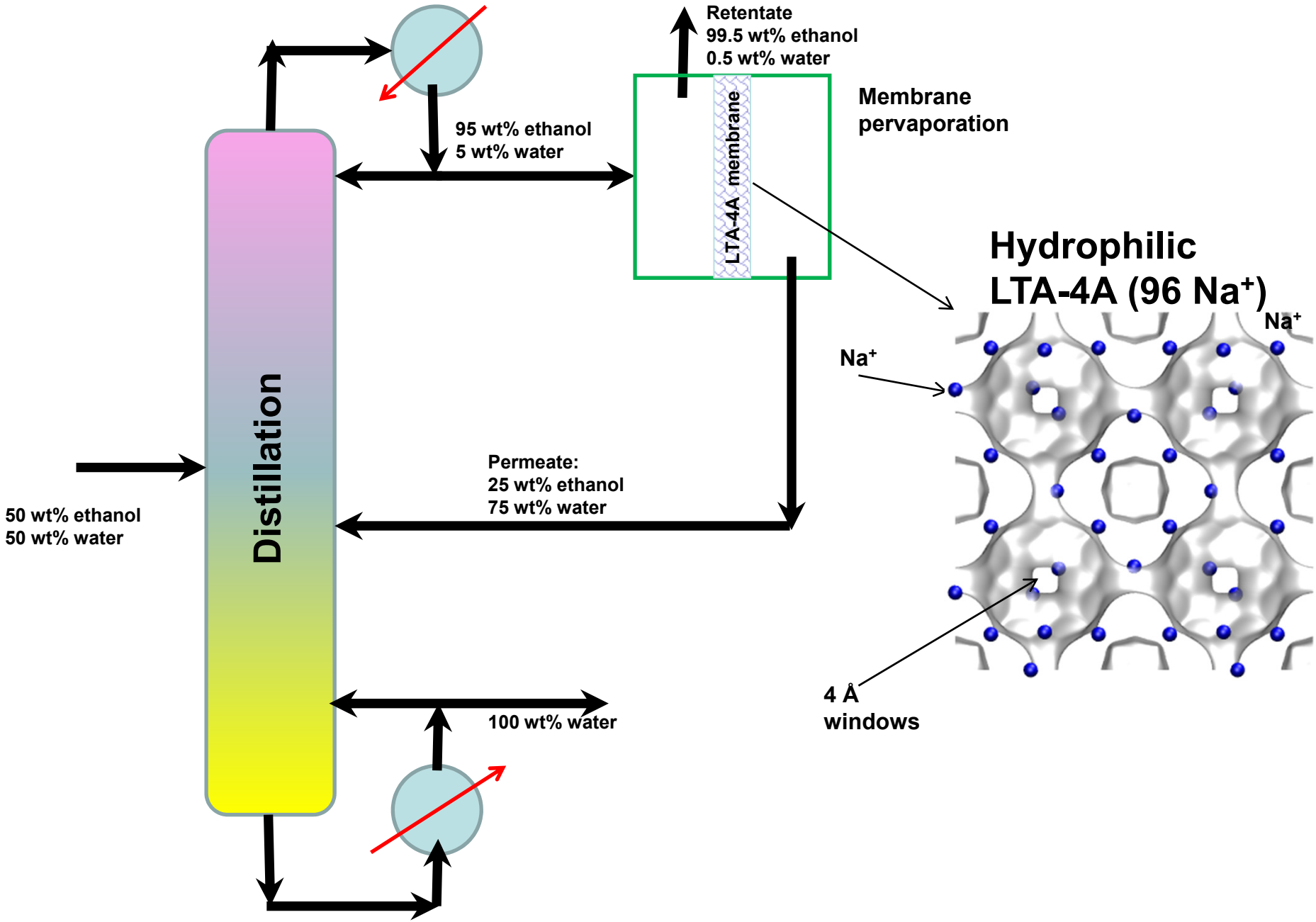

Figure S83

Water and Ethanol adsorption in LTA-4A: Pera-Titus Experiments

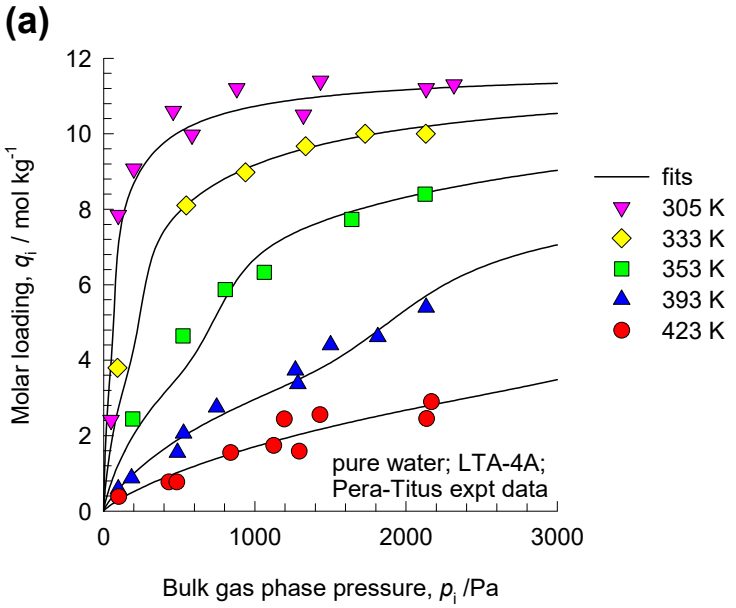

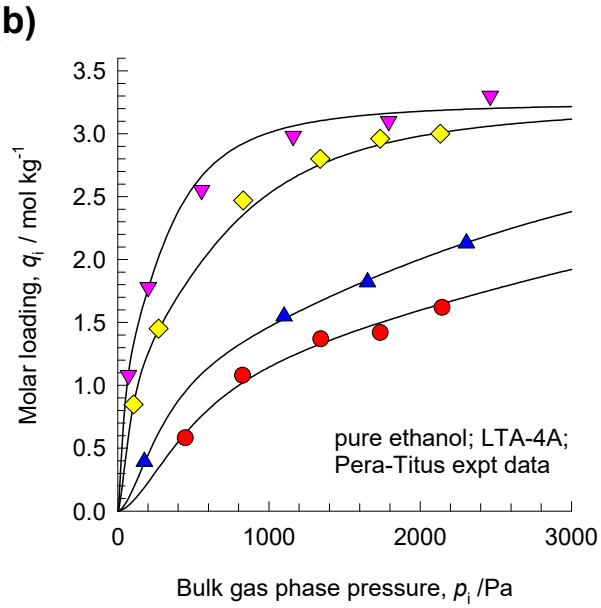

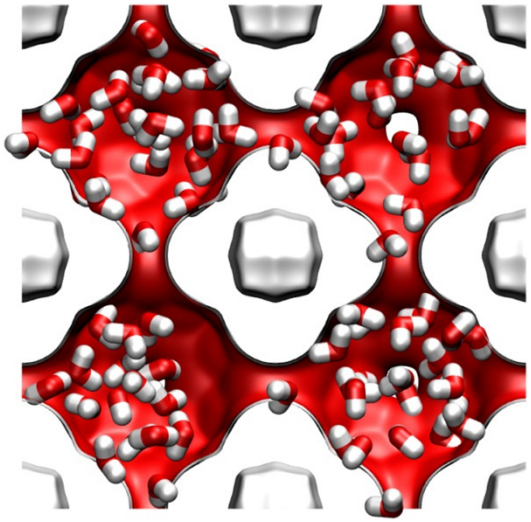

Snapshot of water clustering

Snapshot of ethanol clustering

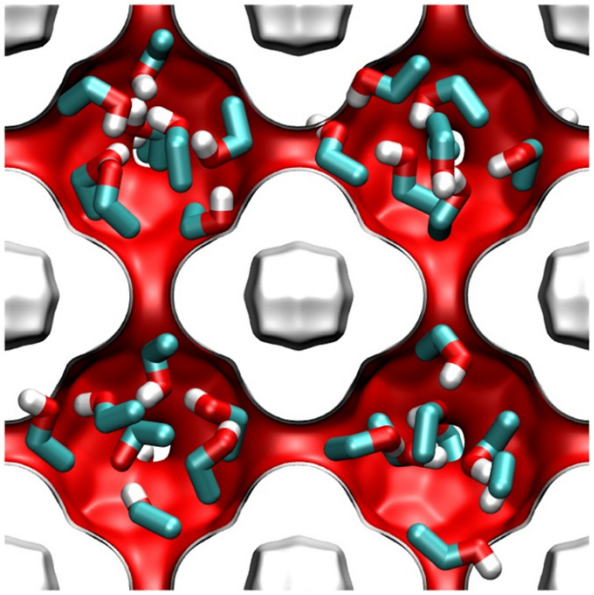

Figure S84

Water/Ethanol in LTA-4A: Pera-Titus Experiments

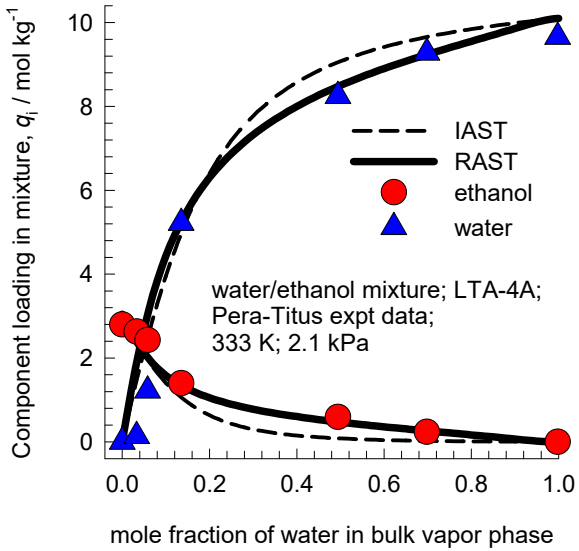

LTA-4A (96 Na+)

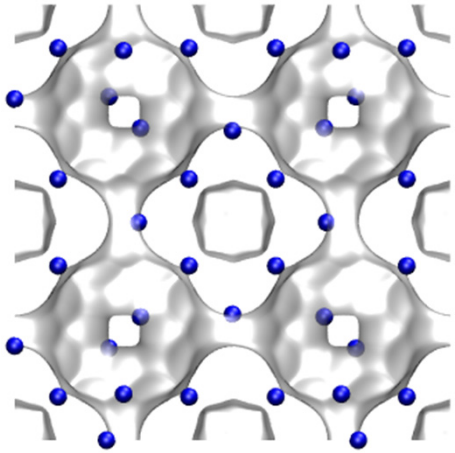

Snapshot of Water/ethanol clustering

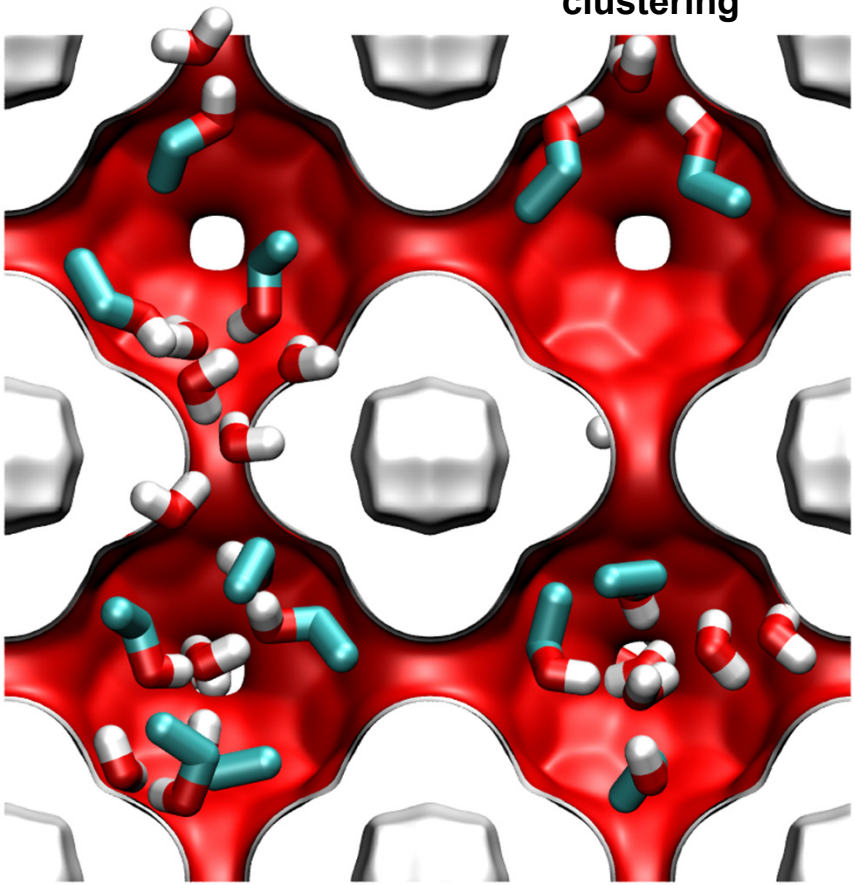

Figure S85

Water/ethanol adsorption in LTA-4A zeolite

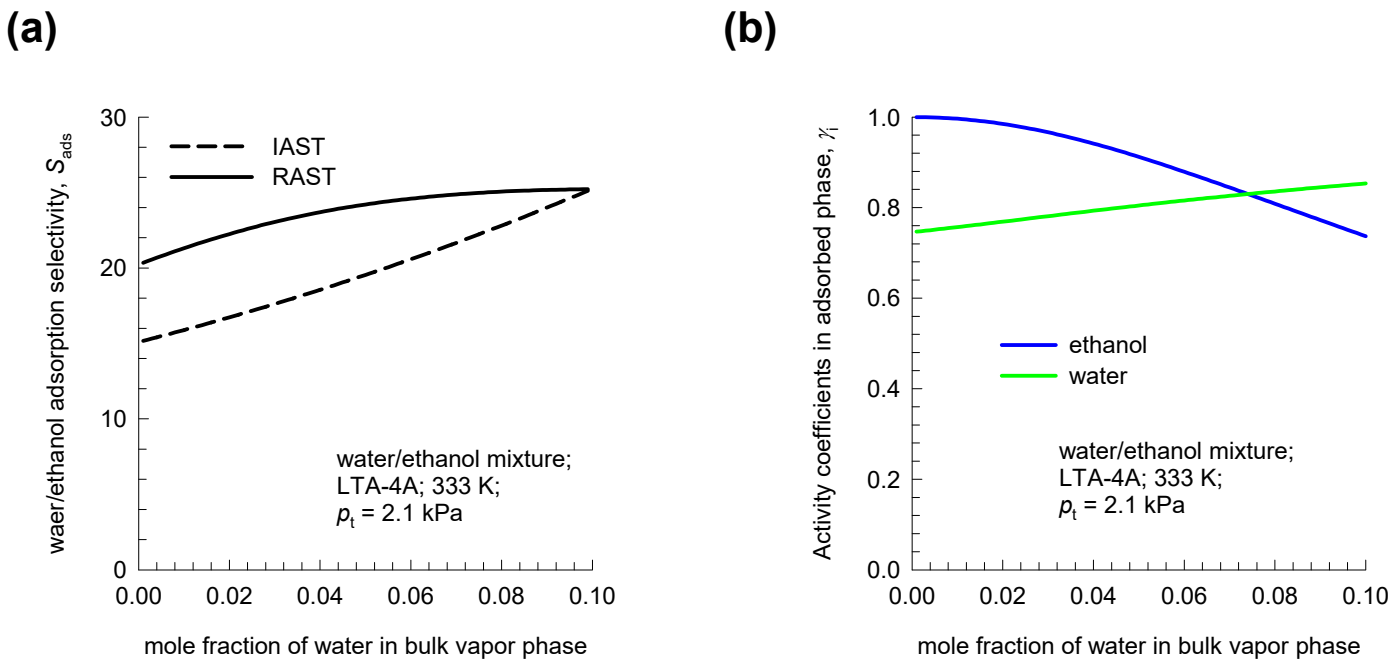

Figure S86

Water/ethanol permeation across LTA-4A

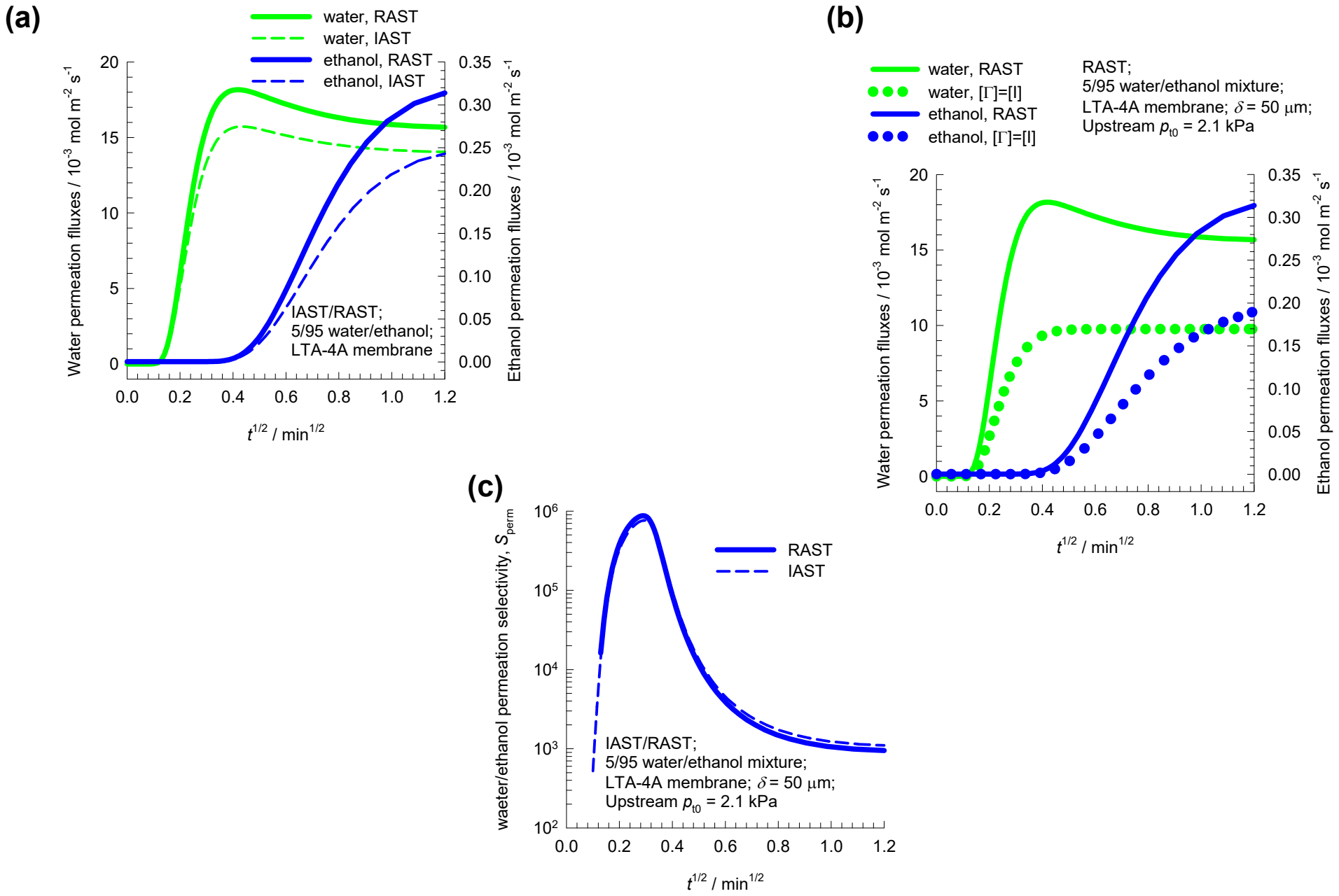

Water/alcohols mixture adsorption in ZIF-71

Figure S87

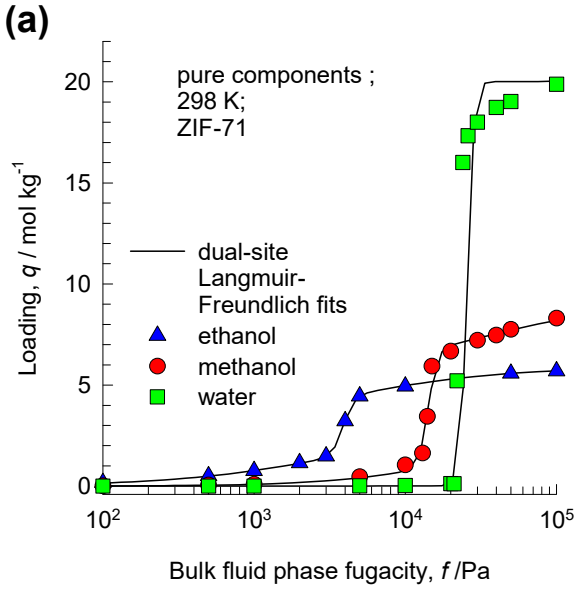

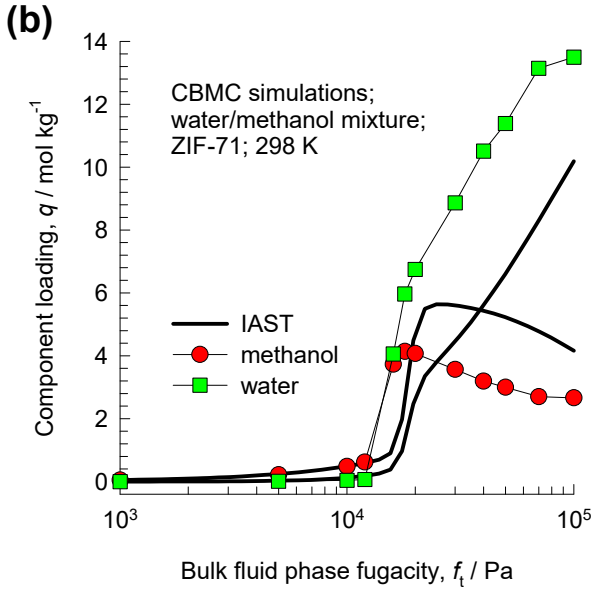

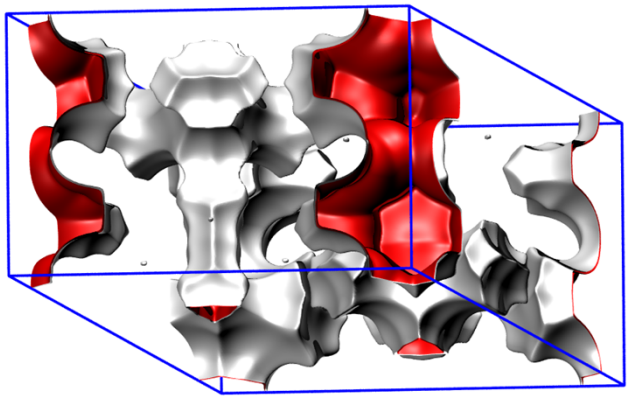

ZIF-71 landscape

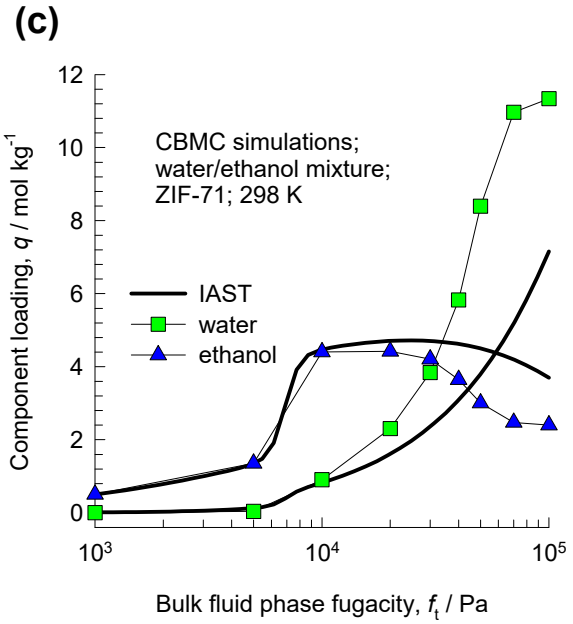

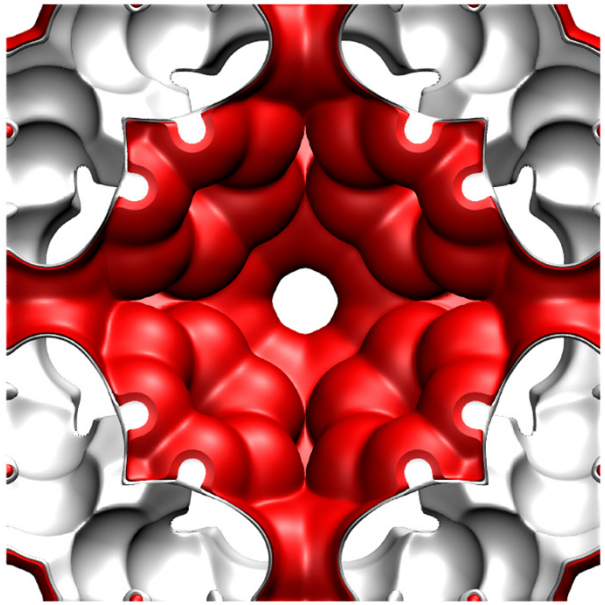

CHA

There are 6 cages per unit cell of CHA.

The volume of one CHA cage is 316.4 Å^3

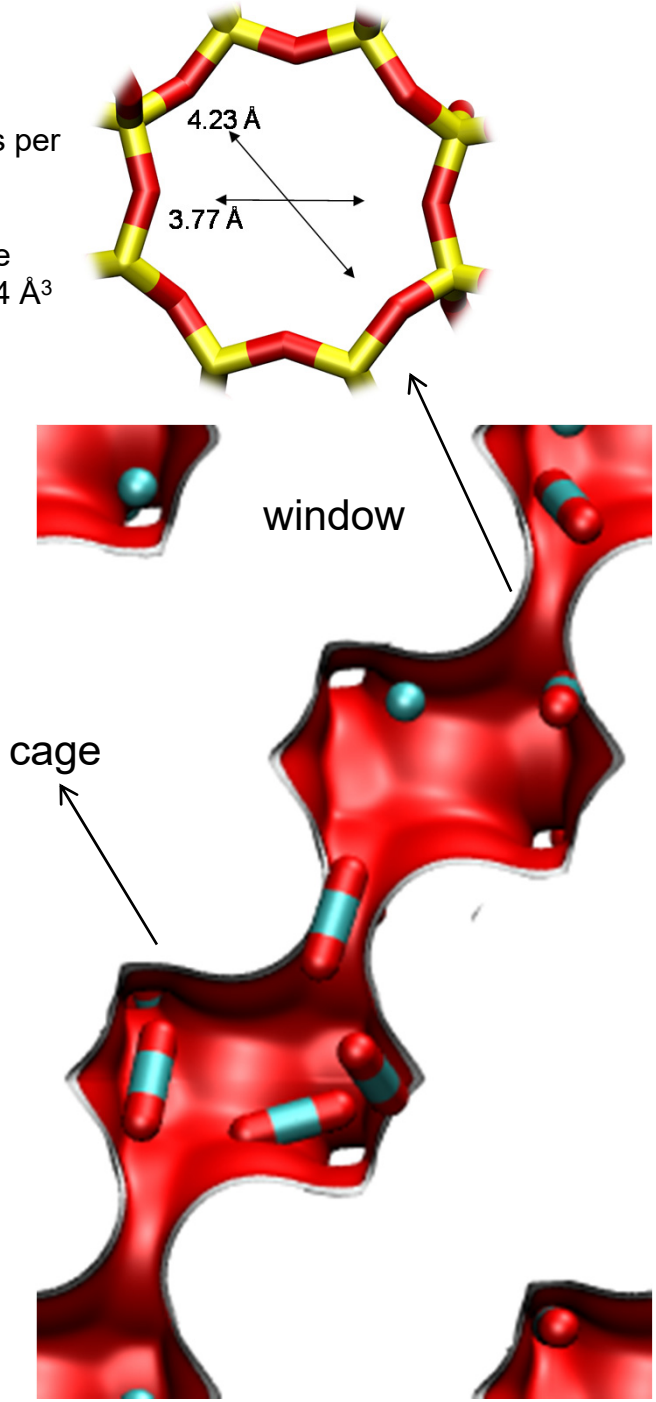

Figure S88

(a)

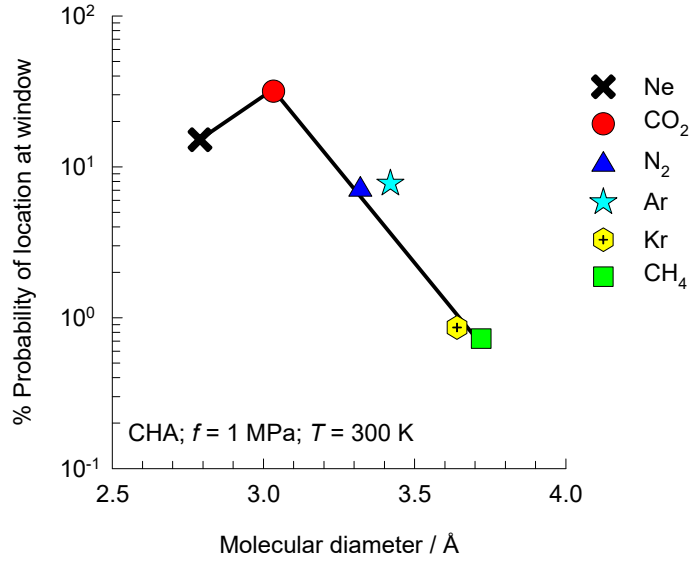

(b)

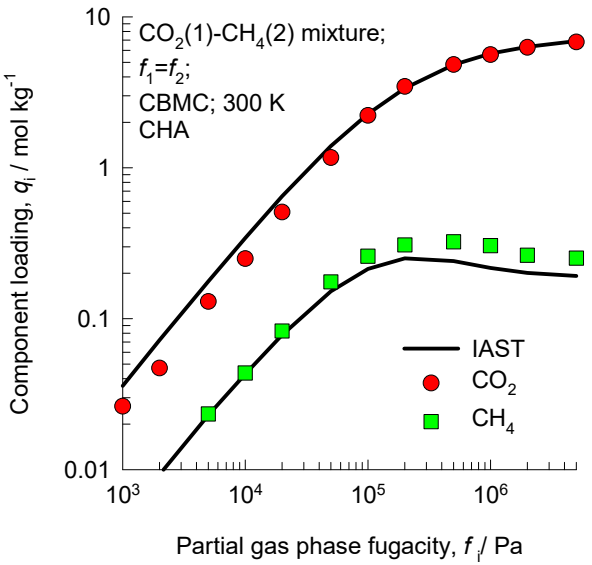

LTA

There are 8 cages per unit cell.

The volume of one LTA cage is 743 Å^3

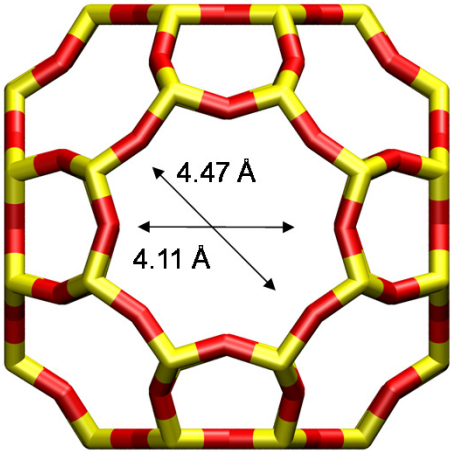

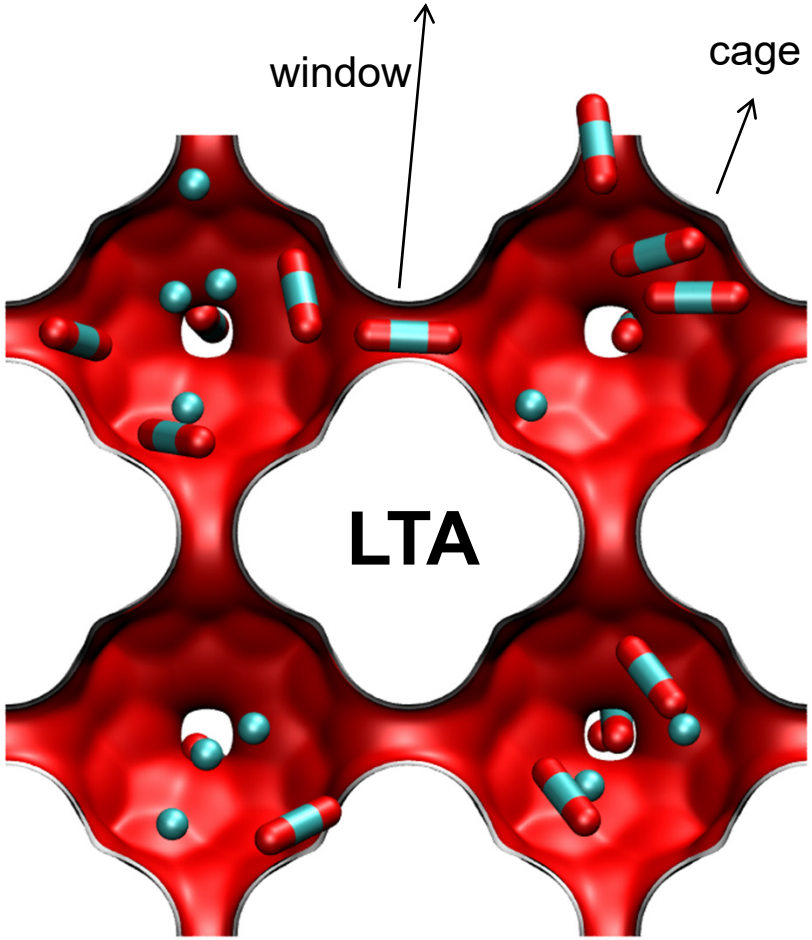

Figure S89

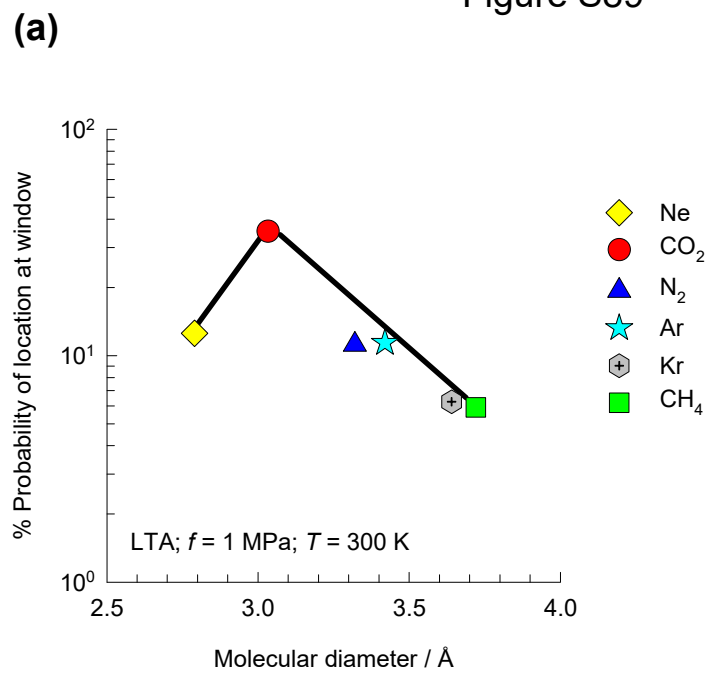

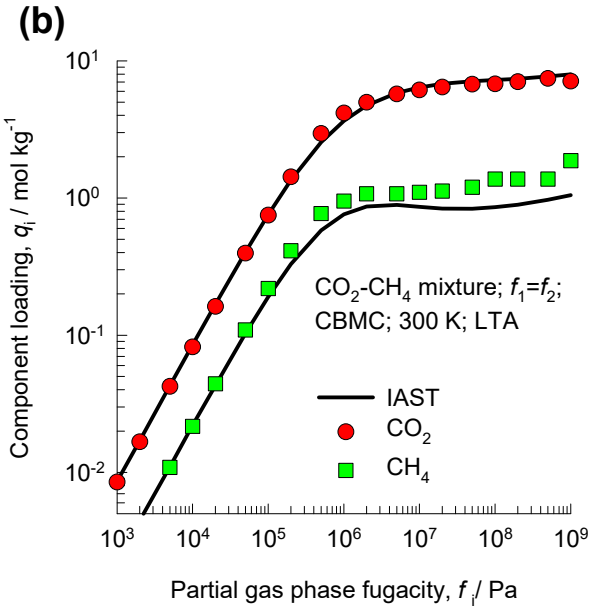

ERI

Figure S90

There are 4 cages per unit cell.

The volume of one ERI cage is 408.7 Å^3

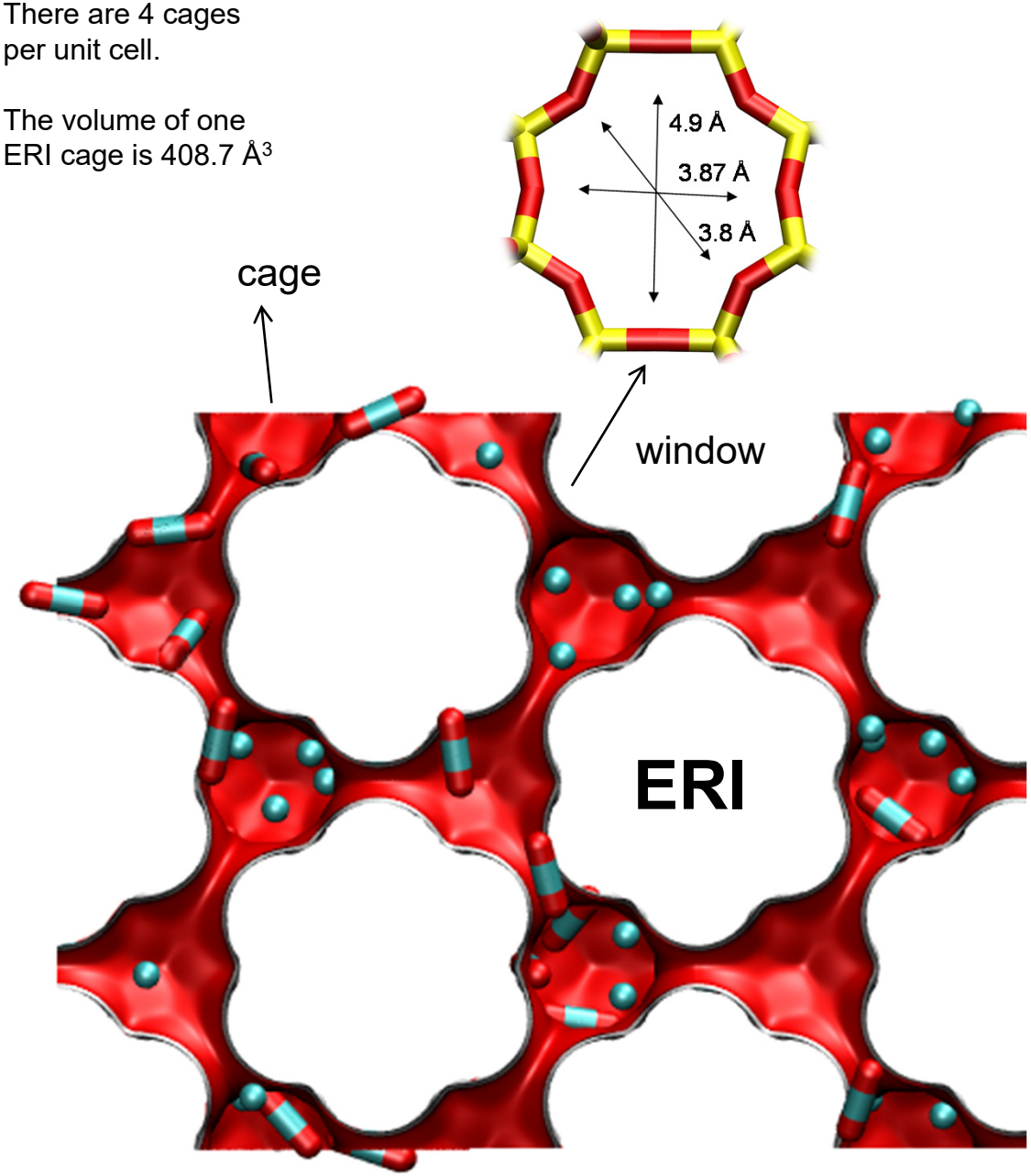

(a)

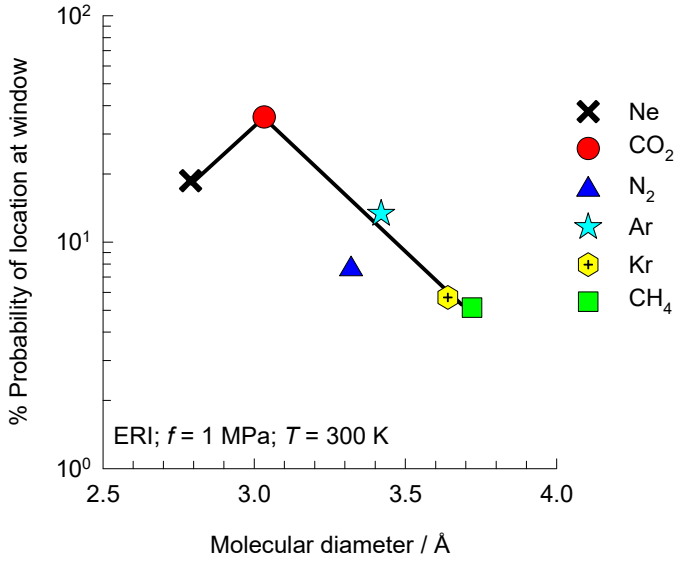

(b)

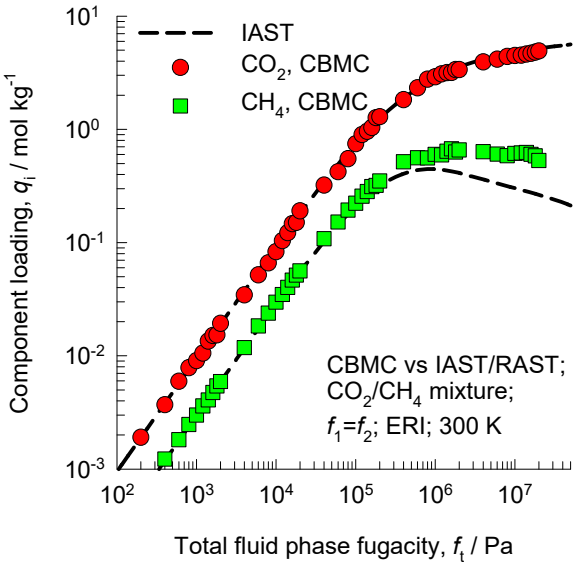

DDR

There are 12 cages per unit cell of DDR.

The volume of one DDR cage is 278 Å^3

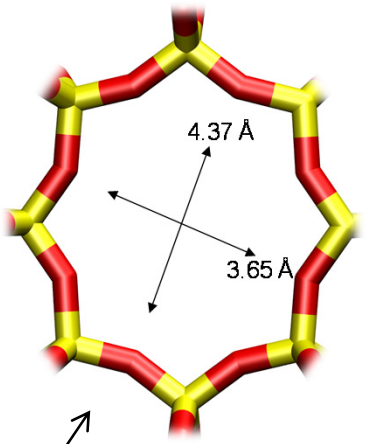

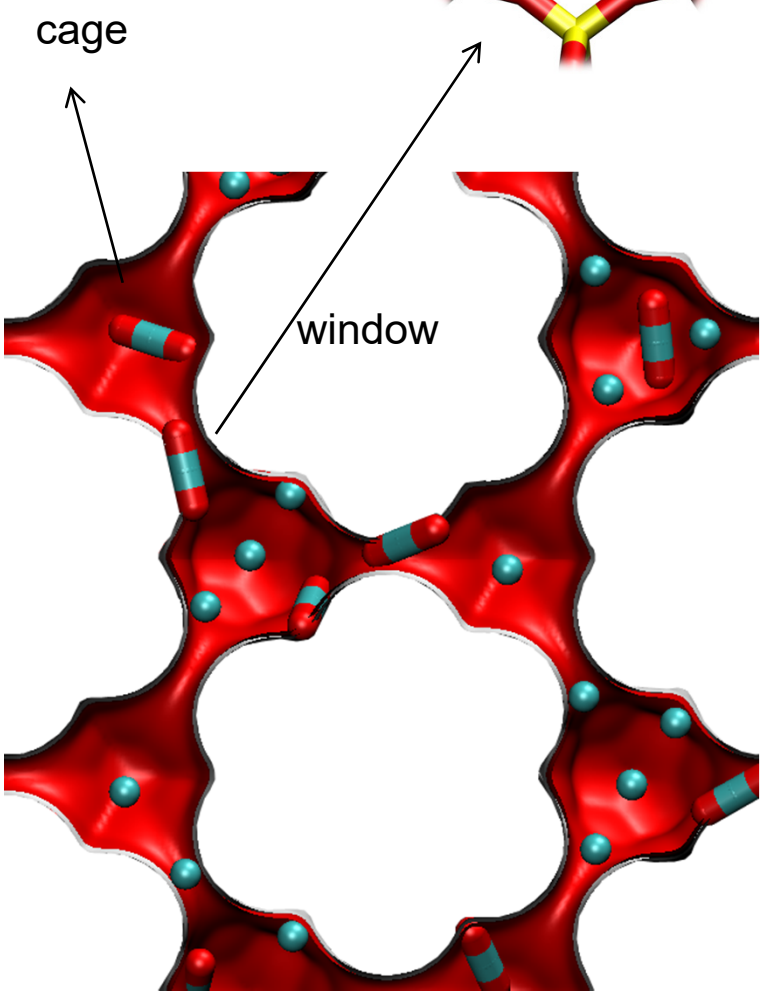

Figure S91

(a)

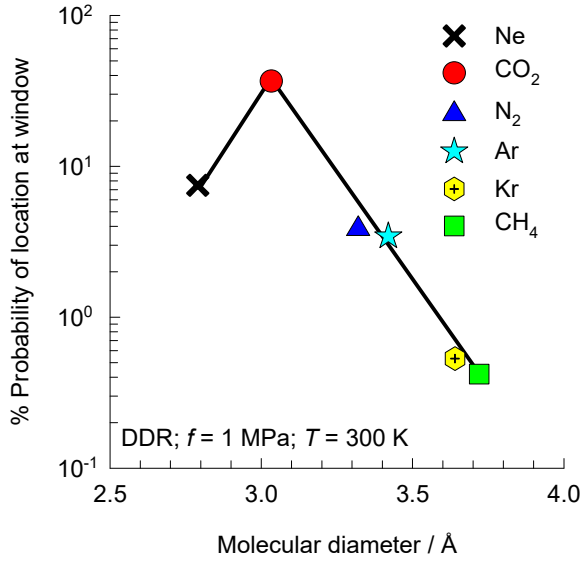

(b)

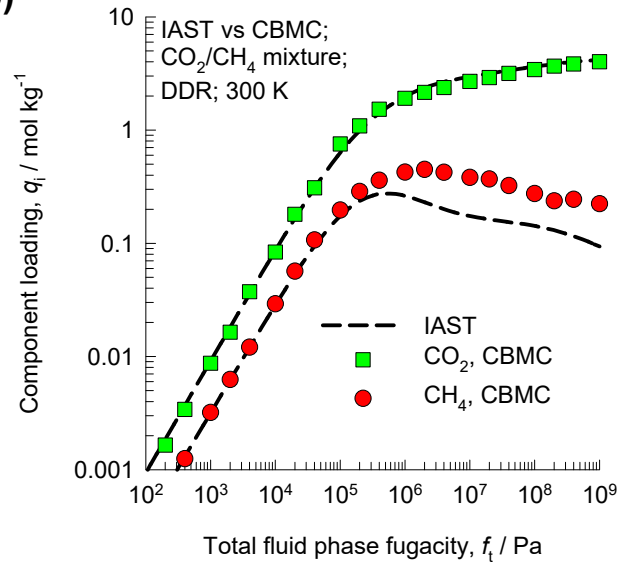

CO_2/CH_4 mixture adsorption in ERI

Figure S92

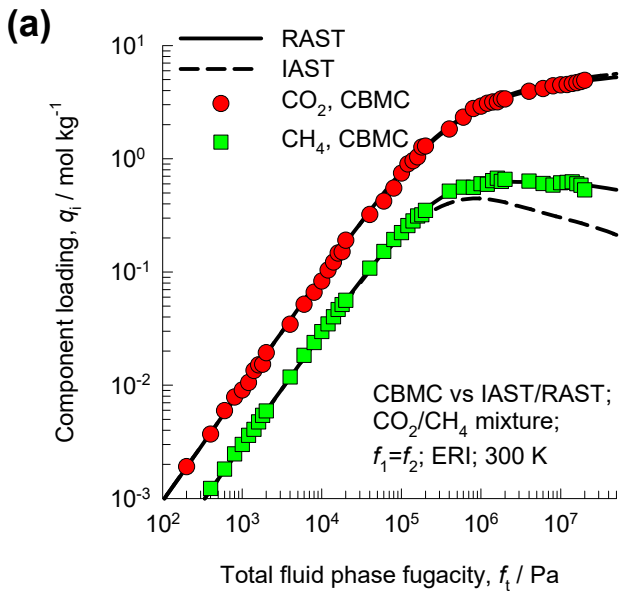

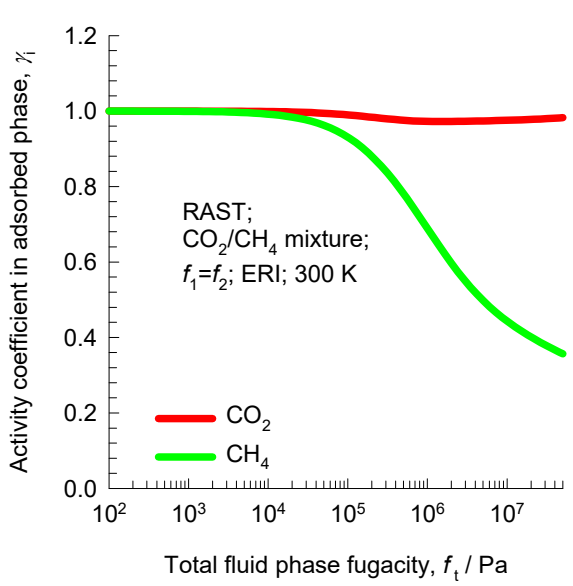

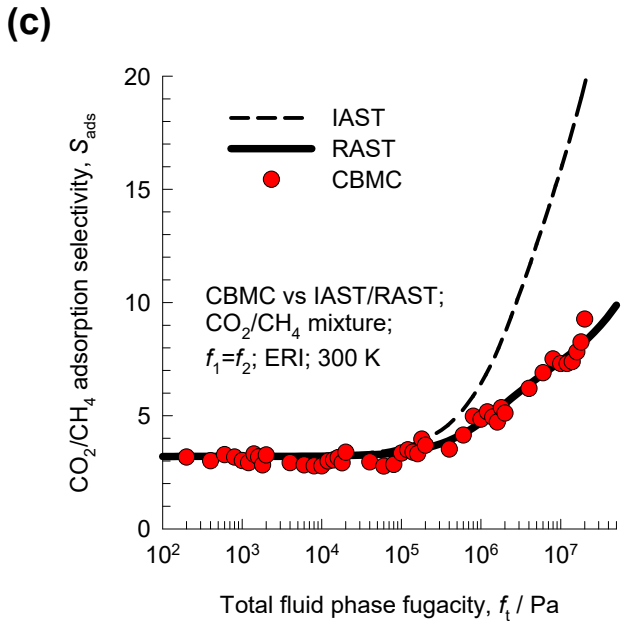

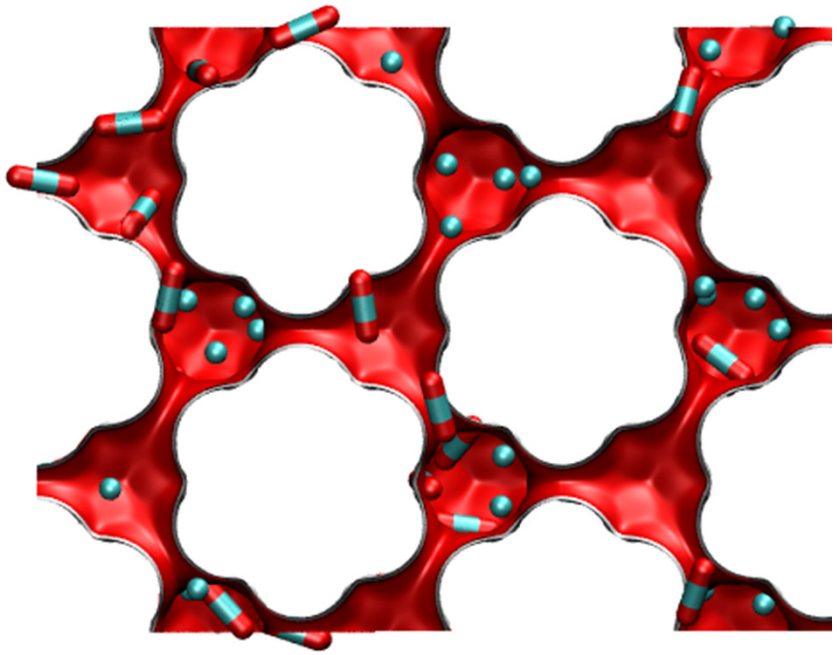

CO_2/CH_4 mixture adsorption in DDR

Figure S93

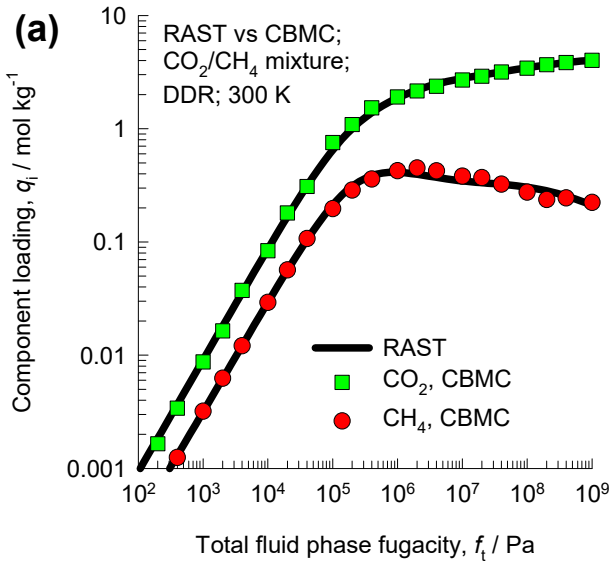

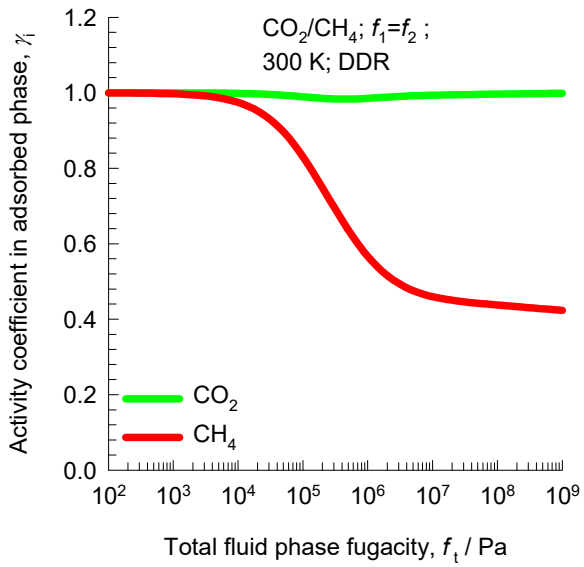

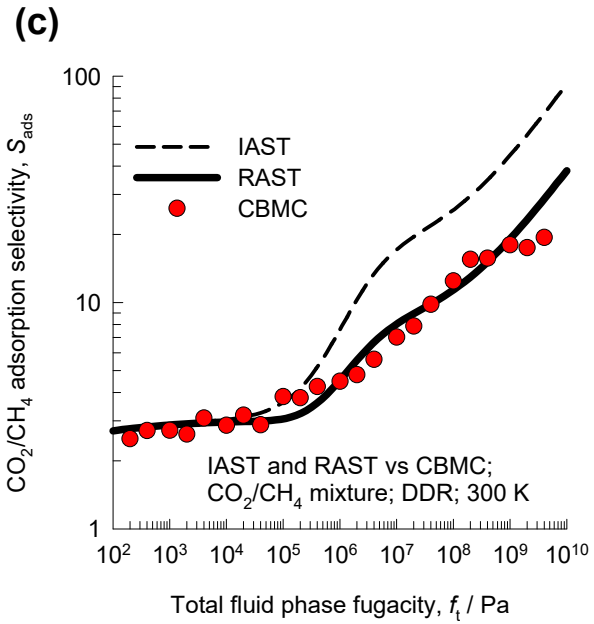

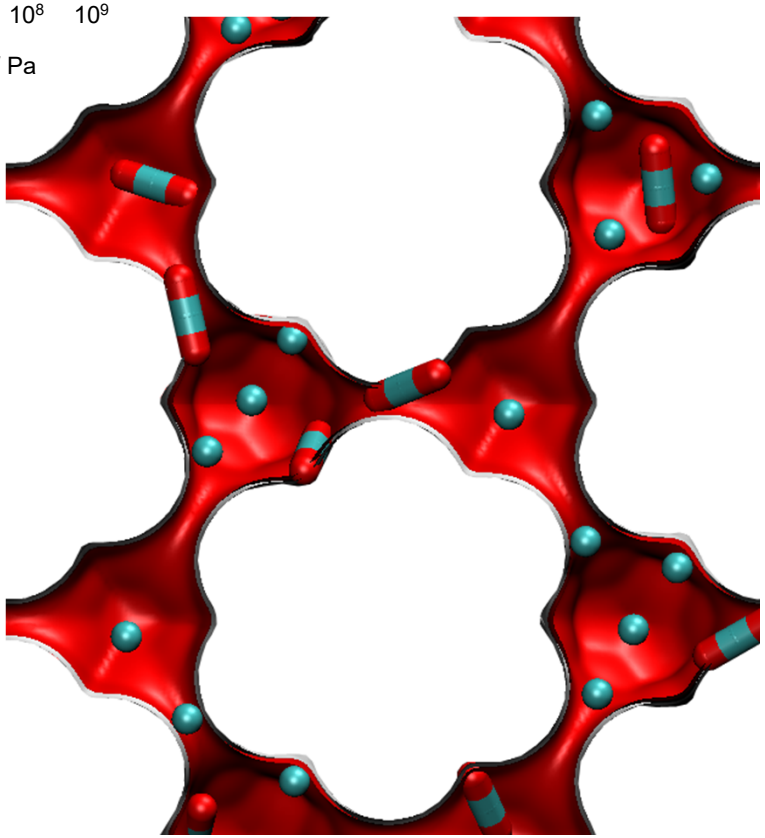

CO_2/CH_4 mixture adsorption in zeolites

Figure S94

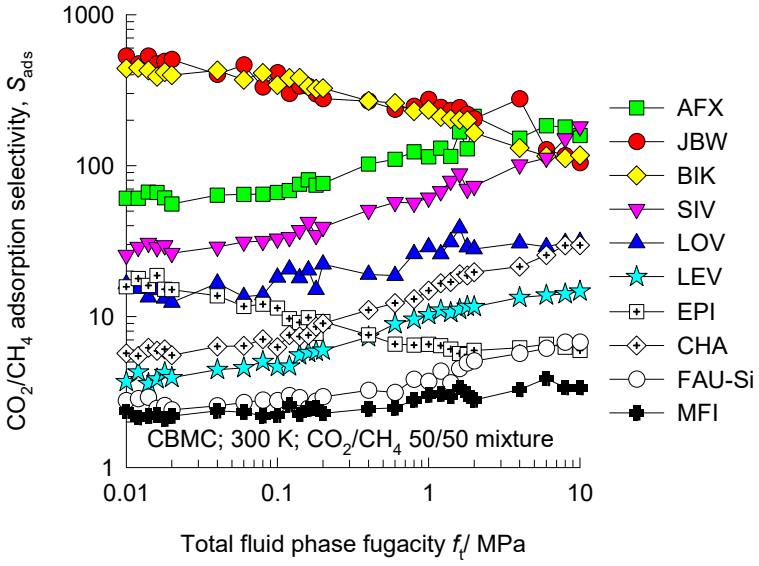

AFX

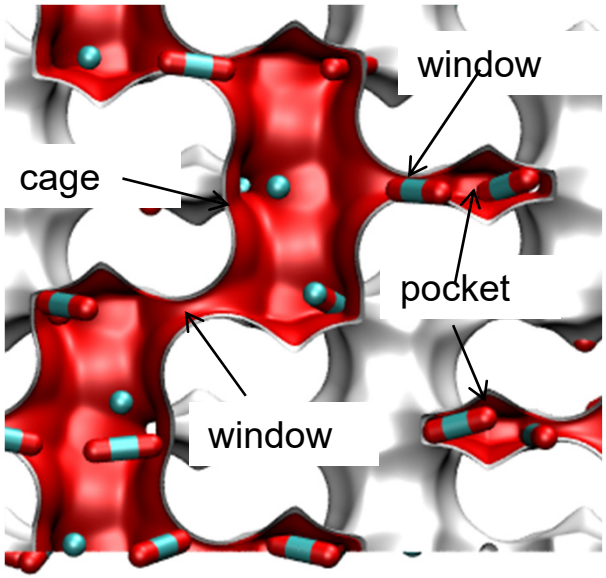

JBW

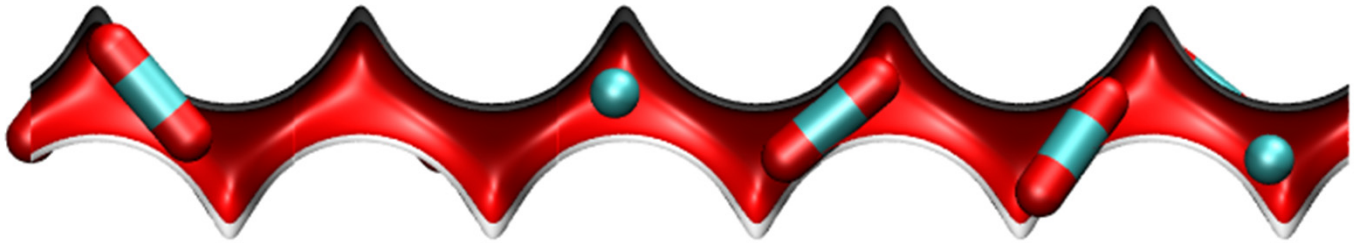

BIK

CO_2/CH_4 mixture adsorption in AFX zeolite

Figure S95

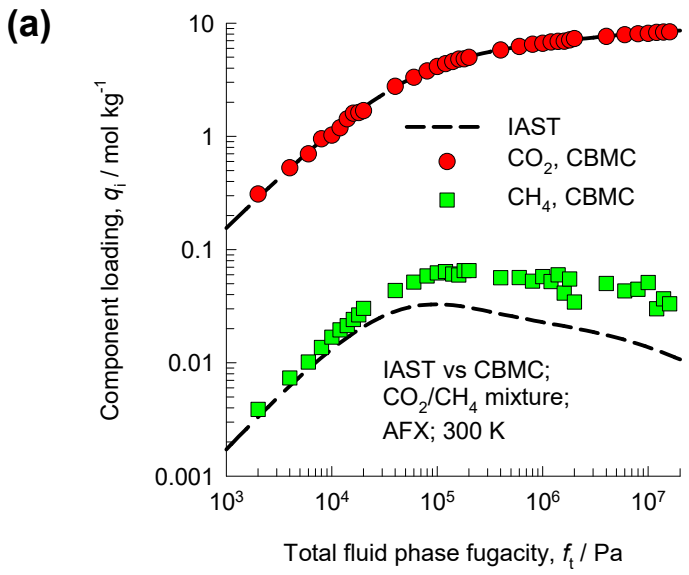

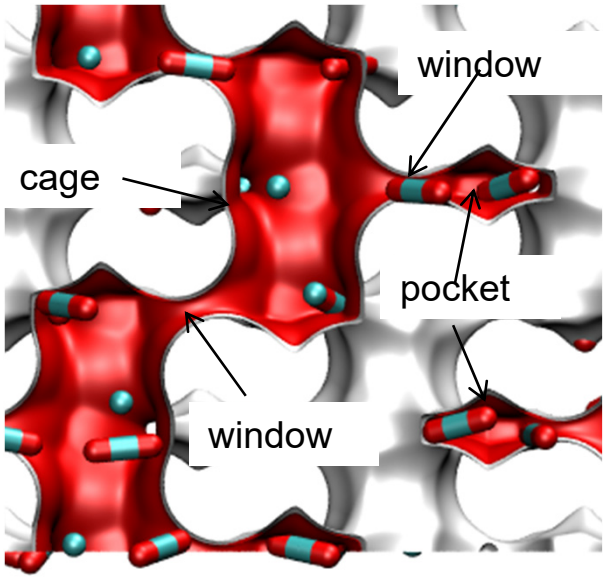

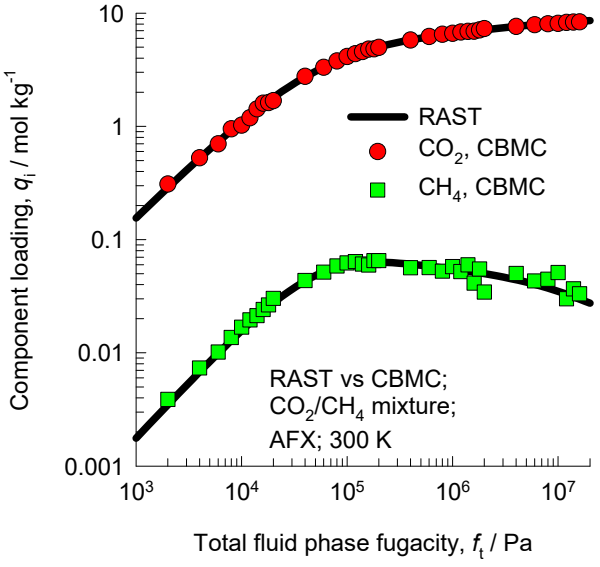

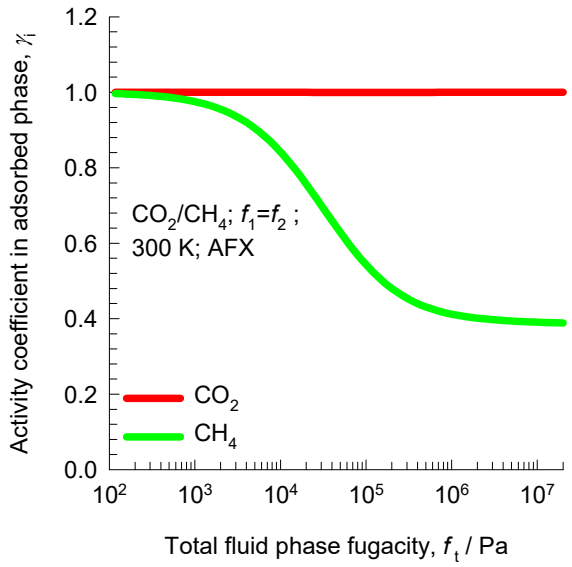

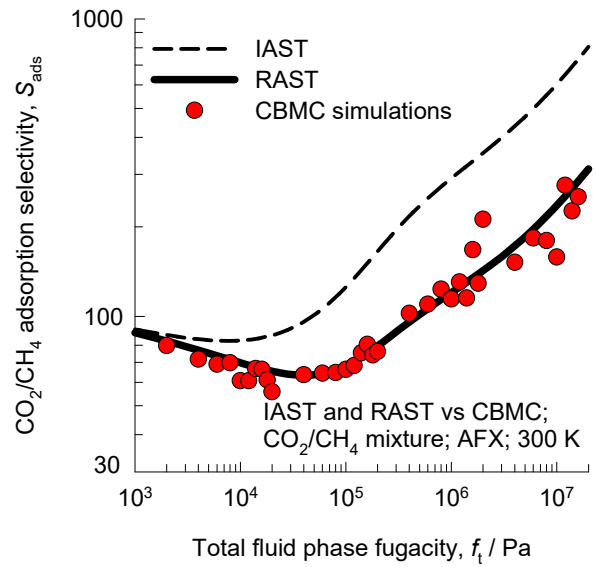

CO_2/N_2 mixture adsorption in AFX zeolite

Figure S96

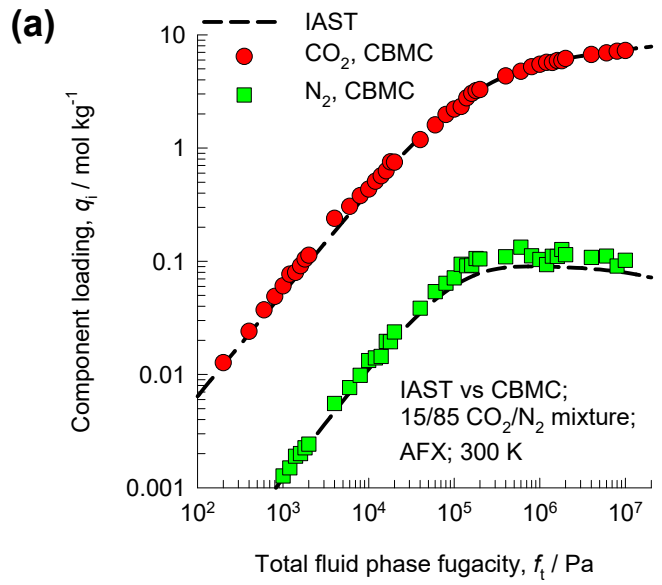

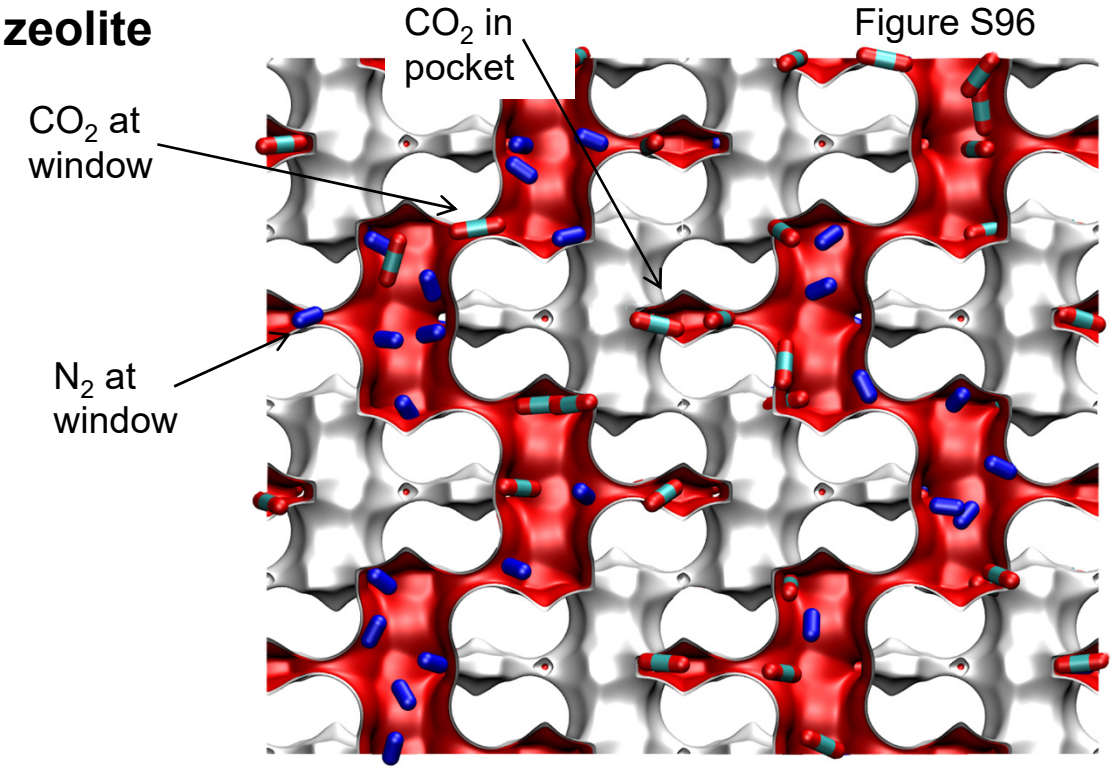

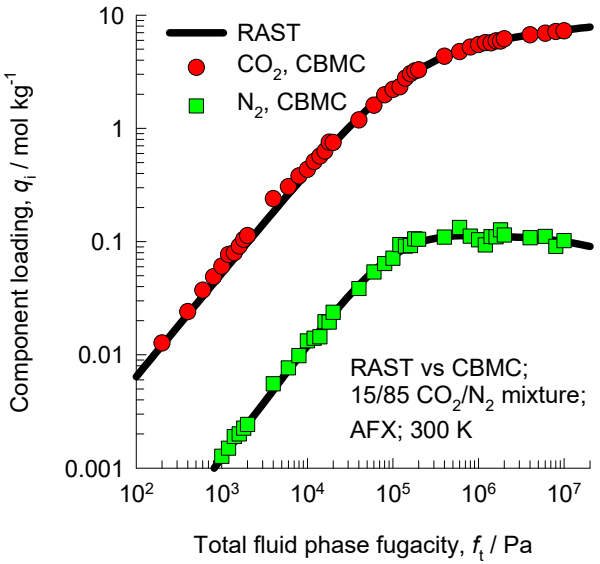

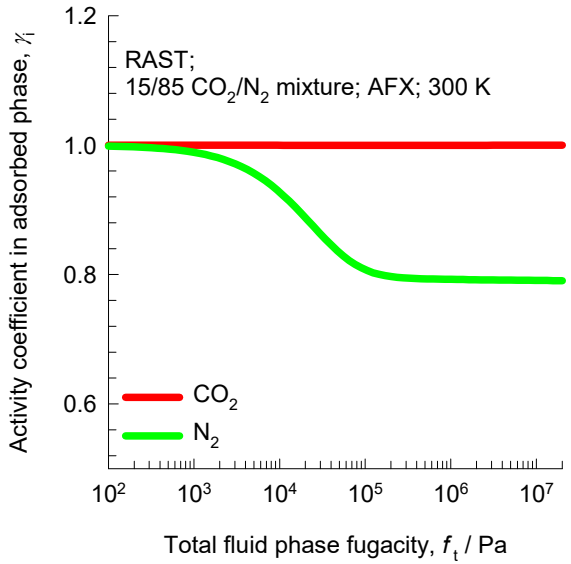

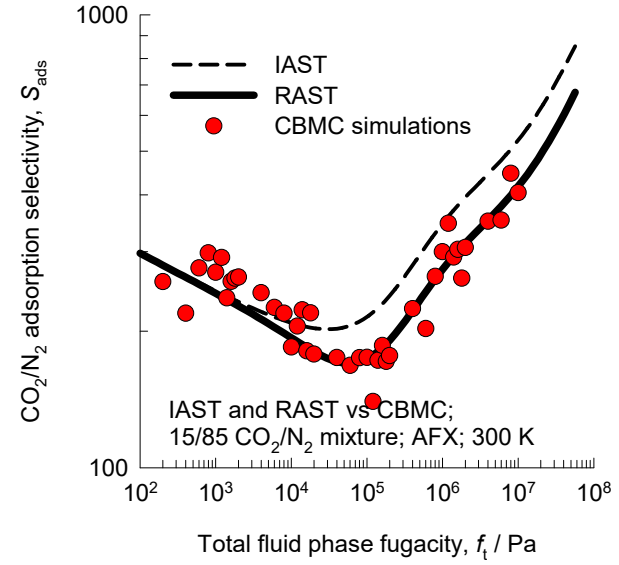

CO_2/CH_4 mixture adsorption in MOR zeolite

Figure S97

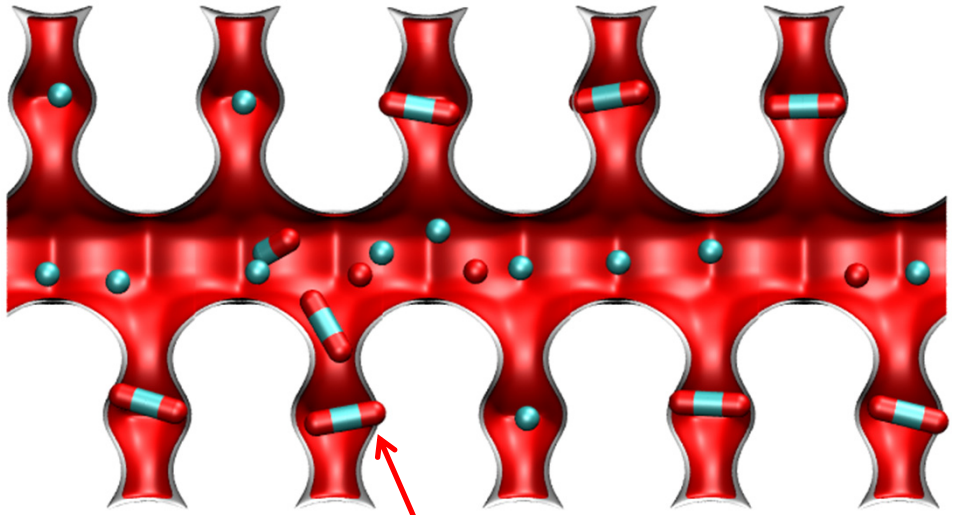

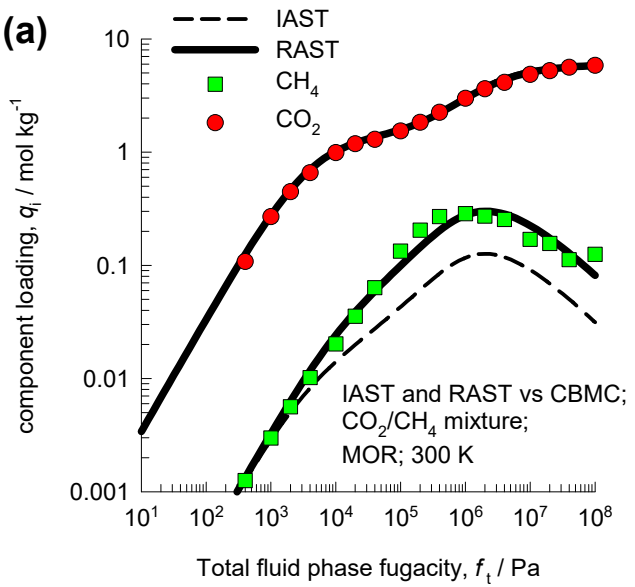

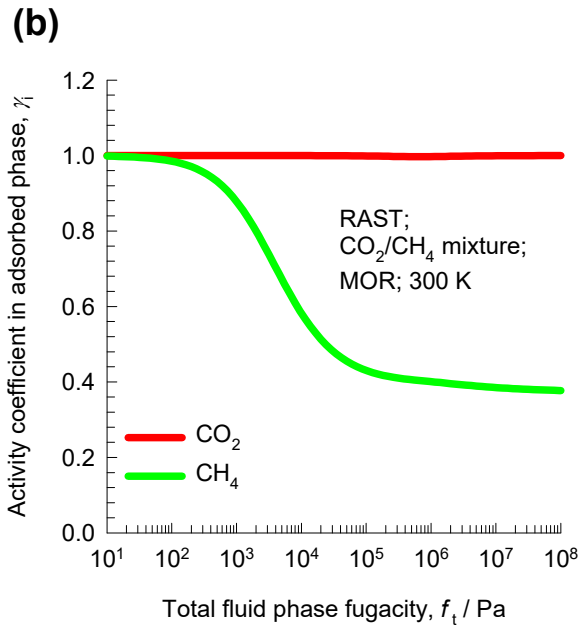

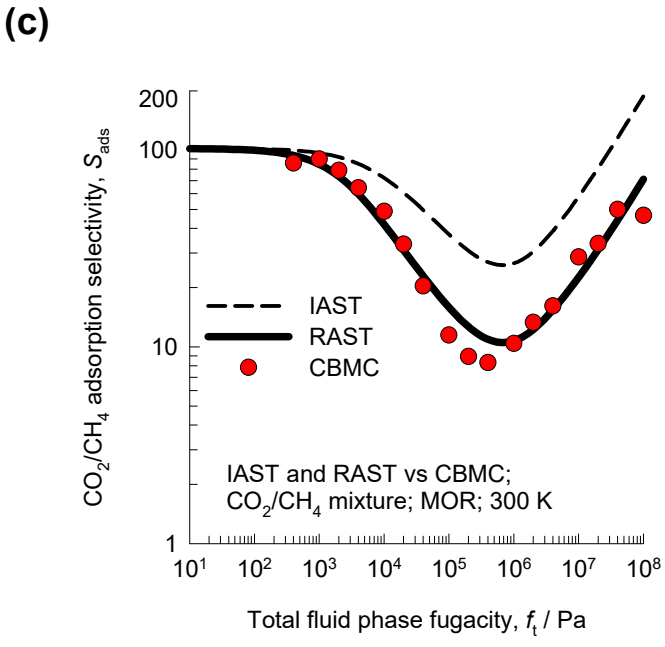

CO_2/CH_4 mixture adsorption in NaX (=13X) zeolite

Figure S98

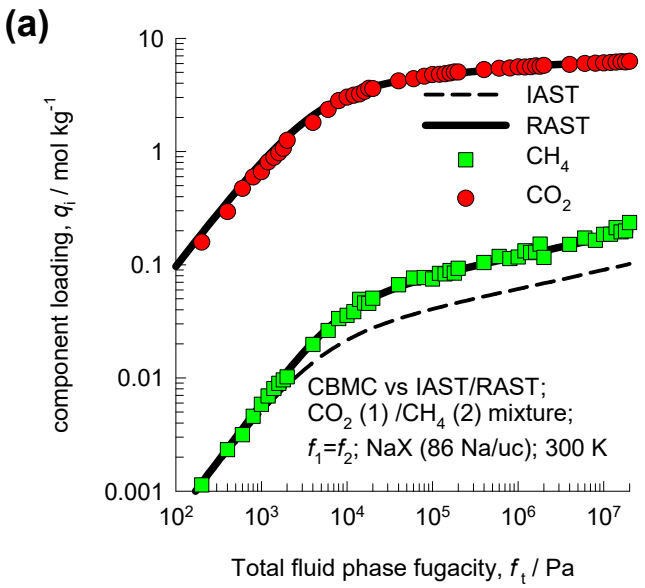

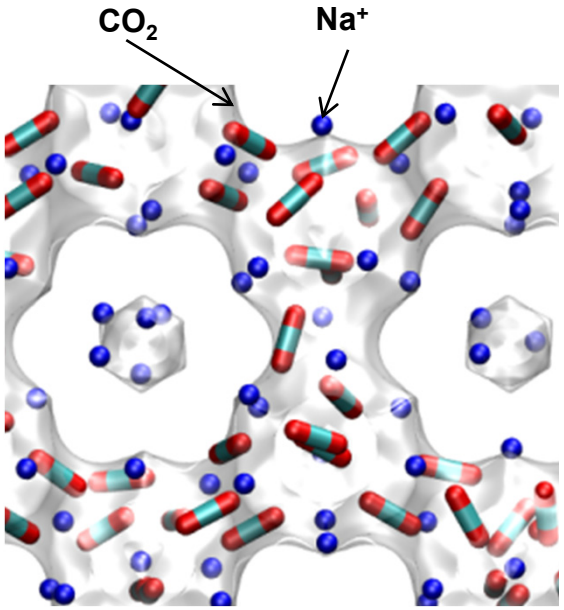

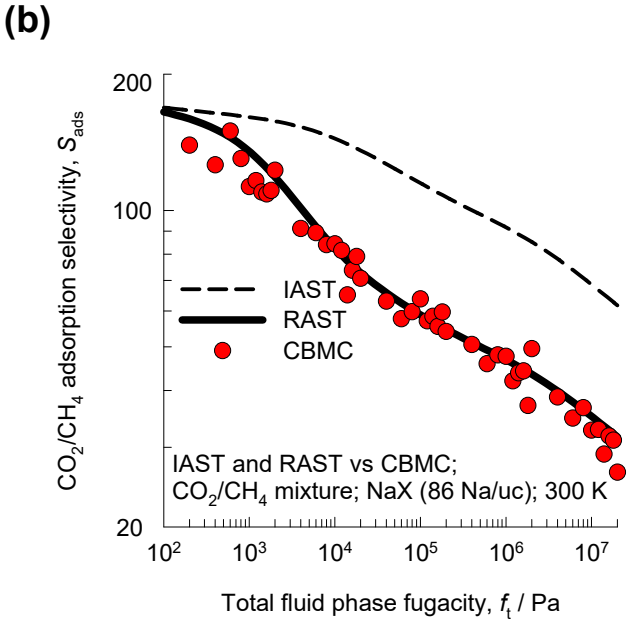

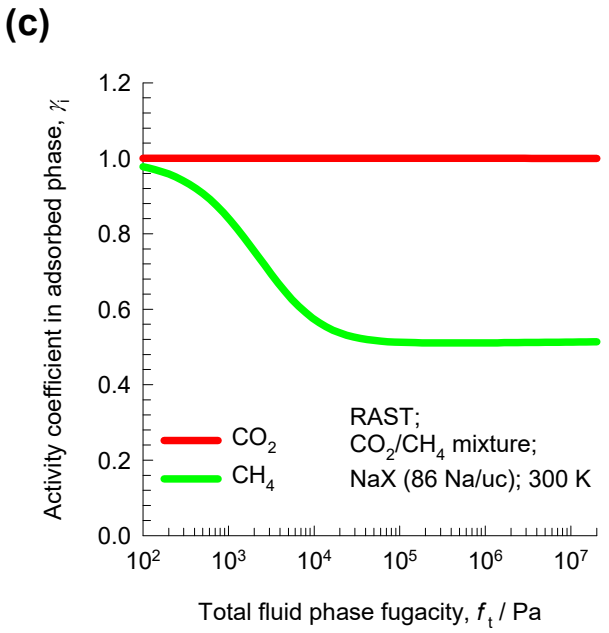

CO_2/N_2 mixture adsorption in NaX (=13X) zeolite

Figure S99

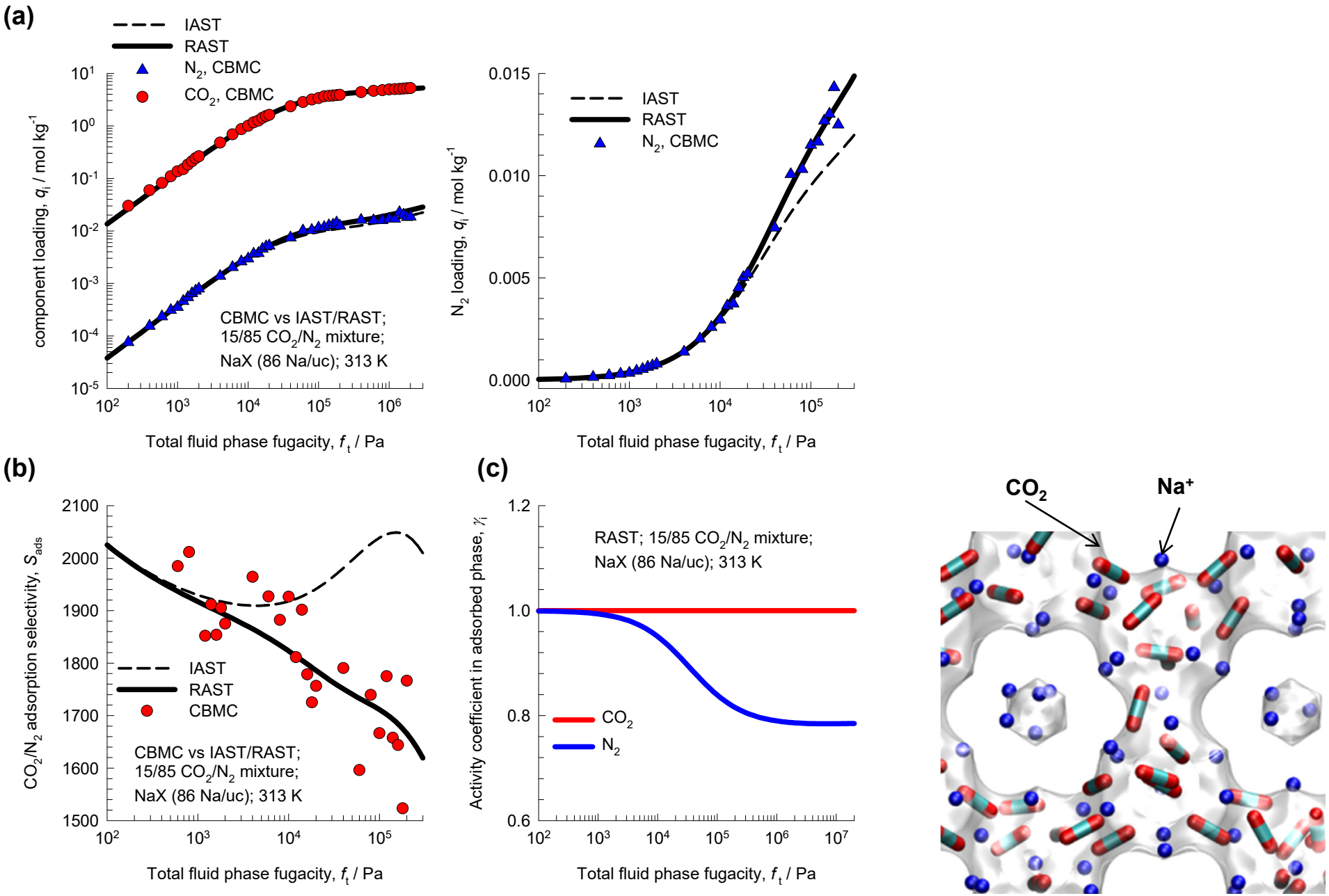

CO_2/H_2 mixture adsorption in NaX (=13X) zeolite

Figure S100

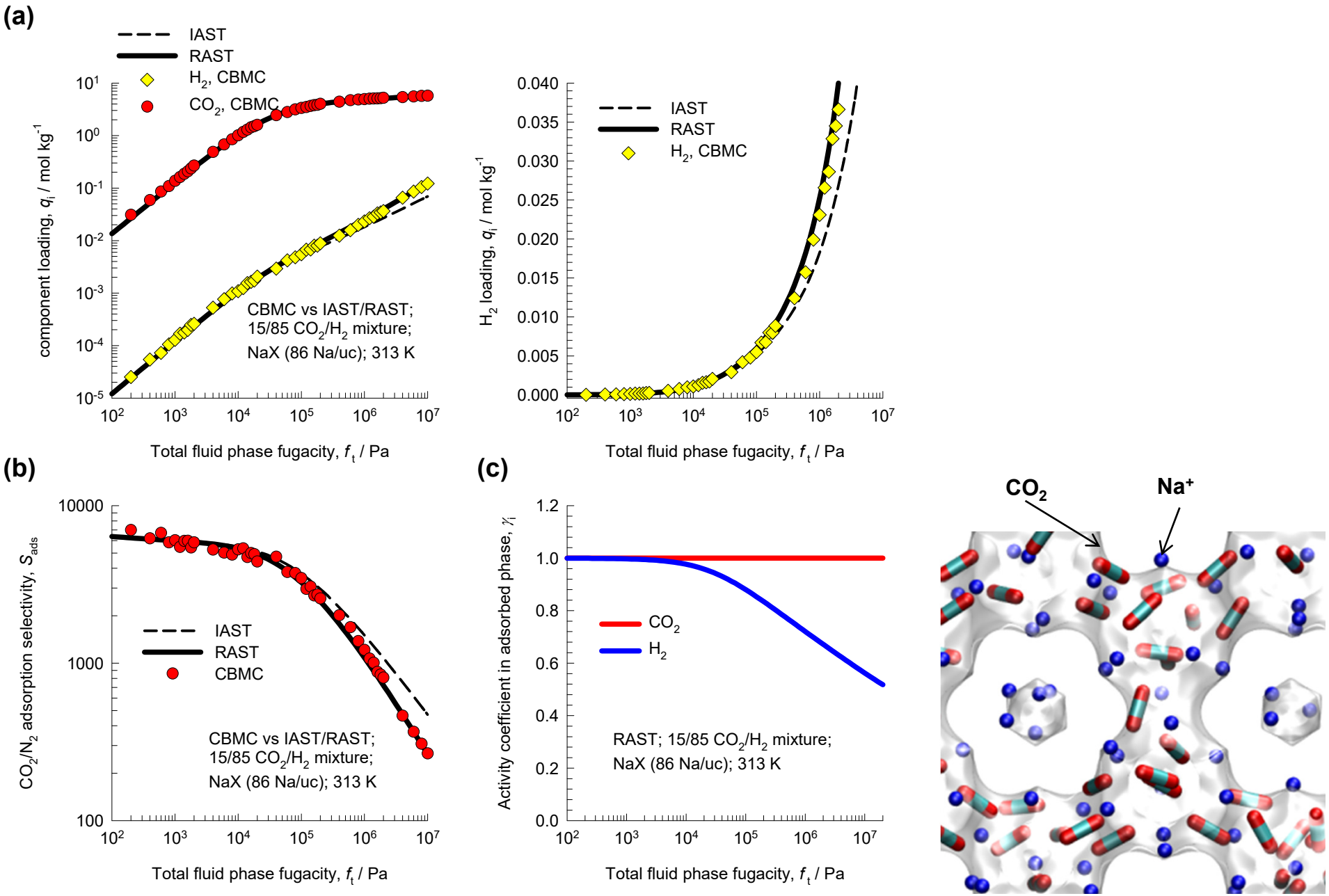

CO_2/CH_4 mixture adsorption in NaX, NaY, and all-silica FAU zeolite

Figure S101

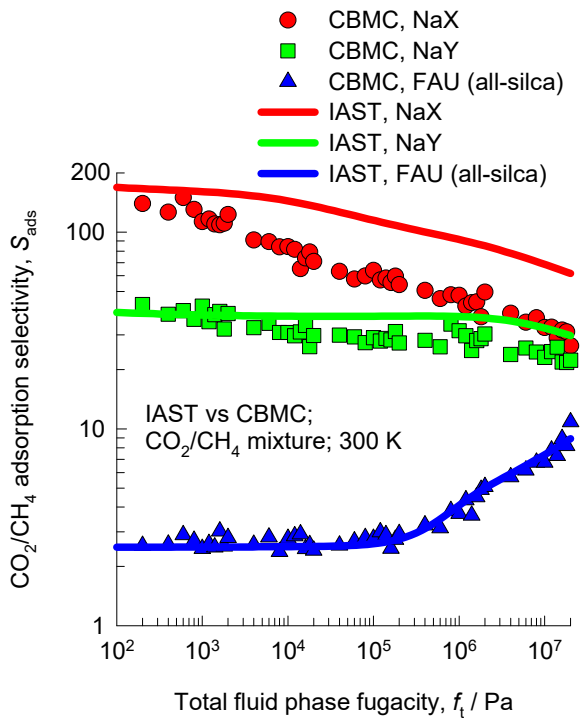

CO_2/CH_4 mixture adsorption in LTA-4A zeolite

Figure S102

(a)

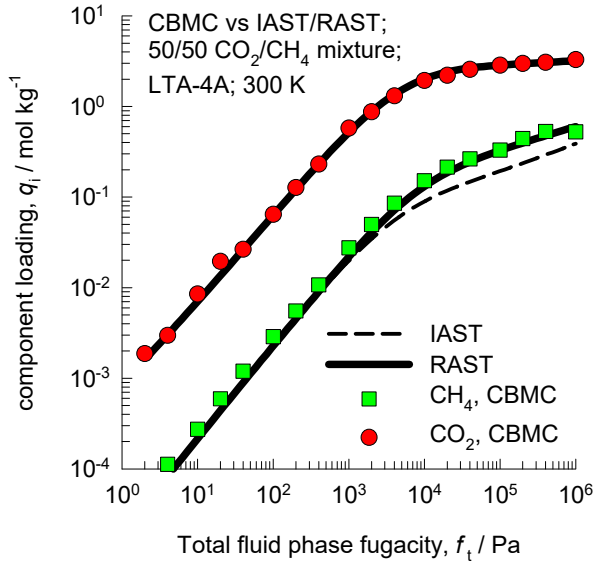

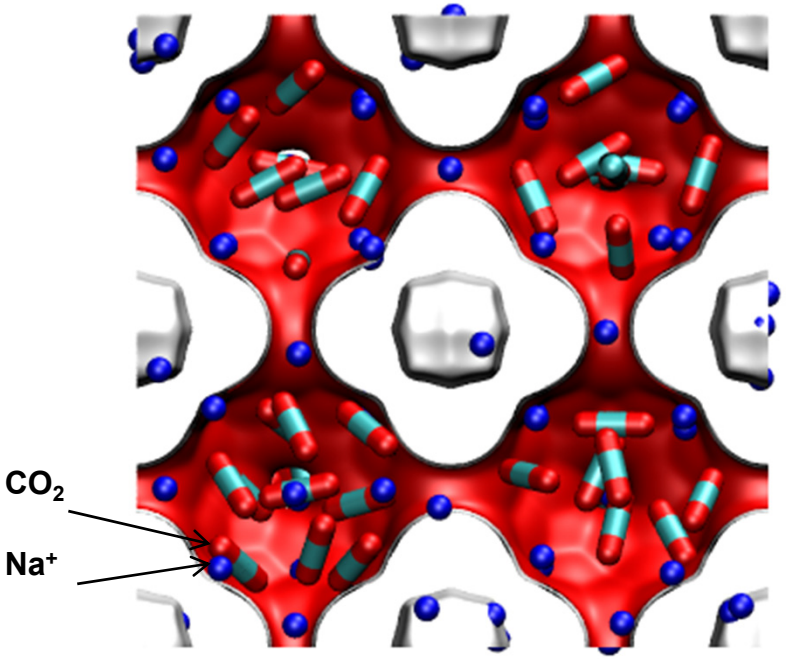

(b)

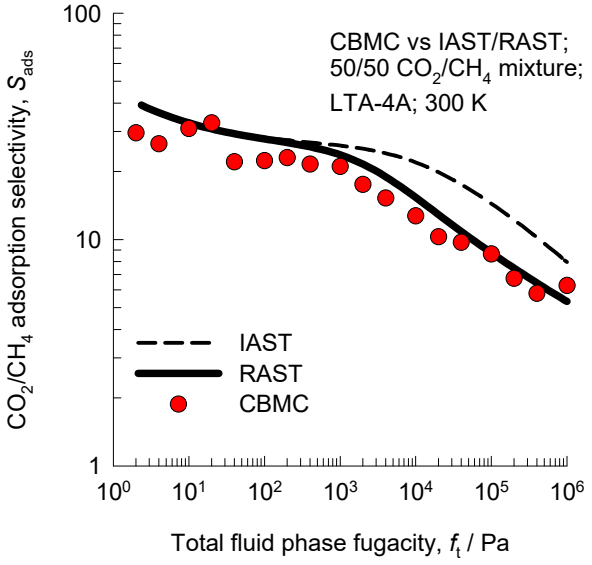

(c)

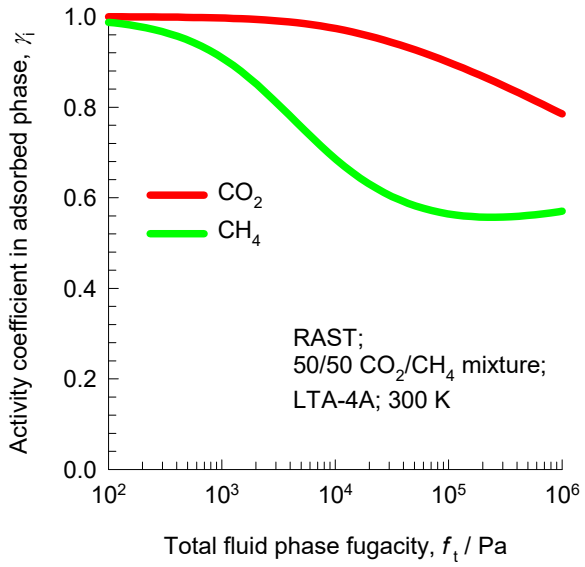

CO_2/CH_4 mixture adsorption in 13X zeolite: Re-analysis of Gholipour-Mofarahi data

Figure S103

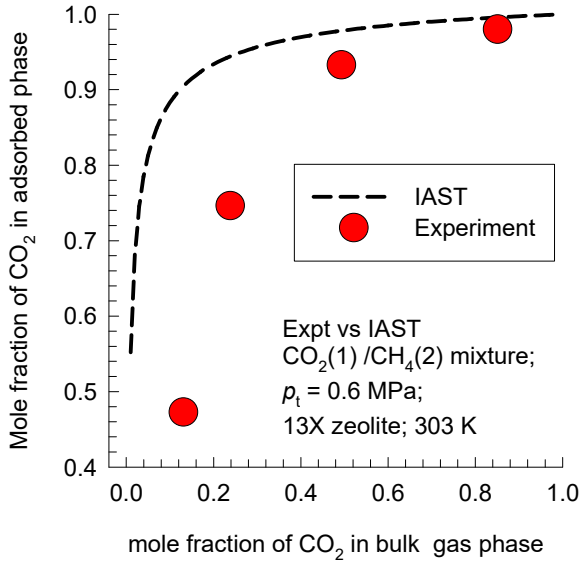

CO_2/N_2 mixture adsorption in 13X zeolite; Re-analysis of data of Hefti et al.

Figure S104

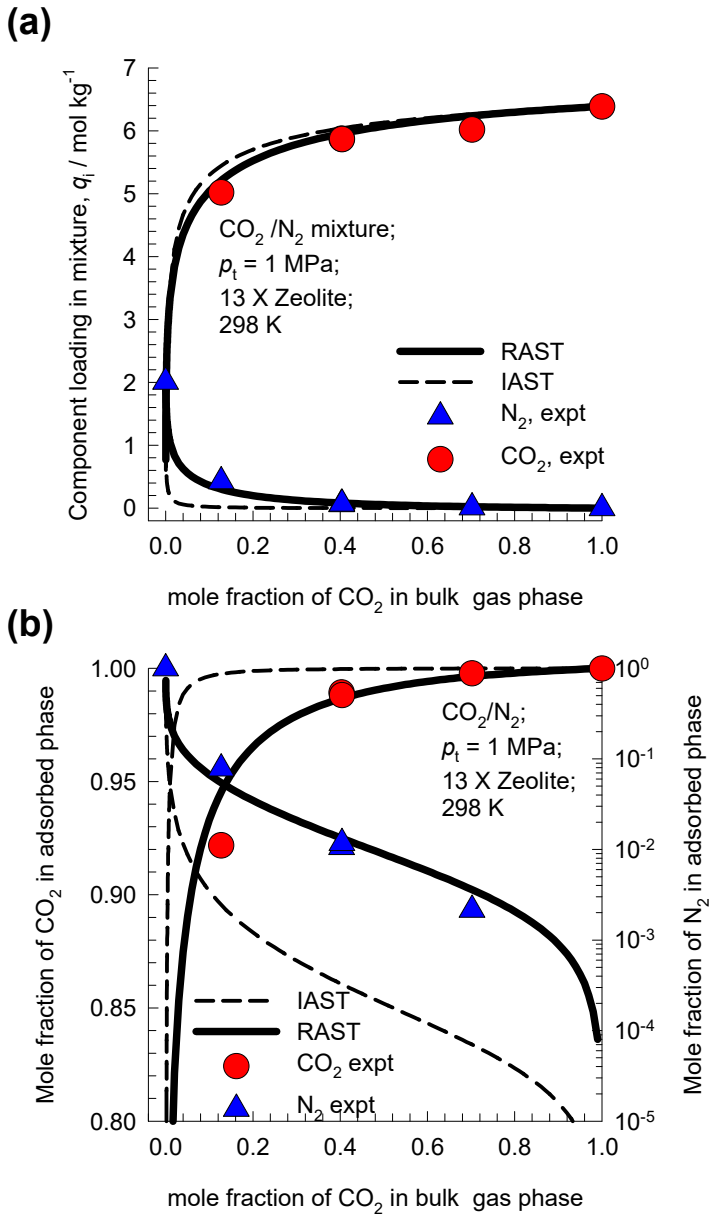

CO_2/C_3H_8 mixture adsorption in NaX zeolite: Siperstein data analysis

Figure S105

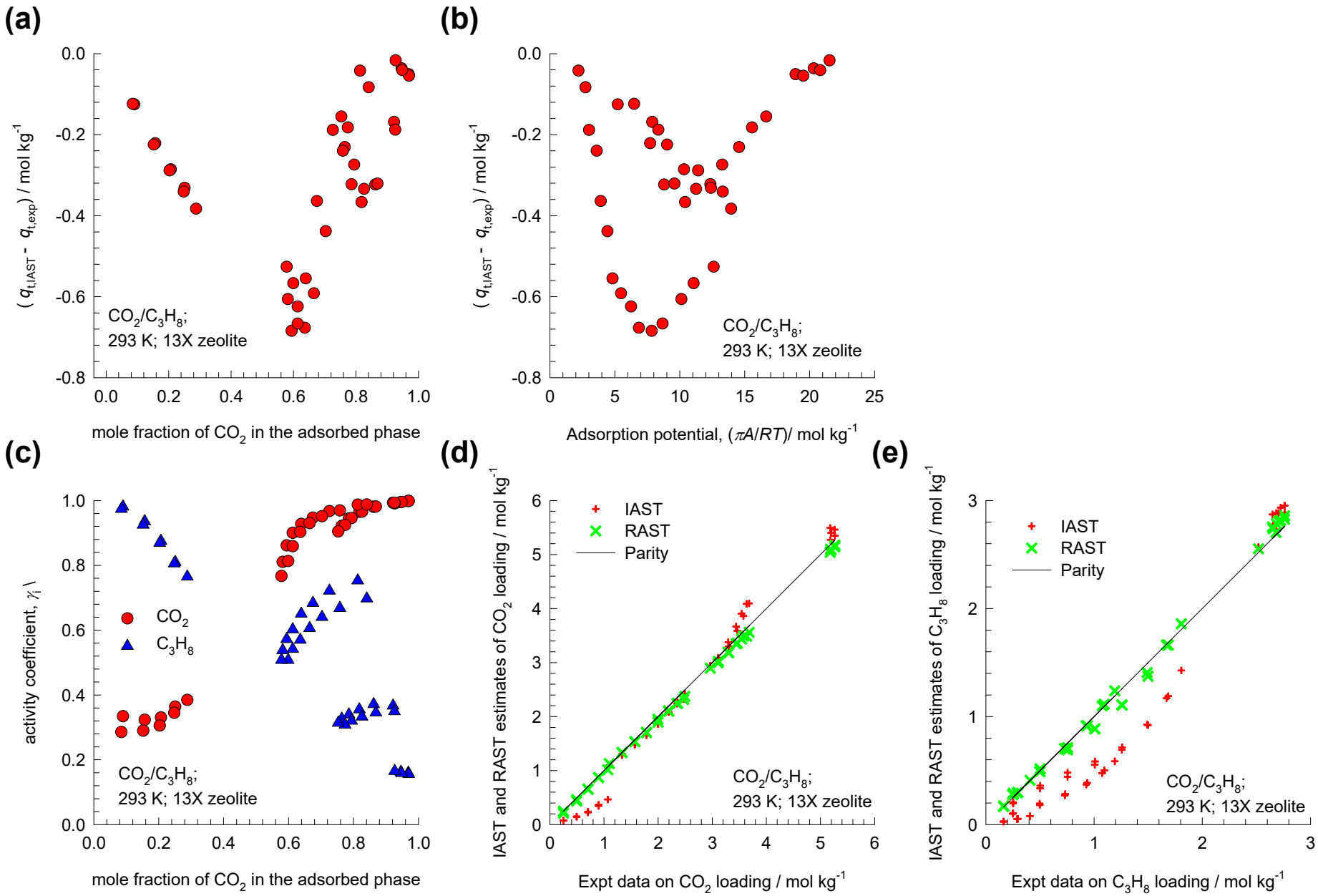

C_2H_4/C_2H_6 mixture adsorption in NaX zeolite: Siperstein data analysis

Figure S106

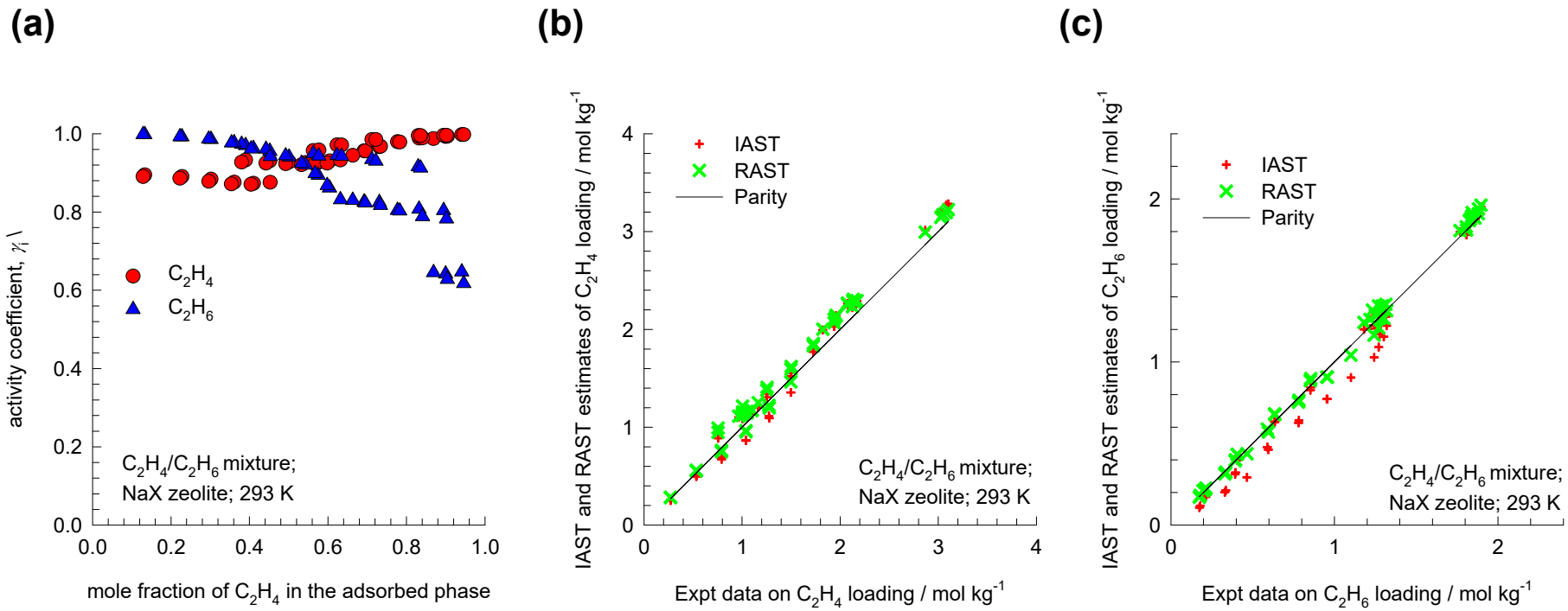

Figure S107

Separation potential for CO_2/C_3H_8/NaX

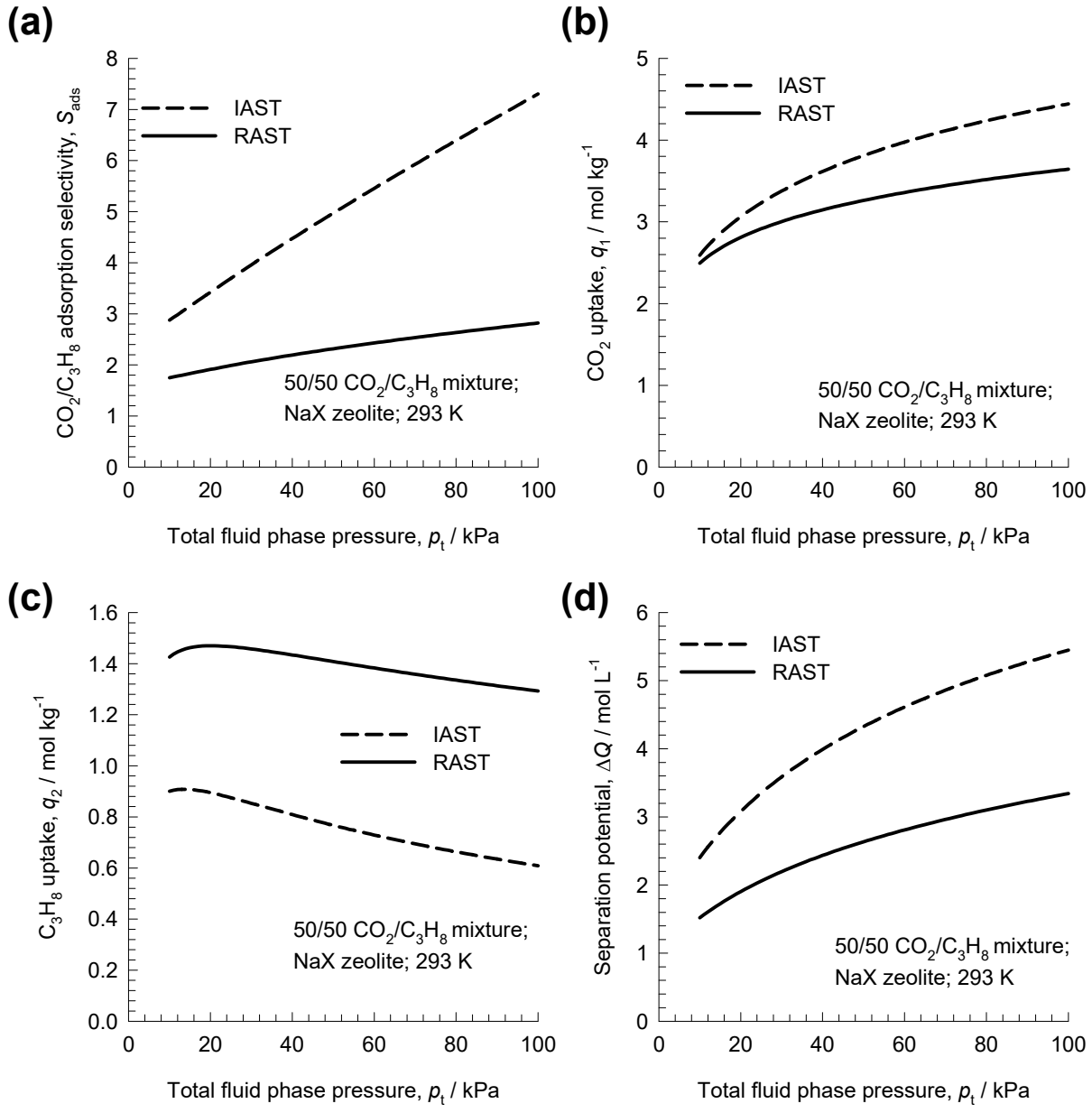

Figure S108

Transient breakthroughs CO_2/C_3H_8/NaX zeolite: RAST vs IAST

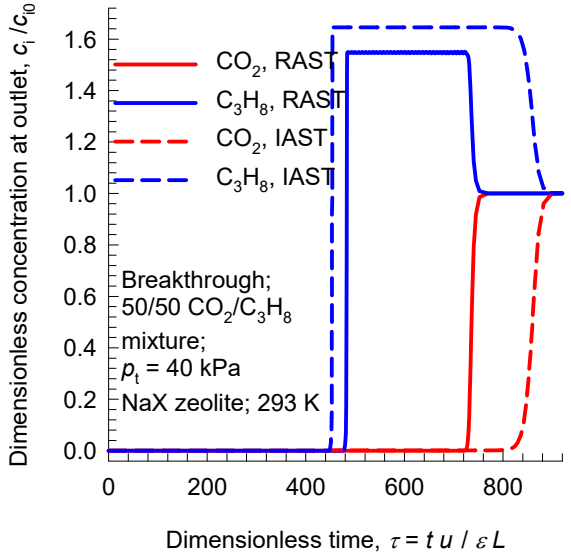

CO_2/C_3H_8 mixture adsorption in NaX zeolite: Costa data analysis

Figure S109

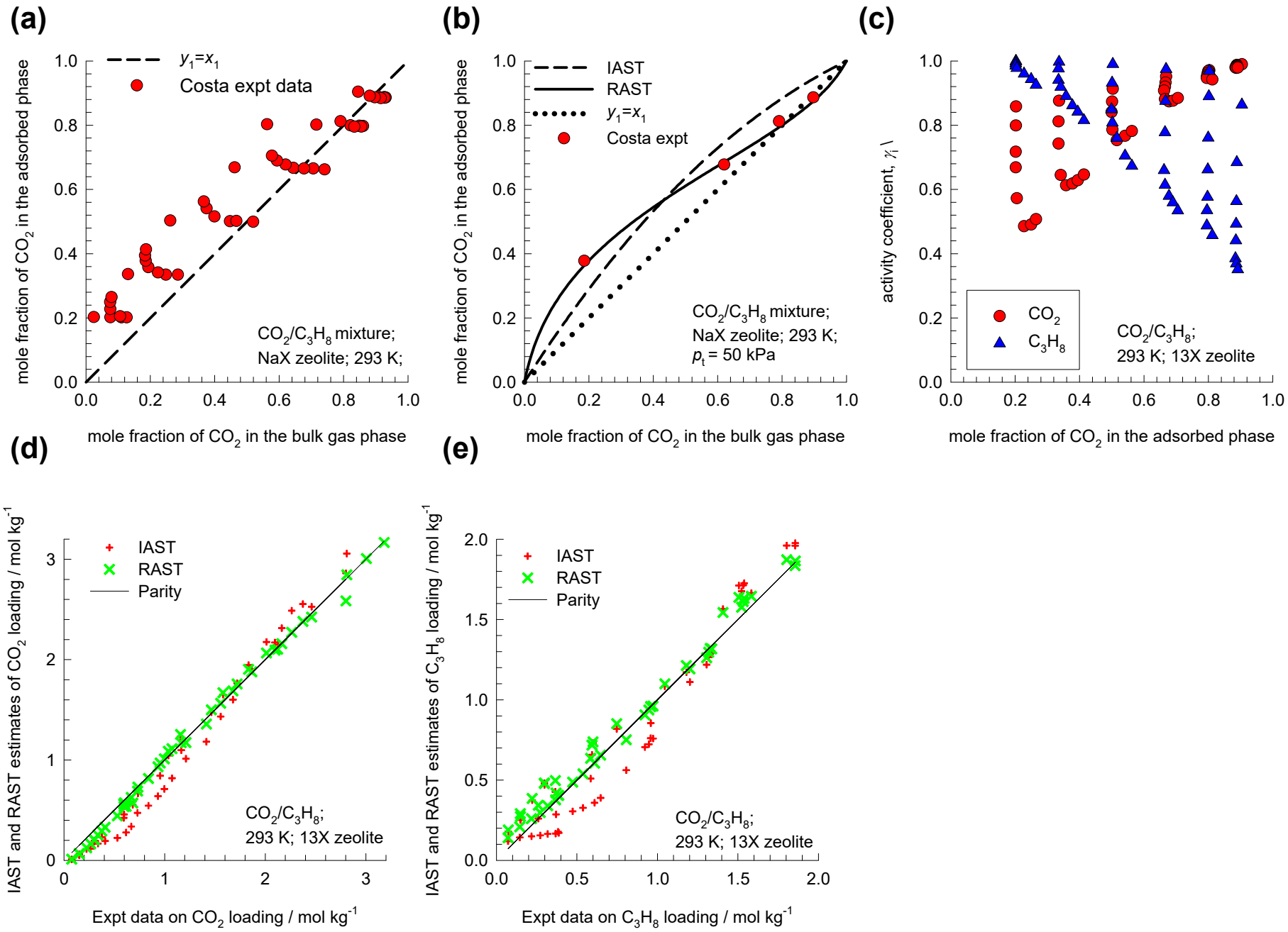

Figure S110

Separation potential for CO_2/C_3H_8/NaX

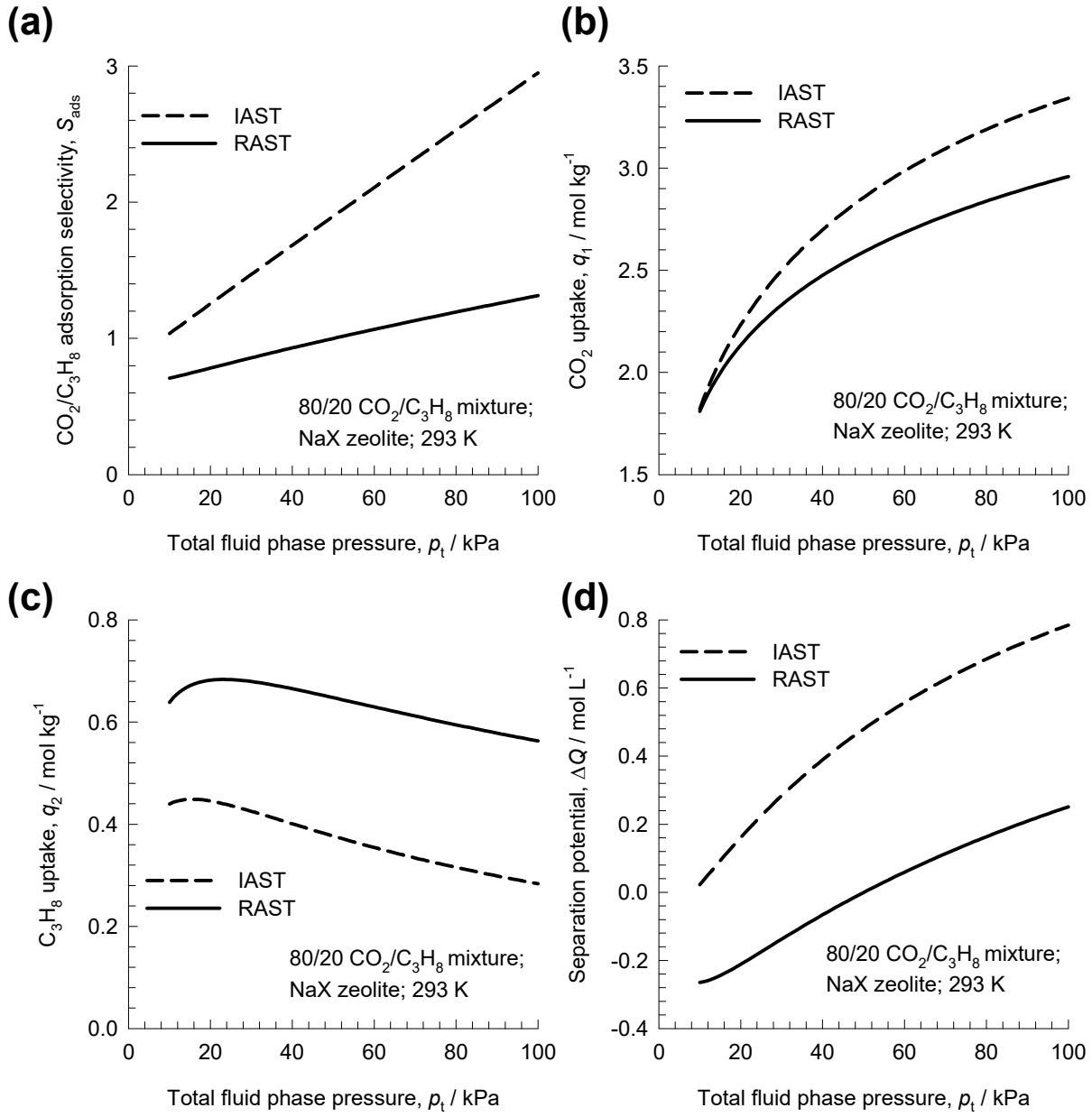

Figure S111

Transient breakthroughs CO_2/C_3H_8/NaX zeolite: RAST vs IAST

(a)

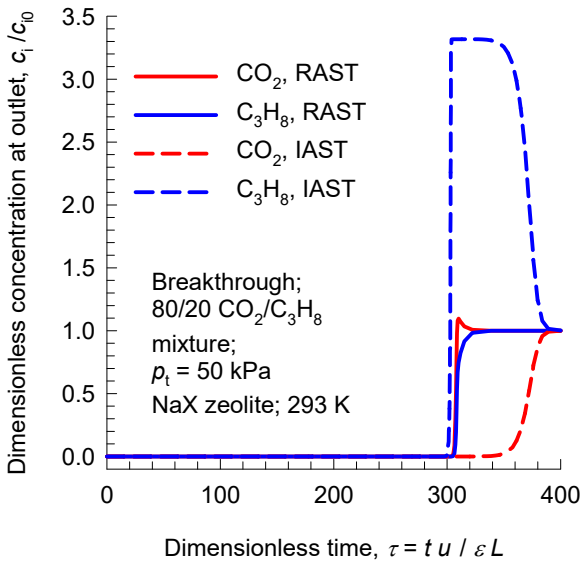

Zoomed-in

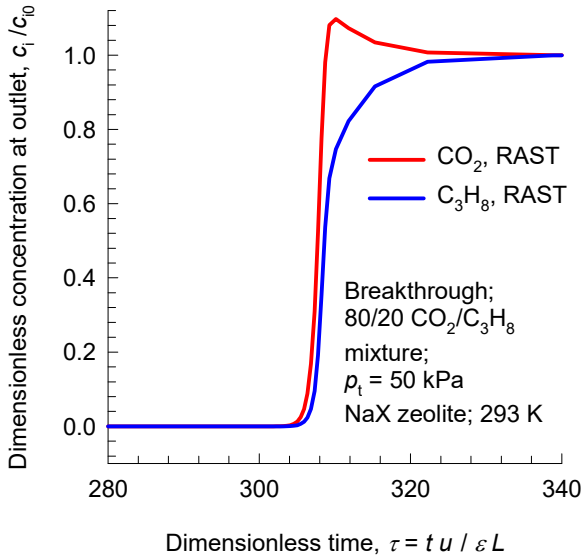

(b)

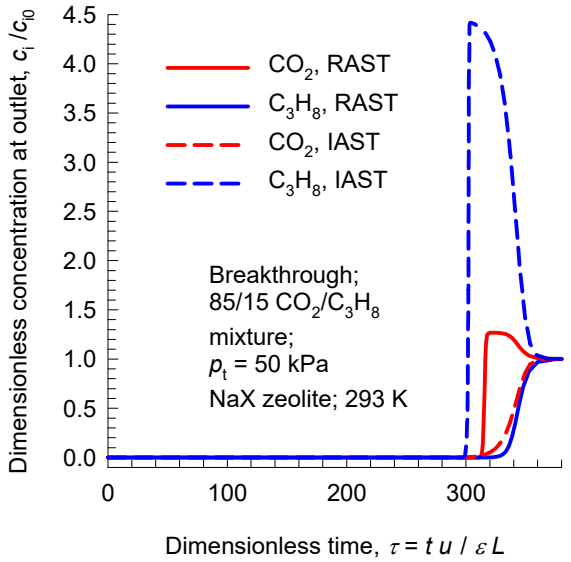

C_3H_6/C_3H_8 mixture adsorption in NaX zeolite: Costa data analysis

Figure S112

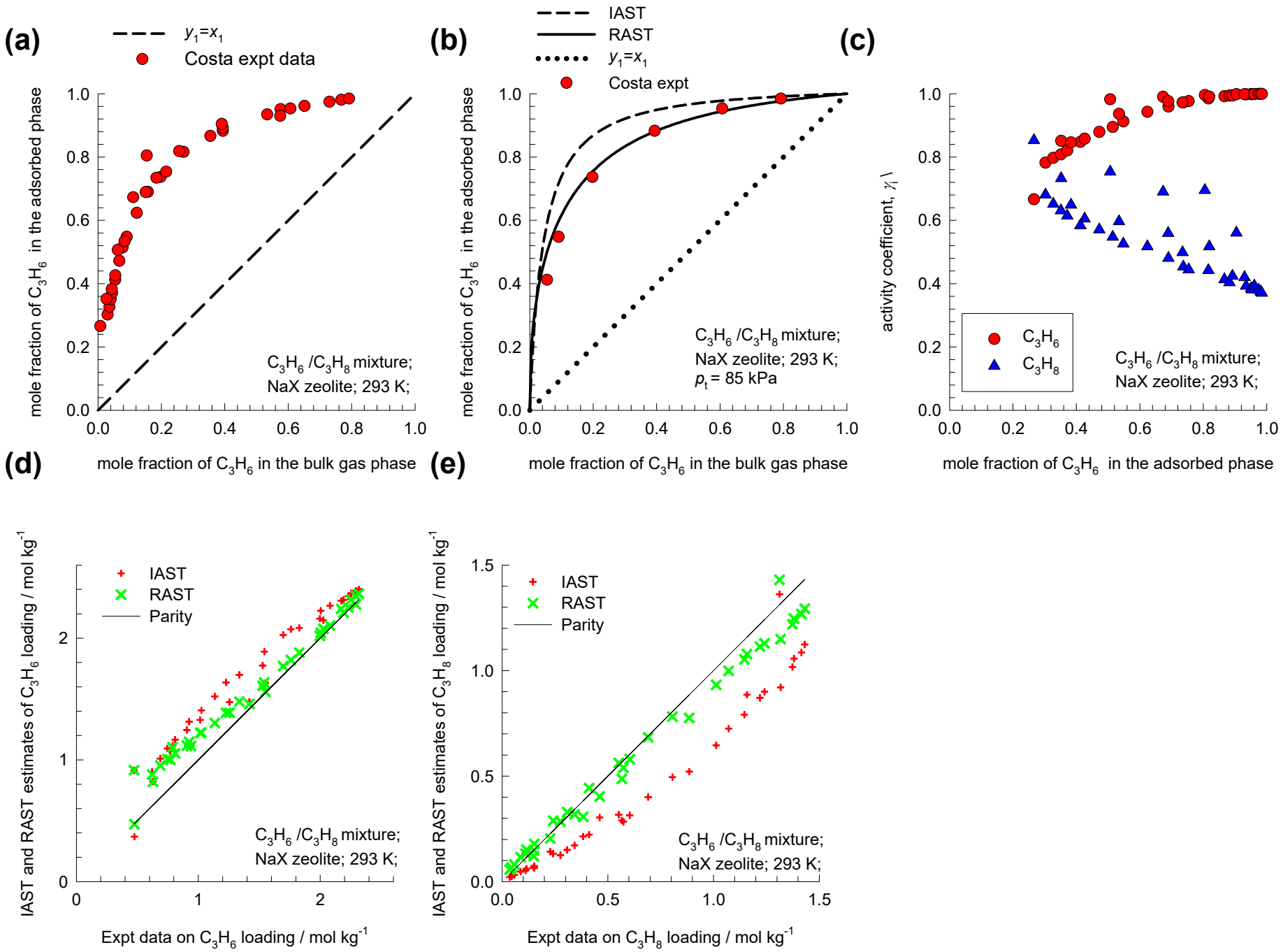

CO_2/C_3H_6 mixture adsorption in NaX zeolite: Costa data analysis

Figure S113

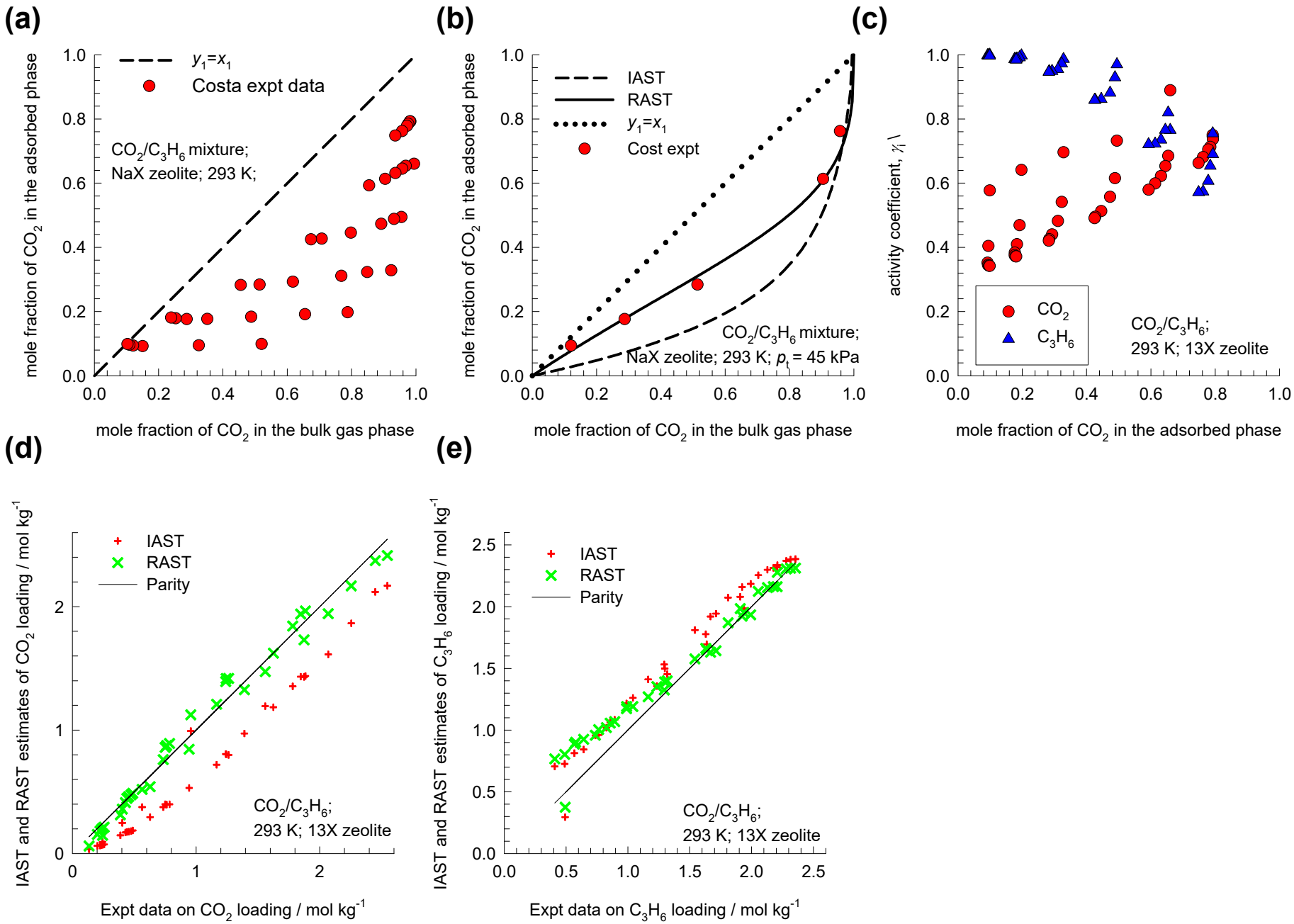

CO_2/C_2H_4 mixture adsorption in NaX zeolite: Costa data analysis

Figure S114

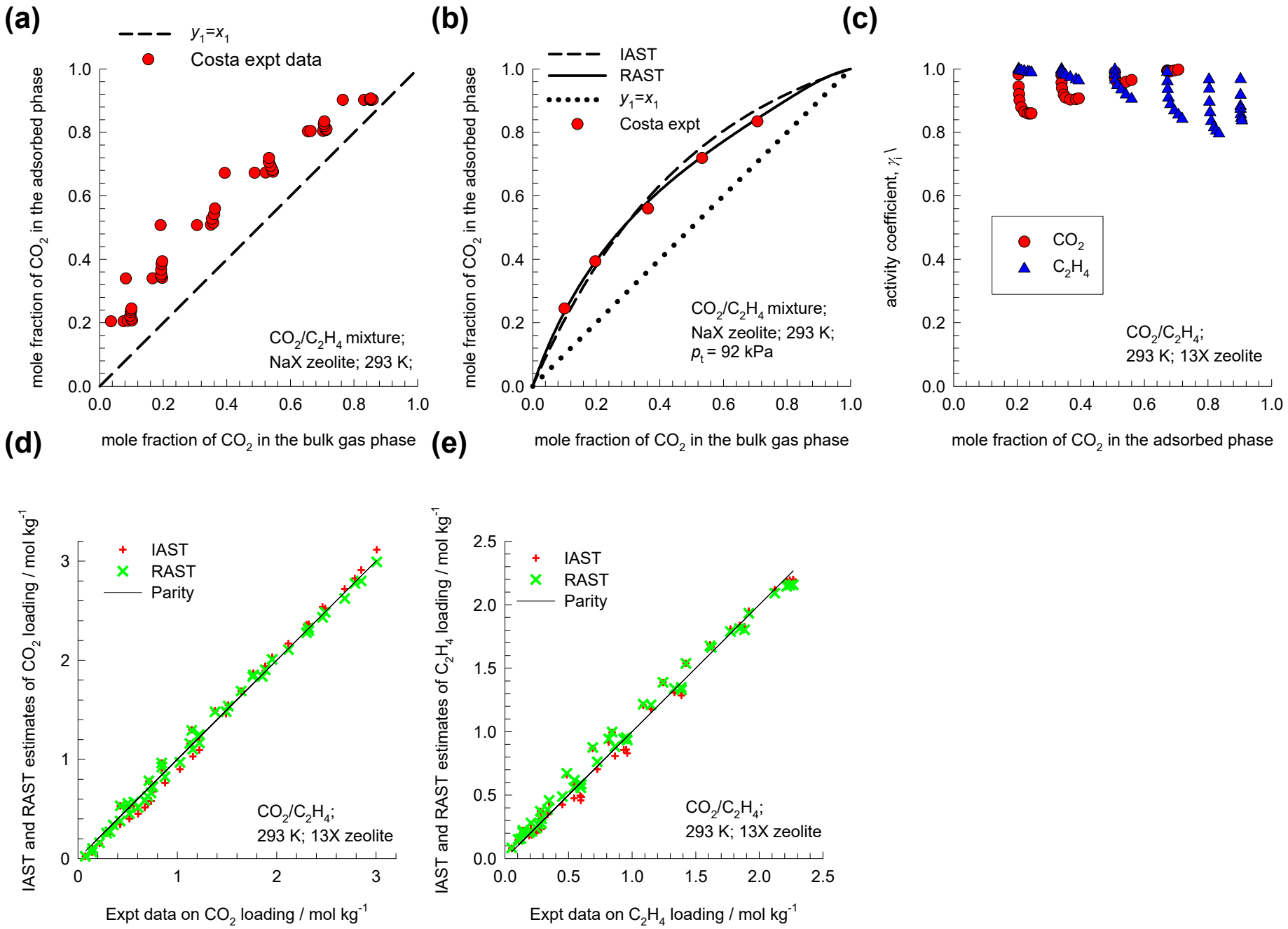

C_2H_4/C_3H_8 mixture adsorption in NaX zeolite: Costa data analysis

Figure S115

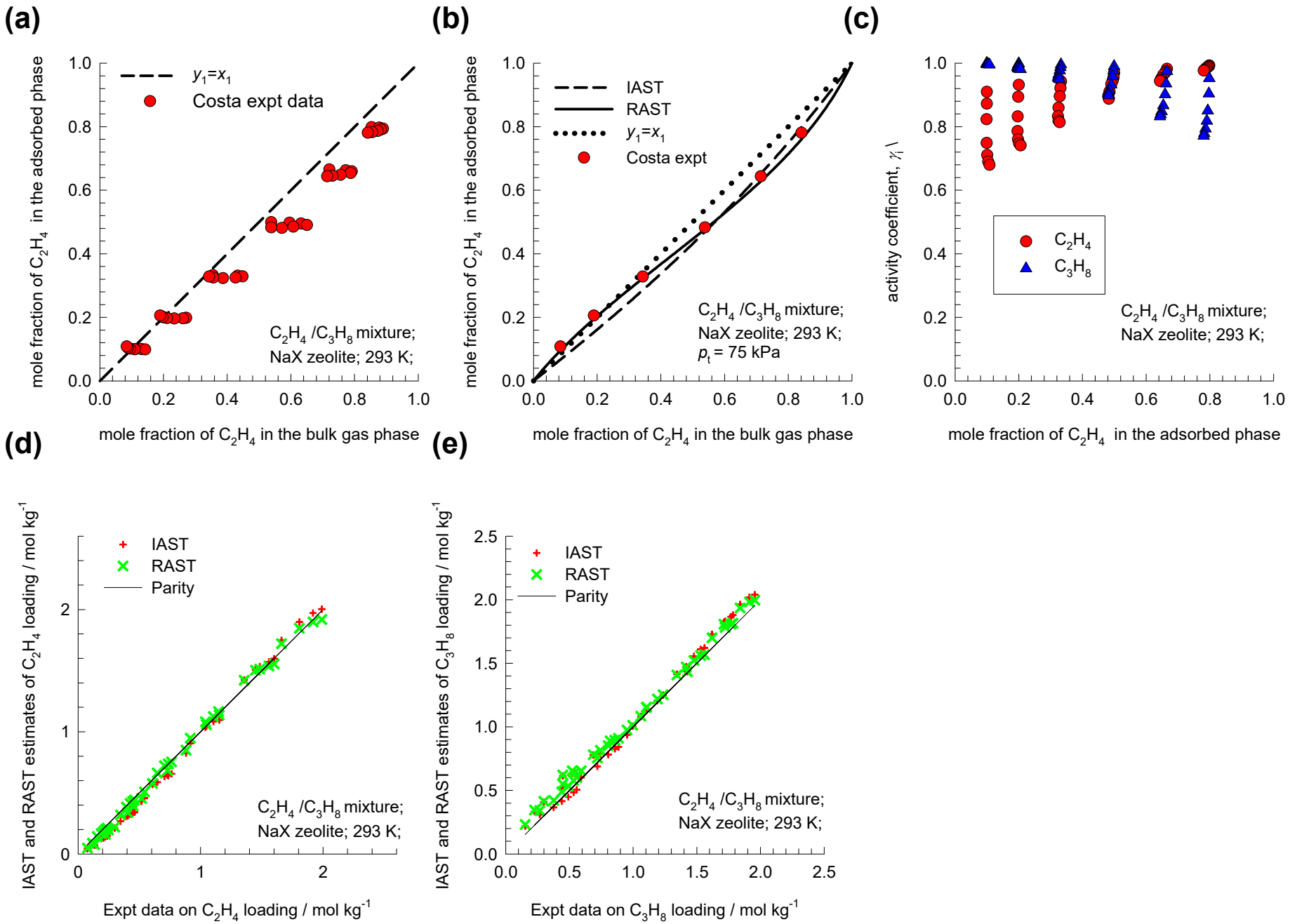

$CO_2/C_2H_4/C_3H_8$ mixture adsorption in NaX zeolite: Calleja data analysis

Figure S116

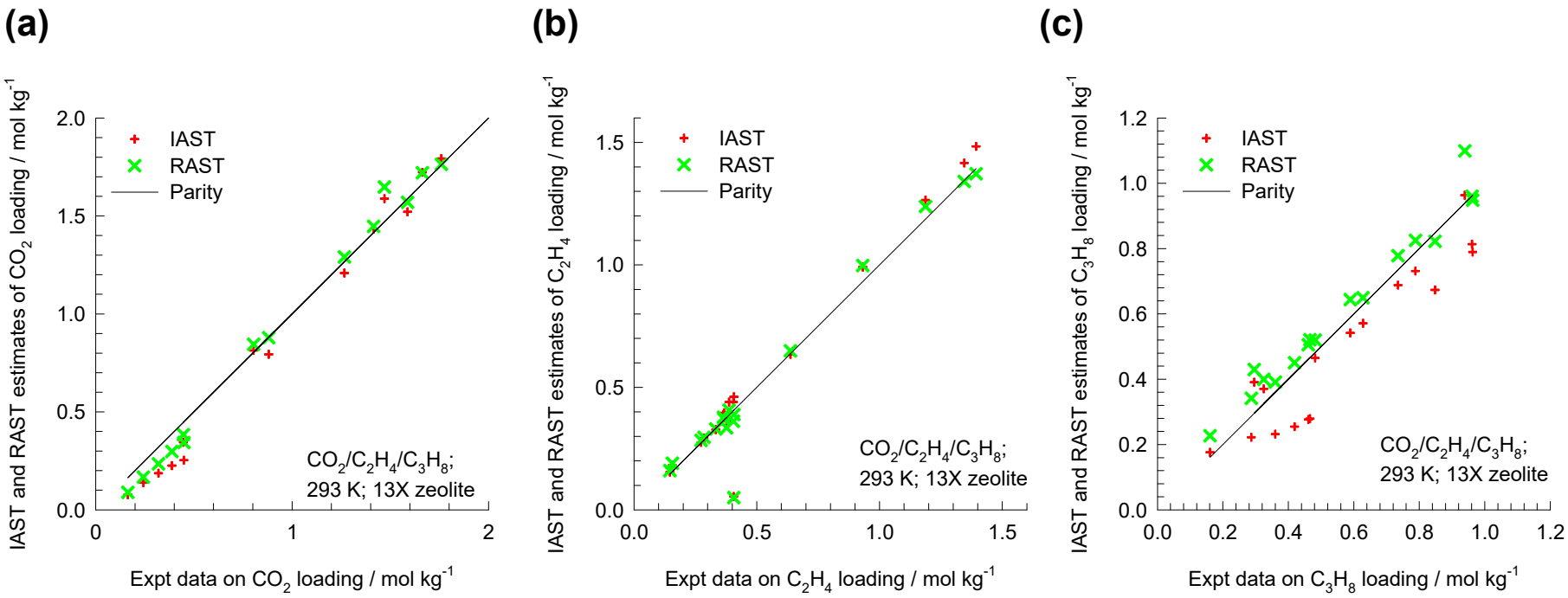

$CO_2/C_3H_6/C_3H_8$ mixture adsorption in NaX zeolite: Calleja data analysis

Figure S117

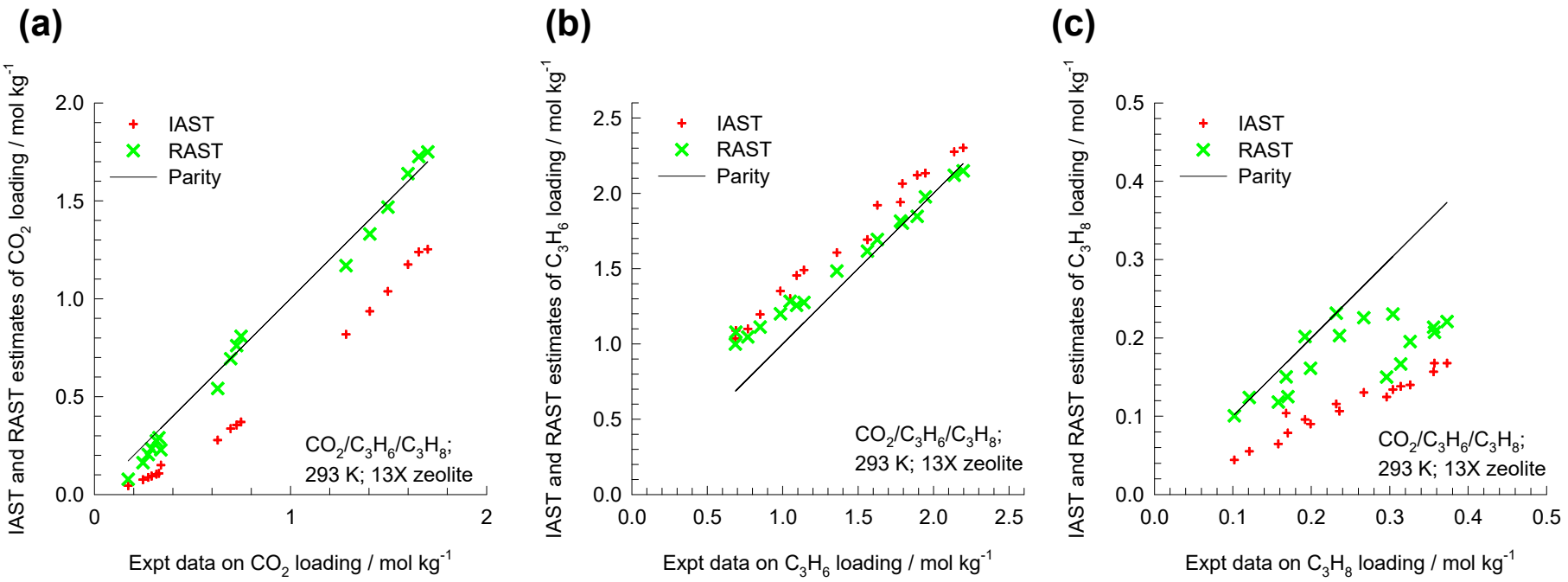

C_2H_4/iso-C_4H_{10} mixture adsorption in 13X zeolite: Hyun data analysis

Figure S118

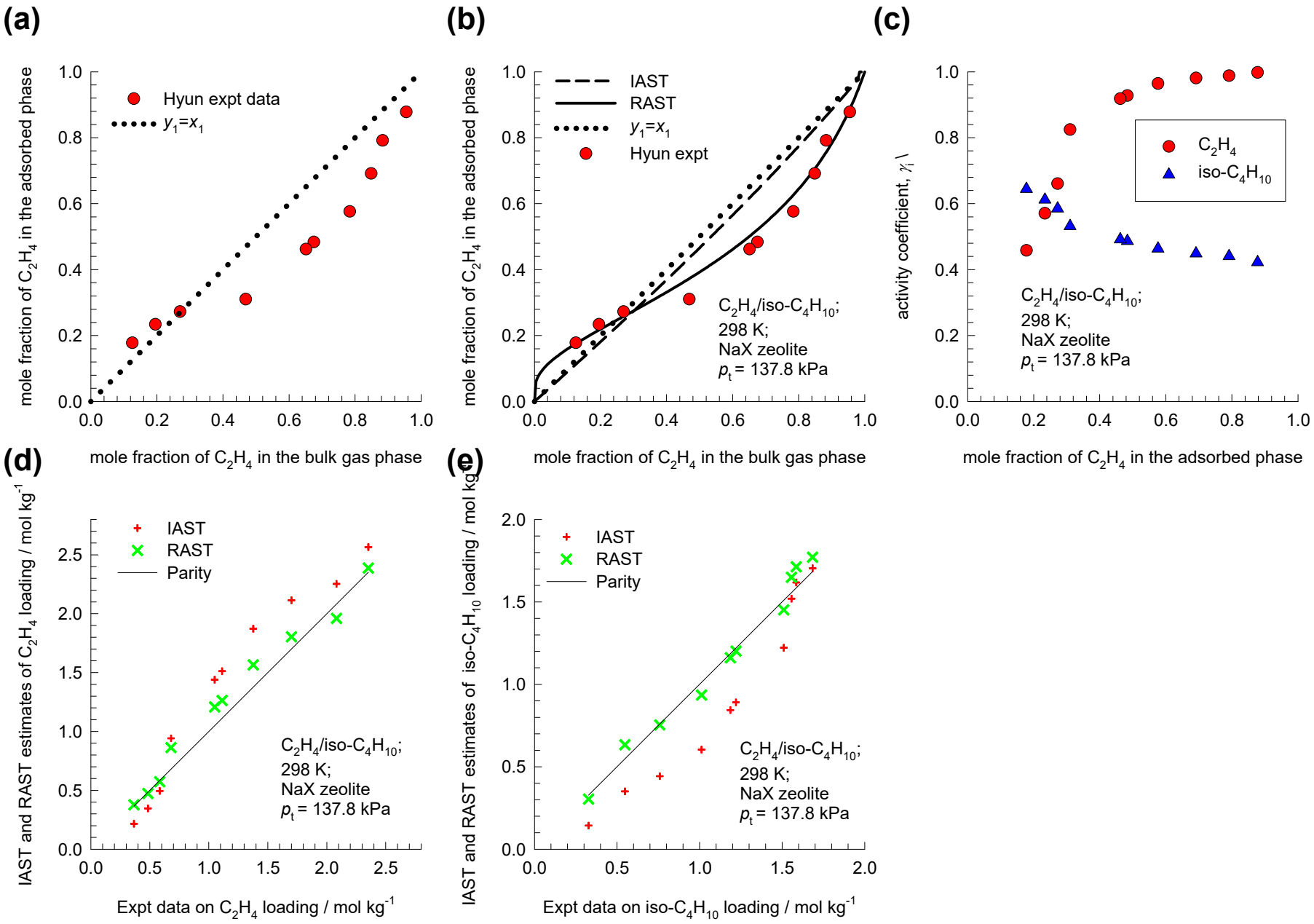

CO_2/C_2H_4 mixture adsorption in ZSM-5 zeolite: Calleja data analysis

Figure S119

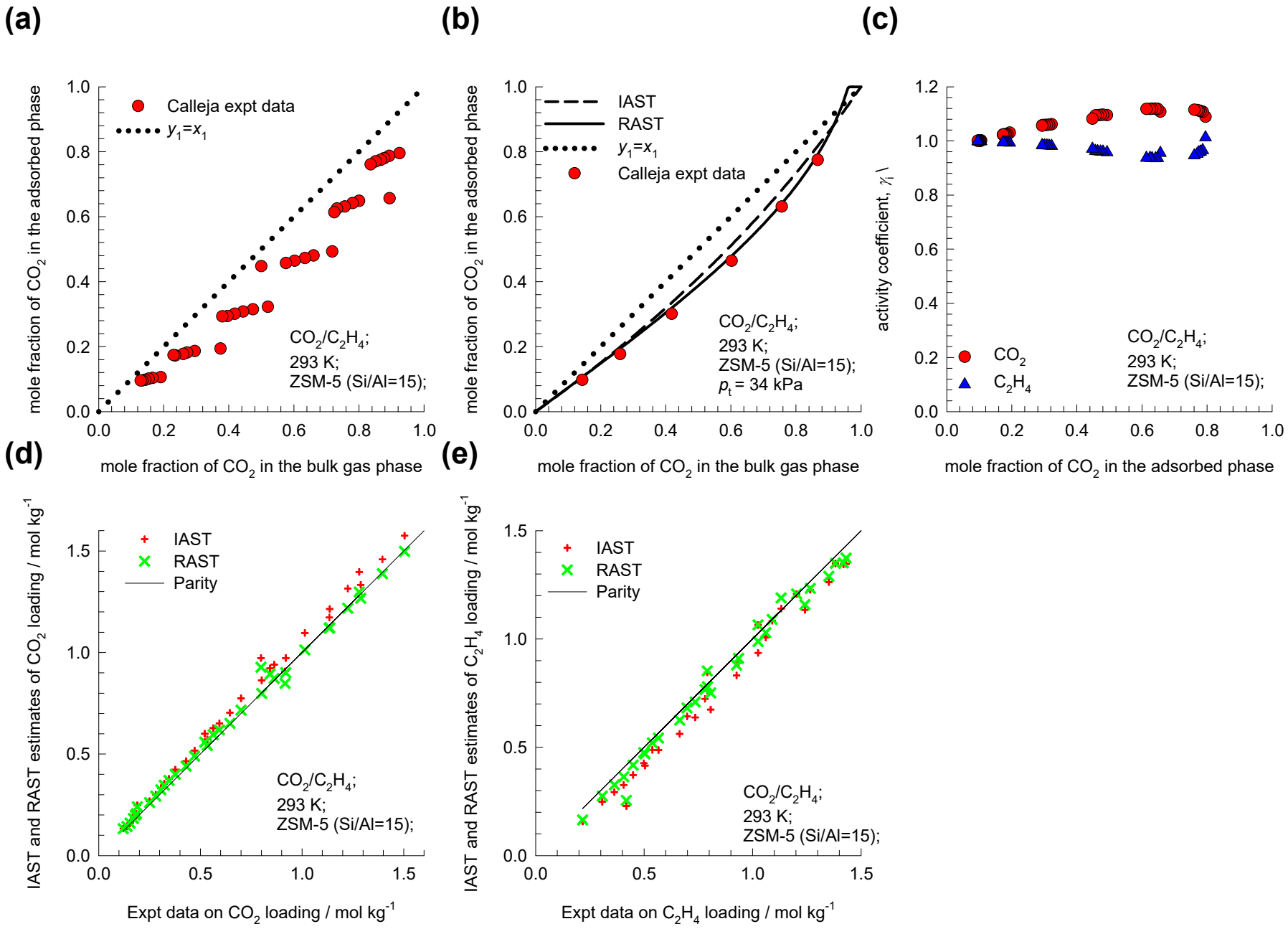

CO_2/C_3H_8 mixture adsorption in ZSM-5 zeolite: Calleja data analysis

Figure S120

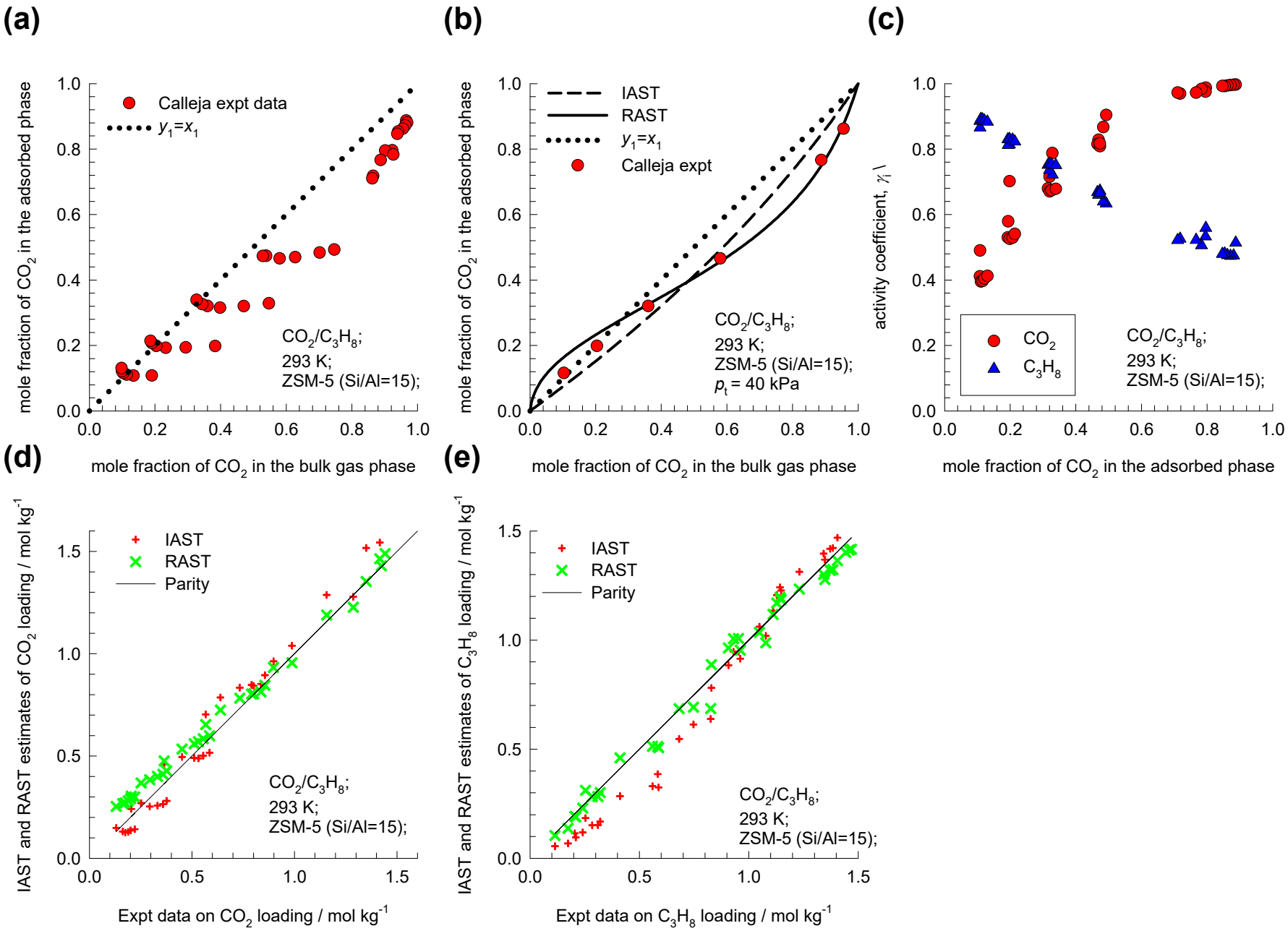

C_2H_4/C_3H_8 mixture adsorption in ZSM-5 zeolite: Calleja data analysis

Figure S121

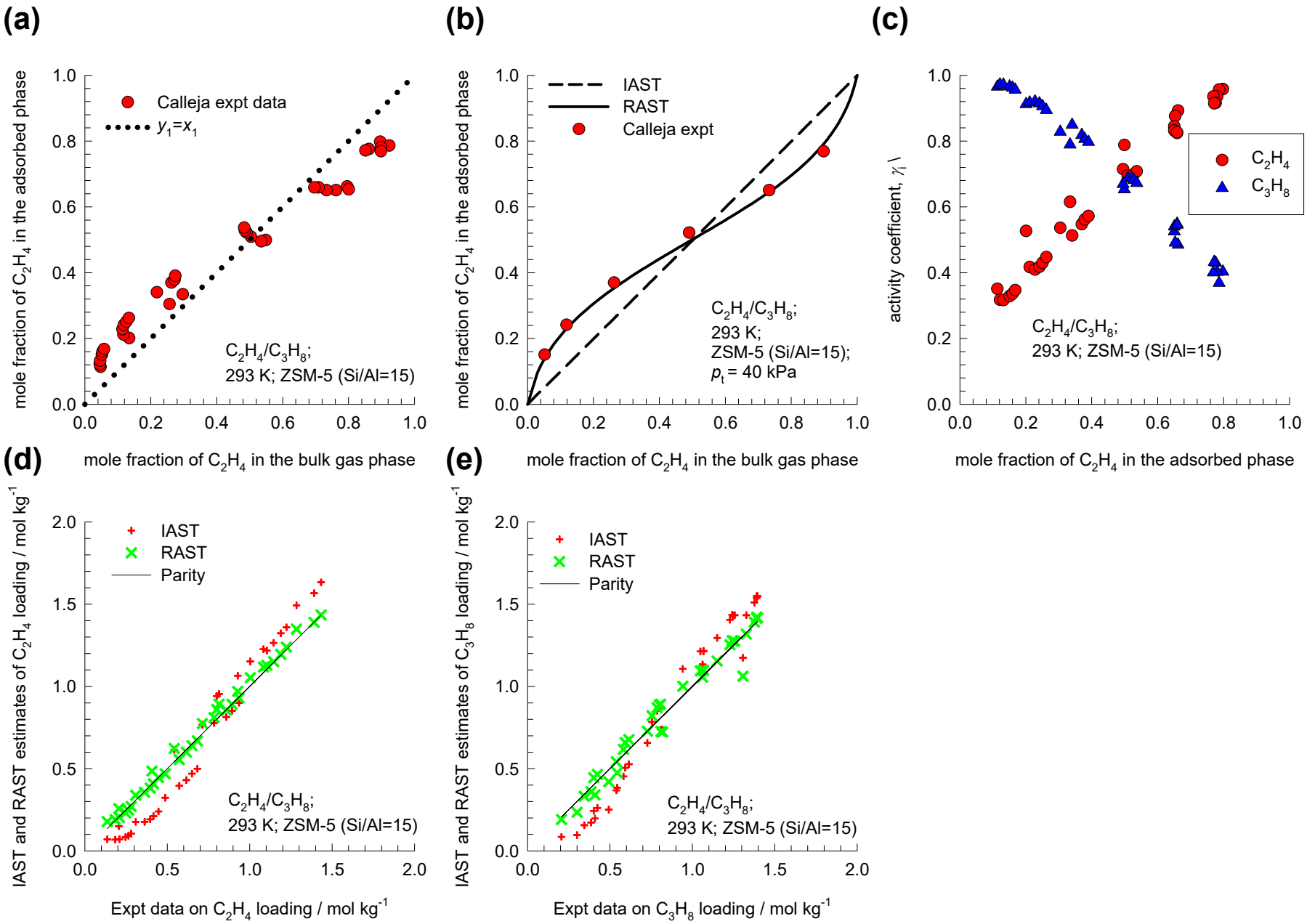

Figure S122

Transient breakthroughs C_2H_4/C_3H_8/ZSM-5 zeolite: RAST vs IAST

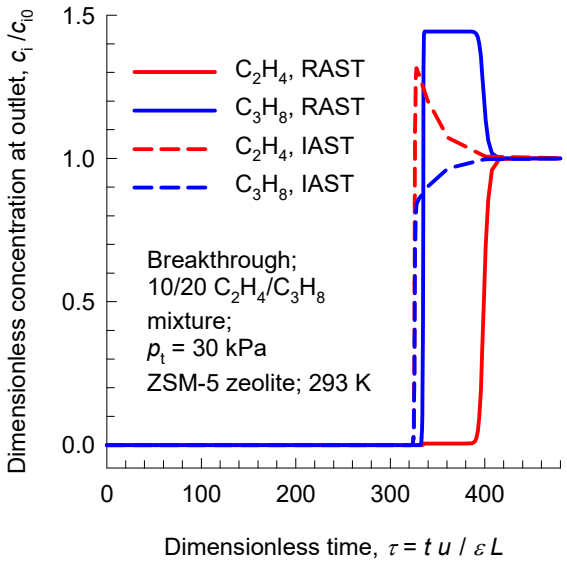

CO_2/C_3H_8 mixture adsorption in H-Mordenite: Talu-Zwiebel data analysis

Figure S123

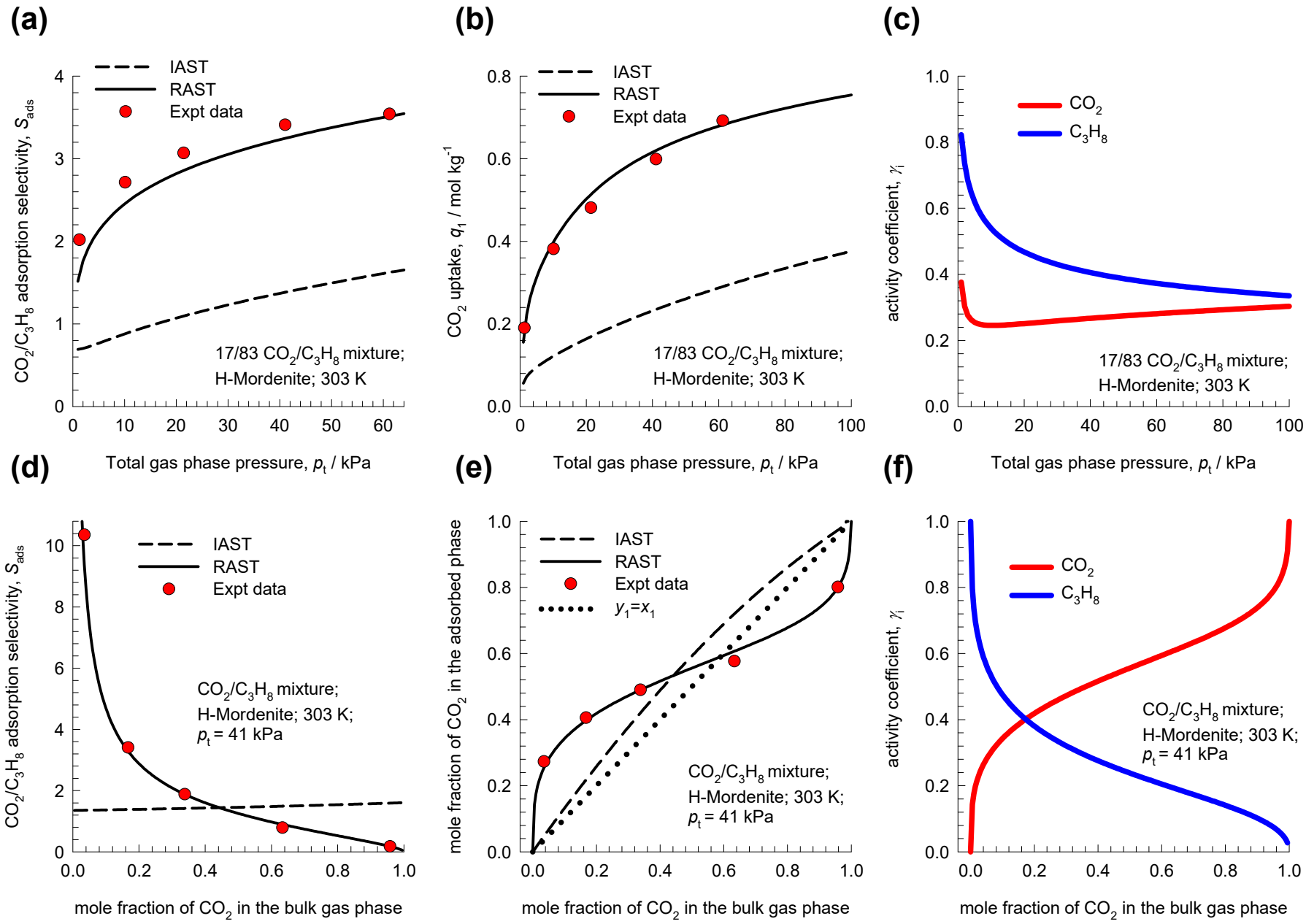

Transient breakthroughs CO_2/C_3H_8/H-MOR: RAST vs IAST

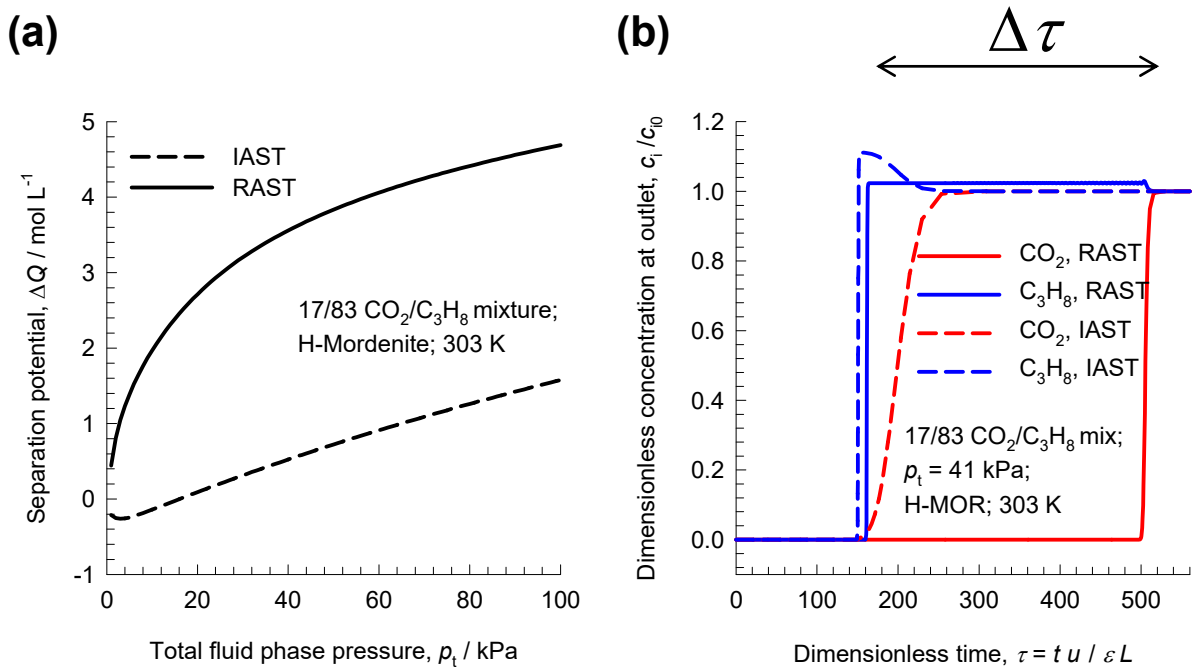

CO_2/H_2S, and C_3H_8/H_2S, mixture adsorption in H-Mordenite: Talu-Zwiebel data analysis

Figure S125

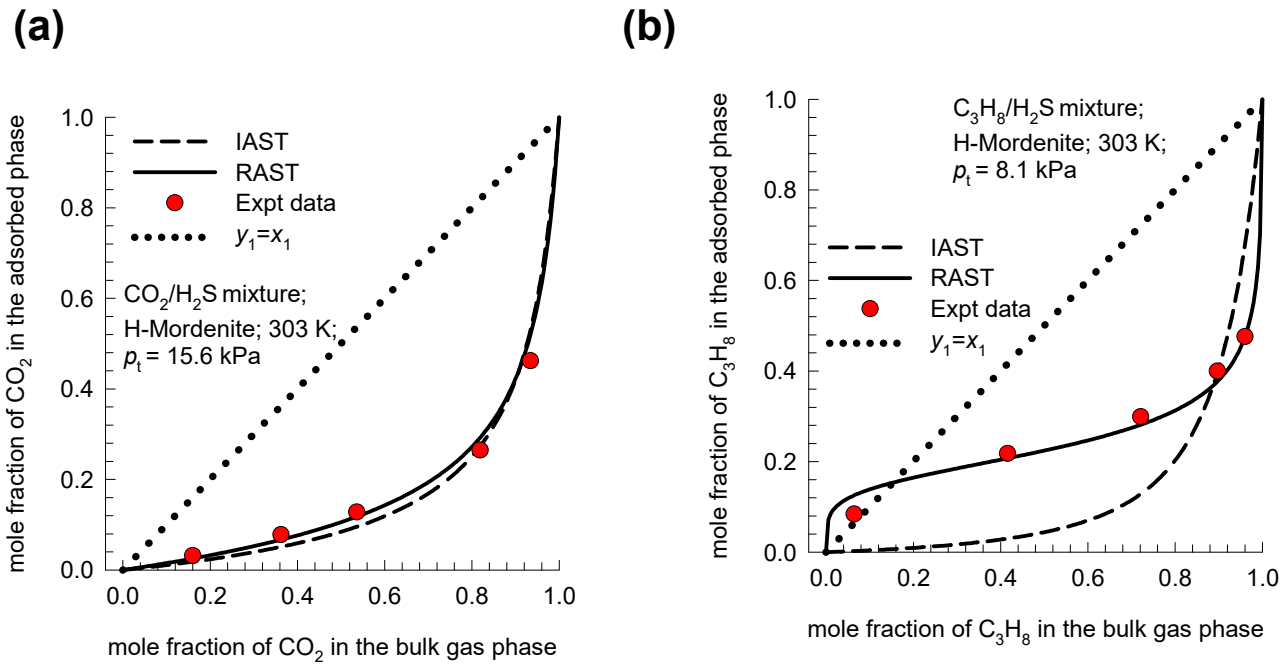

$CO_2/C_3H_8/H_2S$ mixture adsorption in NaX zeolite: Talu-Zwiebel data analysis

Figure S126

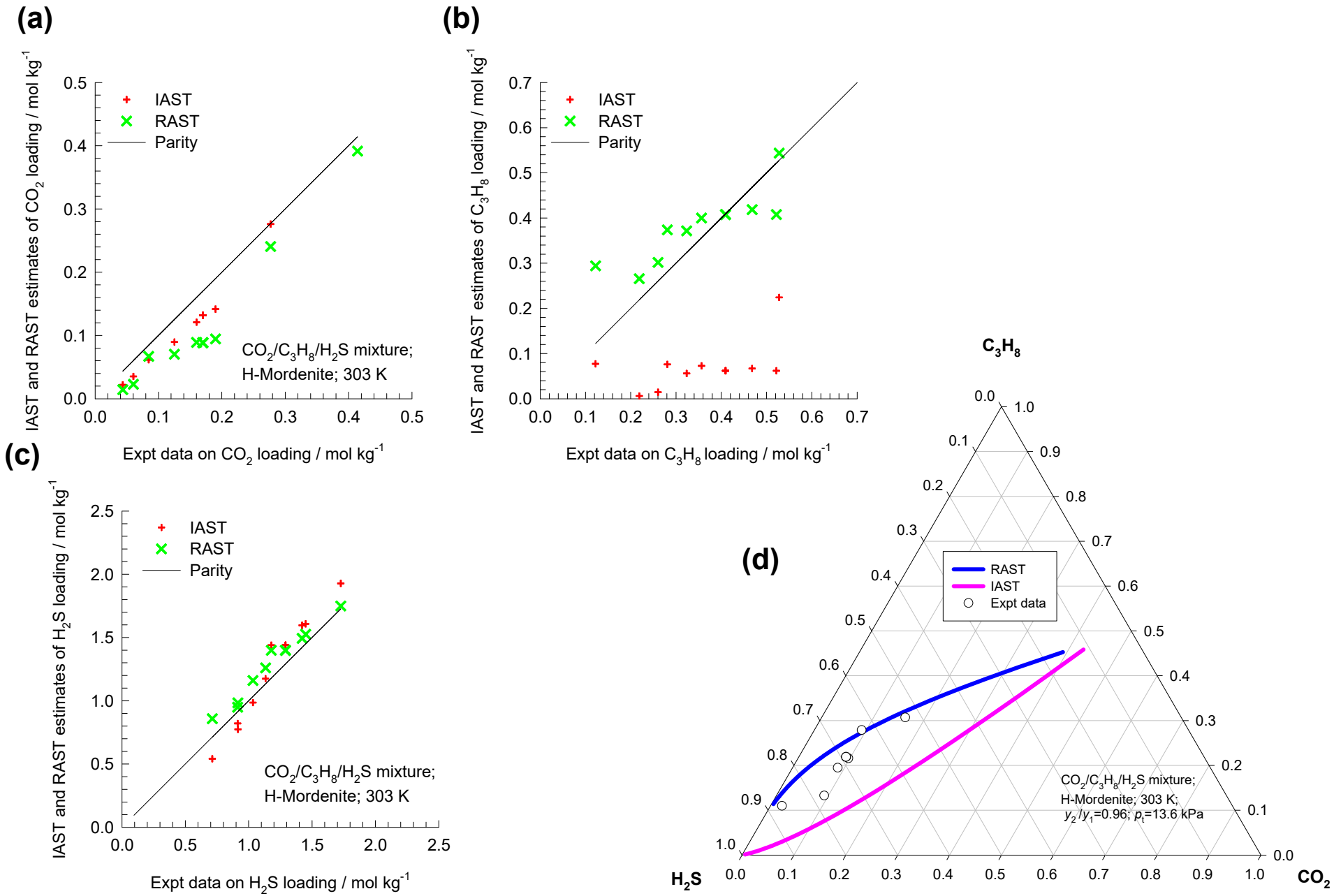

CO_2/CH_4 mixture adsorption in LTA-5A zeolite: Re-analysis of Mofarahi-Gholipour data

Figure S127

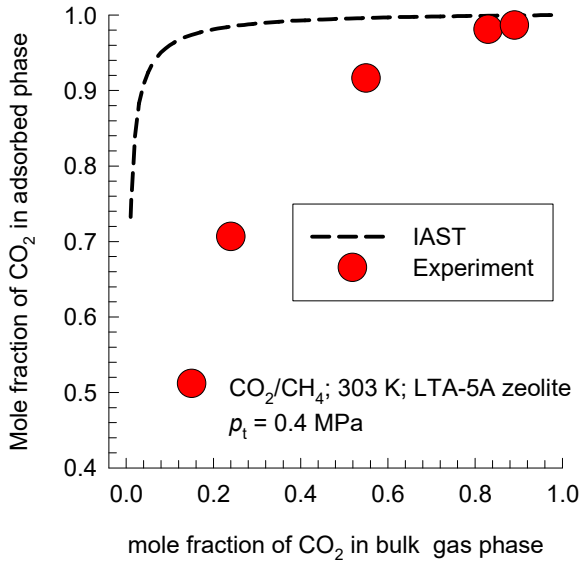

C_2H_4/C_2H_6 mixture adsorption in LTA-5A zeolite: Re-analysis of Mofarahi-Salehi data

Figure S128

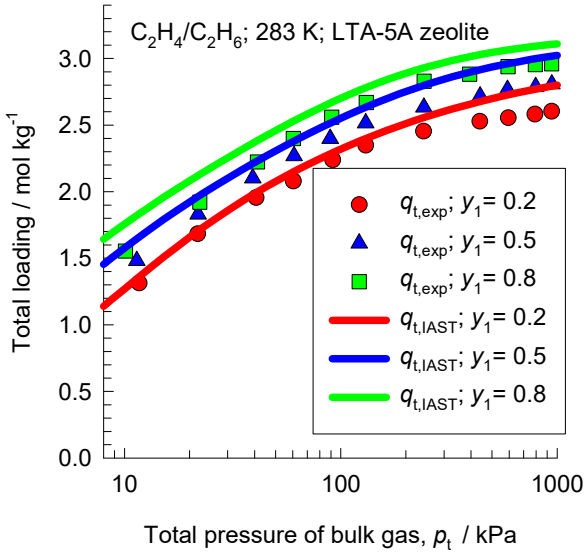

Figure S129

(a) Breakthrough experiment of van Zandvoort et al.

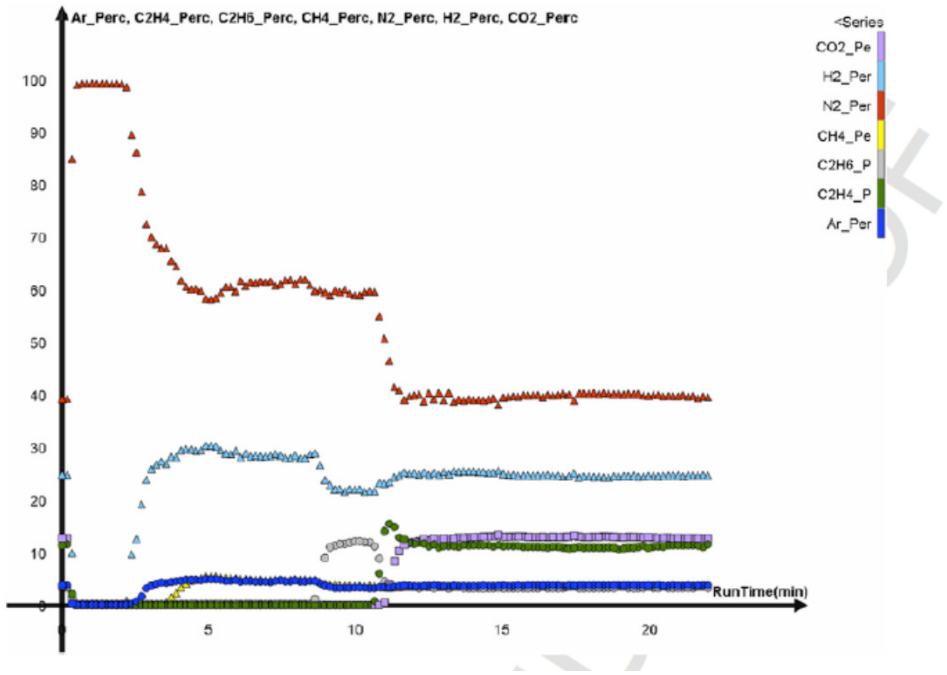

(b) Breakthrough simulation based on IAST

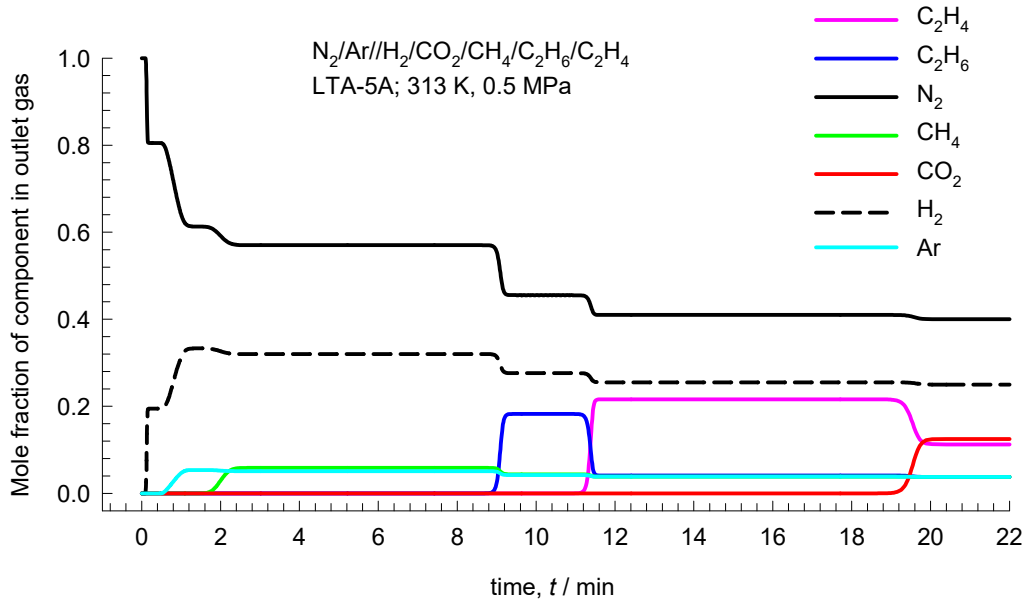

Transient breakthrough of gas mixture in LTA-5A zeolite

CH_4/N_2 adsorption equilibrium in Ba-ETS-4: Expt vs IAST

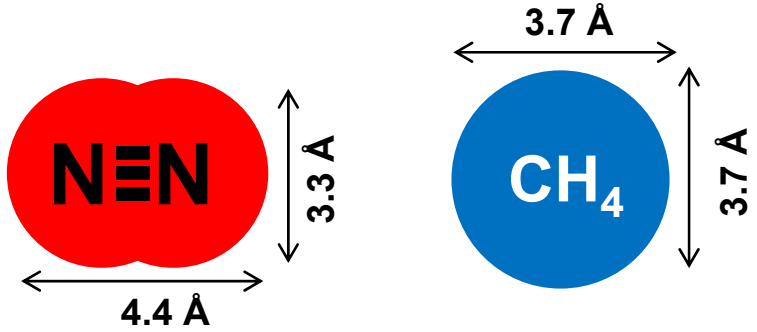

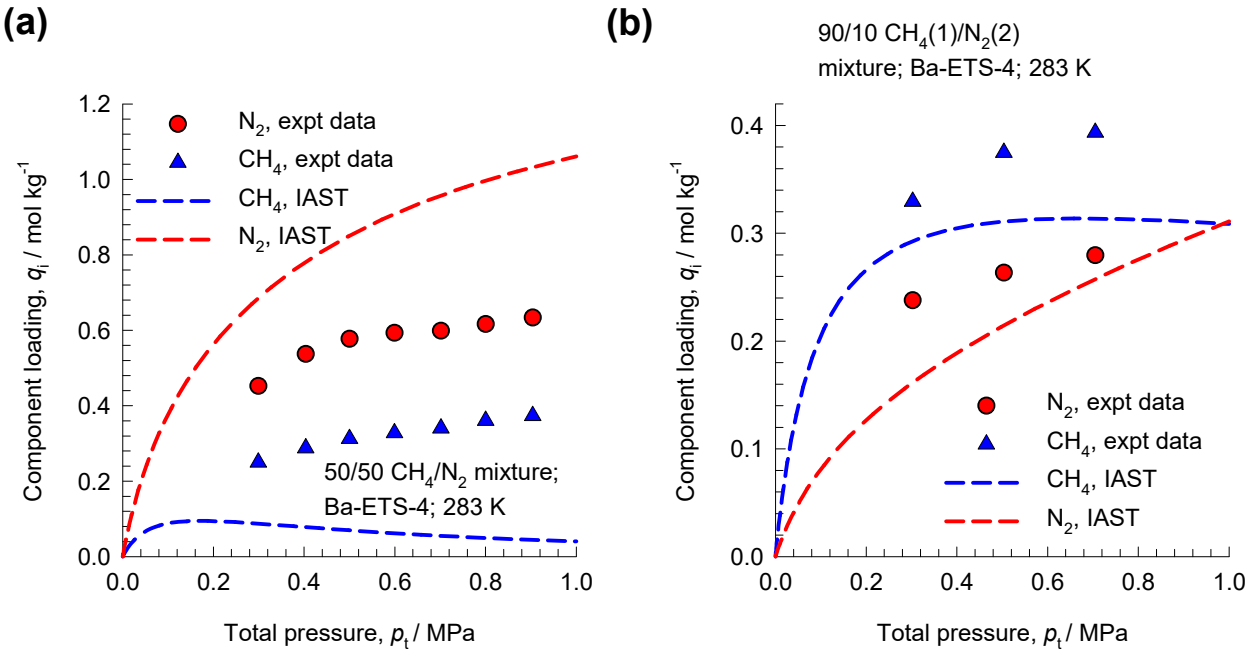

Unary isotherms in MFI zeolite

Figure S131

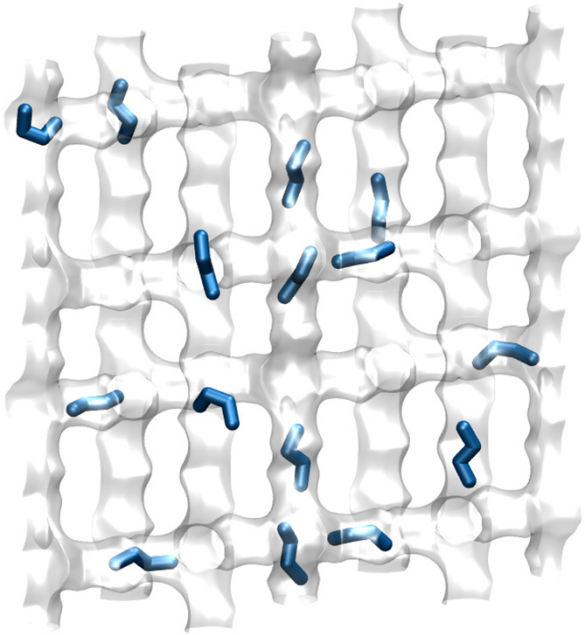

Snapshot of n-butane (nC4) In MFI zeolite

Snapshot of iso-butane (iC4) In MFI zeolite

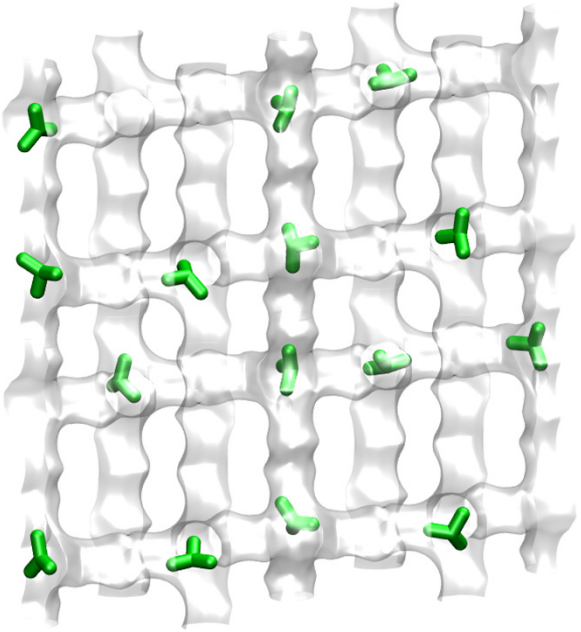

(a)

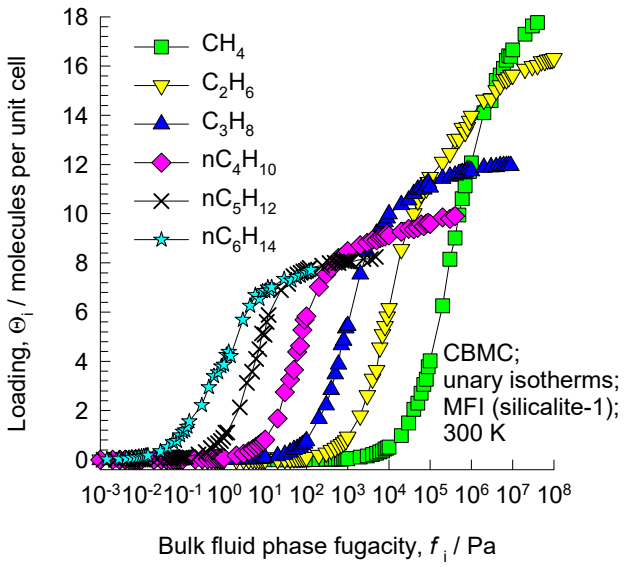

(b)

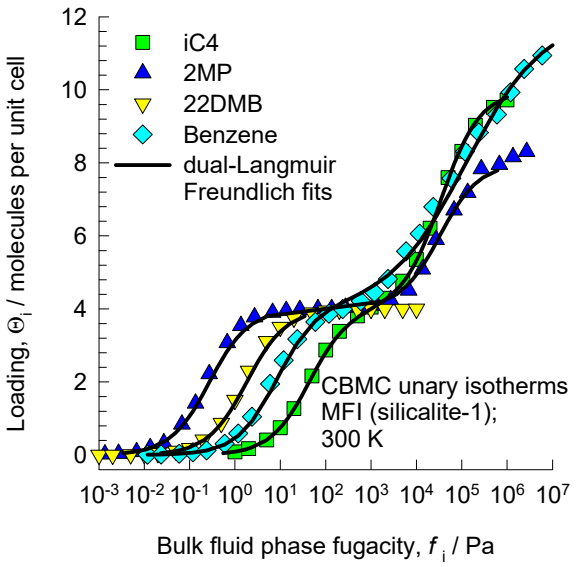

CH_4/Benzene mixture adsorption in MFI zeolite at 300 K

Figure S132

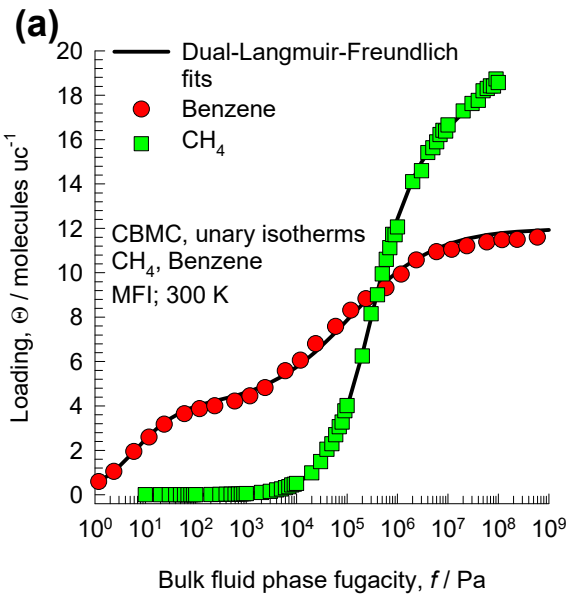

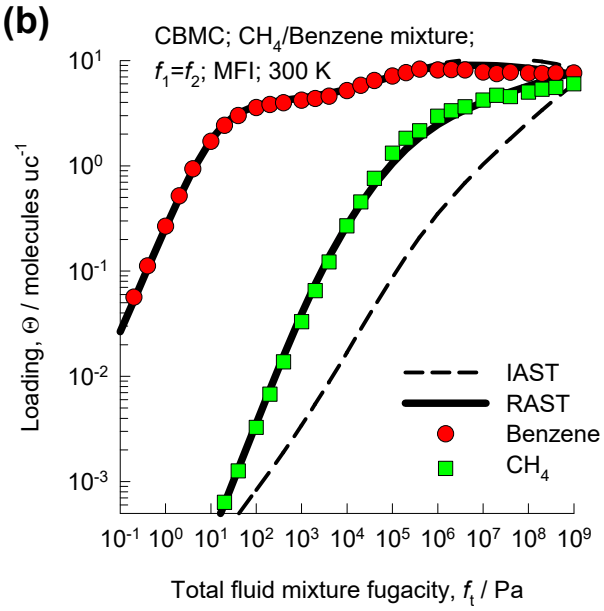

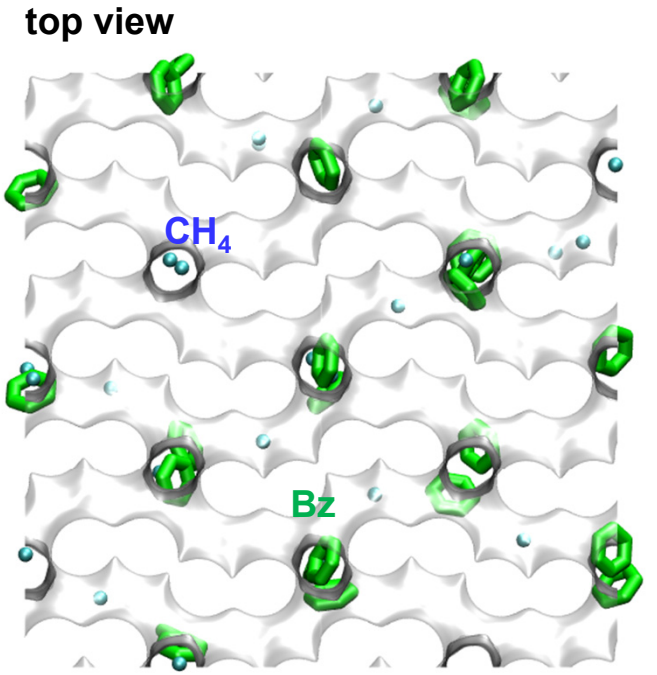

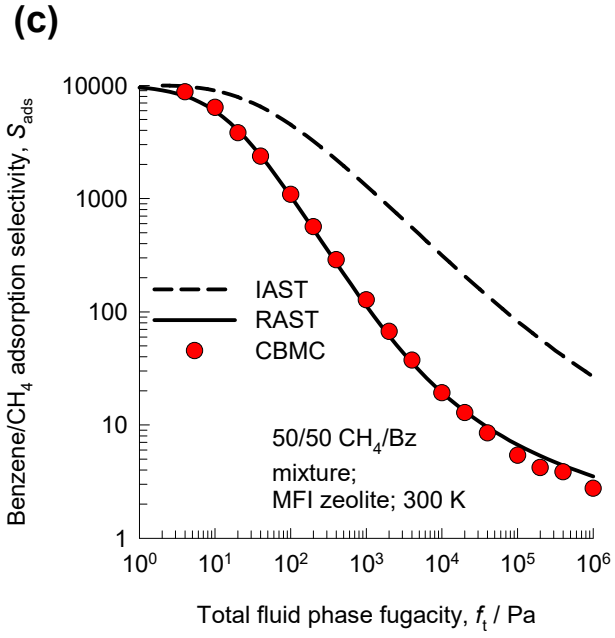

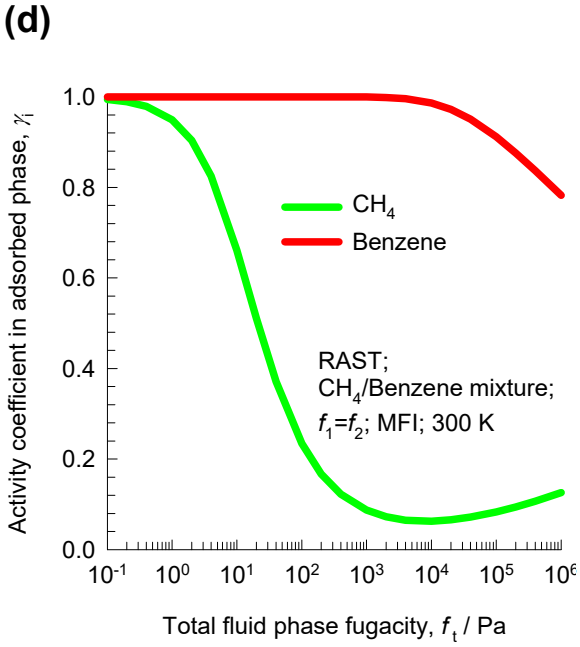

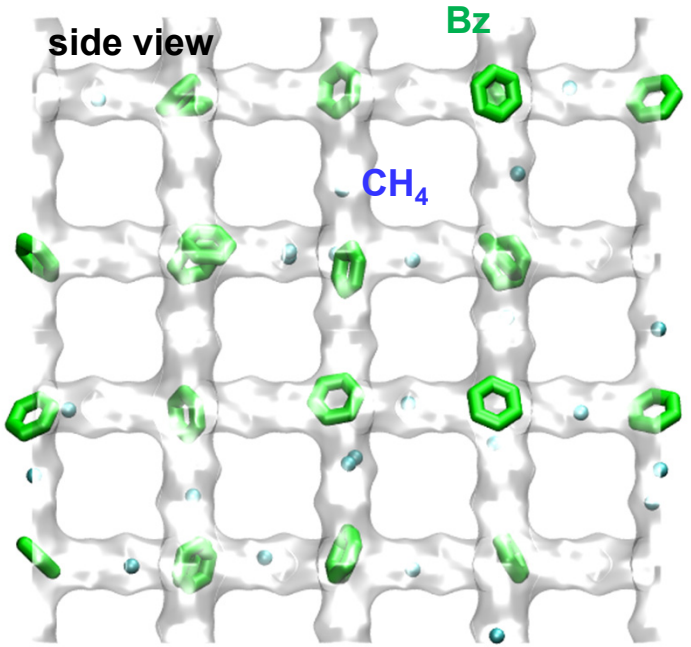

C_2H_4/Benzene mixture adsorption in MFI zeolite at 300 K

Figure S133

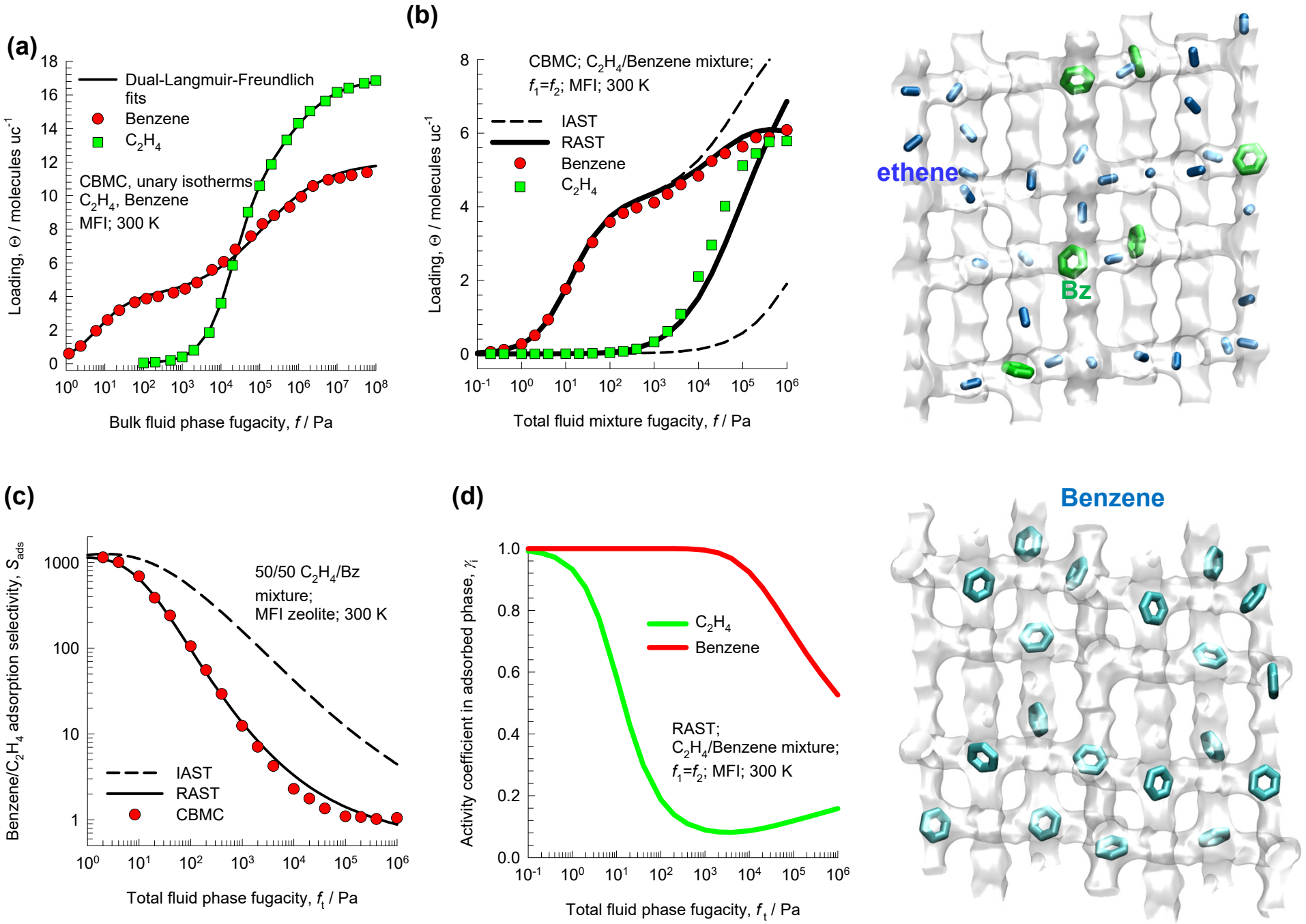

C_2H_4/Benzene mixture adsorption in MFI zeolite at 653 K

Figure S134

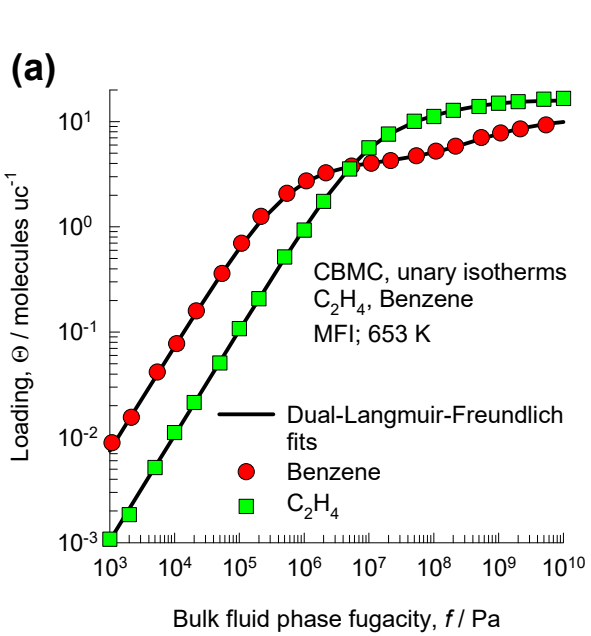

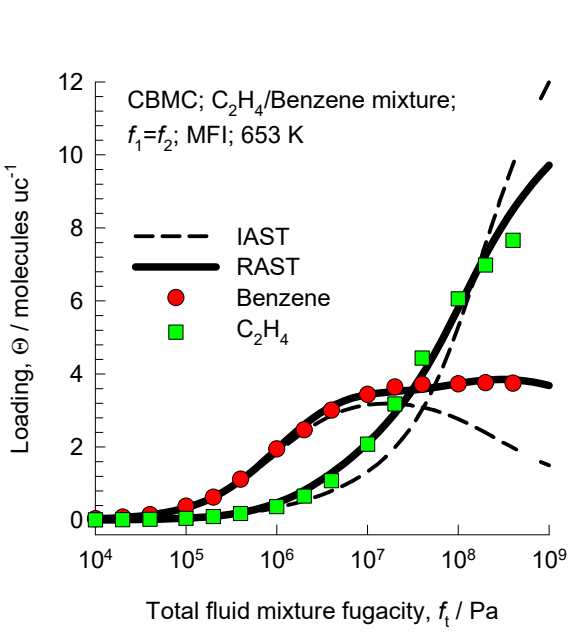

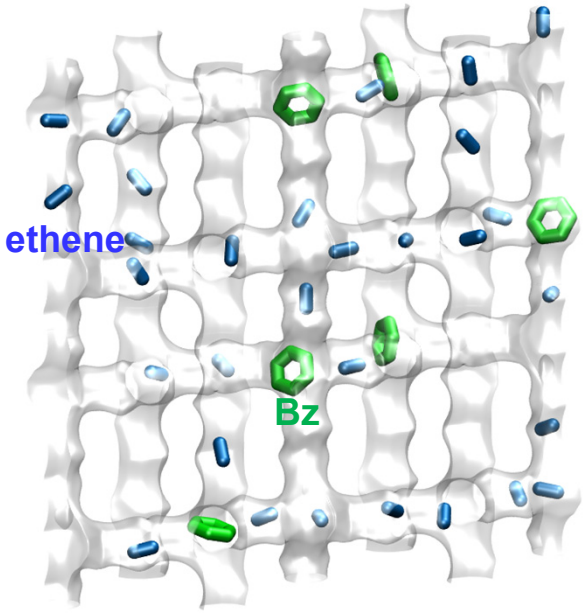

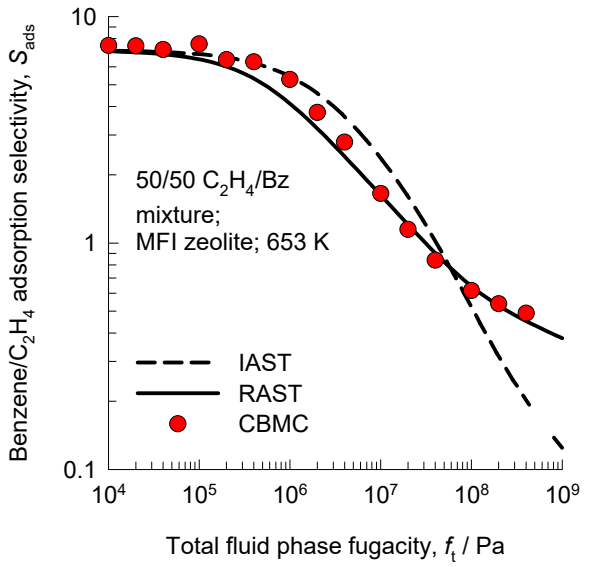

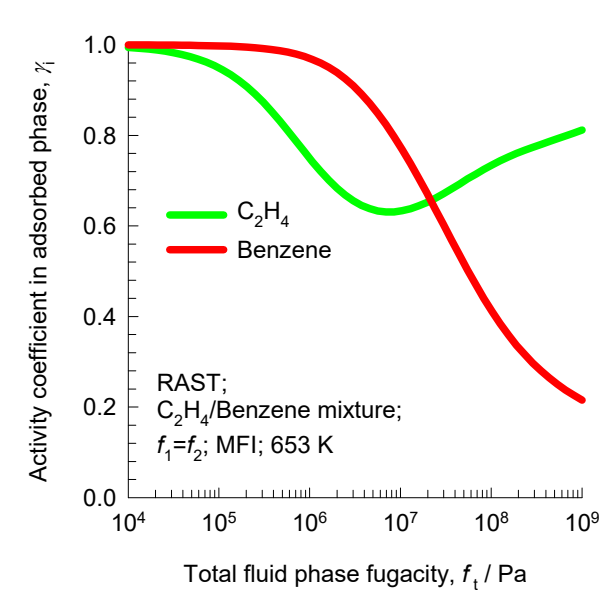

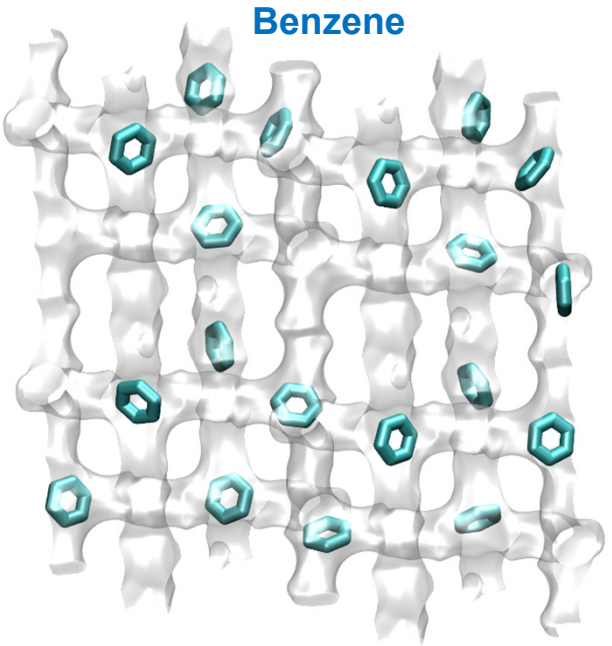

C_3H_6/Benzene mixture adsorption in MFI zeolite at 300 K

Figure S135

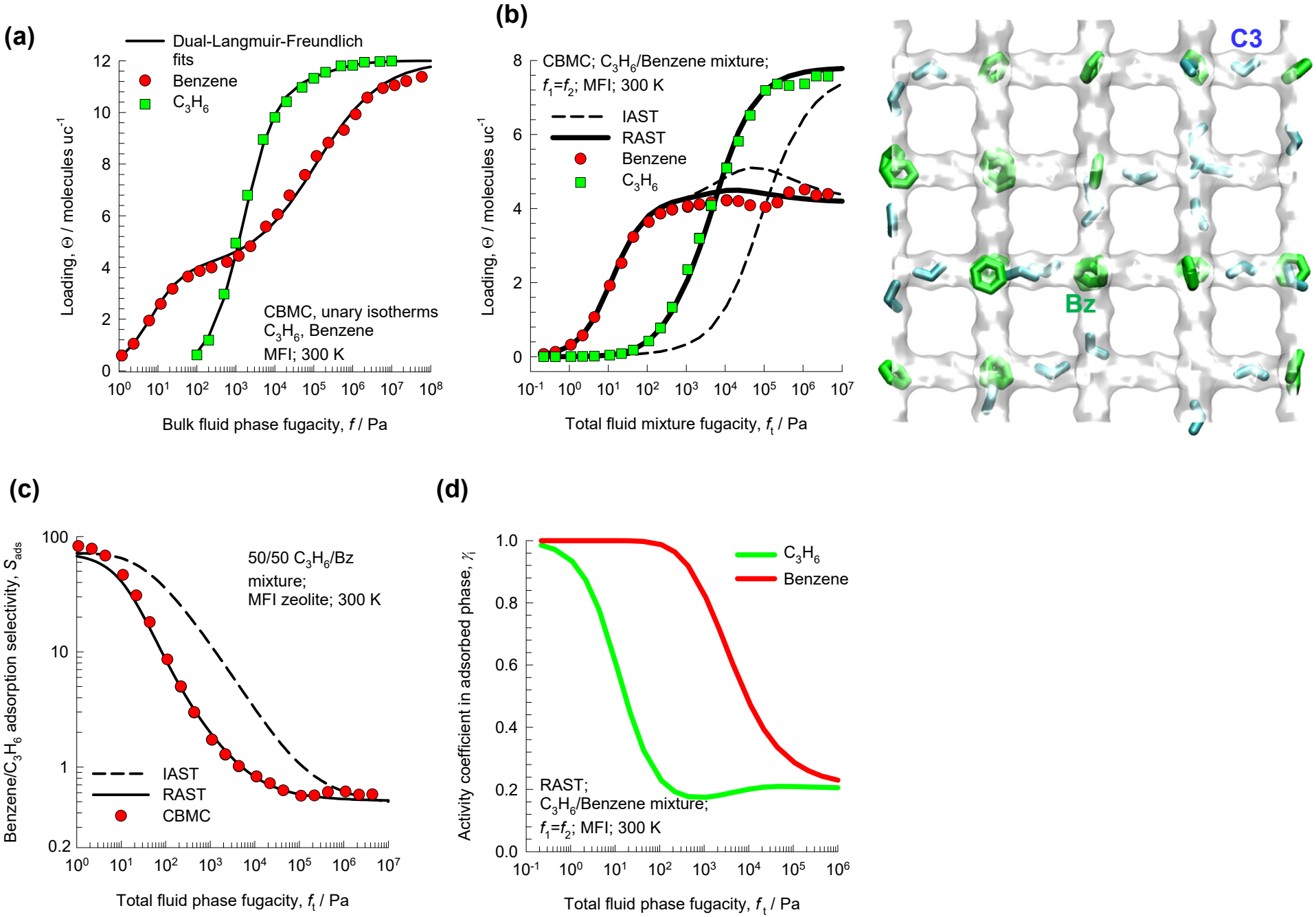

CH_4/iC4 mixture adsorption in MFI zeolite

Figure S136

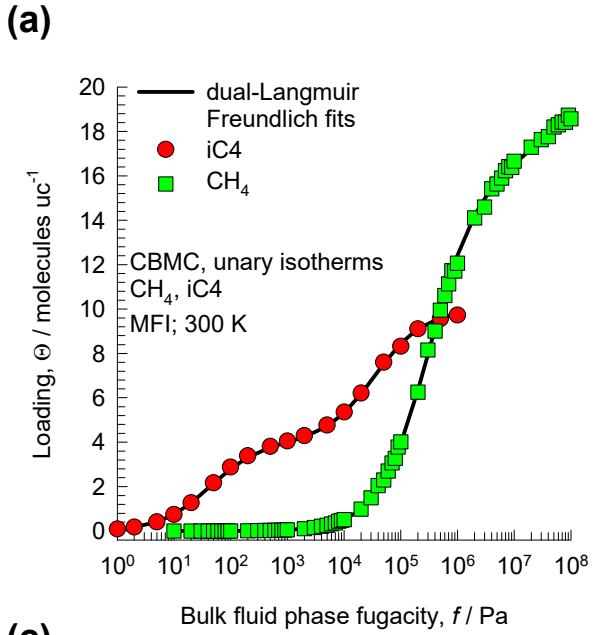

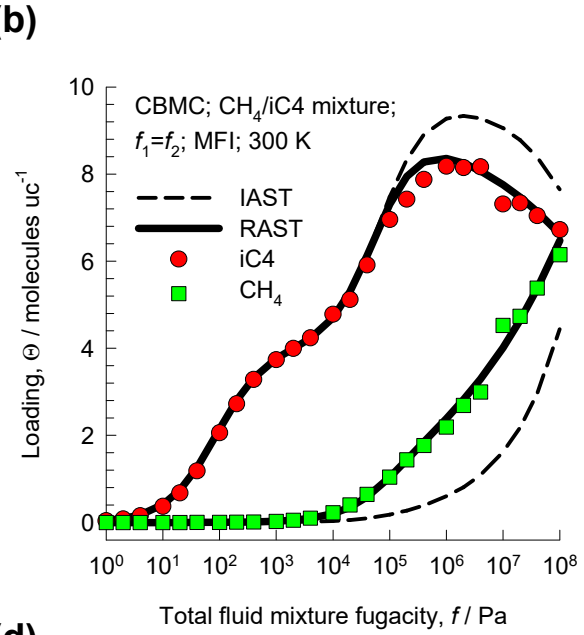

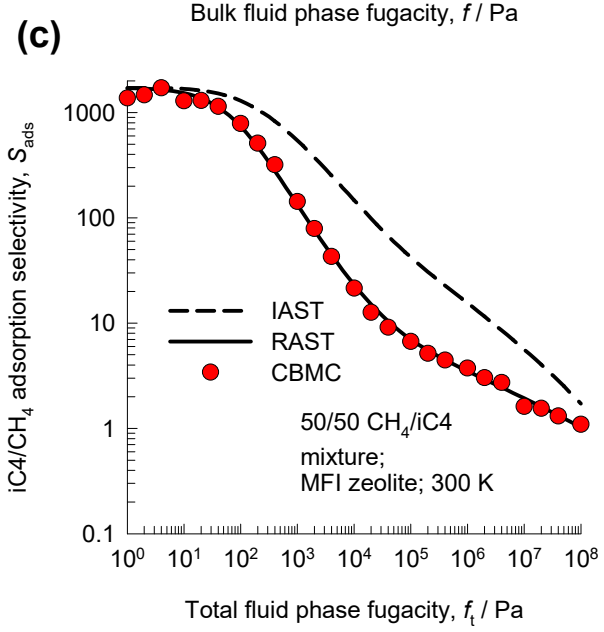

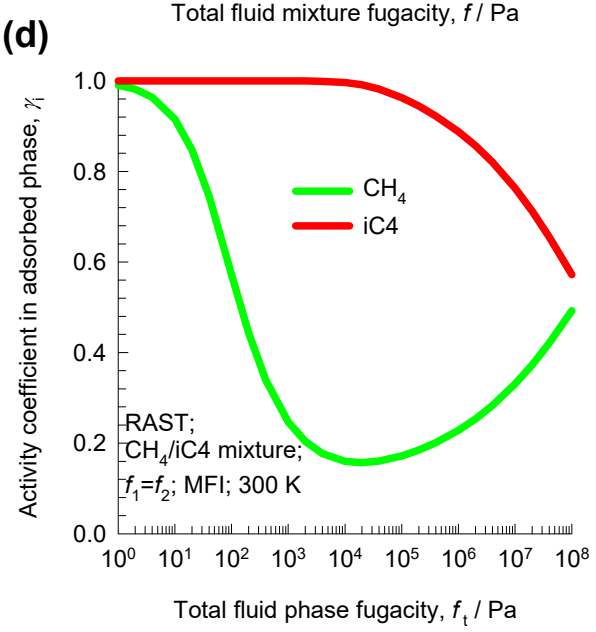

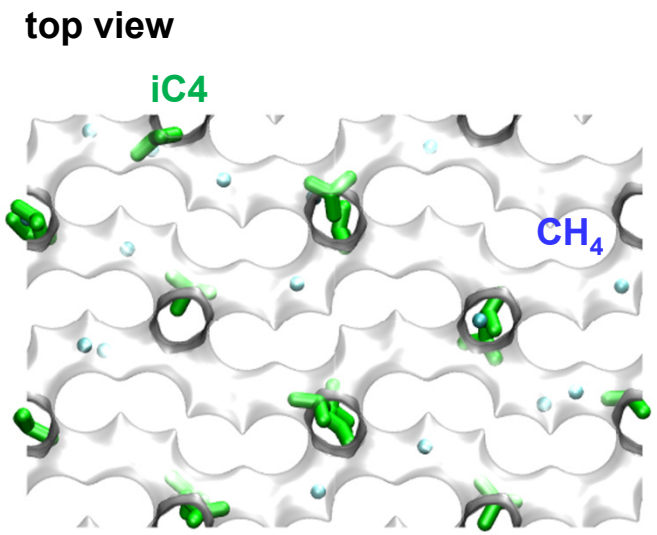

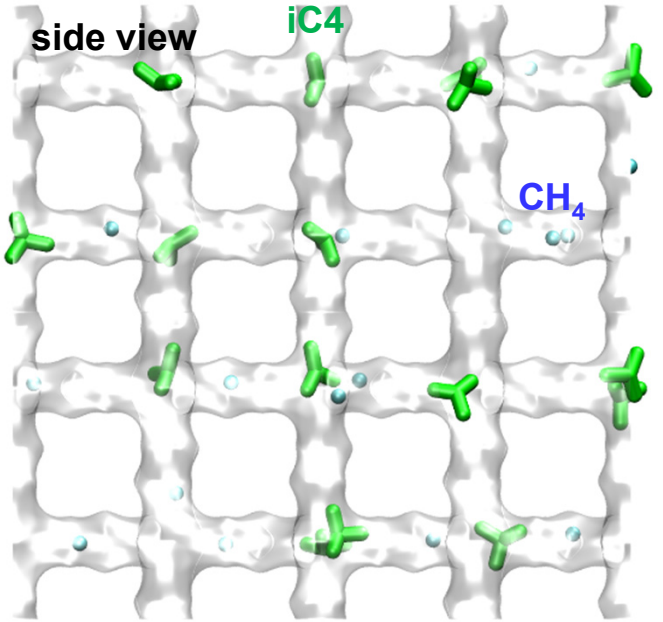

C_2H_6/iC4 mixture adsorption in MFI zeolite

Figure S137

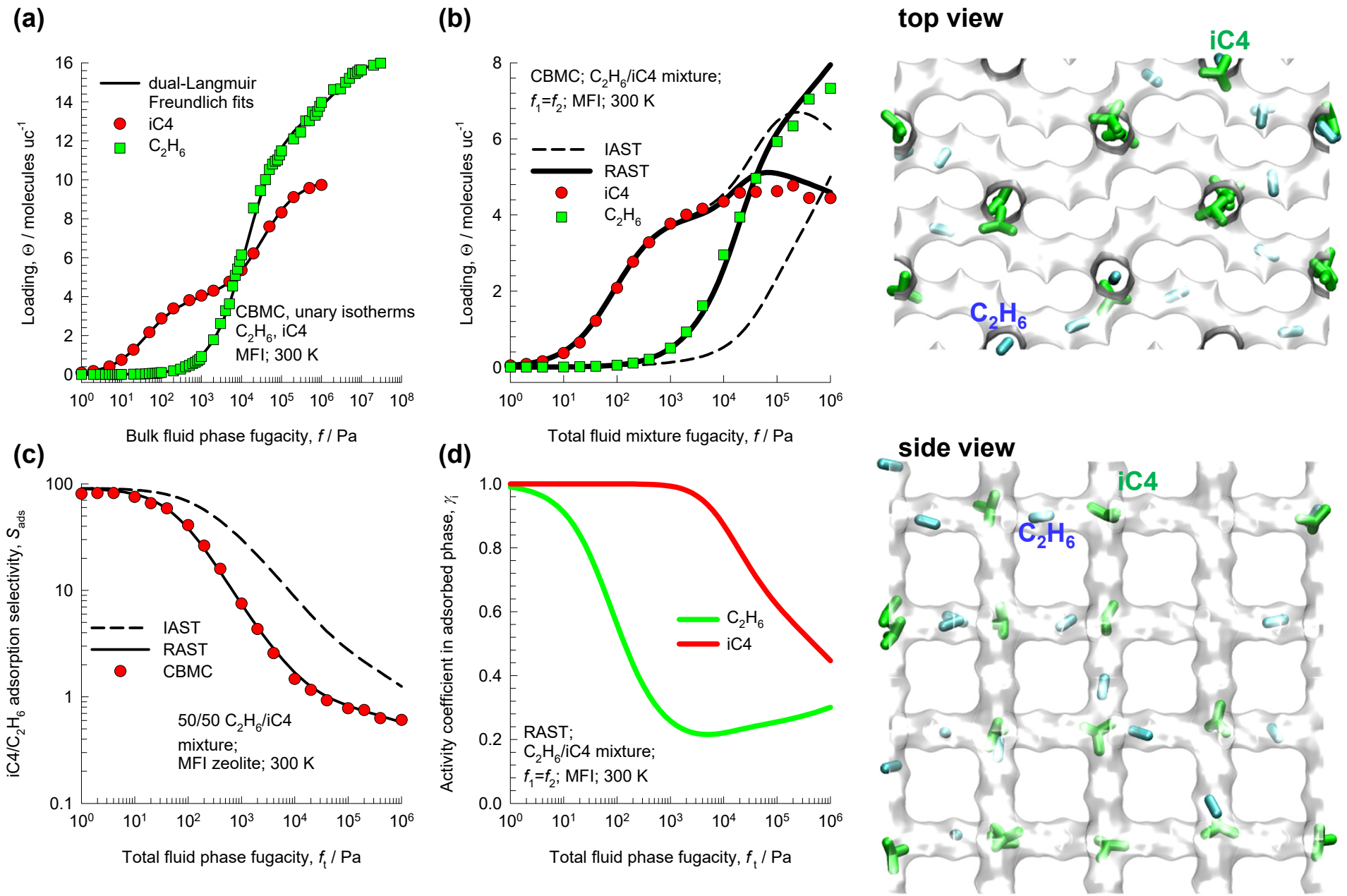

C_3H_8/iC4 mixture adsorption in MFI zeolite

Figure S138

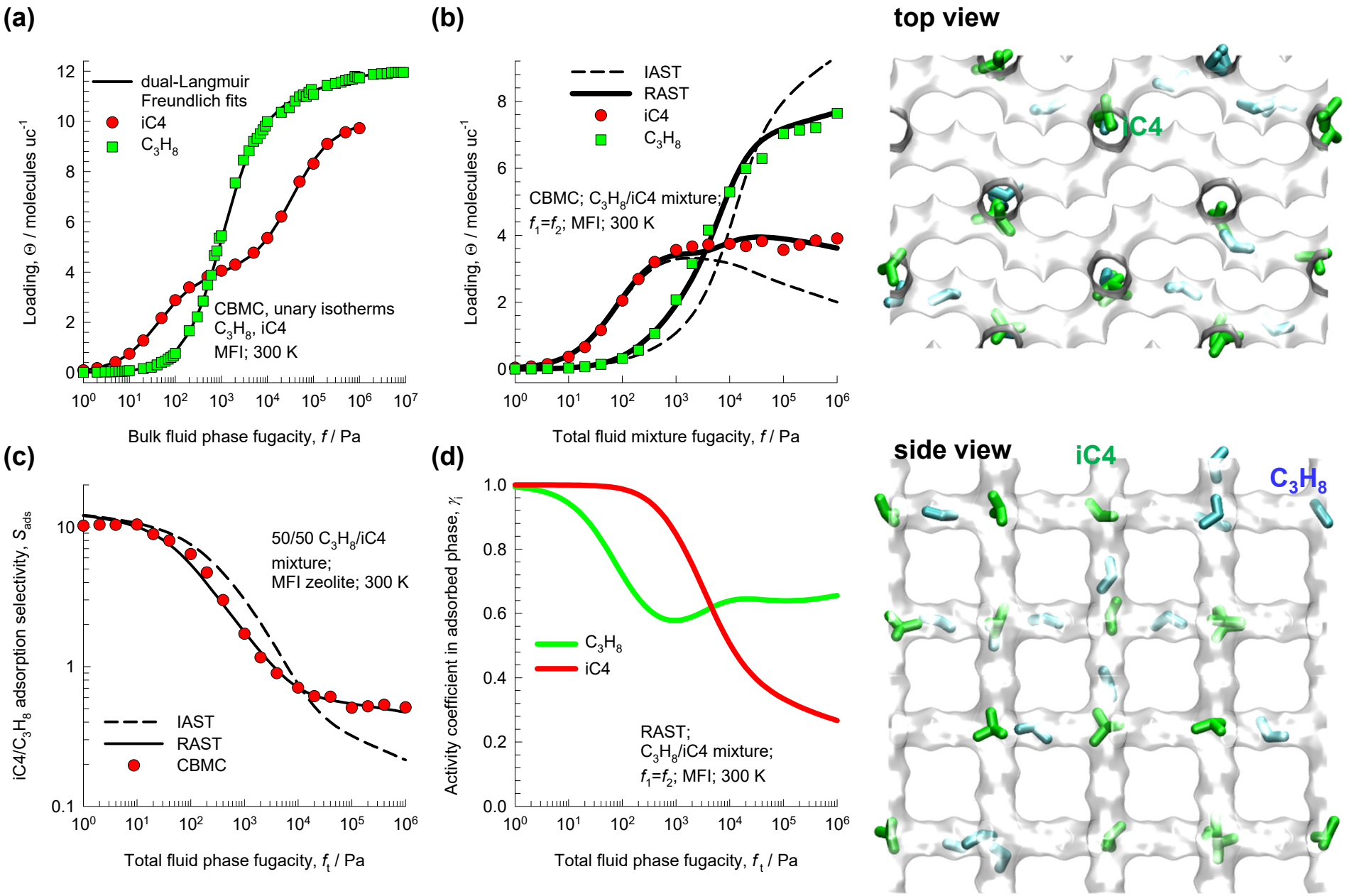

nC4/iC4 mixture adsorption in MFI zeolite

Figure S139

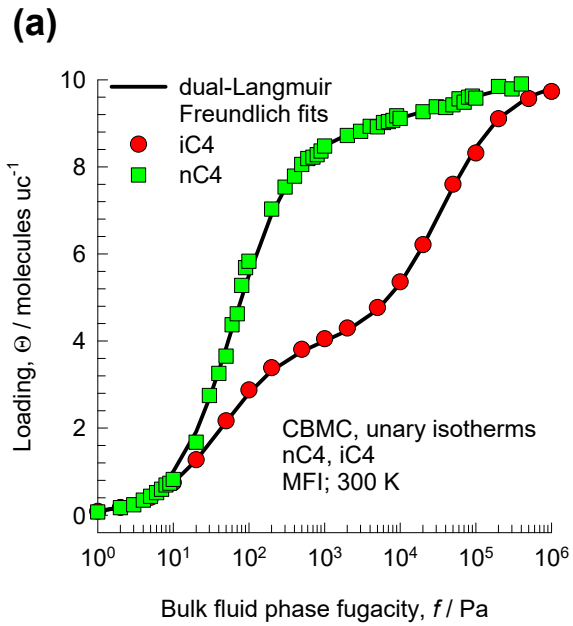

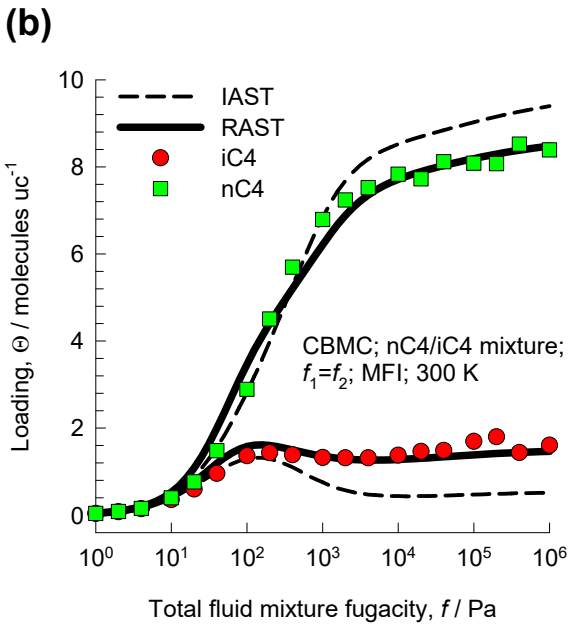

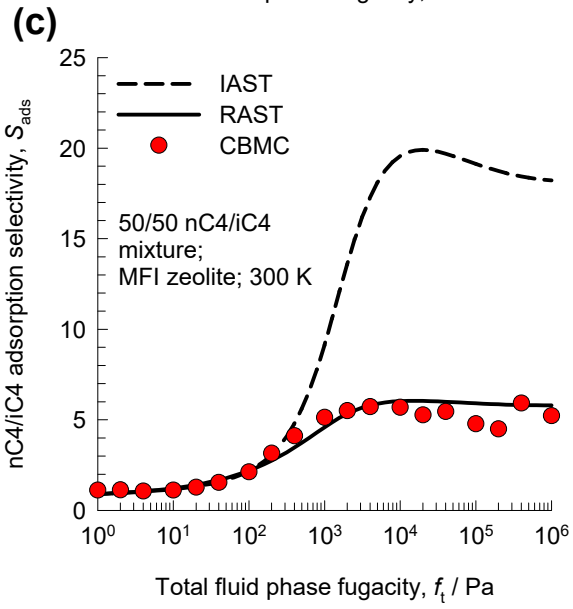

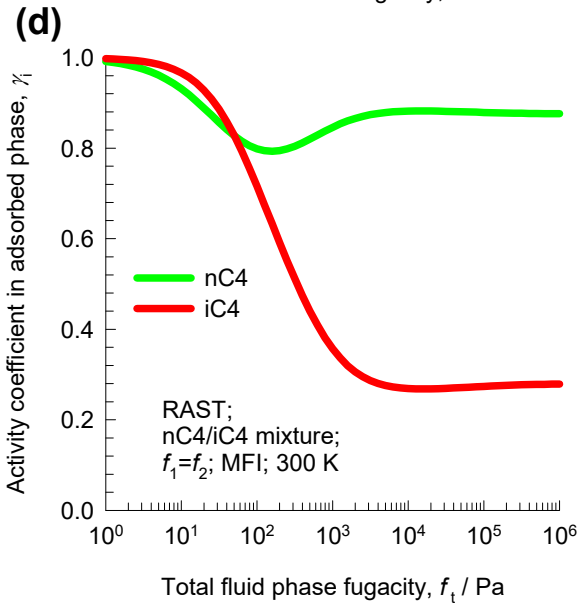

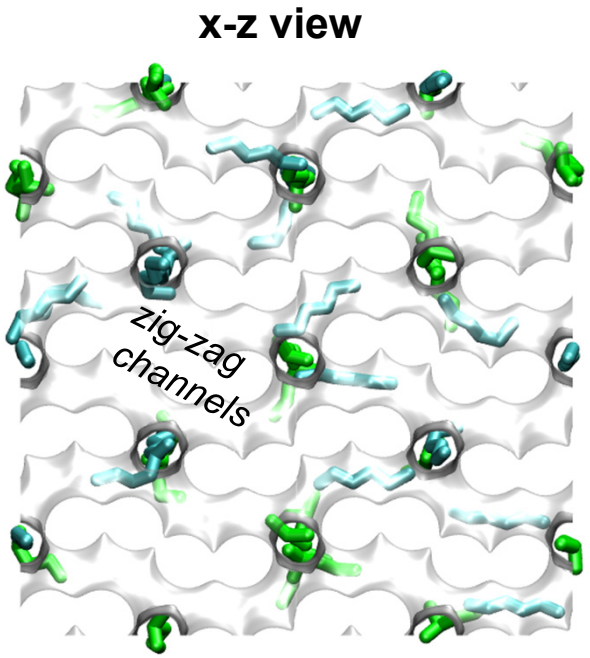

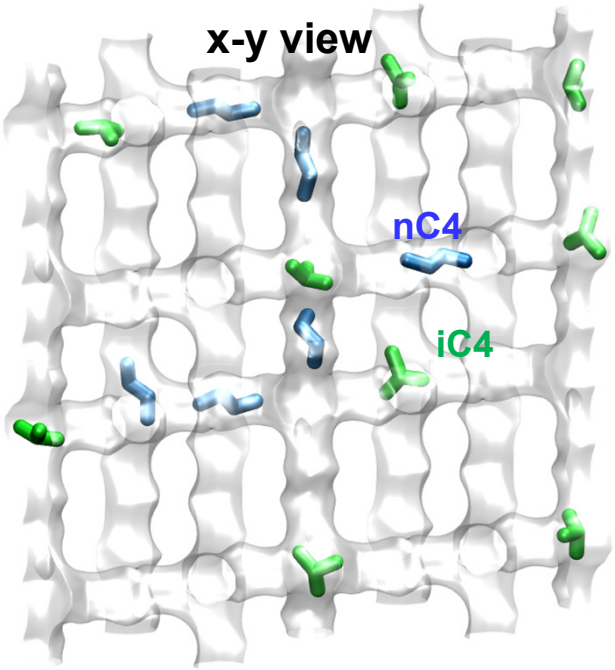

nC6/2MP mixture adsorption in MFI zeolite

Figure S140

(a)

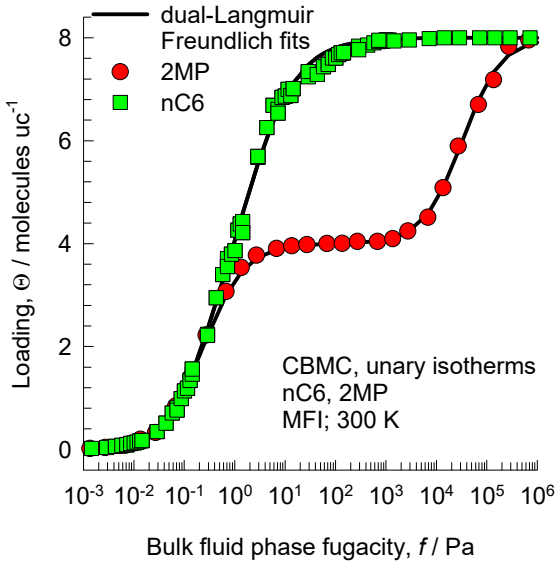

(b)

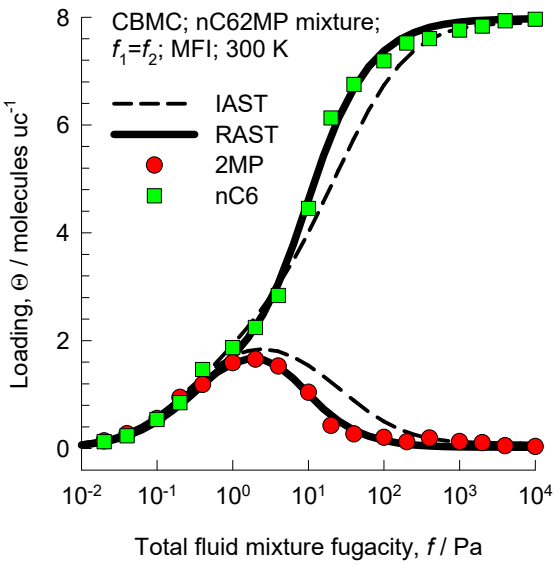

x-z view

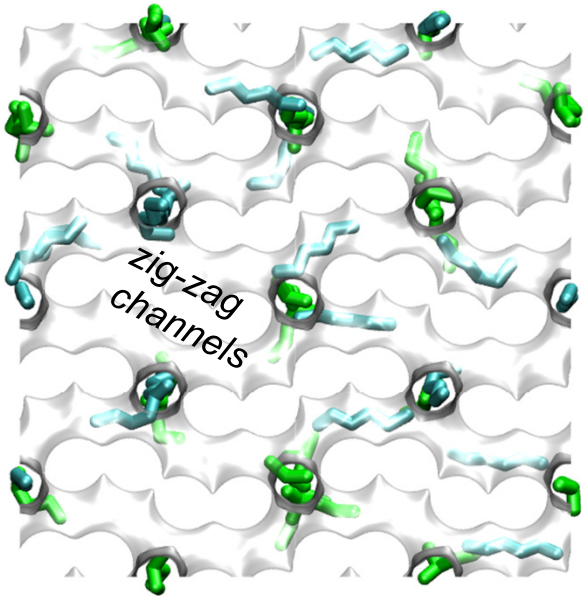

x-y- view

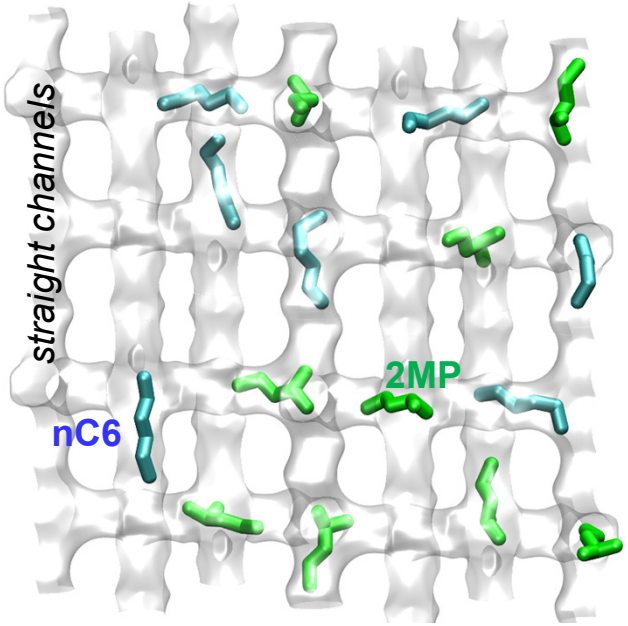

Figure S141

Transient uptake of nC4/iC4 within MFI crystal

(a)

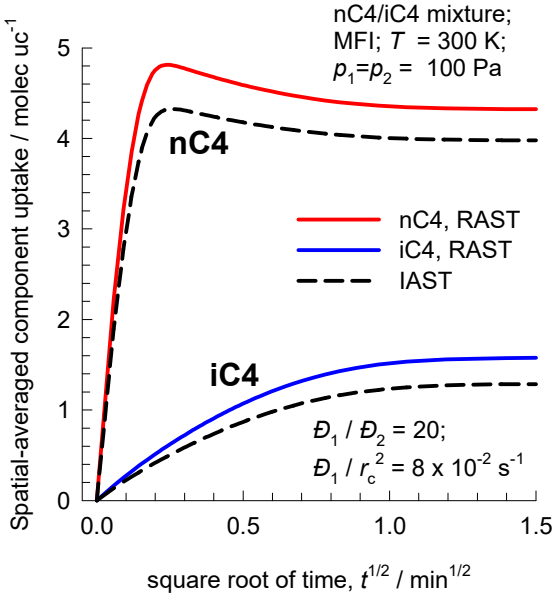

(b)

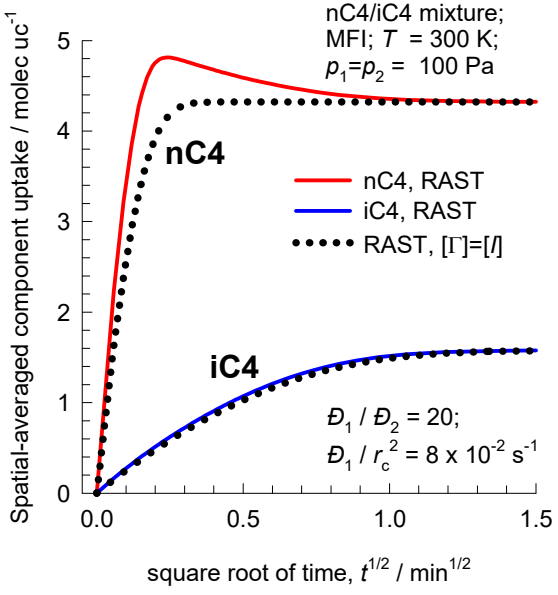

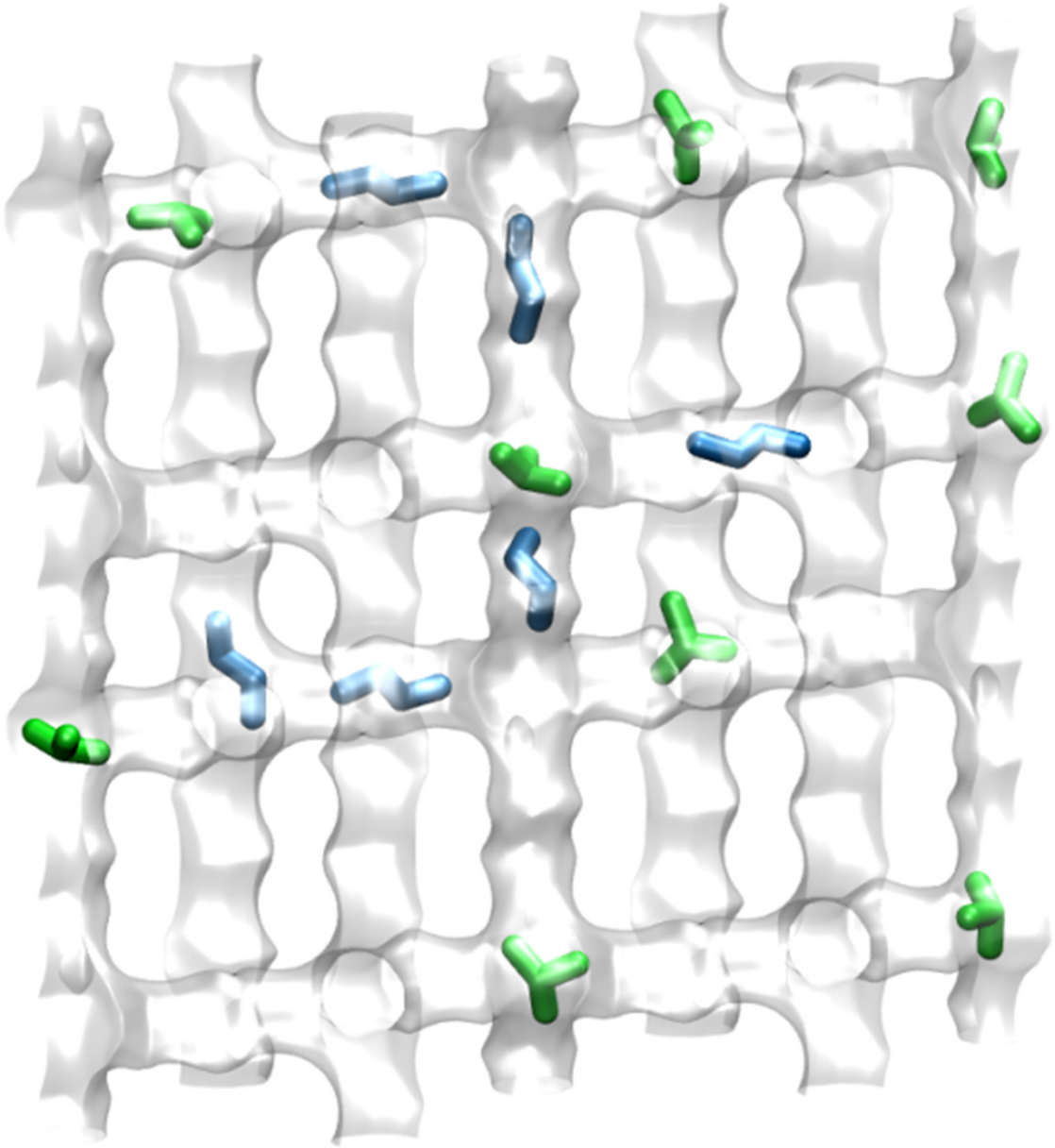

Figure S142

Transient uptake of nC6/2MP within MFI crystal

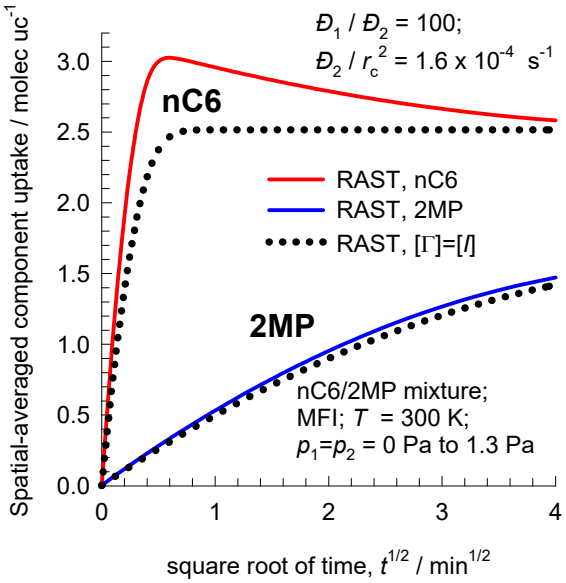

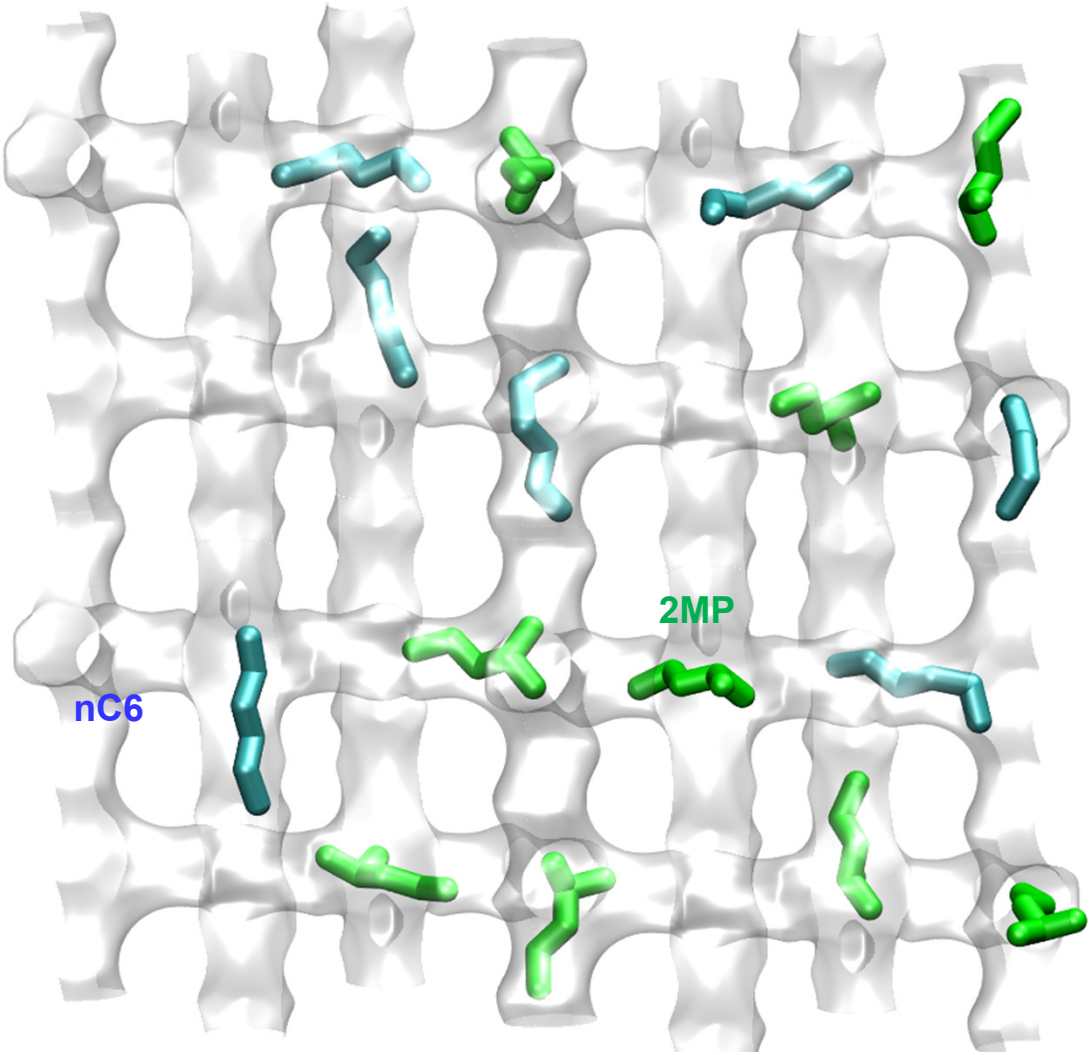

Figure S143

Separation potential for nC4/iC4/MFI

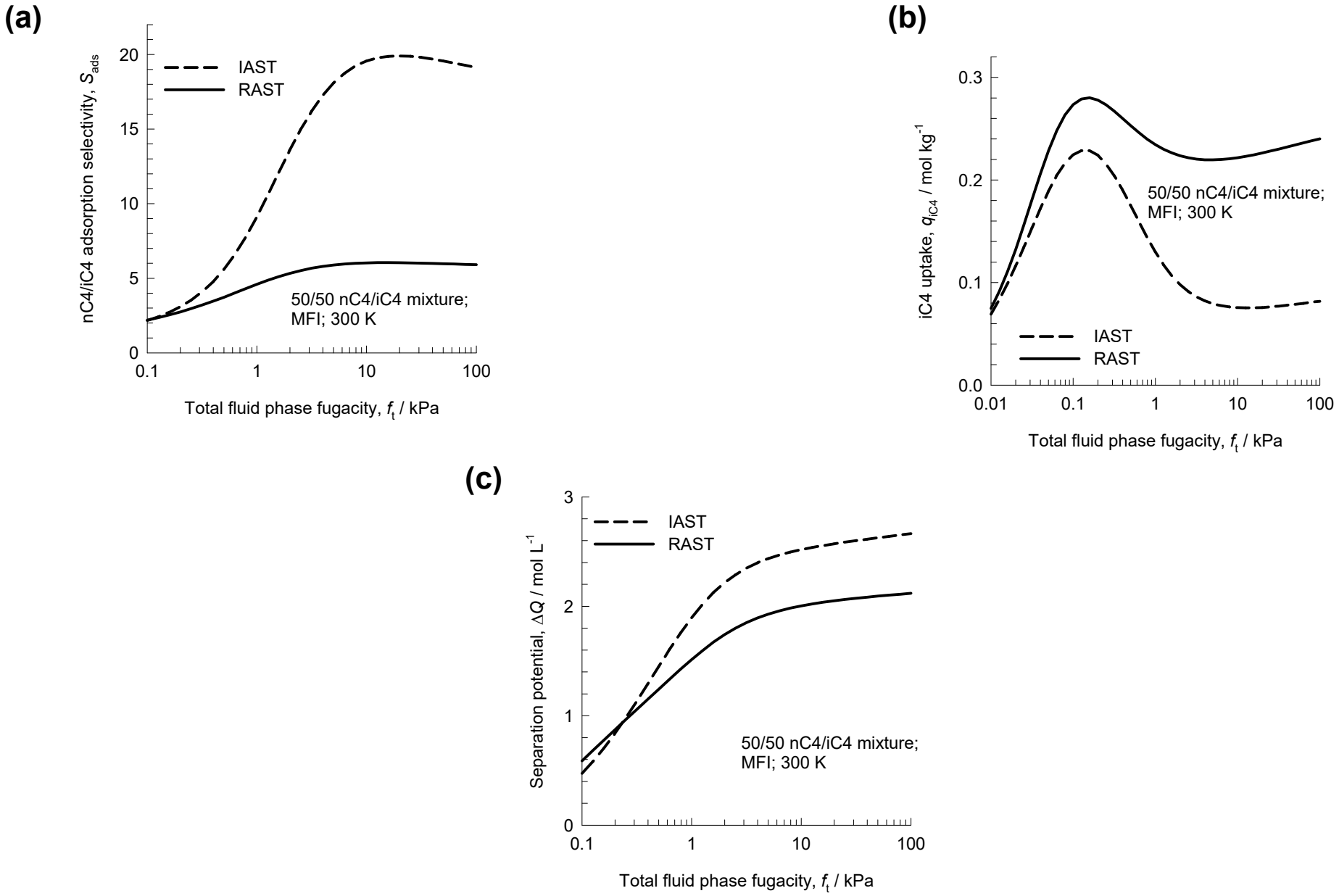

Figure S144

Transient breakthroughs nC4/iC4/MFI: RAST vs IAST

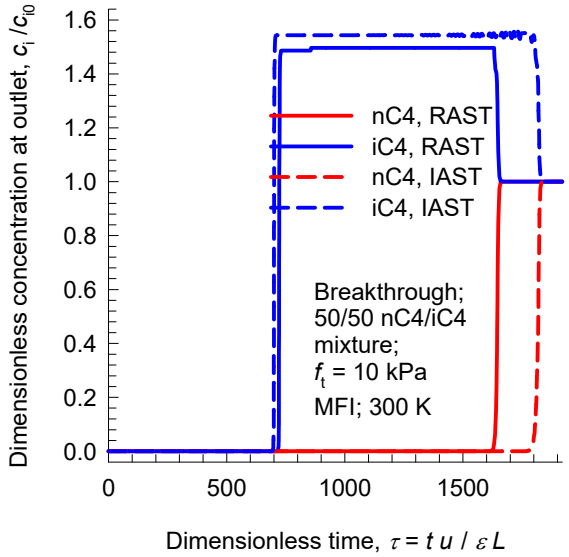

Molecular clustering of CO_2 below critical temperature

Figure S145

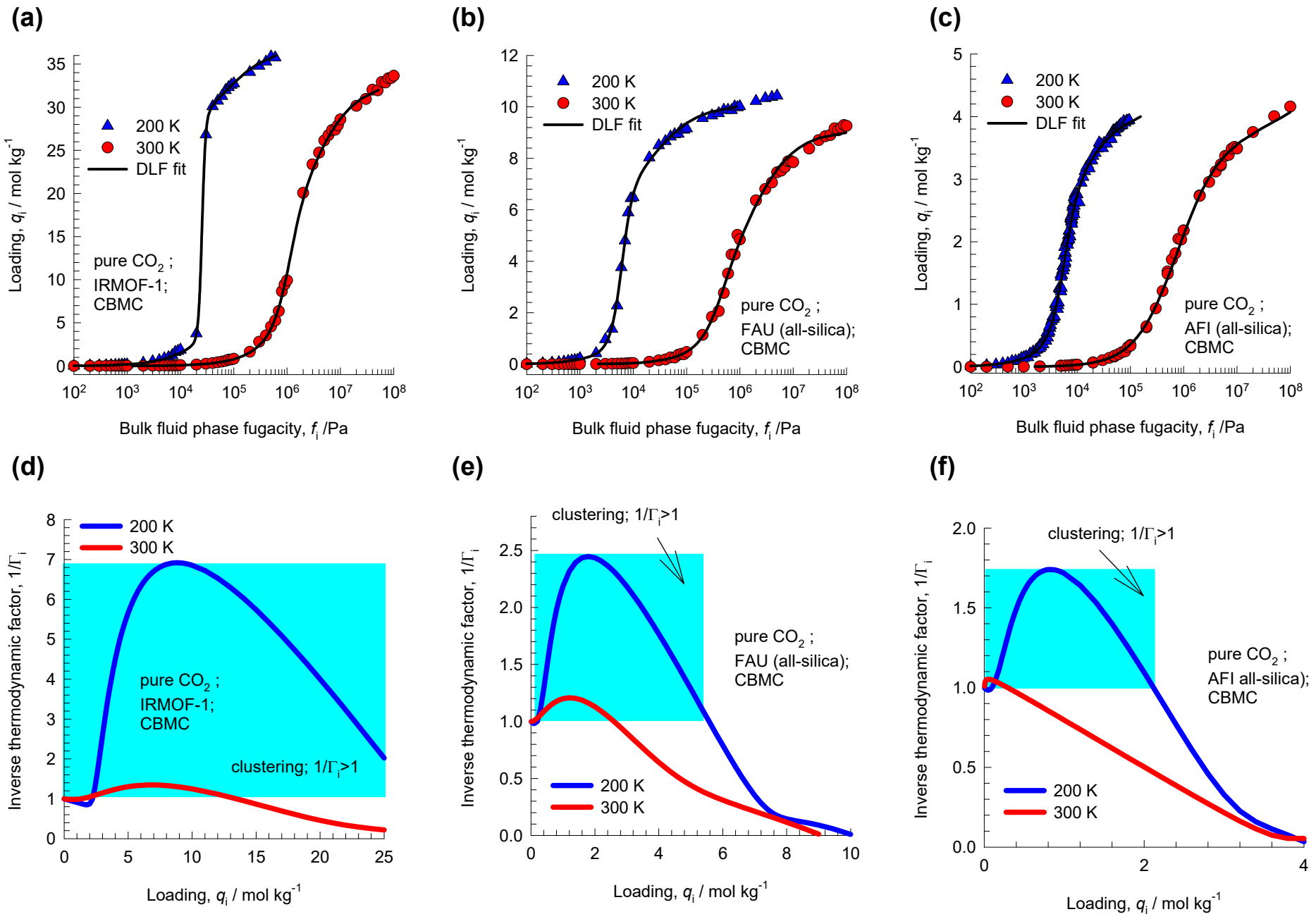

IAST estimates are excellent for CO_2/CH_4 mixture adsorption at 300 K

Figure S146

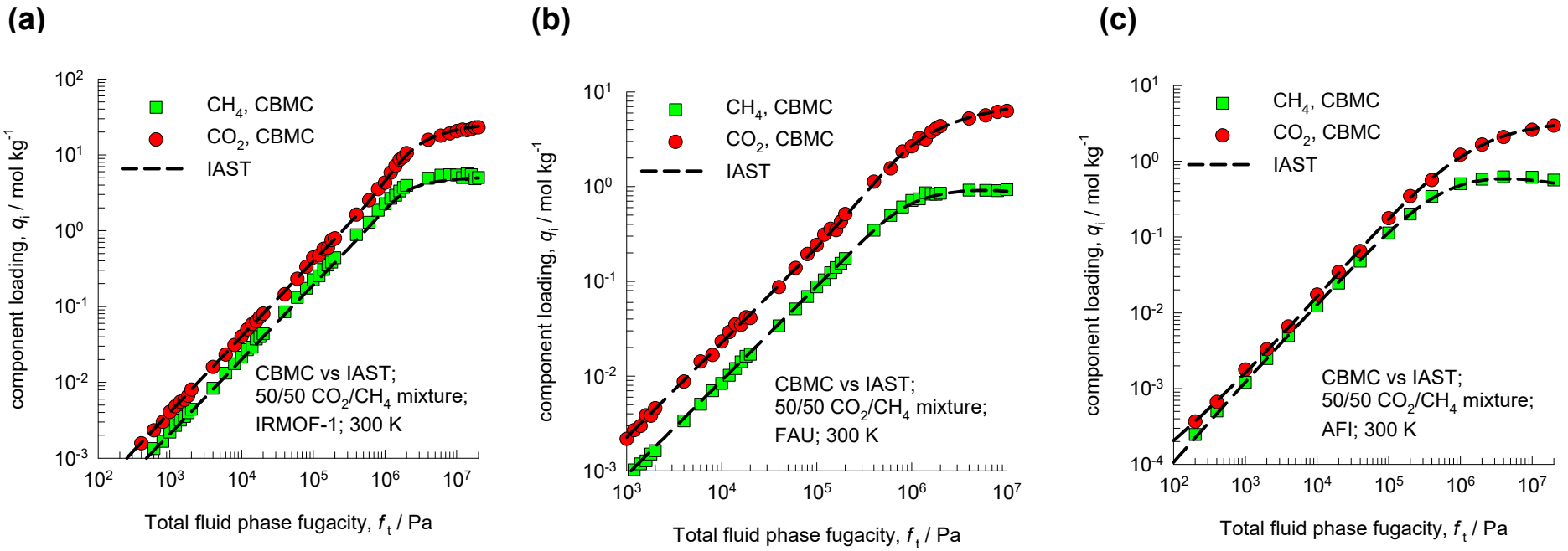

IAST estimates are poor for CO_2/CH_4/IRMOF-1/200 K

Figure S147